Transactions of the ASME®

Technical Editor, **T. H. OKIISHI (1998)**
Associate Technical Editors
Aeromechanical Interaction
R. E. KIELB (1999)
Gas Turbine (Review Chair)
A. KIDD (1997)
Heat Transfer
M. G. DUNN (1999)
Nuclear Engineering
H. H. CHUNG (1996)
Power
D. LOU (1998)
Turbomachinery
R. A. DELANEY (1998)

BOARD ON COMMUNICATIONS
Chairman and Vice-President
R. MATES

OFFICERS OF THE ASME
President, **R. J. GOLDSTEIN**
Executive Director, **D. L. BELDEN**
Treasurer, **J. A. MASON**

PUBLISHING STAFF
Managing Director, Engineering
CHARLES W. BEARDSLEY
Director, Technical Publishing
PHILIP DI VIETRO
Managing Editor, Technical Publishing
CYNTHIA B. CLARK
Managing Editor, Transactions
CORNELIA MONAHAN
Production Coordinator
VALERIE WINTERS
Production Assistant
MARISOL ANDINO

Transactions of the ASME, Journal of Turbomachinery (ISSN 0889-504X) is published quarterly (Jan., Apr., July, Oct.) for $185.00 per year by The American Society of Mechanical Engineers, 345 East 47th Street, New York, NY 10017. Periodicals postage paid at New York, NY and additional mailing offices. POSTMASTER: Send address changes to Transactions of the ASME, Journal of Turbomachinery, c/o THE AMERICAN SOCIETY OF MECHANICAL ENGINEERS, 22 Law Drive, Box 2300. Fairfield, NJ 07007-2300.
CHANGES OF ADDRESS must be received at Society headquarters seven weeks before they are to be effective. Please send old label and new address.
PRICES: To members, $40.00, annually; to nonmembers, $185.00.
Add $24.00 for postage to countries outside the United States and Canada.
STATEMENT from By-Laws. The Society shall not be responsible for statements or opinions advanced in papers or . . . printed in its publications (B7.1, Par. 3).

INDEXED by Applied Mechanics Reviews and Engineering Information, Inc.
Canadian Goods & Services Tax Registration #126148048

Journal of Turbomachinery

Published Quarterly by The American Society of Mechanical Engineers

VOLUME 119 • NUMBER 1 • JANUARY 1997

TECHNICAL PAPERS

TECHNICAL BRIEF

ANNOUNCEMENTS

Flow Visualization in a Linear Turbine Cascade of High Performance Turbine Blades

H. P. Wang

S. J. Olson

R. J. Goldstein

E. R. G. Eckert

Department of Mechanical Engineering,
University of Minnesota,
Minneapolis, MN 55455

Multiple smoke wires are used to investigate the secondary flow near the endwall of a plane cascade with blade shapes used in high-performance turbine stages. The wires are positioned parallel to the endwall and ahead of the cascade, within and outside the endwall boundary layer. The traces of the smoke generated by the wires are visualized with a laser light sheet illuminating various cross sections around the cascade. During the experiment, a periodically fluctuating horseshoe vortex system of varying number of vortices is observed near the leading edge of the cascade. A series of photographs and video tapes was taken in the cascade to trace these vortices. The development and evolution of the horseshoe vortex and the passage vortex are clearly resolved in the photographs. The interation between the suction side leg of the horseshoe vortex and the passage vortex is also observed in the experiment. A vortex induced by the passage vortex, starting about one-fourth of the curvilinear distance along the blade on the suction surface, is also found. This vortex stays close to the suction surface and above the passage vortex in the laminar flow region on the blade. From this flow visualization, a model describing the secondary flows in a cascade is proposed and compared with previous published models. Some naphthalene mass transfer results from a blade near an endwall are cited and compared with the current model. The flows inferred from the two techniques are in good agreement.

Introduction

The secondary flow in a turbine cascade is of interest to both designers and researchers. Current design methods for a turbine blade passage are usually based on two-dimensional flow analysis. However, close to the endwall, flow separation, a horseshoe vortex, a passage vortex, and some small but very intense corner vortices at the junction of the endwall and blade may affect the aerodynamic performance of a turbine and increase the heat transfer from the hot fluid to the blade and endwall surfaces. A comprehensive review of the secondary flow structures in turbine cascades has been presented by Sieverding (1985). Detailed experimental information about secondary flow visualization and the secondary flow patterns can be found in the studies by Jabbari et al. (1992), Langston (1990), Yamamoto (1987a, 1987b), Sonoda (1985), Langston et al. (1977), Marchal and Sieverding (1977), and Chung and Simon (1990), to name just a few.

Several secondary flow models have been published to assist in visualizing the flow patterns and to aid in understanding this complicated flow. Three representative models of the flow pattern, found in the literature, are shown in Fig. 1. Figure 1(*a*) (Langston, 1980) shows a general picture of the evolution and development of two legs of a horseshoe vortex and a passage vortex. The second flow pattern, given by Sharma and Butler (1987) and shown in Fig. 1(*b*), demonstrates that the suction leg wraps itself around the passage vortex instead of adhering to the suction side. The third model, shown in Fig. 1(*c*), is presented by Goldstein and Spores (1988). Based on mass transfer results, they proposed that the suction leg of the horseshoe vortex stays above the passage vortex and travels with it. The location of the suction leg of the horseshoe vortex is the major difference among the three models. It is difficult to follow the suction leg as it moves down the passage. Most pressure or velocity maps in the literature do not give a clear picture of how this leg develops. Its small size combined with a strong stretching in the streamwise direction makes it difficult to detect. Moore and Smith (1984) detected ethylene around the passage vortex core at the exit of a cascade when ethylene was injected at the leading edge suction side. The suction leg appears almost completely mixed with the passage vortex, at least in the exit plane. A similar phenomenon was also observed by Sieverding and Van den Bosche (1983) with their colored-smoke visualization. They found that the suction side leg wraps around the passage vortex. The flow pattern suggested by Jilek (1986) is similar to that in Fig. 1(*c*).

Jabbari et al. (1992) presented a set of oil-lampblack flow visualization photographs on an endwall and blade suction surfaces, which were compared with local mass transfer results. They observed a suction corner vortex in the middle of the passage climbing up and adhering to the suction surface until far downstream. This vortex was also observed by Sonoda (1985) in his kerosene vapor flow visualization.

The present study uses a multiple smoke-wire flow-visualization technique to observe and trace the vortices of interest and compares the flow pattern with results of local mass transfer measurements. A series of photographs and videos have been taken for archival use. Based on the flow visualization results, a new model is presented to better understand the secondary flow.

Experimental Apparatus

Wind Tunnel and Linear Cascade. An open circuit, blower-type wind tunnel is used in these investigations. A 22.4 kW blower is used to drive the flow through a honeycomb flow straightener and three graduated, high-porosity screens before contracting the flow in a 6.25:1 area-ratio contraction. The flow leaves the contraction and enters the test facility, which has a 45.7 cm by 45.7 cm cross section.

A facility for flow visualization and experimental mass transfer tests on gas turbine airfoils and passages has recently been

Contributed by the International Gas Turbine Institute and presented at the 40th International Gas Turbine and Aeroengine Congress and Exhibition, Houston, Texas, June 5–8, 1995. Manuscript received by the International Gas Turbine Institute February 4, 1995. Paper No. 95-GT-7. Associate Technical Editor: C. J. Russo.

built. The test facility following the contraction exit, is shown in a scaled drawing from above in Fig. 2. It is a four-blade, linear cascade, with a high-performance blade profile. Figure 2 also shows two interchangeable sections upstream of the cascade: a straight duct and a grid duct section. The grid duct section has two slots to accommodate turbulence generating grids, but none were used in these investigations. The flow is tripped at the contraction exit, however, to disturb the boundary layer approaching the cascade.

The blade nomenclature is shown in Fig. 3 and the cascade geometry data are given in Table 1. A modern, high-performance blade profile is used in these investigations. The blade profile is specified in Table 2. For these tests, it was necessary to use low-speed flow in order to photograph the smoke traces clearly. A Reynolds number based on the exit velocity and blade chord length of 2.7×10^4 gave good flow visualization results. The undisturbed flow entering the facility from the contraction is highly uniform with a free-stream turbulence intensity less than 0.2 percent, measured at the contraction exit.

Two tail boards trailing the outermost blades, and two flexible bleeds outside the outermost blades, are used to adjust the flow within the three turbine passages. The flow is balanced by comparing pressure measurements, made while using a special pressure measurement blade, on the surfaces of Blades 2 and 3 with each other and with a potential flow calculation. The pressure distribution along the blades is quite sensitive to these adjustments, but good agreement between the blades and the analytical prediction could be achieved. An example of the pressure distribution on the two inner blades is shown in Fig. 4. In addition, measurements of the flow velocity at the midspan of the tunnel show that the flow, measured at the measurement slot shown in Fig. 2 nearest the cascade, varies by less than 2 percent in the cross-stream direction when the tunnel has been balanced using these adjustments.

Flow Visualization. The test section side walls are Plexiglas, which allows unobstructed observation of the flow within the cascade. An extensive smoke-wire flow visualization study has been conducted and video taped with the aid of a laser light sheet. Eight 0.102 mm 304 stainless steel wires were positioned parallel to the endwall ahead of the cascade. The distances from the eight wires to the endwall are 3.2, 6.4, 12.7, 19.1, 25.4, 31.8, 38.1, and 50.8 mm respectively.

A thin layer of light-duty machine oil was applied to the wires, which were electrically heated to produce smoke. A glass rod was used to expand the beam from a He–Ne laser into a sheet to illuminate cross-sectional slices of the flow, made visible by the smoke generation. The smoke traces produced are distinct and can be identified individually as the flow develops in the blade passage.

Photographs of the visualized flow patterns were made using a Nikon N8008s camera with a 1:2.8 105 mm AF Micro Nikkor Lens using Kodak Tmax 3200P film pushed to 6400 speed and shot with an aperture of f2.8 and shutter speed of $\frac{1}{30}$ or $\frac{1}{60}$th of a second. Four sets of video tape have also been produced that follow the vortex flow pattern from different view angles.

Results and Discussion

Inlet Flow Description. Velocity measurements were made to characterize the flow approaching the cascade and to provide some insight into the flow patterns that were observed. Measurements were made using a TSI IFA-100 hot-wire anemometer with a 1218-T1.5 single-wire boundary-layer probe. The flow approaching the cascade was measured at a location 77 cm from the contraction exit, shown as point B in Fig. 2. The mean flow velocity was 0.8 m/s with a turbulence intensity less than 0.2 percent, which gives a Reynolds number based on the blade chord length and exit velocity of 2.7×10^4. The low velocity was necessary to obtain clear flow visualization photographs. At this condition, the displacement thickness was measured to be 4.9 mm and the boundary layer shape factor was found to be 2.48. Due to the low velocity required for flow visualization, the inlet boundary layer remains laminar despite the trip used at the contraction exit.

The flow visualization results to be presented were obtained at these conditions. Typical flow conditions entering the blade section of a real engine are characterized by high turbulence levels, large length scales, and exit Reynolds numbers on the order of 20 to 50 times higher than that used for these flow visualization studies. Additional tests were conducted with higher velocities to produce a turbulent boundary layer at the cascade inlet. The results show a flow pattern similar to that of a laminar inlet boundary layer condition; however, due to the higher velocities, the photographic results were rather poor. In addition, surface flow visualization results at typical engine Reynolds numbers have been conducted with variations in the free-stream turbulence level generated by grids. The flow patterns we infer from the visualizations look similar to one another, although the path and size of the passage vortex are affected by the turbulence level. Other testing is currently under way to examine the effect of turbulence length scale as well. From these additional tests, we conclude that the general flow pattern, described below, is similar to that which would be found at engine conditions.

Flow Visualization. Figures 5–7 contain photographs of the smoke wire patterns. The position of the laser light sheet is indicated by the dashed lines in the left row of the figures and the position of the camera is also indicated.

It was observed in the smoke visualization that the flow exhibits fluctuations in the inlet region of the channel with a frequency of approximately 2.5 Hz. The effect of this on the vortex development is shown in Fig. 5, where sequences of photographs taken at approximately 3.2 frames per second are shown. In this figure, three light sheet positions are shown, with a time sequence of four photographs following them. In Figs. 6 and 7, the positions of the light sheet and camera change in each photograph.

Nomenclature

b = axial chord length of blade
c = chord length of blade
C_{Ps} = static pressure coefficient = $(P_s - P_{s0})/(\rho U_{in}^2/2)$
l = blade span (length between endwalls)
p = pitch length of blades
P_s = local static pressure
P_{s0} = upstream reference static pressure (point A in Fig. 2)
Re_{ex} = exit Reynolds number = $\rho U_{ex} c/\mu$
S_s = curvilinear (streamwise) coordinate along suction side; $S_s = 0$ at stagnation line
t = time
t_0 = reference time for time series photographs
U_{in} = incoming velocity (measured at point B in Fig. 2)
U_{ex} = exit velocity (calculated from incoming velocity and cascade geometry)
V = vortex label, defined in Fig. 8
x = coordinate in axial chord direction, defined in Fig. 3
y = coordinate normal to the axial chord, defined in Fig. 3
z = spanwise coordinate of blade starting from endwall
β_1 = blade inlet angle = 35 deg
β_2 = blade outlet angle = −72.49 deg
μ = dynamic viscosity of air
ρ = density of air

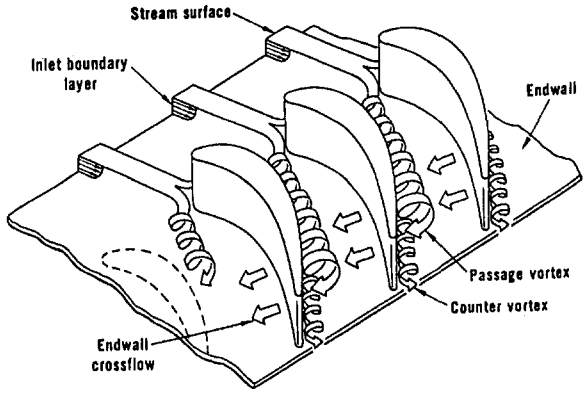

(a) Vortex pattern described by Langston (1980).

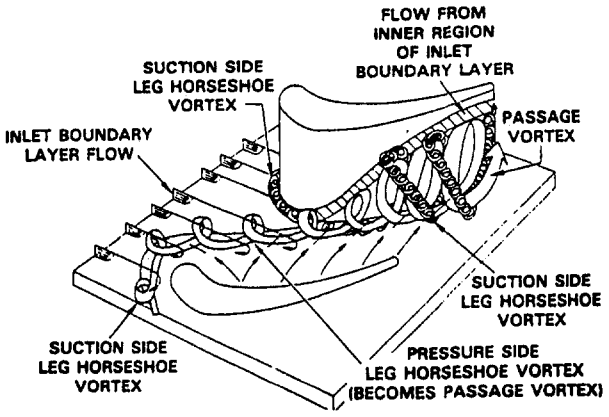

(b) Vortex pattern described by Sharma and Butler (1987).

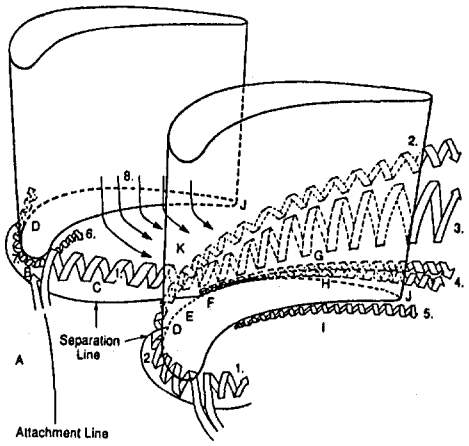

(c) Vortex pattern described by Goldstein and Spores (1988).

Fig. 1 Vortex patterns described in the literature

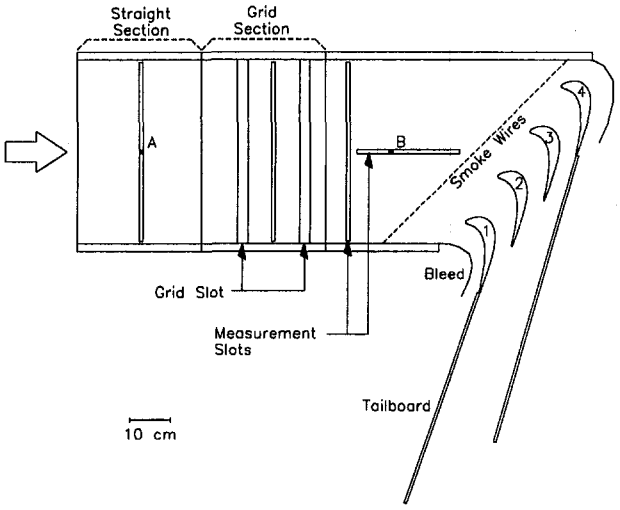

Fig. 2 Turbine cascade viewed from above

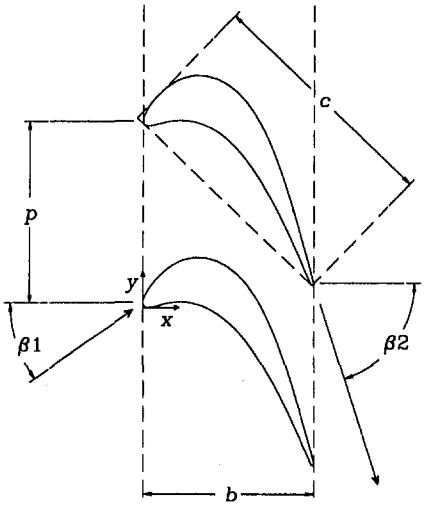

Fig. 3 Turbine blade arrangement

Table 1 Cascade geometry data

Number of blades	4
Chord length of blade - c	184.15 mm
Axial Chord to Chord ratio - b/c	0.704
Pitch to Chord ratio - p/c	0.750
Aspect ratio (Span/Chord) - l/c	2.483
Blade inlet angle - β_1	35°
Blade outlet angle - β_2	−72.49°
Incoming Velocity - U_{in}	0.80 m/s
Exit Velocity - U_{ex}	2.18 m/s
Reynolds Number - Re_{ex} (for all flow visualization)	2.7×10^4

A perspective view of the secondary flow pattern based on the smoke patterns in Figs. 5–7 and the previous observations of Goldstein and Spores (1988) and Jabbari et al. (1992) is shown in Fig. 8. It should be pointed out that the tightness of the spirals representing the vortices in the picture have been chosen for clarity of the presentation. In reality, the passage vortex, for example, was found to turn much less tightly (Sieverding and Van den Bosche, 1983; Sonoda, 1985; Chung and Simon, 1990). Our observation is that the passage vortex makes approximately one and one half rotations as it passes through the cascade. An interpretation of the results will now be presented.

Stagnation Point Flow. The development of a horseshoe vortex at the stagnation line of a cylinder near an endwall depends on the approaching boundary layer and on the boundary layer forming around the cylinder. In previous studies of flow around a cylinder, the cylinder radius was generally larger than the thickness of the approaching boundary layer. A relatively

Table 2 Turbine blade geometry

x/b	y/b	x/b	y/b	x/b	y/b
0.0000	0.0242	0.2365	0.2752	0.7735	-0.1793
0.0014	0.0377	0.2989	0.2886	0.8071	-0.2703
0.0063	0.0550	0.3656	0.2868	0.8383	-0.3621
0.0155	0.0759	0.4328	0.2684	0.8678	-0.4545
0.0296	0.1001	0.4967	0.2348	0.8959	-0.5473
0.0484	0.1269	0.5556	0.1878	0.9229	-0.6404
0.0722	0.1565	0.6083	0.1304	0.9491	-0.7338
0.1014	0.1878	0.6552	0.0646	0.9747	-0.8273
0.1376	0.2200	0.6942	-0.0025	0.9997	-0.9210
0.1822	0.2506	0.7364	-0.0897	1.0000	-0.9235
0.0000	0.0242	0.1147	0.0124	0.7238	-0.3864
0.0009	0.0146	0.1434	0.0190	0.7603	-0.4519
0.0031	0.0079	0.1760	0.0244	0.7950	-0.5183
0.0052	0.0038	0.2133	0.0273	0.8282	-0.5854
0.0070	0.0013	0.2551	0.0256	0.8603	-0.6531
0.0085	0.0000	0.3006	0.0180	0.8914	-0.7212
0.0098	-0.0007	0.3478	0.0035	0.9218	-0.7897
0.0120	-0.0018	0.3950	-0.0175	0.9515	-0.8585
0.0153	-0.0031	0.4412	-0.0452	0.9807	-0.9274
0.0205	-0.0046	0.4857	-0.0789	0.9828	-0.9306
0.0279	-0.0055	0.5286	-0.1184	0.9859	-0.9327
0.0384	-0.0054	0.5695	-0.1626	0.9895	-0.9336
0.0522	-0.0035	0.6088	-0.2112	0.9932	-0.9330
0.0694	0.0003	0.6441	-0.2596	0.9968	-0.9309
0.0903	0.0058	0.6853	-0.3222	0.9992	-0.9276
				1.0000	-0.9235

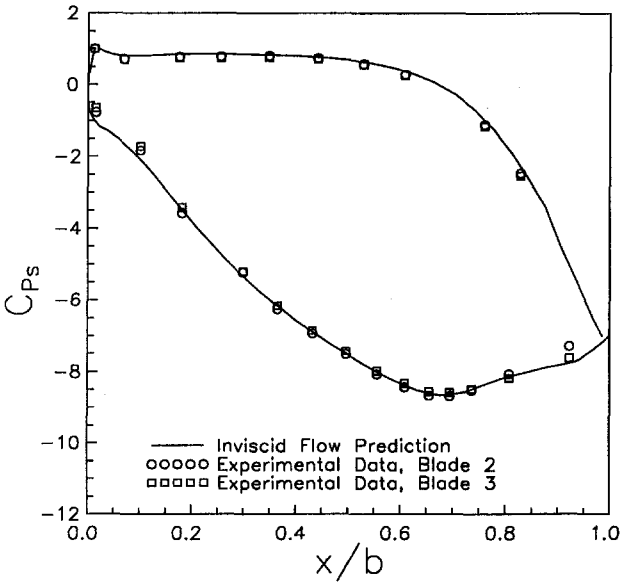

Fig. 4 Pressure coefficient along the surfaces of blades 2 and 3 for $Re_{ex} = 5.4 \times 10^5$

large vortex developed near the corner with smaller vortices close by.

The present high-performance blade has a small radius of curvature, approximately equal in size to the approaching boundary layer thickness. Figure 5 shows that the corner flow near the stagnation line develops two vortices of about equal

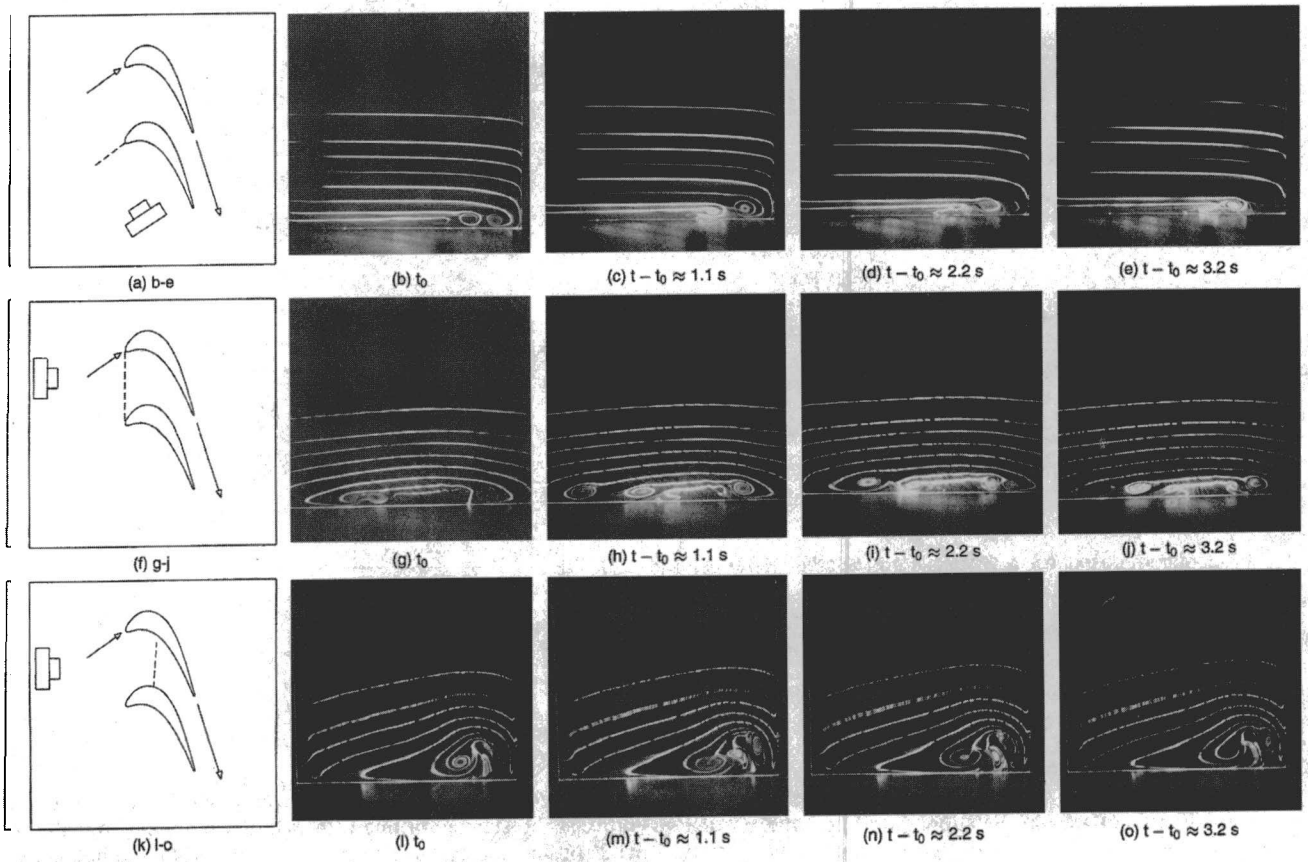

Fig. 5 Leading edge and entrance flow visualization (time series photographs)

sizes at different distances from the blade surface. The fluctuations of flow near the vortices described before causes the arrangement of the vortices to change periodically, as shown in the sequence of photographs in Figs. 5(b–e). The photographs are taken at approximately 3.2 frames per second. The frequency of the vortex movement is about 2.5 Hz. Although the photographs do not follow the motion in one period, they do demonstrate the periodicity of the multivortex structure with varying numbers formed ahead of the blade. Section A–A in Fig. 8 shows two forms that the pressure side leg of the passage vortex takes as it changes periodically.

When the vortices enter the passage, the multi-vortex structure is gradually changed to a single-vortex pattern. It is essentially diminished at the point where the pressure side leg of the horseshoe vortex meets its counterpart from the suction side. The vortices continue to oscillate as they move downstream.

Figures 6 and 7 show slices of the flow in the passage at many locations. It is clear that the major part of the secondary flow is the passage vortex. It is responsible for much of the pressure loss across the cascade and high heat transfer to the blade and endwall. The others involved are the horseshoe vortex pair, and a new counter-rotating wall vortex induced by the passage vortex.

Pressure Side Leg of the Horseshoe Vortex, V_{ph}. It is seen in Figs. 6(f)–(h) and (j)–(l), and depicted in Fig. 8, that due to a strong pressure gradient, the pressure leg of the horseshoe vortex immediately moves toward the suction side after it enters the passage. It entrains the main flow and the inlet boundary layer. This multi-vortex leg is gradually squeezed into a single vortex (Figs. 6(o)–(p)) as it approaches the point where its counterpart, the suction leg from the adjacent blade, joins. This location occurs at approximately 1/4 of the surface distance from the blade leading edge. Goldstein et al. (1995) measured mass transfer on the suction surface of a turbine blade. They found that the maximum mass transfer rate occurs around this location for the case when only the blade is an active mass transfer surface. A contour plot of their naphthalene mass transfer results, Fig. 9, on part of the suction surface is shown here for comparison. Even though the blade geometry used in that study is different from the current one, the basic structure of the secondary flow is expected to be similar. It should be noted that while the flow pattern will be unchanged when the endwall is also an active mass transfer surface, the mass transfer coefficient will be diminished in this area, since the vortex flow is composed primarily of boundary layer fluid.

At the two-leg merging point, the interaction among different flow components, such as the counter-rotating horseshoe legs, the incoming boundary layer, the endwall crossflow, and the mainstream, form an even stronger vortex in the passage, which is called the passage vortex. Since the pressure leg has the same sense of rotation as the passage vortex, Langston (1980) credited this pressure leg as part of the passage vortex.

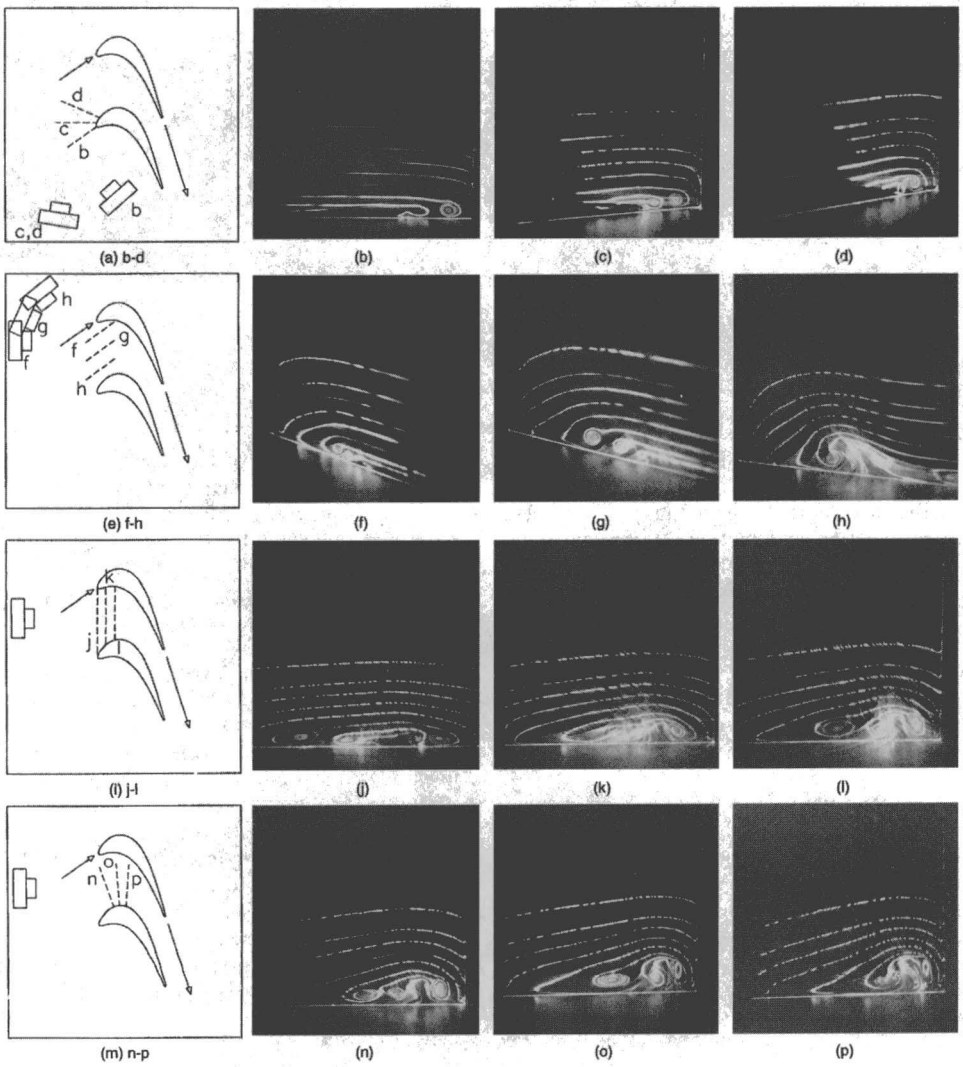

Fig. 6 Flow visualization around the blades

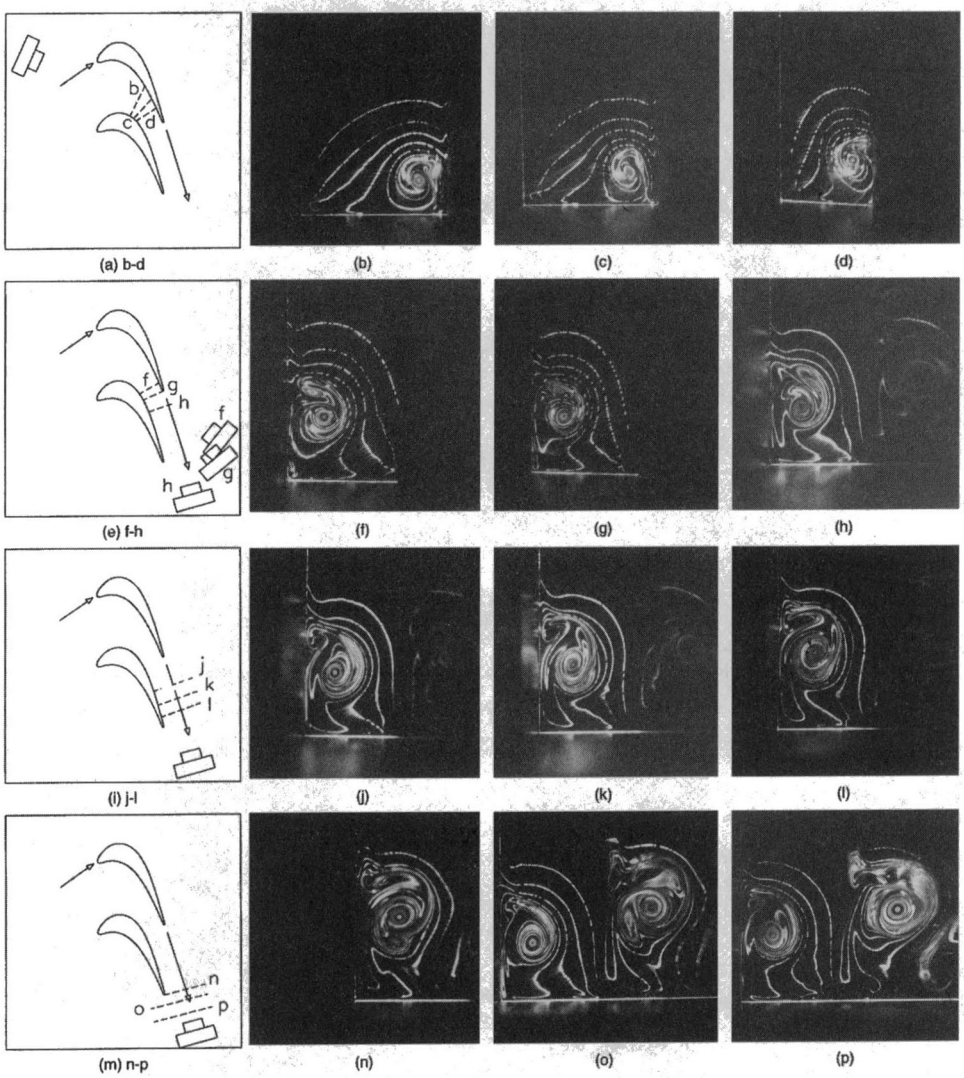

Fig. 7 Flow visualization around the blades (continued)

Passage Vortex, V_p. As mentioned above, the passage vortex consists of many flow components. The pressure leg of the horseshoe vortex is a major part of this vortex. The inlet boundary layer also contributes to it, as seen in Figs. 6(j–l). The inward rotation of the suction and pressure side legs of the horseshoe vortex system funnels part of the inlet boundary layer fluid into a smaller region, gradually extending farther above the endwall. The passage vortex stays close to the suction surface, and rotates in a counterclockwise direction when viewing the flow in the flow direction. In the geometry shown, a strong crossflow enhances its rotation and the vortex is gradually lifted away from the endwall as it travels downstream. As it entrains the main flow and endwall boundary layer, it grows in size, as shown in Fig. 7.

The mass transfer contour map from a blade near an endwall, Fig. 9 given by Goldstein et al. (1995), clearly indicates a triangular region starting near the merging point. The strong upwash motion of the passage vortex gives very high mass transfer close to the corner. The photographs also show how the incoming main flow is revolved by the passage vortex to reach the suction surface.

Suction Side Leg of the Horseshoe Vortex, V_{sh}. The multivortex suction leg quickly evolves to a single vortex as it reaches the merging point, as shown in Figs. 6(j–l). It does not move under the passage vortex, as shown in Figs. 1(a) and 1(b). The stronger pressure side leg pulls the suction leg off the endwall. The sense of rotation of the suction side leg is clockwise when viewed in the flow direction, opposite that of the pressure side leg. As the pressure side leg of the horseshoe vortex system and the suction side leg of the horseshoe vortex system approach each other on the endwall, they constitute a counterrotating vortex pair with the suction leg being weaker (as in Fig. 6(p)).

Farther downstream, the strong rotation by the passage vortex pulls the suction leg away from the suction surface, as seen in Figs. 7(f–h). A similar pattern was also found by Sieverding and Van den Bosche (1983) and Sonoda (1985). The suction leg is wrapped around the passage vortex. This is different from the model in Fig. 1(c), which shows the suction leg moving upward on the suction surface. Nearly one revolution of the suction leg around the passage vortex has been observed at the cascade exit, which is shown in Fig. 7(n). At the exit of the cascade, the suction leg has revolved around the passage vortex and is found near the lower side of the passage vortex near the suction surface. The suction leg remains distinct as it contacts with the passage vortex and moves through the passage. To some extent, the suction leg, like the pressure leg, could be considered as a small part of the larger passage vortex system.

Wall Vortex, V_{wip}. Very close to the suction wall a small and very intense vortex is captured downstream by the camera, shown in Figs. 7(h–n). This vortex originates near the two-

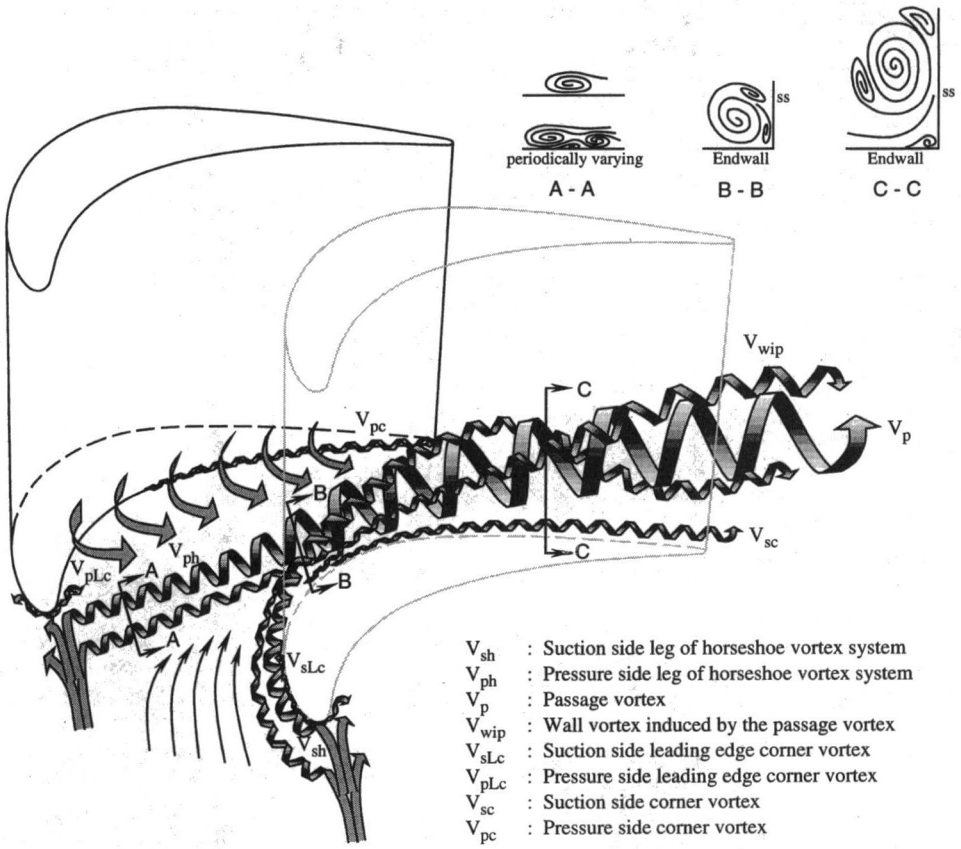

Fig. 8 Interpretation of the vortex flow pattern

leg merging point with a clockwise rotation when viewed in the flow direction and is swept up on the suction wall by the passage vortex. Jabbari et al. (1992) found in their surface flow visualization that the content of this vortex comes from the inlet boundary layer between the saddle points ahead of the cascade. Part of the boundary layer climbs on the wall and part of it stays at the suction-endwall corner. The photographs demonstrate the same flow pattern.

This new wall vortex stays above the passage vortex and counterrotates against it. Even though it has a relatively small size, it has a significant impact on mass transfer from the suction surface. Since it is so close to the wall, the upwash and downwash flows generated by this pair, passage vortex and this new wall vortex, produce a local valley and peak on the naphthalene contour map by Goldstein et al. (1995). Sonoda (1985) also found a similar phenomenon in a vane cascade.

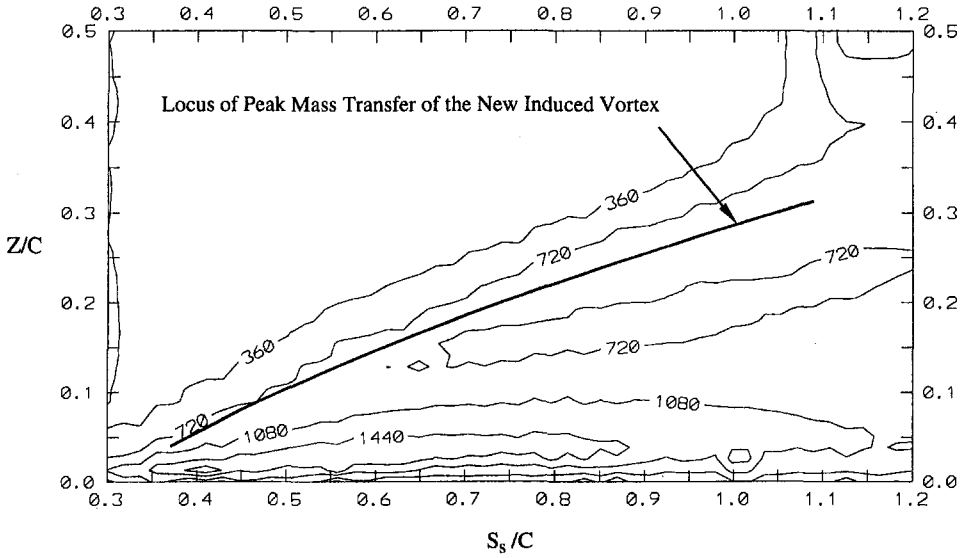

Fig. 9 Sherwood number (mass transfer) distribution on the suction side of a gas turbine blade at $Re_{ex} = 1.73 \times 10^5$, from Goldstein et al. (1995)

Corner Vortices, V_{sLc}, V_{pLc}, V_{sc} and V_{pc}. It is difficult to view a corner vortex with the smoke flow-visualization technique because of its small size. Since the corner vortex at the leading edge is driven by another larger counter-vortex around the edge, it is difficult for smoke to enter it. The surface flow visualization of Jabbari et al. (1992) and the local measurement of naphthalene mass transfer of Goldstein et al. (1995) indicate the existence of the corner vortices. Figure 8 shows the corner vortices based on the results of Jabbari et al. (1992) and Goldstein et al. (1995) although they are not clearly seen in the smoke flow visualization photographs. It is believed that the downstream corner vortex will have an impact on the corner region. These corner vortices may not be present for certain rounded corners near the leading edge.

This secondary flow pattern should be representative of other cascades, even though the leading edge radius, inlet and exit flow angle, inlet boundary layer, pitch, etc., will affect the details of the secondary flow. In particular, the multi-horseshoe-vortex structure formed at the leading edge may vary from cascade to cascade.

Conclusions

Multiple smoke wires and a laser light sheet have been used to view the secondary flow near the endwall of a high-performance blade in a large-aspect-ratio, linear cascade. A multivortex flow pattern with periodic changing of location and number of vortices has been observed ahead of the cascade near the leading edge. Photographs and videos have been taken for archival use. A secondary flow pattern of this cascade is inferred from the flow visualization and compared with earlier mass transfer measurements. General characteristics of the flow are:

1 The two branches of the multiple horseshoe vortex system gradually collapse to two single vortices (a suction leg and pressure leg), which pair with oscillating motion extending downstream. The pressure leg of the horseshoe vortex travels across the passage toward the suction surface, becoming a major part of the passage vortex. It merges with the suction leg of its counterpart at about 1/4 of the surface distance from the leading edge. The passage vortex moves toward the suction side and strengthens itself by entraining the main stream flow when it flows downstream.

2 The suction leg of the horseshoe vortex formed ahead of the leading edge moves above the passage vortex as the pressure leg of the horseshoe vortex merges with it. It wraps itself around the passage vortex due to the strength of the passage vortex becoming a small branch of the overall passage vortex system. The crossflow does not have much effect on this leg.

3 A wall vortex induced by the strong passage vortex is found very close to the suction surface. It starts near the merging point of the suction side and pressure side legs of the horseshoe vortex system and has a high mass transfer rate indicated in the naphthalene mass transfer measurement. The local minimum and peak values of the mass transfer can be explained by the upwash and downwash motions of this vortex pair.

Acknowledgments

We would like to express our thanks to the Air Force Office of Scientific Research, and to the Advanced Turbine Systems at the Department of Energy for their support, and to project monitor Dr. Daniel Fant for his encouragement of our studies.

References

Chung, J. T., and Simon, T. W., 1990, "Three-Dimensional Flow Near the Blade/Endwall Junction of a Gas Turbine: Visualization in a Large-Scale Cascade Simulator," ASME Paper No. 90-WA/HT-4.

Goldstein, R. J., and Spores, R. A., 1988, "Turbulent Transport on the Endwall in the Region Between Adjacent Turbine Blades," ASME *Journal of Heat Transfer,* Vol. 110, pp. 862–869.

Goldstein, R. J., Wang, H. P., and Jabbari, M. Y., 1995, "The Influence of Secondary Flows Near the Endwall and Boundary Layer Disturbance on Convective Transport From a Turbine Blade," ASME JOURNAL OF TURBOMACHINERY, Vol. 117, pp. 657–665.

Jabbari, M. Y., Goldstein, R. J., Marston, K. C., and Eckert, E. R. G., 1992, "Three Dimensional Flow Within Large Scale Turbine Cascades," *Wärme- und Stoffübertragung,* Vol. 27, pp. 51–59.

Jilek, J., 1986, "An Experimental Investigation of the Three-Dimensional Flow Within Large Scale Turbine Cascades," ASME Paper No. 86-GT-170.

Langston, L. S., Nice, M. L., and Hopper, R. M., 1977, "Three-Dimensional Flow Within a Turbine Cascade Passage," ASME *Journal of Engineering for Power,* Vol. 99, pp. 21–28.

Langston, L. S., 1980, "Crossflows in a Turbine Cascade Passage," ASME *Journal of Engineering for Power,* Vol. 102, pp. 866–874.

Langston, L. S., 1990, "Research on Cascade Secondary and Tip-Leakage Flows—Periodicity and Surface Flow Visualization," *Proc. Secondary Flows in Turbomachines,* AGARD CP 469.

Marchal, P. H., and Sieverding, C. H., 1977, "Secondary Flows Within Turbomachinery Bladings," *Proc. Secondary Flows in Turbomachines,* AGARD CP 214.

Moore, J., and Smith, B. L., 1984, "Flow in a Turbine Cascade: Part 2—Measurements of Flow Trajectories by Ethylene Detection," ASME *Journal of Engineering for Gas Turbines and Power,* Vol. 106, pp. 409–413.

Sharma, O. P., and Butler, T. L., 1987, "Predictions of Endwall Losses and Secondary Flows in Axial Flow Turbine Cascades," ASME JOURNAL OF TURBOMACHINERY, Vol. 109, pp. 229–236.

Sieverding, C. H., and Van den Bosche, P., 1983, "The Use of Coloured Smoke to Visualize Secondary Flows in a Turbine-Blade Cascade," *Journal of Fluid Mechanics,* Vol. 134, pp. 85–89.

Sieverding, C. H., 1985, "Recent Progress in the Understanding of Basic Aspects of Secondary Flows in Turbine Blade Passages," ASME *Journal of Engineering for Gas Turbines and Power,* Vol. 107, pp. 248–257.

Sonoda, T., 1985, "Experimental Investigation on Spatial Development of Streamwise Vortices in a Turbine Inlet Guide Vane Cascade," ASME Paper No. 85-GT-20.

Yamamoto, A., 1987a, "Production and Development of Secondary Flows and Losses in Two Types of Straight Turbine Cascades: Part 1—A Stator Case," ASME JOURNAL OF TURBOMACHINERY, Vol. 109, pp. 186–193.

Yamamoto, A., 1987b, "Production and Development of Secondary Flows and Losses in Two Types of Straight Turbine Cascades: Part 2—A Rotor Case," ASME JOURNAL OF TURBOMACHINERY, Vol. 109, pp. 194–200.

Transient Heat Transfer Experiments in a Linear Cascade Via an Insertion Mechanism Using the Liquid Crystal Technique

A. Hoffs

A. Bölcs

Swiss Federal Institute of Technology,
EPFL-LTT,
Lausanne, Switzerland

S. P. Harasgama
ABB Power Generation Ltd.,
Gas Turbine Development,
Baden, Switzerland

An insertion mechanism for a linear cascade allowing the displacement of one measurement airfoil to conduct transient heat transfer experiments is introduced. A basic feature of the system is its capability to work in a continuously running tunnel driven by a compressor at steady-state conditions. The experiment is initiated by pulling the measurement airfoil very rapidly through the sidewalls of the cascade by means of a pneumatic cylinder. Heat transfer measurements were obtained on a turbine airfoil at different exit Mach numbers up to M = 0.8 and exit Reynolds numbers up to Re = 1.2E6. The transient liquid crystal method was used applying a digital image processing system capable of recording and storing the optical signal in real time. Comparisons were performed with measurements conducted in the same test facility using the naphthalene sublimation technique as well as thin film gages. Calculations were made with a two-dimensional boundary layer code.

Introduction

The power output and efficiency level of a gas turbine improves by increasing the turbine inlet temperature. Since these temperatures exceed the maximum allowable blade material temperature, the blades have to be cooled to guarantee safe operating conditions. Hence, knowledge of the detailed heat transfer characteristics is required for the design of airfoils that have to operate for a certain guaranteed number of hours without failure. Principal parameters influencing the heat transfer coefficient along the turbine airfoil are the Reynolds number, the free-stream turbulence, the surface curvature, and the inlet Mach number. Further studies on the influence of the combined effects of these parameters are still needed to validate or to improve numerical predictions.

In the present work, an insertion mechanism creating a step change in temperature to conduct heat transfer measurements on a turbine airfoil in a linear cascade at engine representative Mach and Reynolds numbers is described. The transient liquid crystal technique was used to determine the local heat transfer coefficient on a turbine airfoil based on the assumption of a semi-infinite solid (Ireland and Jones, 1985). Detailed heat transfer characteristics have been obtained for a range of Mach and Reynolds numbers. Comparisons are made with results obtained from the naphthalene sublimation technique (Häring et al., 1995a) and from measurements with thin film gages as well as from calculations with the two-dimensional boundary layer code TEXSTAN (Crawford, 1986).

Martinez-Botas et al. (1995) applied a similar technique for an annular cascade with a blowdown tunnel employing fast-acting shutters before and after the test section. For a continuously running test facility at high velocities, shutters are not appropriate for linear cascades since a large percentage of the working section would be blocked. Harvey et al. (1989) immersed a whole perspex working section of a linear cascade in a heated water tank. With a shutter valve the flow was then initiated for the main test section. The insertion of a model in a flow at low velocity has only been described by Baughn and Xan (1991) for a simple square duct using pneumatic cylinders.

Test Facility and Measuring Equipment

Wind Tunnel. The experiments were performed in a large linear wind tunnel facility with a test section measuring 100 × 340 mm. The test facility is supplied from a continuously running air source delivering a mass flow of 10 kg/s with a maximum pressure ratio of 3.5. The flow temperature in the cascade was adjusted to approximately 45°C to simulate a hot gas flow. The experimental setup for the present study in the linear test facility consists of five airfoils with the measurement airfoil in the center. The isentropic exit Mach number as well as the downstream flow periodicity is regulated by two tailboards and two bypass vanes. Although only five profiles are present in the cascade, a good flow periodicity is obtained (Bölcs and Sari, 1988). Total pressure and total temperature are measured in the settling chamber. The location of the pressure taps for the inlet and outlet flow conditions as well as for the airfoil surfaces have already been described by Häring et al. (1995a). The chord length of the airfoil is 74.5 mm, and the inlet and outlet flow angles are 0 and 71 deg, respectively. The turbulence intensity in the mean flow direction was measured with a hot-wire probe of 5 μm diameter placed 75 mm in front of the airfoils.

Test Airfoil. The heat transfer measurements were conducted on the center airfoil, which is manufactured out of two parts. An aerodynamic part made out of aluminum and equipped with 31 pressure taps was used to determine the Mach number distribution over the surface. The pressure taps are placed on two spanwise lines to check the two dimensionality of the flow field. The other part was made out of plexiglass and covered with a layer of narrow-band encapsulated thermochromic liquid crystals to perform the heat transfer measurements. The initial

Contributed by the International Gas Turbine Institute and presented at the 40th International Gas Turbine and Aeroengine Congress and Exhibition, Houston, Texas, June 5–8, 1995. Manuscript received by the International Gas Turbine Institute February 4, 1995. Paper No. 95-GT-8. Associate Technical Editor: C. J. Russo.

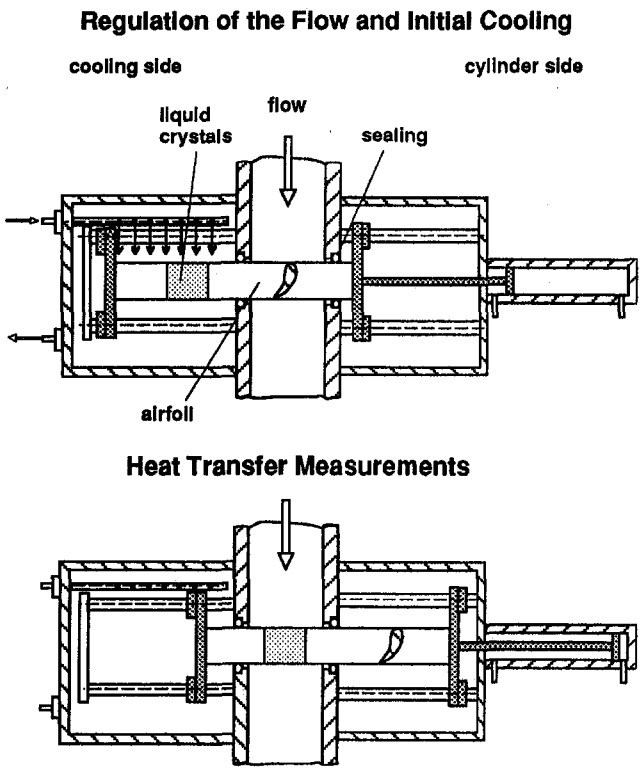

Fig. 1 Insertion mechanism

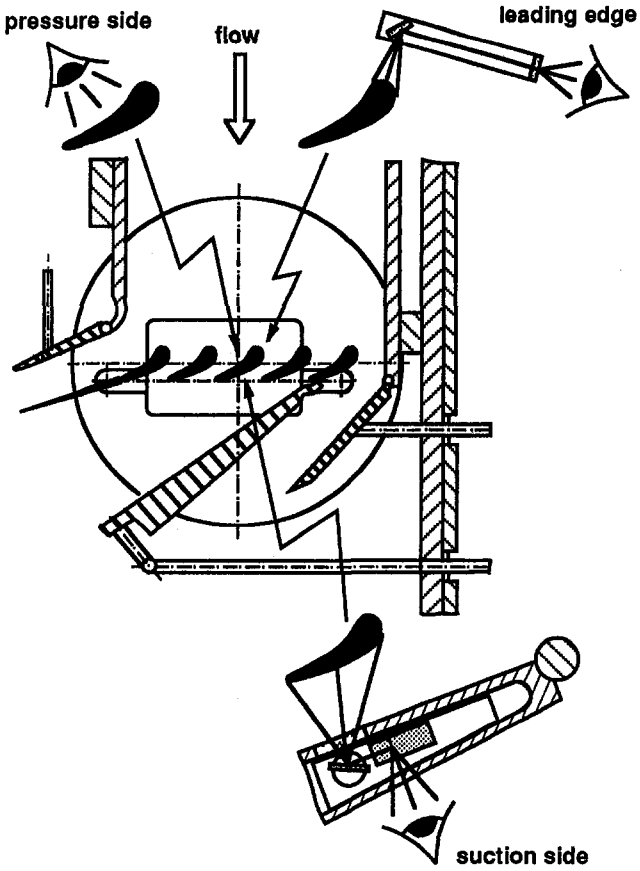

Fig. 2 Viewing of the airfoil surface

temperature was measured with four thermocouples distributed along the airfoil surface.

Insertion Mechanism. The insertion mechanism (Fig. 1) employs a pneumatic cylinder to pull the test airfoil very rapidly through the sidewalls of the linear cascade in less than 0.15 s. The airfoil is guided from both sides of the channel on ball bearings running on cylindrical shafts. The deflection of the airfoil has been calculated as 0.3 mm for an exit Mach number of 0.8. Thus, a gap of 0.5 mm between the cascade walls and the moving airfoil ensures that during the insertion process the liquid crystal layer on the airfoil surface is not damaged. Both sides of the injection mechanism are within sealed chambers, which allow the internal pressure to be above atmospheric. The heat transfer side can be connected to an external thermostat to control the initial temperature to within ±0.15°C. An inflatable seal in the sidewall synchronized with the insertion process allows good isolation from the tunnel during the cooling stage.

The airfoil has to be illuminated and viewed from three sides to provide a full picture of the airfoil surface. The illumination sources are fiber optics connected to a powerful cold light generator. The complete pressure side can be viewed from outside of the cascade with a miniature camera. The leading edge region is observed using an endoscope placed in the cascade close to the outer wall so as not to disturb the flow. The suction side is visualized via an optical mirror system in the tailboard with the camera outside the channel (Fig. 2).

Image Processing System. The present image processing system is based on the hue capturing technique using an automated image processing system. A complete liquid crystal image is taken in real time at the conventional video frame rate of 25 Hz, but only preselected hue values are stored in the random access memory of the computer as a function of their location and time of appearance. For more details the reader is referred to Häring et al. (1995b).

Since the color play of the liquid crystals is always taken under a certain angle with respect to the airfoil surface, the original surface coordinates have to be correlated with the camera picture. For this reason a paper grid was glued on the aerodynamic part of the airfoil to be superimposed numerically with the liquid crystal image.

The evaluation is done on an HP workstation with a Fortran program. A filtering procedure employing time and location windows eliminates random noise. The preselected narrow hue ranges recorded give a range of times at a point as this line

Nomenclature

λ = heat conduction coefficient, W/mK
T = temperature, K
x = depth, m
ρ = density, kg/m^3
c_p = specific heat capacity, J/kgK
t = time, s
α = heat transfer coefficient, W/m^{2}K
M = Mach number
Re = Reynolds number
Pr = Prandtl number
s = surface distance from leading edge
L = chord length
r_0 = recovery factor
θ = nondimensional temperature = $(T_w - T_i)/(T_g - T_i)$
Tu = turbulence intensity, percent
β = flow angle

Subscripts

i = initial
g = free stream
w = wall
L = with respect to the chord length
1 = inlet
2 = outlet

moves over the surface. Thus an average of these times is taken in the analysis to evaluate the heat transfer coefficient.

Calibration of the liquid crystals has been performed in situ under steady-state conditions. The blade was homogeneously heated and the surface temperature corresponding to the liquid crystal hue value was recorded. Each specific viewing position was calibrated to take the different camera viewing positions into account. A narrow-band liquid crystal was used reacting at 30°C with a width of 1°C. The selected hue value was 160 ± 5 on a scale of 0–255 representing the color green.

Heat Transfer Measurement. The technique requires a uniform initial temperature of the model, which is rapidly exposed to a flow at a different temperature for a limited amount of time. It is assumed that within the testing time the penetration of the heating pulse into the model is small compared to the model wall thickness (Ireland and Jones, 1985). Thus, the heat conduction can be considered to be unsteady and one dimensional in a semi-infinite material. The heat equation for transient conduction in a semi-infinite solid is

$$\lambda \frac{\partial^2 T}{\partial x^2} = \rho c_p \frac{\partial T}{\partial t}. \quad (1)$$

With the initial condition

$$T(x, 0) = T_i, \quad (2)$$

the interior boundary condition

$$T(\infty, t) = T_i, \quad (3)$$

and the surface convection boundary condition

$$\left[-\lambda \frac{\partial T}{\partial x}\right]_{x=0} = \alpha(T_g - T_w), \quad (4)$$

the solution for $x = 0$ can be written as

$$\frac{T_w - T_i}{T_g - T_i} = 1 - \exp\left[\frac{\alpha\sqrt{t}}{\sqrt{\rho c_p \lambda}}\right]^2 \operatorname{erfc}\left[\frac{\alpha\sqrt{t}}{\sqrt{\rho c_p \lambda}}\right]. \quad (5)$$

For compressible flow the recovery temperature of the flow was used with $r_0(\mathrm{Pr}) = \mathrm{Pr}^{1/2}$ for laminar and $r_0(\mathrm{Pr}) = \mathrm{Pr}^{1/3}$ for turbulent flow. The curvature effects on normal conduction

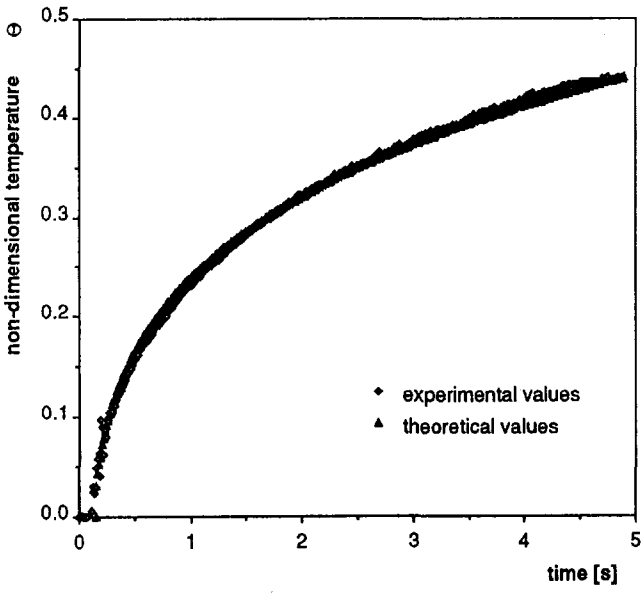

Fig. 3 Insertion process

Table 1 Heat transfer measurements

Test	Re_2 [-]	M_2 [-]	Tu [%]	β_2 [°]
1	340'000	0.23	5	71
2	700'000	0.47	5	71
3	1'160'000	0.76	5	71

are taken into account with a correction factor on the one-dimensional analysis.

The uncertainty in heat transfer coefficient has been estimated with standard methods according to Moffat (1985) and was found to be 7 percent on average. The errors for the initial and total temperatures were estimated to be ±0.15°C, whereas the error for the liquid crystals was estimated to be ±0.20°C. The thermal product $\sqrt{\rho c_p \lambda}$ of plexiglass is 569 ± 29 and the uncertainty in time was determined to be ±0.1 s, which includes the insertion time of the model.

Comparisons. The lower Mach and Reynolds numbers have been compared to measurements conducted with the naphthalene sublimation technique for the same cascade geometry (Häring et al., 1995a). Since the naphthalene sublimation technique is based on a mass/heat transfer analogy, the tests had to be conducted at isothermal conditions to avoid mass transfer due to temperature gradients. It was hence only possible to reproduce the same exit Reynolds numbers for comparison.

Additional heat transfer measurements with thin film gages have been performed using the present insertion mechanism. The measurements and the evaluation have been conducted according to Schultz and Jones (1973). Fifteen gages were applied around the airfoil surface on the center line with a spacing of 10 mm between gages. Since the gages give a continuous temperature response over time, the technique could be used to verify the presence of any instabilities in heat flux during the insertion process.

The TEXSTAN code (Crawford, 1986) has been used to perform boundary layer calculations. The presented calculations made use of the modified Lam and Bremhorst Pressure Term Modification [LBPTM] as suggested by Schmidt and Patankar (1991). The discrete points of the velocity profile have been smoothed for the calculations.

Dullenkopf and Mayle's (1995) correlation was used to compare to the stagnation point heat transfer. The correlation takes the free-stream turbulence intensity into account.

Insertion Process. Thin film gages have been used to determine the influence of the insertion process on the heat transfer possibly caused by the movement of the airfoil together with hot gas entering the cooling box. Measurements of the continous nondimensional temperature value θ were taken versus time. For the same run the heat transfer coefficient was determined, and from this value a theoretical nondimensional temperature θ was calculated. A comparison of these two curves (Fig. 3) shows that the influence of the insertion process is negligible.

Results and Discussion

The objectives of the measurements on the airfoil were to demonstrate the feasibility of the present insertion mechanism and to provide heat transfer distributions at high Mach and Reynolds numbers based on exit conditions and chord length L = 74.5 mm. Table 1 summarizes the tests that were conducted on this cascade.

The isentropic Mach number distribution on the airfoil for all tests is shown in Fig. 4.

On the suction side the flow first strongly accelerates and becomes then almost uniform for the two lower Mach numbers

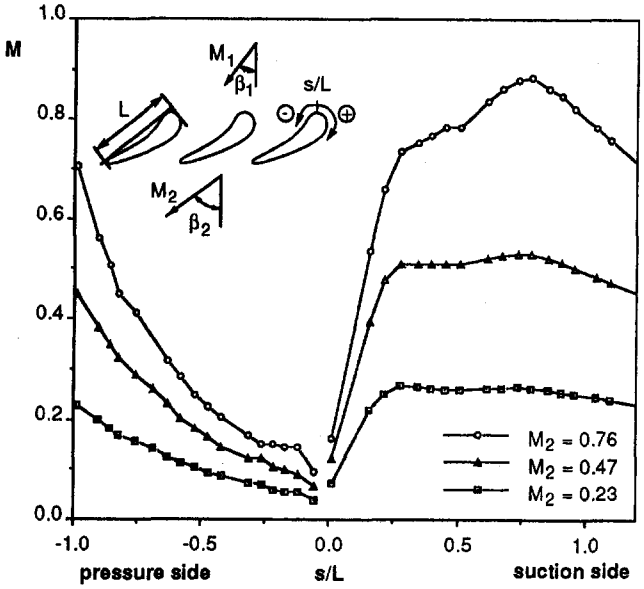

Fig. 4 Airfoil Mach number distribution for all tests

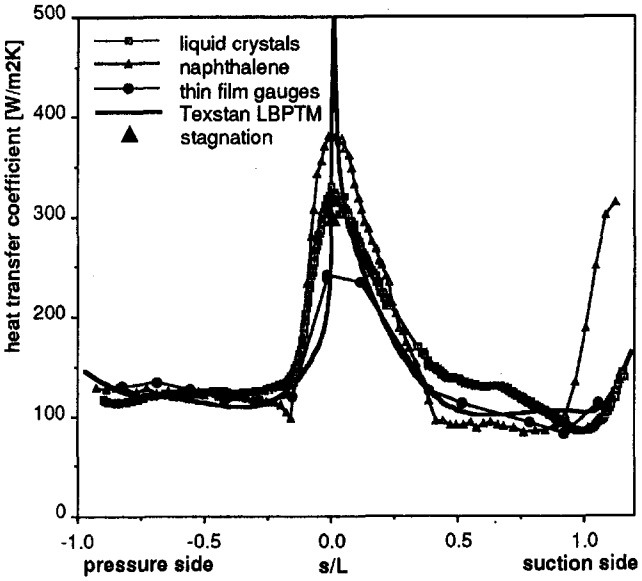

Fig. 6 Test 1, M_2 = 0.23, Re_2 = 340,000, *Tu* = 5 percent

whereas for the high Mach number the velocity is still increasing before it decreases again for all cases toward the trailing edge. On the pressure side the acceleration for the three Mach numbers is almost constant.

The results of test 3 (Re_2 = 1.2e6) are presented in Fig. 5 and show the two-dimensional character of the flow. The figures are projections of the curved airfoil surfaces onto a two-dimensional plane. The lines are equispaced contours of the heat transfer coefficient in steps of 50 W/m^2K.

On the pressure surface a laminar boundary layer develops from the stagnation point and transition occurs close to the trailing edge. On the suction side a laminar boundary layer grows from the stagnation point. A transitional wedge as described by Clark et al. (1992) is present in the center of the flow passage. The phenomenon was only observed for the high Reynolds number and was not taken into account for the spanwise averaging. Close to the trailing edge, the laminar boundary layer proceeds through transition; thereafter the flow becomes fully turbulent near the trailing edge.

The curves in Fig. 6–8 represent spanwise-averaged heat transfer coefficients over 10 mm in the center of the channel (10 percent of full span) along with the comparisons.

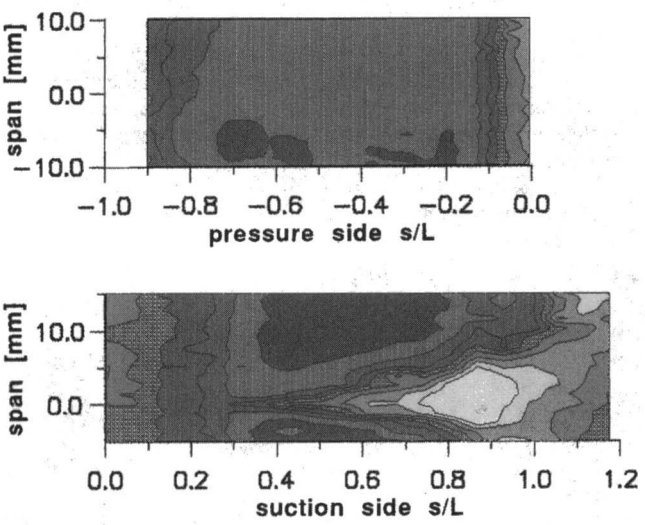

Fig. 5 Two-dimensional heat transfer distribution test 3

For an outlet Mach number of M_2 = 0.23 (Re_2 = 340,000) represented in Fig. 6, all the measurements with different techniques agree well on the pressure side. The higher values at the stagnation point for the naphthalene sublimation technique can be explained by the effect of the mechanical abrasion caused by flow particles during the long testing time. The calculation does not predict the stagnation point well and gives lower values for the leading edge region but agrees quite well further downstream. On the suction side all measurements agree well on the location of transition whereas the naphthalene shows much higher values during the transition itself. Again the calculation predicts lower heat transfer coefficients for the leading edge region but agrees well for the late laminar region and transition.

Figure 7 shows the heat transfer coefficients for an outlet Mach number of M_2 = 0.47 (Re_2 = 700,000). For the pressure side the measurements lay very close together and agree with the calculation. At the stagnation point region both the naphthalene sublimation technique and the calculation predict too high a value for the lower Reynolds number case. On both sides the

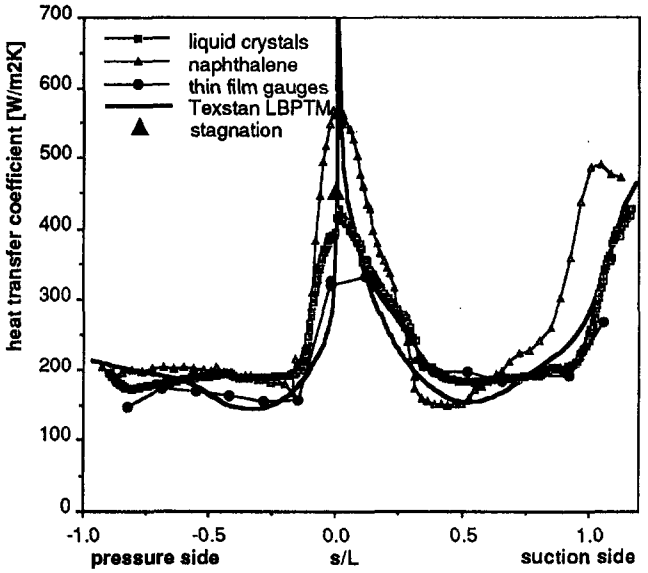

Fig. 7 Test 2, M_2 = 0.47, Re_2 = 700,000, *Tu* = 5 percent

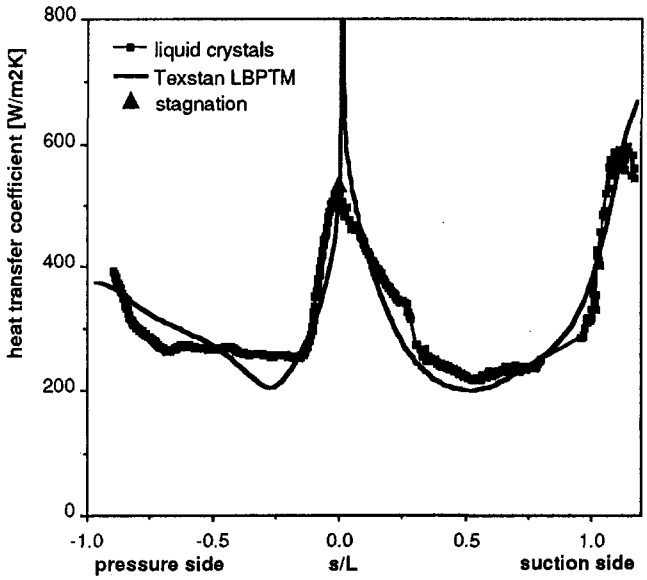

Fig. 8 Test 3, $M_2 = 0.76$, $Re_2 = 1{,}160{,}000$, $Tu = 5$ percent

calculation predicts lower heat transfer for the leading edge region. On the suction side the measurements agree well for most of the laminar region and the transition. For the naphthalene measurements it should be mentioned that the analogy between heat and mass transfer is only fully valid in the incompressible flow region.

The heat transfer coefficients for the high Mach and Reynolds number case ($M_2 = 0.76$, $Re_2 = 1{,}160{,}000$) are shown in Fig. 8. On the pressure side the boundary layer stays laminar until $s/L = 0.7$, where transition begins, which is quite well predicted by the calculation. For the leading edge region lower values are calculated. On the suction side the predicted values stay a little below the measured data but both curves agree well in the transional region. The liquid crystals indicate a turbulent boundary layer close to the trailing edge.

Conclusions

- A fast-acting insertion mechanism to conduct transient heat transfer experiments at engine representative Mach and Reynolds numbers has been developed for a linear cascade supplied by a continously running air source.
- Optical access around the complete airfoil surface could be achieved making use of three different camera arrangements applying mirror and optical lens systems without disturbing the flow.
- The effect of insertion on the heat transfer has been investigated using thin film gages with a continuous time history and found to be negligible.
- Heat transfer coefficients have been obtained for three different exit Mach and Reynolds numbers up to 0.8 and 1.2E6, respectively. They compare well to experiments with the naphthalene sublimation technique and the thin film gages for the two lower Reynolds number cases.
- The comparisons to the calculation TEXSTAN show quite good agreement for all Reynolds numbers except for the leading edge regions, which are less well predicted.

Acknowledgments

The research project is subsidized by ABB, Baden, Switzerland and the "Commission pour l'encouragement de la recherche scientifique" (CERS-KWF), Switzerland. The thin film measurements have been carried out together with Prof. T. V. Jones from Oxford University, England, and the authors are very grateful for his assistance and advice.

References

Baughn, J. W., and Xan, X., 1991, "An Insertion Technique Using the Transient Method With Liquid Crystals for Heat Transfer Measurements in Ducts," presented at the National Heat Transfer Conference, Minneapolis, MN, Jy 28–31.

Bölcs, A., and Sari, O., 1988, "Influence of Deposit on the Flow in a Turbine Cascade," ASME JOURNAL OF TURBOMACHINERY, Vol. 110, pp. 512–519.

Clark, J. P., Magari, P. J., and Jones, T. V., 1992, "On the Distribution of the Heat Transfer Coefficient in Turbulent and 'Transitional' Wedges," *Int. J. Heat Fluid Flow*, Vol. 14, No. 3.

Crawford, M. E., 1986, "Simulation Codes for Calculation of the Heat Transfer to Convectively Cooled Turbine Blades," *Convective Heat Transfer and Film Cooling in Turbomachinery*, VKI-LS 1986-06.

Dullenkopf, K., and Mayle, R. E., 1995, "An Account of Free-Stream-Turbulence Length Scale on Laminar Heat Transfer," ASME JOURNAL OF TURBOMACHINERY, Vol. 117, pp. 401–406.

Häring, M., Bölcs, A., Harasgama, S. P., and Richter, J., 1995a, "Heat Transfer Measurements on Turbine Airfoils Using the Naphthalene Sublimation Technique," ASME JOURNAL OF TURBOMACHINERY, Vol. 117, pp. 432–439.

Häring, M., Hoffs, A., Bölcs, A., and Weigand, B., 1995b, "An Experimental Study to Compare the Naphthalene Sublimation With the Liquid Crystal Technique in Compressible Flow," ASME Paper No. 95-GT-16.

Harvey, N. W., Wang, Z., Ireland, P. T., and Jones, T. V., 1989, "Detailed Heat Transfer Measurements in Nozzle Guide Vane Passages in Linear and Annular Cascades in the Presence of Secondary Flows," AGARD CP 469, Paper 24, Jerusalem.

Ireland, P. T., and Jones, T. V., 1985, "The Measurement of Local Heat Transfer Coefficients in Blade Cooling Geometries," AGARD CP390, Bergen.

Martinez-Botas, R. F., Lock, G. D., and Jones, T. V., 1995, "Heat Transfer Measurements in an Annular Cascade of Transonic Gas Turbine Blades Using the Transient Liquid Crystal Technique," ASME JOURNAL OF TURBOMACHINERY, Vol. 117, pp. 425–431.

Moffat, X. Y., 1985, "Using Uncertainty Analysis in the Planning of an Experiment," ASME *Journal of Fluids Engineering*, Vol. 107, pp. 173–178.

Schmidt, R. C., and Patankar, S. V., 1991, "Simulating Boundary Layer Transition With Low-Reynolds-Number k–Epsilon Models: Part 2—an Approach to Improving the Predictions," ASME JOURNAL OF TURBOMACHINERY, Vol. 113, pp. 18–26.

Schultz, D. L., and Jones, T. V., 1973, "Heat Transfer Measurements in Short-Duration Hypersonic Facilities," NATO Advisory Group for Aeronautical Research and Development AGARDOGRAPH 165.

Transient Liquid Crystal Technique for Convective Heat Transfer on Rough Surfaces

D. N. Barlow
Department of Aeronautics,
United States Air Force Academy,
Colorado Springs, CO

Y. W. Kim
Allied Signal Engines,
Phoenix, AZ

L. W. Florschuetz
Department of Mechanical
and Aerospace Engineering,
Arizona State University,
Tempe, AZ

The local heat transfer coefficients are obtained on a rough planar surface simulating in-service turbine stator vane sections. A transient experimental technique is presented that permits the determination of local heat transfer coefficients for a rough planar surface using thermochromic liquid crystals. The technique involves the use of a composite test surface in the form of a thin foil of stainless steel with roughness elements laminated over a transparent substrate. Tests are conducted on a splitter plate to provide momentum boundary layer thicknesses to roughness heights appropriate for actual turbine stator vanes. Data are reported for two roughness geometries and two free-stream velocities. The range of Reynolds numbers along with the ratio of average roughness value to momentum thickness matches conditions encountered on the pressure side of the first-stage stator vanes in current high performance turbofan engines. A numerical simulation is conducted to validate the test method. Results for the rough surfaces investigated are compared with an available empirical relationship.

Introduction

For some time, it has been recognized that the smooth manufactured surfaces of gas turbines become rough during operation (Tarada and Suzuki, 1993). The hot section surfaces become rough both from the corrosive effects of the high-temperature gas stream and from foreign object deposition. Specifically, recent investigations by Tabbita (1993) of the surface profiles of two Pratt & Whitney (P&W) high-pressure turbine vanes indicate that surface roughness (Ra) values can be on the order of the smooth surface momentum boundary layer thickness (δ_2). Tabbita (1993) reports for an in-service first-stage vane at approximately 15 percent axial chord along the vane's pressure side, the local Ra and original smooth surface δ_2 are on the order of 22.9 μm with a corresponding local Re_x of approximately 1.61×10^5. The effect of roughness on convective heat transfer coefficients (h) at Reynolds numbers applicable to gas turbines is therefore of practical importance.

One of the few analytical relationships available for predicting convective heat transfer for a flat rough surface in external flow is developed by Kays and Crawford (1980) using a thermal law of the wall approach. Constants in the developments are assigned values based on the work of Dipprey and Sabersky (1963) and Pimenta et al. (1975). In order to use this relationship, the equivalent sand roughness of the surface under investigation must be determined. Very extensive measurements of rough pipes were carried out by Nikuradse (1933) who used circular pipes covered on the inside as tightly as possible with sand of a specific grain size glued to the wall. Schlichting (1936) developed the concept of equivalent sand-grain roughness (k_s) as a means of characterizing other types of roughness elements by comparing the equivalent net effect produced by Nikuradse's experiments. Schlichting (1936), using a law of the wall development, determines the k_s for a variety of surfaces in a channel under fully developed flow conditions. Using a law of the wall development for a flat surface, Pimenta et al. (1975) developed a relationship between k_s, boundary layer thickness, and the coefficient of friction for the surface. In this study, the work by Pimenta et al. (1975) is used along with the appropriate momentum integral equation to determine k_s and finally a Stanton number from Kays and Crawford's work (1980). This result is compared to the flat plate experimental results reported here.

Most conventional techniques for heat transfer measurement produce averaged coefficients over segment areas and provide accurate information at only discrete locations. If detailed resolution is desired, the fabrication of the test section becomes complex and expensive. Metzger and Larson (1986) describe an alternative approach along with the theory and experimental method. This transient method uses melting point coatings to determine local heat transfer values. In addition, thermochromic liquid crystal (TLC) has been used extensively by investigators to measure local convection heat transfer rates (Cooper et al., 1975; Hippensteele et al., 1983; Jones and Hippensteele, 1985). More recently, a transient technique using TLC coatings has been developed to obtain both heat transfer coefficients and effectiveness values for the film flow situation (Vedula and Metzger, 1991). These techniques offer several advantages. First, spatially continuous values may be obtained, the resolution of which is based to a large extent on the experimenters' willingness to reduce data. Second, these techniques may be applied to new configurations without the complex and often expensive fabrication requirements of other techniques. Use of liquid crystals on rough surfaces has previously been demonstrated by Wang et al. (1990) who presented a transient technique to investigate heat transfer at rough surfaces with an isolated pin-fin geometry in fully developed channel flows. The present study introduces a different transient approach to local heat transfer measurements, which permits determination of convective heat transfer on rough surfaces with complex surface geometries.

In this study, two surface roughness configurations are investigated with absolute roughness heights of 0.56 mm and 1.14 mm. Data are reported at two main stream velocities of 30 m/s and 50 m/s. The majority of studies have focused not only on smooth surfaces but also on flows with relatively low turbulence levels (<1 percent). In reality however, the turbulence intensity at the leading edge of the first vane stator can be as high as 15 percent or more in engine operating conditions (Mehendale and

Contributed by the International Gas Turbine Institute and presented at the 40th International Gas Turbine and Aeroengine Congress and Exhibition, Houston, Texas, June 5–8, 1995. Manuscript received by the International Gas Turbine Institute February 4, 1996. Paper No. 95-GT-6. Associate Technical Editor: C. J. Russo.

Han, 1992). This turbulence level decreases through the first-stage vane but would be expected to remain as high as 10 percent. As is the work reported in the present study, the work by Mehendale and Han (1992) was conducted at low temperatures and without the presence of combustion products. Work by Moss and Oldfield (1996) has shown that for free-stream intensities above 3 percent, the heat transfer process is enhanced due to the penetration of freestream turbulent eddies deep into the boundary layer. Without the presence of surface roughness, their work has shown increases in Nusselt number up to 35 percent due to free-stream turbulence. The present study uses flows at 6.5 and 8.5 percent turbulence levels and investigates the effect of surface roughness on flat plate heat transfer at appropriate turbulence levels and scaled roughness for the turbomachinery environment. A more complete characterization of the turbulence can be found from Barlow (1994).

Test Apparatus and Measurement Theory

Figure 1 shows a schematic of the first of two experimental apparatuses used for this work. Compressed air is filtered, dried, and orifice metered prior to the test apparatus. The flow passes through an autotransformer controlled tubular heater where the temperature can be accurately set to desired levels. The flow is initially diverted away from the test section by a three-way ball valve until the flow rate and temperature reach steady-state values. Once diverted back to the test section, the flow passes through a rectangular plenum 15.2 cm by 12.7 cm holding a passive turbulence-generating grid. This grid consists of 6.3-mm-dia holes spaced 12.6 mm apart both vertically and horizontally across the plenum. The flow then converges to an opening of 3.81 cm by 7.62 cm over a distance of 20 cm, and passes by a splitter plate where a 0.64-cm-thick bypass occurs across the width of the plate to provide boundary layer thickness control. The main flow then passes through the test section and across the 7.62 cm by 20.3 cm Plexiglas flat plate providing a boundary layer and Reynolds number appropriate for the pressure side turbine vane cases modeled in this work. At a free-stream velocity of 50 m/s, a Reynolds number ($U_\infty X/\nu$) of 1.61×10^5 is produced 57.2 mm downstream of the splitter plate leading edge. This Reynolds number corresponds to that of a typical high performance first stage vane at approximately 15 percent axial chord along the pressure side (Tabbita, 1993). In addition, Tabbita (1993) reports the average surface roughness for such a turbine vane from an in-service engine at approximately this downstream location to be on the order of 22.9 μm or about the same scale as the momentum boundary layer thickness (δ_2) at this location for the manufactured smooth surface. Boundary layer measurements on a smooth surface using the test apparatus shown in Fig. 1 found that for a Reynolds number of 1.61×10^5 the δ_2 at 57.2 mm from the leading

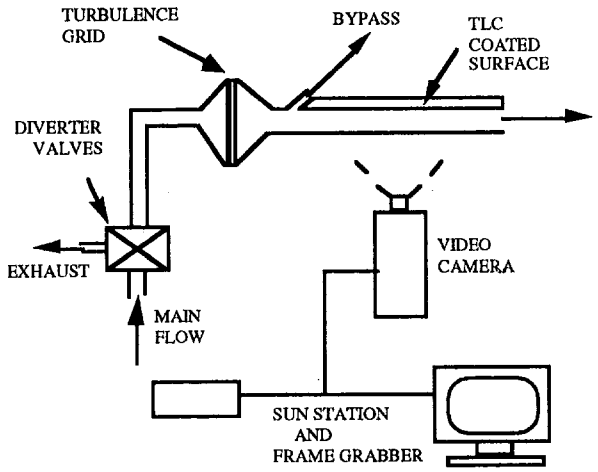

Fig. 1 Plexiglas flat plate test apparatus

edge is 0.203 mm ($\delta_1 = 0.259$ mm). As a result, two roughness designs are chosen for this study that provide a Ra value approaching the experimental δ_2 and a Ra on the order of $0.5\delta_2$.

The test surface is the key to being able to use TLC techniques. In the past (Vedula, 1989), as in Fig. 1, the TLC has most often been applied to the surface directly exposed to the test flow gases. This has been possible because the liquid crystal did not add enough roughness to extend out of the viscous sublayer and the surface could continue to be considered aerodynamically smooth. The surface is then viewed through the flow field and through an adjacent Plexiglas surface.

The measurement of the test surface convection characteristics follows the methods of Metzger and Larson (1986) with the local surface heat flux expressed as:

$$q = h(T_\infty - T_W) \tag{1}$$

In this case, local surface convection behavior is condensed into a constant of proportionality (h) where, for a given flow field and as long as temperature differences are sufficiently small to allow fluid properties to be represented by values independent of temperature, linear convection behavior can be assumed. The experimentation consists of measuring q together with T_W and T_∞, and from them determining h. In this work, local determination of h is made by suddenly exposing the test surface to a steady mainstream flow and observing the transient response of the test surface as indicated by the TLC color display. The wall material, including the test surface, is initially at a uniform temperature at all depths, and the initial response near the surface is governed by a semi-infinite formulation of the transient

Nomenclature

A = area
c_f = friction coefficient
c_p = specific heat of air
h = convective heat transfer coefficient
$\bar{h}$ = laterally averaged heat transfer coefficient
H = absolute local height of roughness elements
$\bar{H}$ = average height of rough surface above base plane
k = thermal conductivity
k_s = equivalent sand-grain roughness
Pr = Prandtl number
Pr_t = turbulent Prandtl number
Ra = average surface roughness
Re_k = roughness Reynolds number = $u_\tau k_s/\nu$
Re_x = Reynolds number = $U_\infty X/\nu$
St = Stanton number = $h/\rho U_\infty c_p$
q = heat transfer rate per unit of area
T = temperature
t = time
U = velocity
V = volume
u_τ = shear velocity
X = distance downstream
Y = distance perpendicular to convective surface
α = thermal diffusivity
δ_2 = momentum thickness of boundary layer
ϵ_H = eddy diffusivity for heat transfer
ρ = density
τ = time step
τ_0 = wall shear stress
ν = kinematic viscosity

Subscripts

i = initial
RS = rough surface
r = reference
s = smooth surface
w = wall
∞ = free-stream state

heat conduction where the surface temperature is given by the classical solution:

$$\frac{T_W - T_i}{T_\infty - T_i} = 1 - \exp\left[\frac{h^2 \alpha t}{k^2}\right] \operatorname{erfc}\left[\frac{h\sqrt{\alpha t}}{k}\right] \qquad (2)$$

By measuring the time (t) required for the surface temperature to reach a prescribed value displayed by the TLC coating, h can be determined. Since true step changes in the applied fluid temperatures are usually not possible and the fluid temperature is a function of time, an additional complication is introduced in the transient experiment. This complication is accounted for by modifying Eq. (2) through use of superposition and Duhamel's theorem (Metzger and Larson, 1986). The actual change is obtained by using a series of steps. The solution is then represented as:

$$T - T_i = \sum_{i=1}^{N} U(t - \tau_i)\Delta T_\infty \qquad (3)$$

where

$$U(t - \tau_i) = 1 - \exp\left(\frac{h^2}{k^2}\alpha(t - \tau_i)\right) \operatorname{erfc}\left(\frac{h}{k}\sqrt{\alpha(t - \tau_i)}\right) \qquad (4)$$

In this technique, the transient surface temperature information provided by the TLC is viewed with video camera/Sun workstation-based image processing system employing a 24-bit frame grabber. The present system employs a normalized threshold method (Barlow, 1994), which permits accurate local temperature determination (±0.11°C) even when the illumination of the surface varies greatly from one area of the test section to another. The TLC displays colors in response to temperature changes as a result of lattice reorientation of the crystal. When sprayed as a thin layer, the TLC is essentially clear and displays color with increasing temperature in sequence of red, green, blue, and back to clear. The nominal temperatures for red, green, and blue displays of the present chiral nematic TLC are 38.4°C, 39.8°C, and 43.5°C, respectively. The process is reversible such that the calibration of temperature remains unchanged for a large number of cycles under laboratory conditions. While all TLC type coatings assume a finite time response for the lattice rotations, Ireland and Jones (1987) have shown that micro-encapsulated chiral nematic coatings on the order of 10^{-3} cm thick require only a few milliseconds for this action. This time lag is negligible in comparison with the thermal transients of the present study. For a rough surface, this technique is not appropriate for several reasons. A TLC layer on the roughened surface will provide a temperature response that sees only the tops of the rough elements. This analysis would fail to take into account the heat transfer occurring on the sides of the roughening elements and would give an inaccurate description of the true heat transfer occurring to the surface. In addition, with any portion of the roughened surface viewed which is not perpendicular to the camera, errors in the calibration of the TLC can occur (Bonnett, 1989).

Figure 2 shows the composite plate developed for the rough surface model. The composite consists of a stainless steel roughened surface sprayed on the non-flow side with a thin layer of black paint followed by the TLC and backed with a 1.5 cm clear epoxy layer. The thermal properties of the chosen epoxy were determined to be similar to Plexiglas (~2 percent) in material testing reported by Barlow (1994).

In this setup, rather than the roughened heat transfer surface being viewed from the front side, it will now be viewed from behind. Stainless steel (k = 14.9 W/mK) was chosen to provide an acceptably small temperature drop across the metal plate, yet limit the lateral conduction. The TLC is then viewed through

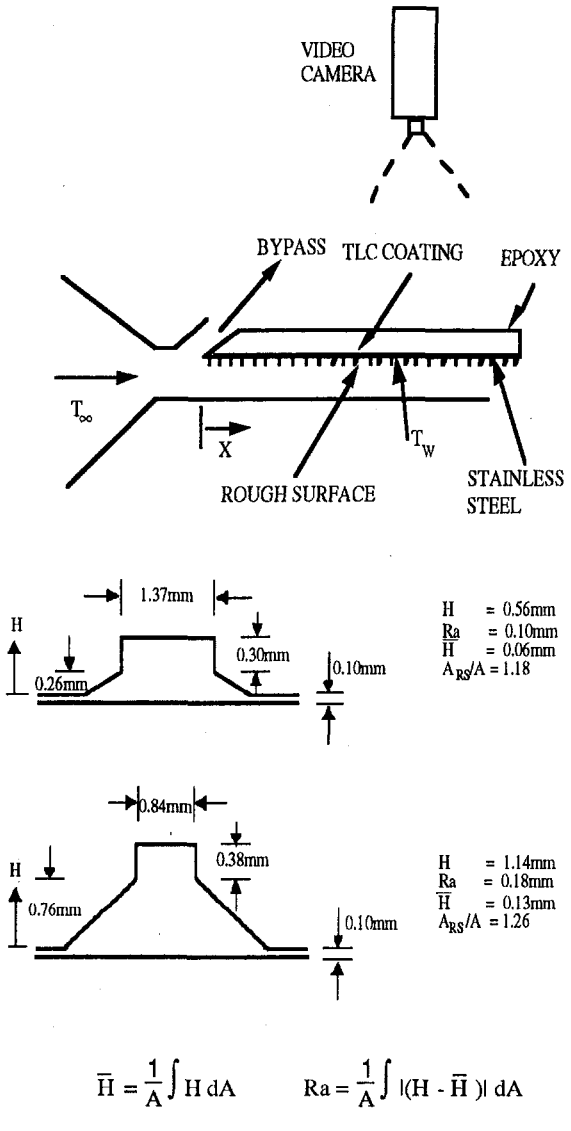

Fig. 2 Composite plate and roughness elements

the epoxy layer, which serves as a semi-infinite conduction medium. This approach provides a temperature time response just below the roughened surface, which is used to determine heat transfer coefficients. The local transient response is spatially averaged to provide relatively local coefficients smoothed on the order of twice the diameter of the roughness columns and in terms of engineering design work should prove valuable.

Metal etching was chosen as a means of producing the rough stainless steel surface. It provides accurate surface geometries and is capable of leaving a very thin surface on the order of 0.08 to 0.1 mm between the roughness elements. One disadvantage of metal etching, however, is the coning at the base of each element due to the acid used in the etching process eating away the manufacturing template. This effect is well modeled and was included in the design of the surface. In order to provide the desired Ra values, two rough surfaces are investigated in this study with absolute roughness heights (H) of 0.56 mm and 1.14 mm. Rough elements are spaced 3.05 mm apart in both spanwise and streamwise directions. However, because the rows are staggered, each element lies 6.1 mm directly downstream of a preceding rough element. A regular pattern (k_s-constant) was chosen so results could more easily be compared to an analytic prediction.

The roughest experimental surface (Ra = 0.18 mm) provides a rough surface on the right order of the roughness (Ra ~ δ_2)

found in operational airfoils under the correct Reynolds number conditions. The other rough surface (Ra = 0.10 mm) permits investigation of the trends of increasing roughness on convective heat transfer. These rough surfaces provide roughness Reynolds numbers (Re_k) greater than 70 over the entire plate under test conditions. This ensures that the roughness under investigation is in the fully rough region. With increasing roughness, the viscous sublayer becomes destabilized and at about $Re_k = 70$ disappears entirely (Kays and Crawford, 1980). At this point, viscosity is no longer a significant variable, and pressure drag becomes the primary mechanism by which shear stress is transmitted to the wall.

Finite difference work indicates that, while there is very little temperature drop across the stainless steel plate during a test run (less than 0.01°C for a 0.1 mm smooth surface and less than 0.14°C for the worst case Ra = 0.18 mm rough surface), there is a difference between the time it takes a Plexiglas test model and the composite test model subject to the same flow conditions to reach the TLC calibration temperature. This time difference exists because of the energy stored in the stainless steel, and thus a time lag is required to increase the stainless steel to the TLC calibration temperature. Specifically, the time that it takes the composite plate to reach the TLC calibration temperature is greater than that for the Plexiglas under the same conditions. Unfortunately, an analytical solution does not exist at present for a composite semi-infinite solid under transient conduction. Therefore, the following model is proposed, the value of which can be judged based on the finite difference results and experimental comparison of Plexiglas and composite plate tests under the same convective conditions presented in this work.

Since the temperature drop across the stainless steel is very small, the conduction in the epoxy semi-infinite solid beneath it can be solved for in the same method as that presented earlier for the Plexiglas model. Due to the energy that it takes to also raise the stainless steel to the TLC calibration temperature, the temperature time response is slower and this method leads to lower heat transfer coefficients when the semi-infinite solid equations are solved for the epoxy portion of the composite. The time lag, the difference between the time that the composite plate reaches the calibration temperature and the time a homogeneous epoxy model under the same conditions reaches the calibration temperature, can be estimated by a lumped capacitance calculation of the stainless steel portion of the composite plate. Since the stainless steel is nearly at a uniform temperature and the Biot number (Bi) is estimated to be less than 0.03 in all cases, where $Bi < 0.1$ is the standard criterion, a lumped capacitance correction is made to the standard semi-infinite solid solution. As presented in the finite difference section, the results are very good, predicting heat transfer coefficients within 1 percent for a smooth surface and within approximately 3 and 5.5 percent for the two rough surfaces. Based on finite difference calculations, this model under predicts the energy into the surface by about 3 percent for the Ra = 0.1 mm surface and about 5 percent for the Ra = 0.18 mm surface.

For this case, where the driving potential is in terms of the free stream temperature, the governing lumped capacitance solution is written as:

$$\frac{T_W - T_i}{T_\infty - T_i} = 1 - \exp\left[\frac{-hA_{RS}t}{V\rho c_p}\right] \tag{5}$$

Here A_{RS} is the wetted surface area of the rough stainless steel surface. Since true step changes in the applied fluid temperature are not possible and the free-stream temperature is a function of time, as was the case for the semi-infinite solid solution, an additional complication is introduced. This is again accounted for by modifying Eq. (5) through the use of superposition and Duhamel's theorem. The solution is then represented by

$$T - T_i = \sum_{i=1}^{N} U(t - \tau_i)\Delta T_\infty \tag{6}$$

where

$$U(t - \tau_i) = 1 - \exp\left(\frac{-h}{V\rho c_p} A_{RS}(t - \tau_i)\right) \tag{7}$$

The time lag correction to the semi-infinite solid solution is applied each time an h is determined in the data reduction. Again, the results of this model are the basis for the composite surface of this study and its success can be seen in the results.

Validation of the Model

The experimental method presented here shows excellent agreement with other experimental methods for obtaining local convection coefficients (Barlow, 1994). In reality, however, lateral conduction effects are present and must be assessed. The greater the gradients in heat transfer coefficient, the greater the significance of the lateral conduction. Lateral conduction in the solid surface smoothes the surface temperature distribution and can potentially reduce the ability of the experimental method to resolve steep variations in heat transfer at the surface. Vedula et al. (1988) used a finite element analysis to assess the effect of lateral conduction. In the present study, a finite difference code is written to assess the effects of lateral conduction in the composite surface and to evaluate the ability of the lumped capacitance model to account for the energy accumulated in the stainless steel during a transient test. Because of the thin stainless steel layer over the entire composite plate, the effects of lateral conduction will be more significant than is the case for a solid Plexiglas model.

The finite difference code written for this numerical analysis relies on a central differencing implicit code using an alternating direction scheme as presented by Patankar (1980). A harmonic mean is employed to model the thermal conductivity at the epoxy stainless steel interface. This technique is covered well in the literature and need not be repeated here. The two-dimensional code was written to permit evaluation of a flat surface or a rough surface. For the rough surface, the ratio of the wetted surface area to planar matches the rough composite plate used for testing. Because the surface convection coefficient distribution is two dimensional, the transient conduction below the surface is generally three dimensional. However, the largest gradient in temperature will be normal to the contours, and the effects of lateral conduction should be adequately described with a two-dimensional analysis correctly oriented. For the case investigated here, the grid runs in the flow direction.

In order to validate the composite plate model for a smooth plate, an h is imposed on the surface that matches that of a turbulent flat plate. The temperature response on the backside of the stainless steel, the location of the TLC layer in actual experiments, is used to back out h using the semi-infinite solid solution with and without the time lag (lumped capacitance) correction. This numerical experiment is carried out for 30 m/s and 50 m/s using two thicknesses of stainless steel, 0.08 mm and 0.13 mm. An example of the results is shown in Fig. 3. In each case, the addition of the lumped capacitance correction to the time that the TLC reaches its calibration temperature improves the model greatly. Even in the worst case of an imposed h corresponding to a free-stream velocity of 50 m/s, the backed out h with a stainless steel thickness of 0.13 mm is within 4 percent of the imposed values. The smooth composite surfaces, which are compared to the results from Plexiglas in the next section, are 0.1 mm thick.

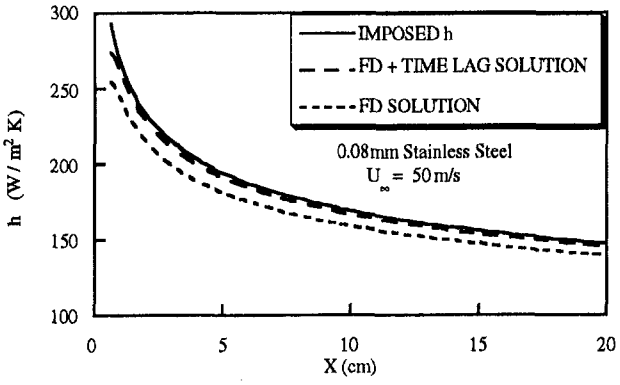

Fig. 3 Finite difference, composite plate model

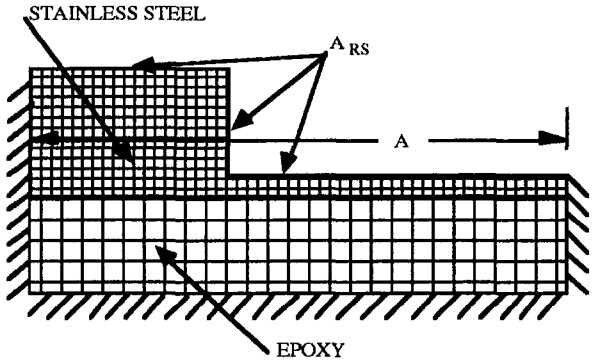

Fig. 5 Rough element numerical element

To experimentally assess the effects of using the composite region and the time lag correction to the semi-infinite solid, a series of identical tests was accomplished using both a Plexiglas and composite test piece. The associated line plot is given in Fig. 4. Clearly, as the finite difference work predicted, the model for the composite plate provides h values that compare well with those determined from the Plexiglas semi-infinite model.

Assessing the model for the rough composite plate is slightly more challenging. The code grid (Fig. 5) is set up to model the area ratio (A_{RS}/A) present for the two rough surfaces tested (A_{RS}/A = 1.18 and 1.26) and to have the same base stainless steel thickness (0.1 mm).

In this work, the reported heat transfer coefficient (h) is for the planar area (A) of the surface, not the wetted surface area (A_{RS}). This is done instead of reporting a convective heat transfer coefficient (h_{RS}) based on the wetted rough surface area where h is more useful to the engine designer who knows the planar area (A) but would have to estimate the wetted surface area of the rough surface (A_{RS}). A convenient result of the model, expounded upon in the theory section, is that the h determined in this method is naturally based on the planar area of the surface.

To assess the model and the use of the planar h, the following numerical experiment is run. For each roughness size a constant h is imposed on the wetted surface area. The transient experiment runs until each grid point on the stainless steel/epoxy interface reaches the calibration temperature of the TLC. As is done in processing the actual data, the time for this one roughness element area to reach the TLC calibration temperature is taken as the average time each grid point (each pixel for the actual experiments) reaches the TLC calibration temperature. From this time, an h is backed out using the semi-infinite solid solution with the lumped capacitance correction.

As expected, the roughness element does enhance the heat transfer, as Fig. 6 indicates. However, the ratio h_{RS}/h for each roughness element is less than the area ratio (A_{RS}/A) providing a fin effectiveness of less than unity. This is physically appropriate because the slight temperature gradients in the stainless steel, with hot spots near the corners of the rough element, result in a lower convection temperature potential for those areas.

To assess whether the calculated planar h models the enhanced heat transfer correctly, an energy storage calculation is accomplished. The time the interface reaches the TLC calibration temperature field in the composite is used to determine the total energy input since the start of the numerical experiment. For example, with the Ra = 0.18 mm surface and an imposed h_{RS} = 150 W/m²K, the total energy into the surface in 19.9 seconds is 160.9 J/m. The h for this experiment is 183.1 W/m²K or 22% greater than h_{RS}. At this point, the planar h of 183.1 W/m²K is imposed on a smooth composite plate with the same mass of stainless steel above the epoxy as for the rough surface. At 19.9 seconds the numerical experiment on the surface is stopped and again the energy into the surface calculated. The result is 153.7 J/m or 4.4 percent less than was actually imposed on the surface. This experiment was carried out for two cases of h_{RS} for each roughness. Table 1 shows that in each case a slight energy deficit occurs. The percent energy deviation provides an indication that h may be under determined by this model by 3 percent for the R = 0.1 mm surface and about 5 percent for the R = 0.18 mm surface.

Based on the comparison, both numerically and experimentally, made of h between data taken with the composite region and those taken with an all Plexiglas model, several conclusions for the experimental work to follow can be made. First, thermal gradients are not severe enough to cause lateral conduction to be a problem for the composite plate model. Second, heat transfer coefficients determined for the rough surfaces should be considered to have a negative bias as large as 5.6 percent. This bias is included in the experimental uncertainty analysis reported in the results section.

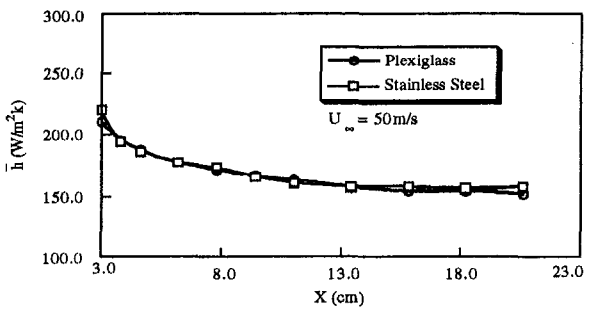

Fig. 4 Experimentally determined h, composite plate versus Plexiglas

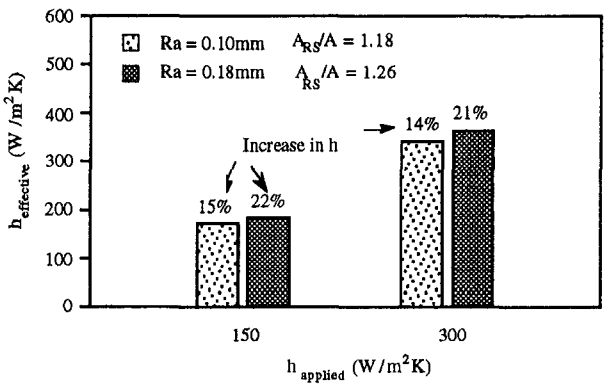

Fig. 6 Increase in heat transfer coefficient due to roughness, finite difference

Table 1 Finite difference, rough element energy deviation

Ra, mm	h_{RS}, W/m^{2}K	h, W/m^{2}K	A_{RS}/A	h_{RS}/h	% Deviation
0.10	150	173	1.18	1.15	-2.3
0.10	300	342	1.18	1.14	-3.1
0.18	150	183	1.26	1.22	-4.4
0.18	300	363	1.26	1.21	-5.6

Available Empirical Correlation

For an aerodynamically smooth surface, Reynolds analogy can be used to relate the convective heat transfer process to the shear stress at the wall. For a smooth surface, the primary mechanism for exchanging both momentum and energy in the turbulent boundary layer is through turbulent exchange. This leads to the equality of the momentum and energy diffusivities within the turbulent boundary layer (Reynolds analogy). For a rough surface, however, Reynolds analogy no longer applies. On a rough surface an apparent sheer stress is transmitted to the surface as the result of dynamic or pressure forces on the area normal to the flow direction, but there is no similar mechanism for heat transfer. The energy can be transferred by turbulent exchange down to the plane of the roughened elements, but the final energy transfer must be through the mechanisms of molecular conduction. The difference in primary mechanism requires a different mixing length model than that used for aerodynamically smooth law-of-the-wall developments.

The majority of studies of uniformly rough surfaces have been conducted for fully developed pipe and channel flows. In these cases, the determination of the skin friction coefficient is very straightforward and is directly related to the static pressure drop in the pipe. For flat surfaces in an external flow environment, the studies are much fewer. In fact, the only available empirical correlation relating flow conditions and surface roughness to surface heat transfer characteristics for flat plate "external" flow is one given by Kays and Crawford (1980):

$$\mathrm{St} = \frac{h}{\rho U_\infty c_p} = \frac{\frac{c_f}{2}}{\mathrm{Pr}_t + \sqrt{\frac{c_f/2}{\mathrm{St}_k}}} \tag{8}$$

In this correlation for Stanton number (St), Pr_t is turbulent Prandtl number and has been shown to be approximately constant for air with a value of 0.9 (Pimenta et al., 1975). c_f is the coefficient of friction, and St_k is the roughness Stanton number. Using a thermal-law-of-the-wall development and the experimental investigation of Dipprey and Sabersky (1963), Pimenta et al. (1975) developed the following correlation for St_k:

$$\mathrm{St}_k = \frac{h}{u_\tau c_p \rho} = C\,\mathrm{Re}_k^{-0.2}\,\mathrm{Pr}^{-0.44} \tag{9}$$

where u_τ is shear velocity

$$\frac{\tau_0}{\rho} = \frac{c_f u_\infty^2}{2} = u_\tau^2 \tag{10}$$

and Re_k is roughness Reynolds number

$$\mathrm{Re}_k = \frac{u_\tau k_s}{\nu} \tag{11}$$

C in Eq. (9) is an empirical constant and is a function of the rough surface geometry. For closely packed spheres, Pimenta et al. (1975) found a value for C of 1.0. k_s is equivalent sand roughness. In order to use this correlation for comparison to the experimental data, the shear velocity must be known at the downstream point where the comparison is made. In addition, the equivalent sand roughness must be determined.

To be able to assign appropriate qualities to these parameters, a boundary layer study was conducted. The boundary layer thickness, momentum thickness, and displacement thickness are determined for each plate at discrete locations downstream. In these cases, the thickness is given as a height above the average surface height ($\bar{H}$) as defined in Fig. 2. Boundary layer measurements were conducted with a Preston tube at locations between the roughness elements. Due to the close proximity of elements, hot-wire measurements proved to be impractical.

With the boundary layer thickness determined for each rough surface at 30 m/s and 50 m/s, it is possible to determine the shear stress at the wall from the appropriate form of the integral momentum equation and thus determine the shear velocity or friction coefficient at those locations.

$$\frac{\tau_0}{\rho U_\infty^2} = \frac{d\delta_2}{dX} + \delta_2 \left| \left(2 + \frac{\delta_1}{\delta_2}\right) \frac{1}{U_\infty} \frac{dU_\infty}{dX} \right| \tag{12}$$

The second term on the right-hand side takes into account the pressure gradient present in the investigated flows. For this work, this term is, in general, more than one order of magnitude smaller than the first term but is included for completeness. From Eqs. (12) and (10), c_f is determined at four downstream locations for each test.

Again, using a law of the wall logarithmic curve fit and the available experimental data, Pimenta et al. (1975) present the following empirical relationship for a rough surface in the fully rough region where no pressure gradient and no transpiration are present:

$$\frac{c_f}{2} = \frac{0.168}{\left[\ln\left(\frac{84\delta}{k_s}\right)\right]^2} \tag{13}$$

It is clearly realized that the law-of-the-wall curve fit will change and thus the correlation given by Eq. (13) if, as in the case of this study, a pressure gradient is present. However, as with the analysis of c_f using the momentum integral equation, the effect is expected to be small for the mild acceleration (<4 percent over the plate length) present in this study. This should provide a k_s of the right order and permit a general comparison between St given by Eq. (8) and the experimental results of this work.

Results and Discussion

Tests are conducted for each rough surface, Ra = 0.1 mm and Ra = 0.18 mm at free-stream velocities of 30 m/s and 50 m/s. In order to provide a more meaningful measure of the heat transfer into the wall in a given area, the coefficients presented are averaged over a roughened elements base area. The 7.62 cm by 20.3 cm rough surface of each composite plate has 1650 elements arranged in rows of 25 elements. This equates to 9.68 square millimeters of base area per element. The video frame grabber system is set up to average 16 pixels in a square pattern to arrive at the time each base area reaches the TLC calibration temperature. Based on experimental uncertainties and the negative bias found in the rough element finite difference work, uncertainties for the locally determined h values are −7 to +4 percent for the Ra = 0.18 mm plate and −6 to +4 percent for the Ra = 0.10 mm plate. The experimental uncertainties are estimated based on the single sample method of Kline and McClintock (1953). h values reported are obtained by laterally averaging the heat transfer coefficients at a given downstream location over the center half of the test surface (Figs. 7 and 8). Figures 9 and 10 provide the rough surface convective heat

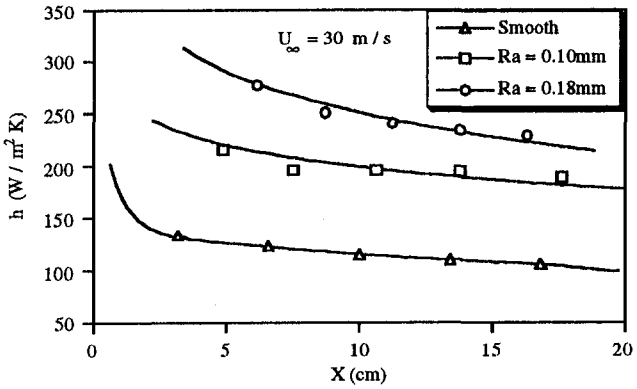

Fig. 7 h, effect of roughness, U_∞ = 30 m/s

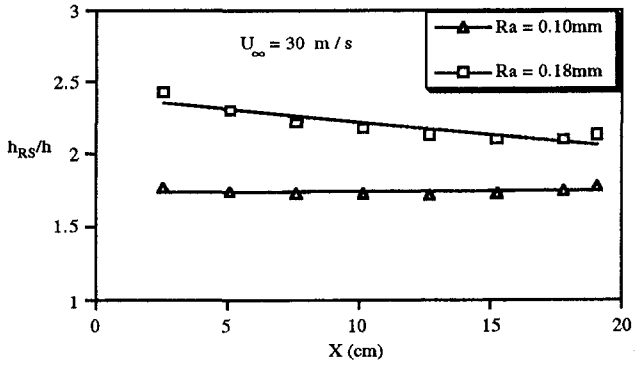

Fig. 9 h_{RS}/h, effect of roughness, U_∞ = 30 m/s

transfer coefficients normalized by the smooth surface coefficients.

It is clear a tremendous penalty is paid in terms of heat transfer to the surface for the increased roughness. For the Ra = 0.1 mm surface, the A_{RS}/A is 1.18 and the increase at both velocities is approximately 70 percent over the smooth surface (h_{RS}/h = 1.70). For the Ra = 0.18 mm surface, A_{RS}/A is 1.26 and h_{RS}/h is approximately 2.2 or over double the heat transfer rate into the surface.

The conclusion here is clearly that the increase in h is due to more than the effect of increased area. The energy transport in the boundary layer has been enhanced by the increased turbulence levels near the surface. As an example and shown in Fig. 11, the boundary layer velocity profile shows a greater momentum deficit near the surface for the rough surface as compared to the smooth surface. This corresponds to the higher drag present on the rough surfaces.

The effect of a rough surface is to thin the viscous sublayer at the wall surface. For $Re_k > 70$, the fully rough surface, the sublayer disappears entirely (Kays and Crawford, 1980). This means ϵ_H no longer goes to zero at the wall, and turbulent transport of momentum and heat is available all the way to the surface. This is in contrast to $Re_k < 70$ where the viscous sublayer, a layer close to the wall that is nearly laminar in nature, is present and turbulent transport is not significant ($\epsilon_H \approx 0$). The absence of the viscous sublayer and high ϵ_H near the wall account for the large increase in the convective heat transfer coefficient.

The profiles clearly indicate the higher momentum deficit present for the rough surfaces and correspond to a higher drag on the surface. By fitting a power law curve to the velocity profiles, momentum thickness and displacement thickness are determined for each case at four downstream locations, X = 22.2, 57.2, 87.4, and 112.8 mm. For a smooth turbulent plate a $\frac{1}{7}$ power low fits the data extremely well. For the Ra = 0.1 mm surface the power low is approximately $\frac{1}{4}$ and for the Ra = 0.18 mm surface approximately $\frac{1}{2.5}$. With this information, the friction coefficient at each downstream location is determined from Eqs. (12) and (10).

Using the boundary layer information for X = 63.5 mm and 87.4 mm where the rate of the change of boundary layer thickness is most accurately known, the k_s for each surface is backed out of Eq. (13). The results are k_s = 1.32 ± .2 mm for the Ra = 0.1 mm surface and k_s = 3.4 ± .5 mm for the Ra = 0.18 mm surface.

The variation in k_s appears to be large, but the effect on the empirical heat transfer coefficient and Stanton number calculated from Eq. (8) is less than 1 percent. This variation in k_s may be present because of the presence of high turbulence level and changing turbulence with downstream location. In this work, the higher k_s is associated with the 57.2 mm downstream location and the lower k_s with the 87.4 mm location. The work done by Schlichting (1936) to determine equivalent sand roughness was accomplished in a water tunnel with very low free-stream turbulence levels and a fully developed flow. Likewise, although this could not be confirmed, the work by Pimenta et al. (1975) was most likely accomplished in a low free-stream turbulence environment. The 4 percent increase in velocity through the present test region makes some variation in the results from Eq. (13) inevitable. The bottom line, however, is this variation has little importance on the predicted Stanton number, which is primarily a function of c_f at any given downstream location.

As far as the magnitude of k_s for each surface, it may initially appear strange these values are 2.4 and 3.0 times larger than the absolute height of the corresponding roughness element. However, a review of Schlichting's (1936) work indicates for densely packed spheres the ratio ks/k is as high as 3.8.

The Stanton numbers from Eq. (9) for the four test situations are matched against the experimental results in Fig. 12. The

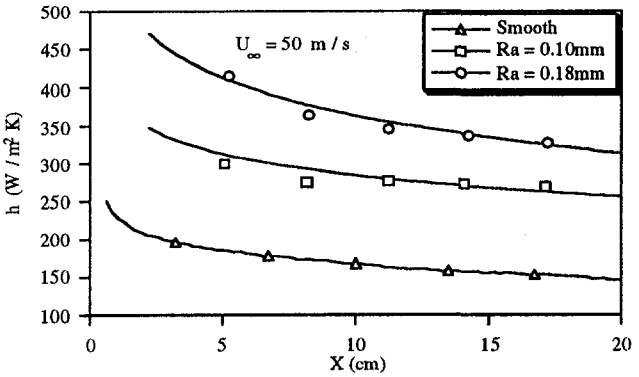

Fig. 8 h, effect of roughness, U_∞ = 50 m/s

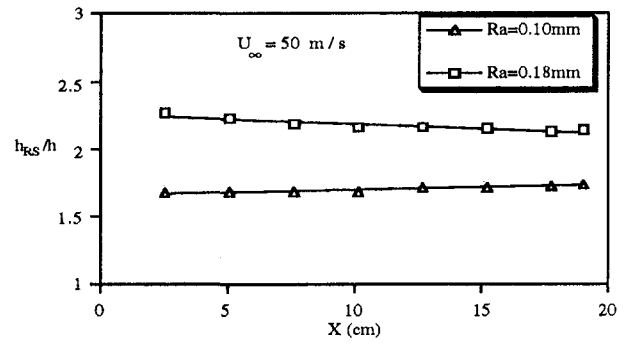

Fig. 10 h_{RS}/h, effect of roughness, U_∞ = 50 m/s

legend is coded where Ra 1V30 corresponds to the Ra = 0.1 mm surface at an entrance velocity of 30 m/s, etc.

In viewing these figures, the lowest Re_k of 171 appears for the Ra = 0.1 mm surface at a location 112.8 mm downstream of the splitter plate leading edge. This means the surface conditions of all tests are, as originally assumed, in the fully rough region. The comparison between experimental and empirical results are very good. The constant in Eq. (9) is left as 1.0 as per Dipprey and Sabersky (1963). This constant can be modified to provide a better match, as can the power coefficient on Re_k. This was not done for this comparison.

One trend to note in viewing Fig. 12 is the slopes of the empirical and experimental linear curve fits are consistently different. This is most likely because of the slight acceleration of the mainflow in the present experimental results. Equation (8) is developed for constant free-stream flow over a rough surface. In analyzing the data in Fig. 12 for each flow condition, the flow moves through the test model from high Re_k to lower Re_k values. At positions further downstream, the boundary layer thickness is smaller and the convection heat transfer coefficient higher than would be the case for a nonaccelerating flow.

Based on the match between the empirical and experimental data in this section, Eq. (8) would seem to be an excellent analytical tool for use in design work.

Closure

This study focuses on obtaining information on the effects of surface roughness on convective heat transfer characteristics for conditions present on the pressure side of a typical high performance first stage turbine vane. The present work presents the experimental apparatus and test model necessary to successfully extend liquid crystal techniques to a rough composite plate.

It is clear a tremendous penalty is paid in terms of heat transfer to the surface for increased roughness on the order of the smooth surface boundary layer momentum thickness. The Ra = 0.1 mm surface showed an increase in heat transfer of 70 percent over a smooth surface at the same flow conditions, while for the Ra = 0.18 mm (Ra ~ δ_2) surface this increase was as high as 120 percent. This increase in heat transfer was much greater than was the increased wetted surface area of the rough surfaces compared to the surface planar area. The conclusion here is the increase in h is due to more than the effect of increased heat transfer area. In this case, the energy transport in the boundary layer has been enhanced by the increased turbulence levels near the surface.

Experimental Stanton numbers compare well with those predicted by an empirical relationship presented by Kays and Crawford (1980). Based on this comparison, Kays and Crawford's (1980) empirical correlation for Stanton number appears to be an excellent analytical tool and, conversely, the empirical correlation tends to validate the experimental model used here.

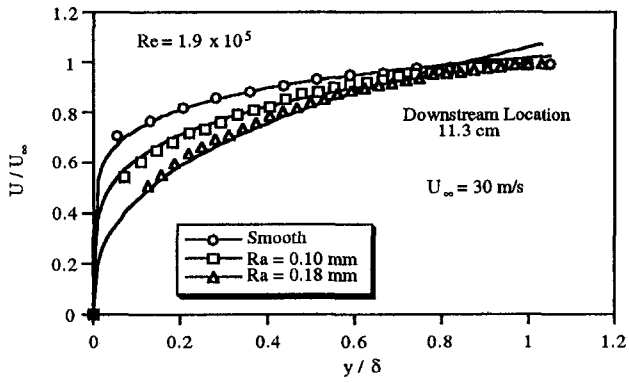

Fig. 11 Boundary layer velocity profile for rough surfaces, X = 112.8 mm, U_∞ = 30 m/s

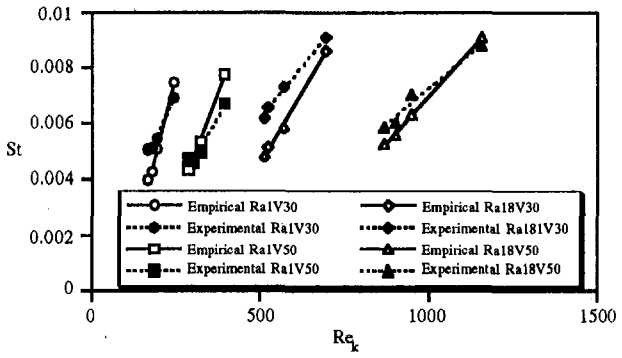

Fig. 12 Stanton number, experimental versus empirical

With the test method validated, this approach could now be applied to random rough surfaces (e.g., irregular rough element height and spacing) more representative of turbomachinery surfaces. It is unclear at this point that Ra values are the correct measure of roughness. Certainly, very different surfaces can have the same Ra values and yet would be expected to have quite different heat transfer and flow characteristics. For the present, quantifying the surface in terms of k_s seems appropriate for the uniformly rough surface. For the irregular rough surface, more representative of hot section surfaces, an appropriate figure of merit that describes roughness in terms of its effect on heat transfer and flow characteristics is not readily apparent but would benefit this area of study greatly.

Acknowledgments

The authors wish to pay their greatest respect to the late Professor Darryl E. Metzger for his guidance and friendship. It was his vision that motivated this effort. In addition, the authors appreciate the support of Matt Meininger of the Air Force Propulsion Laboratory and Martin Tabbitta of United Technologies for their help in determining appropriate test conditions.

References

Barlow, D. N., 1994, "Effect of Surface Roughness on Local Film Cooling Effectiveness and Heat Transfer Coefficients," Ph.D. Dissertation, Arizona State University.

Bonnett, P., 1989, "Applications of Liquid Crystals in Aerodynamic Testing," D. Phil Thesis, Oxford University.

Cooper, T. E., Field, R. J., and Meyer, J. F., 1975, "Liquid Crystal Thermography and Its Application to the Study of Convective Heat Transfer," ASME *Journal of Heat Transfer*, Vol. 97, pp. 442–450.

Dipprey, D. F., and Sabersky, D. H., 1963, *Int. J. of Heat and Mass Transfer*, Vol. 6, pp. 329–353.

Hippensteele, S. A., Russell, L. M., and Stepka, F. S., 1983, "Evaluation of a Method for Heat Transfer Measurements and Thermal Visualization Using a Composite of a Heater Element and Liquid Crystals," ASME *Journal of Heat Transfer*, Vol. 105, pp. 184–189.

Ireland, P. T., and Jones, T. V., 1985, "The Measurement of Local Heat Transfer Coefficients in Blade Cooling Geometries," AGARD Conference on Heat Transfer and Cooling in Gas Turbines, CP 390, Paper 28, Bergen.

Ireland, P. T., and Jones, T. V., 1987, "The Response Time of a Surface Thermometer Employing Encapsulated Thermochromic Liquid Crystals," *Journal of Physics E*, Vol. 20, pp. 1195–1199.

Jones, T. V., and Hippensteele, S. A., 1985, "High-Resolution Heat-Transfer-Coefficient Maps Available to Compound-Curve Surfaces Using Liquid Crystals in a Transient Wind Tunnel," *Developments in Experimental Techniques in Heat Transfer and Combustion*, ASME HTD-Vol. 71, Book No. H00390.

Kays, W. M., and Crawford, M. E., 1980, *Convective Heat and Mass Transfer*, McGraw-Hill Publishing Company, New York.

Kline, S. J., and McKlintock, F. A., 1953, "Describing Uncertainties in Single Sample Experiments," *Mechanical Engineering*, Vol. 75, Jan., pp. 3–8.

Mehendale, A. B., and Han, J. C., 1992, "Influence of High Mainstream Turbulence on Leading Edge Film Cooling Heat Transfer," ASME JOURNAL OF TURBOMACHINERY, Vol. 114, pp. 707–715.

Metzger, D. E., and Larson, D. E., 1986, "Use of Fusion Point Surface Coatings for Local Convection Heat Transfer Measurements in Rectangular Channel Flows With 90-Degree Turns," ASME *Journal of Heat Transfer*, Vol. 108, pp. 48–54.

Moss, R. W., and Oldfield, M. L. G., 1996, "Effect of Free-Stream Turbulence on Flat-Plate Heat Flux Signals: Spectra and Eddy Transport Velocities," ASME JOURNAL OF TURBOMACHINERY, Vol. 118, pp. 461–467.

Myers, G. E., 1971, *Analytical Methods in Conduction,* McGraw Hill, New York.

Nikuradse, J., 1933, "Stromunggesetze in rauhen Rohren," *Forschg. Arb. Ing. Wes.,* No. 361.

Ou, S., Mehendale, A. B., and Han, J. C., 1992, "Influence of High Mainstream Turbulence on Leading Edge Film Cooling Heat Transfer Effect of Film Hole Row Location," ASME JOURNAL OF TURBOMACHINERY, Vol. 114, pp. 716–723.

Patankar, S. V., 1980, *Numerical Heat Transfer and Fluid Flow,* McGraw-Hill, New York.

Pimenta, M. M., Moffat, R. J., and Kays, W. M., 1975, NASA Rep. No. HMT-21, Department of Mechanical Engineering, Stanford University.

Schlichting, H., 1936, "Experimental Untersuchungen zum Rauhigkeits-problem," *Ingenieur-Archiv,* Vol. 7, pp. 1–34.

Schlichting, H., 1979, *Boundary-Layer Theory,* McGraw-Hill, New York.

Tabbita, M. G., 1993, "Results of First Stage Turbine Vane Surface Roughness Investigation," Internal Correspondence, United Technologies Pratt & Whitney.

Tarada, F., and Suzuki, M., 1993, "External Heat Transfer Enhancement to Turbine Blading Due to Surface Roughness," ASME Paper No. 93-GT-74.

Vedula, R. P., 1989, "Film Cooling Effectiveness and Heat Transfer Measurements Using Thermochromic Liquid Crystals," Ph.D. Dissertation, Arizona State University, Tempe, AZ.

Vedula, R. P., Bickford, W., and Metzger, D. E., 1988, "Effects of Lateral and Anisotropic Conduction on Determination of Local Convection Heat Transfer Characteristics With Transient Tests and Surface Coatings," *Collected Papers in Heat Transfer,* ASME HTD-14, pp. 21–27.

Vedula, R. J., and Metzger, D. E., 1991, "A Method for the Simultaneous Determination of Local Effectiveness and Heat Transfer Distributions in Three-Temperature Convection Situations," ASME Paper No. 91-GT-345.

Wang, Z., Ireland, P. T., and Jones, T. V., 1990, "Technique for Measuring Convective Heat Transfer at Rough Surfaces," ASME Paper No. 90-GT-300.

The Influence of Large-Scale High-Intensity Turbulence on Vane Heat Transfer

F. E. Ames
Allison Engine Company,
Indianapolis, IN 46206

An experimental research program was undertaken to examine the influence of large-scale high-intensity turbulence on vane heat transfer. The experiment was conducted in a four-vane linear cascade at exit Reynolds numbers of 500,000 and 800,000 based on chord length. Heat transfer measurements were made for four inlet turbulence conditions including a low turbulence case ($Tu \cong 1$ percent), a grid turbulence case ($Tu \cong 7.5$ percent), and two levels of large-scale turbulence generated with a mock combustor at two upstream locations ($Tu \cong 12$ percent and 8 percent). The heat transfer data demonstrated that the length scale, Lu, has a significant effect on stagnation region and pressure surface heat transfer.

Introduction

Flow features such as high levels of combustor-generated turbulence, hot streaks, and secondary flows all contribute to the difficulty in assessing gas path heat transfer. Unfortunately, few studies exist where these features have been studied and comprehensively documented. Consequently, few heat transfer programs have included relevant and extensively documented inlet conditions.

The focus of this research is to examine the influence of turbulence on vane heat transfer across a relevant range of turbulence boundary conditions. In this study a range of turbulence scales and intensities have been generated and comprehensively documented at two exit Reynolds numbers. The resulting heat transfer from a vane has been determined and compared across these conditions.

Background. Turbulence has been found to have a strong effect on turbine airfoil stagnation region and pressure surface heat transfer. Arts et al. (1990) found a 100 percent increase in heat transfer on the laminar portion of a vane pressure surface for 6 percent grid turbulence. Yet, turbulence levels at the entrance to turbine nozzles can be much higher than 6 percent. Bicen and Jones (1986) measured turbulence levels, based on the bulk exit velocity, ranging from 13 to 20 percent using a model can-type combustor. Ames and Moffat (1990) measured turbulence levels ranging from 15 to 17 percent at the exit of a mock combustor with energy scales ($Lu = 1.5|u'|^3/\epsilon$) ranging from 33 to 50 percent of the exit height.

The component of turbulence normal to a surface is responsible for turbulent mixing in the normal direction and hence heat transfer augmentation. When the turbulent length scale (Lu or Lx) is large compared to the distance from the surface, the distance (or mixing length) the velocity scale will act will be proportional to the distance from the wall. Hunt and Graham (1978) calculated the response of turbulence near a flat surface and found that the normal integral scale, Ly, was proportional to the distance from the surface and that the normal component of turbulence, v', scaled on $y^{1/3}$. This response of Ly and v' near a surface is due to the blocking by the surface of the turbulent eddies, which are large compared to the distance from the surface. Thomas and Hancock (1977), investigating grid generated turbulence near a moving wall, closely corroborated Hunt and Graham's results. Ames and Moffat (1990) studied the influence of large-scale turbulence on turbulent boundary layer heat transfer and successfully used Hunt and Graham's results to develop a correlating parameter. Thole and Bogard (1995) provide a good review of this class of flows and compare several parameters, including Ames and Moffat's for correlating turbulence effects on heat transfer.

Turbulence approaching a stagnation region varies in its response compared to turbulence near a flat wall, but turbulent scale still has an important influence on heat transfer augmentation. Hunt (1973) calculated turbulence approaching a cylindrical stagnation region and found that, similar to a flat plate, the relatively large-scale eddies were blocked by the surface's presence. In addition, Hunt determined that relatively small eddies were amplified by the straining around the surface. Britter et al. (1979) measured turbulence approaching a cylinder and their results corroborate Hunt's earlier calculations. Ames and Moffat (1990) used Hunt's results to develop a correlating parameter for stagnation region heat transfer, which included the effects of energy scale (Lu) and correlated the influence of the large-scale turbulence they generated over a four to one range in diameters within ±4 percent. Van Fossen et al. (1995) studied the effect of integral scale, Lx, on stagnation region heat transfer to an elliptical and cylindrical leading edge and developed a correlation that included a strong dependence on integral scale.

Implications for Heat Transfer. Turbulence intensity and scale as well as characteristic Reynolds number have an important influence on heat transfer augmentation. The pressure surface of a vane subjected to the large-scale high-intensity turbulence of a combustor produces high levels of heat transfer augmentation. In order to develop accurate predictive capabilities for vane heat transfer, the influence of turbulence over a range of relevant characteristics and chord Reynolds numbers needs to be investigated.

The objective of this study was to investigate the influence of large-scale high-intensity turbulence on turbine vane heat transfer. In this study, two levels of mock combustor turbulence and one level of grid turbulence were generated and carefully characterized. The resulting heat transfer to a modern vane was determined. The development of the flow and turbulence through the passageway was characterized and is reported by Ames (1994). Also, the turbulence characteristics and growth of the vane wake were investigated and are reported by Ames (1994) and Ames and Plesniak (1995).

Contributed by the International Gas Turbine Institute and presented at the 40th International Gas Turbine and Aeroengine Congress and Exhibition, Houston, Texas, June 5–8, 1995. Manuscript received by the International Gas Turbine Institute February 3, 1995. Paper No. 95-GT-21. Associate Technical Editor: C. J. Russo.

Experimental Approach

The four vane cascade used in this study is connected to an in-draft blower. The blower is rated at 1.13 m^3/s (2400 scfm) with a pressure rise of 10.3 kPa (1.5 psia). The Plexiglas walled cascade was originally built by Zimmerman (1990) to facilitate three component laser anemometry measurements. The cascade airfoils are 4.5 times scale C3X vanes. The vane profiles are a two-dimensional slice from a first-stage nozzle for a helicopter engine. This vane geometry was previously used by Nealy et al. (1984) for determining heat transfer distributions in a warm cascade rig.

The arrangement of the four-vane cascade is shown schematically in Fig. 1. The cascade has a row of nine static pressure taps across two passages at the inlet, 3.68 cm upstream of the plane of the vane leading edges to monitor inlet static pressure uniformity. The cascade is also instrumented with a row of nine static pressure taps spanning two passages at the exit, 16.35 cm from the inlet plane or 9.37 cm axially downstream from the vane leading edges, to monitor exit static pressure uniformity. The inlet uniformity is set with bleed flow adjustments located below vane 1 and above vane 4. The exit flow uniformity is set by the tailboards, which pivot just downstream from the trailing edge of vanes 1 and 4. The inlet access ports, labeled 1 through 8, accommodated inlet total pressure, temperature, and hot-wire probes used to reference and survey the inlet conditions. The location of the inlet probe access plane is 3.68 cm upstream from the vane leading edge plane.

The coordinates for the 4.5 times scale C3X vane geometry are given by Nealy et al. (1984) and the vane is shown schematically in Fig. 2. The vane true chord length is 14.493 cm and the axial chord is 7.816 cm. The vane spacing is 11.773 cm and the passage has a throat of 3.292 cm. The diameter of the leading edge is 2.337 cm and the diameter of the trailing edge is 0.340 cm. The stagger angle of the vane is 55.47 deg and the calculated air exit angle is 72.4 deg. The height of the vane is 7.62 cm.

The cascade was run at exit Reynolds numbers based on chord length of 800,000 and 500,000 for this study. At sea level take off, exit Reynolds numbers of first-stage vanes would be about 800,000 for a small helicopter engine, could range from one to two million for a medium sized turboprop or turbofan engine, and could range to several million for a large turbofan engine. Exit Reynolds numbers at altitude cruise could easily be a factor of four smaller than these. Hence, the Reynolds numbers investigated in this study fall in the middle of the operating range for aircraft gas turbines.

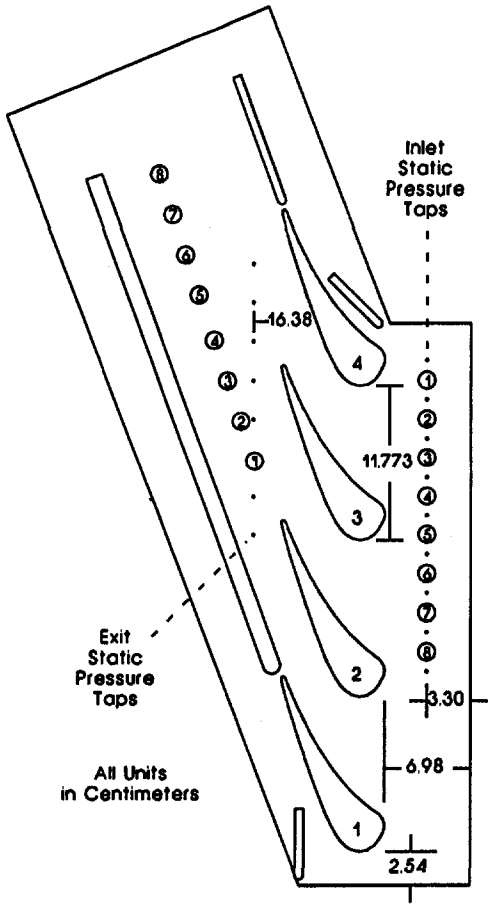

Fig. 1 Schematic of four-vane cascade

Turbulence Generators. Four inlet turbulence boundary conditions were developed for this study. The conditions consisted of a low-turbulence (1.1 percent) base case, a grid-generated turbulence case to produce a moderate level (7.8 percent)

Nomenclature

C = vane chord length, m
Cp = specific heat at constant pressure, J/kg/K
D = leading edge diameter, m
$E_1(k_1)$ = one-dimensional spectrum function for u', $E_1(k_1) = E_1(f)\ U/2\pi$
$E_2(k_1)$ = one-dimensional spectrum function for v', $E_2(k_1) = E_2(f)\ U/2\pi$
f = frequency, 1/s
h = heat transfer coefficient, $W/m^2/K$
k = thermal conductivity, W/m/K
k_1 = wavenumber = $2\pi f/U$
Lu = energy scale = $1.5\ |u'|^3/\epsilon$, m
Lx = longitudinal integral scale of turbulence, m
Ly = surface normal lateral integral scale, m
Ma_{ex} = Mach number based on exit conditions
Nu = Nusselt number = $h\ D/k$
Nu_0 = baseline Nusselt number in the absence of turbulence
P = pressure, Pa
P_s = static pressure, Pa
P_t = total pressure, Pa
Re = Reynolds number
Re_{ex} = exit Reynolds number = $\rho_{ex}\ U_{ex}\ C/\mu$
St = Stanton number = $h/\rho_{ex}\ U_{ex}\ Cp$
St_0 = baseline Stanton number in the absence of turbulence
T = temperature, K
Tu = turbulence intensity = u'/U_∞
Tu_v = normal component turbulence intensity = v'/U_∞
Tu_0 = turbulence level at reference position
U = streamwise velocity, m/s
u' = rms streamwise fluctuation velocity, m/s
v' = rms normal fluctuation velocity, m/s
w' = rms spanwise fluctuation velocity, m/s
X = streamwise distance along the airfoil, m
Y = normal distance from the surface, m
ϵ = turbulent dissipation, m^2/s^3
μ = dynamic viscosity, Pa s
ρ = density, kg/m^3

Subscripts

∞ = references to free-stream conditions
ex = references to exit static pressure tap plane location
in = references to inlet static pressure tap plane location

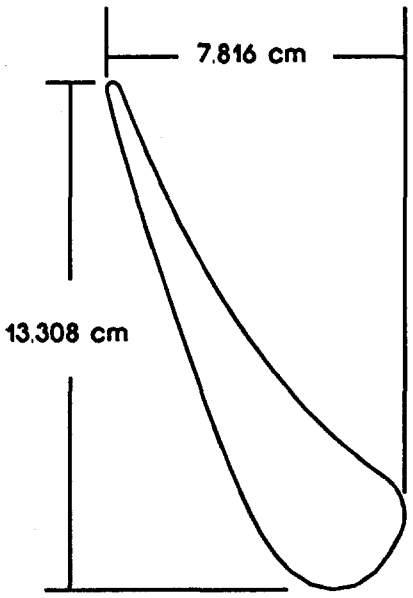

Fig. 2 C3X vane geometry

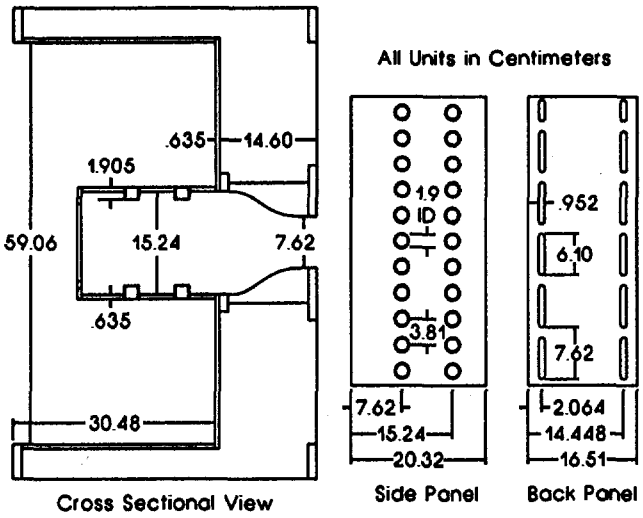

Fig. 3 Schematic of combustor turbulence generator

of relatively small scale (Lu = 1.36 cm) turbulence, and two cases with simulated combustor turbulence to produce a moderate and high level (8.3 and 12.0 percent) of relatively large scale (Lu = 4.26 cm and 3.36 cm) turbulence. The inlet geometry for the low-turbulence condition consisted of an inlet filter to remove dust from the air, two nylon screens to reduce the inlet velocity fluctuations, an eight-to-one two-dimensional contraction nozzle to reduce the level of the streamwise turbulence intensity, and a 25.4-cm-long, 7.62-cm-wide by 42.54-cm-high rectangular section, which was used to connect the two-dimensional nozzle to the cascade.

The inlet geometry for the grid-generated turbulence was the same as the low-turbulence case, except that a grid was installed in the rectangular section. The grid was fabricated from 0.317 cm square steel bars, with a spanwise spacing of 1.524 cm and a pitchwise spacing of 1.588 cm, producing a 63 percent open area grid. The grid was positioned 12.7 cm upstream from the cascade inlet to document the inlet turbulence characteristics at a position 16 cm downstream from the grid. The forward position at 8.9 cm upstream of the cascade inlet, which was in turn 6.98 cm upstream from the vane leading edge plane, placed the grid 15.9 cm upstream from the leading edge of the vanes. The grid was placed in the forward position for all measurements except for documentation of the grid inlet conditions.

A schematic of the simulated combustor is shown in Fig. 3. Air enters at ambient conditions into a 59.06 cm wide by 42.54 cm high plenum, where it is directed through the rear and side panels of the simulator liner. The flow through the back panel slots combines with flow through the first row of holes in the side panels to create a recirculation zone inside the simulator liner. The second row of holes in the side panels simulate dilution jets. The simulator undergoes a two-to-one contraction from the liner into the inlet of the cascade through a 15.24-cm-long nozzle. The flow produced by the rectangular mock combustor is very much like a two-dimensional representation of the flow in a typical annular combustor and the resulting turbulence level and scales are believed to be representative of current technology combustors. While the flow in this mock combustor lacks the density gradients generated by combustion, this mock combustor, like a real combustor, has a relatively long residence time compared to the exit turbulent time scale. The relatively long residence allows time for the small-scale turbulence to decay, leaving only the large energetic motions and the turbulent energies cascading from them. Thus, both mock and real combustor will have energy scales, Lu, that are proportioned on the exit height of the combustor.

The configuration, with the combustor simulator closely attached to the cascade inlet, is referred to as the "close combustor" or comb(1) configuration. The second combustor simulator configuration, referred to as the "far combustor" [comb(2)], adds the 25.4-cm-long rectangular spool between the combustor simulator and the cascade inlet. With the spool section between the simulator and cascade, the combustor-generated turbulence has sufficient time to decay to a level similar to that of the grid turbulence. A more complete description of the turbulence generators, the cascade, and the inlet conditions is given by Ames (1994).

Vane Pressure Distribution. The baseline pressure distribution for the low-turbulence case is given in Fig. 4. The measured pressure distribution, shown with symbols, is compared to a numerical prediction based on a compressible stream function formulation. The analysis assumes the air exit angle is 72 deg. In general, the predicted and measured distributions compare well. The small differences between the predicted and measured pressure distributions are most likely due to the idealizations used in the stream function analysis. For example, the stream function analysis does not account for blockage due to development of the suction and pressure surface boundary layers, separation at the trailing edge, or the separation bubble on the suction surface.

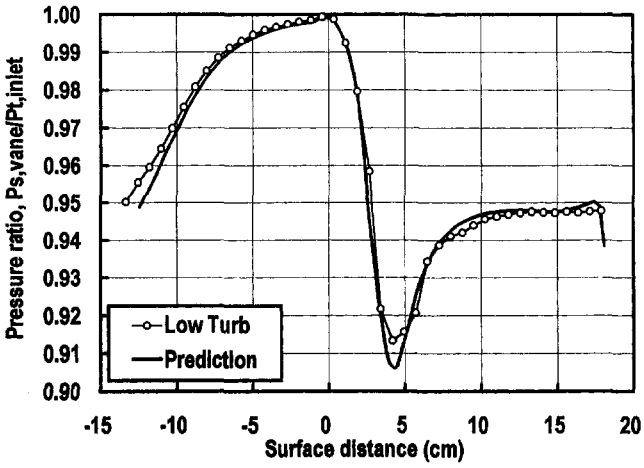

Fig. 4 Comparison of measured and predicted pressure profiles

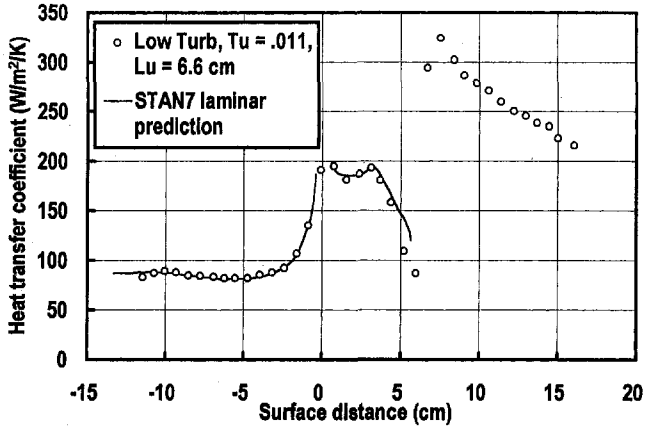

Fig. 5 Comparison of baseline heat transfer test with STAN7, Re_{ex} = 780,000

Heat Transfer Vane Description. The solid epoxy vane used for the heat transfer measurements had fine-gage chromel-alumel thermocouples cast into the surface. The vane was covered with a 0.025-mm-thick Inconel foil used to generate a constant surface heat flux. The heating started at 1 cm from the trailing edge on the pressure surface and ended at 1.45 cm from the trailing edge on the suction surface. Prior to the beginning of heating, the foils were connected to a 0.254-mm-thick and 6.35-mm-wide copper bus bar using resistance welding. A shallow indentation was milled in the airfoil surface to accommodate the bus bars. The Inconel foil was bonded to a 0.127 mm Kapton backing material. The Kapton was adhered to the airfoil surface using a high-temperature acrylic adhesive. The resulting vane surface was aerodynamically smooth and visually attractive.

A heat transfer baselining test was conducted at the low-turbulence condition. The procedure included running the test without heating to obtain the recovery temperatures along the vane. Next, the test was conducted with the vane heated. The thermocouple temperatures for the heated case were input into the finite element analysis. The FEA analysis provided the extra surface normal heat flux due to conduction through the epoxy vane and the surface temperature, which was extrapolated from the vane thermocouples. The heat transfer coefficient was determined from the net surface heat flux and the surface-to-recovery temperature difference. The net heat flux was determined from the foil heat flux plus the conduction heat flux less the radiative heat flux. The radiation loss was estimated by assuming the emissivity of the foil was 0.2 [based on polished Inconel, Siegel and Howell (1981)] and that the foil was radiating to a black body with a temperature equal to the inlet air. The radiative loss was estimated to be no more than 1.5 percent of the total heat flux for the baselining test. A comparison between the experimentally determined heat transfer coefficient and a heat transfer coefficient determined from the measured pressure distribution and a finite difference boundary layer calculation [STAN7, Kays (1987)] is shown in Fig. 5. The comparison on the pressure surface and the laminar part of the suction surface is excellent. The variation at the start of the stagnation point is probably due to the difference between the actual velocity and temperature distributions and the ones input into the boundary layer code. On the suction surface, as the boundary layer develops along the adverse pressure gradient, the code calculates boundary layer separation and cannot continue. The calculated point of separation appears to be near the point where the vane has a laminar separation and then transitions. This comparison between the calculated and predicted heat transfer coefficients along the vane agrees within ±5 percent and gives confidence in the experimental technique. The low-turbulence heat transfer tests were repeated at both the same and a reduced surface heat flux and showed good agreement.

Data Acquisition and Reduction. This experiment used a PC-based data acquisition system. Pressure measurements were made using a Scanivalve and two 6.9 kPa (1 psid) pressure transducers calibrated against an AMETEK dead weight tester. Steady state voltage signals were integrated over 1 power line cycle using an HP digital multimeter with 100 nanovolt sensitivity and 2.5 microvolt accuracy and were averaged over 10 readings. Signals were multiplexed using an HP scanner. The hot-wire signals were collected using an Analog Devices RTI-860 board with simultaneous sample and hold capability and a 200 kHz throughout (50 kHz per channel in simultaneous mode). The hot wires were powered with two DISA 55M system constant-temperature anemometer bridges. The hot-wire signal was biased and amplified to take advantage of the full 12 bit resolution of the data acquisition card. The probes were calibrated against a low free-stream turbulence jet and the calibration was fit to a fourth-order polynomial. Jorgensen's decomposition [see Frota (1982)] was used to determine the instantaneous velocity vector.

Data Uncertainties. The data uncertainties were estimated based on the root mean square method [see Kline and McClintock (1953)]. Determination of total pressure resulted in an absolute uncertainty of about one percent at the inlet and about 0.25 percent at the exit. Determination of the velocity from the pressure at the inlet and exit had an uncertainty of about 2 percent due to the uncertainty in the local static pressure. The mean velocity as determined by single wire had an uncertainty of about two percent. The single largest source of uncertainty in U was due to room temperature variations, which could range by as much as 9°C during some days. The response of the hot wire due to this temperature change was compensated for. The change in anemometer voltage due to the variation in the electronics temperature was not compensated for. The uncertainty in the turbulence level determined from the single wire was estimated to be about 3 percent. The X-wire velocity had an uncertainty of about 3 percent due to random fluctuations, room temperature variation, and errors due to binormal fluctuations (w') [see Wubben (1991)]. The estimated uncertainty in u' and v' was 4 percent for the X-wire. The absolute uncertainty of the heat transfer data was estimated to be ±5 percent. The relative uncertainty of the experimental data was estimated to be ±2.4 percent for run-to-run comparisons.

Inlet Conditions and Turbulence Characteristics. The cross-span distributions of total pressure, velocity, turbulent components, and spectra were taken at circumferential locations 2 and 6 (see Fig. 1). The root mean square variations in total pressure in the central 3 cm of the 7.62 cm span were 0.3, 1.0, 1.0, and 2.8 percent for the low turbulence, comb(1), comb(2), and grid conditions, respectively. Single wire surveys determined that the turbulence levels based on u' were 1.0, 12.8, 8.6, and 7.8 percent for the low turbulence, comb(1), comb(2), and grid condition. Based on X-wire surveys, the ratios of v'/u' for the comb(1), comb(2), and grid conditions were 1.18, 1.09, 1.04. Since the grid was positioned 16 cm upstream from the probe for the turbulence measurements and 15.9 cm upstream from the leading edge for taking the heat transfer data, no correction for decay was needed. For the comb(1) and comb(2) configurations, which allowed for 3.68 cm of decay from the measuring location to the vane leading edge plane, the following method can be used to estimate the decay over this short distance (Ames, 1994):

$$\mathrm{Tu}(X) = 1/[1/\mathrm{Tu}(0) + X/(2Lu)]$$

Records of streamwise velocity versus time were taken to characterize the turbulence scales and dissipation. Forty files of

Table 1 Inlet turbulence characteristics

Condition	Tu	U, m/s	Lx, cm	Lu, cm	ϵ, m^3/s^2
Low turbulence	.011	29.6	5.11	6.64	0.74
Low turbulence	.009	19.3	8.50	18.7	0.045
Comb(1)	.129	29.5	1.70	3.36	2460
Comb(1)	.134	19.5	1.56	3.16	840
Comb(2)	.086	29.3	2.10	4.26	562
Comb(2)	.083	19.3	2.08	4.34	143
Grid	.078	30.5	1.15	1.36	1482
Grid	.075	19.4	1.10	1.10	415

8192 points were taken, analyzed using a fast Fourier transform (FFT) algorithm, and averaged to obtain the one-dimensional spectrum of u' at each location. The spectrum, in log coordinates, was fit to a $-5/3$ slope over the inertial subrange to obtain an estimate for the dissipation, ϵ, using the following relationship [see Ames and Moffat (1990)]:

$$E_1(k_1) = 1.62(18/55)\epsilon^{2/3}k_1^{-5/3}$$

The value for dissipation was then used to estimate a scale, Lu ($Lu \equiv 1.5|u'|^3/\epsilon$), which represents the average size of the energy-containing eddies and is called the energy scale in this paper. Hancock and Bradshaw (1983) use Lu to correlate skin friction but refer to it as the dissipation scale. In addition to Lu, the longitudinal integral scale was determined. First, the autocorrelation in time was calculated using an inverse FFT and the integral time scale was determined by integrating to the first zero crossing. The longitudinal integral scale was estimated by multiplying the integral time scale by the local velocity (Taylor's hypothesis). The inlet averaged values of velocity (U_∞), integral scale (Lx), energy scale (Lu), and dissipation (ϵ) are given in Table 1 for the four turbulence conditions and the two exit Mach numbers (0.27 and 0.17).

One-dimensional spectra were also determined similarly for X-wire data and generally agreed well with the single wire data. Figure 6 compares the one-dimensional spectra of the u' and v' components of turbulence for the close combustor condition. In the inertial subrange, isotropic relations yield that $E_2(k_1) = 4/3\ E_1(k_1)$ (Hinze, 1975). All the single point, two component, inlet spectra match this relationship within 9 percent, indicating the smaller scale eddies show isotropy within experimental accuracy.

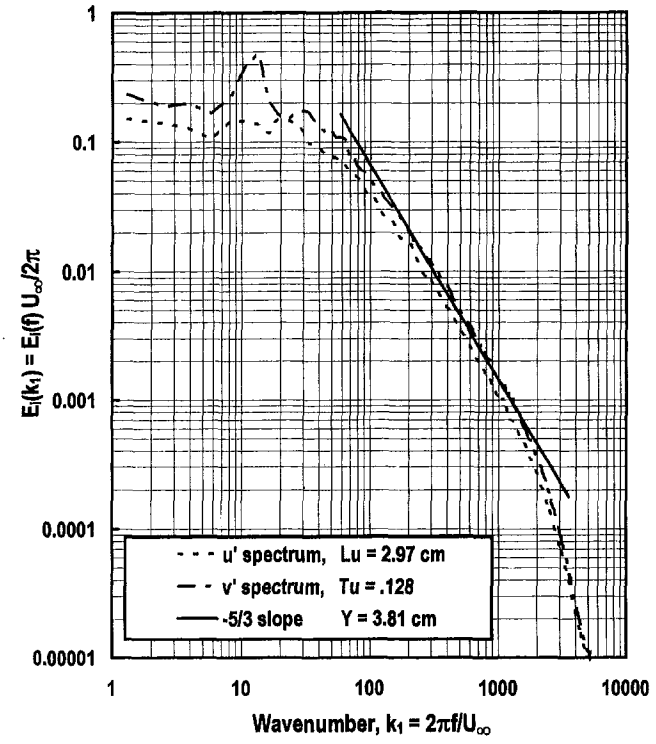

Fig. 6 One-dimensional spectra of u' and v' for comb(1) showing inertial subrange isotropy

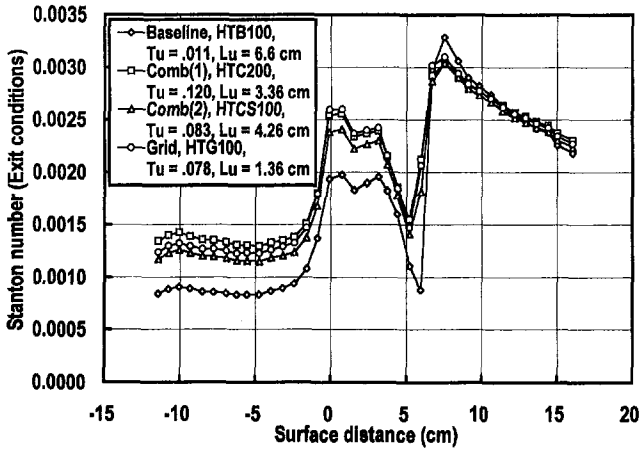

Fig. 7 Effects of turbulence on Stanton number distribution, Re_{ex} = 790,000

Heat Transfer Results

This section examines the influence of turbulence level and scale on vane heat transfer. First, the results of three turbulence cases are compared in terms of Stanton number for the two different Reynolds numbers. Next, the data are examined in terms of Stanton number augmentation comparing the three turbulence levels at constant Reynolds number and then comparing the effect of Reynolds number on the three turbulence cases. Finally, the data are compared in terms of the absolute augmentation of the heat transfer coefficient.

Stanton Number Results. The heat transfer data for the highest Reynolds number comparing the four turbulence conditions are shown in Fig. 7. The elevated turbulence data show a substantial augmentation over the low-turbulence baseline case throughout the region where the boundary layer is laminar. This laminar region includes the stagnation region, all of the pressure surface, and the favorable pressure gradient portion of the suction surface. The main effect of the turbulence on the suction surface is to cause the boundary layer to transition at an earlier location. Based on our low-turbulence laminar calculation for the suction surface, the transition is due to a laminar separation for the low-turbulence case. For the three elevated turbulence cases, the transition occurs earlier and the laminar heat transfer prior to that location is also elevated above the low-turbulence case. These observations suggest there is no laminar separation occurring for the elevated turbulence cases. Other evidence of a laminar separation for the low-turbulence condition includes a measured momentum thickness on the suction surface [reported by Ames and Plesniak (1995)], which is 20 percent thicker than the high turbulence cases. A comparison of the Stanton numbers for the turbulent portion of the suction surface shows only a mild increase in Stanton number. Due to the large turbulence scales of this experiment relative to the thin airfoil boundary layers, the turbulence produces only a small enhancement to the turbulent boundary layer. This observation is consistent with Ames and Moffat (1990) who showed that relatively large-scale turbulence has a significantly reduced effect on thin flat plate turbulent boundary layers.

The Stanton number data near the stagnation region of the vane show that the grid turbulence has a slightly higher augmen-

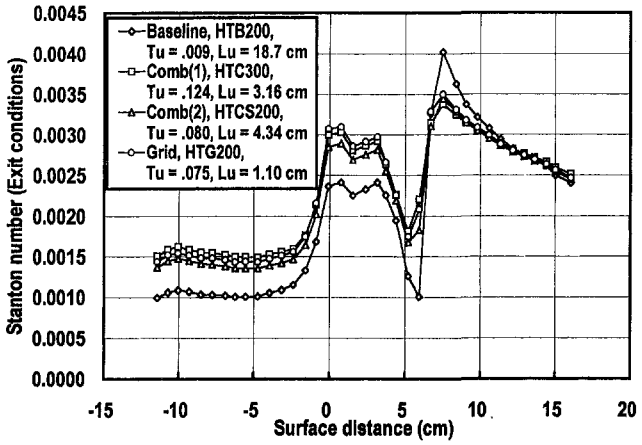

Fig. 8 Effects of turbulence on Stanton number distribution, Re_{ex} = 510,000

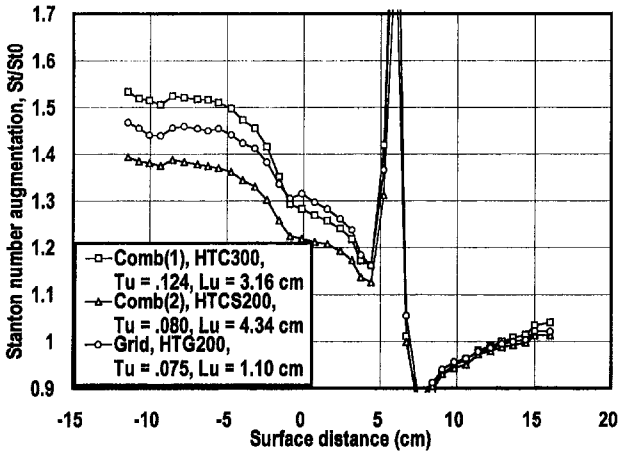

Fig. 10 Influence of turbulence on heat transfer augmentation, Re_{ex} = 510,000

tation than the close combustor [comb(1)] condition and a significantly higher augmentation than the far combustor condition [comb(2)]. Over the pressure surface, the increase in Stanton number due to the grid turbulence is significantly greater than the far combustor condition but lower than the close combustor condition. The legend of Fig. 7 gives values for the inlet turbulence level and scale for the four turbulence conditions showing that the grid has a lower turbulence level and smaller scale than the two combustor turbulence conditions. This result confirms that in addition to turbulence level, the turbulence scale has an important influence on heat transfer.

The heat transfer data for the lowest Reynolds number comparing the four turbulence conditions are shown in Fig. 8. The results are very similar to the results shown in Fig. 7. The main difference between the results is that the lower Reynolds number data have a lower level of augmentation. The transition occurs at about the same location as the higher Reynolds number cases because the suction surface transition on this vane is driven by the adverse pressure gradient.

The level of augmentation to Stanton number relative to the low turbulence case is shown in Fig. 9. The augmentation to the turbulent boundary layer on the suction surface is relatively small. The Stanton number augmentation on the leading edge, shown at 0.0 cm surface distance, ranges from about 25 percent for the far combustor position to about 36 percent for the grid. For the close combustor condition, the augmentation over the pressure surface exceeds 60 percent for most of the surface. The grid and far combustor conditions also produce a high level of augmentation on the pressure surface but lower than the close combustor condition. Figure 10 shows the same comparison for the lower Reynolds number cases.

The ability to predict stagnation region heat transfer is important to the reliability and efficiency of cooled vanes and blades. Ames and Moffat (1990) give a correlation for stagnation region heat transfer with high free-stream turbulence. A good engineering approximation to their correlation is given below:

$$\mathrm{Nu}/\mathrm{Re}_D^{1/2} = 0.95 + 0.038\ \mathrm{Tu}\ \mathrm{Re}_D^{5/12}(Lu/D)^{-1/3}$$

An estimate for the augmentation in the stagnation region can be made by dividing the correlation through by 0.95, the zero-turbulence value of $\mathrm{Nu}/\mathrm{Re}_D^{1/2}$ for air:

$$\mathrm{Nu}/\mathrm{Nu}_0 = 1 + 0.04\ \mathrm{Tu}\ \mathrm{Re}_D^{5/12}(Lu/D)^{-1/3}$$

Using the baseline Stanton number, inlet velocity, and vane leading edge diameter, the correlation predicted the stagnation region Stanton number of the vane within 5 percent for the three turbulence conditions and both Reynolds numbers as shown in Fig. 11.

Based on the work of Ames and Moffat, for a given geometry and Reynolds number, the increase in heat transfer should scale on the relative value of the free-stream dissipation rate to the one-third power (or equivalently $\mathrm{Tu}_\infty\, Lu_\infty^{-1/3}$) provided the turbulent Reynolds number is high enough to support a well-developed inertial subrange. Figure 6 shows the turbulence generated by the combustor simulator for this study passes this criterion.

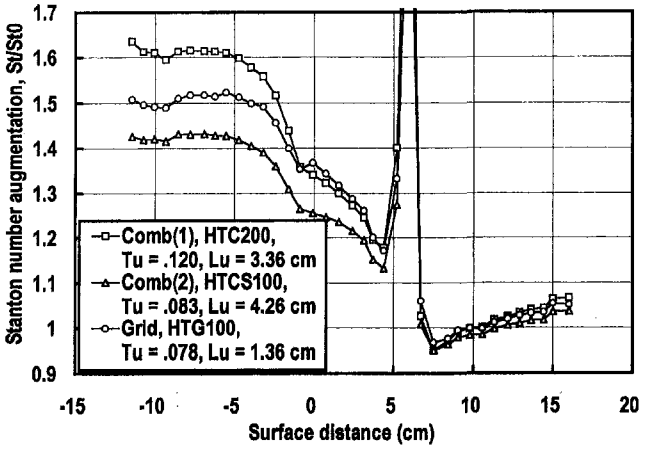

Fig. 9 Influence of turbulence on heat transfer augmentation, Re_{ex} = 790,000

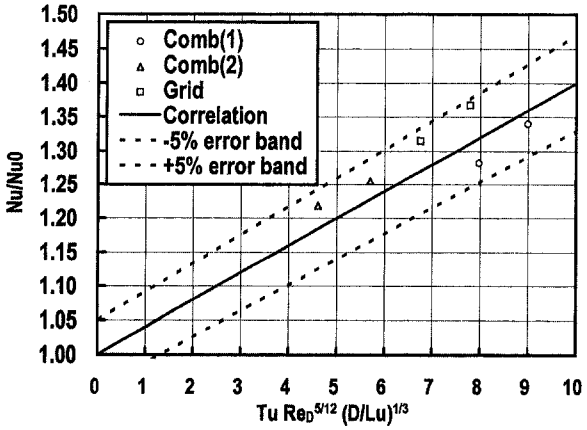

Fig. 11 Correlation of stagnation heat transfer increase

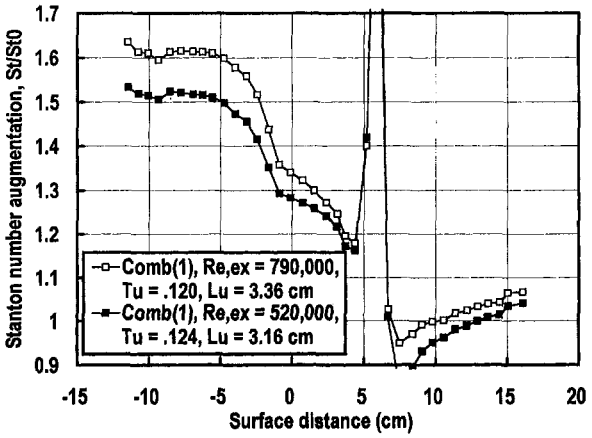

Fig. 12 Influence of Reynolds number on heat transfer augmentation, comb(1)

This $Tu_\infty\ Lu_\infty^{-1/3}$ scaling idea can be used to compare the relative level of augmentation observed to the level estimated by this formula. The average augmentation for the close combustor conditions was 55.6 percent over the entire pressure surface based on the average of local values of augmentation. The grid condition had an average pressure surface augmentation of 47.8 percent, which was 86 percent of the close combustor augmentation compared with an estimate based on $Tu_\infty\ Lu_\infty^{-1/3}$ of 88 percent. The far combustor condition had an average pressure surface augmentation of 38.9 percent or 70 percent of the close combustor augmentation compared to an estimate based on $Tu_\infty\ Lu_\infty^{-1/3}$ of 64 percent. For the lower Reynolds number, the average pressure surface augmentation for the close combustor was 46.4 percent. The low-Reynolds-number grid condition had an average pressure surface augmentation of 41.8 percent or 90 percent of the close combustor condition compared to an estimate of 86 percent. The low Reynolds number far combustor condition had an average augmentation of 34.2 percent, which was 73 percent of the close combustor average compared to an estimate of 58 percent. The relative augmentation estimated by $Tu_\infty\ Lu_\infty^{-1/3}$ generally falls within the uncertainty band of the experiment and supports this scaling argument.

Reynolds number also has an important effect on heat transfer augmentation to a laminar boundary layer. Figure 12 shows the augmentation for the close combustor condition at the two Reynolds numbers. This comparison is similar for the other two turbulence conditions. The influence of Reynolds number on the relative augmentation is clear from this presentation. The data for the three elevated turbulence conditions at the two Reynolds numbers allow an opportunity to estimate the Reynolds number dependence of the relative augmentation. Assuming the form $(St/St_0 - 1) \propto Re_{ex}^m$ with $Tu\ Lu^{-1/3}$ held constant, the Reynolds number dependence of the grid is 0.306, for the close combustor the dependence is 0.413, and it is 0.294 for the far combustor. This dependence on Reynolds number averages to be 0.34. Based on the analysis of Ames and Moffat, the stagnation region augmentation should scale on the $\frac{5}{12}$ power of Reynolds number. Similar reasoning for a flat plate laminar boundary layer suggests augmentation ought to depend on the $\frac{1}{3}$ power of Reynolds number. These data show a dependence ranging from 0.294 to 0.413 and averaging 0.34, which is closer to the flat plate dependence.

The reliability of the turbulence augmentation and Reynolds number scaling arguments can be tested by assuming $(St/St_0 - 1) \propto Tu\ Re_{ex}^{1/3}\ Lu^{-1/3}$ and checking the mean pressure surface augmentation. The results of this check are summarized in Table 2. The predictions are all scaled against the comb(1) condition at the high Reynolds number. The mean Stanton number augmentation ratio agrees within ±4 percent of the estimated value.

Table 2 Pressure surface heat transfer scaling

Condition	Re_{ex}	Tu	*Lu*, cm	St/St_0	Pred
Comb(1)	794,625	.120	3.36	1.556	
Comb(2)	791,033	.083	4.26	1.389	1.355
Grid	778,606	.078	1.36	1.478	1.485
Comb(1)	523,626	.124	3.16	1.464	1.510
Comb(2)	517,309	.080	4.34	1.341	1.294
Grid	506,077	.075	1.10	1.418	1.434

Absolute Heat Transfer Augmentation. The absolute level of augmentation can be determined by subtracting the baseline heat transfer coefficient from the heat transfer coefficient determined for a particular turbulence condition. This absolute increase in the heat transfer coefficient is shown in Fig. 13 for the higher Reynolds number condition. The stagnation region shows the highest absolute increase in the heat transfer coefficient except at the point of early transition. The absolute augmentation on the pressure surface is about 25 to 35 percent lower than the peak increase in the stagnation region. The absolute levels of augmentation for the lower Reynolds number tests have similar trends to those shown in Fig. 13 but are about 30 percent lower.

Conclusions

The present data demonstrated that the length scale, *Lu*, has a significant effect on stagnation region and pressure surface heat transfer. The average heat transfer augmentation from the pressure surface at a constant Reynolds number was found to scale on the one third power of the relative level of dissipation, $\epsilon^{1/3}$, or equivalently the inlet value of $Tu_\infty Lu_\infty^{-1/3}$. The stagnation region heat transfer correlated well on the $Tu\ Re_D^{5/12} \times (Lu/D)^{-1/3}$ parameter of Ames and Moffat. The dependence of heat transfer augmentation on Reynolds number was estimated to scale on the $\frac{1}{3}$ power for the pressure surface. The absolute level of heat transfer coefficient was found to be highest near the stagnation region and declined to about 70 percent of that value over the rest of the pressure surface. The close combustor at a Reynolds number of 800,000 had an average augmentation on the pressure surface of 56 percent.

Acknowledgments

The author is grateful for the support of NASA Lewis Research Center.

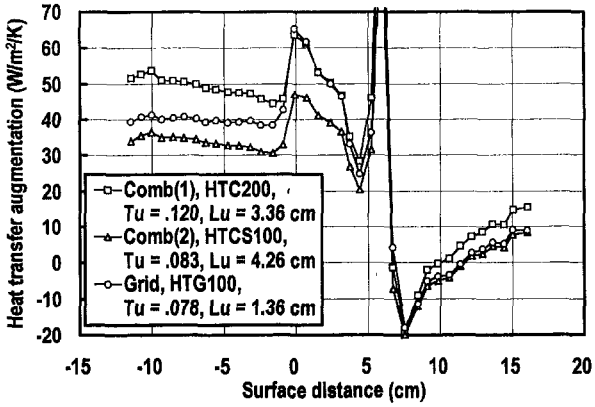

Fig. 13 Comparisons of absolute level of heat transfer augmentation, Re_{ex} = 790,000

References

Ames, F. E., and Moffat, R. J., 1990, "Heat Transfer With High Intensity, Large Scale Turbulence: The Flat Plate Turbulent Boundary Layer and the Cylindrical Stagnation Point," Report No. HMT-44, Thermoscience Division of Mechanical Engineering, Stanford University, CA.

Ames, F. E., 1994, "Experimental Study of Vane Heat Transfer and Aerodynamics at Elevated Levels of Turbulence," NASA CR 4633.

Ames, F. E., and Plesniak, 1995, "The Influence of Large Scale, High Intensity Turbulence on Vane Aerodynamic Losses, Wake Growth, and Exit Turbulence Parameters," ASME Paper No. 95-GT-290; accepted for publication in the ASME JOURNAL OF TURBOMACHINERY.

Arts, T., Lambert de Rouvroit, M., and Rutherford, A. W., 1990, "Aero-thermal Investigation of a Highly Loaded Transonic Linear Turbine Guide Vane Cascade," Technical Note 174, von Karman Institute for Fluid Dynamics, Belgium.

Bicen, A. F., and Jones, W. P., 1986, "Velocity Characteristics of Isothermal and Combusting Flows in a Model Combustor," *Combust. Sci. and Technology,* Vol. 49, p. 1.

Britter, R. E., Hunt, J. C. R., and Mumford, J. C., 1979, "The Distortion of Turbulence by a Circular Cylinder," *J. Fluid Mech.,* Vol. 92.

Frota, M. F., 1982, "Analysis of the Uncertainties in Velocity Measurements and Technique for Turbulence Measurements in Complex Heated Flows With Multiple Hot-Wires," Ph.D. Dissertation, Dept. Mech. Engr., Stanford University, CA.

Hancock, P. E., and Bradshaw, P. 1983, "The Effect of Free-Stream Turbulence on Turbulent Boundary Layers," ASME *Journal of Fluids Engineering,* Vol. 105, p. 284.

Hinze, J., 1975, *Turbulence,* 2nd ed., McGraw-Hill, New York.

Hunt, J. C. R., 1973, "A Theory of Turbulent Flow Round Two-Dimensional Bluff Bodies," *J. Fluid Mech.,* Vol. 61, Part 4, p. 625.

Hunt, J. C. R., and Graham, J. M. R., 1978, "Free-Stream Turbulence Near Plane Boundaries," *J. Fluid Mech.,* Vol. 84, p. 209.

Kays, W. M., 1987, *STAN7, a Finite Difference Boundary Layer Code.*

Kline, S. J., and McClintock, F. A., 1953, "Describing Uncertainties in Single Sample Experiments," *Mech. Engr.,* Jan., p. 3.

Moffat, R. J., 1980, "Experimental Methods in the Thermosciences," Dept. Mech. Engr., Stanford University, CA.

Nealy, D. A., Mihelc, M. S., Hylton, L. D., and Gladden, H. J., 1984, "Measurements of Heat Transfer Distribution Over the Surfaces of Highly Loaded Turbine Nozzle Guide Vanes," ASME *Journal of Engineering for Gas Turbines and Power,* Vol. 106, pp. 149–158.

Siegel, R., and Howell, J. F., 1981, *Thermal Radiation Heat Transfer,* 2nd ed., McGraw-Hill, New York.

Thole, K. A., and Bogard, D. G., 1995, "Enhanced Heat Transfer and Shear Stress Due to High Free-Stream Turbulence," ASME JOURNAL OF TURBOMACHINERY, Vol. 117, pp. 418–424.

Thomas, N. H., and Hancock, P. E., 1977, "Grid Turbulence Near a Moving Wall," *J. Fluid Mech.,* Vol. 82, Part 3, p. 481.

Van Fossen, G. J., Simoneau, R. J., Ching, C. Y., 1995, "The Influence of Turbulence Parameters, Reynolds Number, and Body Shape on Stagnation Region Heat Transfer," ASME *Journal of Heat Transfer,* Vol. 117, pp. 597–603.

Wubben, F. J. W., 1991, "Single and Cross Hot Wire Anemometry in Incompressible Flow," Report LR-663, Faculty of Aerospace Engineering, Delft University of Technology, The Netherlands.

Zimmerman, D. R., 1990, "Three-Dimensional Laser Anemometer Measurements in a Linear Turbine Vane Cascade," *Forum on Turbulent Flows—1990,* ASME FED-Vol. 94, p. 143.

Grid Orthogonality Effects on Predicted Turbine Midspan Heat Transfer and Performance

R. J. Boyle
NASA Lewis Research Center,
Cleveland, OH 44135

A. A. Ameri
University of Kansas,
Center for Research, Inc.,
Lawrence, KS 66045

The effect of five different C-type grid geometries on the predicted heat transfer and aerodynamic performance of a turbine stator is examined. Predictions were obtained using two flow analysis codes. One was a finite difference analysis, and the other was a finite volume analysis. Differences among the grids in terms of heat transfer and overall performance were small. The most significant difference among the five grids occurred in the prediction of pitchwise variation in total pressure. There was consistency between results obtained with each of the flow analysis codes when the same grid was used. A grid-generating procedure in which the viscous grid is embedded within an inviscid type grid resulted in the best overall performance.

Introduction

Among the goals for Navier–Stokes turbomachinery analysis are accurate predictions of blade row losses and turbine blade heat transfer. It has been shown by a number of investigators that the characteristics of the grids used can significantly affect the predicted results. Davis et al. (1988) investigated the effects of blade-to-blade grids of different densities on the prediction of compressor performance. Recently, attention has also been given to the desirability of using grids orthogonal to the blade surfaces. Many applications using **C**-type grids have used grids generated in a manner similar to that proposed by Sorenson (1980) in which the points on the cut line have the same coordinates for both the upper and lower portions of the grid. It was shown by Arnone et al. (1992) that **C**-type grids can be highly skewed, especially for highly turned modern turbine stator blades. The skewing is most evident when a matching condition is enforced on the cut line from the trailing edge to the downstream boundary. If the matching condition is removed the result is less skewed grids. The cut line divides the **C** grid, and extends from the trailing edge to the downstream boundary. Arnone et al. (1992) proposed the use of **C**-type grids for turbine applications in which the requirement for common coordinates along the cut line is not enforced. This procedure allows for greater grid orthogonality at the blade surface, since the numbers of grid cells on the upper and lower surfaces are not necessarily equal. However, this procedure requires interpolation along the cut line, rather than averaging the solution at a common point. Micklow et al. (1993) took this process further, and presented results where the requirement for matching points was not enforced along the periodic boundary of the blade-to-blade grid, as well as along the cut line.

Yeuan et al. (1993) used nonperiodic **H** grids to analyze the performance of a turbine cascade. Turner et al. (1993) advance arguments for the use of modified **H** grids, called **I** grids, to improve flow field calculation accuracy. The **H** grids were modified so as to be more orthogonal to the blade surface, and were recommended for use in calculating the performance of highly turned turbine blades. Because of the rapid changes in heat transfer in the leading edge region, **C** or **O**-type grids are advantageous in comparison to **H** or **I**-type grids for use in Navier–Stokes heat transfer analyses. **C**-type grids have the advantage relative to **O**-type grids in that only a single grid is needed for a blade row passage. **O**-type grids are generally embedded within an **H**-type grid for cascade analyses. The work that is reported in the present paper is concerned with determining the effects of different **C**-type grids on turbine blade heat transfer, as well as turbine blade aerodynamic performance.

The issue of grid size is especially important when one considers that the goal of code development work is to achieve accurate three-dimensional Navier–Stokes solutions while utilizing a reasonable amount of computer resources. It has been shown by Boyle and Giel (1992) that over 50 spanwise grid planes are necessary to achieve grid-independent heat transfer results for a typical turbine blade. If one wishes to limit the size of routine three-dimensional Navier–Stokes calculations to around a half million grid points, then blade-to-blade grids would have a maximum of 10,000 points.

The choice of the best blade-to-blade grid is facilitated by comparisons with experimental data. Arts et al. (1990) presented data for the midspan region of a turbine stator with an exit flow angle of 74 deg. Heat transfer, pitchwise variation in total pressure, as well as overall stator performance data were given. These data were used by Harasagama et al. (1993) to compare different approaches for the prediction of turbine blade heat transfer using boundary layer methods. Luo and Lakshminarayana (1993) used the same experimental data to show the validity of their method for predicting the flowfield and heat transfer in a turbine passage using a Navier–Stokes analysis.

In the present work blade surface heat transfer as well as aerodynamic performance are examined for five different baseline grids. Additional grids were generated to examine other possible grid effects. Three of the five baseline grids have a matching condition imposed along the cut line. Among these three grids two are similar, and differ only in the procedure used to generate them. One was generated using a single grid solution generated using the GRAPE code of Sorenson (1980). The other was generated using the code of Arnone et al. (1992) in which the viscous grid is generated by embedding a near wall grid within a sparse inviscid grid. The third grid that is periodic along the cut line differs from the other two in that the grid in the wake region expands to have nearly uniform pitchwise spacing at the downstream boundary. The two grids without the matching condition differ from each other downstream of the blade row. One extends the periodic boundary in a straight line, so that there is little flow across the periodic boundary downstream of the blade. The other curves the grid, so that there are large flows across the periodic boundary downstream of the blade.

Contributed by the International Gas Turbine Institute and presented at the 39th International Gas Turbine and Aeroengine Congress and Exposition, The Hague, The Netherlands, June 13–16, 1994. Manuscript received by the International Gas Turbine Institute February 4, 1994. Paper No. 94-GT-123. Associate Technical Editor: E. M. Greitzer.

The choice of grid could be significantly affected by the Navier–Stokes solution methodology. The Navier–Stokes analysis were done using a finite difference code developed by Chima (1987), and a finite volume code developed by Arnone et al. (1992). Since the choice of calculation procedure is affected by far more factors than are explored in this paper, the emphasis is on determining the best grid approach for each code. Similarly, since the emphasis is on grid effects, a simple approach is taken to turbulence modeling. An algebraic turbulence model was used for most calculations. Wake profiles are presented using the algebraic model and the two equation turbulence model of Chien (1982).

Description of Analysis

Grid Characteristics. All five grids were of of the same size, 177 × 53. This size was chosen based on requirements for three-dimensional Navier–Stokes analyses. Certainly, two-dimensional Navier–Stokes results could be obtained in a reasonable CPU time for grids of larger sizes. However, based on the required number of spanwise grids for three-dimensional heat transfer analyses, the CPU time and core memory required for three-dimensional analyses might be excessive for blade-to-blade grids significantly greater than 177 × 53. All grids, except grid *A*, had the inlet boundary $0.55c_x$ ahead of the vane. Grid *A* began $0.75c_x$ in front of the vane. All grids had their downstream boundary at $0.84c_x$ behind the vane trailing edge. The downstream boundary was chosen so that the measurement station used by Arts et al. (1990) was midway between the trailing edge and the downstream boundary. The near-wall spacing was held constant at $4 \times 10^{-5}c_x$ for all baseline grids. The effect of variations in the near-wall spacing on predicted results is examined.

The five grids used in the analysis are illustrated in Fig. 1, and will be referred to with the labels A–E. In order to distinguish the individual grid lines, many lines in the figure have been omitted for clarity. Portions of grids *C* and *D* are shown twice. In each view of these two grids different grid lines were omitted in order to best illustrate the comparisons with another grid. Table 1 gives the number of grid spacings used in each of the baseline **C**-type grids. Grid *A* was generated using the GRAPE code of Sorenson (1980). This code obtains a solution to a two-dimensional Poisson partial differential equation in order to generate a **C**-type grid. Grid *B* was generated using the code developed by Arnone et al. (1992), and as can be seen in Fig. 1, this grid is very similar to grid *A*. The principal difference is that a two-step grid generation process was used to generate grid *B*. First a coarse grid, such as might be used in an inviscid analysis, is generated. This initial grid has relatively few lines in the blade-to-blade direction. The grid used for the viscous calculations is obtained by embedding a fine grid over a few cells in the near wall region. The remaining three grids were generated using the same procedure as grid *B*. Grid *C* differed from grid *B* in that the grid lines for small values of η do not maintain a constant spacing from the cut line between the trailing edge and the downstream boundary. For grid *B* these grid lines are maintained at a uniform spacing between the trailing edge and the downstream boundary. Grids *D* and *E* differed from grid *C* in that these two grids were not periodic along the cut line between the trailing edge and the downstream boundary. As can be seen in Fig. 1, grids that are not periodic along the cut line can more easily be made orthogonal to the blade surface. One potential disadvantage of this approach, however, is that the flow solution has to be interpolated along the cut line. Grid *E* differs from grid *D* in that downstream of the blade the periodic boundary is curved so that at the downstream boundary the η = const grid lines are parallel to the axial direction. Grids *A*–*D* are extended downstream of the blade at a constant angle, which is close to the trailing edge angle. When these grids are used, there is only a single wake in the flow field. However, when grid *E* is used, multiple wakes are present in the flow field. The number of wakes depend on the flow angle and the distance between the trailing edge and the downstream boundary. At any given axial location there is only a single passage flow field. Grids *Dn* and *Ea* in Table 1 are similar to grids *D* and *E* respectively, but with more circumferential grid lines.

Table 1 Distribution of circumferential grid

	No. of increments						
	Grid						
Location	A	B	C	D	E	Dn	Ea
Wake-pressure side	40	40	40	56	56	88	128
Blade-pressure side	48	48	48	32	32	32	32
Blade-suction side	48	48	48	64	64	96	96
Wake-suction side	40	40	40	24	24	24	64

Flow Analysis. Two flow analysis codes were run for each of the five grids. One analysis used a finite difference approach, and was developed by Chima (1987). In the discussion that follows, results obtained using this code are labeled as flow code *FC*. The other analysis, developed by Arnone et al. (1992), used a finite volume approach, and employed a multigrid solution scheme. Results obtained using this code are labeled as flow code FA. While the discretization is different between the two analyses, both used a time-marching approach with an explicit four-stage Runge–Kutta scheme to solve the differential equations. Both also employed implicit residual smoothing.

The turbulence model used in both flow analyses for most calculations is a variation of the model developed by Baldwin and Lomax (1978). The main difference between the model used and the Baldwin–Lomax model is in the prediction of the transition location. The transition model given by Mayle (1991) was used. In this model the location of the start of transition as well as the length of transition are given as functions of Reynolds number and turbulence intensity. It was found that estimating the local free-stream turbulence intensity rather than just using the inlet free-stream turbulence intensity gave a better estimate of the vane heat transfer for the cases examined. The local free-stream turbulence intensity was estimated assuming

Nomenclature

c = true chord
c_x = axial chord
$\bar{e}$ = kinetic energy loss coefficient
M_2 = isentropic exit Mach number
P' = total pressure
Re_2 = Reynolds number based on c_x and M_2
s = surface distance
St = Stanton number based on U_{INLET} and ρ
Tu = turbulence intensity
U = velocity
Y = loss coefficient = $\Delta P'/0.5\rho U^2_{EXIT}$
y_1^+ = distance of first grid line from blade
η = direction outward from blade surface
ρ = density

Subscripts

EXIT = exit of computational domain
INLET = inlet of computational domain
M = measurement plane
S = surface of blade

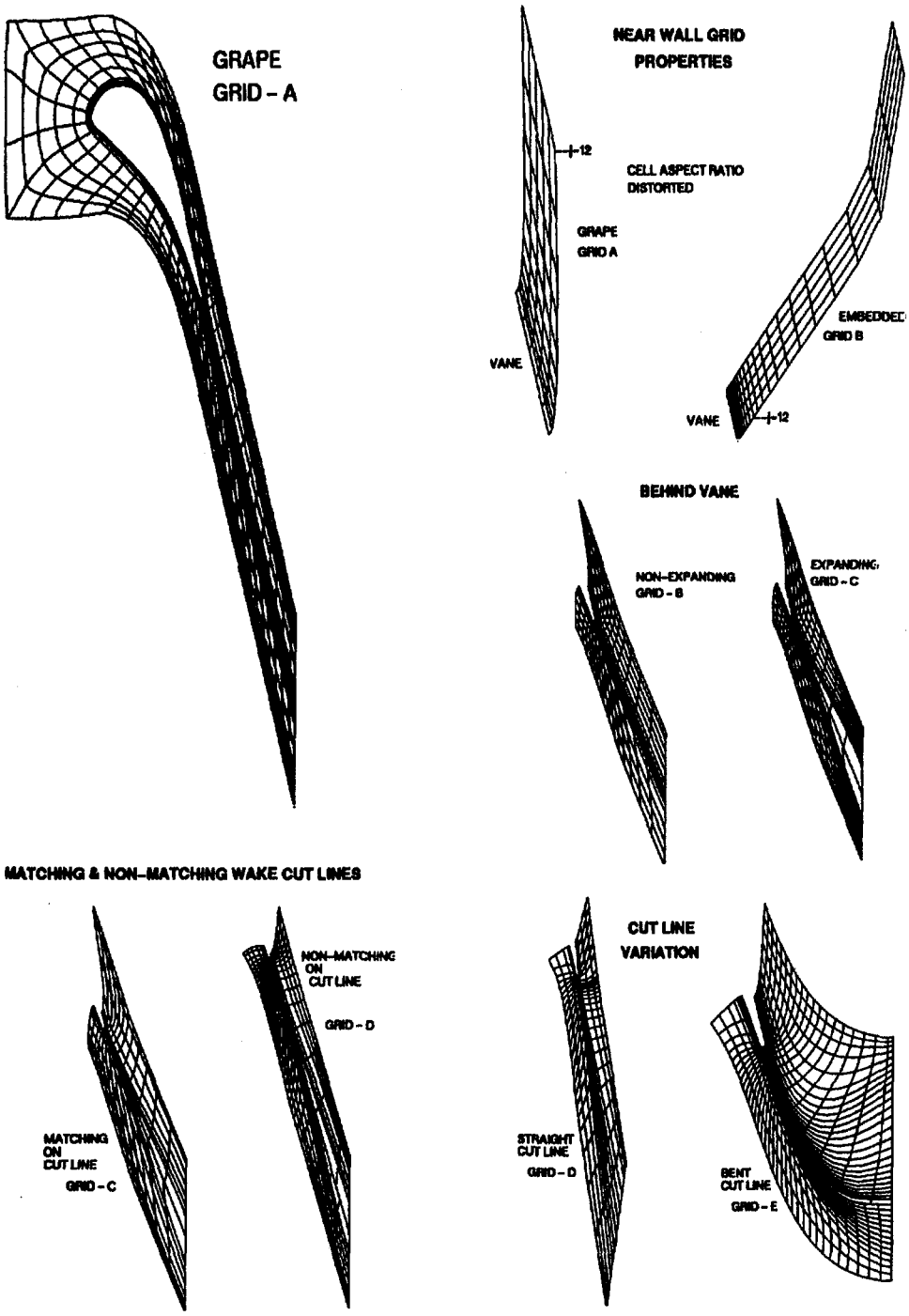

Fig. 1 Description of grids used in analysis, with lines omitted for clarity

that the velocity fluctuations remain constant through the passage. This assumption results in:

$$Tu_S = Tu_{\text{INLET}} U_{\text{INLET}} / U_S$$

The local velocity, U_S, was calculated from the isentropic relationship and the local static-to-inlet total pressure ratio.

Results

Heat Transfer Comparisons. Figures 2 and 3 show the variation in heat transfer among the different grids for the two flow solution codes. Also shown in each figure are the experimental data of Arts et al. (1990). These comparisons are for $\text{Re}_2 = 1.16 \times 10^6$, $Tu_{\text{INLET}} = 1$ percent, and $\text{M}_2 = 0.84$. Because of the low inlet turbulence, transition did not occur even though the Reynolds number is fairly high. The Stanton number predictions shown in Fig. 2 show very high heat transfer just near the trailing edge. These results were obtained by forcing the flow turbulent at the tangent point of the vane trailing edge circle. Since the focus of this work is on the effects of different grids on predicted results, it is useful to show comparisons for a laminar flow case. For laminar flow, questions regarding the implementation of the turbulence model do not arise. For each of the flow analyses, the variation in blade heat transfer among the five grids is small. Except very close to the trailing edge, both codes give nearly the same level of heat transfer for the

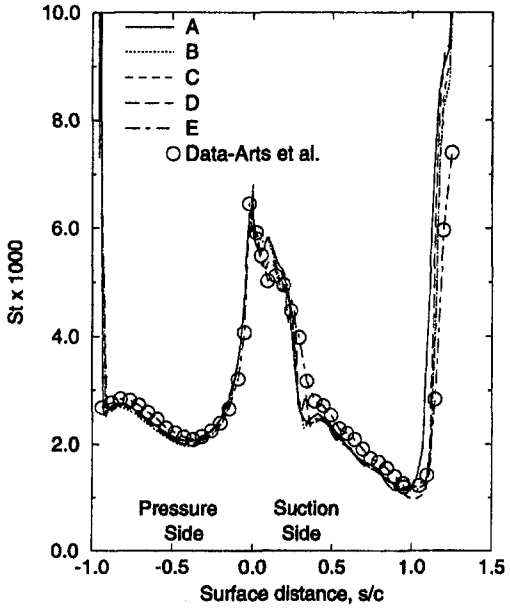

Fig. 2 Stanton number comparisons for $Re_2 = 1.16 \times 10^6$, $Tu = 1$ percent, $M_2 = 0.84$, flow code *FA*

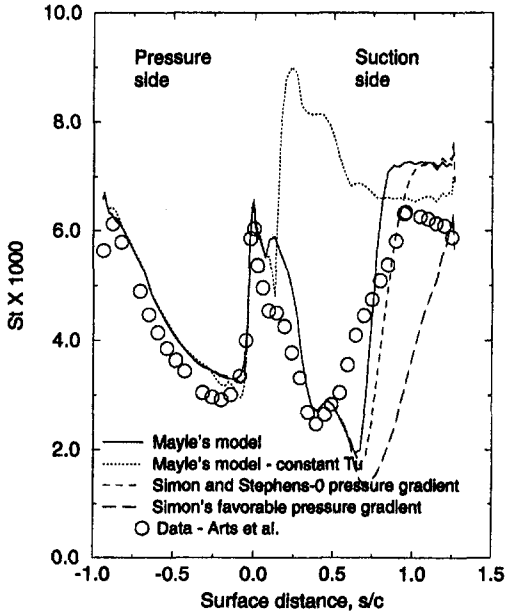

Fig. 4 Effect of transition model assumptions on predicted heat transfer, $Re_2 = 2.1 \times 10^6$, $Tu = 6$ percent, $M_2 = 0.92$, flow code *FC*, grid *C*

same grid. In flow code *FA* the boundary layer was set to be fully turbulent at the beginning of the trailing edge circle. The agreement with the experimental data is generally good, and for this case there is little evidence to prefer one grid over another.

The heat transfer predictions are in good agreement with the experimental data for the low-turbulence-intensity case. Comparisons will next be made for a case with high turbulence intensity, and high Reynolds number. The results of different approaches to modeling the effects of a high-turbulence intensity will be examined prior to showing the grid effects. Figure 4 shows the effects of transition model assumptions on vane surface heat transfer for the highest Reynolds number, 2.1×10^6, and highest turbulence intensity, 6 percent, tested by Arts et al. (1990). The exit Mach number was 0.92. Results are shown for a single grid (grid *C*), and flow solution code (*FC*). The purpose of this figure is to illustrate the significance of the transition model for the heat transfer predictions. The model for the start of transition proposed by Mayle (1991) more accurately predicts the start of transition when the turbulence intensity is adjusted to account for the local inviscid velocity. This is especially evident on the suction surface. Comparing the slope of the predicted heat transfer with the experimental data shows that the length of transition on the suction surface is not well predicted using the intermittency model proposed by Mayle (1991). The predicted transition length is shorter than that indicated by the experimental data. Heat transfer predictions are shown for two additional transition length models. These are the transition length models of Simon and Stephens (1991) and Simon (1994). The model of Simon and Stephens was developed for zero pressure gradient flows, while Simon's model was developed for flows with favorable pressure gradient. The use of Simon's transition length model results in good agreement with the experimental data. Even though suction surface transition began close to the uncovered portion of the suction surface, there was a favorable pressure gradient at the start of transition. These results illustrate the sensitivity of the heat transfer results to transition assumptions. Because of the high free-stream turbulence intensity, pressure surface transition occurs close to the leading edge. The heat transfer on the pressure surface is accurately predicted.

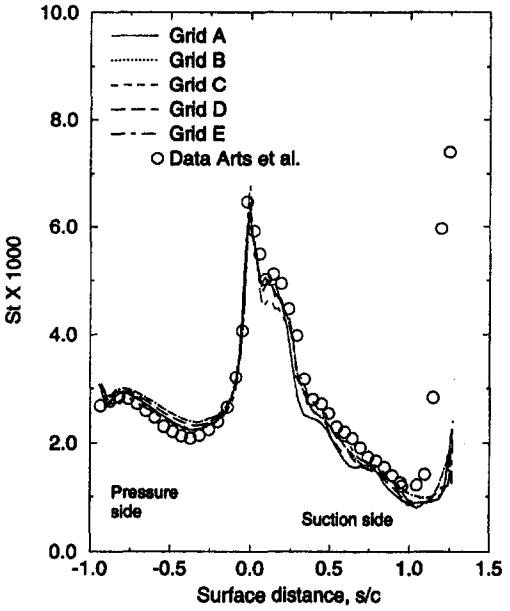

Fig. 3 Stanton number comparisons for $Re_2 = 1.16 \times 10^6$, $Tu = 1$ percent, $M_2 = 0.84$, flow code *FC*

Figure 5 shows the effect of different model assumptions for predicting the effect of free-stream turbulence on blade surface heat transfer. Heat transfer predictions are shown using the model of Forrest (1970), as well as when no augmentation due to free-stream turbulence is assumed. This model for calculating an eddy viscosity due to free-stream turbulence was applied only prior to transition. It was applied in an analogous fashion to the Baldwin–Lomax eddy viscosity model, which is used after transition occurs. The Baldwin–Lomax model for turbulent eddy viscosity is a two-layer model. Predictions are shown when the augmentation model is applied only in the inner layer, when it is applied to both layers, and when it is held constant in the outer layer. This model for the augmentation of eddy viscosity is utilized only prior to transition. The best overall agreement with the experimental data is achieved when the turbulent eddy viscosity in the outer layer is held constant at

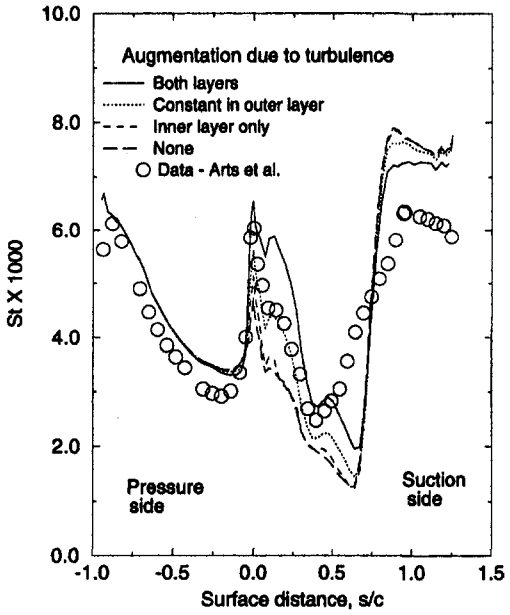

Fig. 5 Effect of model assumptions for free-stream turbulence on predicted heat transfer, $Re_2 = 2.1 \times 10^6$, $Tu = 6$ percent, $M_2 = 0.92$, flow code *FC*, grid *C*

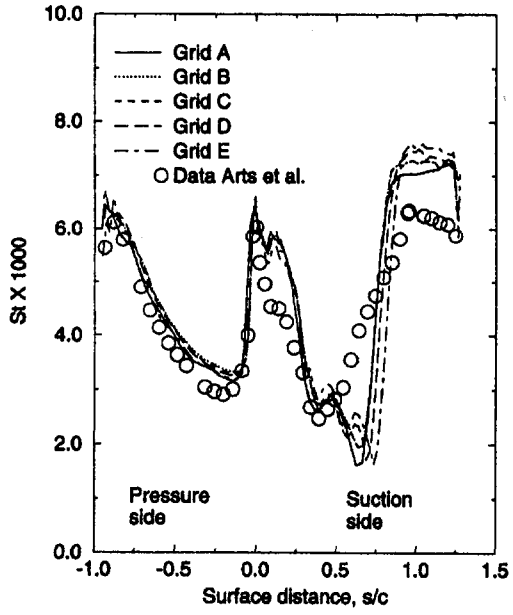

Fig. 7 Stanton number comparisons for $Re_2 = 2.1 \times 10^6$, $Tu = 6$ percent, $M_2 = 0.92$, flow code *FC*

the inner layer value determined at the point where the two layers meet.

A comparison of the heat transfer predictions for the five different grids is given in Figs. 6 and 7. Since this is a relative comparison, only Mayle's transition model is utilized. The use of this model results in a relatively long portion of the suction surface being turbulent, and allows for the comparisons for different grids to be done for a case with turbulent flow on both pressure and suction surfaces. In this case the pressure surface is mostly turbulent, and half of the suction surface is turbulent. The variation in blade surface heat transfer among the five grids is small. The results for this test case are similar to those shown in Figs. 2 and 3 for a case where the vane surface heat transfer was almost entirely laminar.

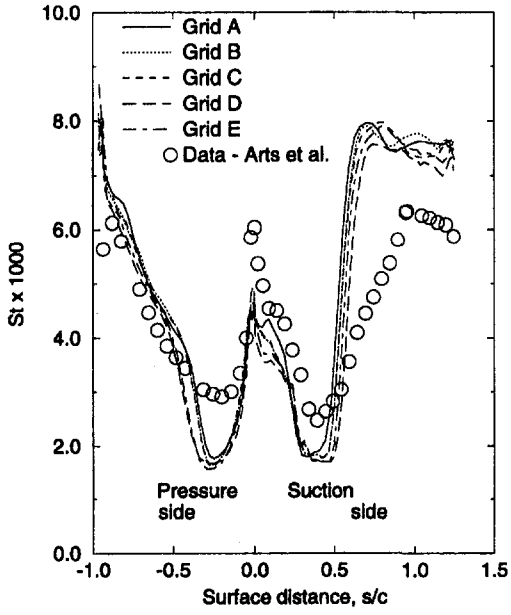

Fig. 6 Stanton number comparisons for $Re_2 = 2.1 \times 10^6$, $Tu = 6$ percent, $M_2 = 0.92$, flow code *FA*

The variation in predicted blade surface heat transfer between the two flow codes for a given grid is somewhat larger than the variation due to different grids for either of the two flow analyses. Part of the differences can be attributed to differences in modeling the turbulent eddy viscosity. In the leading edge region, and prior to transition, flow code *FC* used the model of Forrest (1977), to augment the laminar viscosity for the effects of free-stream turbulence. This model was applied to both the inner and outer regions, since this assumption would magnify any differences due to different grids on the heat transfer. Flow code FA does not increase the viscosity to account for the effect of free-stream turbulence prior to transition. Both flow analyses overpredict the suction surface heat transfer when the flow is fully turbulent.

The results shown in Figs. 2 and 3 are for $Re_2 = 1.16 \times 10^6$, while those in Figs. 6 and 7 are for a Reynolds number nearly twice as large. Since the same grids were used, the value of y_1^+ for the results in Figs. 6 and 7 is greater. The maximum value of y_1^+ for the high Reynolds number case was 3.8. The use of the largest value of y_1^+ that gives accurate results minimizes the amount of near-wall grid stretching, and also allows for the smallest size grid in the blade-to-blade direction. The effect of reducing the near-wall spacing is shown in Fig. 8 for grid *D*, and flow code *FC*. There was virtually no change in the heat transfer as the near-wall spacing was reduced by a factor of 4. Consequently, the relatively large near-wall spacing used for the high Reynolds number analysis is not a cause of the differences between the measured and predicted vane heat transfer.

Reducing the near-wall spacing did not result in better agreement with the experimental heat transfer in the fully turbulent region. To determine whether this disagreement was related to the grid properties, the effect of improving the orthogonality of the grid lines to the vane surface was examined. Figure 9 shows the angle that the grid lines make with the vane surface. If the lines were purely orthogonal, the angle would be 90 deg. Grids *B* and *C* make identical angles with the blade surface, since they differ only downstream of the blade. The embedded grids (*B–E*) have grid lines that maintain a constant angle for the region between the blade surface and the first circumferential inviscid grid line. For the viscous embedded grid this angle is maintained over 20 near-wall spacings. Grid *A* is solved as a single grid, and the angle of the grid line with the blade surface

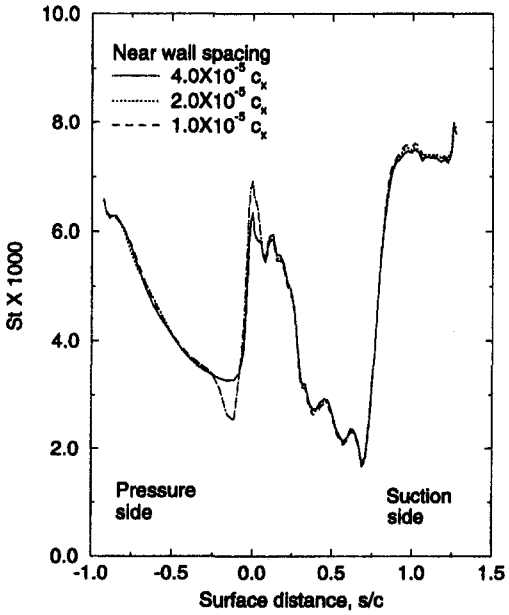

Fig. 8 Grid spacing effects on heat transfer, $Re_2 = 2.1 \times 10^6$, $Tu = 6$ percent, $M_2 = 0.92$, flow code *FC*, grid *C*

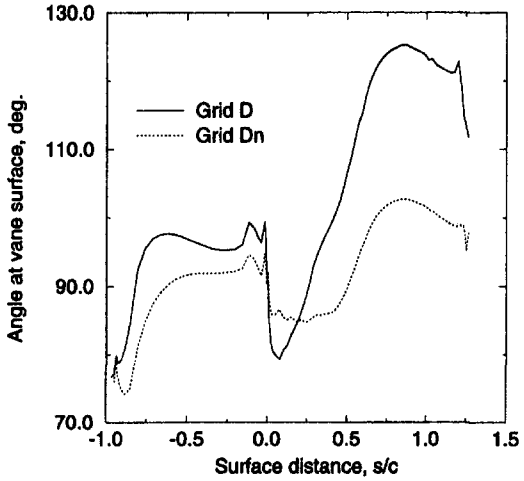

Fig. 10 Angle between grid line and vane surface for grids *D* and *Dn*

continuously varies away from the wall. While grids *B* and *C* have the highest departure from orthogonality, it should be noted that they are both periodic in the wake. Enforcing grid matching along the cut line results in embedded grids that have a higher degree of nonorthogonality at the blade surface than either grids *D* or *E*. While grids that match along the cut line were generated using the procedure discussed by Arnone et al. (1992), they did not recommend doing so because of the higher degree of nonorthogonality at the blade surface. Figure 10 shows the angle of the grid lines with the blade surface for grids *D* and *Dn*. As seen in Table 1, grid *Dn* is significantly larger in size than grid *D*. The use of a larger grid allows for greater orthogonality at the blade surface. However, Fig. 11 shows that the more orthogonal grid did not result in a significantly different heat transfer distribution.

Total Pressure Distribution. Arts et al. (1990) measured the pitchwise variation in total pressure at 0.42 axial chords behind the vane. In the analysis this location was midway between the vane trailing edge and the downstream boundary. Figures 12 and 13 compare the pitchwise variation in total pressure for the five grids and the two flow solvers with the experimental data. For clarity of presentation, the location of minimum pressure was taken as the abscissa origin. Therefore, any variation in flow angle among the grids is not reflected in these figures. The relative grid effects are similar for both flow solvers. For grids *A*–*D* flow solver *FA* resulted in minimum total pressures significantly less than flow solver *FC*. The results obtained using grids *A*–*D* showed the predicted minimum total pressure to be lower than the experimental data. The width of the predicted wake is also smaller than the experimental wake. This indicates that the amount of diffusion in the wake predicted by the turbulence model is too small. Results obtained with flow solver *FC* and grid *A* showed a lower total pressure in the free-stream region than with grids *B*, *C*, or *D*. In this region the data show no loss in total pressure. Results obtained with

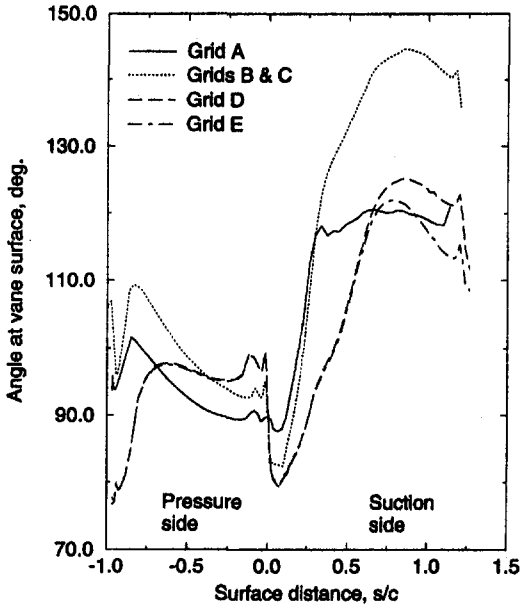

Fig. 9 Angle between grid line and vane surface

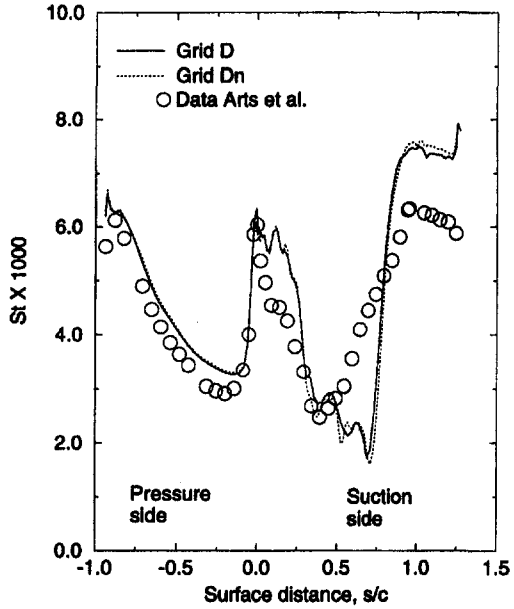

Fig. 11 Stanton number comparisons: grids *D* and *Dn*, $Re_2 = 2.1 \times 10^6$, $Tu = 1$ percent, $M_2 = 0.85$, flow code *FC*

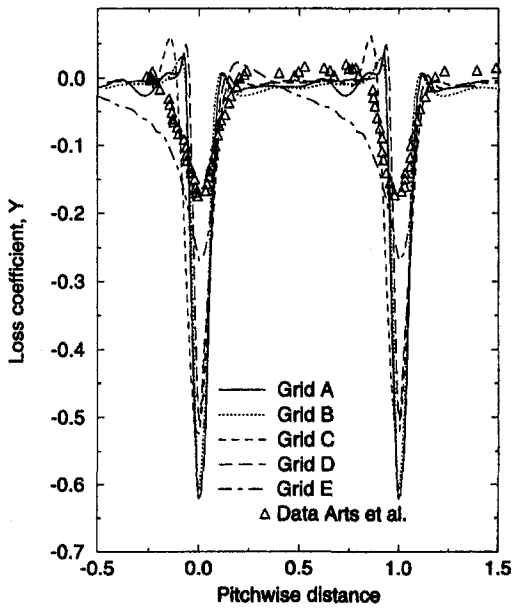

Fig. 12 Pitchwise variation in total pressure, $Re_2 = 1 \times 10^6$, $Tu = 1$ percent, $M_2 = 0.85$, flow code *FA*

flow solver *FA* and grids *A*–*D* showed no loss in total pressure in the free-stream region.

Grid *E* is bent so that the grid is aligned with the axis at the downstream boundary. This bending results in a relatively coarse grid on the suction side of the cut line. The reasonably good agreement between the predicted and measured wakes for grid *E* may have been fortuitous. The numerical diffusion resulting from the coarse grid may have helped to give nearly the correct total diffusion. To verify this hypothesis, an additional bent grid (*Ea*) was generated. Table 1 shows that the number of points in the wake was increased considerably. Figure 14 compares the wake profiles for the two grids. The narrowing of the wake, and lowering of the minimum total pressure, in going to the finer grid is evidenced.

A comparison of the wake profile using a $k-\epsilon$ two-equation turbulence model with the wake profile using the Baldwin–Lomax turbulence model is given in Fig. 15. The results were obtained using grid *D*, and flow code *FA*. The two-equation model is that of Chien (1982), and details of its implementation into the flow code *FA* are given by Ameri and Arnone (1992). The depth of the wake using Chien's model is nearly the same

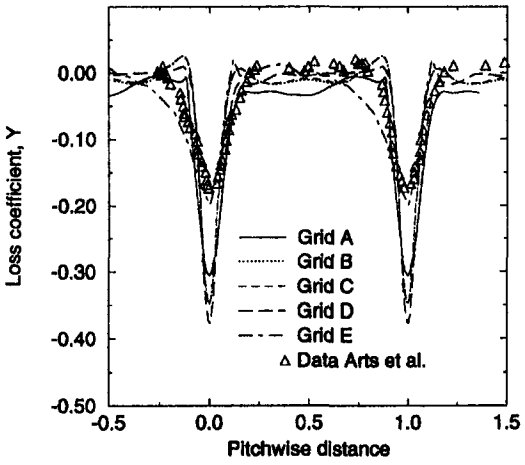

Fig. 13 Pitchwise variation in total pressure, $Re_2 = 1 \times 10^6$, $Tu = 1$ percent, $M_2 = 0.85$, flow code *FC*

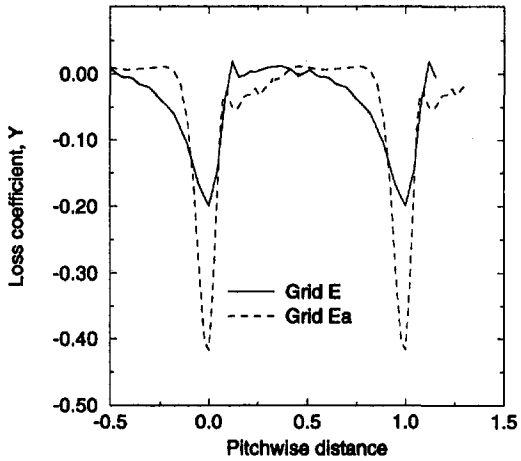

Fig. 14 Grid density effect on total pressure distribution, $Re_2 = 1 \times 10^6$, $Tu = 1$ percent, $M_2 = 0.85$, flow code *FC*

as the wake depth calculated using the Baldwin–Lomax model. The width of the wake is somewhat wider using Chien's model. The wider wake region using Chien's model is due to the the model giving transition on both surfaces close to the leading edge. As shown in Fig. 2, the Baldwin–Lomax model did not result in an early transition.

Overall Loss. Table 2 shows the loss coefficient for the different grids obtained with the two flow solvers at an exit isentropic Mach number of 0.85. Except for the results obtained with flow code *FA* and grid *E*, the highest calculated loss was achieved using grid *A*. The losses for grid *E* are different between flow codes *FA* and *FC*. But, based on the previous discussion, the results using this grid are not expected to be accurate. For both flow codes the loss levels for the other grids are reasonably close to the experimental measurements. The losses calculated using flow code *FC* are slightly lower than those calculated using flow code *FA*. Part of this difference in loss is due to the blade surface boundary layers being tripped near the trailing edge when flow code *FA* was used. The results for grid *D* are in best agreement with the experimental data.

The overall loss increased from 0.030 to 0.057 when Chien's model was used. Part of the increase was the result of the

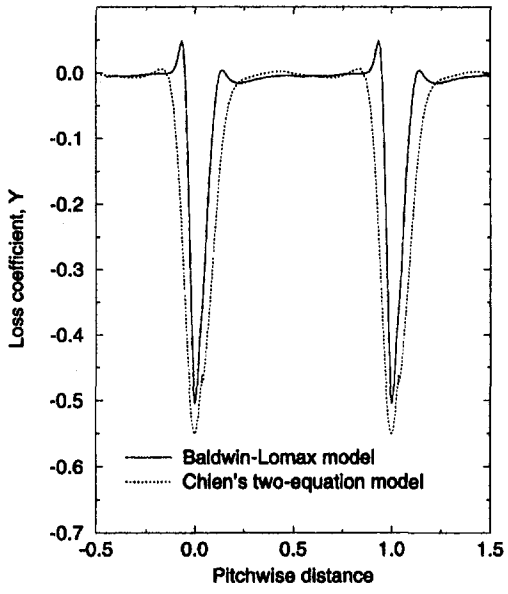

Fig. 15 Wake profiles for Baldwin–Lomax and Chien turbulence models, Grid *D*, flow code *FA*

Table 2 Overall loss coefficient

Flow code	Grid A	B	C	D	E	Dn	Ea
	$\bar{e}$						
FA	.039	.029	.030	.030	.054	.028	.032
FC	.035	.026	.023	.029	.024	.027	.024
Experimental - Arts et al.							0.029

boundary layers being turbulent. A fully turbulent calculation using the Baldwin–Lomax model gave a loss coefficient of 0.041.

Concluding Remarks

The results of this investigation showed that the principle effect of different grid geometries examined was in the pressure distribution behind the vane. Four of the baseline grids resulted in an excessive decrease in total pressure at the center of the wake. The calculated wake was deeper, but more narrow than the experimental data. The implication of this is that the turbulence model used gave insufficient physical diffusion in the wake region. The fifth baseline grid, which was relatively coarse in the wake region, gave good agreement with the experimental data for the minimum pitchwise total pressure. The numerical diffusion caused by the coarse grid resulted in better agreement with the experimental wake profile for this grid. A similar, but denser grid (*Ea*), which resulted in less numerical diffusion, gave wake profiles similar to the other four baseline grids. The relative effect of different grids was the same for either of the two flow codes used.

The effect of different grid geometries on the vane surface heat transfer was small. For the low-turbulence-intensity case the agreement with the experimental data was good. For the high-turbulence–high-Reynolds number case the agreement was influenced by the choice of model to determine transition length and intermittency. The start of transition was better predicted by Mayle's transition model when the local turbulence intensity was taken as a function of the blade pressure distribution. Simon's transition length mode resulted in good agreement with the data. The choice of model to account for free-stream turbulence significantly affected the predicted heat transfer. Forrest's model gave reasonably good agreement with the data when the augmented eddy viscosity was limited in the outer region of the two-layer Baldwin–Lomax turbulence model.

The overall loss distribution was not strongly affected by the choice of grid geometries. Using either flow analysis, the overall loss was reasonably well predicted.

In terms of the overall results, grid *D* appears to be the best choice. This grid has a nonmatching condition along the cut line, and the cut line is extended in a straight line. If it is desired to maintain a matching condition along the cut line, either grids *B* or *C* appear acceptable. Results obtained using either of these grids were nearly identical. From the standpoint of speed of convergence, there was no reason to prefer one grid over another. The number of time steps to obtain a converged solution was about the same for all of the grids. Surface pressure distributions were also similar for each of the baseline grids.

References

Ameri, A. A., and Arnone, A., 1992, "Navier–Stokes Heat Transfer Predictions Using Two-Equation Turbulence Closures," Paper No. AIAA-92-3067.

Arnone, A., Liou, M.-S., and Povinelli, L. A., 1992, "Navier–Stokes Solution of Transonic Cascade Flows Using Non-periodic C-Type Grids," AIAA *Journal of Propulsion and Power,* Vol. 8, No. 2, pp. 410–417.

Arts, T., Lambert de Rouvroit, M., and Rutherford, A. W., 1990, "Aero-thermal Investigation of a Highly Loaded Transonic Linear Turbine Guide Vane Cascade," von Karman Institute for Fluid Dynamics, Belgium, Technical Note 174.

Baldwin, B. S., and Lomax, H., 1978, "Thin-Layer Approximation and Algebraic Model for Separated Turbulent Flows," Paper No. AIAA-78-257.

Boyle, R. J., and Giel, P. W., 1992, "Three-Dimensional Navier–Stokes Heat Transfer Predictions for Turbine Blade Rows," Paper No. AIAA-92-3068.

Chien, K. Y., 1982, "Predictions of Channel and Boundary-Layer Flows With a Low-Reynolds-Number Turbulence Model," *AIAA Journal,* Vol. 20, No. 1, pp. 33–38.

Chima, R. V., 1987, "Explicit Multigrid Algorithm for Quasi-Three-Dimensional Flows in Turbomachinery," AIAA *Journal of Propulsion and Power,* Vol. 3, No. 5, pp. 397–405.

Davis, R. L., Hobbs D. E., and Weingold, H. D., 1988, "Prediction of Compressor Cascade Performance Using a Navier–Stokes Technique," ASME JOURNAL OF TURBOMACHINERY, Vol. 110, No. 4, pp. 520–531.

Forrest, A. E., 1977, "Engineering Predictions of Transitional Boundary layers," AGARD-CP-224.

Luo, J., and Lakshminarayana, B., 1993, "Navier–Stokes Analysis of Turbine Flowfield and External Heat Transfer," *Eleventh ISABE—International Symposium on Air Breathing Engines,* Tokyo, Japan, Vol. 2, pp. 766–780.

Harasagama, S. P., Tarada, F. H., Baumann, R., Crawford, M. E., and Neelakantan, S., 1993, "Calculation of Heat Transfer to Turbine Blading Using Two-Dimensional Boundary Layer Methods," ASME Paper No. 93-GT-79.

Mayle, R. E., 1991, "The Role of Laminar–Turbulent Transition in Gas Turbine Engines," ASME JOURNAL OF TURBOMACHINERY, Vol. 113, pp. 509–537.

Micklow, G. J., Shivaraman, K., and Li, H., 1993, "A Nonperiodic Approach for Computation of Compressible Viscous Flows in Advanced Turbine Cascades," Paper No. AIAA-93-1799.

Simon, F. F., and Stephens, C. A., 1991, "Modeling of the Heat Transfer in Bypass Transitional Boundary-Layer Flows," NASA TP 3170.

Simon, F. F., 1994, "The Use of Transition Region Characteristics to Improve the Numerical Simulation of Heat Transfer in Bypass Transitional Flows," presented at the Fifth International Symposium on Transport Phenomena and Dynamics of Rotating Machinery, Kaanapali, Maui, Hawaii, May 8–11; also NASA TM 106445.

Sorenson, R. L., 1980, "A Computer Program to Generate Two-Dimensional Grids About Airfoils and Other Shapes by the Use of Poisson's Equation," NASA TM 81198.

Turner, M. G., Liang, T., Beauchamp, P., and Jennions, I. K., 1993, "The Use of Orthogonal Grids in Turbine CFD Computations," ASME Paper No. 93-GT-38.

Yeuan, J. J., Hamed, A., and Tabakoff, W., 1993, "Navier–Stokes Computations for Turbulent Flow Predictions in Transonic Turbine Cascade Using a Zonal Approach," ASME Paper No. 93-GT-240.

Passage Flow Structure and Its Influence on Endwall Heat Transfer in a 90 deg Turning Duct: Mean Flow and High Resolution Endwall Heat Transfer Experiments

B. G. Wiedner

C. Camci

Turbomachinery Heat Transfer Laboratory,
Department of Aerospace Engineering,
The Pennsylvania State University,
University Park, PA 16802

Three-dimensional measurements of the mean velocity field have been made in a square-cross-sectional, strongly curved, 90 deg turbulent duct flow. The mean radius to duct width ratio was 2.3. The study was performed as part of an overall investigation of the physics of endwall convective heat transfer. All three components of the velocity vector and the static and total pressure fields were measured using a five-hole probe at four duct cross sections: inlet, 0, 45, and 90 deg. Preliminary turbulence measurements using a single sensor hot wire at the inlet cross section were also obtained to provide streamwise fluctuation levels through the boundary layer. The endwall heat transfer coefficient distribution was determined using a steady-state measurement technique and liquid crystal thermography. A high-resolution heat transfer map of the endwall surface from far upstream of the curve through the 90 deg cross section is presented. The three-dimensional velocity field measurements indicate that a highly symmetric, strong secondary flow develops in the duct with a significant transfer of streamwise momentum to the transverse directions. The cross-stream vorticity components within the measurement plane were estimated using the five-hole probe data and an inviscid form of the incompressible momentum equation. The development of the total and static pressure fields, the three-dimensional mean velocity field, and all three components of the vorticity field are discussed. The endwall heat transfer distribution is interpreted with respect to the measured mean flow quantities.

Introduction

The flow field within a turbine passage creates a complex convective heating pattern on the blade and hub/annulus endwall surfaces. Coupled with the extremely harsh aero thermal environment of the passage, and the thermal limits of the current materials, the complex distribution of heating patterns can lead to local failures of passage component surfaces. Each improvement in the current level of knowledge of the convective heat transfer process has the potential to directly enhance the efficiencies, operating life and size of the passage components.

The first extensive description of the flow characteristics within a linear turbine cascade was given by Langston et al. (1977). The study presented the growth and development of vortical structures within the passage. Langston (1980) provided insight to the endwall boundary layer's dominant streamwise and crossflow features. Additional descriptions of the passage flow structure in cascades have been given by Marchal and Sieverding (1977), Moore and Ransmayr (1984), and Moore and Smith (1984). A relatively recent survey of cascade studies was provided by Sieverding (1985). Studies by Gregory-Smith et al. (1988a, b) have provided a detailed description of the secondary velocities, streamwise vorticity, secondary kinetic energy and turbulent flow characteristics through a cascade passage. Boyle et al. (1988) presented a comparison between the passage flow structure in a vane cascade and a curved duct at equivalent Reynolds numbers. Similar features were found throughout the passages; however, the duct passage showed stronger secondary motion. The study also showed the horseshoe vortex formed at the vane leading edge and endwall junction in the cascade had strong effects on the passage flow only in the leading edge region. The results of Boyle et al. (1988) imply that many conclusions drawn from duct passage studies may be applicable to turbine passage configurations.

Early investigations of the passage flow structure within rectangular ducts have been documented by Humphrey et al. (1977, 1981), and Taylor et al. (1982). Humphrey et al. (1977) presented the streamwise mean velocity of laminar flow in a square duct that passes through a 90 deg bend. A description of a turbulent flow in the same geometry square duct was given by Humphrey et al. (1981). The streamwise and radial components of mean velocity and the associated turbulent stresses were measured with a single component laser-Doppler anemometer. In a continuation of the two previous studies, the effects of inlet boundary layer thickness and duct radius ratio on the development of the secondary flow field were investigated by Taylor et al. (1982) and Enayet et al. (1982). The measurements of Taylor et al. (1982) were expanded to include the third mean component and two more turbulent stresses. Shiragami and Inoue (1989) captured three mean velocity components and the respective turbulence intensities in two strongly curved ducts with a technique based on an electrochemical reaction con-

Contributed by the International Gas Turbine Institute and presented at the ASME Winter Annual Meeting, New Orleans, Louisiana, November 28–December 3, 1993. Manuscript received by The International Gas Turbine Institute April 15, 1993. Associate Technical Editor: T. H. Okiishi. Paper No. 93-WA/HT-52.

trolled by the mass transfer rate. In addition, the turbulent length scale was measured for two radial locations at five streamwise positions. The measurements demonstrated that the turbulent mixing in the bend may be more effective near the outer wall than near the inner radius surface.

Heat transfer studies in duct passages are relatively sparse. Mori et al. (1971) calculated discrete point Nusselt numbers to correlate with their analytic development of a 220 deg square duct bend. The majority of the work presented was an analytical derivation of laminar flow that experiences a constant heat flux boundary condition. Temperature distributions and discrete point Nusselt numbers on the inner radius, outer radius, and endwall surfaces have been measured in a 180 deg bend by Johnson and Launder (1985). Results from experiments conducted at a Reynolds number of about 56,000 indicate that downstream of the 45 deg cross section, the highest heat transfer coefficients exist on the outer radius surface and the lowest on the inner radius surface. Metzger and Larson (1986) used surface coatings with precise melting points to determine Nusselt numbers at discrete points in a 3:1 aspect ratio rectangular channel flow that encountered a 90 deg bend. Nusselt numbers were found on all four sides of the rectangular channel at several streamwise locations for two ducts of different radius ratios. Their results indicated that at given streamwise location, the lowest Nusselt numbers were generally found on the inner radius surface, while the highest Nusselt numbers were observed on the endwall surfaces. Azimuthal averaged Nusselt numbers were shown to increase continually through the duct curvature. Rojas et al. (1987) investigated the endwall heat transfer distributions in two curved diffuser geometries (**C** and **S**-shaped centerlines) of rectangular cross section. The heat transfer results were complimented with mean velocity component measurements in two directions. Higher heat transfer rates were found in regions where the near-wall streamwise velocity gradients and secondary flows were high. Besserman and Tanrikut (1992) applied liquid crystals to the endwall of a 180 deg square cross-sectional duct and used the transient heat transfer measurement technique to construct a Nusselt number distribution on the surface. A comparison with the developing secondary flow in the passage indicated a higher heat transfer rate in regions where the secondary flow impinged on the endwall surface.

The objective of the current study is to provide a detailed description of the mean quantities of the passage flow within a strongly curved 90 deg duct and the resulting convective heat transfer patterns on the endwall surface. In the flow field description, an emphasis has been placed on the development of the mean vorticity field and the induced secondary flow structure. The present work is the second contribution in a series of experimental studies aimed at a comprehensive description of the aerodynamic and heat transfer features of 90 deg turning duct passage flow. The first phase of the study discussed a new technique developed to resolve high-resolution convective heat transfer coefficient distributions on steady-state heat transfer surfaces that have arbitrarily specified external or internal boundaries (Wiedner and Camci, 1993, 1996b). Turbulent flow structure and kinetic energy generation near the endwall surface is also presented in Wiedner and Canci (1996a).

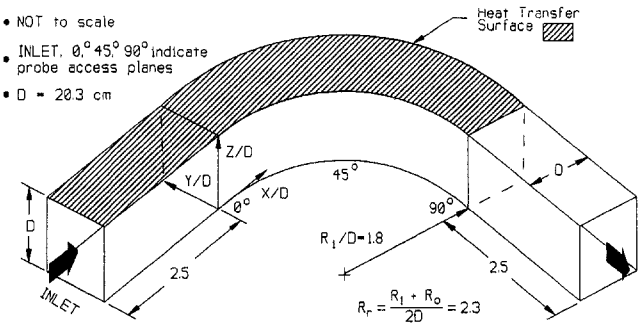

Fig. 1 90 deg duct geometry and coordinate system

Apparatus

Test Facility. The passage geometry under consideration is a square cross-sectional, 90 deg turning duct, Fig. 1. The duct has a radius ratio, $(R_i + R_o)/2D$, of 2.3 and a height/width ratio of 20.3 cm. The flat endwalls are constructed of 1.27-cm-thick acrylic, while the curved side walls are 0.476 cm thick. The turning duct test section was located on the downstream side of an open-loop wind tunnel facility. The facility consisted of an axial air blower, a diffuser that housed multiple screens, a plenum chamber, a high area ratio circular nozzle, a circular to square transition nozzle, a section of constant cross section duct, and the test section. Further details of the facility are provided by Wiedner and Camci (1992) and Wiedner (1993).

The present study utilized two test sections of identical geometry. An aerodynamic duct included probe access slots in the bottom endwall, while an endwall steady-state heat flux surface

Nomenclature

C_{po} = total pressure coefficient = $(p_{o,in,cl} - p_o)/\frac{1}{2}\rho U_{in,cl}^2$
C_{ps} = static pressure coefficient = $(p - p_{in,cl})/\frac{1}{2}\rho U_{in,cl}^2$
D = duct width, m
E = electric field, V/m
h = heat transfer coefficient = $\dot{q}/(T_w - T_{o\infty})$, (W/m^2 K)
H = shape factor = δ_{99}/θ
HSI = hue, saturation, intensity
J = current density, A/m^2
k = thermal conductivity, W/m K
p = local pressure, N/m^2
$\dot{q}$ = heat flux, W/m^2
rms = root mean square
R_i = inner radius, m
R_o = outer radius, m
R_r = radius ratio = $(R_i + R_o)/2D$
Re = Reynolds number = UD/ν
R35C1W = liquid crystal starting to display red at about 35°C with an approximate color bandwidth of 1°C
T = mean temperature, °C
Tu = turbulence intensity = rms$(u')/U*100$
U_{95} = uncertainty based on 95 percent coverage
U, V, W = mean velocity components, m/s
u', v', w' = fluctuating velocity components, m/s
V = electric potential, V
X = streamwise direction
Y = radial direction (horizontal)
Z = vertical direction
δ = heater foil (Inconel) thickness, mm
δ_{99} = boundary layer thickness, @ $U/U_\infty = 0.99$, mm
δ^* = displacement thickness, mm
ρ = resistivity, $\Omega \cdot$m; density, kg/m^3
θ = momentum thickness, mm
ν = kinematic viscosity, m^2/s
σ = conductivity, $(\Omega \cdot m)^{-1}$
Ω = mean vorticity, s^{-1}

Subscripts

cl = duct centerline
cond = conductive
conv = convective
gen = generated
o = total quantity
rad = radiative
w = wall quantity
∞ = free-stream quantity

composite was constructed for the heat transfer duct. Each of the aerodynamic and heat transfer tests was conducted at a Reynolds number of 360,000 based on the inlet centerline velocity (28.3 m/s), duct width, and ambient free stream temperature.

Aerodynamic Measurements

Measurement Locations. Measurement planes were located at the inlet, 0, 45, and 90 deg. The inlet plane was located 55.8 cm upstream of 0 deg (start of curvature), Fig. 1. The measurement planes at 0, 45 and 90 deg were discretized with uniform 30 × 30 grids. The uniformity of the flow field at the inlet plane allowed a 20 × 20 measurement grid to resolve the inlet flow details fully. In each measurement plane the outer edge of the grid was 5 mm from the duct surfaces. The probe access slots were located on the lower (Z/D = 0.0) endwall surface. To minimize leakage affects, the slots were lined with compressible, open cell foam.

Pressure and Velocity Measurements. The total and static pressure fields, and three components of velocity, were measured with a five-hole probe operated in the non-nulled mode. The probe head and shaft were 1.65 mm and 3.18 mm in diameter, respectively. The probe was calibrated at the free-stream Reynolds number for a pitch and yaw range of ±30 deg with a 1 deg alignment accuracy. A complete description of the five-hole probe measurement technique is detailed in Treaster and Yocum (1979). The probe was mounted on a two-degree-of-freedom, high-resolution, traverse system. Traverse motion and data acquisition were controlled by a personal computer. The data acquisition chain consisted of five piezo-resistive solid-state pressure transducers, custom built drivers and amplifiers, and an A/D sampling system. At each measurement location, 1000 samples were acquired over a 2 second interval before time averaging.

Determination of the Vorticity Components. The streamwise component of vorticity, Ω_X, can be resolved from transverse gradients ($\partial/\partial Y$, $\partial/\partial Z$) of the secondary velocity components in a single plane of measurement. To calculate the transverse components of vorticity, Ω_Y and Ω_Z, streamwise gradients ($\partial/\partial X$) of the secondary velocity components are required. Consequently, a single traverse in the $Y-Z$ plane is not suitable for this approach. However, for a steady, inviscid, and incompressible flow field in absence of body forces, the Helmholtz equation can be used to estimate the transverse components of the vorticity vector:

$$\frac{1}{\rho}\vec{\nabla}P_o = \vec{V}\times\vec{\Omega} \tag{1}$$

The vertical and radial components of the Helmholtz equation are, respectively,

$$\Omega_Y = \frac{1}{U}\left(\frac{1}{\rho}(\partial P_o/\partial Z) + V\Omega_X\right). \tag{2}$$

$$\Omega_Z = \frac{1}{U}\left(-\frac{1}{\rho}(\partial P_o/\partial Y) + W\Omega_X\right), \tag{3}$$

Therefore, knowing U, V, and W in a single measurement plane, as well as the gradients of velocity and stagnation pressure in the plane, the complete mean vorticity vector for a steady, inviscid, and incompressible field can be estimated. In the present study, the required gradients have been resolved using a central difference scheme of the measured quantities. The use of the Helmholtz equation has also been applied to resolve the streamwise vorticity component within a cascade passage by Gregory-Smith et al. (1988a).

Experimental uncertainty levels for the measured and derived flow field quantities were estimated using the procedure outlined by Kline and McClintock (1953) and Abernethy et al. (1985). Table 1 summarizes the uncertainty levels for the streamwise mean velocity, static pressure coefficient, and magnitude of the vorticity vector. Within a cross section, the pressure coefficient uncertainty level remained approximately unchanged for the complete range measured, while the streamwise mean velocity component and vorticity magnitude were dependent on the local quantity. The uncertainty levels presented are based on 20:1 odds. A complete description of the error estimates is given by Wiedner (1993)

Heat Transfer Measurements. A steady-state experimental procedure was used to resolve the convective heat transfer coefficient distribution on the endwall surface. The heat transfer measurements used liquid crystal thermography to map the surface temperatures and a finite element numerical routine to determine the local character of the generated surface heat flux. Corrections for radiative and conductive heat flux loss were also applied. A brief summary of the technique is provided here; a detailed description of the heat transfer experimental technique is provided by Wiedner and Camci (1993, 1996b).

Heat Transfer Surface Construction. The heater surface composite consisted of the acrylic endwall (12.7 mm), double-sided tape (0.110 mm), and Inconel 600 foil (0.0254 mm). Several layers of black paint and four layers of chiral nematic encapsulated (R35C1W) liquid crystals were air brush deposited over the Inconel surface. Two thin-foil, *K*-type thermocouples were adhered to the heater surface (beneath the liquid crystal and paint layers) with double sided Kapton tape for calibration of the liquid crystals.

A schematic of the endwall heat transfer test surface geometry is shown in Fig. 2. The surface begins a distance of X/D = 2.5 upstream from the start of curvature of the passage (0 deg) and ends at a streamwise distance of X/D = 0.1 past the 90 deg plane. Large cross-sectional, copper bus bars were located on the ambient side of the endwall surface and attached to the foil with a compression contact. The large cross section insured an equipotential boundary condition at the upstream and downstream foil edges. A 1000 W, variable current DC power supply was used to heat the surface.

Determination of the Generated Surface Heat Flux. Solution of the electrostatic boundary value problem is required to determine the generated surface heat flux on a steady-state surface with arbitrarily specified internal or external boundaries. The voltage potential distribution, $V(x, y)$ for the present heat flux surface configuration and material (Inconel 600) is governed by the Laplace equation,

$$\vec{\nabla}^2 V(x, y) = 0. \tag{4}$$

The boundary conditions are:

(a) uniform potential at the bus bar and heater foil junctions, and

Table 1 Experimental uncertainty estimates for the flow field

Section	U_{95} ($U/U_{in,cl}$)	U_{95} ($C_{p,s}$)	U_{95} ($\|\Omega\|$)
0°	± 0.0096	± 0.006	----
45°	± 0.0098	± 0.006	± 36 sec^{-1}
90°	± 0.0105	± 0.006	± 43 sec^{-1}

values evaluated at $U/U_{in,cl}$ = 1.0 and $|\Omega|$ = 350 sec^{-1}

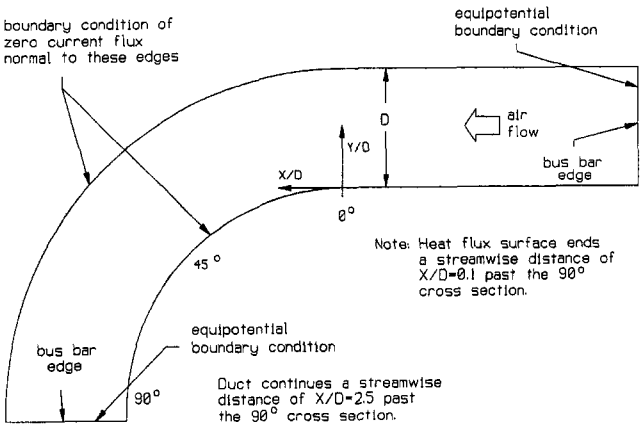

Fig. 2 Endwall heat transfer test surface

(b) zero current flux normal to the unbounded streamwise edges.

From the calculated potential distribution, the electric field, $\vec{E}$, and current density, $\vec{J}$, are determined, respectively,

$$\vec{E} = -\vec{\nabla}V \quad (\text{V/m}) \tag{5}$$

$$\vec{J} = \sigma\vec{E} \quad (\text{A/m}^2) \tag{6}$$

where σ is the conductivity of the heater foil. The generated surface heat flux is determined according to,

$$\dot{q}_{\text{gen}} = \delta\vec{E}\cdot\vec{J}, \quad (\text{W/m}^2) \tag{7}$$

where δ is the thickness of the foil. In the present study, a finite element solution technique was used to solve the described boundary value problem. The heat flux surface geometry was discretized with eight-noded, isoparametric, quadrilateral finite elements. A total of 115 elements and 402 nodes were used. A technique based on variational principles was then applied to solve the potential and current density fields. Details of the numerical method are given in Zienkiewicz (1971) and Camci (1989).

Convective Heat Transfer Coefficient Determination. The heat transfer experiments were performed under steady-state conditions. A run time of approximately two hours was required to reach thermal equilibrium. A high-resolution distribution of the endwall surface temperature was obtained with liquid crystal thermography. The endwall liquid crystal images were captured with a high sensitivity CCD sensor, stored on magnetic tape and later processed using a hue capturing technique. A discussion of the hue capturing technique is given by Camci et al. (1992) and Kim (1991). In addition to the liquid crystal image, several other quantities were recorded during each experiment. The measurements included voltage drop across the bus bars, inlet free-stream temperature, and an array of surface temperature readings from the ambient side of the endwall heat transfer surface. Local heat transfer coefficients on the endwall surface were determined according to,

$$h = \frac{\dot{q}_{\text{conv}}}{(T_w - T_{o\infty})} = \frac{\dot{q}_{\text{gen}} - \dot{q}_{\text{cond}} - \dot{q}_{\text{rad}}}{(T_w - T_{o\infty})} \quad (\text{W/m}^2\,\text{K}) \tag{8}$$

From an experiment, high-resolution, local wall temperatures on the endwall heat transfer surface were determined from the hue attribute contained within the image. Each image corresponded to a distinct voltage drop applied across the bus bars. The surface heat flux generated for each voltage/power level produced a particular hue/temperature distribution defined by the color bandwidth of the liquid crystals.

A black body enclosure model and the assumption of thermal equilibrium between the free-stream air and the unheated duct walls were used to estimate the radiative heat loss. The radiation losses typically accounted for 8–10 percent of the local generated heat flux. Local conduction losses through the acrylic endwall were also estimated. An infrared thermometer was used to record the ambient side surface temperature at multiple points clustered in the endwall region opposite the liquid crystal color band that existed on the forced convection side of the endwall. From the infrared thermometer measurements, a high-density grid of the ambient side endwall temperature distribution was calculated. A two-dimensional interpolation scheme was used to calculate the ambient side temperature grid. The heat flux lost to conduction through the endwall surface was then determined from the two temperature fields. The effects of lateral conduction were investigated in several regions of the endwall surface. The results indicated that the maximum lateral conduction component found increased the total local conduction heat flux by only 0.25 percent of the local generated heat flux. The total heat flux lost to conduction through the endwall was generally 5–8 percent of the generated heat flux.

The free-stream temperature upstream of the test section was measured with a fine wire K-type thermocouple. A recovery factor of unity was assumed based on the low free-stream velocity of the flow. The fine wire thermocouple probe, infrared thermometer, and the surface mount thermocouples used for the liquid crystal calibration were all calibrated against the same mercury thermometer. The experimental uncertainty of the measured parameters and the final convective heat transfer coefficient were estimated according to the procedures given by Kline and McClintock (1953) and Abernethy et al. (1985). Based on a 95 percent confidence interval, the uncertainties were: $\dot{q}_{\text{gen}}$(±1.0 percent), $T_w - T_{o\infty}$(±3.4 percent), and h(±3.8 percent). Higher uncertainties were found in the conductive and radiative heat flux losses; however, their small magnitudes relative to the generated surface heat flux produced only a minor influence in the heat transfer coefficient uncertainty. In addition, the exact nature of the finite element numerical technique results in a low measurement uncertainty of the generated heat flux. A complete description of the heat transfer measurement uncertainties are provided by Wiedner (1993) and Wiedner and Camci (1996b, 1993).

Results and Discussion

Streamwise and Secondary Velocity Fields. The development of the velocity and pressure fields is shown in Figs. 3–9. In each of the contour and vector plots presented, the streamwise flow is out of the page. The measured quantities have been referenced to the inlet centerline conditions. The inlet conditions were measured a distance of $X/D = 2.75$ upstream of the 0 deg (start of curvature) plane. The streamwise velocity was symmetric across the inlet plane with relatively uniform boundary layer thicknesses on all surfaces (Fig. 3(a)). The upper endwall ($Z/D = 1.0$) mean velocity and turbulent fluctuation profiles are shown in Fig. 3(b) and the characteristics of the inlet endwall boundary layer are summarized in Table 2. Secondary velocity vectors at the inlet plane were typically less than 3 percent of the free-stream velocity in the X direction.

The influence of the 90 deg bend geometry is apparent in the pressure coefficient contours measured at the 0 deg cross section, Fig. 4(a). A horizontal (radial) pressure gradient is developed across the duct cross section with a higher pressure near the outer radius surface than near the inner radius. The increase in pressure near the outer surface and decrease near the inner surface results in a pressure difference across the passage equivalent to 35 percent of the inlet dynamic pressure. In addition, the local horizontal pressure gradient near the inner radius surface is greater than the pressure gradient near the outer surface. With the exception of the outer radius near wall region, a general

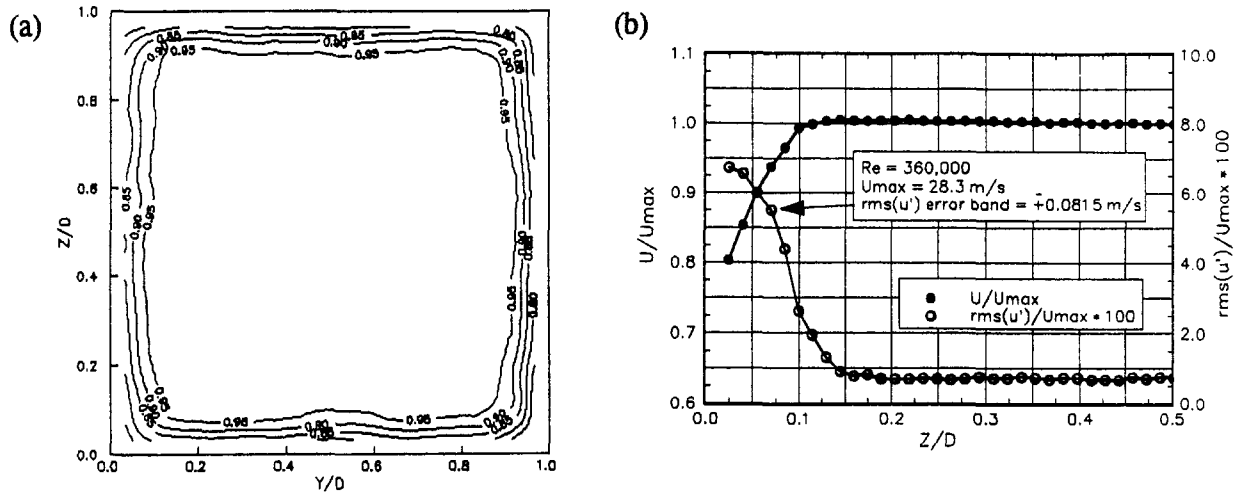

Fig. 3 Streamwise velocity contours at the inlet cross section ($X/D = -2.75$): (*a*) $U/U_{in,cl}$ contours, (*b*) $U/U_{in,cl}$ and turbulent velocity fluctuation ($\text{rms}(u')/U_{in,cl}$) profiles

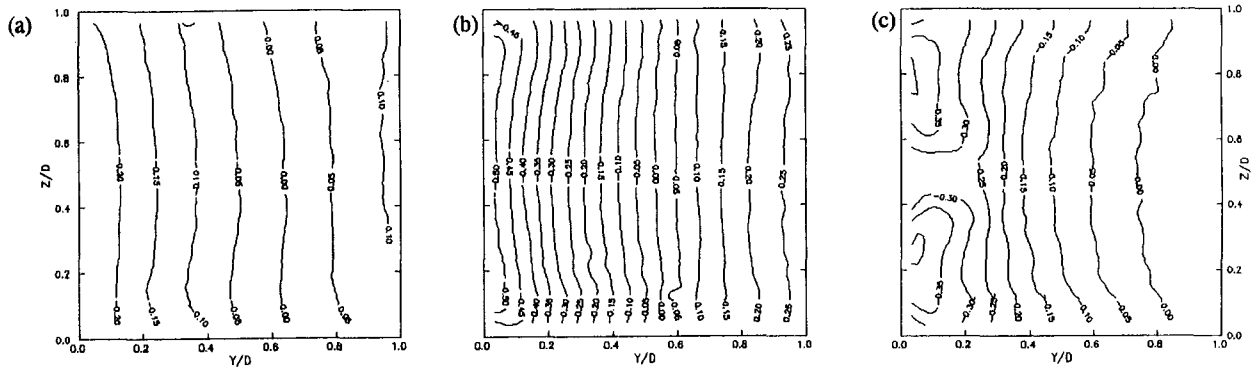

Fig. 4 Static pressure coefficient, $C_{ps} = (p_s - p_{s,in,cl})/0.5\rho U^2_{in,cl}$: (*a*) 0 deg, (*b*) 45 deg, (c) 90 deg

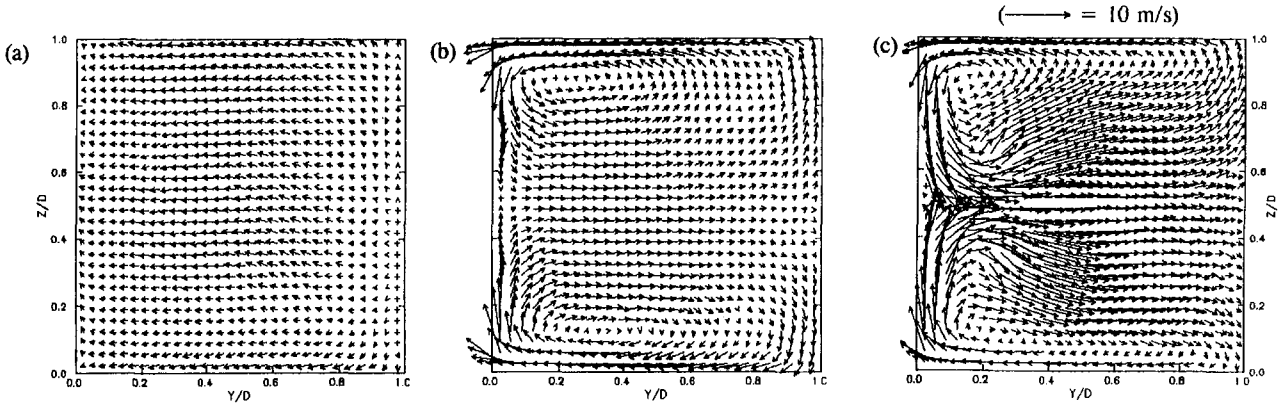

Fig. 5 Secondary mean velocity vectors: (a) 0 deg, (b) 45 deg, (c) 90 deg

migration of secondary flow toward the inner radius surface occurs, Fig. 5(a). A typical secondary velocity magnitude in this plane is 6 percent of the free-stream velocity magnitude. In the outer radius surface near-wall region, secondary flow is seen to move away from the plane of symmetry, $Z/D = 0.5$, toward the endwalls. In accordance with the adverse streamwise pressure gradient near the outer wall and the favorable streamwise pressure gradient near the inner wall, the streamwise velocity contours indicate a deceleration and acceleration, respectively (Fig. 6(a)). A qualitative representation of the streamwise velocity distribution, Fig. 7(a), shows the gradient of the streamwise velocity component in the core of the passage to be uniform. The upper surface endwall boundary layer has grown to an approximate height of 40 mm and remains uniform across the surface, Fig. 8(a). The total pressure coefficient contours indicate a slight increase in the thickness of the high loss region near the outer radius compared to the inner radius surface, Fig. 9(a).

A difference in pressure equivalent to 75 percent of the inlet dynamic pressure existed across the duct at the 45 deg cross section, Fig. 4(b). Similar to the 0 deg plane, the local horizontal pressure gradient increases from the outer radius surface

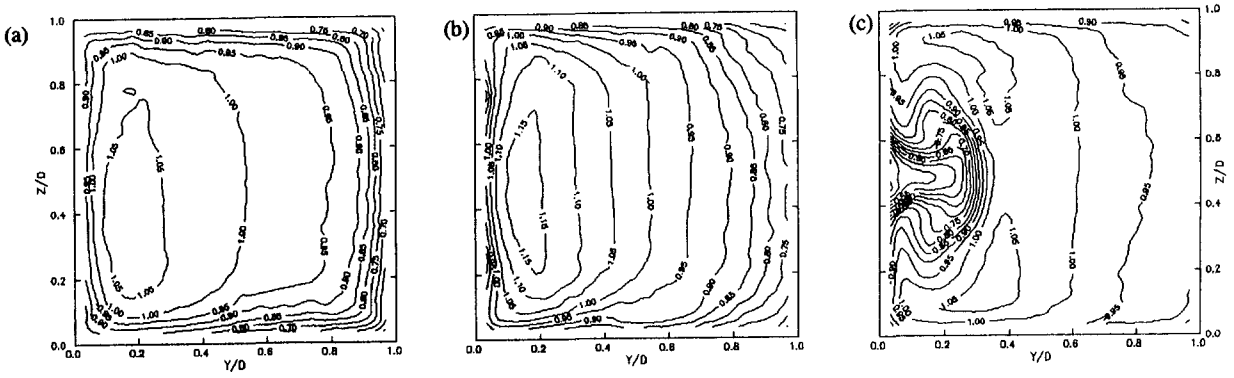

Fig. 6 Streamwise mean velocity, $U/U_{in,cl}$: (*a*) 0 deg, (*b*) 45 deg, (*c*) 90 deg

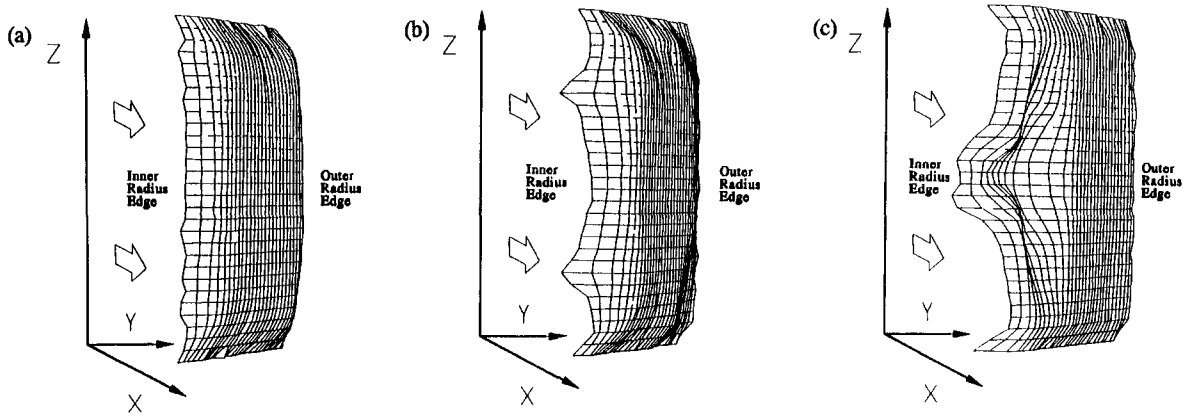

Fig. 7 Streamwise mean velocity surface contours: (*a*) 0 deg, (*b*) 45 deg, (*c*) 90 deg

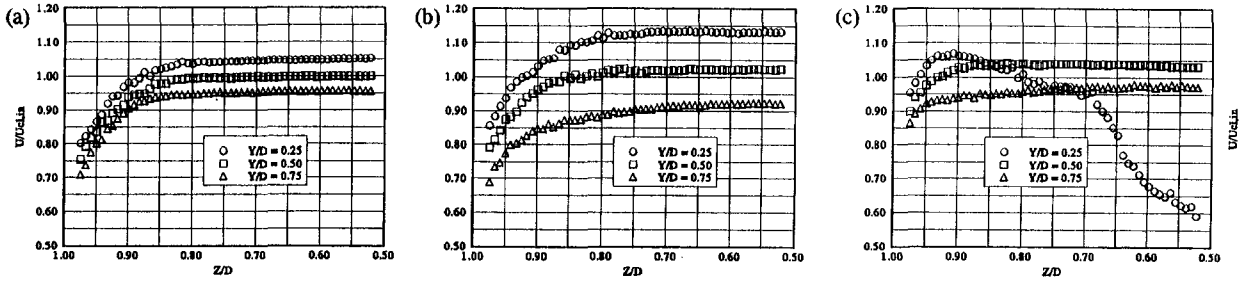

Fig. 8 Endwall mean velocity profiles, $U/U_{in,cl}$: (*a*) 0 deg, (*b*) 45 deg, (*c*) 90 deg

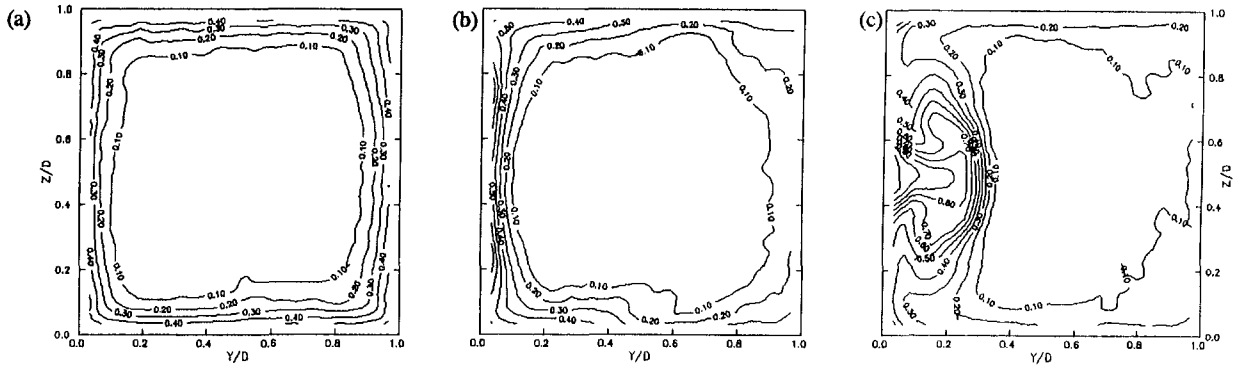

Fig. 9 Total pressure coefficient, $C_{po} = (p_{o,in,co} - p_o)/0.5\rho U^2_{in,cl}$: (*a*) 0 deg, (*b*) 45 deg, (*c*) 90 deg

Table 2 Endwall inlet boundary layer characteristics 55.8 cm ($X/D = -2.75$) upstream from the start of curvature (0 deg) at the endwall centerline

δ_{99}	25.4 mm
δ^*	4.6 mm
θ	2.6 mm
H	1.8
Tu_∞	0.7 % at Z/D=0.84
Tu_{max}	6.8% at Z/D=0.975

to the inner radius surface. Also, along the inner radius surface higher local pressures exist near the two endwall corners. The secondary velocity vectors indicate strong crossflows along the endwall from the outer to inner radius surfaces with the maximum crossflow velocity (33.7 percent of $U_{in,cl}$) occurring 38 mm ($Y/D = 0.188$) from the inner radius surface (Fig. 5(b)). The endwall crossflow encounters an adverse pressure gradient as it approaches the inner radius corner, causing a deceleration followed by intense turning. The low-momentum flow from the endwall moves onto the inner radius surface and toward the passage plane of symmetry. Near the inner radius surface and plane of symmetry intersection, the secondary velocity components become negligibly small. Turning of the high streamwise velocity component produces centrifugal forces, which result in secondary flow from the inner radius surface toward the outer radius surface in a direction parallel to the plane of symmetry. At the outer radius surface the secondary flow turns toward the endwalls. The outer radius/endwall corner regions indicate an acceleration of the secondary velocity vectors toward the endwall where impingement and turning occur. The complete secondary velocity pattern forms the counterrotating passage vortices common in passage flows with streamwise curvature. The streamwise velocity component indicates continued acceleration near the inner radius surface and deceleration in the outer radius region, Figs. 6(b) and 7(b). The peak streamwise velocity occurs between $0.1 < Y/D < 0.2$, with a stronger radial gradient in velocity across the passage compared to the 0 deg plane. Within the core region, variations in the streamwise velocity component are two dimensional. The streamwise velocity profiles indicate that the high-momentum-deficit regions near the endwall surface are thicker than at the 0 deg plane. In addition, a gradient in local endwall boundary layer thickness occurs with less momentum deficit near the inner radius surface, Fig. 8(b). Low total pressure losses exist throughout the outer radius region of the duct and high losses near the inner radius surface (Fig. 9(b)). Two distinct loss cores are present near the inner radius surface at $Z/D = 0.25, 0.75$. A total pressure loss equivalent to 70 percent of the inlet dynamic pressure exists within these cores. The high total pressure losses incurred near the inner radius surface are a consequence of high local mean velocity gradients. In turn, the local velocity gradients develop as the result of accumulation of low energy endwall boundary layer fluid that was displaced by the horizontal/radial pressure gradient. At the 90 deg cross section, the pressure gradient from the inner to outer radius surfaces has decreased to 45 percent of the inlet dynamic pressure (Fig. 4(c)). Like the 0 and 45 deg planes, the local pressure gradient is stronger near the inner radius than the outer radius. However, unlike the adverse streamwise pressure gradient exhibited in the outer radius region between 0 and 45 deg, a pressure decrease has occurred in the outer radius region, $0.4 < Y/D < 1.0$, between the 45 and 90 deg planes. The inner radius/endwall corner regions show an increase in pressure as does the region near the inner radius surface and plane of symmetry intersection. Each of these areas corresponds to a region in which the secondary flow velocity components experience strong deceleration. Throughout the cross section, the passage vortices are stronger at the 90 plane than at the 45 deg plane (Fig. 5(c)). Also, the largest secondary velocity vectors are located along the inner radius surface (40 percent of $U_{in,cl}$ at $Z/D = 0.3, 0.7$) rather than along the endwall. In the region near the intersection of the plane of symmetry and inner radius surface, the secondary flow is strong with intense rotation toward the core of the passage. Several secondary velocity vectors in this region indicate that the interaction of the two primary passage vortices has generated a new pair of counterrotating vortices. Further evidence of this second pair of counterrotating vortices will be presented in the discussion of the streamwise vorticity structure.

The streamwise velocity component at the 90 deg plane is shown in Figs. 6(c) and 7(c). An immense redistribution of the streamwise momentum has occurred between the 45 and 90 deg cross sections. The low-momentum fluid that had begun to coalesce near the inner radius surface at the 45 deg cross section has moved across the inner radius surface toward the plane of symmetry and radially outward into the passage core. In addition, high-momentum fluid from the core has been convected to the outer radius surface, away from the plane of symmetry, and along the endwalls toward the inner radius surface. At the 90 deg plane, the outer 70 percent of the passage contains low-loss/high-momentum fluid ($C_{p,o} \leq 0.2$). The two high total pressure loss regions that existed near the inner radius surface ($Z/D = 0.25, 0.75$) at the 45 deg cross section have been displaced toward the plane of symmetry, met, and moved out into the passage to form a large T-shaped high total pressure loss core with the root extending from the inner radius surface (Fig. 9(c)). The highest total pressure loss region is found at the root of the loss core near the inner radius surface ($C_{p,o} \approx 1.1$). Recall that this area indicated an intense interaction of the two primary passage vortices in addition to the generation of a second vortex pair. Further evidence of the redistribution of the passage flow at 90 deg is seen in the three endwall streamwise velocity surveys (Fig. 8(c)). In the outer radius region, $Y/D = 0.75$, a high shear, thin boundary layer and accelerated local free stream exist, while, near the inner radius surface, $Y/D = 0.25$, a thin, highly three-dimensional endwall boundary layer exists.

Vorticity Field. At the inlet and 0 deg cross sections, the distribution of the vorticity field is primarily restricted to the passage boundary layers. Negligible streamwise vorticity existed at either cross section. Figures 10–13 show the three components of vorticity and the magnitude of the vorticity vector that existed at the 45 and 90 deg cross sections. At the 45 deg cross section, the streamwise component of vorticity, Ω_X, indicates an increase along the endwall boundary layers from the outer radius surface to the inner surface. A maximum magnitude of 750 s^{-1} exists near the inner radius corner. The horizontal component of vorticity, Ω_Y, is primarily confined to the endwall regions and remains at approximately the same strength as the 0 deg cross section. The vertical component, Ω_Z, is limited to the inner radius surface. Low levels of the vertical vorticity component are shown near the outer radius surface. This event coexists with the low total pressure loss region near the outer radius surface previously described. The highest level of vertical vorticity corresponds with the high total pressure loss cores that exist near the inner radius surface. The vorticity vector magnitude indicates the highest levels along the endwalls and inner radius surface with peaks (>850 s^{-1}) in the inner radius corner regions.

At the 90 deg cross section, the endwall regions exhibit a gradient in the streamwise vorticity, Ω_X, with the lower levels near the outer radius surface and the higher levels near the inner radius surface. The maximum streamwise vorticity magnitudes

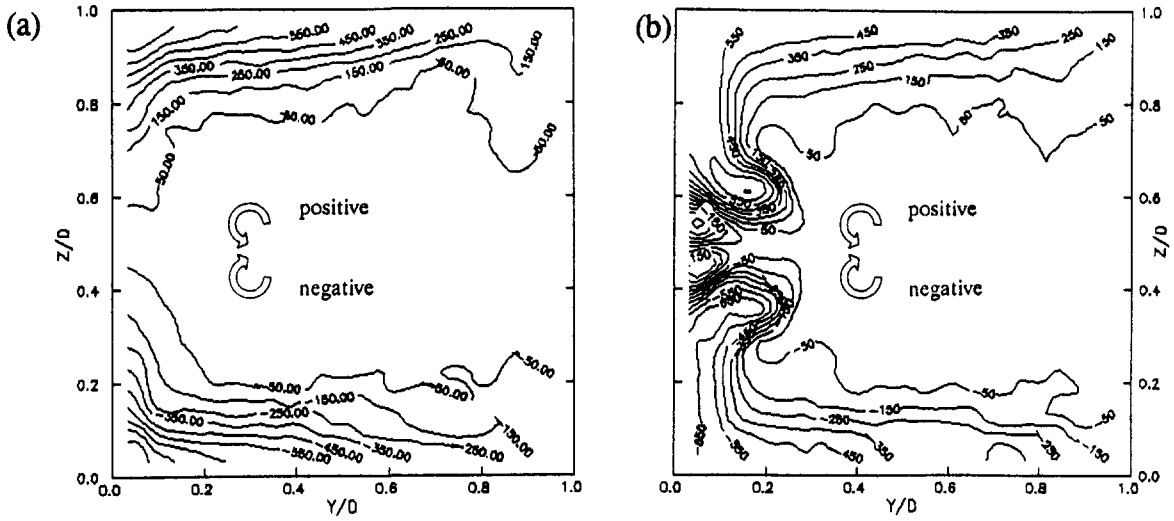

Fig. 10 Streamwise mean vorticity, Ω_X: (*a*) 45 deg, (*b*) 90 deg

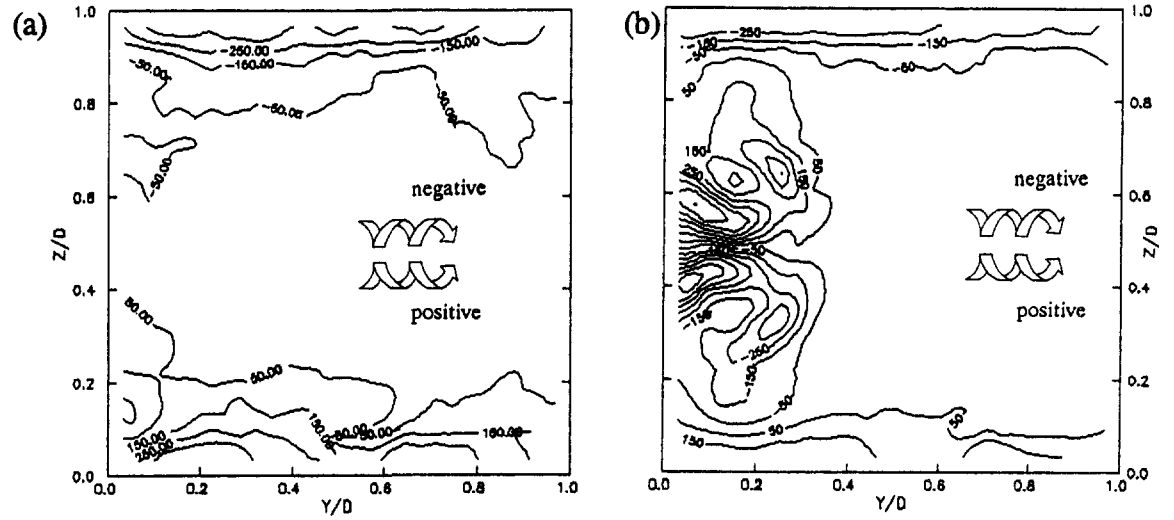

Fig. 11 Horizontal/radial mean vorticity, Ω_Y: (*a*) 45 deg, (*b*) 90 deg

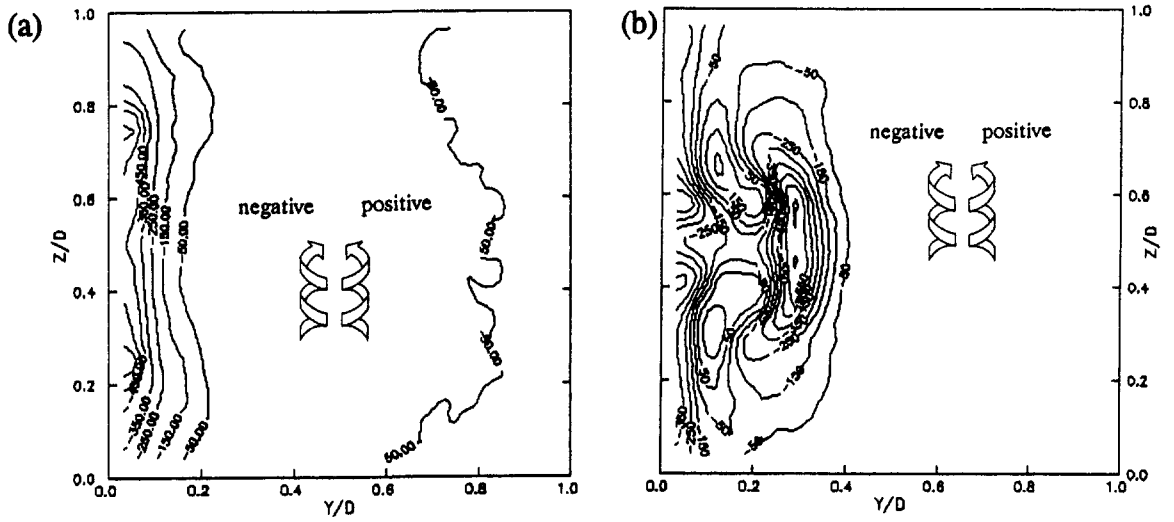

Fig. 12 Vertical mean vorticity, Ω_Z: (*a*) 45 deg, (*b*) 90 deg

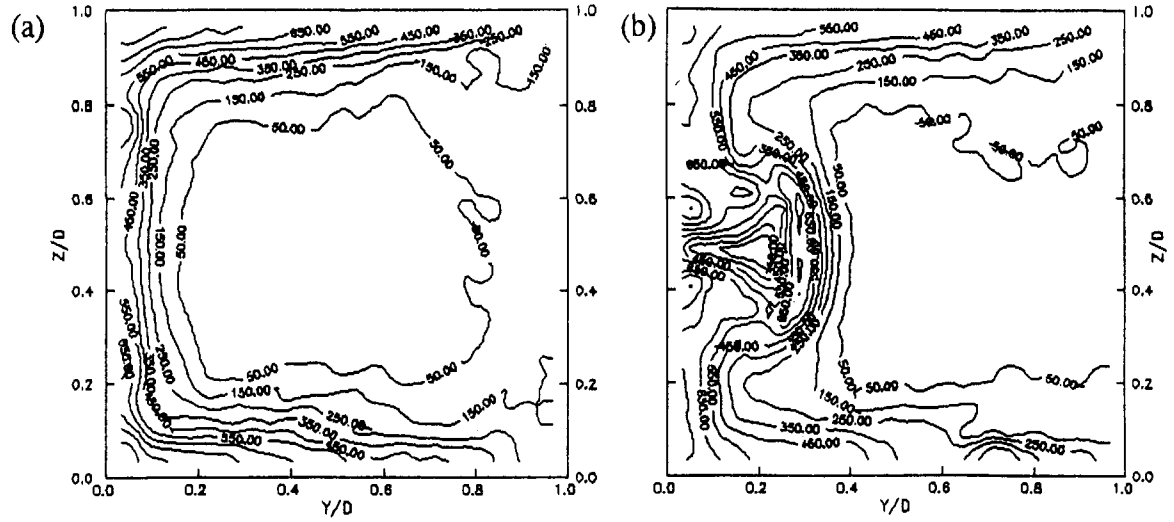

Fig. 13 Mean vorticity vector magnitude, $|\Omega|$: (*a*) 45 deg, (*b*) 90 deg

are located along the inner radius surface and within the high total pressure loss core along the plane of symmetry ($0.0 < Y/D < 0.2$). A new pair of oppositely directed streamwise vorticity components is shown in the inner radius region along the plane of symmetry. Their evolution results from the intense interaction of the two primary counterrotating vortices and the inner radius surface. The horizontal vorticity component is no longer confined to the endwall regions. Though not as intense in magnitude as the streamwise component, horizontal vorticity exists throughout the high loss region near the inner radius surface. Similar to the 45 deg cross section, the vertical vorticity component is concentrated near the inner radius surface ($0.0 < Y/D < 0.4$). With the exception of the endwall regions, the outer radius region of the passage is free of strong vortical action. However, the majority (>60 percent) of the passage cross section contains high levels of vorticity.

Endwall Heat Transfer. The convective heat transfer coefficient distribution for the endwall surface is shown in Fig. 14. Several distinct regions of interest on the endwall have been labeled $A-G$ and paths I and II. The entry region prior to the 90 deg turn shows a continual decrease in the heat transfer coefficient on the test surface from the inlet to the 0 deg cross section (A). The decline in heat transfer in the streamwise direction is governed by the growth of the hydrodynamic and thermal boundary layers. Narrow regions of high heat transfer with strong gradients in the cross-stream direction are shown near the inner and outer radius corners (B). Specific corner flows, as described by Brundett and Baines (1964), Gessner (1973), and others, in these regions may be responsible for the higher heat transfer levels. These strong gradient regions in the straight inlet section of the duct coincide with the regions that have the highest turbulent velocity fluctuations, Fig. 3(b). It should be noted that the conduction heat loss through the sidewalls could also result in a slight increase in the uncertainty of the heat transfer coefficient in this region. Further details of the fluid mechanics in the corner region are required to quantify the contribution to endwall heat transfer. Steep gradients in the heat transfer coefficient along the outer radius surface within the 90 deg bend (C) are also clearly visualized. The passage vortex may produce significant vorticity near the outer and inner radii corner regions. The cross-stream velocities that indicate the strong vorticity content in these regions are shown in Figs. 5(b) and 5(c). Vorticity augmentation is much more significant near the inner radius corner than near the outer radius corner. The augmentation of the magnitude of the mean vorticity vector near the corner regions is shown in Figs. 13(a) and 13(b). It is likely that the location of the mean vorticity magnitude derived from three-dimensional mean velocity data coincide with the regions of enhanced turbulent flow activity. The points on the endwall surface under the influence of these high turbulent kinetic energy regions could experience enhanced turbulent heat transport from the endwall.

An enhancement in heat transfer (D) followed by a low region of heat transfer (E) occurs near the inner radius surface between the 0 and 35 deg cross sections where the initial development of cross-stream velocities takes place. Similar patterns were observed in the cascade results of Goldstein and Spores (1988). They attributed the high heat transfer zone to a local highly turbulent flow that resulted from the transverse pressure gradient turning the endwall boundary layer. In regions D and E, shown in Fig. 14(a), a highly accelerated boundary layer on the convex inner surface and the endwall boundary layer merge together in the corner region. The mean flow in this corner region after the 0 deg section is highly three dimensional. The endwall boundary layer fluid starts to develop the secondary velocities in a direction from the outer wall to convex inner wall between the 0 and 45 deg locations. Between the inlet section and the 0 deg section, the inlet endwall boundary layer on the heat transfer surface is not subject to streamwise curvature. The inlet flow away from the corners has almost a two-dimensional mean flow structure, as shown in Figs. 3, 4(a), 5(a), and 7(a). Immediately after the 0 deg section, near region D, this structure is severely disturbed by the immediate development of centrifugal forces, static pressure gradient in the Y direction, stagnation pressure gradient in the Z direction, and the highly accelerated boundary layer on the inner radius side wall. Region D experiences a locally enhanced mode of turbulent heat transport (77–82 W/m^2 K) due to its highly strained mean flow structure. Immediately downstream of region D a relatively reduced heat transfer coefficient island (E) (67–72 W/m^2 K) exists. Turbulent momentum and heat exchange in this region may be reduced due to further acceleration of the fluid near the inner radius wall between the 20 and 45 deg cross sections. Further investigation of the heat transfer behavior in the corner region immediately downstream of the 0 deg section in conjunction with the mean flow and turbulent flow field is currently under consideration.

At the 0 deg cross section, a gradient in the heat transfer coefficient exists with the higher levels near the inner radius surface and the lower levels near the outer radius surface (F). The favorable and adverse pressure gradients near the inner and outer radius surfaces, respectively, resulted in accelerated

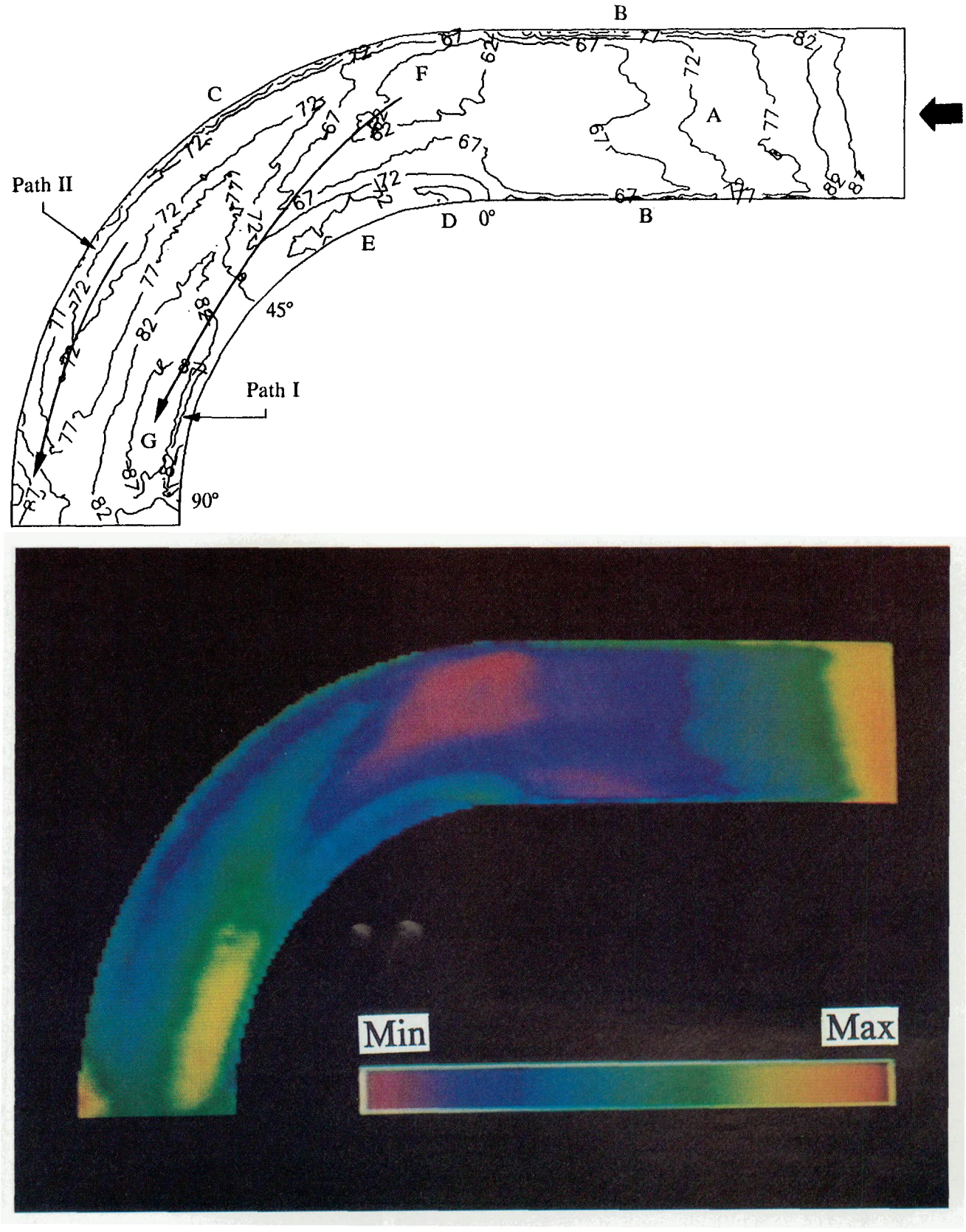

Fig. 14 Endwall convective heat transfer coefficient, h (W/m^{2}K)

streamwise velocity near the inner surface and decelerated streamwise velocity near the outer radius surface. As the flow moves into the bend, the outer radius half of the passage endwall continues to show a decrease in the heat transfer level, while the heat transfer level on the inner radius half continues to increase. Beginning from the minimum heat transfer level established in the outer radius half and continuing across the passage endwall toward the inner radius surface, a path of increasing

heat transfer level occurs (Path I). This path forms the characteristic wedge shape that has been described by Graziani et al. (1980) and can also be seen in the cascade results of Gaugler and Russell (1984), Goldstein and Spores (1988), and Boyle and Russell (1989). The path crosses the 45 deg cross section at an approximate value of $Y/D = 0.25$. The secondary velocity vector map at this cross section (Fig. 5(*b*)) indicated the highest secondary velocity vectors adjacent to the endwall occurred at this position. Similar circumstances are apparent at the 90 deg cross section, Fig. 5(*c*).

As discussed, the region of high endwall heat transfer near the inner radius surface (*G*) is seen to coincide with high levels of local secondary velocity. Traversing the endwall radially inward, a decrease in the heat transfer coefficient occurs as the inner radius surface and endwall corner is approached. This decrease in heat transfer may be the result of the secondary velocity deceleration followed by the abrupt turning of the flow onto the inner radius surface. The secondary flow conditions are similar to those present in a longitudinal vortex. Eibeck and Eaton (1987) showed a decrease in the Stanton number on the upwash side of the vortex.

Finally, in the outer radius region of the passage endwall between the 45 and 90 deg cross sections, the streamwise pressure gradient changes from adverse to favorable. This pressure gradient reversal results in an acceleration of the streamwise velocity. The endwall heat transfer coefficient distribution in this region indicates a path of increasing heat transfer that continues through the 90 deg cross section, Path II. The elevated heat transfer coefficient values (87–92 W/m^2 K) measured near the outer surface corner at the 90 deg section lie in this path of increasing heat transfer.

Conclusions

The fluid dynamic features and endwall heat transfer coefficient patterns have been reported for a strongly curved, 90 deg turning duct. A detailed map of the convective heat transfer coefficient on the endwall surface and the mean flow characteristics at four streamwise cross sections are presented (inlet, 0, 45, 90 deg). The influence of the duct curvature on the pressure field was apparent throughout the passage curvature. Two primary counterrotating passage vortices developed as a result of the inertial and pressure force balance. Between the 0 and 45 deg cross sections, an adverse streamwise pressure gradient existed in the outer radius region and favorable streamwise pressure gradient existed in the inner radius region. These pressure gradients resulted in a streamwise deceleration and acceleration, respectively. Between the 45 and 90 deg cross sections, a favorable streamwise pressure gradient existed in the outer radius region. Streamwise accelerations and a migration of the vorticity field toward the inner radius surface resulted. High secondary flows traversed the endwall from the outer to inner radius surfaces. At the 90 deg section, the highest secondary velocity vectors had moved onto the inner radius surface.

The local heat transfer behavior on the endwall surface is closely related to the structure of the three-dimensional mean flow and the associated turbulent flow field. When the endwall boundary layer develops in the curved section of the duct, cross-stream components of the velocity vector are enhanced due to the generation of the passage vortex. The endwall boundary layer is also subject to streamwise curvature. The interaction of the endwall boundary layer with the inner and outer radius side wall boundary layers creates complex local wall heating rate distributions in the corner regions. Elevated levels of local heat transfer coefficients on the endwall coincide with the flow regions that have high levels of vorticity magnitude. High levels of heat transfer on the endwall were also found near the regions of high secondary velocity adjacent to the endwall and in regions where the streamwise velocity gradient was positive. Regions of low heat transfer were associated with local streamwise decelerations.

Several of the endwall heat transfer characteristics that exist in cascade studies were present in the turning duct passage. These results suggest that the simplified turbine passage model can sufficiently represent many of the dominant fluid dynamic and resulting endwall heat transfer properties present in cascade models. Duct flows also represent a natural progression for computational studies aimed at resolving the details of the more complex, complete turbine stage. A successful interpretation of local high and low heat transfer regions require an extensive evaluation of the local turbulent flow characteristics. A detailed investigation of the local turbulent flow features is currently under progress.

Acknowledgments

The authors would like to acknowledge the support of NASA Lewis Research Center, Internal Fluid Mechanics Division for the continuation of this experimental program through Grant No. NAG-3-989. The program was monitored by S. A. Hippensteele. Some of the equipment used in the program was obtained through National Science Foundation equipment Grant No. CTS-8906452.

References

Abernethy, R. B., Benedict, R. P., and Dowdell, R. B., 1985, "ASME Measurement Uncertainty," ASME *Journal of Fluids Engineering,* Vol. 107, pp. 161–164.

Besserman, D. L., and Tanrikut, S., 1992, "Comparison of Heat Transfer Measurements With Computations for Turbulent Flow Around a 180 deg Bend," ASME JOURNAL OF TURBOMACHINERY, Vol. 114, pp. 865–871.

Boyle, R. J., and Russell, L. M., 1989, "Experimental Determination of Stator Endwall Heat Transfer," NASA TM-101419.

Boyle, M. T., Simonds, M., and Poon, K., 1988, "A Comparison of Secondary Flow in a Vane Cascade and a Curved Duct," *Heat Transfer in Gas Turbine Engines and Three Dimensional Flows,* ASME HTD-Vol. 103, pp. 85–93.

Brundett, E., and Baines, W. D., 1964, "The Production and Diffusion of Vorticity in Duct Flow," *Journal of Fluid Mechanics,* Vol. 19, pp. 375–394.

Camci, C., 1989, "An Experimental and Numerical Investigation of Near Cooling Hole Heat Fluxes on a Film Cooled Turbine Blade," ASME JOURNAL OF TURBOMACHINERY, Vol. 111, pp. 63–70.

Camci, C., Kim, K., and Hippensteele, S. A., 1992, "A New Hue Capturing Technique for the Quantitative Interpretation of Liquid Crystal Images Used in Convective Heat Transfer Studies," ASME JOURNAL OF TURBOMACHINERY, Vol. 114, pp. 765–775.

Eibeck, P. A., and Eaton, J. K., 1987, "Heat Transfer Effects of a Longitudinal Vortex Embedded in a Turbulent Boundary Layer," ASME *Journal of Heat Transfer,* Vol. 109, pp. 16–24.

Enayet, M. M., Gibson, M. M., and Yianneskis, M., 1982, "Measurements of Turbulent Developing Flow in a Moderately Curved Square Duct," *Int. J. Heat Fluid Flow,* Vol. 3, pp. 221–224.

Gaugler, R. E., and Russell, L. M., 1984, "Comparison of Visualized Turbine Endwall Secondary Flows and Measured Heat Transfer Patterns," ASME *Journal of Engineering for Gas Turbines and Power,* Vol. 106, pp. 168–172.

Gessner, F. B., 1973, "The Origin of Secondary Flow in Turbulent Flow Along a Corner," *Journal of Fluid Mechanics,* Vol. 58, pp. 1–25.

Goldstein, R. J., and Spores, R. A., 1988, "Turbulent Transport on the Endwall in the Region Between Adjacent Turbine Blades," ASME *Journal of Heat Transfer,* Vol. 110, pp. 862–869.

Graziani, R. A., Blair, M. F., Taylor, J. R., and Mayle, R. E., 1980, "An Experimental Study of Endwall and Airfoil Surface Heat Transfer in a Large Scale Turbine Blade Cascade," ASME *Journal of Engineering for Power,* Vol. 102, pp. 257–267.

Gregory-Smith, D. G., Graves, C. P., and Walsh, J. A., 1988a, "Growth of Secondary Losses and Vorticity in an Axial Turbine Cascade," ASME JOURNAL OF TURBOMACHINERY, Vol. 110, pp. 1–8.

Gregory-Smith, D. G., Walsh, J. A., Graves, C. P., and Fulton, K. P., 1988b, "Turbulence Measurements and Secondary Flows in a Turbine Rotor Cascade," ASME JOURNAL OF TURBOMACHINERY, Vol. 110, pp. 479–485.

Humphrey, J. A. C., Taylor, A. M. K., and Whitelaw, J. H., 1977, "Laminar Flow in a Square Duct of Strong Curvature," *Journal of Fluid Mechanics,* Vol. 83, pp. 509–527.

Humphrey, J. A. C., Whitelaw, J. H., and Yee, G., 1981, "Turbulent Flow in a Square Duct With Strong Curvature," *Journal of Fluid Mechanics,* Vol. 103, pp. 443–463.

Johnson, R. W., and Launder, B. E., 1985, "Local Nusselt Number and Temperature Field in Turbulent Flow Through a Heated Square-Sectioned U-Bend," *Int. J. Heat Fluid Flow,* Vol. 6, pp. 171–180.

Kim, K., 1991, "A New Hue Capturing Technique for the Quantitative Interpretation of Liquid Crystal Images used in Convective Heat Transfer Studies," Ph.D. Thesis, The Pennsylvania State University, Aerospace Engineering Department.

Kline, S. J., and McClintock, F. A., 1953, "Describing Uncertainties in Single-Sample Experiments," *Mechanical Engineering,* Vol. 75, Jan., pp. 3–8.

Langston, L. S., Nice, M. L., and Hooper, R. M., 1977, "Three-Dimensional Flow Within a Turbine Cascade Passage," ASME *Journal of Engineering for Power,* Vol. 99, pp. 21–28.

Langston, L. S., 1980, "Crossflows in a Turbine Cascade Passage," ASME *Journal of Engineering for Power,* Vol. 102, pp. 866–874.

Marchal, P., and Sieverding, C. H., 1977, "Secondary Flows Within Turbomachinery Blading," *Secondary Flows in Turbomachines,* AGARD CP-214.

Metzger, D. E., and Larson, D. E., 1986, "Use of Melting Point Surface Coatings for Local Convection Heat Transfer Measurements in Rectangular Channel Flows With 90-deg Turns," ASME *Journal of Heat Transfer,* Vol. 108, pp. 48–54.

Moore, J., and Ransmayr, A., 1984, "Flow in a Turbine Cascade: Part 1—Losses and Leading-Edge Effects," ASME *Journal of Engineering for Gas Turbines and Power,* Vol. 106, pp. 400–408.

Moore, J. and Smith, B. L., 1984, "Flow in a Turbine Cascade: Part 2—Measurement of Flow Trajectories by Ethylene Detection," ASME *Journal of Engineering for Gas Turbines and Power,* Vol. 106, pp. 409–413.

Mori, Y., Uchida, Y., and Ukon, T., 1971, "Forced Convective Heat Transfer in a Curved Channel With a Square Cross Section," *Int. J. Heat Mass Transfer,* Vol. 14, pp. 1787–1805.

Rojas, J., Whitelaw, J. H., and Yianneskis, M., 1987, "Forced Convective Heat Transfer in Curved Diffusers," ASME *Journal of Heat Transfer,* Vol. 109, pp. 866–871.

Shiragami, N., and Inoue, I., 1989, "Turbulent Velocity Profile and Turbulent Statistical Quantities in a Rectangular Bend," *Int. J. Engineering Fluid Mechanics,* Vol. 2, pp. 157–176.

Sieverding, C. H., 1985, "Recent Progress in the Understanding of Basic Aspects of Secondary Flows in Turbine Blade Passages," ASME *Journal of Engineering for Gas Turbines and Power,* Vol. 107, pp. 248–257.

Taylor, A. M. K. P., Whitelaw, J. H., and Yianneskis, M., 1982, "Curved Ducts With Strong Secondary Motion: Velocity Measurements of Developing Laminar and Turbulent Flow," ASME *Journal of Fluids Engineering,* Vol. 104, pp. 350–359.

Treaster, A. L., and Yocum, A. M., 1979, "The Calibration and Application of Five-Hole Probes," *ISA Transactions,* Vol. 18, No. 3, pp. 23–34.

Wiedner, B. G., and Camci, C., 1992, "A Low Speed, Transient Facility for Propulsion Heat Transfer Studies," *Proc. International Symposium on Heat Transfer in Turbomachinery,* organized by the International Centre for Heat and Mass Transfer, ICHMT, Athens, Greece.

Wiedner, B. G., 1993, "Passage Flow Structure and Its Influence on Endwall Heat Transfer in a 90° Turning Duct," Ph.D. Thesis, The Pennsylvania State University, Aerospace Engineering Department.

Wiedner, B. G., and Camci, C., 1993, "A Technique for the Determination of Local Heat Flux on Steady State Heat Transfer Surfaces With Arbitrarily Specified External and Internal Boundaries," *Gas Turbine Heat Transfer,* ASME HTD-Vol. 242, pp. 21–31.

Wiedner, B. G., and Camci, C., 1996a, "Passage Flow Structure and Its Influence on Endwall Heat Transfer in a 90° Turning Duct: Turbulent Stresses and Turbulent Kinetic Energy Production," ASME Paper No. 96-GT-251.

Wiedner, B. G., and Camci, C., 1996b, "Determination of Convective Heat Flux on Steady-State Heat Transfer Surfaces With Arbitrarily Specified Boundaries," ASME *Journal of Heat Transfer,* Vol. 118, pp. 850–856.

Zienkiewicz, O. C., 1971, *The Finite Element Method in Engineering Science,* McGraw-Hill, London.

Measurement and Computation of Heat Transfer in High-Pressure Compressor Drum Geometries With Axial Throughflow

C. A. Long

A. P. Morse

Thermo-Fluid Mechanics Research Centre,
University of Sussex,
Brighton, Sussex, United Kingdom

P. G. Tucker
A.P.E.M.E.,
University of Dundee,
Fife, Scotland,
United Kingdom

This paper makes comparisons between CFD computations and experimental measurements of heat transfer for the axial throughflow of cooling air in a high-pressure compressor spool rig and a plane cavity rig. The heat transfer measurements are produced using fluxmeters and by the conduction solution method from surface temperature measurements. Numerical predictions are made by solving the Navier–Stokes equations in a full three-dimensional, time-dependent form using the finite-volume method. Convergence is accelerated using a multigrid algorithm and turbulence modeled using a simple mixing length formulation. Notwithstanding systematic differences between the measurements and the computations, the level of agreement can be regarded as promising in view of the acknowledged uncertainties in the experimental data, the limitations of the turbulence model and, perhaps more importantly, the modest grid densities used for the computations.

1 Introduction

Improvements in the power and thermal efficiency of gas turbine engines rely on increasing turbine inlet temperatures and advances in cooling technology. Cooling air is bled from the compressor and is routed to the various engine components by the so-called Internal Air System. If components are not adequately cooled, component failures will occur, but too much cooling air will of course reduce overall engine performance.

Figure 1 shows a schematic diagram of a section through an aero-engine high-pressure compressor. The compressor spool comprises an outer drum and a series of disks, which partition the interior into a number of cavities, sealed at the periphery or shroud. Cooling air passes axially through the compressor spool, flowing between the bores of adjacent disks as shown in the figure. Some of this flow enters the cavities and a parasitic temperature rise occurs as a result of heat transfer from the disk surfaces and the shroud. A knowledge of the heat transfer is therefore important for two reasons: (*i*) to be able to predict the temperature of the turbine cooling air, and (*ii*) to be able to predict the temperature, stress, and radial growth of the compressor disks.

Farthing et al. (1992b) experimentally investigated the flow structure in a simplified high-pressure compressor configuration comprising a single rotating cavity with an axial throughflow of cooling air. The isothermal (or unheated) flow structure was characterized by a toroidal vortex driven by the central throughflow. In the main, the flow was axisymmetric. However, various modes of vortex breakdown were found to occur (governed by the cavity gap ratio, $G = s/b$, and the Rossby number, $\mathrm{Ro} = W/\Omega a$), some of which resulted in nonaxisymmetric flow and some in axisymmetric flow but with a reversal at the cavity exit. For a heated cavity, the nonisothermal flow structure is always three dimensional. It appears that rotationally induced buoyancy forces cause heated air inside the cavity to be destabilized. As a consequence of the resulting motion, some (perhaps 10–20 percent) of the central throughflow enters the cavity through one or more radial arms. Asymmetry in the flow is required to provide the Coriolis force, through a circumferential pressure gradient, necessary to sustain a radial flow outside the disk boundary layers.

Farthing et al. (1992a) correlated measurements of the disk heat transfer and Long and Tucker (1994a) presented measurements of the heat transfer from the peripheral shroud. In both cases, a cavity with a gap ratio of $G = 0.13$ was used, and it was suggested that the heat transfer was a function of a rotational Grashof number, $\mathrm{Gr} = \Omega^2 r \beta \Delta T L^3/\nu^2$ (the choice of characteristic length, L, is discussed more fully later in this paper).

Full three-dimensional, time-dependent, laminar computations for fairly low values of axial and rotational Reynolds numbers ($\mathrm{Re}_Z \approx 2 \times 10^3$ and $\mathrm{Re}_\phi \approx 1 \times 10^4$) were made by Long and Tucker (1994b). There was encouraging quantitative agreement with the experimental flow visualization, carried out using laser-illuminated smoke, of Farthing et al. (1992b). Results presented also illustrated the complex flow structure, which is significantly influenced by the cavity surface temperature distribution. Further studies were undertaken by Tucker (1993) in which both laminar and turbulent solutions were obtained.

Three-dimensional, time-dependent computations of this flow require considerable computing resources. Iacovides and Chew (1993) investigated the potential for using two-dimensional axisymmetric steady-state solutions (using a one-equation energy model with prescribed algebraic length scale and also a mixing length model) to estimate the disk heat transfer when the Rossby number is high ($\mathrm{Ro} \approx 35$). The superior performance of the one-equation model was noted and comparison with limited experimental results showed some agreement (similar magnitudes of disk heat transfer and the trend in the difference between the two disks).

In this paper we report on further three-dimensional time-dependent computations for this flow. The CFD computations are used to model the flow in two different experimental rigs

Contributed by the International Gas Turbine Institute and presented at the 40th International Gas Turbine and Aeroengine Congress and Exhibition, Houston, Texas, June 5–8, 1995. Manuscript received by the International Gas Turbine Institute February 22, 1995. Paper No. 95-GT-185. Associate Technical Editor: C. J. Russo.

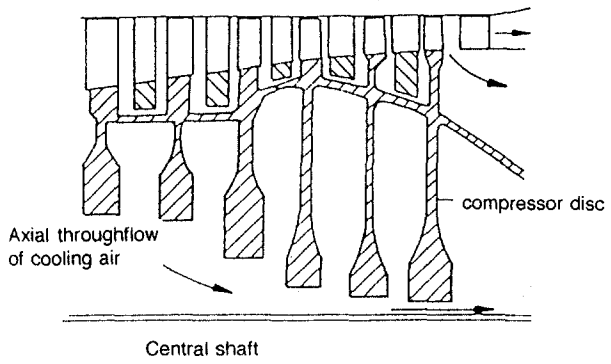

Fig. 1 Simplified arrangement of a high-pressure compressor drum

for a range of operating conditions, some of which are representative of those found in real aero-engines. These rigs are described in Section 2 and the analysis of the experimental data in Section 3. A mixing length turbulence model is used and a description of this, together with that of the numerical model, is given in Section 4. The computations are discussed and comparisons made with the experimental data in Section 5.

2 Experimental Apparatus

Two separate experimental rigs are discussed. These will be referred to as Apparatus (a), the rotating cavity rig, and Apparatus (b), the high-pressure compressor spool rig. Discussion of most of the details for Apparatus (a) is given by Northrop (1984). Later modifications to the apparatus, which include the addition of a shroud heater system and a local air temperature measurement probe, are described by Long and Tucker (1994a).

Data for Apparatus (b) were supplied by an engine manufacturer (no experimental measurements were taken from this apparatus by the authors). The data comprised measured metal and air temperatures, and cavity pressures at various times for a number of different tests. Discussion of most of the details for Apparatus (b) is given by Tucker (1993). However, for the sake of completeness, brief descriptions of both Apparatus (a) and (b) will be given here.

2.1 The Rotating Cavity Rig, Apparatus (a). Figure 2(a) shows a schematic diagram of experimental Apparatus (a). The rotating cavity comprises two separate disks and a peripheral shroud, all of which rotate at a common angular velocity Ω. The cavity has an outer radius, $b = 484.5$ mm, and the disks are separated by an axial distance, $s = 65$ mm ($G = 0.134$). The maximum speed of 4000 rpm corresponds to a rotational Reynolds number of $\mathrm{Re}_\phi \approx 5 \times 10^6$. Air is fed into and out of the cavity by two co-rotating pipes with an inner radius, $a = 45$ mm. The peripheral shroud is made from a carbon-fiber epoxy–resin composite. The basic construction of both the upstream and downstream disks is identical, but the positioning of the instrumentation is slightly different. Each disk is fitted with electrical heaters and the shroud is heated by stationary "fire bar" heaters mounted in a curved cradle with a reflective inner surface. In addition to the air inlet temperature, the air temperature inside this rig is also measured, using three 0.15 mm copper-constantan thermocouples protruding from the surface of a stainless steel supporting tube fastened diametrically across the cavity (see Long and Tucker, 1994a, for further details).

The front and back faces of the disks are covered with 1-mm-thick glass fiber instrumentation mats. The surface temperatures for each disk are measured using thermocouples made of 0.15-mm-dia copper-constantan wires. There are 13 thermocouples on the outside face of each disk, 23 on the inside face

Nomenclature

a, b = inner and outer radius of cavity
A_n = coefficients ($n = 0, 1, 2 \ldots, 5$)
C_p = specific heat at constant pressure
$G = s/b$ or s'/b gap ratio
$\mathrm{Gr} = \Omega^2 r \beta \Delta T L^3/\nu^2$ rotational Grashof number
k = thermal conductivity
l, l_0 = mixing length
L = characteristic length
m = mass flow rate
n = arbitrary exponent
$\mathrm{Nu} = qL/\Delta Tk$ local Nusselt number
$p = P - \rho\Omega^2 r^2/2$ = reduced static pressure
P = static pressure
$\mathrm{Pr} = \mu C_p/k$ = Prandtl number
q = heat flux
r, z, θ = radial, axial, and tangential coordinates
R = characteristic gas constant
$\mathrm{Re}_Z = 2Wa/\nu$ = axial Reynolds number
$\mathrm{Re}_\phi = \Omega b^2/\nu$ = rotational Reynolds number
Ri = Richardson number
$\mathrm{Ro} = W/\Omega a$ = Rossby number
s or s' = axial gap between the disks
S = source term
t = time
$t^* = \Omega t$ dimensionless time
T = static temperature
u, v, w = radial, tangential and axial velocity components in a coordinate system rotating at Ω rad/s
V = voltage
W = bulk average velocity at cavity inlet
$X = r/b$ = dimensionless radius
y = distance from wall
y_+ = wall-distance Reynolds number
α_0, α_1 = Gosman under relaxation factors
$\beta = 1/T$ = volumetric expansion coefficient
Γ = diffusion coefficient
Δt = time step
$\Delta t^* = \Omega \Delta t$ = dimensionless time-step length
ΔT = temperature difference
δ = boundary layer thickness
ϵ = emissivity
$\lambda = -2\mu/3$ = viscosity coefficient
ν = kinematic viscosity
μ = dynamic viscosity
ρ = density
τ = shear stress
ϕ = generalized transport variable
ω = circumferentially averaged rotational speed of fluid core between the disks
Ω = rotational speed of the disks

Subscripts

avg = average value
cav = value inside the cavity
eff = effective (laminar + turbulent) value
in = value at the cavity inlet
max = maximum value
new, old = new and old values
r, z, θ = radial, axial, and tangential components
R = radiative value
s, sh = pertaining to the disk and shroud surface, respectively
shaft = pertaining to the central shaft
t = turbulent value
tot = total value
u, v, w, T = pertaining to the variables u, v, w, and T
ϕ = pertaining to the generalized transport variable

Superscript

* = dimensionless quantity (for T)

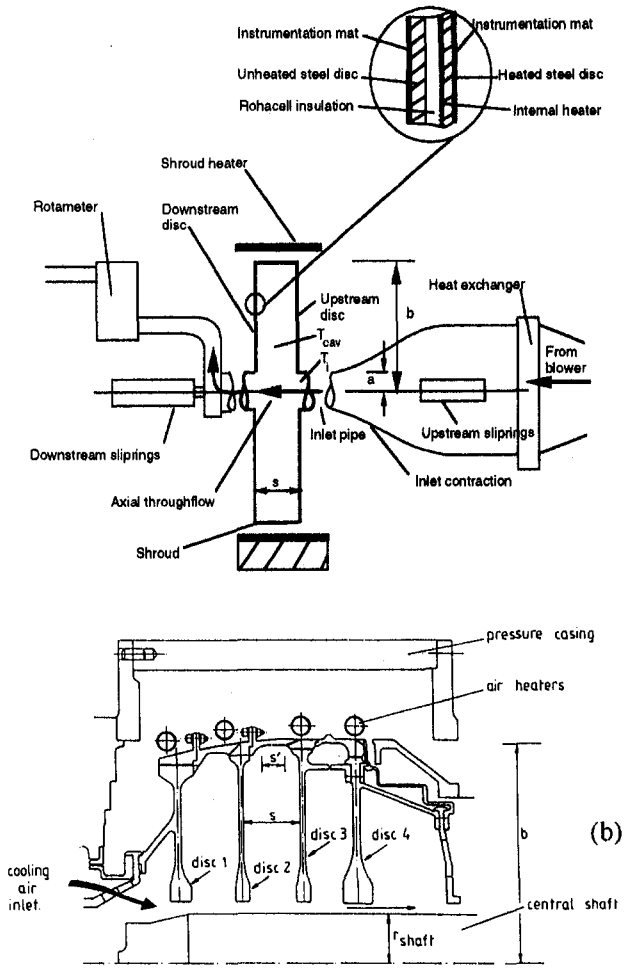

Fig. 2 Diagrams of the two experimental rigs: (*a*) apparatus (*a*), the rotating cavity rig; (*b*) apparatus (*b*), the high-pressure compressor spool rig

of the upstream disk, and 18 on the inside face of the downstream disk. The front face of each disk is also instrumented with eight RdF heat fluxmeters fixed into slots 10 mm wide and 0.7 mm deep using an epoxy resin. The inner cylindrical surface of the shroud is also instrumented with two fluxmeters, each of which contains a thermocouple to measure the local shroud temperature. The shroud fluxmeters are secured by several strips of Kapton tape, which surrounds them and provides a surface with a uniform thermal resistance.

The total (radiative and convective) heat flux, q_{tot}, from the fluxmeters is given by:

$$q_{tot} = A_0 V \{[A_1 + (4A_2T_s)]^{1/2} + A_2V\} \text{ W/m}^2, \quad (1)$$

where V is the output voltage (in mV), T_s the surface temperature (in °C) and A_0, A_1, and A_2 are calibration constants (discussed by Long, 1991).

2.2 The High-Pressure Compressor Spool Rig, Apparatus (b). A cross section illustrating the salient features of Apparatus (b) is shown in Fig. 2(b). The compressor spool, which comprises a number of cavities, is housed inside a pressure casing. Passing through the center of the compressor spool is a rotating shaft of radius r_{shaft} = 45 mm. The rotational speed of the shaft is independent of the four disks: The shaft can rotate synchronously with the disks or corotate/counterrotate at a different speed. The disks are made of titanium and have an outer radius, b = 200 mm, an inner radius, a = 58 mm, and are separated by an axial gap of s = 50 mm (G = 0.25). The maximum disk speed and test pressure are 12,000 rpm and 3.2 bar (absolute), respectively, enabling rotational Reynolds numbers up to $Re_\phi \approx 1 \times 10^7$. A simulated axial throughflow of cooling air (with a maximum flow rate of 0.36 kg/s) enters the apparatus through inlet ports indicated on the upstream (left) side of the diagram and leaves as shown on the downstream (right) side of the diagram. Hot air jets are used to heat the outer radius of the spool to a maximum surface temperature of approximately 600 K. The disks themselves are heated by conduction from the shroud region. Figure 3(a) shows the cavity formed by disks 2 and 3 and the outer bounding shroud for which the experimental data were supplied. The positions of the air and metal temperature thermocouples are also shown.

3 Data Analysis

The data for Apparatus (a) were obtained for constant values of Re_Z, Re_ϕ, surface temperature level and distribution. However, for Apparatus (b), where the data had rapid initial thermal transients, measurements were analyzed only after these initial transients, where the conditions became relatively steady. This is because, during such transients, there is a change in the radial temperature distribution, which (as found by Farthing et al., 1992a) significantly affects the Nusselt numbers.

A smoothing technique described by Long (1984) is used to smooth the fluxmeter and temperature signals with time. These smoothed data are then interpolated into 100 equal time-steps and a suitable fit (using Bessel interpolation or cubic splines) obtained for the radial temperature distribution at each of these time-steps. These temperatures are used as boundary conditions

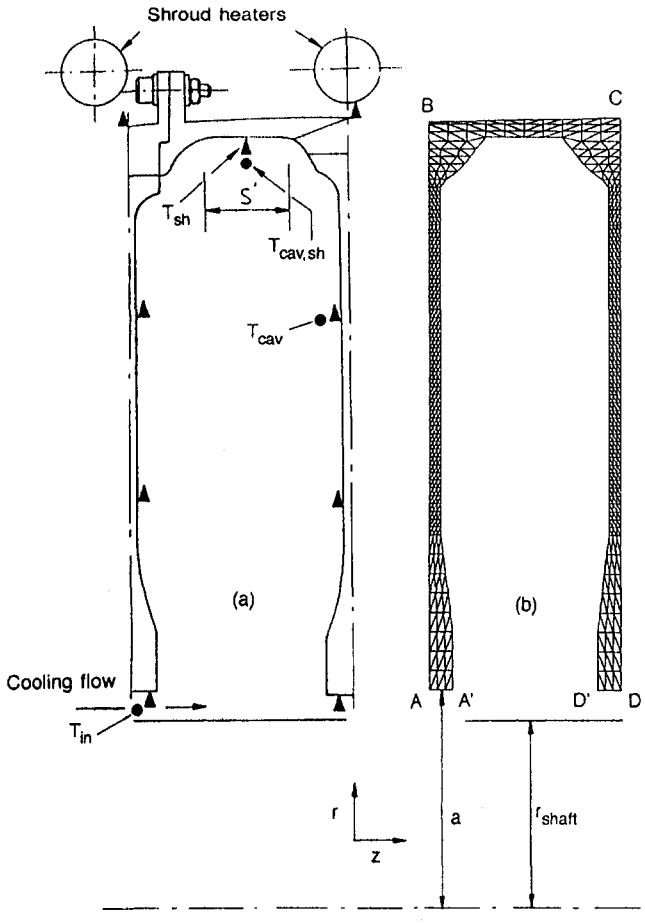

Fig. 3 Region of interest on experimental Apparatus (*b*) between disks 2 and 3: (*a*) actual geometry, ● denotes an air temperature thermocouple, ▲ a metal temperature thermocouple; (*b*) finite element mesh used in the conduction analysis

for the solution of the transient conduction equation, which in cylindrical-polar coordinates is

$$r^{-1}\partial[rk(\partial T/\partial r)]/\partial r + \partial[k(\partial T/\partial z)]/\partial z = \rho Cp\,\partial T/\partial t. \quad (2)$$

The computed temperature field at each time step is differentiated using second-order backward differences to give surface heat fluxes. The measured fluxes from both the transient conduction solution and the fluxmeters are total heat fluxes, q_{tot}, from which the radiative heat flux, q_R, must be subtracted to give the convective flux, q. The radiative fluxes are estimated using the method described by Long (1986). For Apparatus (a), the cavity surfaces are covered with a matt-finish instrumentation mat for which the emissivity ϵ is sufficiently close to unity that these surfaces can be treated as black. For Apparatus (b), the emissivities of the cavity surfaces are significantly different from unity and are treated as gray. The variation of emissivity with temperature, T (in K), is evaluated using a fit of tabulated data for titanium taken from Touloukian and DeWitt (1970): $\epsilon = 0.1 + 3.57 \times 10^{-4}\,T$. For Apparatus (a), the view factors are calculated using tabulated algebraic expressions. For Apparatus (b), since the cavity geometry is more complicated, a numerical integration procedure is used to compute the view factors and this is discussed by Tucker (1993). The Nusselt numbers ($\mathrm{Nu} = qL/k\Delta T$) are based on the convective heat flux and taken as time-averaged values over a period where the temperatures change little with time. For Apparatus (b), Eq. (2) is solved using the finite-element technique (see Tucker and Long, 1992). Convergence of the discretized finite-element equations is accelerated using a simple multigrid procedure with two grid levels (a fine and a coarse grid). Since, for Apparatus (b), there can be significant variations in disk temperature (from bore to rim and also during the test), the thermal conductivity, k, is evaluated as a function of temperature at each of the finite element nodes and at each time step ($k = 2.22 + 0.0136T$ W/mK, where T is in K).

The finite element mesh used for the conduction analysis is shown in Fig. 3(b). The letters A', A, B, C, D, D' are used to denote the different treatment of boundary conditions. In the midplane of the disks (i.e., along lines AB and DC), the disks are treated as adiabatic ($\partial T/\partial z = 0$). This assumption has been used by Farthing et al. (1991) and, for relatively thin disks with a large radial temperature gradient, is considered to be a reasonable assumption. At the disk bores, cooling air flows through the narrow gap $r_{shaft} \le r \le a$. The regions AA' and DD' are therefore each assumed to be isothermal and at the temperature obtained from the thermocouples located on the disk bores (see Fig. 3(a)). For the region at the outer radius of the shroud (BC), the temperatures are obtained by linear interpolation of the measurements from the thermocouples located on the outside surface of the shroud. On the cavity surface ($A'D'$), quadratic curves (generated using a Bessel interpolation) are used to obtain the temperature distribution between the experimentally measured locations. The influence of different forms of curve on predicted heat transfer was investigated by Tucker and Long (1992), and for the geometry considered and number of data points supplied, the form of interpolation used here was considered to be the most appropriate. For each test, the initial conditions were obtained from the solution of the steady-state equation, setting $(\partial T/\partial t)_{t=0} = 0$ in Eq. (2).

4 Numerical Method

Relative to the disks, the flow structure inside the cavity is slow moving ($\omega \approx \Omega$), so that the terms in the energy equation associated with frictional heating can justifiably be ignored. (Comparisons between numerical predictions with and without viscous dissipation, for the highest rotational Reynolds number considered here, show variations in local Nusselt number less then 5 percent.) This allows the formal stagnation enthalpy equation to be substituted by one in which the temperature is the dependent variable: No source terms arise with consequent savings in CPU time. The variation of air density with pressure and temperature is calculated using the ideal-gas equation of state, $\rho = P/RT$, where R is the characteristic gas constant.

Table 1 Diffusion coefficients for Eq. (3)

ϕ	$\Gamma_{\phi,z}$	$\Gamma_{\phi,r}$	$\Gamma_{\phi,\theta}$
w	$2\mu_{eff} + \lambda$	μ_{eff}	μ_{eff}
u	μ_{eff}	$2\,\mu_{eff} + \lambda$	μ_{eff}
v	μ_{eff}	μ_{eff}	$2\,\mu_{eff} + \lambda$
T	$\frac{k}{Cp} + \frac{\mu_t}{Pr_t}$	$\frac{k}{Cp} + \frac{\mu_t}{Pr_t}$	$\frac{k}{Cp} + \frac{\mu_t}{Pr_t}$

The time-dependent equations describing the conservation of momentum and energy in 3D for such a flow can be represented in a common form for the general transport variable ϕ by

$$\partial(\rho\phi)/\partial t + \partial(\rho w\phi)/\partial z + r^{-1}\partial(\rho ru\phi)/\partial r + r^{-1}\partial(\rho v\phi)/\partial\theta = \partial(\Gamma_{\phi,z}\partial\phi/\partial z)/\partial z + r^{-1}\partial(\Gamma_{\phi,r}r\partial\phi/\partial r)/\partial r + r^{-2}\partial(\Gamma_{\phi,\theta}\partial\phi/\partial\theta)/\partial\theta + S_\phi. \quad (3)$$

The diffusion coefficients, Γ_ϕ, that occur in Eq. (3) are listed in Table 1, where $\lambda = -2\mu_{eff}/3$ and μ_{eff} is the effective (= laminar + turbulent) viscosity. The turbulent Prandtl number was assigned a value of 0.9.

The source terms, S_ϕ, when $\phi = w$, u, v, and T are as follows:

$$S_w = -\partial p/\partial z + \partial(\lambda r^{-1}\partial(ru)/\partial r)/\partial z + \partial(\lambda r^{-1}\partial v/\partial\theta)/\partial z + r^{-1}\partial(\mu r\partial u/\partial z)/\partial r + r^{-1}\partial(\mu\partial v/\partial z)/\partial\theta;$$

$$S_u = -\partial p/\partial r + \partial(\mu\partial w/\partial r)/\partial z + \partial(\lambda\partial w/\partial z)/\partial r + \partial(\lambda r^{-1}\partial v/\partial\theta)/\partial r + r^{-1}\partial(\mu r\partial(vr^{-1})/\partial r)/\partial\theta - 2\mu r^{-2}(\partial v/\partial\theta) + 2\rho v\Omega + u\partial(\lambda r^{-1})/\partial r - 2\mu u/r^2 + \rho v^2/r;$$

$$S_v = -r^{-1}\partial p/\partial\theta - \rho uvr^{-1} - \mu vr^{-2} - vr^{-1}\partial\mu/\partial r + r^{-1}\partial(\mu\partial w/\partial\theta)/\partial z + r^{-2}\partial(\mu r\partial u/\partial\theta)\partial r + r^{-1}\partial(\lambda\partial w/\partial z)\partial\theta + r^{-2}\partial(\lambda\partial(ru)/\partial r)/\partial\theta + 2\mu r^{-2}\partial u/\partial\theta - 2\rho u\Omega;$$

$$S_T = 0.$$

Note that p is here the reduced static pressure, measured relative to the local static pressure for solid-body rotation of the cavity air.

The continuity equation in time-dependent form is given by:

$$\partial\rho/\partial t + \partial(\rho w)/\partial z + r^{-1}\partial(\rho ur)/\partial r + r^{-1}\partial(\rho v)/\partial\theta = 0. \quad (4)$$

4.1 Initial and Boundary Conditions. Some predictions were used as initial conditions for other solutions; for example, converged solutions for a lower axial Reynolds number or shroud temperature, or made on a coarser grid, would be used to generate initial conditions for solutions with a higher axial Reynolds number, shroud temperature, or finer grid. For solutions where such an approach was not used, the initial conditions inside the cavity (i.e., for $a \le r \le b$, $0 < \theta \le 2\pi$, and $0 \le z$

$\leq s$) were set as: $u = v = w = 0$; $P = 1.03 \times 10^5$ Pa; $T = T_{in}$ and $\rho = P/RT_{in}$.

For $t > 0$, the disk and shroud surface temperatures were specified (the precise form will be stated as appropriate later in the paper) and, on these boundaries, $u = v = w = 0$. At the cavity inlet (i.e., $z = 0$, $r \leq a$, and for $0 < \theta \leq 2\pi$), $T = T_{in}$, $u = v = 0$, and a constant uniform profile was stipulated for the axial velocity, $w = W$. At the cavity outlet ($z = s$, $r \leq a$, and for $0 < \theta \leq 2\pi$), for Apparatus (a), $\partial\phi/\partial z = 0$, where $\phi = u$, v, w, or T. For Apparatus (b), these differential outlet boundary conditions resulted in convergence difficulties and evidence of flow reversal at the cavity outlet. Although this flow reversal could indicate the occurrence of vortex breakdown (which is not inconsistent with experimental evidence, albeit obtained from rigs with a different inlet radius ratio and without a central shaft), in order to reduce computing time and therefore make computations for Apparatus (b) viable, the following outlet boundary conditions were used: $\partial T/\partial z = 0$, $u = v = 0$, and $w = W$. The sensitivity to the cavity outlet boundary conditions suggests that the flow there is strongly elliptic in nature and that the accuracy of solutions could be greatly improved if the downstream cavity were included in the calculation. This is, however, unrealistic at present due to limitations in CPU time and storage requirements.

4.2 Numerical Method. Full details of the solution method used for the three-dimensional, time-dependent, numerical work presented here are given by Tucker (1993) and so only a brief discussion follows. The equations of motion are solved in a coordinate system rotating at the cavity angular velocity and discretized using a control volume formulation with an implicit time scheme. The grids used in the momentum equations are staggered. The HYBRID scheme of Spalding (1972) and also a stabilized (Tucker, 1993) version of the CONDIF scheme of Runchal (1987) are used to interpolate variables from the main grid points onto the mesh control volume faces. The pressure field over the computational domain is obtained from the continuity equation using the SIMPLEC method of Van Doormal and Raithby (1984). Solution of the discretized equations is accelerated by the use of a nonlinear multigrid algorithm with a V-cycle.

Convergence of solutions is improved by adding a slightly modified form of the term proposed by Gosman et al. (1976) to the radial momentum equation. In the current nomenclature, the term is $\alpha_0\rho|v + \alpha_1\Omega r|(u_{old} - u_{new})/r$, where a_0 and a_1 are in effect underrelaxation factors and the subscripts "old" and "new" denote values at the previous and current iterations. For the current predictions, $\alpha_1 = 2$ and α_0 was varied in the range 0.5–1.0.

4.3 Modeling of Turbulence. Although the flow in a heated rotating cavity with an axial throughflow is here assumed to be turbulent, it should be noted that the conditions under which laminar–turbulent transition occurs are not, as yet, known. Farthing et al. (1992a) showed the disk heat transfer (for $2 \times 10^4 \leq \mathrm{Re}_z \leq 1.6 \times 10^5$ and $2 \times 10^5 \leq \mathrm{Re}_\phi \leq 5 \times 10^6$) to be correlated by $\mathrm{Re}_z^{0.3}$ and $\mathrm{Gr}^{0.25}$. The significance here is the exponent of the Grashof number, a value normally associated with laminar free convection. It is quite likely that both the axial Reynolds number and the Grashof number affect transition. It is also considered likely that laminar and turbulent conditions could co-exist, as for example in a cavity with superimposed radial flow (Owen et al., 1985) where there can be a turbulent source region yet laminar Ekman layers on the disks.

Transitional flows in rotating disk geometries can perhaps best be handled by the use of low-Reynolds-number energy-dissipation (k–ϵ) models. Indeed, Morse (1991a, b) and Morse and Ong (1992) have obtained very good predictive agreement for the flow and heat transfer in various geometries over a wide range of operating conditions. However, such models require fairly dense clustering of grid nodes in near-wall regions to obtain sufficient resolution of the rapidly changing turbulence quantities for the predictions to be sensibly grid-independent. This approach is viable for two-dimensional flow computations, but not generally for three-dimensional flows. Here, to reduce CPU time and core memory requirements, the mixing length model of Koosinlin et al. (1974) is used with the original Van Driest formula for near-wall damping. Full details regarding the implementation of the turbulence model are provided by Chew and Vaughan (1988), but a brief description will be given here.

The turbulent viscosity is calculated from

$$\mu_t = \rho l^2[(\partial u/\partial z)^2 + (\partial v/\partial z)^2 + (\partial w/\partial r)^2 + (r\partial(v/r)/\partial r)^2]^{1/2}, \quad (5)$$

where l is the mixing length and θ derivatives are ignored. The mixing length increases linearly with wall distance, but is damped according to the Van Driest formula very close to the wall, i.e.,

$$l = A_0 y\{1 - \exp(-y_+/26)\}, \quad (6)$$

where $A_0 = 0.42$, y is the distance from the wall, and y_+ ($= y(\tau_s/\rho)^{0.5}/\nu$) is a nondimensional wall distance involving the resultant wall shear stress, τ. Koosinlin et al. and Chew and Vaughan both used a modified Van Driest formulation involving the local shear stress, but for the flow considered here, numerical experiments showed little difference in predicted heat transfer using the two formulations, while Eq. (6) was preferable from the viewpoint of computational stability and also less demanding of CPU time. The limiting value of the mixing length is specified as

$$l = A_1\delta, \quad (7)$$

where δ is a boundary layer thickness, defined as the point where the shear stress falls to 1 percent of its value at the wall, and $A_1 = 0.085$. At cylindrical surfaces, the mixing length is modified according to

$$l = l_0(1 - A_2\,\mathrm{Ri}), \quad (8)$$

where l_0 is the base value from Eq. (6) or (7), $A_2 = 5$ (a value selected by Koosinlin et al. to give the best agreement of their numerical predictions with experimental data), and Ri is a gradient Richardson number given by

$$\mathrm{Ri} = (2v/r^2)(\partial(rv)/\partial r)/[(\partial w/\partial r)^2 + (r\partial(v/r)/\partial r)^2]. \quad (9)$$

4.4 Convergence Criteria. The parameters used to monitor convergence were the normalized residuals and also the root-mean square (rms) change in all the variables. The latter is defined as $\mathrm{rms}_\phi = (\Sigma(\phi_{new} - \phi_{old})^2/[\Sigma(\phi_{new})^2])^{1/2}$, where the summation applies over the entire solution domain. The discretized equations are not under-relaxed and, at the end of a time step, $\mathrm{rms}_\phi < 10^{-5}$ and typically an order of magnitude smaller than this. For all variables, this constitutes a suitably strict convergence criterion.

The residual of the pressure correction equation was made dimensionless by dividing by m_{cav}, the net mass flow rate of fluid actually entering the cavity (typically 0.1 to 15 percent of the throughflow rate). For the energy equation, the product of flow rate entering the cavity and the maximum temperature difference between the cavity walls and the incoming air was used to normalize the residuals, while, for the momentum equations, the normalizing factor was taken as m_{cav} multiplied by appropriate reference velocities. All normalized residuals were required to exhibit a convergence error of less than 1 percent at the end of the iteration within each time step.

Computations were performed on a Solbourne 5E/905-128 computer using double-precision FORTRAN. For Apparatus (a), on average approximately 15 hours of CPU time were required to advance 1 s in simulated time, and for Apparatus (b), on average, approximately 500 hours. Solutions were con-

Table 2 Dimensionless parameters for cases considered

Case	Re_z	Re_ϕ	$\beta\Delta T_{max}$	Apparatus
I	2.0×10^3	2.0×10^5	0.185	a
II	2.0×10^3	2.0×10^5	0.314	a
III	2.0×10^4	2.0×10^5	0.270	a
IV-VII	2.3×10^4	3.0×10^6	0.262	b

sidered to be steady and independent of initial conditions when the disk surface Nusselt number distribution did not vary significantly (<2 percent variation over a time period $t^* = 25$) or the variation was seen to be cyclic. Several different flows were used to validate the code: These are discussed by Tucker (1993).

5 Discussion of Results

Numerical predictions will be presented for seven different test cases, numbered I to VII. Values of the axial and rotational Reynolds numbers and the buoyancy parameter, $\beta\Delta T_{max}$, for which the flow conditions are modeled are summarized in Table 2. Cases IV–VII are for the same flow conditions, but different grid densities are used (see Table 5).

Figure 4 shows typical radial variations of dimensionless surface temperature ($T^* = (T - T_{in})/(T_{s,max} - T_{in})$) for both Apparatus ($a$) and ($b$). The disk surface temperature increases with radius, differences in the form of the temperature distributions being due to differences in the heating systems used. For Apparatus (a), the upstream and downstream disks have similar temperature distributions; for Apparatus (b), the downstream disk is hotter (by about 10 K) than the upstream.

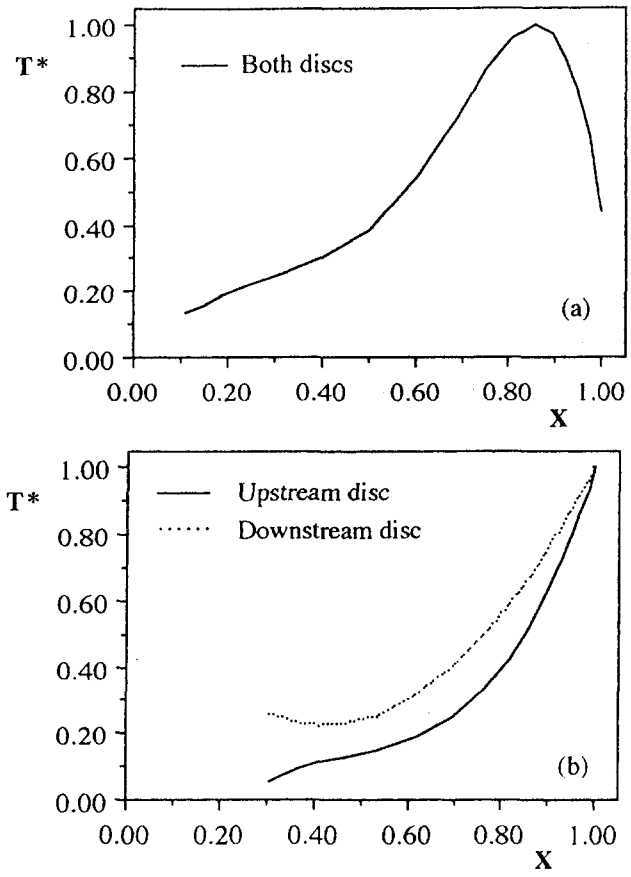

Fig. 4 Typical variations of dimensionless disk surface temperature with radius for the test cases used in the numerical predictions: (*a*) Apparatus (*a*); (*b*) Apparatus (*b*)

Table 3 Coefficients of Eq. (10) for the test cases considered

Cases	I-II	III	IV - VII	
Apparatus	(a)	(a)	(b)	
Discs	both	both	upstream	downstream
A_0:	0.1806	0.1175	-0.556	0.6253
A_1:	2.6587	-0.6109	3.743	-1.923
A_2:	-10.11	10.49	-7.213	2.297
A_3:	17.32	-38.00	5.026	3.4×10^{-4}
A_4:	-9.157	57.99	–	–
A_5:	–	-29.54	–	–

These surface temperatures were used as boundary conditions for the predictions, being specified as polynomials of the form, and the coefficients used are shown in Table 3:

$$T^* = \sum A_n X^n \ (n = 0, 1, 2 \ldots 5). \qquad (10)$$

The maximum disk surface temperatures, the nondimensional radius where these occur, the air inlet temperatures, average shroud temperatures, and shroud boundary conditions are summarized in Table 4.

For cases I and II, the shroud temperature was actually measured in the experiments; there was little variation across the axial width of the shroud and so the temperature is assumed constant in the modeling. For Case III, where an insulated shroud was used in the experimental work, an adiabatic shroud is assumed (so it is not necessary to specify a shroud temperature). For cases IV–VII, where there were also shroud temperature measurements, the shroud temperature was assumed to vary linearly between the upstream and downstream disc surface temperatures at $X = 1$.

The number of pressure correction sweeps, axial and radial grid expansion factors, number of axial, radial and tangential grid nodes, number of multigrid levels, time-step size and time at which solutions are presented are summarized in Table 5.

In order to reduce CPU time, the solution for Case II was started from the solution for Case I. The solution for Case III was started from a solution with $Re_z \approx 2 \times 10^3$ (not presented here). Also the solution for Case V was started from the solution for Case IV, and the solutions for Cases VI and VII started from that for Case V.

Table 4 Details of thermal boundary condition for cases considered

Case	$T_{s,max}$ (K)	X	T_{in} (K)	$T_{sh,ave}$ (K)	Shroud
I	347.0	0.82	286.0	339.0	isothermal
II	347.0	0.82	286.0	339.0	isothermal
III	379.0	0.82	293.0	--	adiabatic
IV-VII	382.0	1.00	302.5	379.5	isothermal

Table 5 Numerical details of cases considered

Case:	I	II	III	IV	V	VI	VII
	Apparatus (a)				Apparatus (b)		
No. of Pressure Correction Sweeps	8	8	50	18	18	18	18
Axial Grid Expansion Factor	1.10	1.10	1.10	1.20	1.20	1.20	1.20
Radial Grid Expansion Factor	1.21	1.21	1.21	1.23	1.23	1.23	1.23
No. of axial grid nodes	17	17	17	17	17	33	17
No. of radial grid nodes	21	21	21	21	21	21	37
No. of tangential grid nodes	40	40	40	1	40	40	40
Multigrid levels in z & r directions	3	3	2	1	1	1	1
Multigrid levels in θ direction	3	3	2	1	1	1	1
Dimensionless time-step $\Omega\Delta t$	0.63	0.63	0.41	0.58	0.58	0.58	0.58
Dimensionless time $t^* = \Omega t$	804	917	245	21000	7500	170	175

5.1 Description of the Flow Structure. The essential features of the flow structure computed from Case VI (see Tables 2 and 4) are shown in Fig. 5. The cavity rotates in a clockwise sense and the throughflow passes from left to right. The computed flow field at $t^* = 170$ is "seeded" with tracer particles of equal density to the cavity air at two places, near the bore ($0 < z/s < 1$, $r/b = 0.36$, and $0 < \theta \leq 2\pi$) and near the shroud ($0 < z/s < 1$, $r/b = 0.98$, and $0 < \theta \leq 2\pi$). The resulting tracks, produced using a numerical particle tracker and a Silicon Graphics workstation, of the particles are shown for a period of 0.5 s from the computed velocity field at a single time step.

Two regions are apparent in the flow. An inner region occurs where fluid entering the cavity peels off from the central throughflow and spirals radially outward, then, after reversing on itself, moves back in to mix with the central throughflow and leaves the cavity. A second region is seen near the shroud, where fluid destabilized by heating moves radially inward; it then cools by mixing with the inner region and by convection to the disk surfaces and moves radially outwards. This free convection mechanism is shown by the numerous counter-rotating vortices near the shroud. It is also interesting to note that mixing between the two regions is limited to a distinct interface between them and does not occur throughout the entire cavity. Little of the fluid seeded in the inner region appears in the outer region, and conversely, little of the fluid seeded in the outer region appears in the inner region.

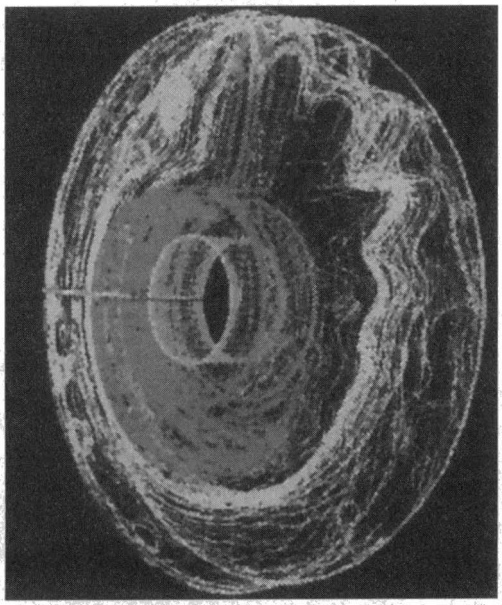

Fig. 5 Visualization of the predicted flow structure for Apparatus (*b*), Case VI, $Re_\phi = 3.2 \times 10^6$ and $Re_z = 2.3 \times 10^4$

Comparison between an axisymmetric solution (Case IV) and a three-dimensional solution (Case V) shows that treating the flow as axisymmetric results in velocities several orders of magnitude lower. Correspondingly, the mass flow rate entering the cavity, expressed as a percentage of the axial throughflow air mass flow rate, is 0.1 percent for the axisymmetric prediction (which is consistent with the axisymmetric computations of Hennecke et al., 1971) and over 5 percent for the three-dimensional prediction. It is therefore very unlikely that an axisymmetric prediction will be able to model faithfully the flow in an entire cavity with axial throughflow. However, there are considerable computational advantages to such an approach and under certain conditions (high Rossby number for example), a two-dimensional axisymmetric solution might give acceptable results (see Iacovides and Chew, 1993).

5.2 Shroud Heat Transfer. The variation of measured and predicted values of average shroud Nusselt number ($Nu = qL/k\Delta T$) with Grashof number ($Gr = \Omega^2 b\beta\Delta T L^3/\nu^2$) is shown in Fig. 6; the choice of characteristic length, L, and temperature difference, ΔT, is discussed fully below. The measured values are from both Apparatus (*a*) and (*b*); the predictions are made using the HYBRID scheme. For the measurements from Apparatus (*a*), $G = 0.134$, $Re_z = 8 \times 10^4$, $2 \times 10^5 \leq Re_\phi \leq 2 \times 10^6$, and, for Apparatus (*b*), $G = 0.25$, $1.9 \times 10^4 \leq Re_z \leq 10.5 \times 10^4$, $3 \times 10^6 \leq Re_\phi \leq 6.25 \times 10^6$. Also shown on the figure are correlations for free convection from a horizontal surface, heated with a constant surface temperature, facing upward and in a gravitational field (Gebhart et al., 1988); in the current nomenclature, these are given by

$$Nu = 2^{(1-3n)} A_0 \, Pr^n Gr^n. \qquad (11)$$

For the laminar regime ($2.2 \times 10^4 \leq Gr\,Pr \leq 8 \times 10^6$), $A_0 = 0.54$ and $n = \frac{1}{4}$; for the turbulent regime ($8 \times 10^6 \leq Gr\,Pr \leq 1.6 \times 10^9$), $A_0 = 0.15$ and $n = \frac{1}{3}$.

Long and Tucker (1994a) have shown that measured values of shroud heat transfer in a rotating cavity with an axial throughflow of cooling air for $10^6 < Gr < 3 \times 10^8$ are correlated reasonably well by Eq. (11), provided that the cavity air temperature, T_{cav}, is used as a reference temperature in the definition of the Nusselt and Grashof numbers, so $\Delta T = T_{sh} - T_{cav}$. For Apparatus (*a*), T_{cav} is taken as the temperature at $X = 0.867$ and for Apparatus (*b*) at $X = 0.96$, corresponding to

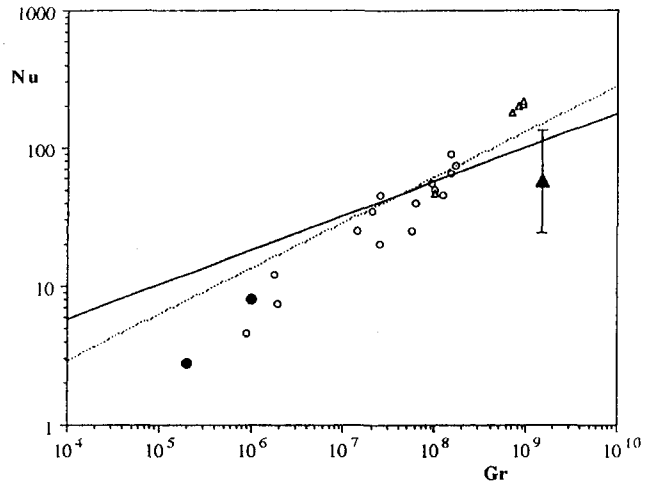

Fig. 6 Variation of shroud Nusselt number with Grashof number for Apparatus (*a*), the rotating cavity rig and Apparatus (*b*), the high-pressure compressor spool rig:

- ○ Experimental measurement, Apparatus (*a*)
- △ Experimental measurement, Apparatus (*b*)
- ● Numerical predictions, Apparatus (*a*), Cases I–II (17 × 21 × 40 grid)
- ▲ Numerical prediction, Apparatus (*b*), Case VII (17 × 37 × 40 grid)
- I Maximum and minimum values for Case VII
- —— Gebhart et al. (1988) laminar flow
- - - Gebhart et al. (1988) turbulent flow

the locations where these temperatures were measured (see Fig. 3(*a*)). Long and Tucker used the ratio of shroud surface area to perimeter, $L = s/2$ as the characteristic length in Nu and Gr. This choice of length scale is recommended by Goldstein et al. (1973) for free convection from horizontal plates. For the shroud heat transfer results presented here, the characteristic length will, again, be based on the shroud half width. However for Apparatus (*b*), L is based on an effective width, $L = s'/2$, where $s' = 23$ mm.

For Apparatus (*b*), only the prediction for Case VII (with the most radial grid nodes to resolve the shroud boundary layer) is shown on the graph, using the symbol ▲ for the shroud-averaged value and a vertical line denoting the variation from maximum to minimum values. For Case IV (two-dimensional axisymmetric solution), the predicted average shroud Nusselt number is approximately 2; for cases V and VI it is approximately 25. These values are considered unrealistic in comparison to the result for case VII ($Nu_{avg} \approx 60$) and illustrate the importance of good radial grid resolution in the shroud boundary layer.

As can be seen from Fig. 6, the numerical result for Apparatus (*a*), at $Gr \approx 1 \times 10^6$, is in good agreement with experimental measurement for similar values of Grashof number. The predictions for Apparatus (*b*) are lower, relative to the experimental data, than for Apparatus (*a*). It is considered that the conditions of higher Grashof number in Apparatus (*b*) produce steeper velocity gradients that are less well resolved by the grids used. It is quite likely that agreement will be improved with further refinement of the grid in the radial direction. However, due to CPU time limitations, this has not been possible. In addition, for the conditions of Apparatus (*b*), a higher level of turbulence is expected that will highlight any deficiencies in the mixing length model used for the current predictions. Use of more sophisticated turbulence models, such as the one-equation energy model of Iacovides and Chew (1993) or a low-Reynolds-number k–ϵ model (e.g., Morse and Ong, 1992) might further improve agreement, although these would necessitate refinement of the finite-difference mesh, which appears to underpin the problems encountered here.

5.3 Disk Heat Transfer. The radial variations of circumferentially averaged disk surface Nusselt numbers for Case III (see Tables 2 and 4) are shown in Fig. 7. The dashed line represents the prediction made using the HYBRID scheme, the full lines the bounded CONDIF scheme, and symbols are used for the fluxmeter measurements. For the results presented, the cavity air temperature was not measured and so the air temperature at the cavity inlet is used as the reference temperature for the local Nusselt number ($Nu = qr/k_{in}(T_s - T_{in})$). The numerical predictions are presented for the range $X > 0.3$, where there are fluxmeter readings, and $X < 0.9$, because of the lack of measured temperatures, which leads to uncertain modeling of the boundary conditions in this region. Examination of results at previous and subsequent time steps revealed that, for $0.35 < X < 0.45$, there is approximately a ±20 percent variation in the predicted values of Nu with time and the lines shown correspond to the midpoint of this variation. For $X > 0.45$, there is no significant variation of Nu with time.

For the experimental conditions of Fig. 7, the general low level of heat flux ($Nu = 30$ at $X = 0.8$ and $\Delta T = 80$°C corresponds to a heat flux of 200 W/m^2) can result in significant uncertainty in the experimental data. Considering this and also the limitations of the numerical approach, it is considered that

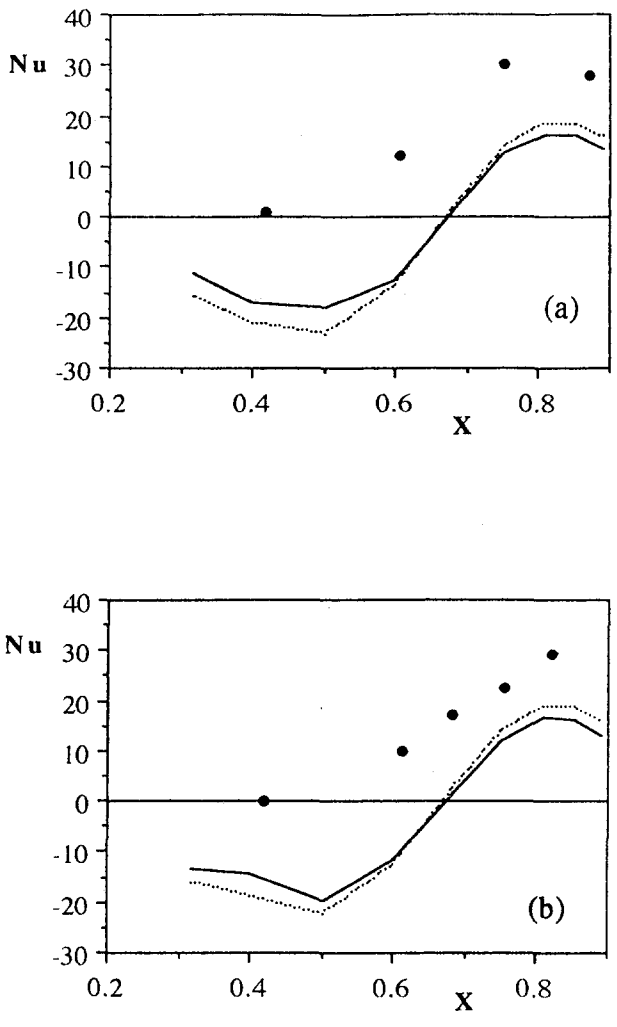

Fig. 7 Measured and predicted (Case III) radial variation of circumferentially averaged disk surface Nusselt number for Apparatus (*a*) with adiabatic shroud: $Re_\phi = 2 \times 10^5$, $Re_Z = 2 \times 10^4$, $\beta\Delta T_{max} = 0.27$, $G = 0.134$ and $a/b \approx 0.1$: (*a*) upstream disk; (*b*) downstream disk:

- ● Fluxmeter measurement
- ... Numerical prediction (HYBRID)
- —— Numerical prediction (CONDIF)

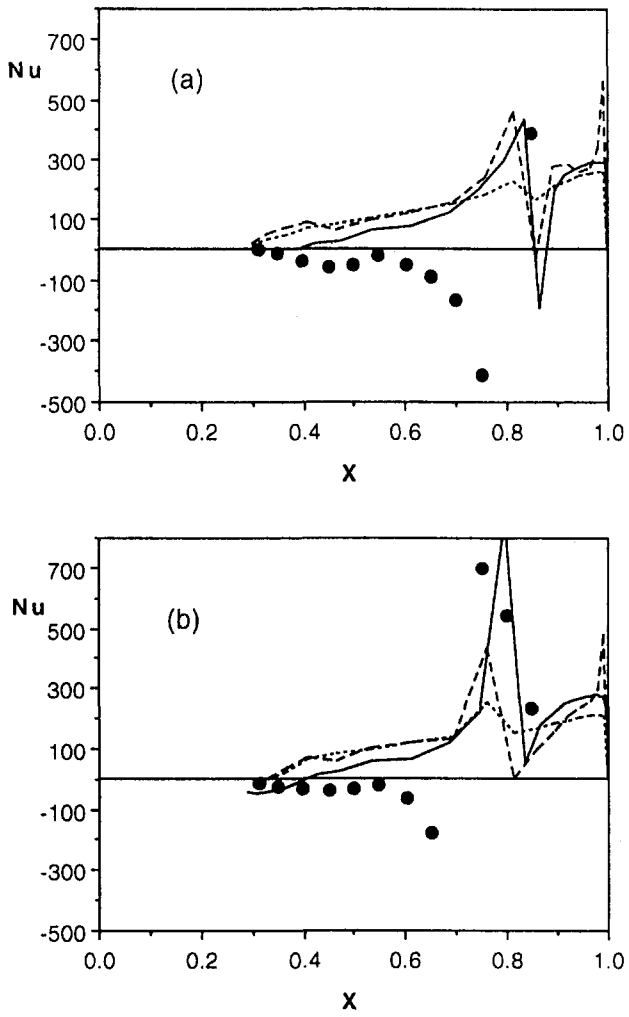

Fig. 8 Radial variation of circumferentially averaged disk surface Nusselt number for cases V–VII; Apparatus (*b*) with $Re_\phi = 3 \times 10^6$, $Re_z = 2.3 \times 10^4$, $\beta \Delta T_{max} = 0.26$ $G = 0.25$ and $a/b \approx 0.3$: (*a*) upstream disk; (*b*) downstream disk:

- ● **Experimental measurement**
- ··· **Numerical prediction (17 × 21 × 40 grid, Case V)**
- - - **Numerical prediction (33 × 21 × 40 grid, Case VI)**
- —— **Numerical prediction (17 × 37 × 40 grid, Case VII)**

there is reasonable agreement between the numerical predictions and experimental results if not generally in the magnitude of the Nusselt number, then at least in the trend of the radial distribution. The numerical results show the disk surface Nusselt number to be negative in the region $X < 0.65$, indicating that heat is being convected into the disk surface. This is not present in these experimental results (although it has been observed in others) and it is suggested that the cause lies in both experimental uncertainty and limitations with the three-dimensional model. At $X \approx 0.4$, the CONDIF scheme gives values of Nu closer to the fluxmeter measurements than the HYBRID scheme. However, the difference between these two solutions is within the error bounds of the experimental data, so it is not possible to comment on which offers the better prediction.

The radial variation of circumferentially averaged disk surface Nusselt number for Cases (V–VII) (see again Tables 2 and 4) is shown in Fig. 8. For the axisymmetric solution (Case IV), the Nusselt numbers are nearly two orders of magnitude lower than those obtained from the three-dimensional predictions and are omitted from the graph. For cases V and VI the CONDIF scheme is used and, for Case VII, the HYBRID scheme. Comparison here is made with experimental results obtained from the transient conduction analysis (see Section 3). The cavity air temperature was measured (at $z/s \approx 0.81$ and $X \approx 0.78$) and so is used as the reference temperature when defining the local disk surface Nusselt number ($Nu = qr/k_{cav}(T_s - T_{cav})$). At $X \approx 0.8$ on the upstream disk and $X \approx 0.7$ on the downstream disk, there is a discontinuity in the measured values of Nu where $T_{cav} = T_s$.

As can be seen, increasing the number of axial grid nodes from 17 (Case V) to 33 (Case VI) suggests that the predictions for $x \leq 0.6$ are fairly independent of the number of axial grid nodes. However, increasing the number of radial grid nodes from 21 (Case V) to 37 (Case VII) shows the solutions to be radial-grid dependent and also results in better general agreement with the experimental data. The agreement is improved toward the shroud ($X > 0.8$); elsewhere, significant discrepancies are mostly attributable to errors in the transient conduction analysis with sparse temperature measurements, the influence of the discontinuity mentioned above, and finally, toward the disk bores, to the questionable validity of the adiabatic midplane assumption (see Section 3). These factors are in addition to the usual uncertainties in the numerical results due to limitations imposed on grid size and choice of turbulence model by realistic CPU times.

6 Conclusions

A three-dimensional, time-dependent CFD code, using a mixing length turbulence model, has been applied to predict the flow and heat transfer in rotating cavities with axial throughflow. Two different experimental rigs have been modeled. Apparatus (*a*) has a cavity gap ratio of $G = 0.134$, $a/b = 0.1$, and no central shaft; Apparatus (*b*) has $G = 0.25$, $a/b = 0.29$, and a central shaft. Predictions are obtained for $Re_\phi = 2 \times 10^5$ with $Re_z = 2 \times 10^3$ and $Re_z = 2 \times 10^4$ in Apparatus (*a*) and $Re_\phi = 3 \times 10^6$ and $Re_z = 2.3 \times 10^4$ in Apparatus (*b*). A two-dimensional axisymmetric solution gives velocities several orders of magnitude lower than the three-dimensional predictions. Limitations with CPU time and storage requirements have demanded the use of fairly coarse grids and a simple turbulence model.

A numerical particle tracker has been used to visualize the computed flow field for Apparatus (*b*). This shows two regions of flow: an inner region where fluid enters the cavity by spiralling radially outward and then inward, and an outer region of counter-rotating vortices induced by free convection. The two regions do not merge; mixing between them takes place at their interface.

For Apparatus (*a*), there is reasonably encouraging agreement between the predicted disk and shroud heat transfer and experimental fluxmeter measurements. For Apparatus (*b*), the agreement is less satisfactory. Some of the discrepancy is attributable to experimental uncertainty (too few temperature measurements and a questionable, but necessary, midplane boundary condition assumption for conduction inside the disk), some to uncertainties in the numerical results due to limited grid size and simplistic turbulence model. It is envisaged that improvements could be made regarding the turbulence modeling, but even so, this is likely to increase significantly the already large CPU times. The way ahead could lie with the bringing together of several heuristic local models for the different regions of the flow, each of less generality but significantly less demanding of computing resources than the three-dimensional time-dependent numerical approach.

Acknowledgments

The authors wish to thank the organizations that have funded this research, notably the Engineering and Physical Sciences Research Council, Rolls-Royce plc, and MTU GmbH.

References

Note: TFMRC reports are available from the Thermo-Fluid Mechanics Research Centre, School of Engineering, University of Sussex, Brighton BN1 9QT, England.

Chew, J. W., and Vaughan, C. M., 1988, "Numerical Predictions for the Flow Induced by an Enclosed Rotating Disc," ASME Paper No. 88-GT-127.

Farthing, P. R., Long, C. A., and Rogers, R. H., 1991, "Measurement and Prediction of Heat Transfer From Compressor Discs With a Radial Inflow of Cooling Air," ASME Paper No. 91-GT-53.

Farthing, P. R., Long, C. A., Owen, J. M., and Pincombe, J. R., 1992a, "Rotating Cavity With Axial Throughflow of Cooling Air: Heat Transfer," ASME JOURNAL OF TURBOMACHINERY, Vol. 114, p. 229.

Farthing, P. R., Long, C. A., Owen, J. M., and Pincombe, J. R., 1992b, "Rotating Cavity With Axial Throughflow of Cooling Air: Flow Structure," ASME JOURNAL OF TURBOMACHINERY, Vol. 114, p. 237.

Gebhart, D., Jaluria, Y., Mahajan, R. L., and Sammakia, B., 1988, *Buoyancy-Induced Flows and Transport.* Hemisphere Publishing Corporation, New York, p. 227.

Goldstein, R. J., Sparrow, E. M., and Jones, D. C. 1973, "Natural Convection Mass Transfer Adjacent to Horizontal Plates," *Int. J. Heat Mass Transfer,* Vol. 16, p. 1025.

Gosman, A. D., Koosinlin, M. L., Lockwood, F. C., and Spalding, D. B., 1976, "Transfer of Heat in Rotating Systems," ASME Paper No. 76-GT-25.

Hennecke, D. K., Sparrow, E. M., and Eckert, E. R. G., 1971, "Flow and Heat Transfer in a Rotating Enclosure With Axial Throughflow," *Wärme und Stoffübertragung,* Vol. 4, p. 222.

Iacovides, H., and Chew, J. W., 1993, "The Computation of Convective Heat Transfer in Rotating Cavities," *Int. J. Heat and Fluid Flow,* Vol. 14, p. 146.

Koosinlin, M. L., Launder, B. E., and Sharma, B. I., 1974, "Prediction of Momentum, Heat and Mass Transfer in Swirling Turbulent Boundary Layers," ASME *Journal of Heat Transfer,* Vol. 96, p. 204.

Long, C. A., 1984, "Transient Heat Transfer in a Rotating Cylindrical Cavity," D. Phil. Thesis, University of Sussex, England.

Long, C. A., 1985, "Transient Analysis of Experimental Data From the MkII Rotating Cavity Rig," Report No. 85/TFMRC/76. School of Engineering and Applied Sciences, University of Sussex, England.

Long, C. A., 1986, "Transient Analysis of Temperature Measurements on Discs of the RB 199 H.P. Vented-Rotor Compressor," Report No. 86/TFMRC/87. School of Engineering and Applied Sciences, University of Sussex, England.

Long, C. A., 1991, "A Calibration Technique for Thermopile Heat-Flux Gauges," *Proc. Sensor 91 Conference,* Nuremberg, Germany, Vol. IV, Paper No. B12.2, p. 247.

Long, C. A., and Tucker, P. G., 1994a, "Shroud Heat Transfer Measurements From a Rotating Cavity With an Axial Throughflow of Air," ASME JOURNAL OF TURBOMACHINERY, Vol. 116, p. 525.

Long, C. A., and Tucker, P. G., 1994b, "Numerical Computation of Laminar Flow in a Heated Rotating Cavity With an Axial Throughflow of Air," *Int. J. of Num. Meths. for Heat and Fluid Flow,* Vol. 4, p. 347.

Morse, A. P., 1991a, "Application of a Low Reynolds Number $k-e$ Turbulence Model to High-Speed Rotating Cavity Flows," ASME JOURNAL OF TURBOMACHINERY, Vol. 113, p. 98.

Morse, A. P., 1991b, "Assessment of Laminar-Turbulent Transition in Closed Disc Geometries," ASME JOURNAL OF TURBOMACHINERY, Vol. 113, p. 131.

Morse, A. P., and Ong, C. L., 1992, "Computation of Heat Transfer in Rotating Cavities Using a Two-Equation Model of Turbulence," ASME JOURNAL OF TURBOMACHINERY, Vol. 114, p. 247.

Northrop, A., 1984, "Heat Transfer in a Cylindrical Rotating Cavity," D. Phil. Thesis, School of Engineering and Applied Sciences, University of Sussex, England.

Owen, J. M., Pincombe, J. R., and Rogers, R. H., 1985, "Source-Sink Flow Inside a Rotating Cylindrical Cavity," *J. Fluid Mech.,* Vol. 155, p. 233.

Runchal, A. K., 1987, "CONDIF: A Modified Central-Difference Scheme for Convective Flows," *Int. J. for Num. Meths. in Engng.,* Vol. 24, p. 1593.

Spalding, D. B., 1972, "A Novel Finite-Difference Formulation for Differential Expressions Involving Both First and Second Derivatives," *Int. J. for Num. Meths. Engng.,* Vol. 4, p. 551.

Touloukian, Y. S., and DeWitt, D. P., 1970, *Thermophysical Properties of Matter, Vol. 7, Thermal Radiative Properties,* IFI/Plenum, New York.

Tucker, P. G., and Long, C. A., 1992, "A Finite Element Analysis of Compressor Disc Heat Transfer Using the Transient Conduction Method With Sparse Boundary Collocation Points," *Proc. 2nd Int. Conference on Advanced Comp. Methods in Heat Transfer.* HT/92, Milan, Computational Mechanics Publications and Elsevier Applied Science, Vol. 1, p. 409.

Tucker, P. G., 1993, "Numerical and Experimental Investigation of Flow Structure and Heat Transfer in a Rotating Cavity With an Axial Throughflow of Cooling Air," D. Phil. Thesis, School of Engineering, University of Sussex, England.

Van Doormaal, J. P., and Raithby, G. D., 1984, "Enhancements of the SIMPLE Method for Predicting Incompressible Fluid Flows," *Num. Heat Transfer,* Vol. 7, p. 147.

Heat Transfer From Air-Cooled Contrarotating Disks

J.-X. Chen

X. Gan[1]

J. M. Owen

School of Mechanical Engineering,
University of Bath,
Bath, United Kingdom

A superposed radial outflow of air is used to cool two disks that are rotating at equal and opposite speeds at rotational Reynolds numbers up to 1.2×10^6. One disk, which is heated up to 100°C, is instrumented with thermocouples and fluxmeters; the other disk, which is unheated, is made from transparent polycarbonate to allow the measurement of velocity using an LDA system. Measured Nusselt numbers and velocities are compared with computations made using an axisymmetric elliptic solver with a low-Reynolds-number $k-\epsilon$ turbulence model. Over the range of flow rates and rotational speeds tested, agreement between the computations and measurements is mainly good. As suggested by the Reynolds analogy, the Nusselt numbers for contrarotating disks increase strongly with rotational speed and weakly with flow rate; they are lower than the values obtained under equivalent conditions in a rotor–stator system.

1 Introduction

In most gas turbines, a turbine disk rotates close to either a stationary casing or another corotating turbine disk. In some engines, and in some designs of future engines, two adjacent disks may rotate in opposite directions. Such contrarotating turbines could be used to drive the contrarotating fans of future generations of ultra-high-bypass-ratio engines, and an additional advantage is that contrarotating turbine stages remove the need for an intermediate row of stator vanes, thereby reducing the size and weight of the engine.

Recent research in contrarotating disks has produced a number of papers, most of which are concerned with the fluid dynamics of the problem. Graber et al. (1987) reported extensive experimental measurements obtained from a pressurized rotating-disk rig in which the two disks could be rotated, in either direction, to produce rotational Reynolds numbers up to $\mathrm{Re}_\phi = 1.6 \times 10^7$, typical of those found in gas turbines. For their contrarotating-disk tests, a *stationary* shroud (or cylindrical casing) was used to seal the periphery of the system. A superposed radial inflow or outflow of air could be supplied, and the measurements of frictional moment coefficients, C_m, on one of the rotating disks, showed that neither the magnitude nor the direction of the flow rate had a significant effect on C_m. However, the value of C_m for a contrarotating disk with no superposed flow is approximately twice that of the equivalent rotor-stator case, where one disk is rotating and the other is stationary.

Morse (1991) and Kilic et al. (1996) carried out computations for the contrarotating-disk case using elliptic solvers and (different) low-Reynolds-number $k-\epsilon$ turbulence models. Their computed moment coefficients were in close agreement with each other and with the correlation of Dorfman (1963) for the free-disk case (that is, a single disk rotating in a quiescent environment), where

$$C_m = 0.491\ (\log_{10} \mathrm{Re}_\phi)^{-2.58} \qquad (1.1)$$

Like the experiments of Graber et al. the computations showed that, with no superposed flow, the moment coefficients for contrarotating disks are approximately twice those of the rotor–stator case. However, whereas a superposed radial outflow has little effect on C_m for contrarotating disks, it has a large effect for the rotor–stator system. In the latter case, C_m approaches the free-disk value (and consequently, the contrarotating-disk value) as the flow rate approaches the free-disk entrainment rate (that is, the flow rate entrained by the free disk).

A combined computational and experimental study of the flow and heat transfer associated with air-cooled contrarotating disks has recently been completed at the University of Bath. Velocity and heat transfer measurements were obtained for rotational Reynolds numbers up to $\mathrm{Re}_\phi \simeq 1.2 \times 10^6$ over the range $-1 \le \Gamma \le 0$, where Γ is the ratio of the speed of the slower disk to that of the faster one: $\Gamma = 0$ corresponding to the rotor–stator case and $\Gamma = -1$ to disks rotating at equal and opposite speeds. Computations of the flow were made using an elliptic solver with a low-Reynolds-number $k-\epsilon$ turbulence model, and further details of the computed and measured flows are given by Gan et al. (1995) and by Kilic et al. (1994a, b, 1996). The principal features of the flow are outlined below, and the flow structures for $\Gamma = 0$ and $\Gamma = -1$ are shown schematically in Fig. 1.

When there is no superposed flow between the disks, then, depending on the value of Γ, Batchelor-type flow (Batchelor, 1951) or Stewartson-type flow (Stewartson, 1953) can occur. For $\Gamma = 0$, Batchelor-type flow comprises radial outflow in a boundary layer on the rotating disk (the rotor), and radial inflow in a boundary layer on the stationary disk (the stator); between the boundary layers is a core of rotating fluid in which the radial component of velocity is zero and there is an axial flow from the stator to the rotor. For $\Gamma = -1$, Stewartson-type flow comprises a radial outflow in boundary layers on both disks, between which is a recirculating core of fluid that is entrained into the outflowing boundary layers; the tangential component of velocity in this core is very small.

For contrarotating disks there is a double transition: from laminar to turbulent flow and from Batchelor-type to Stewartson-type flow, depending on Γ and Re_ϕ. For $\Gamma = 0$, transition from laminar to turbulent Batchelor-type flow occurs at $x^2\mathrm{Re}_\phi \simeq 2 \times 10^5$. For $\Gamma = -1$, laminar flow can occur in the boundary layers but, even at local Reynolds numbers as low as $x^2\mathrm{Re}_\phi = 2 \times 10^4$, the flow in the core always appears to be turbulent. (For $\Gamma = -1$, laminar Batchelor-type flow can be computed but it appears not to exist in practice.) For $-1 < \Gamma < 0$, a two-cell structure can occur: Batchelor-type flow with a rotating core occurs in the (radially) outer cell, and Stewartson-type flow with a nonrotating recirculating core occurs in the inner cell.

[1] Present address: European Gas Turbines Ltd, Whetstone, Leicester LE8 6LH, United Kingdom.

Contributed by the International Gas Turbine Institute and presented at the 40th International Gas Turbine and Aeroengine Congress and Exhibition, Houston, Texas, June 5–8, 1995. Manuscript received by the International Gas Turbine Institute February 22, 1995. Paper No. 95-GT-184. Associate Technical Editor: C. J. Russo.

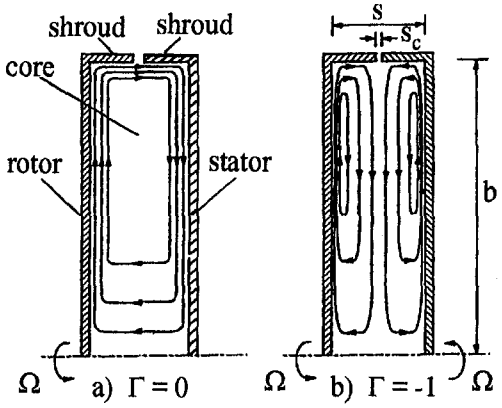

Fig. 1 Schematic diagram of flow structure (no superposed flow)

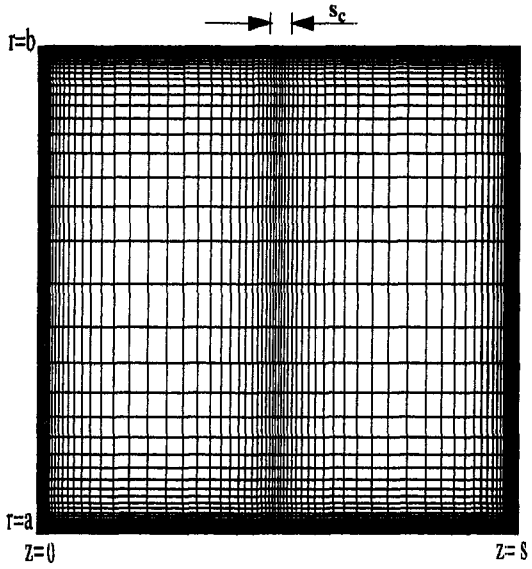

Fig. 2 Typical computational grid (92 radial × 78 axial nodes) (not to scale)

For $\Gamma = -1$, a superposed radial outflow of fluid divides the flow structure into two regions: a source region near the inlet, where fluid is entrained into a free-disk-type boundary layer on each disk, and an outer recirculating region where Stewartson-type flow occurs. The nondimensional flow rate, C_W, entrained by the turbulent free disk can be approximated by

$$C_W = 0.22\ \mathrm{Re}_\phi^{0.8} \tag{1.2}$$

It is convenient to define the turbulent flow parameter, λ_T, as

$$\lambda_T = C_W\ \mathrm{Re}_\phi^{-0.8} \tag{1.3}$$

where $\lambda_T = 0.22$ corresponds to the free-disk entrainment rate; in most turbine-disk cooling applications, $\lambda_T < 0.22$. Gan et al. (1995), using an argument based on free-disk entrainment in the source region, suggested that the nondimensional radius of the source region, x_e, could be approximated by

$$x_e = 1.37\ \lambda_T^{0.385} \tag{1.4}$$

These papers were concerned with the fluid dynamics of the problem, whereas this one concentrates principally on the heat transfer from contrarotating disks for $\Gamma = -1$. The computational method and experimental apparatus are outlined in Sections 2 and 3, and the comparisons between computations and measurements are discussed in Section 4.

2 Computational Method

An "in-house elliptic code" was used to solve the incompressible, axisymmetric, conservation equations for mass, momentum, energy, and turbulence quantities together with a low-Reynolds-number $k-\epsilon$ turbulence model (Morse, 1988, 1991). Turbulent heat fluxes were computed from the temperature gradients using a turbulent Prandtl number. The code has been used successfully to compute the flow and heat transfer for the free-disk case and for rotor-stator systems; details are given by Chen et al. (1993a, b, 1996).

A typical grid distribution for the contrarotating disks is shown in Fig. 2. For most tests, a nonuniform grid with 92 radial and 78 axial nodes was used, and a geometric expansion/contraction factor was employed to achieve a fine grid near the disks: for all computations reported here, the grid point closest to the disk was set to ensure that $y^+ < 1.0$. Grid-independence tests were conducted by making computations with a fine (92 × 78) and a coarse (68 × 68) grid: There was no graphic difference between the two sets of velocity profiles and the Nusselt numbers differed by less than 2 percent.

In the experiments, the disks were spaced a distance s apart and flow entered the system at $r = a$ through a gauze tube attached to each disk (see Section 3) and left through a small axial clearance, s_c, between the contrarotating shrouds at $r =$

Nomenclature

a = inner radius of disk
b = outer radius of disk
C_m = moment coefficient = $M/0.5\ \rho\Omega^2 b^5$
C_p = specific heat at constant pressure
C_w = nondimensional mass flow rate = $\dot{m}/\mu b$
G = gap ratio = s/b
G_c = shroud-clearance ratio = s_c/b
k = thermal conductivity; turbulent kinetic energy
$\dot{m}$ = mass flow rate
M = moment on rotating disc
Nu = Nusselt number = $q_o r/k(T_o - T_{\mathrm{ref}})$
Pr = Prandtl number of air
q_o = convective heat flux from disk to air
r = radial coordinate
R = recovery factor
Re_ϕ = rotational Reynolds number = $\rho\Omega b^2/\mu$
s = axial gap between disks
s_c = shroud clearance
T = temperature
U_τ = friction velocity = $\sqrt{(\tau_w/\rho)}$
V_r, V_ϕ, V_z = velocity components in r, ϕ, z directions
x = nondimensional radius = r/b
x_e = nondimensional radius of source region
y = distance normal to wall
y^+ = wall-distance Reynolds number = $\rho U_\tau y/\mu$
z = axial coordinate from heated disk
ϵ = turbulent energy dissipation rate
Γ = ratio of speed of slower disk to that of faster one
λ_T = turbulent flow parameter = $C_w \mathrm{Re}_\phi^{-0.8}$
μ = dynamic viscosity
ϕ = tangential coordinate
ρ = density
τ_w = total wall shear stress
Ω = angular speed of disc

Subscripts

ad = adiabatic value
I = inlet value
o = surface of rotating disk
ref = reference value
1, 2 = unheated, heated disk

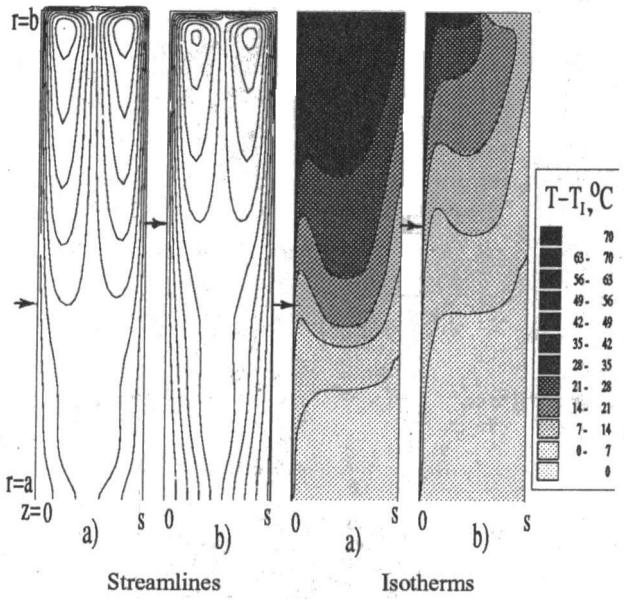

Fig. 3 Computed streamlines and isotherms for $\Gamma = -1$: (*a*) $C_W = 4026$, $Re_\phi = 1.14 \times 10^6$ ($\lambda_T = 0.0575$); (*b*) $C_W = 9351$, $Re_\phi = 1.19 \times 10^6$ ($\lambda_T = 0.129$); ↑ x_e (Eq. (1.4))

b. The computational geometry matched the experimental one: $a/b = 0.13$, $G = s/b = 0.12$, $G_c = s_c/b = 0.01$. No-slip conditions were used for the velocities on all solid surfaces, and at the inlet, $r = a$, the flow was assumed to enter uniformly in the radial direction and the inlet temperature, T_I, was specified; for $0 \leq z/s < \frac{1}{2}$, $V_\phi = \Omega a$, and for $\frac{1}{2} < z/s \leq 1$, $V_\phi = -\Omega a$. At the outlet, $r = b$, the flow was assumed to leave uniformly in the radial direction, and the radial derivatives of the tangential component of velocity and the temperature were assumed to be zero. In the experiment, only one disk was heated and thermocouples were used to measure its temperature; in the computations, the temperature of the heated disk was obtained using interpolation of the measured temperatures, and the unheated disk and shrouds were assumed to be adiabatic.

Computed streamlines and isotherms for $\Gamma = -1$ and $Re_\phi \simeq 1.1 \times 10^6$ are shown in Fig. 3 for the geometry and thermal conditions corresponding to the experimental apparatus; the left-hand disk is heated and the right-hand one is adiabatic. The streamlines show that the flow entering at $r = a$ forms a source region outside of which recirculation occurs. The arrows indicate the radial extent of the source region given by the free-disk-entrainment model, Eq. (1.4), which overestimates the computed size. The isotherms show that inside the source region the air temperature is equal to that at inlet, T_I, and outside recirculation causes the air temperature to increase with radius. At the larger radii, the temperature of the adiabatic disk is greater than T_I.

3 Experimental Apparatus

The apparatus, which is shown in Fig. 4, was essentially the same as that described by Chen et al. (1996) and so only the salient features are described here.

Two disks of 762 mm diameter were rotated independently at speeds up to 1500 rpm; the speed was measured with an uncertainty of 1 rpm. Disk 1, which was unheated, was made from transparent polycarbonate; disk 2, which could be radiantly heated, was made from steel. A carbon-fiber shroud was attached to the periphery of each disk, and the axial clearance between the contrarotating shrouds was less than 4 mm ($G_c \simeq 0.01$); the axial spacing between the two disks was approximately 46 mm ($G \simeq 0.12$).

A radial outflow of air could be supplied through rotating gauze tubes of 100 mm diameter ($a/b \simeq 0.13$) attached to the center of the disks (see Fig 4). The air was supplied to the rig from a centrifugal compressor, via a stationary and a rotating tube attached to the center of the upstream disk. The flow rate was measured, with an uncertainty of around 3 percent, using an orifice plate in the stationary tube; leakage was minimized by the use of seals between the stationary and rotating tubes. It should be pointed out that the gauze tubes were intended to produce a uniform radial flow at inlet to the system; velocity measurements showed that this was not achieved.

The back face of the steel disk (disk 2) could be heated electrically by stationary radiant heaters to produce a maximum temperature of approximately 100°C (around 70°C above that of the cooling air at inlet). Ten thermocouples and ten RDF thermopile fluxmeters (three of which subsequently broke) were embedded in a glass-fiber "mat," 0.8 mm thick, bonded to the front face of the disk. The signals were taken out through an IDM slip-ring assembly, and the voltages were measured in a Schlumberger computer-controlled data-logger. By taking the average of 100 sets of data, the random uncertainties were 0.03°C for the thermocouple readings. The overall uncertainties were estimated to be around 0.5°C for the thermocouples and 5 percent for the flux meters. (Chen et al., 1996, show good agreement between measured and computed Nusselt numbers for the free-disk case, which gives confidence in the accuracy of the fluxmeter measurements.)

The reference temperature, T_{ref}, used in the definition of the Nusselt number (see Nomenclature) was based on the *adiabatic-disk-temperature*, $T_{o,ad}$, employed by Chen et al. (1996) for their rotor–stator experiments:

$$T_{ref} = T_{o,ad} = T_I + \tfrac{1}{2} R\Omega^2 r^2 / C_p \qquad (3.1)$$

R being the recovery factor ($R \simeq Pr^{1/3}$). Ideally, the adiabatic-disk temperature should be based on the *local* air temperature and the *local* velocity difference ($\Omega r - V_\phi$), but it was only possible to measure the inlet air temperature, T_I, in the experiments. In practice, $\Omega^2 r^2 / 2C_p \leq 1$°C, but, as shown below, the computed difference between the local air temperature and T_I can be significant.

Radiation from the heated disk was also significant and it was necessary to estimate a correction for the radiative flux. The glass-fiber mat had an emissivity of approximately 0.95, and the fluxmeters measured the total heat flux (convection and

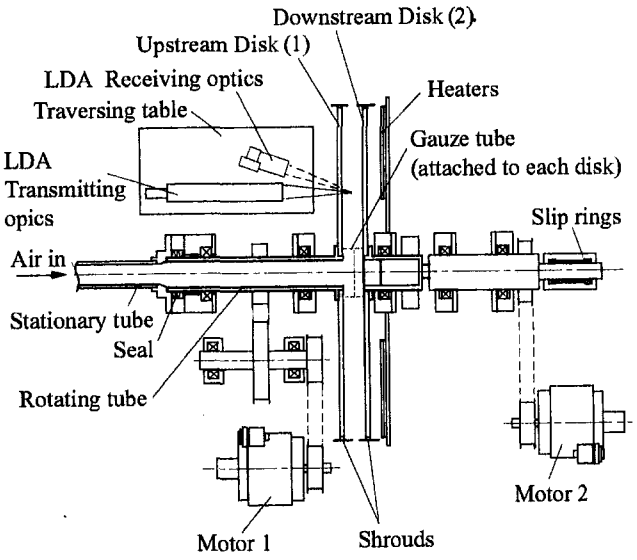

Fig. 4 Schematic layout of the rotating-disk rig and LDA system

radiation). Chen et al. (1996) assumed that the polycarbonate disk was opaque to infrared radiation and that its temperature (which was not measured) was equal to that of the cooling air at inlet. Using these assumptions, they estimated the radiative heat flux from the steel disk and produced corrections for the measured flux. In practice, the corrections, which can be as large as 10 percent of the measured flux, are likely to be overestimates of the radiation as the temperature of the polycarbonate disk can be higher than that of the cooling air (as discussed in Section 2).

The radial and tangential components of velocity were measured using a TSI laser-Doppler anemometer (LDA) operating in an off-axis back-scatter mode with the optical axis normal to the transparent polycarbonate disk. The Doppler frequency was measured with an IFA 750 burst correlator, and the estimated uncertainty in the measured tangential component of velocity was less than 0.5 percent of the disk speed. Positional uncertainty and scatter from the disk surfaces made it difficult to obtain accurate measurements close to either disk, particularly the steel one.

4 Comparison Between Computations and Measurements

4.1 Velocity Measurements. The radial and tangential components of velocity were measured at $x = 0.6, 0.7, 0.8$, and 0.85 for $2500 \le C_W \le 9700$ and $1.3 \times 10^5 \le \mathrm{Re}_\phi \le 1.3 \times 10^6$ ($0.05 \le \lambda_T \le 0.3$). Many comparisons between computations and measurement for the case of superposed flow and $\Gamma = -1$ have been presented by Gan et al. (1995), who used a different elliptic solver and a different version of the low-Reynolds-number $k-\epsilon$ turbulence model from those used in this paper. Although the two computational codes produced very similar results, for completeness some comparisons between velocity measurements and computations using the current code are shown in Figs 5 and 6.

Figure 5 shows comparisons between the computed and measured velocities for $\mathrm{Re}_\phi = 1.14 \times 10^6$ and $C_W = 4026$ ($\lambda_T = 0.0574$). The agreement is good except near $z/s = 1$, where accurate LDA measurements are difficult to make. For this value of λ_T, the measurements are outside the source region and the negative values of V_r in the core show that recirculation is occurring. The continuous shear in V_ϕ from $+\Omega r$ at $z/s = 0$ to $-\Omega r$ at $z/s = 1$ produces very little rotation in the core between the boundary layers.

Figure 6 for $\mathrm{Re}_\phi = 1.19 \times 10^6$ and $C_W = 9351$ ($\lambda_T = 0.129$) shows a distinct skew in the measured radial components of velocity, particularly at the smaller values of x. As mentioned in Section 3, gauze tubes were used in an attempt to create a uniform radial inlet; in practice, the flow impinges on the downstream disk, causing a skewed flow. Except near the disk surfaces, the measured values and computations are in better agreement at the larger values of x where inlet effects are attenuated. For $\lambda_T = 0.129$, the source region extends to $x \simeq 0.6$ (as shown in Fig. 3) and recirculation occurs at larger values of x.

Comparison between the computations and measurements at other values of Re_ϕ and C_W show similar effects to those described above. The source region increases as λ_T increases, and agreement between the computed and measured velocities tends to be better in the recirculation zone outside the source region.

4.2 Thermal Measurements. Figure 7 shows the computed and measured temperature distributions for $\Gamma = -1$ and for four values of Re_ϕ and C_W. For the heated disk ($z/s = 0$), the measured temperature and fitted curve, which provides the thermal boundary conditions for the computations, are shown. Also shown are the computed curves for the temperature of the adiabatic disk ($z/s = 1$) and for the air in the midplane ($z/s = \frac{1}{2}$). The nondimensional radius of the source region, x_e, calculated from Eq. (1.4), is also shown.

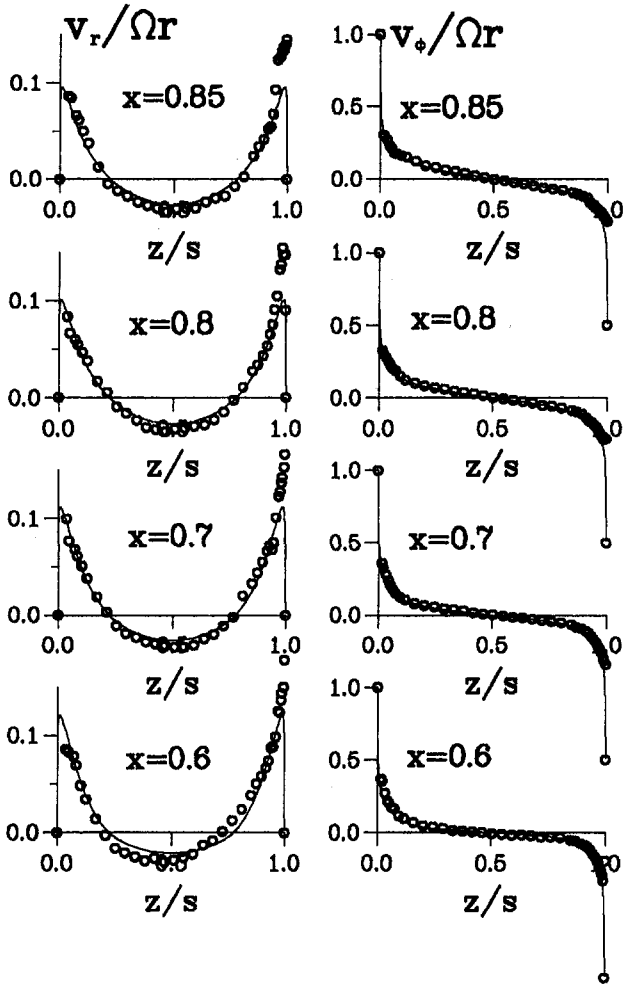

Fig. 5 Computed and measured velocity profiles for $\Gamma = -1$, $\mathrm{Re}_\phi = 1.14 \times 10^6$, and $C_W = 4026$ ($\lambda_T = 0.0574$): —— computations; ○ experimental data

Although the measured distribution of temperature on the heated disk is similar for all four cases, the computed temperatures of the adiabatic disk and the air depend strongly on λ_T. The size of the source region increases as λ_T increases, and for $x < x_e$ the temperature of the adiabatic disk is virtually equal to that of the air at inlet to the system. For $x > x_e$, the temperatures of the air and the adiabatic disk both increase with radius, the air temperature being intermediate between that of the two disks.

Figures 8–11 show comparisons between the computed and measured Nusselt numbers for $\mathrm{Re}_\phi \simeq 2 \times 10^5$ to 1.1×10^6. The uncorrected measurements are based on the fluxmeter readings, and the corrected values include the radiation correction discussed in Section 3. In Fig. 11, the Nusselt numbers for $\Gamma = 0$ (the rotor-stator results of Chen et al. 1996) are shown together with those for $\Gamma = -1$. It should be noted that the values of Re_ϕ and C_W for $\Gamma = 0$ are slightly different from the values used here for $\Gamma = -1$; it was not possible to carry out experiments at identical conditions for both cases.

Before discussing the heat transfer results, it is useful to consider the implications of the Reynolds analogy (see, for example, Owen and Rogers, 1989). For the case where the thermal boundary conditions are similar to those for the tangential component of velocity, and where the (true) *adiabatic disk temperature* is used as the reference temperature for the Nusselt number, it can be shown that the average Nusselt number is proportional to the product $C_m\mathrm{Re}_\phi$, where C_m is the moment coefficient. In Section 1, it was noted that a superposed radial

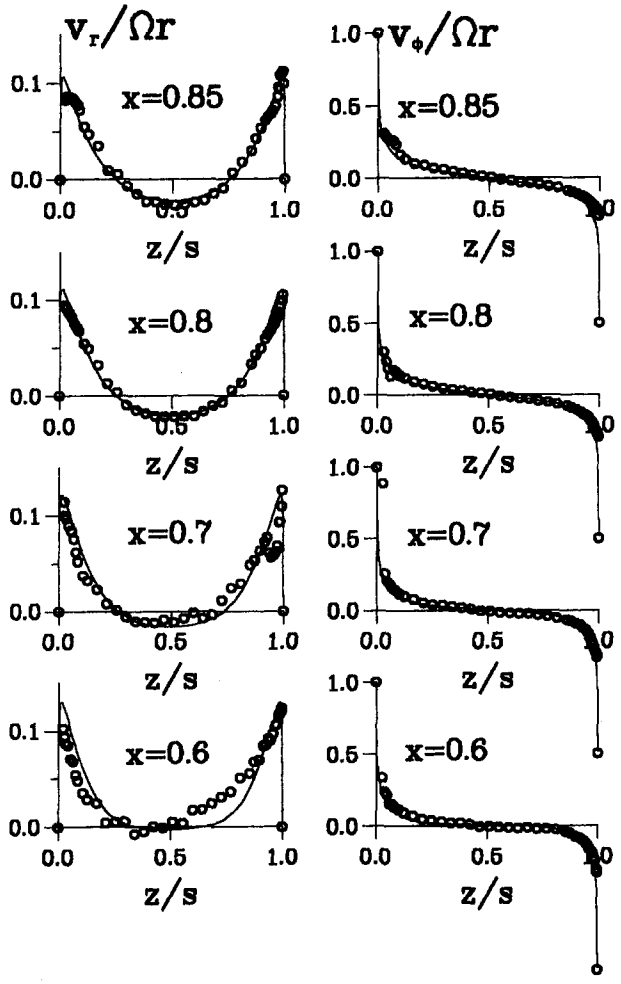

Fig. 6 Computed and measured velocity profiles for $\Gamma = -1$, $Re_\phi = 1.19 \times 10^6$, and $C_W = 9351$ ($\lambda_T = 0.129$): —— computations; ○ experimental data

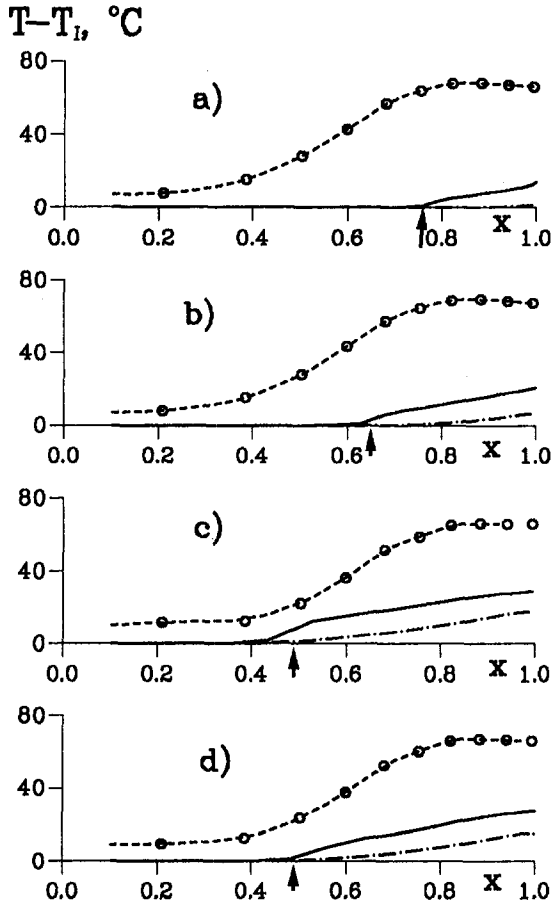

Fig. 7 Temperature distributions for $\Gamma = -1$: (*a*) $Re_\phi = 3.70 \times 10^5$, $C_W = 6128$ ($\lambda_T = 0.215$); (*b*) $Re_\phi = 3.62 \times 10^5$, $C_W = 3920$ ($\lambda_T = 0.140$); (*c*) $Re_\phi = 6.21 \times 10^5$, $C_W = 3896$ ($\lambda_T = 0.0904$); (*d*) $Re_\phi = 1.11 \times 10^6$, $C_W = 6130$ ($\lambda_T = 0.0894$); - - - heated disk (fitted); ○ measured data; — · — adiabatic disk (computed); —— air in midplane (computed) ↑ x_s (Eq. (1.4))

flow has little effect on C_m, which suggests (according to the Reynolds analogy) that the flow rate should have little effect on Nu. This is, however, an oversimplification, as the superposed flow affects the thermal boundary conditions, and the reference temperature used here is based on the inlet air temperature (which can be measured easily) and not on the local air temperature (which cannot be measured easily). It was also noted above that the size of the source region increases as λ_T increases: Inside the source region, the air temperature is close to the inlet temperature, T_I, and outside it increases with radius. Consequently, T_I is more appropriate as a reference temperature for Nu inside the source region than it is outside. It follows therefore that the Reynolds analogy is more appropriate for the larger values of λ_T, where the source region covers most of the heated disk, than for the smaller values.

Turning now to Figs. 8, 9, and 10, it can be seen that the Nusselt numbers, both measured and computed, increase with increasing Re_ϕ and with increasing radius over most of the disk surface. For a given value of Re_ϕ, the effect of C_W is relatively small, particularly for the larger values of λ_T in Figs. 8 and 9. These effects are consistent with the Reynolds analogy: In Fig. 10, the reduction in Nu with decreasing C_W is attributed to the reduction in the size of the source region and the consequent increase in the temperature of the cooling air referred to above.

The computed Nusselt numbers in Figs. 8, 9, and 10 tend to underestimate the measured values, although the agreement between the computed and corrected values of Nu improves as Re_ϕ increases: In Fig 10, the agreement is very good. For these

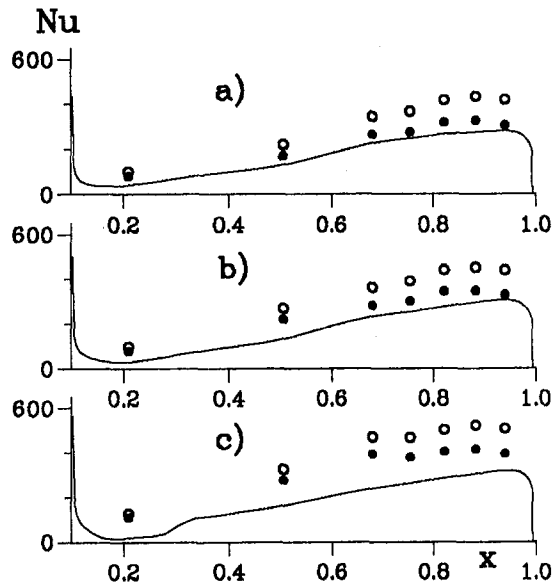

Fig. 8 Computed and measured Nusselt numbers for $\Gamma = -1$: (*a*) $Re_\phi = 2.09 \times 10^5$, $C_W = 3939$ ($\lambda_T = 0.218$); (*b*) $Re_\phi = 2.10 \times 10^5$, $C_W = 6121$ ($\lambda_T = 0.338$); (*c*) $Re_\phi = 2.24 \times 10^5$, $C_W = 9718$ ($\lambda_T = 0.510$); —— computation, ○ uncorrected data, ● corrected data

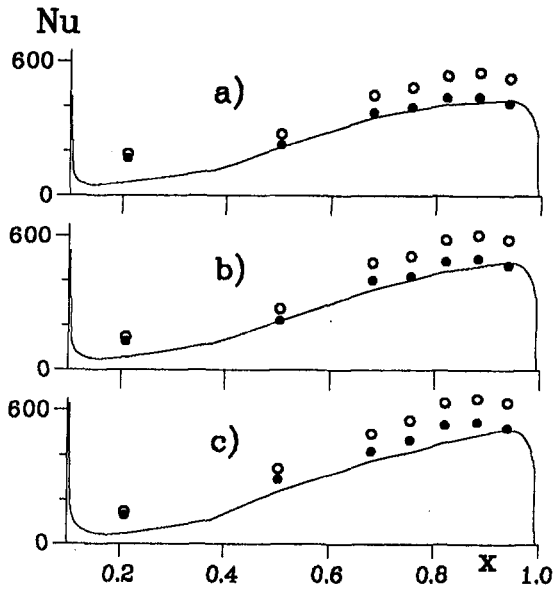

Fig. 9 Computed and measured Nusselt numbers for $\Gamma = -1$: (*a*) $Re_\phi = 3.62 \times 10^5$, $C_W = 3920$ ($\lambda_T = 0.140$); (*b*) $Re_\phi = 3.70 \times 10^5$, $C_W = 6128$ ($\lambda_T = 0.215$); (*c*) $Re_\phi = 3.84 \times 10^5$, $C_W = 9643$ ($\lambda_T = 0.329$); —— computation; ○ uncorrected data; ● corrected data

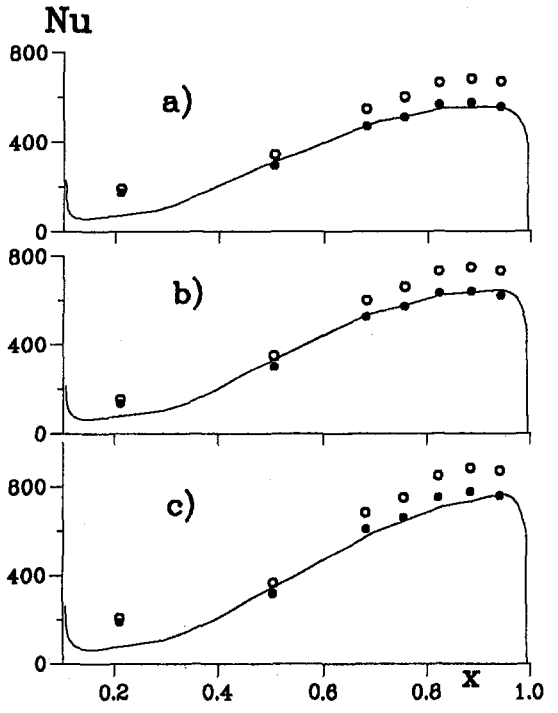

Fig. 10 Computed and measured Nusselt numbers for $\Gamma = -1$: (*a*) $Re_\phi = 6.21 \times 10^5$, $C_W = 3896$ ($\lambda_T = 0.0904$); (*b*) $Re_\phi = 6.36 \times 10^5$, $C_W = 6131$ ($\lambda_T = 0.139$); (*c*) $Re_\phi = 6.79 \times 10^5$, $C_W = 9724$ ($\lambda_T = 0.210$); —— computation; ○ uncorrected data; ● corrected data

results the computations show that the temperature of the adiabatic disk is never more than 20°C greater than T_I. As the radiation correction described in Section 3 was based on the assumption that the temperature of the unheated disk was equal to T_I, the corrected Nusselt numbers are believed to be more accurate than the uncorrected values.

Figure 11 for $Re_\phi \simeq 1.1 \times 10^6$ shows the comparison between the results for $\Gamma = -1$ and $\Gamma = 0$. Although the trends for the computational and experimental results are similar for both values of Γ, the computed and measured Nusselt numbers for

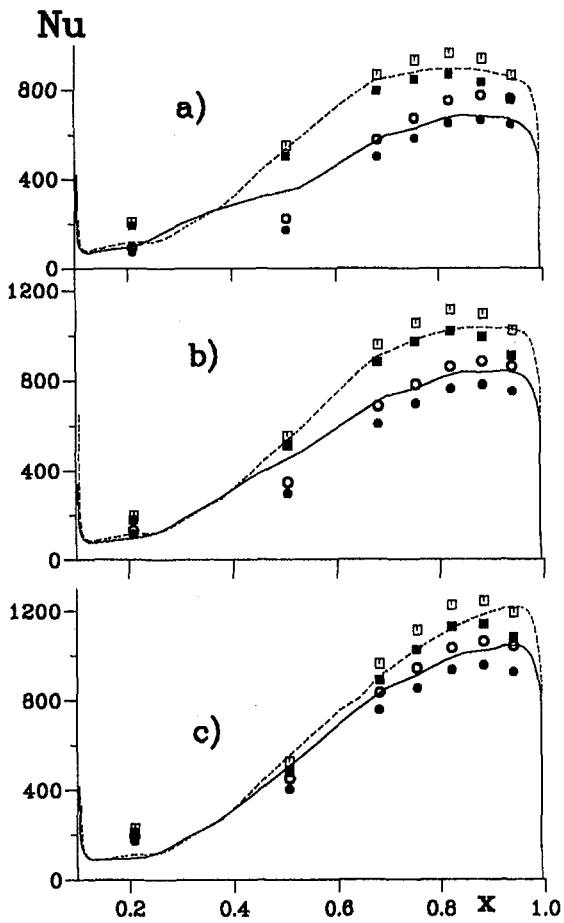

Fig. 11 Computed and measured Nusselt numbers for $\Gamma = -1$ and $\Gamma = 0$: (*a*) $Re_\phi = 1.09 \times 10^6$, $C_W = 3926$ ($\lambda_T = 0.0581$); (*b*) $Re_\phi = 1.11 \times 10^6$, $C_W = 6130$ ($\lambda_T = 0.0894$); (*c*) $Re_\phi = 1.18 \times 10^6$, $C_W = 9720$ ($\lambda_T = 0.135$); $\Gamma = -1$: —— computation, ○ data; $\Gamma = 0$: - - - computation, □ data (solid symbols refer to corrected data)

$\Gamma = 0$ are significantly higher than those for $\Gamma = -1$. It was stated in Section 1 that the value of C_m for contrarotating disks is greater than that for the equivalent rotor–stator case, although the difference reduces as the flow rate approaches the free-disk-entrainment rate. The Reynolds analogy suggests therefore that the Nusselt numbers for $\Gamma = -1$ should be *higher,* not *lower,* than those for $\Gamma = 0$. The main reason for this paradox is that, according to the computations, the air temperature in the recirculating core for $\Gamma = -1$ is higher than that in the nonrecirculating core for $\Gamma = 0$; the increase in air temperature causes a decrease in heat transfer.

In summary, the measured effects of Γ, Re_ϕ, and C_W on Nu are mainly well predicted by the computational method. The agreement is worst at the lowest Reynolds number tested ($Re_\phi \simeq 2 \times 10^5$) where the computations underpredict the measured values. For the higher values of Re_ϕ, the differences between the computations and the corrected Nusselt numbers are attributed to the uncertainties in both the computations and the measurements.

5 Conclusions

Velocity and heat transfer measurements, made in a heated rotating-disk rig with a radial outflow of cooling air, have been compared with computations made using an elliptic solver incorporating a low-Reynolds-number $k-\epsilon$ turbulence model. For $\Gamma = -1$ (the contrarotating case), comparisons are made for $Re_\phi \simeq 2 \times 10^5$ and 1.1×10^6 and $3900 < C_W < 9700$ ($0.06 < \lambda_T < 0.5$).

Both computations and experiments show trends consistent with the Reynolds analogy: For a given radial location, Nu increases strongly with Re_ϕ and weakly with C_W. The size of the source region and the temperature distribution in the cooling air depend strongly on λ_T: a large value of λ_T is associated with a large source region and with a small increase in the air temperature in the recirculation zone outside the source region.

Comparison with results for $\Gamma = 0$ (the rotor–stator case) shows that, under equivalent conditions, the Nusselt numbers for $\Gamma = -1$ are significantly less than those for $\Gamma = 0$.

Overall, the measured velocity distribution and Nusselt numbers are well predicted by the computational method.

Acknowledgments

This work has been carried out with the support of the UK Engineering and Physical Sciences Research Council and the Defence Research Agency.

References

Batchelor, G. K., 1951, "Note on a Class of Solutions of the Navier–Stokes Equations Representing Steady Rotationally-Symmetric Flow," *Quart. J. Mech. Appl. Math.,* Vol. 4, pp. 29–41.

Chen, J.-X., Owen, J. M., and Wilson, M., 1993a, "Parallel-Computing Techniques Applied to Rotor–Stator Systems: Fluid Dynamics Computations," *Proc. 8th Intl. Conf. Numer. Meth. Laminar Turbulent Flow,* Swansea, Pineridge Press, pp. 899–911.

Chen, J.-X., Owen, J. M., and Wilson, M., 1993b, "Parallel-Computing Techniques Applied to Rotor–Stator Systems: Thermal Computations," *Proc. 8th Intl. Conf. Numer. Meth. Thermal Problems,* Swansea, Pineridge Press, pp. 1212–1226.

Chen, J.-X., Gan, X., and Owen, J. M., 1996, "Heat Transfer in an Air-Cooled Rotor–Stator System," ASME JOURNAL OF TURBOMACHINERY, Vol. 118, pp. 444–451.

Dorfman, L. A., 1963, *Hydrodynamic Resistance and the Heat Loss of Rotating Solids,* Oliver and Boyd, Edinburgh.

Gan, X., Kilic, M., and Owen, J. M., 1995, "Flow Between Contrarotating Discs," ASME JOURNAL OF TURBOMACHINERY, Vol. 117, pp. 298–305.

Graber, D. J., Daniels, W. A., and Johnson, B. V., 1987, "Disk Pumping Test," Air Force Wright Aeronaut. Lab., Report No. AFWAL-TR-87-2050.

Kilic, M., Gan, X., and Owen, J. M., 1994a, "Superposed Flow Between Two Discs Contrarotating at Differential Speeds," *Int. J. Heat Fluid Flow,* Vol. 15, pp. 438–446.

Kilic, M., Gan, X., and Owen, J. M., 1994b, "Transitional Flow Between Contrarotating Discs," *J. Fluid Mech.,* Vol. 281, pp. 119–135.

Kilic, M., Gan, X., and Owen, J. M., 1996, "Turbulent Flow Between Two Discs Contrarotating at Different Speeds," ASME JOURNAL OF TURBOMACHINERY, Vol. 118, pp. 408–413.

Morse, A. P., 1988, "Numerical Prediction of Turbulent Flow in Rotating Cavities," ASME JOURNAL OF TURBOMACHINERY, Vol. 110, pp. 202–215.

Morse, A. P., 1991, "Application of a Low Reynolds Number $k-\epsilon$ Turbulence Model to High-Speed Rotating Cavity Flows," ASME JOURNAL OF TURBOMACHINERY, Vol. 113, pp. 98–105.

Owen, J. M., and Rogers, R. H., 1989, *Flow and Heat Transfer in Rotating Disc Systems, Vol. 1: Rotor Stator Systems,* Research Studies Press, Taunton (Wiley, New York).

Stewartson, K., 1953, "On the Flow Between Two Rotating Coaxial Disks," *Proc. Camb. Phil. Soc.,* Vol. 49, pp. 333–341.

Evaluation of the Interaction Losses in a Transonic Turbine HP Rotor/LP Vane Configuration

I. K. Jennions[1]
G. E. Aircraft Engines,
Cincinnati, OH 44135

J. J. Adamczyk
NASA Lewis Research Center,
Cleveland, OH 44135

Transonic turbine rotors produce shock waves, wakes, tip leakage flows, and other secondary flows that the downstream stators have to ingest. While the physics of wake ingestion and shock interaction have been studied quite extensively, few ideas for reducing the aerodynamic interaction losses have been forthcoming. This paper aims to extend previously reported work performed by GE Aircraft Engines in this area. It reports on both average-passage (steady) and unsteady three-dimensional numerical simulations of a candidate design to shed light on the interaction loss mechanisms and evaluate the design. The results from these simulations are first shown against test data for a baseline configuration to engender confidence in the numerical approach. Simulations with the proposed newly designed rotor are then performed to show the trade-offs that are being made in such designs. The new rotor does improve the overall efficiency of the group and physical explanations are presented based on examining entropy production.

Introduction

High pressure (HP) aircraft engine turbines adopt either one or two-stage configurations. Two-stage turbines are longer and weigh more but are considerably easier to design (being subsonic) and even with the increase in overall surface area are usually more efficient. Single-stage designs offer the advantages of shorter length, lighter weight, and possible lower parts cost but, being highly loaded, are transonic and suffer efficiency penalties from shock losses and high loadings. In addition, cooling plays a major role in the design of HP turbines, protecting the blade metal from the extremely hot flowpath gases. It will only be indirectly addressed in this paper as here the emphasis is on the aerodynamic design. Both rotor designs investigated are capable of being cooled using current technology.

Transonic blades typical of single-stage designs have been investigated experimentally for a number of years; the first papers concentrated on aerodynamic shock formation (Sieverding, 1973) and the base pressure encountered in such configurations (Sieverding et al., 1979). Later, investigations included heat transfer measurements (Arts and Heider, 1994) and trailing edge coolant ejection (Sieverding et al., 1996). Computations to match the data produced by these experiments have been ongoing (Arnone and Stecco, 1991; Turner et al., 1993; Heider and Arts, 1994), focusing on the accurate prediction of these single blade row results.

The extension of these single blade row calculations to steady-state solutions was made using a mixing plane approach (Dawes, 1991; Arnone and Stecco, 1991) and by an alternate average-passage approach (Adamczyk et al., 1990). The latter was aimed at overcoming some perceived shortfalls in the mixing plane approach (see below) and attempts to solve, within modeling limitations, the time average of the multistage unsteady flow.

Unsteady stage interactions have been investigated both at Oxford University (Johnson et al., 1990) and MIT (Guenette et al., 1989; Abhari et al., 1992) where the focus has been primarily on heat transfer measurements. At the same time the development of unsteady flow solvers, first in two dimensions (Rai, 1987; Giles, 1990; Rangwalla et al., 1992) and more recently in three dimensions (Madavan and Rai, 1989; Chen et al., 1994) has complemented these efforts at understanding the physical flow phenomena involved. Fritsch and Giles (1995) compared results obtained with an unsteady code against those obtained using a steady mixing plane approach, showing that a jump in entropy occurs at the mixing plane that is not present in the unsteady calculation. This jump would also not be present in the average-passage approach.

Although these research activities have been pursued for some years, papers on the design of single-stage HP turbines to reduce the subsequent interaction loss with the LP turbine do not seem to be common. The present paper seeks to fill this gap. The paper continues a line of work that has been under way at General Electric Aircraft Engines (GEAE) for some years now, aimed at understanding the interaction loss mechanisms between a transonic HP rotor and the first-stage LP vane.

Problem

In 1982, GEAE ran a cascade and subsequent rig test in which a LP vane was tested in a cascade configuration and then behind an HP rotor (Fig. 1). Results from this test indicated that a significant penalty (5.6 percent loss in efficiency) was encountered when the LP vane ran behind the HP stage (Fig. 2). Consequently, a program of work was initiated to understand the nature of the interaction loss, with the eventual goal of changing the design to reduce this penalty. Preliminary quasi-three-dimensional unsteady calculations on the midspan region of the nozzle performed with the Rotor1 code (Rai, 1987) showed large unsteady pressure fluctuations on the LP vane. Although no clear causal relationship was established between these fluctuations and loss, it was hypothesized that the fluctuations were due to rotor shock waves striking the vane and that reducing the strength of these shocks would improve the efficiency significantly.

Based on this hypothesis, design activity was initiated to reduce the strength of the shocks from the rotor, and thus to reduce the circumferential static pressure gradient and hence decrease the unsteady vane loading. This design was executed using an artificial intelligence design shell (Engineous) coupled with an inviscid, unstructured, adaptive blade-to-blade code

[1] Present address: ABB Power Generation Ltd.

Contributed by the International Gas Turbine Institute and presented at the 40th International Gas Turbine and Aeroengine Congress and Exhibition, Houston, Texas, June 5–8, 1995. Manuscript received by the International Gas Turbine Institute March 7, 1995. Paper No. 95-GT-299. Associate Technical Editor: C. J. Russo.

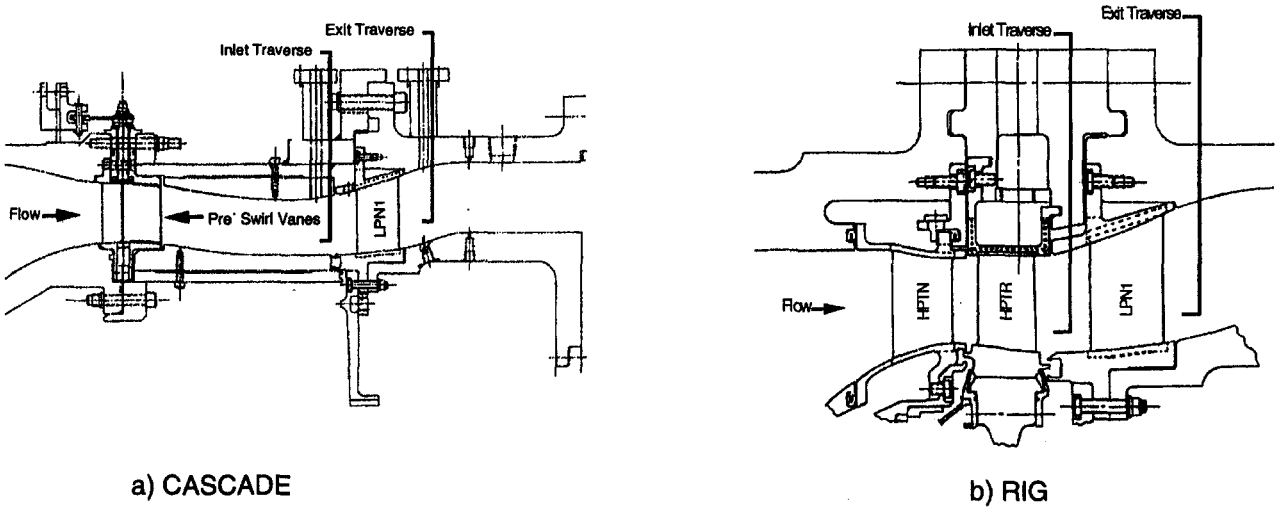

Fig. 1 Test configuration

(NOVAK2D). Traditional parameters that were known to influence shock strength including wedge angle, unguided turning, overturning, and trailing edge thickness were allowed to vary. The overall optimization process became a balance between the relative strengths of the shocks emanating from the suction and pressure surfaces near the trailing edge of the blade in order to produce the most homogeneous flow possible onto the downstream blade. The geometry and aerodynamic loading were reported by Shelton et al. (1993a). The design was executed and resulted in a blade named MIDOS (MInimized DOwnstream Shock). The idea was subsequently tested as a linear cascade at VPI (Shelton et al., 1993b), the results downstream of the rotor at the design exit Mach number of 1.13 being shown in Fig. 3. The blade-to-blade variation of static pressure is significantly reduced with the new design showing that the design objective had been met. However, it was found that, due to an increase in the rotor trailing edge thickness necessary to reduce the shock strength, the overall loss of the rotor had increased (Fig. 4) and the flow nonuniformity as measured by the relative total pressure had increased (Fig. 5), i.e., wakes were thicker and deeper.

As the wakes were thicker and still no clear relationship existed between the fluctuating vane loads and loss, it was unclear as to whether or not this design would improve overall performance. Based on these issues it was decided to conduct a series of numerical experiments to examine the interaction loss process. These simulations would hopefully quantify the loss process and establish if indeed the new design would lead to a net overall performance improvement. The findings from these simulations, i.e., the baseline and MIDOS configurations are the subject of this paper.

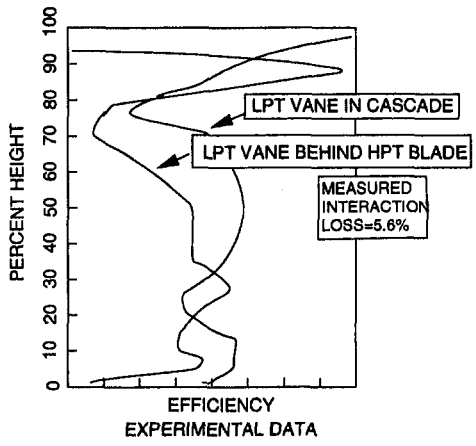

Fig. 2 Efficiencies for vane in cascade and behind HP rotor

Prior to showing the direct comparison between the two different rotor cases, the credibility of the codes being used is established. Both the average-passage code (VSTAGE, Adamczyk et al., 1996) and the unsteady code (UNCLE, Chen et al., 1994) are run against the existing baseline experimental data to show that the numerical error bands are well within the interaction loss levels that are trying to be controlled by the redesign. With confidence that it is valid to use these tools on the baseline configuration, results from the new rotor are then presented and discussed. In order to compare the two designs properly, the steady and unsteady entropy contributions are examined and conclusions reached.

Cascade Results

The geometry tested is as shown in Fig. 1(a), the computational grid extending from the vane inlet traverse plane to the vane exit traverse plane. The upstream preswirl vane produced an almost uniform (compared to the rig) inlet swirl angle and total pressure profile for the vane. VSTAGE was run as a single blade row simulation for this study with a computational grid of 33 × 33 × 131 (142,659 points), corresponding closely to the grid density used for the stage solutions. Inlet conditions of total pressure, total temperature, and swirl angle were taken from the experimental traverse and the downstream static pressure was set in the same way. Comparison between measured and computed results for total pressure and swirl angle are shown in Fig. 6. The group of experimental data points between 70 and 90 percent span is somewhat questionable but, taking this into account, agreement is quite reasonable. Efficiency for the cascade is shown later when it is compared to that behind the HP stage; it compares quite well to the measured values.

Baseline Results

With the full HP stage in front of the LP vane, the configuration is shown in Fig. 1(b). In order to restrict the computations to the area of interest, only the HP rotor and LP vane were modeled; the HP vane was thought to be of secondary importance. The inlet conditions for the HP rotor were taken from a throughflow match of the experimental data with the static pressure downstream of the vane coming from the measured values. In the rig, both the HP vane and rotor cooling flow circuits were flowing for the test. The only appreciable effect that this

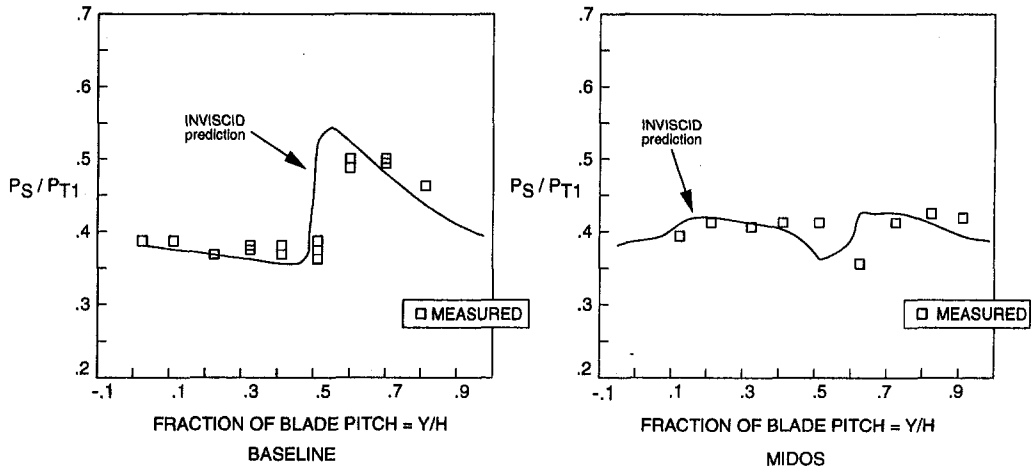

Fig. 3 Circumferential static pressure variations from VPI tests

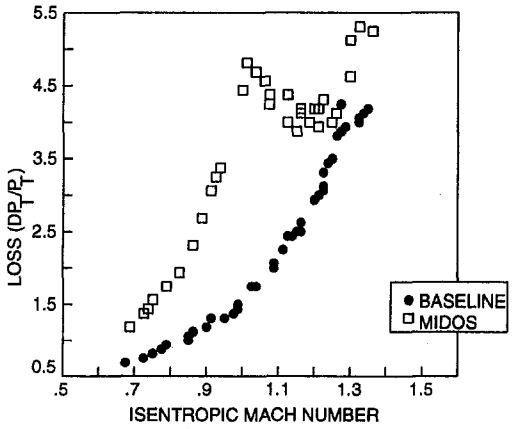

Fig. 4 Loss versus Mach number from VPI tests

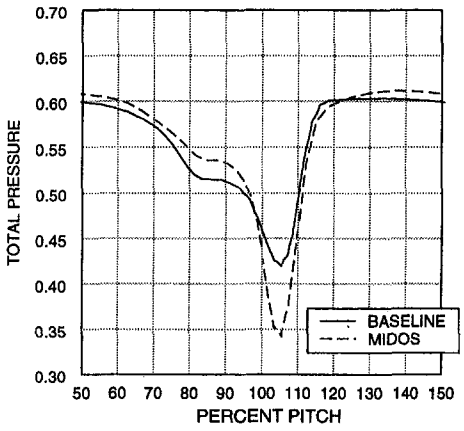

Fig. 5 Relative total pressure versus percent pitch at exit of rotor

has on the results is in terms of total temperature and for that reason the total temperature comparisons are not presented.

Two simulations were performed on this configuration. First, VSTAGE was run on the HP rotor/LP vane stage with the boundary conditions just described. Then a three-dimensional unsteady simulation of the LP vane, achieved by moving the rotor exit boundary condition past the vane, was performed using the UNCLE code. The results from both of these will be described here.

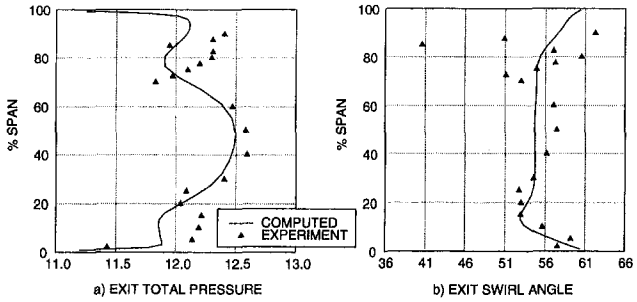

Fig. 6 Comparison of exit total pressure and swirl angle with experimental data

The inlet and exit conditions predicted by the VSTAGE code for the LP vane are shown in Fig. 7 along with the experimental data. The incoming total pressure is well predicted including the flattening of the profile in the 20 percent span close to the hub. The same overall match is achieved at vane exit, but with the experimental data still showing the hub pressure rise, while VSTAGE predicts a more conventional drop off. The inlet swirl angles show the classic counterrotating vortices from the rotor. These persist through the vane in the computation while the data show a flattening of the profile. Part of the modeling in VSTAGE accounts for "mixing" due to an upstream blade as the flow passes through subsequent blade rows. Clearly, the mixing is not sufficient and the model could be better calibrated on this case. The exit static pressure is deliberately set higher than that measured in order to achieve realistic static pressures at exit from the rotor. Further decreasing the exit static would lead to the interblade statics dropping further and hence the rotor operating off-design. This pressure anomaly is not fully understood, but it appears that the code is not predicting a sufficiently high discharge coefficient for the vane, a problem that may be remedied by running a fully unsteady stage calculation.

A three-dimensional unsteady simulation of the vane only was performed in order to determine the effects of true unsteadiness on the results. Recall that VSTAGE solves for the time average of the unsteady flow, subject to some modeling limitations. This means that while convected vorticity from one blade row into the next can be simulated, any loss due to unsteady shock interaction would not be captured by this simulation and hence the need for the unsteady simulation. The unsteady code static pressure on the suction and pressure surface of a vane passage at midspan is plotted as a function of axial chord and time in Fig. 8. The time intervals are a quarter of the rotor

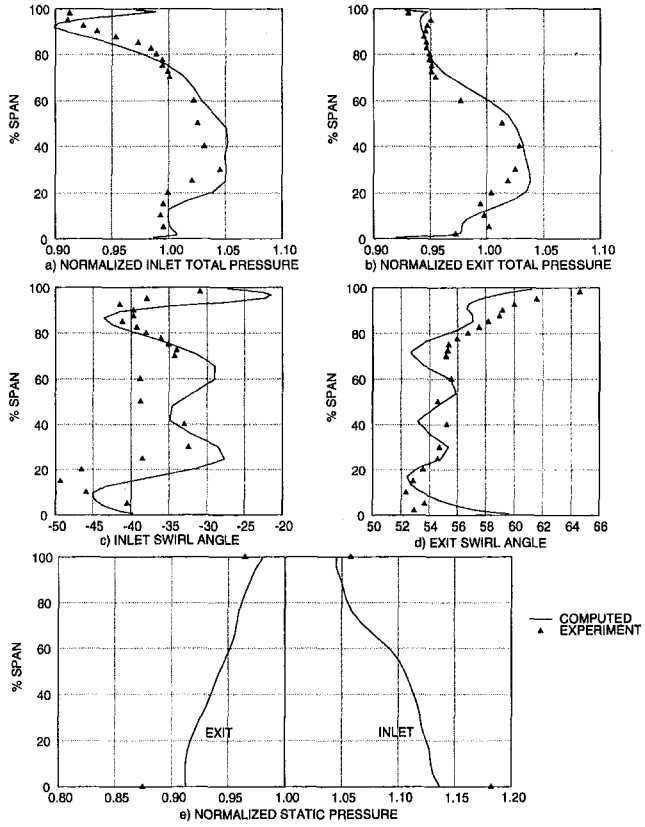

Fig. 7 Comparison of predicted and experimental conditions at inlet and exit of LP vane

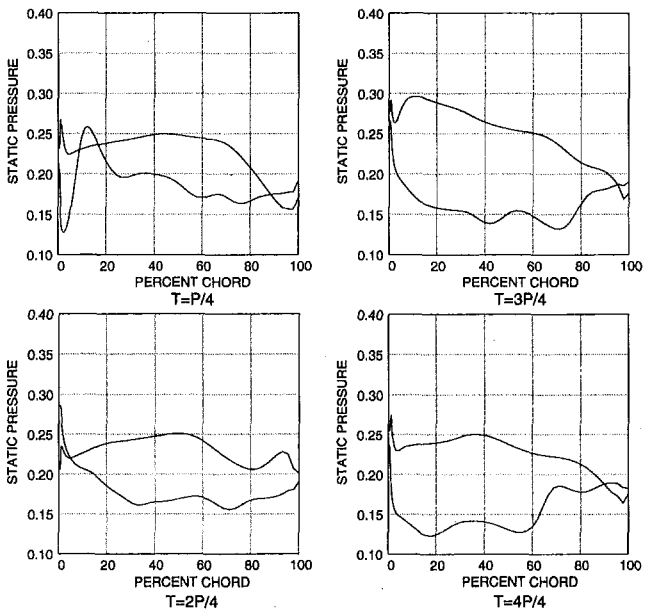

Fig. 8 Unsteady static pressure distribution at midspan: baseline case

passing time cycle apart. There is a very significant change in the static pressure during one blade passing cycle, particularly near the leading edge. These results are qualitatively similar to those produced much earlier by a quasi-three-dimensional unsteady code that prompted the MIDOS design.

Figure 9 summarizes these runs by showing the calculated efficiencies from the LP vane in cascade (from VSTAGE) and that calculated behind the HP rotor (from UNCLE). The same

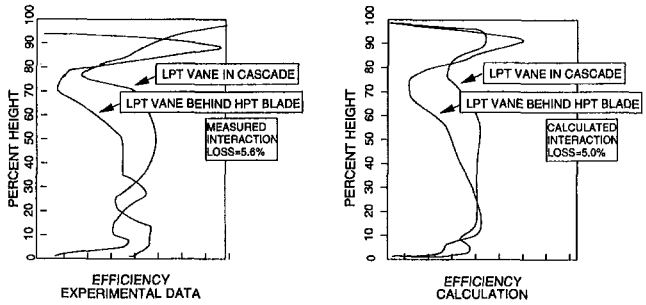

Fig. 9 Efficiencies for vane in cascade and behind HP rotor

interaction loss is seen in the computations as was observed in the experiment, giving rise to confidence in the ability of these codes to reproduce the physics of the interaction loss. The next section will apply these codes to the analysis of the group with a new rotor.

The VSTAGE simulation employed a 33 × 33 × 257 grid (279,873 points) and took some 30 flips and 6.7 CRAY C-90 CPU hours to converge. The UNCLE simulation used a 33 × 33 × 113 grid (123,057 points), which, starting from the average-passage generated starting solution, took 12 blade passings and 2.9 CRAY C-90 hours to produce a repeating solution. This incredibly short time is due almost entirely to the use of the average-passage solution, which produces such a remarkably good starting solution that it could be mistaken for a snapshot of the true unsteady solution. Using this procedure, UNCLE is really solving a small perturbation problem rather than the more daunting unsteady flow process from a uniform starting guess. This combination of timings makes the VSTAGE UNCLE code combination very attractive in a design system.

MIDOS Results

The newly designed MIDOS rotor was simulated in a similar manner to the baseline. First, an average-passage run was made, followed by an unsteady simulation of the LP vane. Gridding and numerical parameters were set to be the same as for the baseline. Figure 10 shows the pressure distribution on the suc-

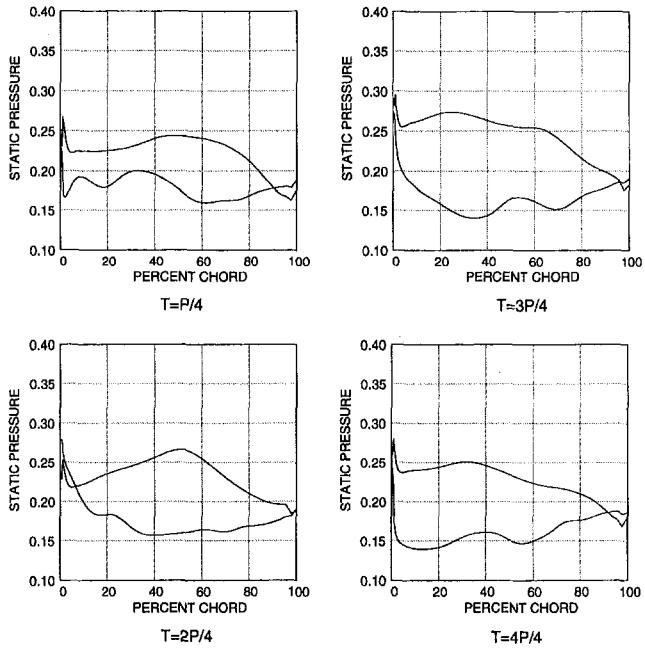

Fig. 10 Unsteady static pressure distribution at midspan: MIDOS case

Table 1 MIDOS versus baseline efficiency gains

	HP Rotor	LPT Vane	Group
Average-Passage	-0.22	+1.6	+0.5
UNCLE (Unsteady)	-0.22	+2.2	+0.6

tion and pressure surface of a vane passage at four instances in time. The plots for the baseline configuration are taken from Fig. 8 and appear on the left of Fig. 10; the plots for the MIDOS configuration are on the right. The time intervals are identical to those in Fig. 8. At time one-quarter, the pressure difference across the vane passage is near its minimum value while at time three-quarter, the pressure difference across the passage is near its maximum value. Comparing the plots for the baseline configuration to those for the MIDOS configuration shows the unsteady pressure loading for the MIDOS configuration is less than that for the baseline. Figure 10 also shows the magnitude of the steep pressure gradients on the suction surface, which will be shown to be attributed to the incoming shock, is less for the MIDOS configuration than the baseline. The reduced amplitude of the unsteady pressure loading of the MIDOS configuration clearly indicates that the MIDOS design has achieved its objectives. Finally, note that the time mean pressure distribution is nearly identical from both configurations.

Table 1 presents a summary of the efficiency change between the MIDOS and baseline configurations. Results are presented from the average-passage and unsteady simulations for the HP rotor, LP vane and the group, which consists of the HP rotor and the LP vane. The appendix gives the mathematical definition for each of these efficiencies. Since in the unsteady simulations the rotor was not included, the rotor efficiency is assummed to be equal to that obtained from the average-passage simulations. The first thing to observe is that the average-passage and unsteady simulations are in fair agreement, which implies that the unsteady shock vane interaction is playing a weak role and that the loss process is dominated by mixing, which the average-passage code is capable of accounting for. Secondly, the HP turbine efficiency for MIDOS is 0.22 points lower than that for the baseline. This is in agreement with the findings of Shelton et al. (1993a) and arises from the thicker trailing edge of the MIDOS rotor needed to minimize the downstream pressure nonuniformity. This loss may be offset when trailing edge cooling effects are included. However, in sharp contrast to the loss in rotor efficiency, the vane efficiency is improved as a results of operating behind the MIDOS rotor. This improvement in vane efficiency in turn yields a net gain in the group (HP rotor and LP vane) efficiency of 0.6 points, a nontrivial amount. The question left unanswered is to why the improvement in vane efficiency is realized. What flow processes have led to this gain? The answer to this question is attempted in the next section.

Loss Reduction

The efficiencies that have just been cited are a measure of the irreversibility of the process. For an unsteady flow the only flow variable that can be directly related to this irreversibility is the entropy. For an unsteady flow the entropy is governed by the following equation:

$$\rho \frac{Ds}{Dt} = \frac{1}{T}\frac{\partial u_i}{\partial x_i}\tau_{ij} - \frac{q_i}{T^2}\frac{\partial T}{\partial x_i} - \frac{\partial}{\partial x_i}\frac{1}{T}q_i \qquad (1)$$

wherein s denotes the entropy of a fluid particle, ρ the density, D/Dt is the substantial derivative, T the temperature, u_i the Cartesian velocity components, τ_{ij} the viscous stress, x_i the Cartesian coordinates, and q_i the heat flux vector. Assuming a Stokesian, Newtonian fluid and Fourier's equation for heat flux transfer by conduction:

$$q_i = -k\frac{\partial T}{\partial x_i} \qquad (2)$$

Eq. (1) becomes:

$$\rho \frac{Ds}{Dt} = \underbrace{\frac{\mu}{T}e_{ij}e_{ij}}_{(1)} + \underbrace{\frac{k}{T^2}\frac{\partial T}{\partial x^i}\frac{\partial T}{\partial x^i}}_{(2)} + \underbrace{\frac{\partial}{\partial x^i}\frac{k}{T}\frac{\partial T}{\partial x_i}}_{(3)} \qquad (3)$$

where μ is the coefficient of viscosity (i.e., both laminar and turbulent), k the thermal conductivity (i.e., both laminar and turbulent), and e_{ij} the strain rate tensor. Both of the terms labeled (1) and (2) are positive definite and thus lead directly to the production of entropy. Term (1) is associated with viscous dissipation while (2) is associated with thermal dissipation. Term (3) may either increase or decrease the entropy of a fluid particle depending upon the heat transfer to the particle. In the present study, term (2) was found to be nearly an order of magnitude smaller than term (1) and thus will be neglected in the analysis to follow. Term (1) will be used to detect features in the unsteady flow field that lead to the production of entropy and hence generate loss.

In the evaluation of term (1) it is assumed that the coefficient of viscosity is constant throughout the flow field. Since the primary use of term (1) is in identifying features outside the viscous wall layers that lead to loss generation; this latter assumption appears reasonable.

With term (2) neglected, averaging Eq. (3) in time and across the flow channel yields

$$\frac{d}{dx}\overline{\overline{s\rho uA}} = \int \overline{\frac{\mu}{T}e_{ij}e_{ij}}\,dA \qquad (4)$$

where the first overbar signifies a time average, and the second an area average. The variable A is the flow stream cross-sectional area and u the axial velocity component. The contribution of term (3) to Eq. (4) vanishes because the external boundaries in the present study are adiabatic. Equation (4) shows the direct relationship that exists between the entropy flux and the viscous dissipation, thus justifying the use of the viscous dissipation as a detector of flow features associated with the generation of loss.

The analysis of loss production for the baseline and MIDOS designs begins with Fig. 11, which shows the time-averaged entropy flux through the vane operating downstream of both rotors plotted against the nondimensional axial distance from the inlet to the exit of the unsteady simulation computational domain. The location of the vane leading and trailing edge is noted on the plots. The entropy flux has been normalized by the value of the entropy flux of the baseline configuration at the exit of the computational domain. In addition, for the MIDOS configuration the normalized entropy flux has been shifted by the difference between the entropy flux of the baseline and MIDOS configuration at the exit of the computational domain. Thus for both configurations the entropy flux at the exit of the domain is one. Recall that the efficiency of the MIDOS rotor is less than the baseline, but that the efficiency of the vane operating downstream of the MIDOS rotor is greater than when operating downstream of the baseline rotor. Plots labeled (a) and (b) in Fig. 11 show that the entropy flux generated from the vane midchord to the exit of the computational domain is nearly identical for the two configurations. However, the entropy flux generated from the inlet of the computational domain to the vane leading edge is lower for the MIDOS configuration than for the baseline. Thus the increase in efficiency of the MIDOS group is the result of a reduction in loss generation forward of the vane leading edge. Figure 11 also shows lines labeled (c) and (d) from which the contribution to the entropy flux from the hub to 20 percent of span and from 80 percent of span to the shroud has been omitted. As in plots (a) and (b), the entropy flux generated from the vane midchord to the

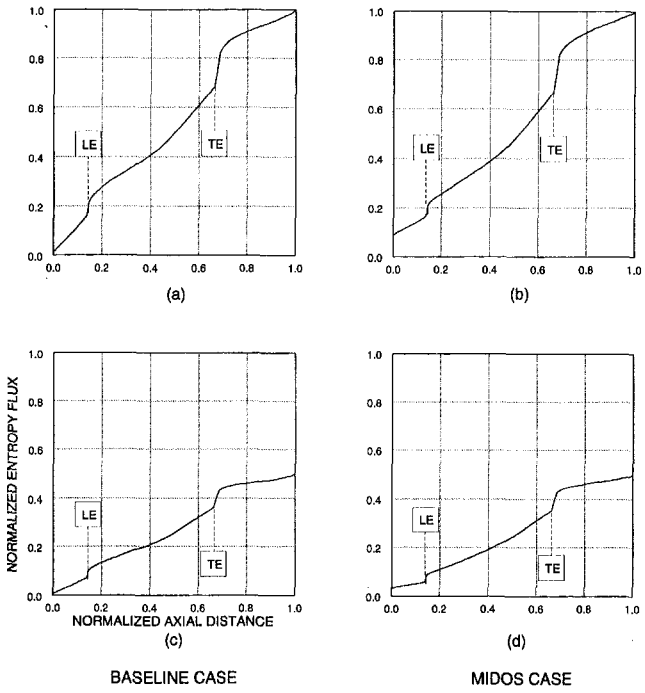

Fig. 11 Time-averaged entropy flux versus normalized axial distance (0.0 = computational inlet; 1.0 = computational exit): (*a*) & (*b*) nondimensional with respect to exit conditions; (*c*) & (*d*) inner and outer 20 percent removed

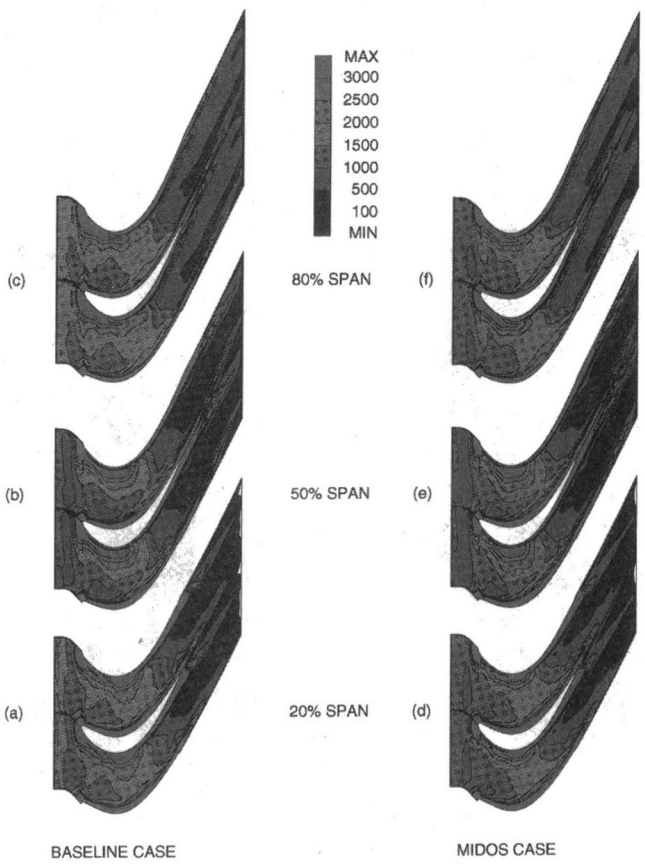

Fig. 12 Contour plot of time-averaged dissipation function

exit of the computational domain is nearly identical for the two configurations. The differences that exist between plots (*c*) and (*d*) are forward of midchord. It will be shown that the reduced loss of the MIDOS configuration is the result of a weaker unsteady shock system relative to that for the baseline configuration. Note, however, that for both configurations there is a significant contribution to total entropy flux generated from the end-wall region as indicated by the difference between plots (*a*) and (*c*) compared to plot (*a*) for the baseline configuration, while for the MIDOS design the difference between plots (*b*) and (*d*) compared to plot (*b*).

Extending this idea of separating out the entropy generated in various regions of the flow, Table 2 is obtained. The first column in the table gives the percentage of the contribution to overall loss for the baseline configuration, the second column that for the MIDOS design, while the third is the difference. Excluding the numbers in the third column, the first row is the contribution associated with the outer 20 percent of span (i.e., outer endwall region), the second row that associated with the inner 20 percent of span (i.e., inner endwall region), while the column sum of the next three rows gives the contribution of the core flow region. From this it is noted that the MIDOS design has less loss in the core flow region upstream of the vane leading edge, a difference of 4.2 percent, over the corresponding baseline loss. There are also loss reductions which arise in the endwall regions. Going back to Fig. 11 one observes, by comparing the difference between plots (*a*) and (*c*) to the difference between plots (*b*) and (*d*), that most of the gains in the endwall regions occur forward of the vane midchord. The loss reduction associated with the MIDOS design in the core flow region forward of midchord extended into the endwall regions. Table 2 also shows that the major loss creating regions of the flow are near the endwalls, probably caused by secondary flow and mixing in these regions. Subsequent designs could best concentrate on these regions as those of greatest potential benefit.

Table 2 Percent contributions to overall loss*

	Baseline	MIDOS	Δ
80% Span To Shroud	28.1	25.5	-2.6
Hub To 20% Span	21.8	19.3	-2.5
Remaining Flow: Inlet– LE	7.5	3.3	-4.2
Remaining Flow: LE – TE	32.7	33.6	+0.9
Remaining Flow: TE – Exit	9.9	10.3	+0.4
Totals	100.0	92.0	-8.0

* Given as % of Total Baseline Loss

Figure 12 shows blade-to-blade contour plots of the time-averaged normalized viscous dissipation function at 20, 50, and 80 percent of span. The contour plots on the left are for the baseline while those on the right are for the MIDOS configuration. The contour plots show that the level of dissipation forward of the leading edge is higher for the baseline configuration than it is for the MIDOS configuration. This result is consistent with the results previously shown for the entropy flux. In addition, note that the dissipation contours forward of the vane are nonaxisymmetric. Animating the results of the unsteady simulation revealed the nonaxisymmetic pattern arises because of the interaction between the incoming wakes and the reflected shock system. The downstream side of the incoming wake suppressed entropy generation from the shock while the upstream side augmented it. The line seen is thus the locus of the reflected shock and the upstream side of the wake as they pass through each other.

Within the passage region and the region surrounding the leading edge, the dissipation extends far beyond the viscous wall layers. The dissipation in these regions results from the straining of the incoming wakes by the time mean velocity field and the reflected shock system. However, the entropy flux results, as discussed previously, showed that the integrated ef-

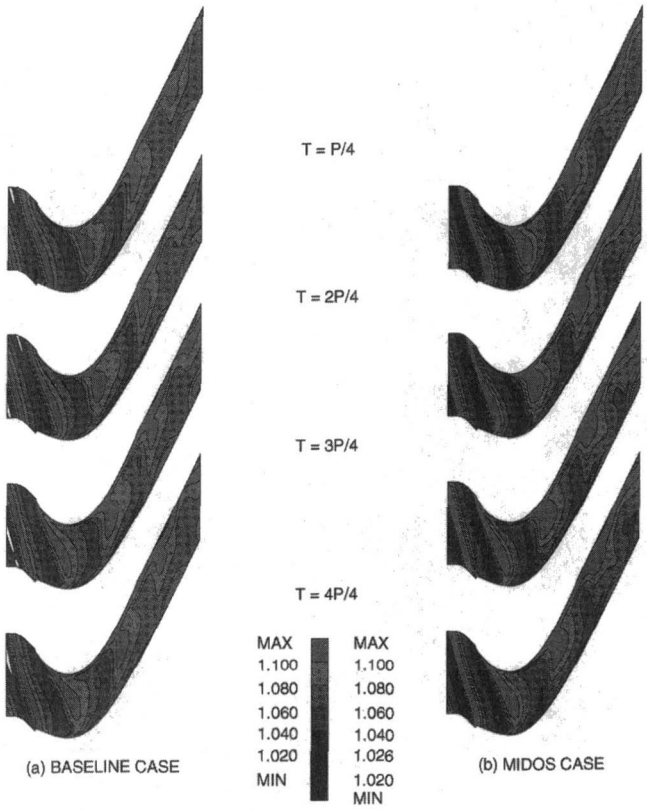

Fig. 13 Contours of entropy as a function of time at midspan

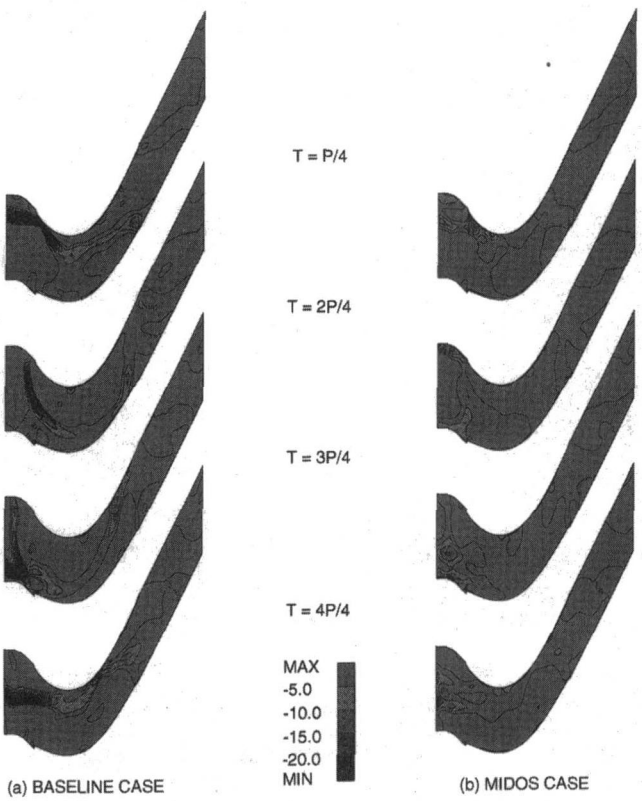

Fig. 14 Divergence of velocity as a function of time at midspan

fect of the in-passage dissipation is nearly the same for both configurations.

Downstream of the trailing edge the dissipation is confined to the wake region. The dissipation at midpitch for both configurations is nearly zero. This suggests that the wakes and shocks have mixed out or are confined to the sides of the vane passage. Which process is responsible for the low level of dissipation at midpitch will be addressed shortly.

The final set of figures (13, 14, and 15) is intended to illustrate the unsteady flow processes that lead to the generation of entropy for the baseline and MIDOS configuration. All the unsteady results are for midspan and are representative of the loss generation processes that occur away from the end-wall regions. The first set of figures shows the entropy contours at the time intervals shown in Fig. 8. The baseline results are on the left while the MIDOS results are on the right. Both sets of results show clear evidence of the incoming wakes with the wakes from the MIDOS configuration having larger variations in entropy. Because the wakes from the MIDOS rotor have a greater velocity defect, they transport further across the vane passage than the wakes from the baseline rotor. For both configurations, by the time an incoming wake has passed the vane trailing edge a significant portion of the wake has drifted across the passage and become part of the vane wake. The drift and subsequent piling up of the rotor wakes on the vane suction surface is greater for the MIDOS configuration than for the baseline, a consequence of the "Kerrebrock–Mikolajczak" effect (Kerrebrock and Mikolajczak, 1970). This drift of the wake fluid is responsible for the low levels of dissipation at midpassage downstream of the vane throat. For both configurations, the straining of the wake forward of the vane throat by the time mean velocity field is very noticeable. This straining leads to the generation of entropy outside of the viscous wall layers. A final observation regarding these plots is the lack of any apparent evidence of the structure of the incoming shock system and the loss attributed to this system.

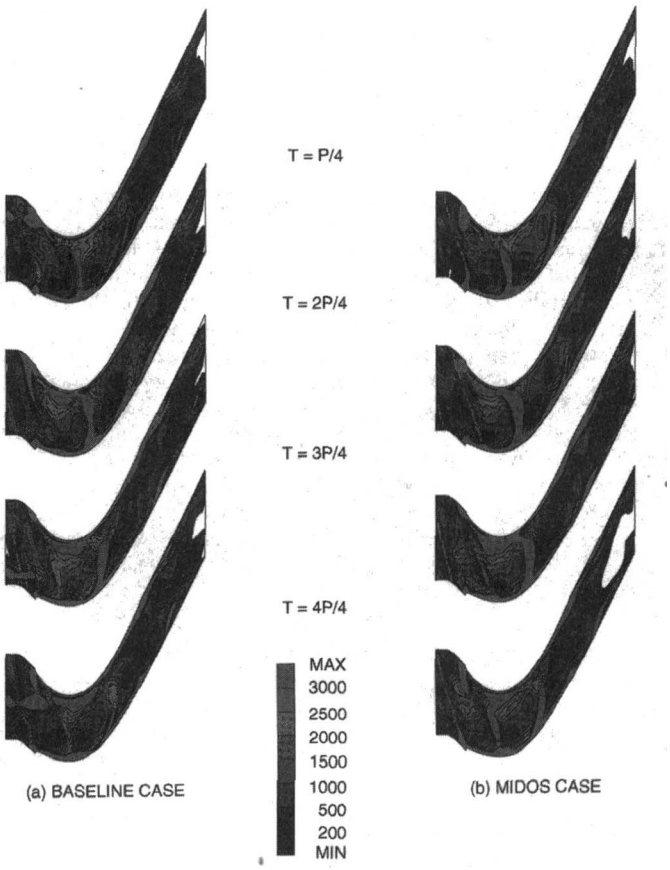

Fig. 15 Dissipation function as a function of time at midspan

Figure 14 shows the divergence of the velocity field at the times corresponding to those for the plots in Fig. 13. The contours on the plots for the MIDOS configuration, which are on the right, are a factor of two smaller then those for the baseline configuration, which are on the left, a consequence of the design objective being met. The divergence of the velocity field is equal to minus the logarithmic time derivative of the density of a fluid particle. Negative values of the divergence, which are the only ones shown, correspond to regions of compression while positive values are regions of expansion. A shock front appears as a ridge of large negative values of the divergence of velocity. The first thing to note in Fig. 14 is the well-defined structure of the incoming shock system for both configurations. The baseline has a single shock entering the vane while the MIDOS configuration has two. The shock for the baseline configuration is stronger than either shock for the MIDOS configuration. Upon striking the vane, the incoming shock from the baseline configuration is reflected into a shock, which propagates both upstream and downstream. The region in which the reflected shocks originate will be shown to be a region of entropy production. For the MIDOS configuration the reflected shock system is very weak, the upstream propagating shock system is barely evident, while the downstream shock system is sufficiently weak to be nonresolvable. Upon exiting forward of the vane passage both the shock of the baseline configuration and the MIDOS configuration are nearly circumferential.

The next set of plots (Fig. 15) show the viscous dissipation at the times corresponding to those for the plots in Figs. 13 and 14. The plots for the baseline configuration are on the left, while those for the MIDOS configuration are on the right. Apart from the viscous wall layers and the vane wakes, the large values of the viscous dissipation for either configuration is confined to the region surrounding shocks, the leading edge, and the incoming wakes. Forward of the leading edge the dissipation associated with the shock system of the baseline configuration is larger than that for the MIDOS configuration. The increase in dissipation is the result of the Baseline configuration having a stronger unsteady shock system, which reduces the efficiency of the baseline configuration relative to the MIDOS configuration. The dissipation associated with the reflected shock system of the baseline configuration within the passage is far larger than that of the MIDOS configuration. However because the rotor wakes of the MIDOS configuration are deeper, the dissipation they generate is greater than that of the baseline. The integral of the time-averaged dissipation outside of the viscous wall layers within the vane passage was found to be nearly identical for the two configurations.

The dissipation downstream of the trailing edge is the result of the shear within the vane wake and the shear within that portion of a rotor wake that has migrated across the vane passage. The integral of the time-averaged dissipation outside of the viscous wall layers over the region of flow downstream of the trailing edge for the baseline and MIDOS configuration were nearly identical.

In summary the plots presented in Figs. 13, 14, and 15 show that the efficiency gains of the MIDOS configuration over the baseline is a direct result of a weaker unsteady shock system in the region of flow forward of the vane leading edge. The unsteady shock system is composed of the incoming shock from the rotor and its reflection by the vane. The loss generation process involves the interaction of the shock system with the incoming rotor wakes.

Conclusions

A numerical study was undertaken to examine the potential of reducing the interaction losses between a transonic high-pressure turbine rotor and the downstream low-pressure turbine vane by reducing the strength of the rotor trailing edge shock system. The numerical study made use of two codes, the first of which predicts the time-averaged flow field surrounding a particular blade row, while the second predicts the underlying unsteady flow surrounding that blade row. Two configuration were simulated. The baseline configuration was used as the reference by which performance gains or losses were assessed. Data from the baseline configuration were also available and were used to calibrate the predictive capability of the codes used in the study.

The numerical simulations showed that the MIDOS rotor, which was designed to have a weak trailing edge shock system, was two tenths of a percent less efficient than the baseline rotor with its strong trailing edge shock structure because of a larger trailing edge thickness. However, the low-pressure turbine vane operating downstream of the MIDOS rotor was 2.2 percent more efficient than the same vane operating downstream of the baseline rotor. The gain in efficiency of the vane operating downstream of the MIDOS rotor produced a net gain in group efficiency of six tenths of a percent over the group efficiency of the baseline configuration.

The gain in efficiency of the MIDOS configuration over that of the baseline is attributed to the unsteady flow processes taking place forward of the vane leading edge. For the baseline configuration a reflected shock system is generated within the vane passage, which is stronger than that generated by the MIDOS configuration. Upon exiting the vane passage, the reflected shock of the baseline configuration becomes circumferential, and upon encountering the incoming rotor shock and wake generates a greater increase in entropy than the reflected shock system of the MIDOS configuration. The entropy rise within and downstream of the vane passage is nearly identical for the two configurations.

Acknowledgments

The authors wish to thank General Electric Aircraft Engines for providing the data used in this study. The authors also wish to cite the constructive suggestions of Mr. D. Cherry, Mr. M. Pearson, and Dr. M. Turner and the encouragement of Dr. M. Suo, from the Heat Transfer and Turbine Aero group at G.E. Aircraft Engines. Finally, the authors wish to acknowledge the assistance of Mr. M. Celestina, Dept. of Aeromechanics, Nyma, Inc., and Dr. J. P. Chen, NSF Engr. Research Center, Miss. State Univ. in the execution of the numerical simulations and the NASA NAS project for the computing support.

References

Abhari, R. S., Guenette, G. R., Epstein, A. H., and Giles, M. B., 1992, "Comparison of Time-Resolved Turbine Rotor Blade Heat Transfer Measurements and Numerical Calculations," ASME JOURNAL OF TURBOMACHINERY, Vol. 114, pp. 818–827.

Adamczyk, J. J., Celestina, M. L., and Chen, J. P., 1996, "Wake-Induced Unsteady Flows: Their Impact on Rotor Performance and Wake Rectification," ASME JOURNAL OF TURBOMACHINERY, Vol. 118, pp. 88–95.

Adamczyk, J. J., Celestina, M. L., Beach, T. A., and Barnett, M., 1990, "Simulation of Three-Dimensional Viscous Flow Within a Multistage Turbine," ASME JOURNAL OF TURBOMACHINERY, Vol. 112, pp. 370–376.

Arnone, A., and Stecco, S. S., 1991, "Transonic Cascade Flow Prediction Using the Navier–Stokes Equations," ASME Paper No. 91-GT-313.

Arts, T., and Heider, R., 1994, "Aerodynamic and Thermal Performance of a Three Dimensional Annular Transonic Nozzle Guide Vane, Part 1: Experimental Investigation," AIAA Paper No. 94-2929.

Chen, J. P., Celestina, M. L., and Adamczyk, J. J., 1994, "A New Procedure for Simulating Unsteady Flows Through Turbomachinery Blade Passages," ASME Paper No. 94-GT-151.

Fritsch, G., and Giles, M. B., 1995, "An Asymptotic Analysis of Mixing Loss," ASME JOURNAL OF TURBOMACHINERY, Vol. 117, pp. 367–374.

Dawes, W. N., 1991, "Multi-blade Row Navier–Stokes Simulations of Fan-Bypass Configurations," ASME Paper No. 91-GT-148.

Dawes, W. N., 1995, "A Simulation of the Unsteady Interaction of a Centrifugal Impeller With Its Vaned Diffuser: Flow Analysis," ASME JOURNAL OF TURBOMACHINERY, Vol. 117, pp. 213–222.

Dawes, W. N., 1994, "A Numerical Study of the Interaction of a Transonic Compressor Rotor Overtip Leakage Vortex With the Following Stator Blade Row," ASME Paper No. 94-GT-156.

Giles, M. B., 1990, "Stator/Rotor Interaction in a Transonic Turbine," AIAA *Journal of Propulsion,* Vol. 6, p. 621.

Guenette, G. R., Epstein, A. H., Giles, M. B., Haimes, R., and Norton, R. J. G., 1989, "Fully Scaled Transonic Turbine Rotor Heat Transfer Measurements," ASME JOURNAL OF TURBOMACHINERY, Vol. 111, pp. 1–7.

Heider, R., and Arts, T., 1994, "Aerodynamic and Thermal Performance of a Three Dimensional Annular Transonic Nozzle Guide Vane, Part 2: Assessment of a Three Dimensional Navier-Stokes Solver," AIAA Paper No. 94–2930.

Kerrebrock, J. L., and Mikolajczak, A. A., 1970, "Intra-Stator Transport of Rotor Wakes and Its Effect on Compressor Performance," ASME *Journal of Engineering for Power,* Vol. 92, pp. 359–368.

Johnson, A. B., Oldfield, M. L. G., Rigby, M. J., and Giles, M. B., 1990, "Nozzle Guide Vane Shock Wave Propagation and Bifurcation in a Transonic Turbine Rotor," ASME Paper No. 90-GT-310.

Madavan, N. K., and Rai, M. M., 1989, "Grid Refinement Studies of Turbine Rotor–Stator Interaction," AIAA Paper No. 89-0325.

Rai, M. M., 1987, "Navier-Stokes Simulations of Rotor–Stator Interaction Using Patched and Overlaid Grids," AIAA *Journal of Propulsion and Power,* Vol. 3, pp. 387–396.

Rangwalla, A. A., Madavan, N. K., and Johnson, P. D., 1992, "Application of an Unsteady Navier–Stokes Solver to Transonic Turbine Design," AIAA *Journal of Propulsion and Power,* Vol. 8, pp. 1079–1086.

Shelton, M. L., Gregory, B. A., Lamson, S. H., Moses, H. L., Doughty, R. L., and Kiss, T., 1993a, "Optimization of a Transonic Turbine Airfoil Using Artificial Intelligence, CFD and Cascade Testing," ASME Paper No. 93-GT-161.

Shelton, M. L., Gregory, B. A., Doughty, R. L., Kiss, T., and Moses, H. L., 1993b, "A Statistical Approach to the Experimental Evaluation of Transonic Turbine Airfoils in a Linear Cascade," ASME JOURNAL OF TURBOMACHINERY, Vol. 115, pp. 366–375.

Sieverding, C. H., Arts, T., Dénos, R., and Martelli, F., 1996, "Investigation of the Flow Field Downstream of a Turbine Trailing Edge Cooled Nozzle Guide Vane," ASME JOURNAL OF TURBOMACHINERY, Vol. 118, pp. 291–300.

Sieverding, C. H., 1973, "Experimental Data on Two Transonic Turbine Blade Sections and Comparison With Various Theoretical Methods," VKI LS 59, *Transonic Flows in Turbomachinery.*

Sieverding, C. H., Stanislas, M., and Snoech, J., 1979, "The Base Pressure Problem in Transonic Cascade," ASME Paper No. 79-GT-120.

Turner, M. G., Liang, T., Beauchamp, P. P., and Jennions, I. K., 1993, "The Use of Orthogonal Grids in Turbine CFD Computations," ASME Paper No. 93-GT-38.

APPENDIX

The efficiencies stated in Table 1 are defined as follows:

$$\eta_{\text{HP Rotor}} = \left[\frac{1 - \left(\frac{p_{s,\text{exit}}}{P_{TR,\text{exit}}} \right)^{[(\gamma-1)/\gamma]}}{1 - \left(\frac{p_{s,\text{exit}}}{P_{TR,\text{inlet}}} \right)^{[(\gamma-1)/\gamma]}} \right]$$

$$\eta_{\text{LP Vane}} = \left[\frac{1 - \left(\frac{p_{s,\text{exit}}}{P_{T,\text{exit}}} \right)^{[(\gamma-1)/\gamma]}}{1 - \left(\frac{p_{s,\text{exit}}}{P_{T,\text{inlet}}} \right)^{[(\gamma-1)/\gamma]}} \right]$$

$$\eta_{\text{Group}} = \left[\frac{T_{T,\text{inlet}} - T_{T,\text{exit}}}{T_{T,\text{inlet}} - T_{T,\text{inlet}} \left(\frac{P_{T,\text{exit}}}{P_{T,\text{inlet}}} \right)^{[(\gamma-1)/\gamma]}} \right]$$

where T_T is the total temperature, P_T the total pressure, p_s the pressure. The subscripts inlet and exit refer to inlet and exit conditions respectively, while the subscript *TR* refers to the relative total conditions.

A Navier–Stokes Analysis of Airfoils in Oscillating Transonic Cascades for the Prediction of Aerodynamic Damping

R. S. Abhari
The Ohio State University,
Columbus, OH 43210

M. Giles
Oxford University,
Oxford, United Kingdom

An unsteady, compressible, two-dimensional, thin shear layer Navier–Stokes solver is modified to predict the motion-dependent unsteady flow around oscillating airfoils in a cascade. A quasi-three-dimensional formulation is used to account for the streamwise variation of streamtube height. The code uses Ni's Lax–Wendroff algorithm in the outer region, an implicit ADI method in the inner region, conservative coupling at the interface, and the Baldwin–Lomax turbulence model. The computational mesh consists of an O-grid around each blade plus an unstructured outer grid of quadrilateral or triangular cells. The unstructured computational grid was adapted to the flow to better resolve shocks and wakes. Motion of each airfoil was simulated at each time step by stretching and compressing the mesh within the O-grid. This imposed motion consists of harmonic solid body translation in two directions and rotation, combined with the correct interblade phase angles. The validity of the code is illustrated by comparing its predictions to a number of test cases, including an axially oscillating flat plate in laminar flow, the Aeroelasticity of Turbomachines Symposium Fourth Standard Configuration (a transonic turbine cascade), and the Seventh Standard Configuration (a transonic compressor cascade). The overall comparison between the predictions and the test data is reasonably good. A numerical study on a generic transonic compressor rotor was performed in which the impact of varying the amplitude of the airfoil oscillation on the normalized predicted magnitude and phase of the unsteady pressure around the airfoil was studied. It was observed that for this transonic compressor, the nondimensional aerodynamic damping was influenced by the amplitude of the oscillation.

Introduction

One of the most complicated and challenging areas of turbomachinery design and development is the prediction of airfoil vibratory stresses (Rao, 1991). These vibratory stresses arise from the excitation and consequent vibration of blades at the structure's modal frequencies by an external source (called forced response), or through self-excitation (called flutter).

In forced response vibration, the frequency of a source of excitation, such as upstream distortion, coincides with a fundamental modal frequency of the blade somewhere within the operating range. In the Campbell diagram, the modal frequencies of the airfoil are typically plotted against the rotational speed, as well as the most obvious sources of excitation. The intersection of a mode with a source of excitation, known as a "crossing," could result in unacceptable vibratory stresses. To avoid a crossing, designers typically attempt to alter the modal frequencies of the airfoil by changing the blade structure such as by changing thickness, taper, and chord. In propulsion applications, however, some crossings within the operating envelope generally do occur. In these cases, the knowledge of the vibratory response of the airfoils is critical in order to avoid blade failure. The designers need to determine the significance of a blade response at the crossings within the operating envelope. A typical approach consists of considering the aerodynamic forces acting on the airfoils in two separate categories; the forcing function, which refers to the amplitude and phase of the unsteady pressure field around the airfoil as it moves through the nonuniform excitation field, and the aerodynamic damping, which is the term used to refer to the unsteady aerodynamic force generated by the oscillatory movement of the airfoil. The amplitude of the blade oscillation, which is a direct measure of the vibratory stress, is determined by the balance of the forcing function with the structural and aerodynamic damping forces opposing the vibration. In certain applications such as in bladed disks (blisks), the structural damping tends to be much less than the aerodynamic terms. In these applications, when the excitation is due to some aerodynamic nonuniformity, the balance of the aerodynamic forcing function and damping determines the level of response.

Flutter excitation is a different type of vibratory response in which, at certain conditions, the external flow around the blade sustains the oscillatory motion of the airfoil. At conditions under which the unsteady pressure force generated by motion of the blade extracts energy from the flow field, any perturbation could grow into airfoil flutter. The knowledge of the aerodynamic damping at many interblade phase angles (IBPA) is critical in determining flutter boundaries.

In recent years, a number of methods utilizing linearized models (Verdon and Casper, 1982; Whitehead, 1982) have been used to predict aerodynamic damping as well as forcing function. In such approaches, the unsteady equations of the motion are linearized with respect to small harmonic perturbation. The predicted normalized amplitude and phase of the aerodynamic damping terms are thus assumed to be independent of the magnitude of the small (relative to blade characteristic length) harmonic motion. An objective of the present study is to examine

Contributed by the International Gas Turbine Institute and presented at the 40th International Gas Turbine and Aeroengine Congress and Exhibition, Houston, Texas, June 5–8, 1995. Manuscript received by the International Gas Turbine Institute February 13, 1995. Paper No. 95-GT-182. Associate Technical Editor: C. J. Russo.

this assumption numerically for typical amplitudes of blade vibration encountered in transonic flow. A nonlinear Euler code with moving grid technique was reported by He (1990) to predict the aerodynamic damping for the Fourth Standard Configuration, which compared well with the experimental measurements.

In the present study, an unsteady quasi-three-dimensional Navier–Stokes code was modified to include airfoil oscillatory movement. This modification included the addition of a moving grid formulation to model airfoil solid body oscillation. This code was validated by comparing its predictions to a number of analytical and experimental test cases. The first validation case is that corresponding to the subsonic unsteady flow over an axially oscillating flat plate cascade with laminar boundary layer flow. A common feature of most CFD validations is the scarcity of available reliable data, with the situation being rather grave for oscillating airfoils in realistic transonic test conditions. In fact, the only complete sets of data available to the authors were obtained from the Aeroelasticity Workshop report compiled and edited by Bölcs and Fransson (1986). In the second test case, the predictions for the Fourth Standard Configuration at high subsonic conditions are compared to the experimental data. This part is very similar to the work of He (1990), in which an inviscid code with blade motion was used. In the third case, the experimental conditions of the Seventh Standard Configuration at transonic conditions are simulated and the unsteady loads are compared to the experimental data. In the final test case, by using the profile of a transonic compressor blade at 90 percent span, the code is used in a numerical experiment to study the nonlinearity of unsteady loads with respect to the amplitude of airfoil movement in a pure bending mode.

Numerical Method

The numerical procedure used to model this flow is a two-dimensional, Reynolds-averaged, unsteady multiblade row Navier–Stokes code, UNSFLO, developed by Giles (1988). This is a coupled viscous/inviscid code in which the thin shear layer Navier–Stokes equations are solved on a body-fitted boundary layer grid using an implicit algorithm, while the Euler equations are solved on an outer inviscid grid using an explicit algorithm. The interface between the two regions is handled in a conservative manner. Quasi-three-dimensional effects are included through the specification of a streamtube thickness in the third dimension. Here, the Euler equations are solved using a generalization of Ni's Lax–Wendroff algorithm (Ni, 1981). Full second-order accuracy is achieved. The inviscid grid is an unstructured mesh composed of an arbitrary mix of quadrilateral and triangular cells. The viscous grid is an O-type mesh about each blade for which an ADI (alternating-direction-implicit) method with Roe's flux-difference splitting gives third-order upwinding for the residual operator and first order upwinding for the implicit operator. The Baldwin–Lomax (1978) algebraic turbulence model is used in the viscous part of the solution with the location of the boundary layer transition specified. For the calculations presented herein, transition was assumed to occur at the leading edge.

To better capture the shock and wake structures of airfoil cascades, the computational grid was adapted to the flow. A grid-independent solution at steady state was obtained by refining the computational grid to the point where further refinement does not alter the solution. The grid adaptation encompassed a fairly broad area around the flow features of concern (for example, width of the wake). By using time-accurate graphic flow visualization, details of the predicted unsteady fluid flow were thoroughly investigated. This investigation typically included a determination of the quality of the adapted grid for the particular unsteady problem. Within the scope of the present work, the impact of the grid dependence on the unsteady calculations was not investigated.

The code utilizes an innovative space–time coordinate transformation, "time-tilting" (Giles, 1988), to permit arbitrary reduced frequencies while incurring little penalty in the computational time. A method of accounting for the temporal periodicity used here is known as the "Direct Store" (Erdos and Alzner, 1978). In this method, the primitive variables for a complete period, which were stored previously, are used to update the periodic boundary condition while accounting for a specified phase lag (i.e., IBPA). The advantage of this approach is that for low reduced frequency oscillations, the complete problem can be solved for a single blade passage, considerably reducing the computational grid size and the solution time. The study of the application Direct Store and its limitation has been reported in detail by He (1990). Direct Store is in fact a temporal linearization of periodic boundary conditions. This fact combined with the large storage requirements are the main disadvantages of the approach. The solution was assumed to be converged when the maximum error between two following periods at any point was less than 1E-3, which typically required anywhere between 3 and 10 periods depending on the particular test case. Many more details on this code and its verification may be found from Giles (1991), Giles and Haimes (1993), and Abhari et al. (1992).

Moving Grid Approach

The moving blade formulation was the approach proposed by Giles (1991). To model the motion of the airfoil, the code was modified in such a way that the wall nodes moved according to the prescribed harmonic motion for each period. The position of the mesh points within the O-grid were then updated in such a way as to maintain the original relative grid distribution, while the interface between the viscous and inviscid grid remained stationary, see Fig. 1. This approach allowed the inviscid solver to remain unchanged and the moving grid modifications were only needed for the viscous solver.

Nomenclature

$\tilde{C}_P$ = real amplitude of the unsteady perturbation pressure coefficient per unit amplitude
C_f = skin friction coefficient
F = flux terms in x
G = flux terms in y
n = normal vector direction
p = pressure
q = heat flux
Re_x = Reynolds number based on x
t = time
U = primitive variables
u = velocity in x direction
U_0 = free-stream velocity
V = defined in Eq. (2)
v = velocity in y direction
W_{pc} = nondimensional unsteady aerodynamic work on an airfoil integrated over one oscillation cycle
X = distance along the chord
x = axial direction
y = tangential direction
ϵ = amplitude of oscillation
Ξ = aerodynamic damping coefficient = $-(W_{pc}/\pi\epsilon)$
τ = skin friction
ω = frequency
Ω = control volume

Subscripts

0 = stagnation conditions
b = blade
x = axial direction
y = tangential direction

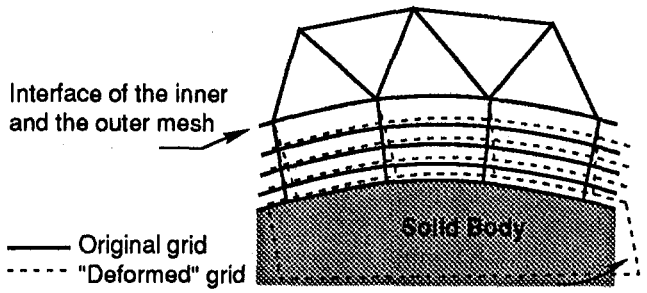

Fig. 1 Illustration of the movement of mesh relative to blade

Consider the two-dimensional Navier–Stokes equations being solved on a fixed (in time) control volume Ω,

$$\iint_\Omega \left(\frac{\partial U}{\partial t} + \frac{\partial (F - V_x)}{\partial x} + \frac{\partial (G - V_y)}{\partial y} \right) dxdy = 0 \quad (1)$$

where the viscous terms are given by

$$V_x = \begin{bmatrix} 0 \\ \tau_{xx} \\ \tau_{xy} \\ u\tau_{xx} + v\tau_{xy} - q_x \end{bmatrix}, \quad V_y = \begin{bmatrix} 0 \\ \tau_{xy} \\ \tau_{yy} \\ u\tau_{xy} + v\tau_{yy} - q_y \end{bmatrix} \quad (2)$$

Now assume that the boundary of this control volume is moving at velocity $\vec{u}_b$ and has an outward pointing unit normal vector $\vec{n}$. Due to the motion of the control volume boundary $\partial\Omega$,

$$\frac{d}{dt} \iint_\Omega U dxdy = \iint_\Omega \frac{\partial U}{\partial t} dxdy + \int_{\partial\Omega} U(\vec{u}_b \cdot \vec{n}) ds \quad (3)$$

The second term in Eq. (3) corresponds to the volume being swept out by the moving boundary. Combining Eqs. (1) and (3),

$$\frac{d}{dt} \iint_\Omega U dxdy = -\iint_\Omega \left(\frac{\partial (F - V_x)}{\partial x} + \frac{\partial (G - V_y)}{\partial y} \right) dxdy + \int_{\partial\Omega} U(\vec{u}_b \cdot \vec{n}) ds \quad (4)$$

or

$$\frac{d}{dt} \iint_\Omega U dxdy = -\int_{\partial\Omega} (F - V_x) n_x + (G - V_y) n_y - U(\vec{u}_b \cdot \vec{n}) ds \quad (5)$$

In addition to the extra flux terms represented by the third term on the right-hand side of Eq. (5), the wall boundary conditions were also modified to account for the grid movement. A complete description of the changes to the solver and the boundary conditions is given by Giles (1991).

Comparisons and Discussions

Oscillating Flat Plates. The initial validation test case modeled an axially oscillating flat plate cascade at zero incident with laminar boundary layer. The geometry was composed of flat plates of 0.004 m thickness, 1 m length in cascade with a solidity of one. This low blockage and low solidity was chosen to minimize the pressure gradients within the cascade. The leading edges of the plates were elliptical to avoid a leading edge separation and the flow Reynolds number based on length was 100,000. The computational grid, shown in Fig. 2, was composed of an O-grid (21 points across) coupled to a structured rectangular H-grid (60 × 150). The O-grid was closely packed near the surface to better resolve the boundary layer. The turbulence model was turned off and the flow was assumed to be laminar. In Fig. 3, the predicted steady-state skin friction coefficient versus axial length along the plate is shown, with the Blasius solution also being plotted for comparison. This figure demonstrates the accuracy of the present code against a closed form analytical prediction. It is observed that, over 80 percent of the length of the plate, the predicted result closely matches that of the Blasius solution. Toward the trailing edge of the plate, the numerical solution diverges from the analytical prediction, presumably because of the pressure gradient generated due to the finite trailing edge blockage.

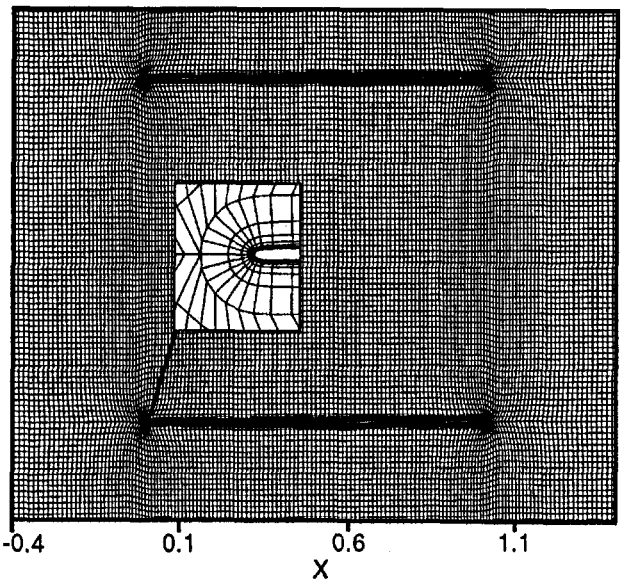

Fig. 2 Computational grid for flat plate test case, inviscid (60 × 150) mesh points, 21 points across O-grid

By performing a low-frequency first-order asymptotic expansion, Moore (1951) showed that for a small harmonic perturbation of the external velocity superimposed on a mean velocity over a flat plate in laminar flow, the nonsteady friction coefficient is given by Eq. (6). This case is analogous to an infinite

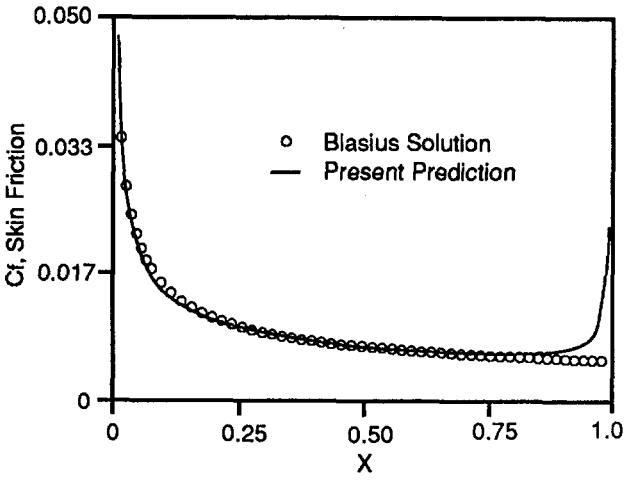

Fig. 3 Comparison of numerical prediction against Blasius solution of flat plate skin friction coefficient distribution versus axial surface length

flat plate performing a small-amplitude oscillation in the direction of the mean flow:

$$\frac{2}{3\epsilon}\left(\frac{C_f\sqrt{\mathrm{Re}_x}}{0.664}-1\right) \cong e^{i\omega t}\left\{1+0.944\left(\frac{\omega x}{U_0}\right)^2+1.705\,i\left(\frac{\omega x}{U_0}\right)\right\} \quad (6)$$

where ϵ and ω are the amplitude and frequency of the oscillation. The unsteady flow over the oscillating flat plate was then simulated by moving the cascade of the flat plates at a small amplitude (ϵ/length = 0.00004) with zero IBPA. The numerical prediction of the unsteady friction coefficient (scaled to be similar to the left-hand side of Eq. (6)) for a reduced frequency ($\omega x/U_0$) of 0.68, is plotted versus the nondimensional time in Fig. 4. The first-order prediction of Moore (right-hand side of Eq. (6)) is also plotted. It is observed that the phase and amplitude of the predicted results agree reasonably well with the first-order analytical solution.

Fourth Standard Configuration. This annular turbine cascade test case was experimentally investigated at Lausanne Institute of Technology and the results were included in the aeroelasticity workshop report by Bölcs and Fransson (1986). This cascade represented a typical section of a turbine airfoil that had exhibited flutter instability in the first bending mode. In the experiments reported, the cascade of airfoils was oscillated in the first bending mode at high speed conditions. Surface unsteady pressures at the 0, 90, −90, and 180 deg IBPAs were measured. Present simulations were performed at the exit Mach number of 0.9, matching the conditions reported in the experiment. The computational grid consisted of a structured (80 × 20) H-grid with rectangular mesh coupled to an O-grid with 21 points across the viscous region.

In Fig. 5, the steady-state Mach number contours of the flow are shown. The steady-state surface pressure distribution around the airfoil is plotted against the length in Fig. 6. The length is nondimensionalized with respect to the chord to match the convention used in the reporting of the experimental results. It is observed that with the exception of the slight overprediction of the acceleration on the front portion of the suction surface, the prediction reasonably matches the data. The code was then used to simulate the unsteady pressure distribution around the airfoil. In this experiment, the amplitude and interblade phase angle of the airfoils were well controlled. By utilizing Direct Store boundary conditions, a single passage computational domain was used. In order to check the accuracy of the Direct Store boundary conditions for the 180 deg test case, two passages were modeled with the exact periodicity imposed at the boundaries. The results were almost identical to the solution with Direct Store. In Fig. 7, the predicted amplitudes and phase angles for the first harmonics of the unsteady pressure are compared to the experimental test data for three IBPA, −90, 180,

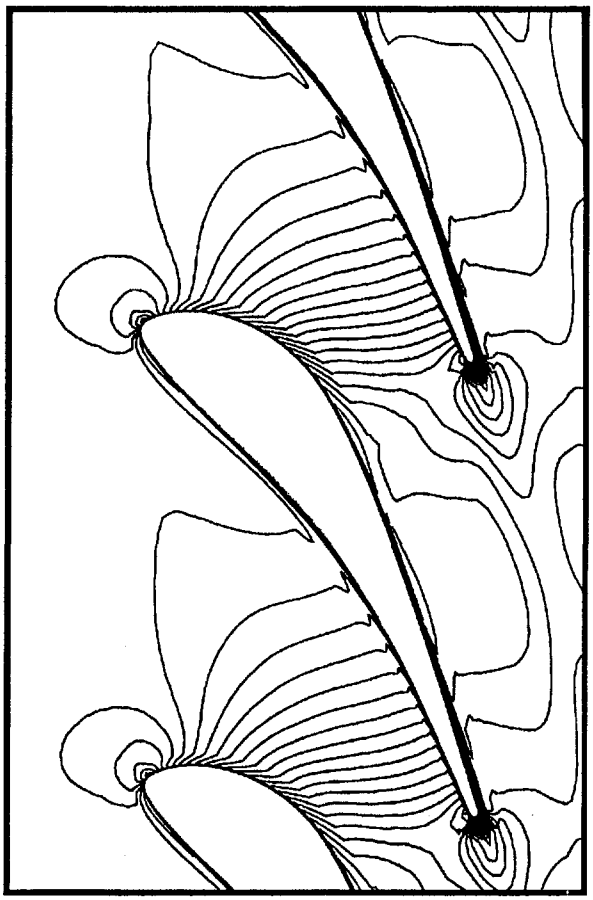

Fig. 5 Predicted steady-state Mach number contour distribution (increment of 0.04) for the Fourth Standard Configuration, 0.9 blade exit Mach number

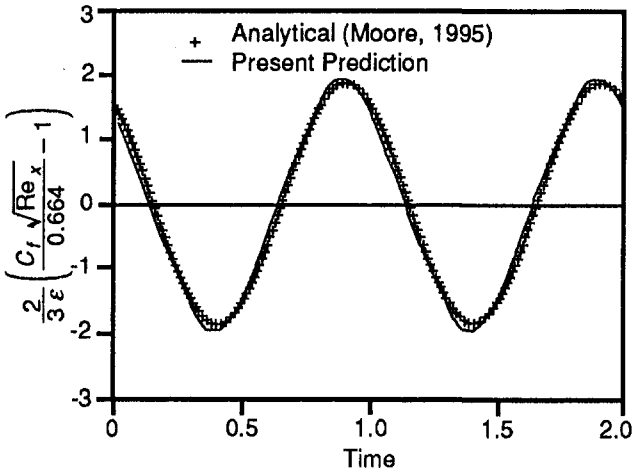

Fig. 4 Comparison of numerical prediction of unsteady skin friction against the first order perturbation analysis (Moore, 1955) presented versus time

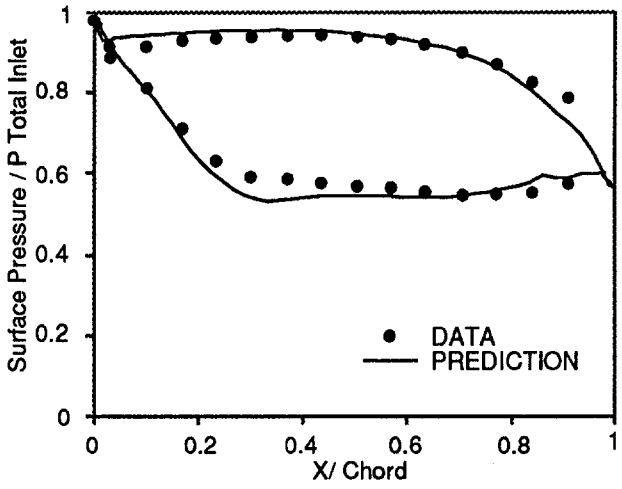

Fig. 6 Comparison of the data and the predicted surface pressure distribution for the Fourth Standard Configuration, at blade exit Mach number of 0.9

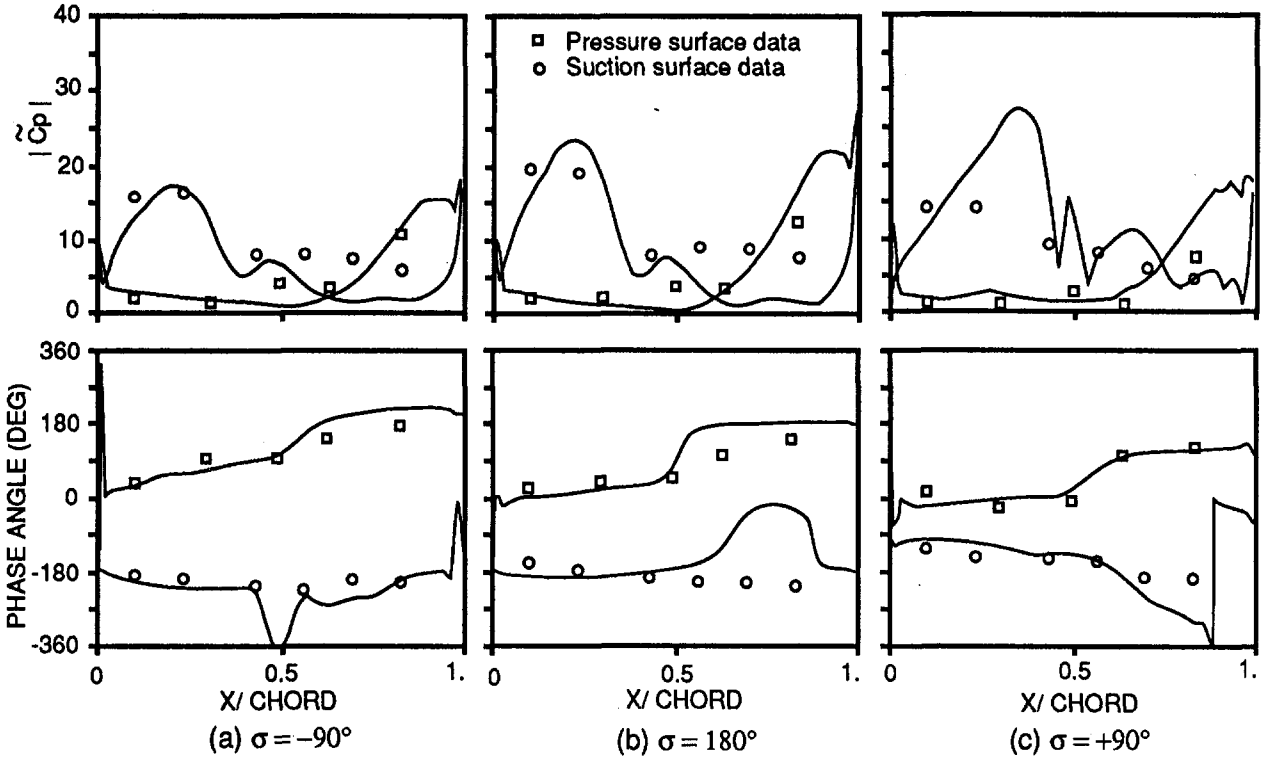

Fig. 7 Comparison of the prediction and the measured data for the amplitude and phase angle distribution of the first harmonic of unsteady surface pressure coefficient at: (*a*) IBPA = −90 deg, (*b*) IBPA = 180 deg, (*c*) IBPA = +90 deg

and 90 deg. The code does a reasonably good job of predicting the unsteady pressures with the largest discrepancy in the pressure coefficient amplitude occurring in the front portion of the suction surface for the +90 deg IBPA and at the back of the suction surface for the −90 and 180 deg IBPA. A direct outcome of the present simulations is that the work per cycle, also known as the aerodynamic damping, is easily calculated by integrating the results. The normalized form of the aerodynamic damping as defined by Bölcs and Fransson (1986) is plotted against the measured values in Fig. 8. Additionally, the simulations were also performed for −135, −45, +45, and +135 deg IBPA conditions. The inviscid prediction of He (1990) for the same airfoil and test conditions is also included in the figure. Again, the code does a reasonably good job of predicting the amplitude and the shape of the measurements. The value of the aerodynamics damping becomes negative, signifying instability, from approximately −165 to −10 deg IBPA.

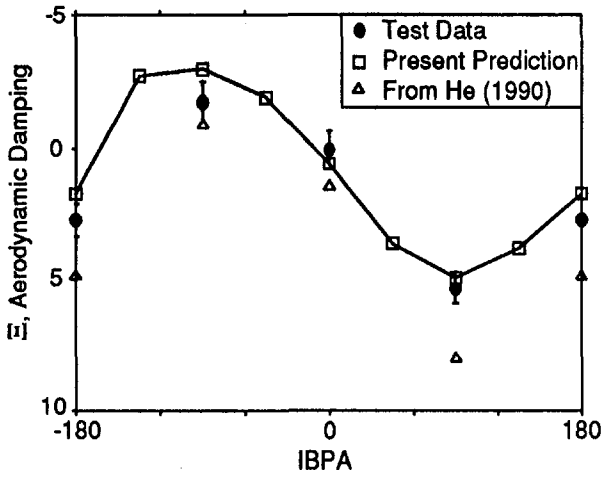

Fig. 8 Comparison of the aerodynamic damping and IBPA made between present prediction, an inviscid calculation (He, 1990), and measured data

Seventh Standard Configuration. Another test case from the aeroelasticity workshop report by Bölcs and Fransson (1986) used for validation is the Seventh Standard Configuration. This cascade of five airfoils (with solid walls on either side) represented the tip section of a typical compressor airfoil, with the geometry being taken from the 87 percent tip section of the second stage of a five-stage axial compressor. The airfoils were oscillated in the pitching mode. Due to the relatively high frequencies used in this study, certain experimental difficulties were encountered in maintaining a constant amplitude and phase angles between airfoils. In the test case studied, the compressor was operated with an inlet Mach number of 1.315 and exit Mach number of 1.25. The computational grid consisted of an unstructured triangular grid with adaptation near the leading edge, coupled to the O-grid for the viscous calculations. The grid adaptation was used to improve the capturing of the bow shock near the leading edge. The Mach number contour distribution, illustrating the predicted complex shock structure of this compressor, is shown in Fig. 9.

The experimental conditions were initially considered to be represented by the pitching amplitude of the center airfoil. Direct Store was used, which significantly reduced the computational time. In Fig. 10, the predicted amplitudes and phase angles of the first harmonic of the unsteady pressure are compared to the experimental data. The test condition corresponds to the nominal 180 deg IBPA and the center airfoil pitching angle of 0.00122 rad. The prediction seems to miss entirely the peaks in the amplitude of pressure, and the phase angle neither follows the level nor the trend of the data.

It was believed that this large discrepancy could be due to the relatively large variation in the tested phase and amplitude of the airfoils within the cascade. This was investigated by numerically simulating the complete five blade rows without

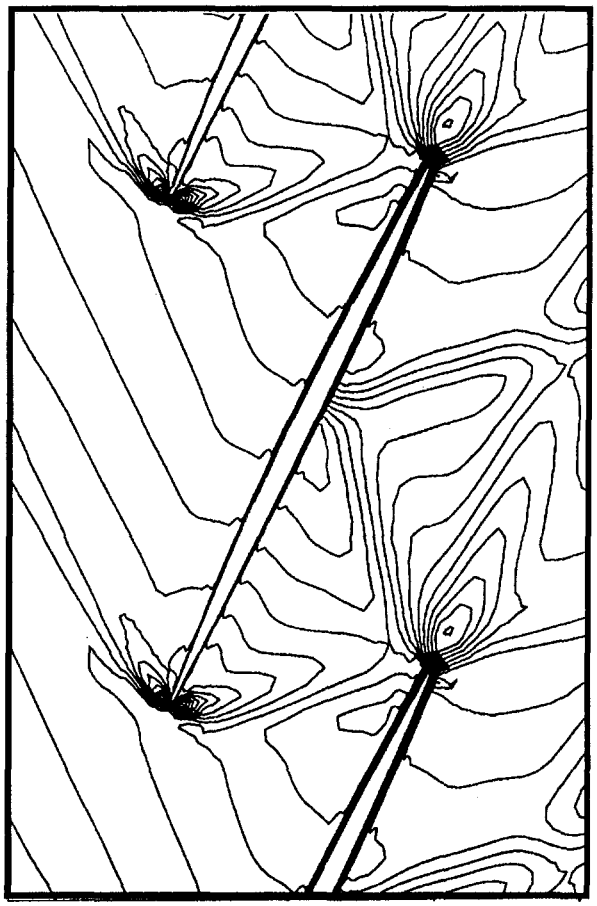

Fig. 9 Predicted steady-state Mach number contour distribution (increment of 0.04) for the Seventh Standard Configuration, blade exit Mach number of 1.25

using Direct Store. Each blade was moved at the measured amplitude and phase of oscillation and the nonperiodicity due to the presence of side walls was ignored. The experimental values of IBPA varied from 173 to 187 deg, and the amplitude of the oscillation from 0.52 to 1.27 times the value for the center airfoil. The predicted results for the center airfoil were then compared against the measurements. In Fig. 11, the predicted amplitudes and phase angles of the first harmonic of the unsteady pressure for the center blade of the five passage model are compared to the experimental data. It is observed that the numerical solution does a reasonably good job of predicting the amplitude and the phase of the unsteady pressure, with the largest discrepancy occurring in the phase relationship toward the trailing edge of the blade. The large difference between the results of Figs. 10 and 11 represents a strong aerodynamic coupling, which seems to exist between adjacent airfoils in a transonic cascade.

A Transonic Compressor Tip Section. The cross section of a typical first-stage axial transonic compressor at 90 percent span was used in a numerical experiment to study the impact of nonlinearities on aerodynamic damping under primarily bending conditions. A finite element analysis of the complete airfoil was used to determine the modal response of the airfoil. The conditions of interest used in the present simulation corresponded to a purely bending mode. The computational mesh consisted of an unstructured triangular grid, which was adapted to the flow to better capture the shock and wake structure. The grid adaptation strategy involved two sweeps in which first the grid was adapted to the second gradient of pressure (for shocks) and then to the gradient of entropy (for wakes). The resulting mesh, shown in Fig. 12, had a fairly distributed packing in the passage shock region. During the unsteady simulations, the movement of the passage shock was checked and found to be well within the packed-grid region.

An O-grid with 21 points across was used in the viscous region with stretching away from the walls. The results presented here correspond to the peak efficiency condition with a 1.35 relative inlet Mach number. The Mach number contour distribution is shown in Fig. 13, illustrating the predicted shock and wake structure of this compressor. The grid adaptation scheme resulted in a well-defined shock at the entrance to the flow passage. There was no predicted boundary layer separation anywhere on the airfoil.

Direct Store was utilized in the unsteady simulations. To check the validity of the Direct Store approach, a calculation at 0 deg IBPA was performed using the exact time tilting boundary condition. The results were found to be almost identical to the Direct Store approach. Based on this result, a number of other similar validations, and the results of He (1990), it was assumed that, for the present application, the temporal linearization of the lagged periodic boundary condition did not affect the accuracy of the final solution.

A number of simulations were performed in which the airfoils were oscillated in bending motion with the IBPA being changed in increments of 45 deg. The amplitude of the oscillation corresponded to 0.06 and 0.25 percent of the chord, which represented a realistic forced response range for this type of compressor. The steady-state boundary layer displacement thickness at the point of the shock impingement on the pressure surface was predicted to be 0.24 percent of the chord. The predicted aerodynamic damping for two amplitudes of the motion over the range of the IBPAs are presented in Fig. 14. The line through

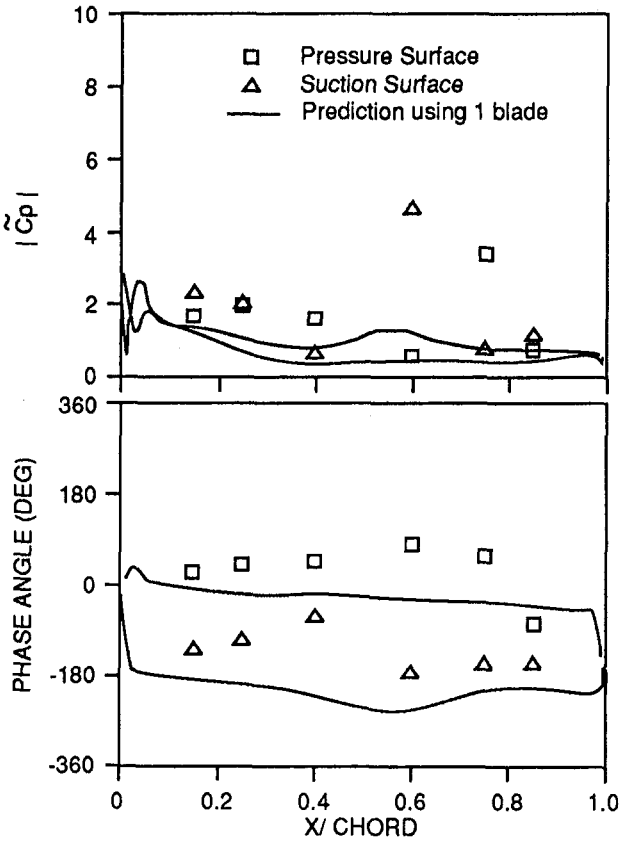

Fig. 10 Comparison of the prediction (modeling a single passage) and data for the amplitude and phase angle distribution of the first harmonic of unsteady surface pressure at 180 deg IBPA, 7th Standard Configuration

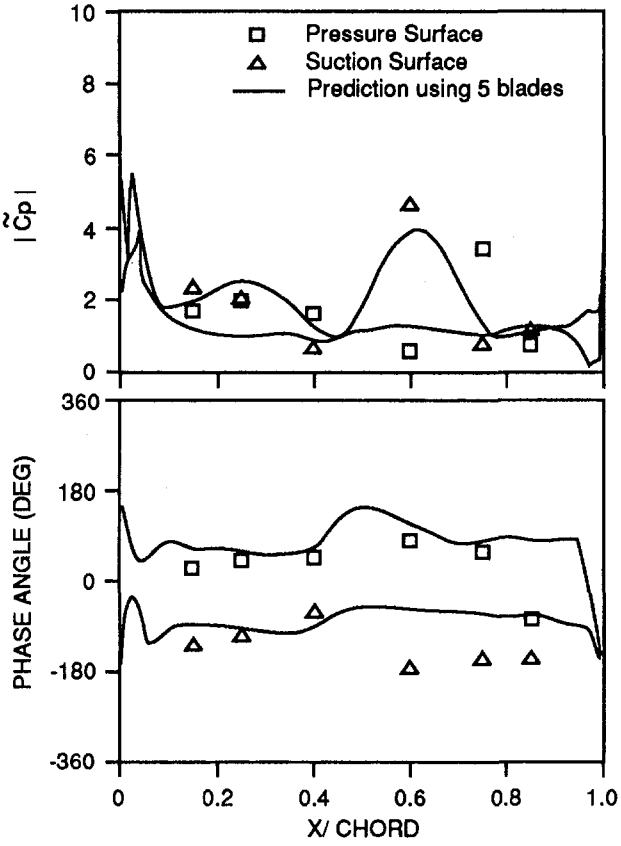

Fig. 11 Comparison of the prediction (with five passages, modeling the entire cascade) and data for the amplitude and phase angle distribution of the first harmonic of unsteady surface pressure coefficient at 180 deg IBPA for the Seventh Standard Configuration

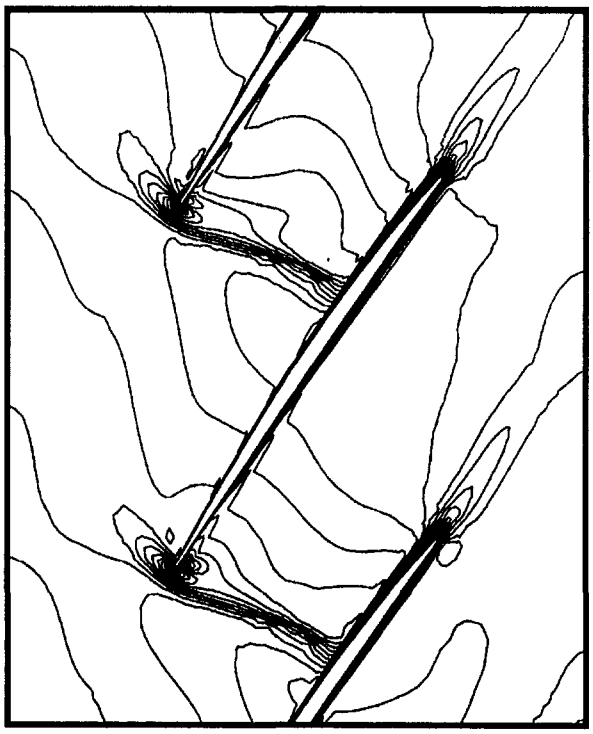

Fig. 13 Predicted steady-state Mach number contour distribution (increment of 0.04) for the transonic compressor at peak efficiency condition

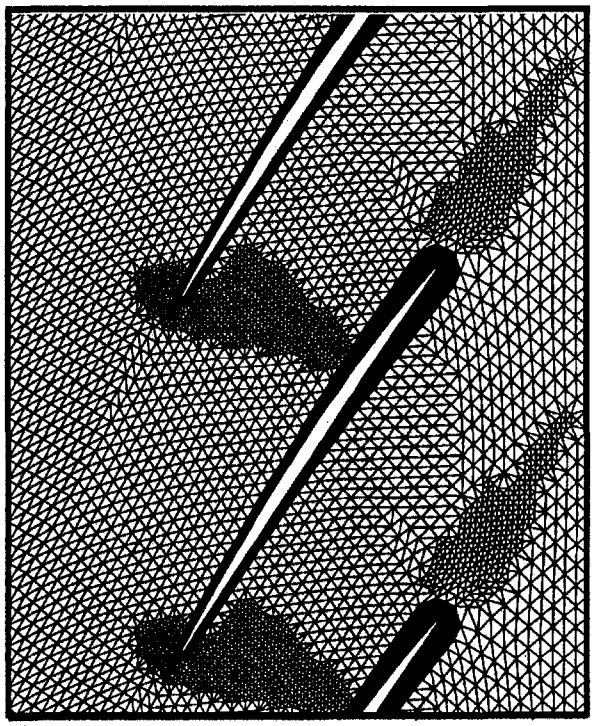

Fig. 12 Computational grid of the section of the modeled transonic compressor

the predicted values is merely to show the sinusoidal nature of the aerodynamic damping with respect to IBPA. It is observed that, in this instance, the amplitude of the oscillation does influence the level of aero-damping by as much as 14 percent within the IBPA range. In Fig. 15, the unsteady pressure coefficient (first harmonic) and the associated phase angle distributions for both amplitudes at −135 deg IBPA are plotted against the length along the chord. On the pressure surface, the predicted unsteady pressure coefficients for the two amplitudes are almost identical up to 65 percent of the length, which was the point of shock impingement. On the suction surface, the amplitudes of the unsteady pressure distributions are different throughout for the two cases. There was very little difference in the phase angle distributions. It should be noted that the aerodynamic damping

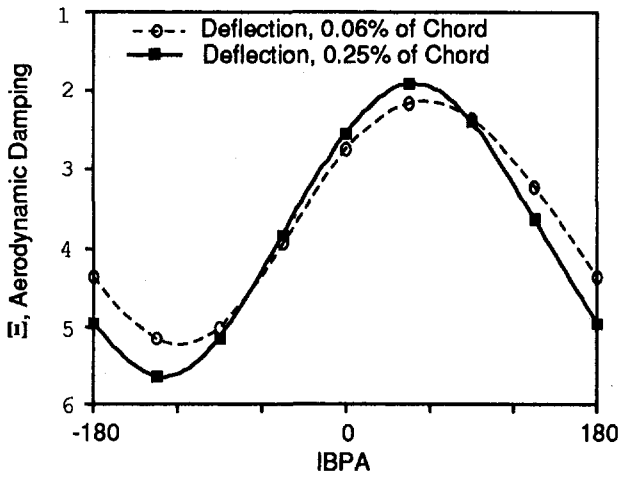

Fig. 14 Predicted aerodynamic damping versus IBPA for the transonic compressor in bending with amplitude of oscillation of 0.06 and 0.25 percent of chord

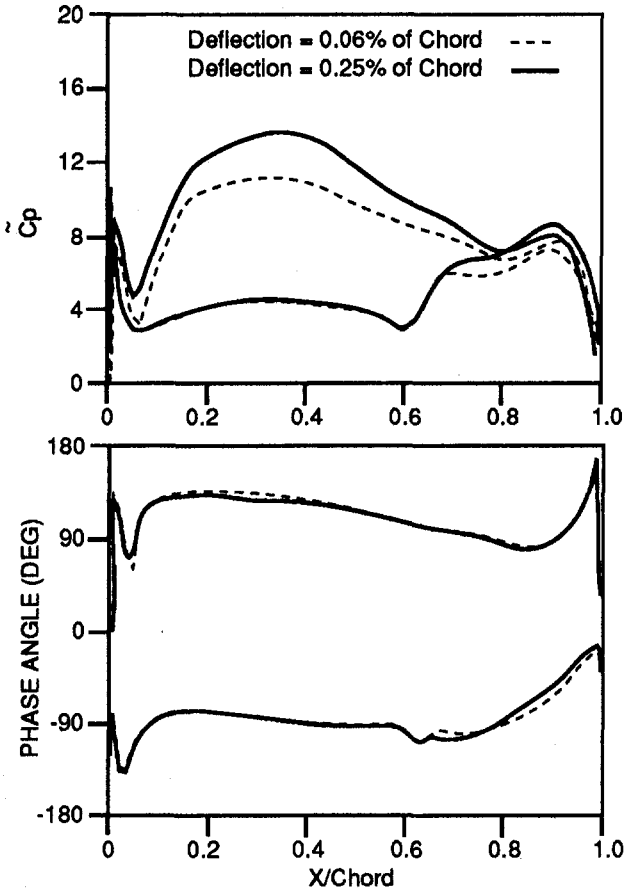

Fig. 15 Predicted amplitude and phase angle distribution of the first harmonic of unsteady surface pressure coefficient for a transonic compressor, bending deflections of 0.06 and 0.25 percent of chord, IBPA of −135 deg

parameter presented is nondimensionalized with respect to the amplitude of the oscillation. A linearized code would predict identical nondimensional results for different amplitudes of oscillation.

It is worth noting that the same numerical experiment was performed for a subsonic axial compressor (not shown) over a range of oscillation amplitudes, very little difference in the aerodynamic damping was observed. The limited experience gained from using this code on a handful of geometries and flow conditions, has been that the influence of the amplitude of oscillation under bending and torsion on nondimensional aerodynamic damping was only significant for certain transonic compressors operating near peak efficiency.

Summary and Conclusions

A quasi-three-dimensional unsteady, multiblade row, Navier–Stokes CFD code was enhanced by the addition of a moving grid capability to predict the flow around oscillating airfoils. The computational mesh consisted of either a structured or an unstructured triangular grid in the inviscid region and an O-grid in the viscous region. To better capture the shocks and wakes structures, steady-state flow adaptation of the unstructured grid was also used. The harmonic solid body movement of the airfoil was simulated by the movement of the blade surface at each time step with redistribution of the mesh within the O-grid. The viscous solver was modified to account for the extra flux terms due to the mesh movement. The interface of the viscous and inviscid grids remained unaffected by the blade movement and as such the inviscid mesh and the flow solver were untouched.

The comparison between the prediction of unsteady surface friction for an axially oscillating flat plate with analytical solution showed reasonably good agreement. To further validate the code, comparisons of experimental data and predictions for the Fourth and Seventh Standard Test cases were also presented. The results show that the present code does a reasonably good job of predicting the flow around oscillating airfoils in a cascade.

A numerical study was also performed in which the impact of varying the amplitude of the airfoil oscillation on the aerodynamic damping was studied. It was observed that for the present transonic case, the nondimensional aerodynamic damping was changed by as much as 14 percent when the amplitude of the oscillation was changed from 0.06 to 0.25 percent of chord. This change was primarily due to the change in the amplitude of the nondimensional unsteady pressure coefficient on the suction surface of the blade downstream of the passage shock. The present result illustrates that for certain conditions, linearized approaches for the prediction of the aerodynamic damping would be insufficient to provide an accurate model of the flow.

Acknowledgments

This study was sponsored by Textron Lycoming (now Allied Signal Engines) whose permission to publish this work is acknowledged. The stimulating comments of Dr. A. Sehra, R. Stockton and S. Tatakis are also greatly appreciated.

References

Abhari, R. S., Guenette, G. R., Epstein, A. H., and Giles, M. B., 1992, "Comparison of Time-Resolved Turbine Rotor Blade Heat Transfer Measurements and Numerical Calculations," ASME JOURNAL OF TURBOMACHINERY, Vol. 114, pp. 818–827.

Baldwin, B. S., and Lomax, H., 1978, "Thin Layer Approximation and Algebraic Model for Separated Turbulent Flows," AIAA Paper No. 78-257.

Bölcs, A., and Fransson, T. H., eds., 1986, "Aeroelasticity in Turbomachines, Comparison of Theoretical and Experimental Cascade Results," Communication de Laboratoire de Thermique Appliquee et de Turbomachines, No. 16, EPFL, Lausanne, Switzerland.

Erdos, J. I., and Alzner, E., 1978, "Computation of Unsteady Transonic Flows Through Rotating and Stationary Cascades," NASA CR-2900.

Giles, M. B., 1988, "UNSFLO: A Numerical Method for Unsteady Inviscid Flow in Turbomachinery," MIT Gas Turbine Laboratory Report No. 195.

Giles, M. B., 1991, "UNSFLO: A Numerical Method for the Calculation of Unsteady Flow in Turbomachinery," MIT Gas Turbine Laboratory Report No.

Giles, M. B., and Haimes, R., 1993, "Validation of a Numerical Method for Unsteady Flow Calculations," ASME JOURNAL OF TURBOMACHINERY, Vol. 115, pp. 110–117.

He, L., 1990, "An Euler Solution for Unsteady Flows Around Oscillating Blades," ASME JOURNAL OF TURBOMACHINERY, Vol. 112, pp. 714–722.

Moore, F. K., 1951, "Unsteady Laminar Boundary Layer Flow," NACA TN 2471.

Ni, R.-H., 1981, "A Multiple Grid Scheme for Solving the Euler Equations," *AIAA Journal,* Vol. 20, No. 11, pp. 1565–1571.

Rao, J. S., 1991, *Turbomachine Blade Vibration,* Wiley, New York.

Verdon, J. M., and Casper, J. R., 1982, "Development of a Linear Unsteady Aerodynamics for Finite Deflection Cascades," *AIAA Journal,* Vol. 20, No. 9.

Whitehead, D. S., 1982, "The Calculations of Steady and Unsteady Transonic Flow in Cascades," Cambridge University Engineering Dept., Report CUED/A-Turbo/TR118.

The Influence of Neighboring Blade Rows on the Unsteady Aerodynamic Response of Cascades

K. C. Hall

P. D. Silkowski

Department of Mechanical Engineering and Materials Science,
Duke University,
Durham, NC 27708

In this paper, we present an analysis of the unsteady aerodynamic response of cascades due to incident gusts (the forced response problem) or blade vibration (the flutter problem) when the cascade is part of a multistage fan, compressor, or turbine. Most current unsteady aerodynamic models assume the cascade to be isolated in an infinitely long duct. This assumption, however, neglects the potentially important influence of neighboring blade rows. We present an elegant and computationally efficient method to model these neighboring blade row effects. In the present method, we model the unsteady aerodynamic response due to so-called spinning modes (pressure and vorticity waves), with each mode corresponding to a different circumferential wave number and frequency. Then, for each mode, we compute the reflection and transmission coefficients for each blade row. These coefficients can be obtained from any of the currently available unsteady linearized aerodynamic models of isolated cascades. A set of linear equations is then constructed that couples together the various spinning modes, and the linear equations are solved via LU decomposition. Numerical results are presented for both the gust response and blade vibration problems. To validate our model, we compare our results to other analytical models, and to a multistage vortex lattice model. We show that the effect of neighboring blade rows on the aerodynamic damping of vibrating cascades is significant, but nevertheless can be modeled with a small number of modes.

1 Introduction

The fluid flow through turbomachinery blade rows is inherently unsteady due to the relative motion of neighboring blade rows. In part, this is by design. Only through unsteady flow processes can the total enthalpy of the fluid be changed. Although this unsteady interaction is directly responsible for the work done on the fluid, the resulting unsteady aerodynamic loads acting on the blades are also sources of noise and forced response. Additionally, as we will show, the close proximity and relative motion of neighboring blade rows can significantly modify the aeroelastic stability of a blade row.

A key assumption of most of the currently available aerodynamic models of flutter, forced response, and acoustic response of cascades is that the cascade is isolated in an infinitely long duct. In fact, these phenomena are significantly influenced by the presence of neighboring blade rows. Recent experiments by Manwaring and Wisler (1993), for example, have shown that multistage effects are indeed significant in the forced response problem. Manwaring and Wisler obtained measurements of the unsteady aerodynamic force due to wake crossing in General Electric's Low Speed Research Turbine (LSRT). These measurements showed that for a stator–rotor–stator geometry, the upstream stator had a significant influence on the unsteady forced response of the downstream stator, an effect not modeled by single blade row analyses.

Two families of computational techniques are currently available to solve rotor–stator interaction-type problems. The most widely used are time-marching techniques. Using this approach, the governing equations of fluid motion are "marched" in time from one time level to the next simulating the flow through the turbomachine. A number of investigators (e.g., Rai, 1989a, b; Giles, 1988) have time marched the Euler and Navier–Stokes equations to obtain the unsteady flow due to rotor/stator interaction. For example, Rai (1989a, b) has time marched the Navier–Stokes equations to compute unsteady rotor/stator interaction. One difficulty with Rai's approach (and others) is that the computational domain must be periodic in the circumferential direction. Thus, for example, if the rotor has 72 blades and the stator has 66 blades, the computational domain can be reduced to 12 rotor blades and 11 stator blades but no further, leading to very large computational times. Rai circumvents this difficulty by modifying the geometry to force periodicity with fewer blades. Giles' (1988) has time marched the Euler equations to solve the rotor/stator interaction problem. Giles introduced the concept of "time inclining," a novel technique to reduce the number of blade passages required in the computation (e.g., from 12:11 to 1:1) without the errors incurred by modifying the geometry. The method, however, cannot be extended to more than two blade rows. While the time marching techniques are able to model the complex unsteady interactions between a rotor and a stator, they are still computationally very expensive, too expensive for use in routine design.

Contributed by the International Gas Turbine Institute and presented at the 40th International Gas Turbine and Aeroengine Congress and Exhibition, Houston, Texas, June 5–8, 1995. Manuscript received by the International Gas Turbine Institute February 11, 1995. Paper No. 95-GT-35. Associate Technical Editor: C. J. Russo.

The other family of techniques includes the so-called "time linearized" analysis techniques (see, e.g., Verdon, 1987; Whitehead and Grant, 1981; Hall and Crawley, 1989; Hall, 1993; Hall and Clark, 1993; Hall and Lorence, 1993). Using this approach, one first solves for the time-averaged "steady" flow through a blade row using the nonlinear governing fluid equations. One then linearizes the governing equations assuming that the unsteadiness in the flow is small compared to the mean flow, is harmonic in time, and has a fixed interblade phase angle. The resulting linear small disturbance equations are discretized on a computational mesh of a single blade passage, and solved using Gaussian elimination or an iterative technique for each interblade phase angle and frequency of interest. The advantage of this approach is that it is computationally very efficient, typically requiring two orders of magnitude less computer time than the time marching approach.

Unfortunately, without modification, the time-linearized analyses can only be applied to a single blade row. The reason is that when two or more blade rows are involved, the relative motion due to the rotation of the rotors produces a *shifting* of the frequencies of the acoustic, vortical, and entropic waves as they propagate from one blade row to the next. The frequency shift is analogous to the familiar Doppler shift. Furthermore, when waves emanating from the rotor impinge on the upstream stator, for example, waves will be reflected back toward the rotor. These reflected waves will have a multiplicity of *shifted* frequencies and *scattered* interblade phase angles, violating the assumption that the solution is harmonic in time with a fixed interblade phase angle.

A number of investigators have attempted to modify the frequency domain techniques to model rotor/stator interactions. An analytical approach was taken by Kaji and Okazaki (1970) using an acceleration potential technique. They distributed pressure doublets over both the rotor and stator. By satisfying the no-flux condition through the airfoils, they solved for all the doublet strengths simultaneously. However, this was done using only the fundamental frequency and interblade phase angle, and therefore the interaction was only partially modeled. Hanson (1992) later extended this method, using vortex singularities, retaining multiple interblade phase angles and frequencies.

In 1988, the first author (Hall) suggested in an unpublished report that conventional frequency domain solvers could be used to characterize the reflection and transmission of spinning modes through individual blade rows of a multistage machine. Between the blade rows, the unsteady flow is composed of so-called spinning modes. The individual cascades can then be coupled via the spinning modes to obtain the behavior of the multistage machine. Hall developed an analysis technique in which the rotor and stator of a single stage were coupled via a single family of acoustic and vortical waves (single frequency and interblade phase angle in each blade row). Hanson (1993) later extended this technique to include multiple frequencies and multiple interblade phase angle waves, and used the method to analyze the acoustic behavior of a single stage. Buffum (1993) applied a similar technique to predict the aeroelastic stability of a stator/rotor/stator system. Buffum, however, retained only superresonant modes, and did not model the phenomena of mode scattering.

In this paper, we generalize the mode coupling technique to analyze unsteady flows associated with flutter and forced response in multiple blade row machines. Numerical results are compared to other theoretical results and to a time-marching vortex lattice method to demonstrate the ability of the code to predict accurately unsteady flows through multiple blade rows using a relatively small number of spinning modes. Furthermore, we show that coupling between blade rows significantly modifies the aerodynamic damping of cascades, even in the case of subresonant flutter.

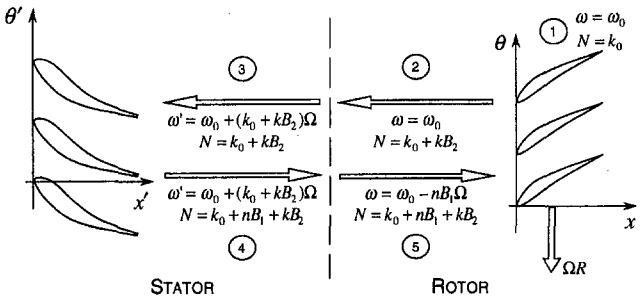

Fig. 1 Schematic showing kinematics of frequency shifting and mode scattering

2 Theory

In this section, we develop a model of unsteady flow through a single stage (stator plus rotor). The analysis, however, with very minor modifications, is applicable to multistage machines. In Section 2.1, we discuss the kinematic behavior of unsteady flow through multiple blade rows. In Section 2.2, we characterize the reflection and transmission properties of individual blade rows. In Section 2.3, we discuss the propagation of waves through the duct between the blade rows. Finally, in Section 2.4, we assemble the results of Sections 2.1–2.3 into a small system of linear equations that describes the unsteady flow through the stage.

2.1 Modal Content. To illustrate the physical process to be modeled, consider a single stage as shown in Fig. 1. A row of rotor blades with B_2 blades is situated behind a row of stator blades with B_1 blades. We assume that the flow is two dimensional (in the axial and circumferential directions), and that the unsteadiness in the flow is small compared to the mean flow. Therefore, in each blade row, the unsteady flow will be governed by linear variable coefficient equations (for example, the linearized potential equation or the linearized Euler equations). Furthermore, between the blade rows, where the time-averaged mean flow is uniform, the governing equations are linear equations with constant coefficients. Thus, the unsteady flow in these regions may be thought of as composed of *eigenmodes,* sometimes referred to as spinning modes; the shapes of these eigenmodes are Fourier modes in the circumferential direction.

Consider first the case of the rotor in isolation in an infinitely long duct. Suppose that the cascade of blades vibrates in plunge in a traveling wave mode with interblade phase angle σ_0 and temporal frequency ω_0. Mathematically, the plunging velocity $\dot{h}$ of the mth blade in the cascade is given by

$$\dot{h}(m, t) = \dot{h}_0 \exp[j(\omega_0 t + m\sigma_0)] \qquad (1)$$

where $\dot{h}_0$ is the complex amplitude of the plunging velocity. The interblade phase angle is related to the number of nodal diameters k_0 in the traveling wave mode by $\sigma_0 = 2\pi k_0/B_2$. In the frame of reference of the rotor, pressure waves (spinning modes) with frequency ω_0 will radiate away from the rotor both upstream and downstream. In addition, vorticity waves with frequency ω_0 will be convected downstream (in the present analysis, we neglect entropy waves, although such waves could be readily included). The radiated waves must have the same phase shift over one blade gap as the original interblade phase angle. Therefore, the radiated waves can take on all interblade phase angles given by

$$\sigma_k = \sigma_0 + 2\pi k = 2\pi N_k / B_2 \tag{2}$$

where k takes on all integer values, and N_k is the number of nodal diameters of the wave. Thus, the unsteady flow upstream of the rotor may be expressed by

$$\mathbf{u}(x, \theta, t) = \sum_{i=1}^{1} \sum_{k=-\infty}^{+\infty} c_{ik} \bar{\mathbf{u}}_{ik} \exp\{j[\omega_0 t + \alpha_{i,k} x + (k_0 + kB_2)\theta)]\} \tag{3}$$

where x is the distance in the axial direction, θ is the circumferential distance (in radians) around the rotor in a frame of reference attached to the rotor, and t is time. In Eq. (3), $\mathbf{u}$ is a vector describing the unsteady flow field, e.g., $\mathbf{u}$ could be the vector of primitive flow variables. The index i denotes the type of radiated wave; $i = 1$, 2, and 3 correspond to upstream moving pressure waves, downstream moving pressure waves, and vorticity waves, respectively. The vector $\bar{\mathbf{u}}_{ik}$ is the eigenmode of the (i, k)th mode, and $\alpha_{i,k}$ is the corresponding axial wave number of the wave. Finally, the scalar constant c_{ik} denotes how much of a given eigenmode is present in the solution. Note that Eq. (3) contains only $i = 1$ type waves, that is, upstream going pressure waves. Downstream of the rotor, a similar sum would describe the unsteady flow, but with $i = 2$ and 3.

When viewed in the rotor frame of reference, all of the waves have the same temporal frequency ω_0 as the original disturbance in the rotor. However, in the stator frame of reference, the frequency of each k mode will appear *shifted.* This is readily seen if we make the change of coordinates

$$x' = x + \Delta x \tag{4}$$

$$\theta' = \theta - \Omega t \tag{5}$$

$$t' = t \tag{6}$$

where the primed coordinates are fixed to the stator frame of reference, Ω is the rotation rate of the rotor, and Δx is the axial separation of the leading edges of the stator and the rotor. Substitution of Eqs. (4)–(6) into Eq. (3) gives

$$\mathbf{u}(x', \theta', t') = \sum_{i=1}^{1} \sum_{k=-\infty}^{+\infty} c_{ik} \bar{\mathbf{u}}_{ik} \exp\{-j\alpha_{i,k}\Delta x\} \times \exp\{j[\omega_k' t' + \alpha_{i,k} x' + (k_0 + kB_2)\theta']\} \tag{7}$$

where $\omega_k' = \omega_0 + (k_0 + kB_2)\Omega$. Thus we see that the frequency is *shifted* when viewed in the stator frame of reference. Hence, a single initial excitation frequency in the rotor frame of reference produces a multiplicity of frequencies and interblade phase angles in the stator frame of reference.

The unsteady waves impinging on the stator will produce an unsteady aerodynamic load on the stator, and excite additional pressure and vorticity waves which radiate away from the stator. These radiated waves, which may be thought of as *reflected* and *transmitted* waves, will have the same interblade phase angle as the incident wave plus integer multiples of 2π. Hence, these additional waves reflected into the region downstream of the stator will have the form

$$\mathbf{u}(x', \theta', t') = \sum_{i=2}^{3} \sum_{n=-\infty}^{+\infty} \sum_{k=-\infty}^{+\infty} c_{ink} \bar{\mathbf{u}}_{ink} \exp\{-j\alpha_{i,n}\Delta x\} \times \exp\{j[\omega_k' t' + \alpha_{i,nk} x' + (k_0 + nB_1 + kB_2)\theta']\} \tag{8}$$

when viewed in the stator frame of reference, where the number of nodal diameters N_{nk} is equal to $k_0 + nB_1 + kB_2$ with n and k taking on all integer values. When viewed in the rotor frame of reference, the waves have the form

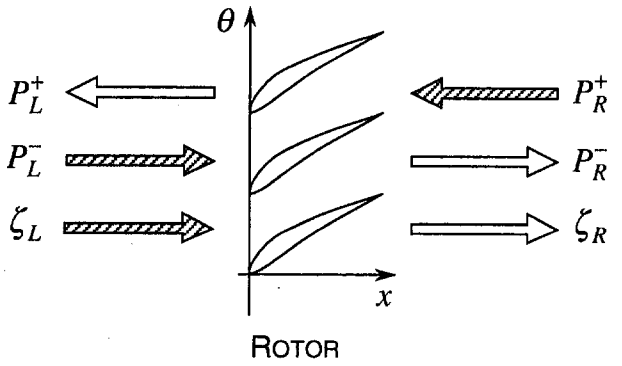

Fig. 2 Schematic showing definition of incident (shaded) and reflected and transmitted (unshaded) waves

$$\mathbf{u}(x, \theta, t) = \sum_{i=2}^{3} \sum_{n=-\infty}^{+\infty} \sum_{k=-\infty}^{+\infty} c_{ink} \bar{\mathbf{u}}_{ink} \times \exp\{j[\omega_{nk} t + \alpha_{i,nk} x + (k_0 + nB_1 + kB_2)\theta]\} \tag{9}$$

where $\omega_{nk} = \omega_0 - nB_1\Omega$. Note that the frequency as viewed in the rotor frame does not depend on k. Therefore, an original disturbance with a single interblade phase angle and frequency will *scatter* into a number of discrete nodal diameters, and *shift* into a number of discrete frequencies. Note that the mode numbers n and k, along with the knowledge of the original excitation frequency, interblade phase angle, blade counts, and wheel speed, determines the frequency and interblade phase angle of a given spinning mode.

2.2 Reflection and Transmission Coefficients. We now consider the interaction of the spinning modes with the blade rows themselves. Incident waves will impinge on a given blade row from both the upstream and downstream sides. These waves will interact with the blade row producing *reflected* and *transmitted* waves at the same frequency as the incident waves when viewed in the frame of reference of the blade row in question. Consider the case of incident pressure and vorticity waves with mode numbers n, k impinging on the rotor (see Fig. 2). We may express the radiated pressure and vorticity waves as

$$\begin{Bmatrix} P_L^+ \\ P_R^- \\ \zeta_R \end{Bmatrix}_{nj} = \begin{bmatrix} w_{11} & w_{12} & w_{13} \\ w_{21} & w_{22} & w_{23} \\ w_{31} & w_{32} & w_{33} \end{bmatrix}_{njnk} \begin{Bmatrix} P_R^+ \\ P_L^- \\ \zeta_L \end{Bmatrix}_{nk} \tag{10}$$

for integer $j = -\infty$ to ∞ where P^+, P^-, and ζ denote the complex amplitude of the upstream going pressure wave, the downstream going pressure wave, and the downstream going vorticity wave. The subscripts L and R denote the upstream and downstream (left and right) sides of the blade row. The matrix $\mathbf{W}$ is a matrix of transmission and reflection coefficients. Note that a single incident wave with mode numbers n, k in principle produces an infinite number of reflected and transmitted waves with mode numbers n, j, where j takes on all integer values. Conversely, an infinite number of incident waves contribute to a single family of outgoing waves. We may express this result as

$$\begin{Bmatrix} P_L^+ \\ P_R^- \\ \zeta_R \end{Bmatrix}_{nj} = \sum_{k=-\infty}^{\infty} \begin{bmatrix} w_{11} & w_{12} & w_{13} \\ w_{21} & w_{22} & w_{23} \\ w_{31} & w_{32} & w_{33} \end{bmatrix}_{njnk} \begin{Bmatrix} P_R^+ \\ P_L^- \\ \zeta_L \end{Bmatrix}_{nk} + \begin{Bmatrix} b_1 \\ b_2 \\ b_3 \end{Bmatrix}_{nj},$$

$$j = -\infty \quad \text{to} \quad \infty \tag{11}$$

Also, in Eq. (11) we have included an inhomogeneous term b_{nj}. Such a term would arise, for example, if the blades of the cascade were prescribed to vibrate, or from a prescribed viscous wake trailing behind the stator blades.

It will be convenient to rearrange Eq. (11) as follows:

$$\sum_{k=-\infty}^{\infty} [\mathbf{A}_{njnk}\mathbf{u}_{L,nk} + \mathbf{B}_{njnk}\mathbf{u}_{R,nk}] = \mathbf{b}_{nj}, j = -\infty \quad \text{to} \quad \infty \tag{12}$$

where

$$\mathbf{u}_{L,nk} = \begin{Bmatrix} P_L^+ \\ P_L^- \\ \zeta_L \end{Bmatrix}_{nk}, \quad \mathbf{u}_{R,nk} = \begin{Bmatrix} P_R^+ \\ P_R^- \\ \zeta_R \end{Bmatrix}_{nk}$$

and

$$\mathbf{A}_{njnk} = \begin{bmatrix} \delta_{jk} & -w_{12} & -w_{13} \\ 0 & -w_{22} & -w_{23} \\ 0 & -w_{32} & -w_{33} \end{bmatrix}_{njnk}$$

$$\mathbf{B}_{njnk} = \begin{bmatrix} -w_{11} & 0 & 0 \\ -w_{21} & \delta_{jk} & 0 \\ -w_{31} & 0 & \delta_{jk} \end{bmatrix}_{njnk}$$

and δ_{jk} is the Kroneker delta function. A similar set of equations are applied to the stator, i.e.,

$$\sum_{n=-\infty}^{\infty} [\mathbf{A}_{jknk}\mathbf{u}_{L,nk} + \mathbf{B}_{jknk}\mathbf{u}_{R,nk}] = \mathbf{b}_{jk}, \quad j = -\infty \quad \text{to} \quad \infty \tag{13}$$

Note that the equations in this section merely describe the kinematics of the reflection and transmission of waves through a stator or rotor. To obtain the actual reflection and transmission coefficients $\mathbf{W}$ and the inhomogeneous terms $\mathbf{b}$ requires an unsteady aerodynamic theory. In the present study, we use a modified version of the two-dimensional compressible flat-plate cascade theory and computer code "LINSUB" developed by Whitehead (1987) based on the theory of Smith (1972). We note, however, that more sophisticated linearized theories could be used as well.

2.3 Interrow Coupling. Having described the behavior of the individual blade rows, we now consider the aerodynamic coupling of the blade rows. The blade rows "communicate" with one another through the spinning modes. For example, an outgoing pressure wave (spinning mode) from the rotor propagating upstream becomes an incident pressure wave to the stator. This may be expressed as

$$\mathbf{E}_{nk}\mathbf{u}^1_{R,nk} + \mathbf{u}^2_{L,nk} = 0 \tag{14}$$

where the superscripts 1 and 2 refer to the first and second blade rows respectively (stator and rotor for the situation depicted in Fig. 1). The matrix $\mathbf{E}_{nk}$ describes the propagation of the spinning modes through the duct, and is given by

$$\mathbf{E}_{nk} = \begin{bmatrix} -e^{i\alpha_{1,nk}\Delta x} & 0 & 0 \\ 0 & -e^{i\alpha_{2,nk}\Delta x} & 0 \\ 0 & 0 & -e^{i\alpha_{3,nk}\Delta x} \end{bmatrix} \tag{15}$$

where Δx is the axial spacing from the leading edge of the stator to the leading edge of the rotor.

The axial wave number $\alpha_{i,nk}$ in Eq. (15) depends on the steady flow properties in the duct between the blade rows, the mode numbers (n, k), and the frequency ω_{nk}. For downstream propagating vorticity waves, the wave number is given by

$$\alpha_{3,nk} = -\frac{\beta_{nk}V + \omega_{nk}}{U} \tag{16}$$

where U and V are the axial and tangential components of velocity, respectively, and ω_{nk} is the temporal frequency associated with the wave (V and ω_{nk} must be viewed in the same frame of reference). Also, β_{nk} is the circumferential wave number given by $\beta_{nk} = (k_0 + nB_1 + kB_2)/R$ where R is the radius of the machine. For pressure waves, the wave number is given by

$$\alpha_{i,nk} = \frac{U(\omega_{nk} + \beta_{nk}V) \pm a\sqrt{(\omega_{nk} + \beta_{nk}V)^2 - (a^2 - U^2)\beta_{nk}^2}}{a^2 - U^2} \tag{17}$$

Note that for certain conditions, the wave numbers will be complex, and the waves will be "cut-off." Cut-off waves are attenuated, and no acoustic energy is carried along the duct. For other conditions, the wave numbers will be purely real, and the waves are "cut-on," i.e., they propagate along the duct without attenuation.

Finally, upstream of the stator and downstream of the rotor, we require that there be no incoming waves. This condition may be expressed by

$$\mathbf{C}\mathbf{u}^1_{L,nk} + \mathbf{D}\mathbf{u}^2_{R,nk} = 0 \tag{18}$$

where

$$\mathbf{C} = \begin{bmatrix} 0 & 0 & 0 \\ 0 & 1 & 0 \\ 0 & 0 & 1 \end{bmatrix}, \quad \mathbf{D} = \begin{bmatrix} 1 & 0 & 0 \\ 0 & 0 & 0 \\ 0 & 0 & 0 \end{bmatrix} \tag{19}$$

2.4 Assembled System of Equations. Next, we put together these relationships to obtain a linear system of equations describing the unsteady flow in the stage. Of course, the infinite sums in Eqs. (11) and (13) must be truncated. As an example, we consider the case where four spinning modes are retained in the model: $(n, k) = (0, 0), (0, 1), (1, 0)$, and $(1, 1)$. The resulting linear system of equations then has the form given by Eq. (20). Superscripts denote the blade row number. Equation (20) describes the interaction of the various n, k modes in the rotor and stator. This equation is solved using lower-upper (LU) decomposition to determine the amount of each mode present in the unsteady flow. Knowing this, one can then compute the unsteady lift and moment acting on the airfoils in a postprocessing operation. Finally we note that although Eq. (20) was derived for the special case of a single stage (stator plus rotor), the approach is easily extended to multiple stages, and results are presented in the next section of unsteady flow through a three and one-half stage machine.

$$
\begin{bmatrix}
A^1_{0000} & B^1_{0000} & & & & & A^1_{0010} & B^1_{0010} & & & & & & & & \\
 & E_{00} & I & & & & & & & & & & & & & \\
 & & A^2_{0000} & B^2_{0000} & & & & & A^2_{0001} & B^2_{0001} & & & & & & \\
C & & & D & & & & & & & & & & & & \\
\hline
 & & & & A^1_{0101} & B^1_{0101} & & & & & A^1_{0111} & B^1_{0111} & & & & \\
 & & & & & E_{01} & I & & & & & & & & & \\
 & & A^2_{0100} & B^2_{0100} & & & & & A^2_{0101} & B^2_{0101} & & & & & & \\
 & & & & C & & & & & D & & & & & & \\
\hline
A^1_{1000} & B^1_{1000} & & & & & A^1_{1010} & B^1_{1010} & & & & & & & & \\
 & & & & & & & & E_{10} & I & & & & & & \\
 & & & & & & & & & A^2_{1010} & B^2_{1010} & & & & A^2_{1011} & B^2_{1011} \\
 & & & & & & C & & & & D & & & & & \\
\hline
 & & & & A^1_{1101} & B^1_{1101} & & & & & A^1_{1111} & B^1_{1111} & & & & \\
 & & & & & & & & & & & E_{11} & I & & & \\
 & & & & & & & & & A^2_{1110} & B^2_{1110} & & & A^2_{1111} & B^2_{1111} \\
 & & & & & & & & & & C & & & & D
\end{bmatrix}
\times
\begin{bmatrix}
u^1_{L,00} \\ u^1_{R,00} \\ u^2_{L,00} \\ u^2_{R,00} \\ \hline
u^1_{L,01} \\ u^1_{R,01} \\ u^2_{L,01} \\ u^2_{R,01} \\ \hline
u^1_{L,10} \\ u^1_{R,10} \\ u^2_{L,10} \\ u^2_{R,10} \\ \hline
u^1_{L,11} \\ u^1_{R,11} \\ u^2_{L,11} \\ u^2_{R,11}
\end{bmatrix}
=
\begin{bmatrix}
b^1_{00} \\ 0 \\ b^2_{00} \\ 0 \\ \hline
b^1_{01} \\ 0 \\ b^2_{01} \\ 0 \\ \hline
b^1_{10} \\ 0 \\ b^2_{10} \\ 0 \\ \hline
b^1_{11} \\ 0 \\ b^2_{11} \\ 0
\end{bmatrix}
\tag{20}
$$

3 Results

3.1 Code Validation. Before using the present analysis to study the aeroelastic stability of rows of airfoils, we first present a number of numerical examples designed to validate the present method. In this section, we compare our numerical results to two other theories: a similar coupled mode analysis developed by Hanson (1993, 1994), and a rotor/stator vortex lattice method developed by the authors specifically to test the present method.

First, consider Configuration A, a rotor/stator combination with the geometry given in Table 1. In this example, we assume that the upstream rotor generates a viscous wake which then interacts with the downstream stator. Note that the rotor speed for this example is such that the rotor and stator carry no steady load. The interrow spacing is 1.5 times the rotor blade chord. The upwash acting on the stator due to the rotor wake is modeled using the wake model of Kemp and Sears (1955). We assume that the viscous wake trailing the rotor blades is due to an airfoil profile drag coefficient of 0.02. Note, however, that only the first circumferential harmonic of the viscous wake upwash is retained. Thus, the original excitation is at a single interblade phase angle and temporal frequency. Results of the present theory are shown in Fig. 3. Shown are the magnitudes of the harmonic components of unsteady coefficient of lift [$C_L = L/(\rho U^2 c)$] acting on the rotor (vane passing frequency and twice vane passing frequency) and stator (blade passing frequency and twice blade passing frequency) as a function of the relative Mach number M of the flow into the rotor. Also shown for comparison are the results computed by Hanson (1993, 1994) using his collocation method. In both theories, the same nine spinning modes were retained, $(n, k) = (0, -1), (0, 0), (0, 1), (0, 2), (-1, -2), (-1, -1), (-1, 0), (-1, 1)$, and $(-1, 2)$. It is reassuring, although perhaps not surprising, that the two essentially equivalent theories are in excellent agreement. Note that even though the original excitation acts on the stator only, unsteady lift acts on both blade rows. This is to be expected since the (0, 1) mode, which is directly excited by the original disturbance, is cut-on over the entire Mach number range providing a significant coupling mechanism.

Next, we compare the present coupled mode analysis to an incompressible time-marching vortex–lattice model developed by the authors for this purpose. Using our vortex–lattice model, the blades and wakes of multiple cascades are modeled with a

Table 1 Cascade parameters for Configuration A

		Rotor	Stator
Cascade Index		1	2
Number of Blades	B	38	50
Chord	c	1.00	0.57
Gap-to-Chord Ratio	G	0.75	1.00
Stagger Angle	Θ	–60°	0°
Relative Velocity	U	1.0	0.5
Forced Response Case			
Relative Mach Number	M	$0.60 \le M \le 0.90$	$0.30 \le M \le 0.45$
Excitation Frequency	ω_0		7.255
Excitation Phase Angle	σ_0		–273.6°
Flutter Case			
Relative Mach Number	M	0.7	0.35
Excitation Frequency	ω_0	1.0	
Excitation Phase Angle	σ_0	$-180° \le \sigma_0 \le 180°$	
Rotation Speed	ΩR	–0.866	0.0

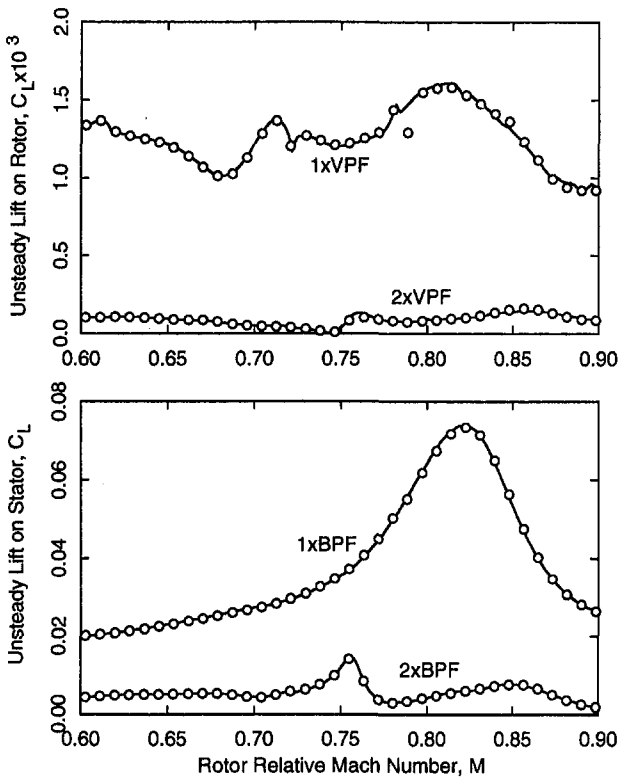

Fig. 3 Unsteady lift on rotor (top) and stator (bottom) of Configuration A due to interaction with Kemp–Sears wake: ○, present method; ——, Hanson collocation method (1993, 1994)

Table 2 Cascade parameters for Configuration B

		Stator	Rotor	Stator
Cascade Index		1	2	3
Number of Blades	B	72	72	72
Chord	c	1.00	1.00	1.00
Gap-to-Chord Ratio	G	0.75	0.75	0.75
Stagger Angle	Θ	45°	−45°	45°
Relative Velocity	U	1.0	1.0	1.0
Relative Mach Number	M	0.0, 0.7	0.0, 0.7	0.0, 0.7
Excitation Frequency	ω_0		1.0	
Excitation Phase Angle	σ_0		$-180° \leq \sigma_0 \leq 180°$	
Rotation Speed	ΩR	0.0	−1.414	0.0

number of vortex elements. At the quarter-chord of each element is placed a point vortex. At the three-quarter chord point of each element we place a collocation point. We start the solution with all of the vorticity equal to zero. Then, at each time step, we adjust the vorticity at each of the elements on the blades so that flow tangency is satisfied. The vorticity at the first point behind each airfoil is selected to satisfy the requirement that circulation be conserved. In the remainder of the wake, the vorticity is simply convected from one time step to the next assuming a rigid wake. Finally, we increment the position of the rotor, and repeat the entire process. The result is a time-accurate simulation of incompressible flow through multiple blade rows.

Consider "Configuration B," a stator/rotor/stator configuration (see Table 2). The interrow spacing for the case considered here is 0.2 times the blade chord, and the axial Mach number M is zero (incompressible flow). Shown in Fig. 4 is the computed time history of the unsteady coefficient of lift [$C_L = L/(\rho U \dot{h}_0 c)$] on the reference blades of Configuration B due to plunging motion of the rotor blades at an interblade phase angle σ_0 of 90 deg. Results are shown for both the coupled mode analysis and the vortex lattice model. For the case considered here, the rotor blades plunge with a reduced frequency $\omega_0 c/U$ of 1.0 (based on relative velocity and chord). The coupled mode analysis used one mode ($n = k = 0$) in one case, and 25 modes ($-2 \leq n \leq 2$, $-2 \leq k \leq 2$) in another. The time-marching vortex–lattice model used 40 panels per blade. Note that after the initial transients associated with the start of the vortex–lattice method have decayed away, there is generally excellent agreement between the two methods, especially when the coupled mode analysis uses 25 modes. Even using just one mode, the coupled mode analysis does a good job of predicting the low-frequency component of the unsteady lift. The largest discrepancies occur at the times when a blade intersects the shed wake of the upstream blade row. At these instances, there is an abrupt change in the slope of the lift. Physically, a slope discontinuity indicates that the unsteady response contains significant high-frequency content, and one would expect that a large number of spinning modes would be needed to model the unsteady flow accurately. Nevertheless, our results indicate that a modest number of modes is required to obtain good agreement with the "exact" time-marching solution.

3.2 Aerodynamic Damping Calculations. Having validated the model, we next consider the aeroelastic stability of the rotors of Configurations A and B. Consider the time history of the unsteady lift due to plunging motion of the rotor blades of configuration B (see, e.g., Fig. 4). Clearly the unsteady lift contains the original excitation frequency plus numerous shifted frequencies. However, on average, the unsteady lift at the shifted frequencies does no aerodynamic work on the vibrating rotor blades. Therefore, the aeroelastic stability is governed by the real part of the lift at the original (fundamental) excitation frequency. (The "aerodynamic damping" is proportional to the negative of the real part of the coefficient of lift, C_L. If the aerodynamic damping plus the structural damping is negative, then the cascade will flutter.)

The first example we consider is Configuration A as before, but now the excitation is due to a plunging vibration of the rotor blades with a reduced frequency $\omega_0 c/U$ of 1.0. Figure 5 shows the real and imaginary parts of the fundamental harmonic of the unsteady lift for a range of interblade phase angles. These results were computed using the present coupled mode analysis with 1 mode ($n = k = 0$) and 25 modes ($-2 \leq n \leq 2$, $-2 \leq k \leq 2$). The two solutions are in almost perfect agreement, indicating that most of the coupling for this example occurs through a single mode (at least the coupling that affects the fundamental harmonic). Also shown in the figure is the unsteady lift computed for the rotor in isolation using LINSUB (Whitehead, 1987) without coupling, i.e., the conventional approach. For this example, coupling has a small effect on the

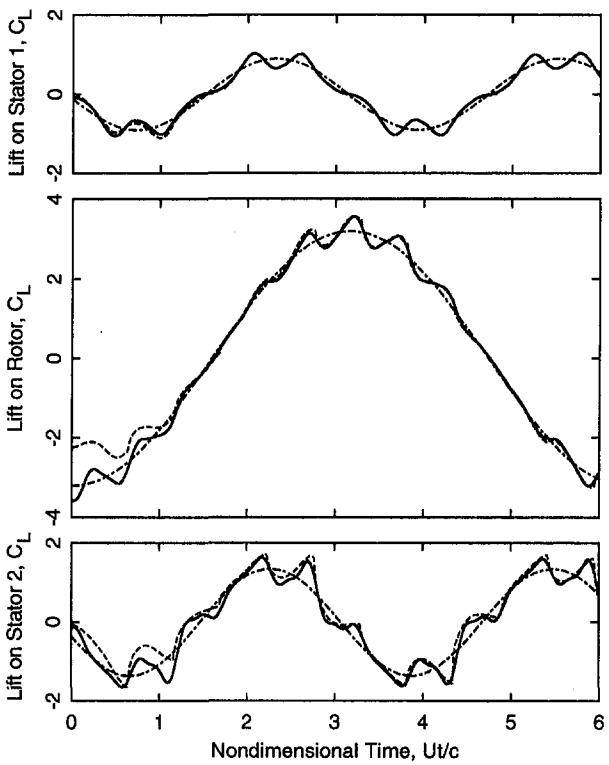

Fig. 4 Time history of unsteady lift on reference blades of Configuration B due to plunging motion of the rotor blades, $\omega_0 c/U = 1.0$, $\sigma_0 = 90$ deg: - - -, vortex–lattice code; — - —, present analysis using 1 mode; ——, present analysis using 25 modes

unsteady lift in the superresonant region (-91.1 deg $\leq \sigma_0 \leq$ 19.5 deg), and almost no effect in the subresonant region.

Next, we consider the aeroelastic stability of Configuration B. Shown in Fig. 6 is the fundamental harmonic of the unsteady lift as a function of interblade phase angle for the original Case B configuration, but for a relative Mach number M of 0.7 in both the rotor and the stator. Shown is the unsteady lift on the reference blade of the rotor computed using one, nine, or 25 modes for a range of interblade phase angles. Note that the three computed results all agree fairly well with one another over most of the interblade phase angle range, indicating that the primary coupling between blade rows for this case is due to a single mode. Over a portion of the interblade phase angle range, more modes are required to obtain a "converged" solution, but certainly no more than 9 modes ($-1 \leq n \leq 1$, $-1 \leq k \leq 1$). Also shown in Fig. 6 is the unsteady lift computed using LINSUB. Note that this unsteady lift is significantly different than the unsteady lift for a rotor surrounded by stator blade rows, even for interblade phase angles in the subresonant region. This should not be too surprising since the vorticity waves are always "cut-on." These waves propagate downstream from the rotor and impinge on the downstream stator. In the stator frame of reference, some of these waves have quite high frequency, and therefore excite superresonant pressure waves that propagate upstream and interact with the rotor. Furthermore, even cut-off pressure waves will interact with adjacent blade rows if the interrow gap is small or the interblade phase angle of the mode is small.

Next, we again consider plunging motion of the rotor of Configuration B with M = 0.7, but now vary the interrow spacing between blade rows. In one case, the axial spacing is 0.2 chords (as before). In the other, the axial gap is 1.0 chord. Shown in Fig. 7 is the fundamental harmonic of unsteady lift acting on the reference blade of the rotor. In both cases, nine modes were used in the coupled mode analysis. The two solu-

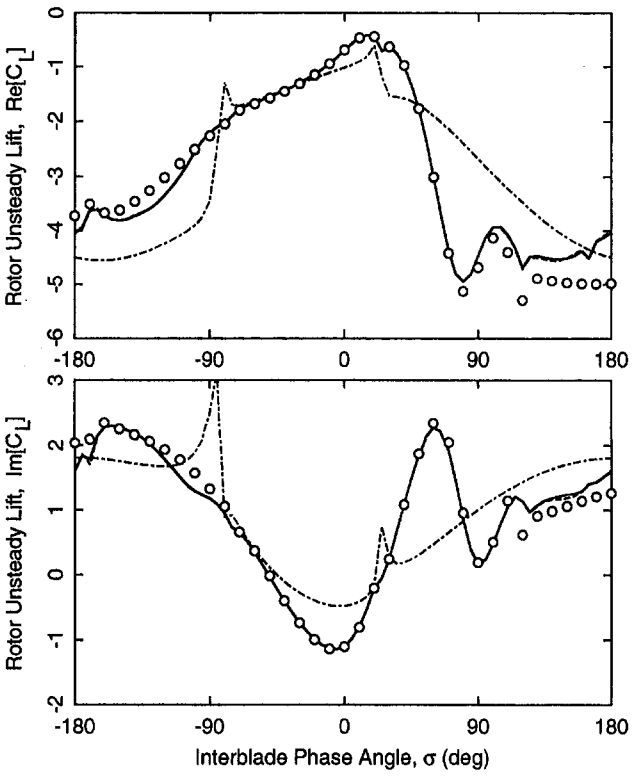

Fig. 6 Fundamental harmonic of unsteady lift on rotor blades of Configuration B due to plunging motion of rotor blades, $\omega_0 c/U$ = 1.0: — – —, LINSUB (Whitehead, 1987); ○, present method with 1 mode; – – – – –, 9 modes; ——, 25 modes

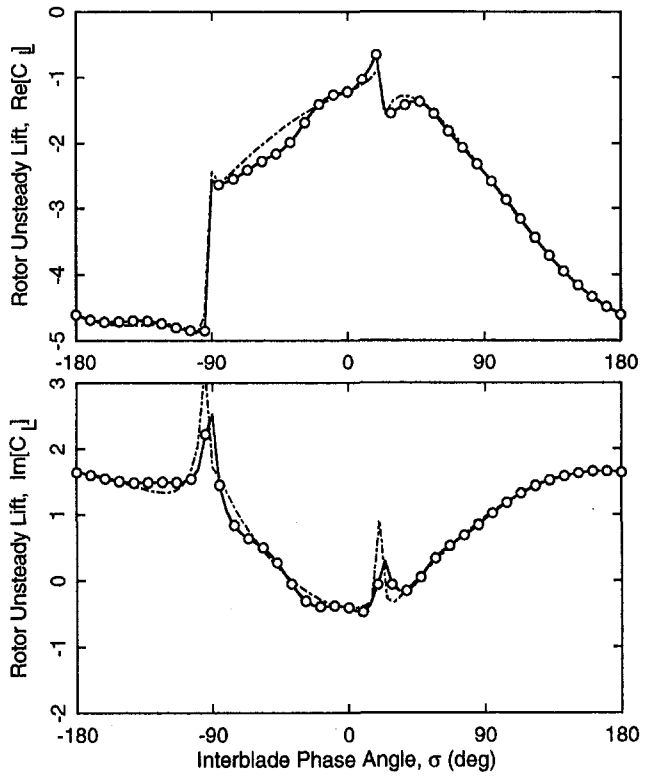

Fig. 5 Fundamental harmonic of unsteady lift on rotor blades of Configuration A due to plunging motion of rotor blades, $\omega_0 c/U$ = 1.0: — – —, LINSUB (Whitehead, 1987); ——, present method with 1 mode; ○, 25 modes

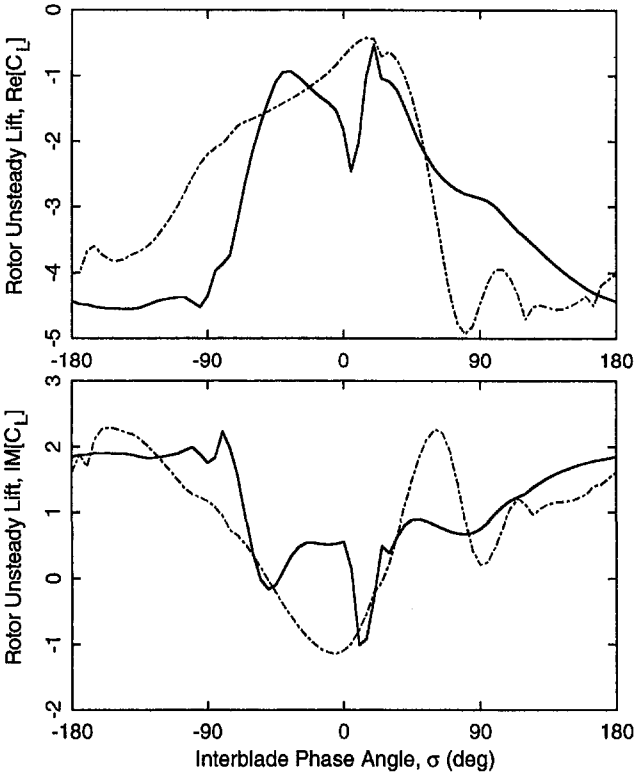

Fig. 7 Fundamental harmonic of unsteady lift on rotor blades of Configuration B due to plunging motion of rotor blades, $\omega_0 c/U$ = 1.0: — – —, present method with axial gap = 0.2 chords; ——, present method with axial gap = 1.0 chord

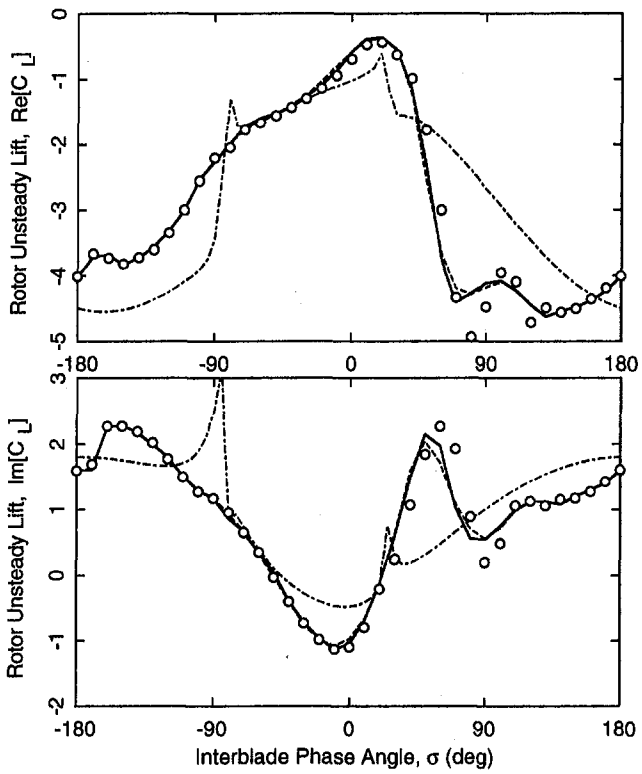

Fig. 8 Fundamental harmonic of unsteady lift on rotor blades of Configuration B due to plunging motion of rotor blades, $\omega_0 c/U$ = 1.0: — - —, 1 blade row; ○, 3 blade rows; - - - - -, 5 blade rows; ——, 7 blade rows

tions are seen to differ markedly, demonstrating the importance of the axial spacing of neighboring blade rows on aeroelastic damping. These results suggest that axial spacing plays an important role in the aeroelastic stability of blade rows.

Next, we investigate the influence of multiple blade rows surrounding a vibrating blade row. We consider again Configuration B (stator/rotor/stator), but now with 1 blade row (rotor), 3 blade rows, (stator/rotor/stator), 5 blade rows (rotor/stator/rotor/stator/rotor), and 7 blade rows (stator/rotor/stator/rotor/stator/rotor/stator). In all cases, only the blades of the middle rotor vibrate in plunge with a reduced frequency of 1.0, and nine modes were included in the coupled mode analysis. Shown in Fig. 8 is the fundamental harmonic of the unsteady lift for a range of interblade phase angles. Note that as more blade rows are added to the system, the unsteady lift is modified. However, the most significant change occurs when the system goes from a rotor in isolation, to a rotor surrounded by an upstream and downstream stator row. Adding more blade rows beyond this point has a more modest effect on the unsteady lift.

4 Discussion and Summary

In this paper, we have presented an analysis for computing unsteady flows in multistage fans, compressors, and turbines. Using the present method, conventional frequency domain solution techniques are used to compute reflection and transmission coefficients that describe the response of an isolated blade row to a single incident interrow wave. These reflection and transmission coefficients are then used to construct a linear system of equations that describes how multiple blade rows will behave together. Although the reflection and transmission coefficients were computed in this study using a flat-plate cascade theory, the method is general, and other more realistic linearized analyses could be used to obtain the reflection and transmission coefficients. For example, replacing the LINSUB model for the isolated blade rows with a more sophisticated flow model—such as a linearized Euler analysis (Hall and Clark, 1993)—would result in a model capable of predicting the potentially important influence of turning and "mode trapping" as described by Hanson (1993). Furthermore, there is no difficulty in analyzing unsteady flows through rotor/stator configurations with unequal blade counts in the blade rows. Finally, the method can be applied to machines with any number of blade rows, although the number of modes one must retain in the model will generally increase with increasing number of blade rows.

For flutter calculations, a relatively small number of modes (say ten to 25 modes) is required to obtain satisfactory estimates of the aerodynamic damping. We found that the aerodynamic damping of an isolated cascade of vibrating airfoils differs markedly from the aerodynamic damping when the cascade is surrounded by neighboring blade rows. We also found that the interrow spacing significantly affects the aerodynamic damping of a blade row. This result also suggests that in some cases adjusting the interrow spacing may be used to passively control blade flutter.

Finally, although the results in this paper are preliminary, we would argue that the current generation of unsteady time-linearized flow solvers, which model a given blade row as isolated in an infinitely long duct, may not correctly predict the aerodynamic damping of vibrating blades. The method presented in this paper provides a framework to incorporate the influence of neighboring blade rows into these time-linearized aerodynamic solvers.

Acknowledgments

This work was supported in part by a gift from Stress Technologies Incorporated. This material is based upon work supported by the National Science Foundation under Grant No. GTS-9157908. The Government has certain rights in this material. The authors are indebted to Dr. Donald B. Hanson of Pratt & Whitney for substantial technical advice, and for providing numerical data that appear in this paper.

References

Buffum, D. H., 1993, "Blade Row Interaction Effects on Flutter and Forced Response," Paper No. AIAA-93-2084; also NASA TM 106438.

Giles, M. B., 1988, "Calculation of Unsteady Wake/Rotor Interaction," *Journal of Propulsion and Power,* Vol. 4, No. 4, pp. 356–362.

Hall, K. C., 1993, "Deforming Grid Variational Principle for Unsteady Small Disturbance Flows in Cascades," *AIAA Journal,* Vol. 31, No. 5, pp. 891–900.

Hall, K. C., and Clark, W. S., 1993, "Linearized Euler Predictions of Unsteady Aerodynamic Loads in Cascades," *AIAA Journal,* Vol. 31, No. 3, pp. 540–550.

Hall, K. C., and Crawley, E. F., 1989, "Calculation of Unsteady Flows in Turbomachinery Using the Linearized Euler Equations," *AIAA Journal,* Vol. 27, No. 6, pp. 777–787.

Hall, K. C., and Lorence, C. B., 1993, "Calculation of Three-Dimensional Unsteady Flows in Turbomachinery Using the Linearized Harmonic Euler Equations," ASME JOURNAL OF TURBOMACHINERY, Vol. 115, pp. 800–809.

Hanson, D. B., 1992, "Unsteady Coupled Cascade Theory Applied to the Rotor/Stator Interaction Noise Problem," DGLR/AIAA Paper No. 92-02-084.

Hanson, D. B., 1993, "Mode Trapping in Coupled 2D Cascades-Acoustic and Aerodynamic Results" AIAA Paper No. 93-4417.

Hanson, D. B., 1994, private communication.

Kaji, S., and Okazaki, T., 1970, "Generation of Sound by Rotor–Stator Interaction," *J. Sound and Vibration,* Vol. 13, No. 3, pp. 281–307.

Kemp, N. H., and Sears, W. R., 1955, "The Unsteady Forces Due to Viscous Wakes in Turbomachines," *Journal of the Aeronautical Sciences,* Vol. 22, No. 7, pp. 478–483.

Manwaring, S. R., and Wisler, D. C., 1993, "Unsteady Aerodynamics and Gust Response in Compressors and Turbines," ASME JOURNAL OF TURBOMACHINERY, Vol. 115, pp. 724–740.

Rai, M. M., 1989a, "Three-Dimensional Navier–Stokes Simulations of Turbine Rotor–Stator Interaction: Part I—Methodology," *Journal of Propulsion and Power,* Vol. 5, No. 3, pp. 307–311.

Rai, M. M., 1989b, "Three-Dimensional Navier–Stokes Simulations of Turbine Rotor–Stator Interaction: Part II—Results," *Journal of Propulsion and Power,* Vol. 5, No. 3, pp. 312–319.

Smith, S. N., 1972, "Discrete Frequency Sound Generation in Axial Flow Turbomachines," Aeronautical Research Council Reports and Memoranda, R. & M. No. 3709.

Verdon, J. M., 1987, "Linearized Unsteady Aerodynamic Theory," *AGARD Manual on Aeroelasticity in Axial Flow Turbomachines, Vol. 1, Unsteady Turbomachinery Aerodynamics* (AGARD-AG-298), M. F. Platzer and F. O. Carta, eds., Neuilly sur Seine, France, Chap. 2.

Whitehead, D. S., 1987, "Classical Two-Dimensional Methods," *AGARD Manual on Aeroelasticity in Axial Flow Turbomachines, Vol. 1, Unsteady Turbomachinery Aerodynamics* (AGARD-AG-298), M. F. Platzer and F. O. Carta, eds., Neuilly sur Seine, France, Chap. 3.

Whitehead, D. S., and Grant, R. J., 1981, "Force and Moment Coefficients of High Deflection Cascades," *Proc. 2nd International Symposium on Aeroelasticity in Turbomachines,* P. Suter, ed., Juris-Verlag, Zurich, pp. 85–127.

Three-Dimensional Unsteady Flow and Forces in Centrifugal Impellers With Circumferential Distortion of the Outlet Static Pressure

A. Fatsis

S. Pierret

R. Van den Braembussche

Turbomachinery Department,
von Karman Institute for Fluid Dynamics,
Rhode-St-Genèse, Belgium

This paper describes the numerical investigation of the centrifugal impeller response to downstream static pressure distortions imposed by volutes at off-design operations. An unsteady three-dimensional Euler solver with nonreflecting upstream and downstream boundary conditions and phase-lagged periodicity conditions is used for this purpose. The mechanisms governing the unsteady flow field are analyzed. A parametric study shows the influence of the acoustic Strouhal number on the amplitude of the flow perturbations. Radial forces calculated on backward leaned and radial ending centrifugal impellers show nonnegligible influence of the impeller geometry.

Introduction

Centrifugal compressor impellers are exposed to downstream circumferential static pressure distortions when followed by nonaxisymmetric volutes operating at off-design conditions. The static pressure distortion propagates upstream and creates a circumferential variation of the blade loading and forces in the impeller. A first consequence is a nonzero radial force on the shaft and extra load on the bearings. It also means unsteady flow in the rotating blade passages resulting in blade vibrations and additional noise. This increases losses and decreases the operating range of the compressor.

Experimental studies on the flow in centrifugal compressor impellers with downstream static pressure distortion (Pfau, 1967; Uchida et al., 1987; Sideris, 1988) indicate a nonlinear variation of the outlet flow with large variations in the volute tongue region. Nonnegligible circumferential flow variations are also detected upstream of the impeller, resulting in a variation of incidence.

The unsteadiness of the incompressible flow in a channel of length L is normally characterized by the reduced frequency,

$$\Omega = \frac{fL}{V} \tag{1}$$

where V is the speed by which a particle is transported through the channel. However, the acoustic Strouhal number is more appropriate to characterize compressible flows. It is defined as the product of the reduced frequency times the Mach number:

$$\mathrm{Sr} = \Omega M = \frac{fL}{c} \tag{2}$$

It relates the time needed by a pressure wave to travel a distance L to the period of the pressure perturbation $1/f$.

In turbomachinery applications, L is normally defined as the length of a blade passage, whereas f is the number of rotations per second times the number of perturbation waves around the circumference.

Contributed by the International Gas Turbine Institute and presented at the 40th International Gas Turbine and Aeroengine Congress and Exhibition, Houston, Texas, June 5–8, 1995. Manuscript received by the International Gas Turbine Institute February 11, 1995. Paper No. 95-GT-33. Associate Technical Editor: C. J. Russo.

Unsteady effects are small for $\mathrm{Sr} \ll 1$ and the quasi-steady flow can be evaluated by means of steady calculations. For $\mathrm{Sr} > 0.1$ accurate results can be obtained only by means of unsteady flow calculations.

A one-dimensional unsteady model to predict the impeller response to a downstream circumferential static pressure distortion was developed by Lorett and Gopalakrishnan (1986). The model, applicable only to incompressible flows, assumes constant outlet relative flow angle. It calculates the radial force acting on the impeller in function of the circumferential nonuniformity of the outlet static pressure, neglecting the circumferential variation of the radial and tangential momentum.

Better predictions can be obtained by the two-dimensional unsteady models of Morfiadakis et al. (1991), and Badie et al. (1992) who solve the two-dimensional unsteady potential flow equations by means of singularity or finite element method. Croba (1992) calculates the incompressible unsteady two-dimensional Navier–Stokes flow using the $k-\epsilon$ model for turbulence. Sideris (1988) uses a quasi-three-dimensional unsteady Euler model to predict the unsteady flow variations in the blade-to-blade surface at the shroud. All these models, however, fail to provide information about the three-dimensional effects in the impeller.

The present numerical study aims to predict the three-dimensional unsteady flow in centrifugal impellers, and the unsteady forces and torques acting on the impeller shaft and blades. A parametric study is carried out to find the conditions that give rise to large amplitudes of flow quantities and forces oscillations. Computations are done on impellers with backward leaned and with radial ending blades to evaluate the influence of the impeller geometry.

Numerical Method

Flow unsteadiness due to circumferential inlet and outlet pressure distortions is influenced mainly by wave propagation and to a lesser extent by viscous phenomena. This justifies the use of an unsteady three-dimensional Euler solver instead of a full three-dimensional Navier–Stokes solver. This simplification results in an affordable computer time, and it can give useful information on the dynamics of the flow in the case where the impeller is not heavily loaded and flow separation is limited.

The space discretization of the three-dimensional Euler equations is done by means of the finite volume technique with a second order spatial accuracy in smooth grids (Fatsis, 1993). The Runge–Kutta four-step scheme with single evaluation of the dissipative terms providing second-order accuracy for nonlinear equations is used for the time integration (Jameson et al., 1981). Extensive testing of the method by Sideris (1988) in special test cases for which analytical solutions exist has demonstrated the accuracy of this scheme for unsteady flow predictions.

Impermeable wall boundary conditions are imposed on the solid walls by considering only the static pressure distribution when computing the convective fluxes. The evaluation of the Jameson-type artificial dissipation on the solid walls is done by means of high order extrapolation polynomials in order to minimize the dissipative fluxes (Fatsis and Van den Braembussche, 1994). They also describe the three-dimensional inlet/outlet nonreflecting boundary conditions based on the Fourier decomposition and showed that the upstream location of the inflow boundary has a negligible effect on the solution.

Special problems related to unsteady flow are the nonperiodicity of the flow and the definition of the time step. They are discussed in the following two sections.

Phase-Lagged Periodicity Conditions. Since the downstream static pressure is not uniform around the circumference, the flow variables will be different on each stagnation pseudo-streamline so that the classical periodicity conditions cannot be applied any longer. A point rotating with the impeller will experience the same flow conditions only after a complete rotation.

There are two methods to simulate this phenomenon numerically. The first one is to extend the numerical domain in the circumferential direction such that it contains all the blades of the impeller and to calculate the whole impeller flow at once. This leads to computer storage problems in three dimensions, because all the flow variables at each individual blade passage have to be stored in memory.

The alternative way is to consider only one blade channel as computational domain, and to simulate the circumferentially nonuniform flow field by employing phase-lagged periodicity conditions. A modified version of the phase-lagged periodicity conditions of Erdos and Alzner (1977) is used in the present study.

The computational domain under consideration is the one defined by *ABCDNMLK*, on Fig. 1. The flow variables at the boundaries *AB*, *KL*, and *CD*, *MN* are not equal anymore because the static pressure in *D* and *N* is different. Suppose that the flow is calculated at NCIRC different circumferential positions of the rotor within one rotation. The blades will then have rotated over a pitch after n computations

$$n = \frac{\text{NCIRC}}{N_{bl}} \tag{3}$$

Calculating the unsteady flow at the ith circumferential position

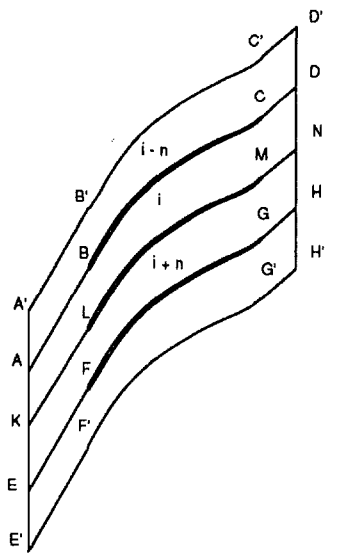

Fig. 1 Phase-lagged periodicity conditions

($i = 1, \ldots,$ NCIRC), the necessary information above the boundary *ABCD* and below the boundary *KLMN* (Fig. 1) can be obtained from the computations done in neighboring passages at positions $i - n$ and $i + n$, respectively.

The flow variables at the blade position $i - n$ have been updated shortly before, during the actual rotation when calculating the flow in the previous pitch. The flow variables at the blade position $i + n$ are not yet known at the current rotation, and are set equal to the values at the position $i + n -$ NCIRC obtained at the previous rotation.

Using information from the previous rotation means that the nonperturbed solution is used to calculate the flow during the first rotation, which slows down the convergence to a periodic state.

Phase-lagged periodicity conditions have to be adjusted each time the impeller has rotated over the distance between two successive grid points. The method therefore only requires the storage of the information needed to define the flow on the stagnation pseudo-streamlines *AB*, *CD*, *KL*, and *MN* at each circumferential position during one rotation. This also includes the flow quantities in adjacent points, which are required to calculate the second and fourth order artificial dissipation terms.

Definition of Time Step. For a time-accurate simulation of the unsteady phenomena occurring during one impeller rotation, the numerical time step must be related to the rotational speed and to the angular displacement of the impeller between two successive computations. This time step has to be the same for all the points composing the numerical domain, which means that local time stepping can no longer be used.

Nomenclature

$\vec{F}$ = force
L = length of blade channel
M = Mach number
N_{bl} = number of the impeller blades
NCIRC = number of angular positions of impeller
P = static pressure
R = radius
S = surface
Sr = acoustic Strouhal number
V = absolute velocity
W = relative velocity
c = speed of sound
f = frequency of unsteadiness
n = number of positions per blade pitch
t = time
Δt = time step
Ω = reduced frequency
α = absolute flow angle
β = relative flow angle
ρ = density
ω = nondimensional rotational impeller speed

Subscripts

m = meridional
r = radial
z = axial
θ = circumferential
0 = total conditions
2 = impeller trailing edge

The time needed for one rotation is $2\pi/\omega$, so that the nondimensional time needed for the impeller to rotate from one position to the next is:

$$\Delta t' = \frac{2\pi}{\omega \times \text{NCIRC}} \tag{4}$$

The numerical time step Δt is also limited by the stability condition. It has to be smaller than (or equal to) the smallest numerical time step evaluated by the *CFL* restriction. If $\Delta t'$, as defined by Eq. (4), is bigger than Δt, then J = INTEGER $(\Delta t'/\Delta t)$ iterations have to be done at each impeller position before rotating the impeller to the next position.

A small error is introduced by the assumption that the rotor outlet conditions are unchanged during J intermediate time steps. However, increasing the NCIRC to decrease $\Delta t'$ will not help because it requires a finer grid and as a consequence Δt will decrease accordingly.

The number of time steps required for one full rotation is $J \times$ NCIRC. The nondimensional numerical time step to be used for the computations is:

$$\Delta t'' = \frac{\Delta t'}{J} = \frac{2\pi}{J \times \omega \times \text{NCIRC}} \tag{5}$$

Fourier analysis of the imposed pressure distortion and a parametric study of the impeller response, discussed in a later section, indicate that time variations should be correctly modeled only up to the fifth harmonic of the rotational frequency. The time step required for a time accurate calculation of the fifth harmonic is much larger than the one defined by Eq. (5) so that it does not result in any additional condition.

Acceleration Techniques. Convergence to a periodic solution can be accelerated by doubling the numerical domain. The phase-lagged boundary conditions are then applied to two blade passages defined by *ABCDHGFE*, Fig. 1. The solution on the line *KL* and *MN* will no longer depend on the results below that stagnation pseudo-streamline, obtained at previous rotation, but is now obtained from a calculation at the current rotation. As a consequence information related to the downstream pressure distortion spreads much faster over the calculation domain, which favors the convergence.

Convergence to a periodic solution of the single pitch and double pitch calculations is compared in Fig. 2. This shows the variation of the density in a fixed point in the flow field after each rotation when the rotor has returned to the same position. These values are constant when convergence has been reached. The density at the leading edge (diamonds and circles) and at the upstream boundary (triangles and squares) is shown. One can see that the double pitch calculations converge already after 15 rotations whereas the single pitch needs more than 40 rotations.

Another method to accelerate the convergence to a periodic solution is the use of grid refinement. This technique, which is also used to speed up the convergence in steady-state computations, is even more effective here. Computing the flow first on a coarse grid allows larger time steps, which promotes the spread of the distortion over the flow field. Having reached a satisfactory convergence level on the coarse grid, the solution is interpolated on the fine grid and the computations are continued until final convergence is reached. The aim of implementing this technique is not really to build a multigrid time accurate solver, but to achieve a cheap and faster propagation of the phase-lagged periodicity conditions.

Convergence obtained with this acceleration technique, is shown in Fig. 3. Six rotations are done using the coarse grid and the modified phase-lagged periodicity conditions. The solution is then interpolated on the fine grid, and six more rotations are computed. The time needed for the first six rotations on the coarse grid is negligible when compared to the fine grid one, and the convergence is reached more quickly than with the original method. The total CPU time needed using this method is essentially the time needed by the fine grid. It is reduced to about one third of its original value.

Validation

Except where specified differently, all calculations have been done on an impeller designed at the von Karman Institute (VKI impeller) with 20 blades at 40 deg backward lean angle. Computations are done using an *H*-grid having 86 points in the axial direction; 60 of them between leading and trailing edge, 15 points from hub to shroud, and 15 points from pressure to suction side.

An experimentally defined circumferential static pressure distribution (Sideris, 1988) corresponding to higher than optimum mass flow is specified as outflow boundary condition. The initial solution used for the time-accurate computations is the steady-state solution corresponding to a circumferentially uniform downstream static pressure.

The nondimensionalized static pressure variation calculated at different locations, is presented in Fig. 4 versus the number of rotations. These results are obtained for the VKI impeller at a rotational speed of 22,000 rpm, with 3360 time steps per rotation and corresponding to an acoustic Strouhal number Sr = 0.25. The upper curve shows the saw-tooth pressure profile imposed at the outflow boundary. The other three curves show the calculated static pressure variation at a blade trailing edge, leading edge, and at a point on the inflow boundary (located one blade pitch upstream), respectively. It can be seen that the amplitude of the computed variations gradually increases from the first to the fourth rotation and that full convergence to periodic flow is obtained after about eight rotations. This is due to the time needed for a perturbation to propagate from the outlet to the inlet and is a consequence of the way the phase-lagged periodicity conditions are implemented. Infor-

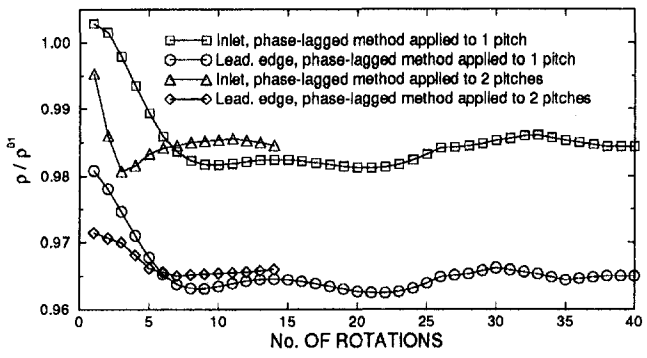

Fig. 2 Convergence history of the unsteady flow computations

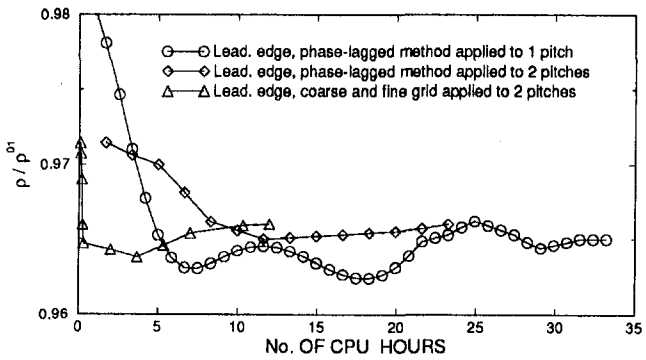

Fig. 3 Convergence history versus the computer time needed for convergence

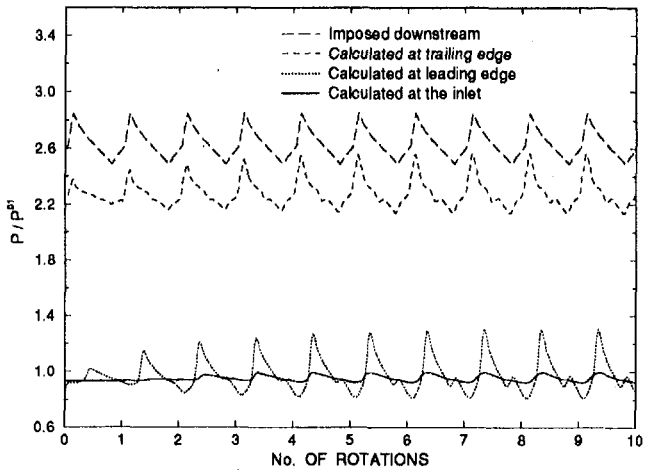

Fig. 4 Convergence history of the time accurate computations, Sr = 0.25

mation obtained at previous rotation is used when calculating the flow at the current one. Consequently, the results of the first rotation are partly influenced by the steady-state solution and it takes several rotations before the unsteady flow is fully established everywhere. The static pressure profiles at trailing and leading edge are distorted due to pressure wave reflections in the impeller.

The absence of any flow perturbation due to the upstream boundary condition has been verified by comparing the results obtained with the two upstream extensions of the calculation domain. The inflow boundary of the short domain is located one pitch upstream of the blade leading edge, whereas the long domain extends three pitches upstream. A sinusoidal static pressure profile with a 90 deg period is imposed on the downstream boundary of the backward leaned impeller. Variations of the nondimensional mass flow per blade channel are presented in Fig. 5. Results obtained with the short domain are indicated with smooth lines, whereas the results with the long domain are indicated by a crossed line.

One can see that, at the trailing edge, the shape of the mass flow variation is sinusoidal corresponding to the imposed sinusoidal static pressure profile. At the leading edge, the profile is asymmetric. This is due to the fact that the propagation velocity is higher at the high-pressure part of the wave (where the temperature and speed of sound are higher) than at the low-pressure part of the wave. As a consequence, the wave is distorted as it propagates through the blade channel with a more abrupt pressure rise. This results in a more abrupt decrease in local mass flow, as observed on Fig. 5.

A phase shift between the signal at the trailing edge, leading edge, and upstream position is also observed. This is due to the fact that a perturbation needs some time to travel through a blade channel of nonzero length, and because the leading edge of a given channel is not at the same circumferential position as the trailing edge.

Comparing the results of the short upstream domain (smooth lines) with the ones obtained with the long upstream domain (crossed lines) shows almost no influence of the location of the upstream boundary on the solution. One can conclude from this that the nonreflecting boundary conditions correctly simulate an infinite upstream channel, and are not responsible for the reduction in mass flow variation between the leading edge and inlet boundary. As will be shown later, this reduction is due to a redistribution of the fluid over the neighboring channels because of the circumferential nonuniformity of the pressure at the impeller inlet.

Results

Mach Number Distributions. The method has first been used to study the flow distortion in the VKI impeller operating at 22,000 rpm. The pressure distortion imposed at the outlet is the experimental one shown by the upper curve in Fig. 4. This condition corresponds to a Strouhal number of Sr = 0.25.

Figures 6–8 show the Mach number distribution on the shroud, mean and hub streamsurface during one rotation. One observes large variations in Mach number at different circumferential positions that are due to pressure waves traveling upstream and downstream.

The flow is choked at the shroud streamsurface for circumferential positions 0 deg $< \theta <$ 90 deg (Fig. 6). In this case the pressure waves, which propagate upstream, can only modify the extent of the supersonic flow by changing the position and strength of the shock. They cannot propagate up to the leading edge. At θ = 135 deg the shock has disappeared, and the flow field is subsonic also at the shroud. At higher values of θ, the flow progressively reaccelerates and choking appears again at θ = 270 deg, but for a shorter time. Although the imposed pressure distortion has only one maximum per rotation, one observes two maxima per rotation in the Mach number distribution, are one at 45 deg, the other at 270 deg. It seems that the pressure waves, reflected at leading edge, travel twice upstream and downstream during one rotation. This is in agreement with the value of the acoustic Strouhal number Sr = 0.25 which is half the one corresponding to resonance, as will be shown in a later section. Similar phenomena, but less pronounced occur at mean and hub streamsurfaces (Figs. 7, 8) where the flow is fully subsonic at all positions.

One also observes that the classical periodicity conditions (equal Mach number or pressure on suction and pressure side at the trailing edge) are no longer satisfied. This is due to the fact that one is plotting here the Mach number distributions on the pressure and suction sides of one channel and not on the same blade. It is made possible by the phase-lagged periodicity conditions.

Inlet and Outlet Flow Distortion. The circumferential variation of the mass averaged from hub to shroud relative flow angle (β_2), absolute flow angle (α_2), radial velocity (V_{R2}), and absolute tangential velocity ($V_{\theta 2}$) at R/R_2 = 1.028, are shown in Fig. 9. In the same figure, stars (*) represent a quasi-steady solution obtained by imposing the local value of the distorted pressure as back pressure in a three-dimensional steady flow calculation. The circumferential distance of 33 deg corresponds to the blade channel in front of the volute tongue.

Predictions based on the three-dimensional unsteady model show variations much larger than the ones predicted by the

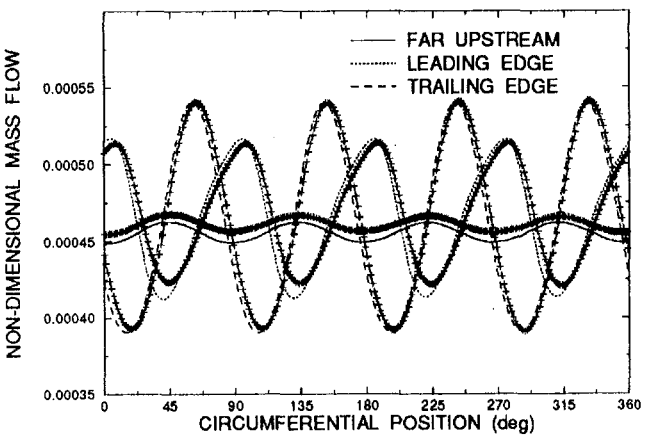

Fig. 5 Nondimensional mass flow within a blade channel during one rotation for different axial positions for short and long upstream domain

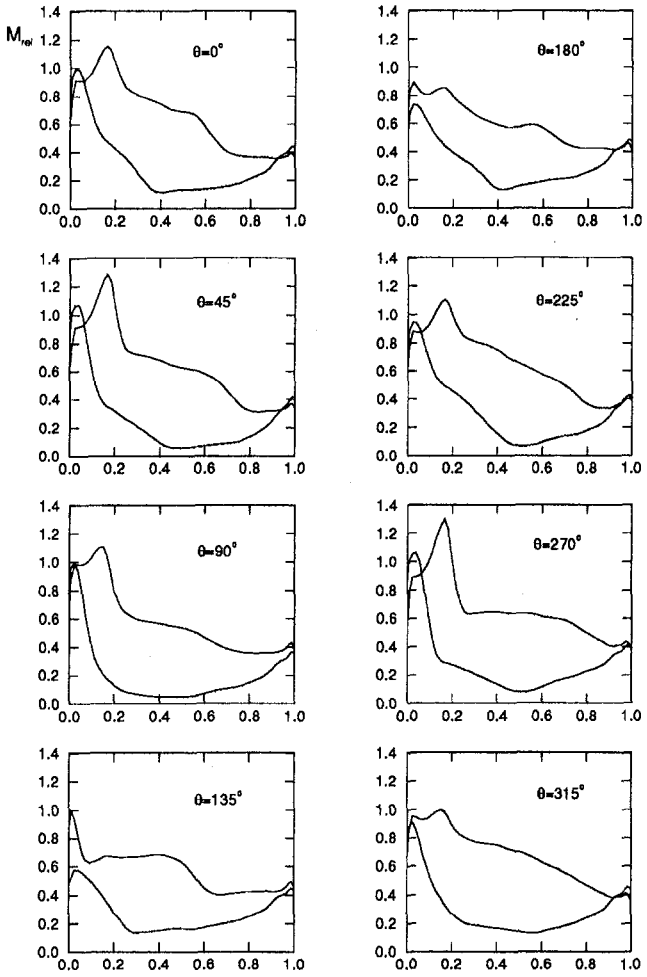

Fig. 6 Relative blade Mach number versus the blade length at shroud streamsurface during one rotation

quasi-steady computations. This indicates that, although the acoustic Strouhal number of this test case is relatively low, quasi-steady calculations cannot give reliable results. These results also make clear that the constant outlet relative flow angle assumption, generally used in one-dimensional models, is not correct.

The β_2 distribution in Fig. 9(a) shows a significant variation close to the tongue, due to a sudden increase of the static pressure at this position. A second peak occurs at 200 deg, where the imposed static pressure changes smoothly. This second distortion must therefore be attributed to the reflections of pressure waves in the impeller channels. The amplitude of the second pulse is smaller because of damping in the blade passage.

The other flow parameters also show a bimodal variation per rotation with larger amplitude than the quasi-steady results.

The circumferential variation of the mass-averaged β, α and of the nondimensional V_z, V_θ at leading edge is shown in Fig. 10. The circumferential position is again defined by the trailing edge location as in Fig. 9. In this way one can directly compare the flow conditions at the leading edge and at the trailing edge of a blade channel.

Although the shroud section is choked, one observes a slight increase in axial velocity for 0 deg $< \theta <$ 120 deg. This increase of mass flow is possible because it occurs simultaneously with a decrease in relative flow angle (Fig. 10(a)), resulting from an increased prerotation of an incoming flow (Fig. 10(d)). One should also keep in mind that the values shown are averaged over the blade height from hub to shroud. The axial velocity can still increase at the hub even when the shroud section is choked.

The sudden decrease of axial velocity at θ = 120 deg occurs when the impeller unchokes due to the upstream propagating static pressure waves. It is followed by a gradual increase of axial velocity up to the position where choking occurs again at θ = 270 deg. Large variations in the absolute and relative flow angle and absolute tangential velocity can be observed. The alternation in sign of the absolute tangential velocity corresponds to two counterrotating vortices upstream of the impeller where the total circulation has not yet changed. These findings are in agreement with the conclusions of Pfau (1967).

There is a 90 deg phase shift between the point where the downstream static pressure has a sudden increase and the point where the axial velocity at leading edge drops abruptly. This shift corresponds to the time needed by the pressure wave to travel from the outlet to the leading edge. One can conclude from this that there is no direct interaction between the high downstream static pressure and the high relative flow angle and incidence at θ = 33 deg.

Parametric Study

A parametric study has been made to find out how the impeller distortion changes with the acoustic Strouhal number. A sinusoidal static pressure profile with the same amplitude as the saw-tooth one has been specified at the downstream boundary for this purpose. The acoustic Strouhal number is changed by varying the number of sinusoidal waves around the impeller periphery.

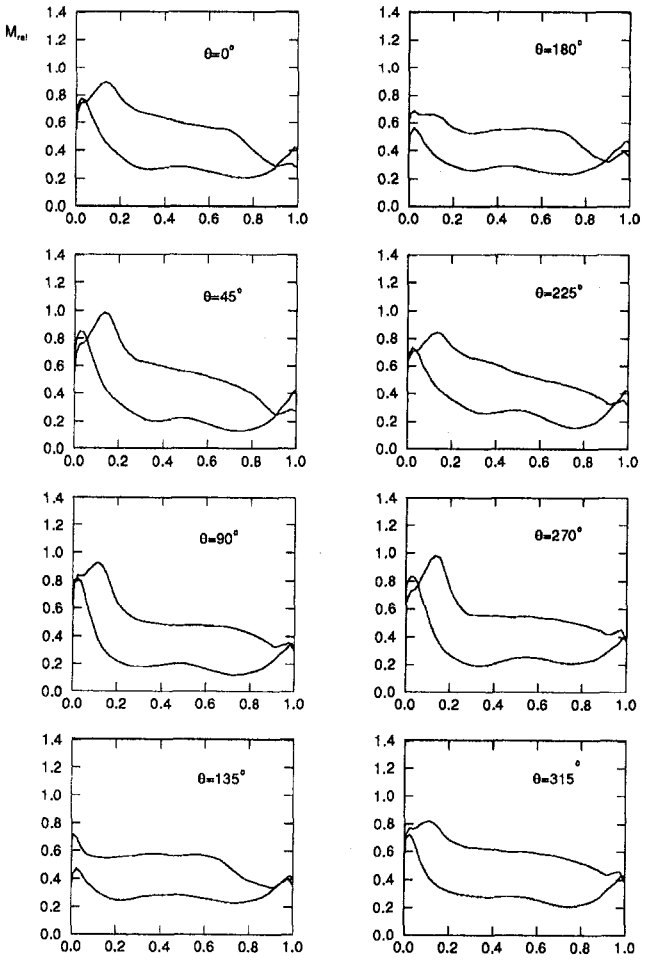

Fig. 7 Relative blade Mach number versus the blade length at mean streamsurface during one rotation

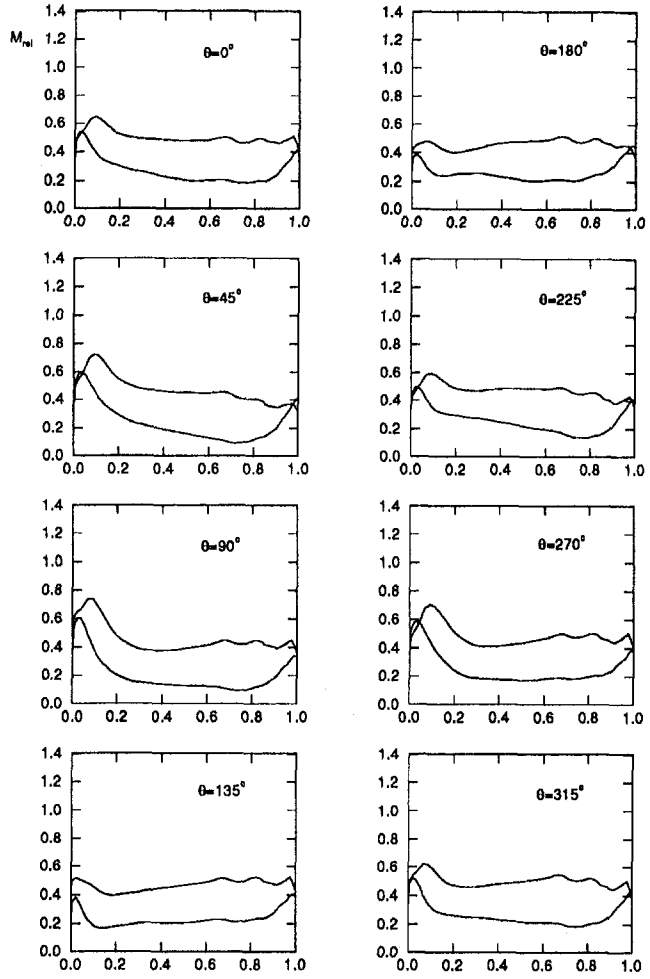

Fig. 8 Relative blade Mach number versus the blade length at hub streamsurface during one rotation

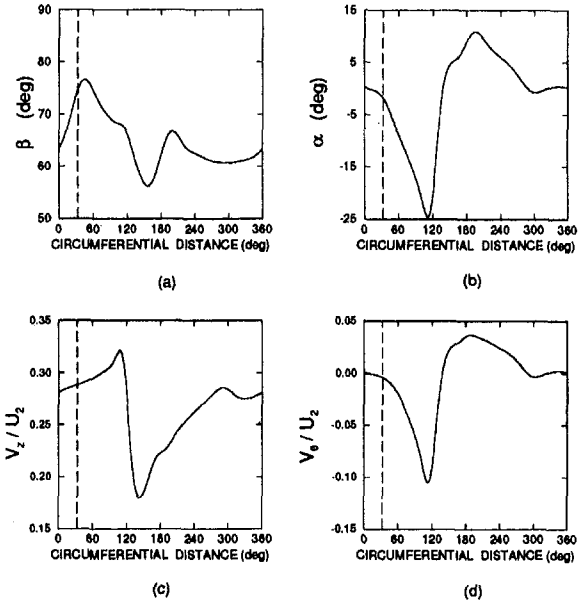

Fig. 10 Circumferential distribution of mass-averaged β, α, V_Z, V_θ at leading edge, Sr = 0.25 (- - - tongue position)

This study has been made for two different flow conditions. For each of them, a constant time step over the numerical domain given by Eq. (5) was used. The first one has fully subsonic flow inside the impeller rotating at 10,000 rpm. One wave per circumference perturbation corresponds to Sr = 0.1. The variation of $\Delta\beta_2$ at radius $R/R_2 = 1.028$ is shown in Fig. 11. A gradual increase in $\Delta\beta_2$ with Sr occurs up to the acoustic Strouhal number Sr = 0.5. This maximum is due to resonance of the pressure waves in the blade-to-blade channel and can be explained as follows. A compression wave at the downstream boundary propagates upstream where it is reflected at the leading edge and turns back as an expansion wave. It will reflect on the outlet as a compression wave of larger amplitude if this occurs in a time equal to the period of the perturbation. This is

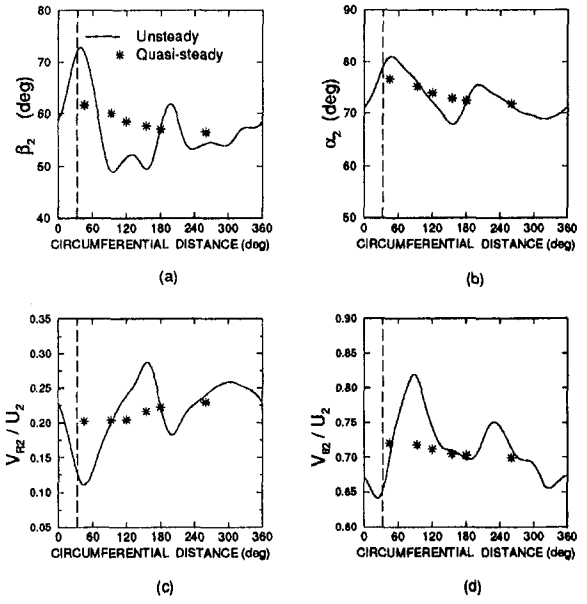

Fig. 9 Circumferential distribution of mass-averaged β_2, α_2, V_{R2}, $V_{\theta 2}$ at $R/R_2 = 1.028$, Sr = 0.25 (- - - tongue position)

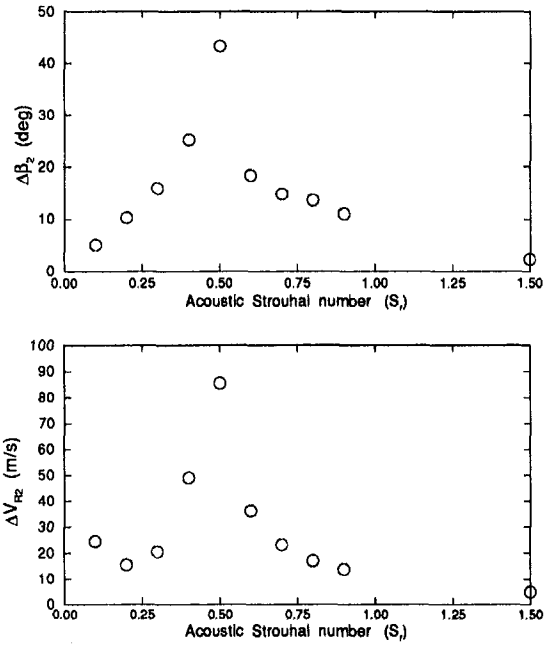

Fig. 11 Variation of amplitude $\Delta\beta_2$, ΔV_{R2} in function of the acoustic Strouhal number (Sr) for subsonic flow in the impeller

repeated at each period, and the amplitude of the perturbation increases until it is limited by the artificial dissipation term added in the equations. At higher or lower Strouhal numbers, the expansion waves returning to the outlet counteract the waves generated by the static pressure perturbation and the amplitude decreases. Similar observations are made for the variation of ΔV_{R2}.

A different distribution is observed at 22,000 rpm where the flow in the impeller is transonic, Fig. 12. The acoustic Strouhal number for one wave per circumferential perturbation is 0.25. The distribution of $\Delta\beta_2$ at the same radial position is completely different. One now observes two peaks in the $\Delta\beta_2$ and in the ΔV_{R2} distributions. They correspond to Sr = 0.5 and 1.0, respectively. Choked flow is observed for only these two Strouhal numbers.

The compression waves generated at the downstream boundary cannot travel along the whole blade channel because they cannot propagate upstream of the supersonic pocket. They are attenuated by a displacement of the shock, which results in much lower amplitudes for the $\Delta\beta_2$ and ΔV_{R2} variations. It is not clear why there is a second peak at Sr = 1.0 but it could be the result of a reduction of the effective length of the channel by the shock.

Computation of Forces

The circumferential variation of blade loading results in a different blade force at each circumferential position and as a consequence in a nonzero force on the shaft.

Two methods have been used to compute the forces and torques resulting from the outlet circumferential static pressure distortion. A Cartesian coordinate system is used to define the forces and torques acting on each individual blade and on the impeller shaft. The y axis is from the shaft center toward the volute tongue, and the x axis perpendicular to it.

The first method integrates the pressure over the impeller surface.

$$\vec{F} = \iint_{\vec{S}_{i,j,k}} P_{i,j,k} d\vec{S}_{i,j,k} \tag{6}$$

The total force acting on the impeller is obtained by adding the forces on all blades and the hub surface. In the case of a shrouded impeller the pressure on the inner and outer side of the shroud should also be integrated. The latter is not predicted by the Euler solver but can be obtained by a suitable model, e.g., the one proposed by Childs (1992).

The second method applies the momentum and pressure balance on a control volume which contains the space between the impeller inlet and outlet. The total force $\vec{F}$ is given by:

$$\vec{F}_{\Delta MR} + \vec{F}_{\Delta M\theta} + \vec{F}_P = \vec{F} \tag{7}$$

where $\vec{F}_P$ is the static pressure forces at inlet and outlet, and $\vec{F}_{\Delta MR}$, $\vec{F}_{\Delta M\theta}$ are the forces due to the change of radial and tangential momentum. Written in summation form, the previous equation is:

$$\left(\sum_k \sum_j \rho \vec{V} \vec{S} \vec{V}_R\right)_{\text{out}} - \left(\sum_k \sum_j \rho \vec{V} \vec{S} \vec{V}_R\right)_{\text{in}} + \left(\sum_k \sum_j \rho \vec{V} \vec{S} \vec{V}_\theta\right)_{\text{out}} - \left(\sum_k \sum_j \rho \vec{V} \vec{S} \vec{V}_\theta\right)_{\text{in}} + \left(\sum_k \sum_j P \vec{S}\right)_{\text{out}} - \left(\sum_k \sum_j P \vec{S}\right)_{\text{in}} = \vec{F} \tag{8}$$

The indices j, k run from suction to pressure side, and from hub to shroud, respectively.

This method computes the total force acting on the impeller, and not on a single blade because the momentum balance gives the forces acting on the whole channel and not on each surface.

The flow velocity and static pressure at each circumferential position are obtained from the computation of the unsteady flow field at a given impeller position.

Both methods predict different forces when applied to the same geometry using the results obtained with a coarse grid ($43 \times 11 \times 11$ points). Repeating both calculations on a finer grid ($86 \times 15 \times 15$) shows almost identical results, which are close to the ones obtained from the pressure integration method on a coarse grid. One can conclude from this that the momentum balance method is more sensitive to the grid density than the pressure integration method.

Although the momentum balance method does not allow the calculation of forces on individual blades, it allows the evaluation of the individual contributions to the radial force. This is important in the context of an experimental definition of the radial forces in function of the flow quantities at the impeller inlet and outlet. It can answer the question of whether it is sufficient to integrate the static pressure distortion over the impeller outlet circumference or should one also account for the variation in radial and tangential velocity.

In order to evaluate the dependence of the forces on the impeller geometry, calculations have been done on both the VKI impeller, described previously, and the Eckardt "O" type impeller with 20 radial ending blades. The latter rotates at 14,000 rpm and calculations are made with the same number of grid points as for the VKI impeller. The contributions to the total force, divided by the impeller outlet section, are shown in Fig. 13. The direction of the total force is typical for higher than optimal mass flow operations, and is confirmed by many experimental observations (i.e., Iversen et al., 1960; Meier-Grotian, 1972).

Results of the backward-leaned impeller are shown by full lines and show that the largest contribution is from the circumferentially nonuniform outlet static pressure distribution. The force component due to nonuniform outlet radial momentum is in the opposite direction and is much smaller. The contribution of the inlet tangential momentum, which is also small, is due to the nonzero absolute tangential velocity at leading edge, and is nearly perpendicular to the other ones. The remaining contributions are less significant.

The dashed lines give the force components for the Eckardt "O" impeller with radial ending blades. Pressure force is al-

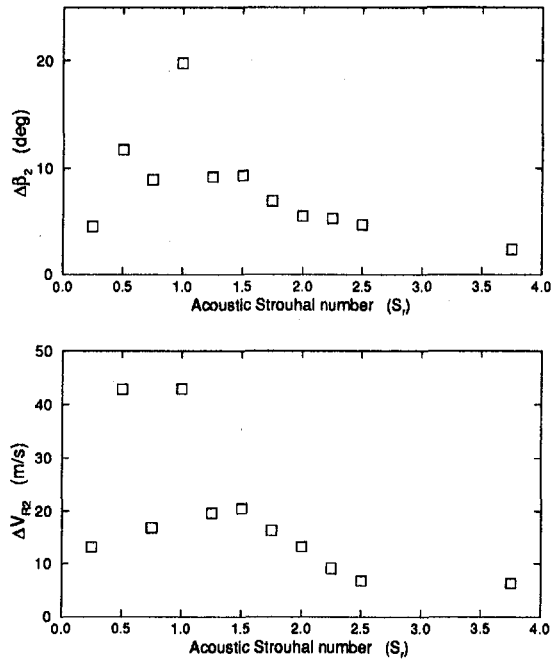

Fig. 12 Variation of amplitude $\Delta\beta_2$, ΔV_{R2} in function of the acoustic Strouhal number (Sr) for transonic flow in the impeller

most totally compensated by the force due to radial momentum at the outlet, so that the total force is much smaller than for the VKI impeller. The contribution of the nonuniform tangential momentum at the outlet is also nonnegligible.

The different contributions to the radial forces by the radial momentum in a radial ending and backward leaned impeller can be explained as follows. The increase or decrease of the relative velocity is due to the disequilibrium between the pressure rise by the impeller and the imposed outlet pressure. In case of a backward-leaned impeller, any increase in relative velocity immediately involves a decrease of tangential velocity and as a consequence a decrease in pressure rise. As a result the disequilibrium is smaller and the velocity changes are smaller. This kind of corrective action results in a smaller change in radial velocity. The change in radial momentum that is proportional to V_R^2 and the resulting radial force is smaller.

The pressure rise in radial ending impellers is nearly independent of the radial velocity because it does not involve a change in V_θ, so that the radial velocity and radial momentum change is larger.

The different contributions of the tangential momentum at the impeller outlet can also be explained by means of Fig. 14. The increase in radial velocity, due to the circumferential decrease in static pressure, results in a decrease of the tangential velocity for backward-leaned blades, as indicated on Fig. 14(*a*). As a consequence, the product $\rho \cdot V_{m2} \cdot S \cdot V_{\theta 2}$ is almost constant along the periphery. The contribution of the tangential momentum to the radial force is thus negligible.

In case of radial ending blades, an increase in mass flow does not alter the tangential component of the absolute velocity $V_{\theta 2}$ (dotted line velocity triangle in Fig. 14(*b*)). The product $\rho \cdot V_{m2} \cdot S \cdot V_{\theta 2}$ is not constant along the periphery because only V_{m2} has changed. The outlet tangential momentum is therefore not uniform circumferentially, resulting in a significant component to the radial force.

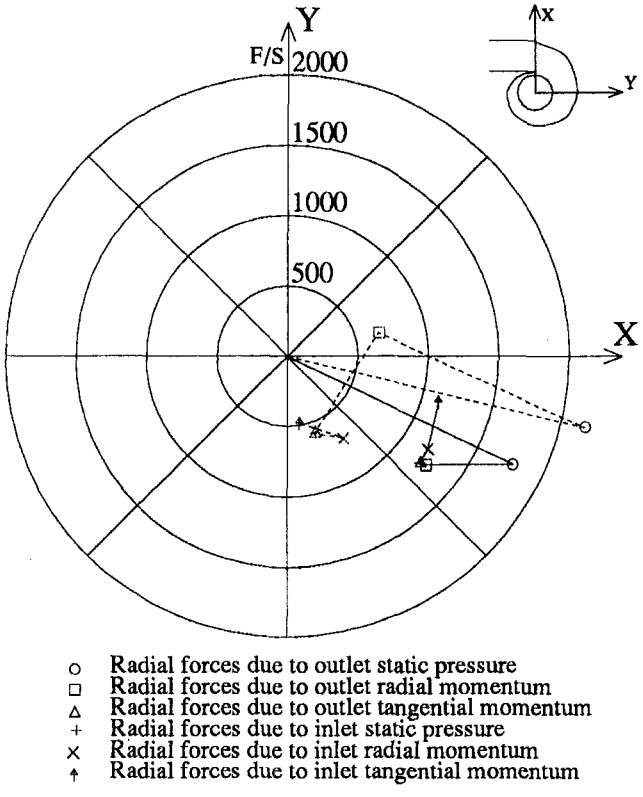

Fig. 13 Components of radial force in impeller with backward leaned (continuous lines), and radial ending blades (dashed lines)

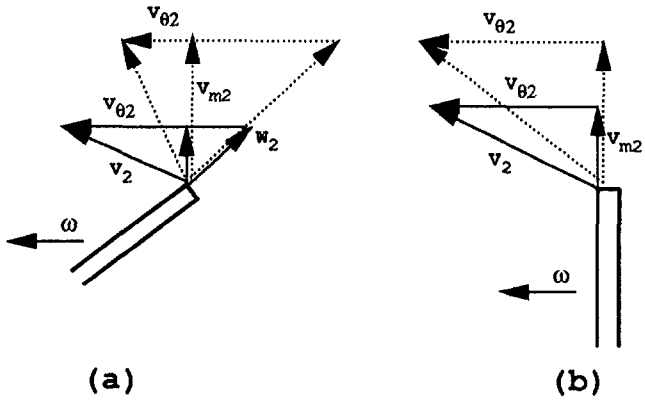

Fig. 14 Difference in tangential momentum distribution between impeller with (*a*) backward leaned blades, and (*b*) radial ending blades

Conclusions

The three-dimensional unsteady Euler calculations give valuable information about unsteady flows in impellers at affordable computer time and cost, especially when the appropriate acceleration techniques are implemented.

It has been shown that the nonreflecting upstream boundary conditions correctly simulate transparent walls to the incident pressure waves, and that their location does not affect the solution.

Calculations of the blade Mach number distribution in the impeller show that the flow unsteadiness is governed by pressure wave propagation in the blade to blade channels.

The variation of the impeller outlet flow is much larger than that obtained from quasi-steady calculations. The latter are applicable only in cases of very low Strouhal numbers.

The assumption of constant outlet relative flow angle used in many existing one-dimensional models is incorrect at Strouhal numbers greater that 0.1.

The flow perturbation extends upstream of the impeller. Two counterrotating vortices divide the inlet into a region of large and a region of lower average incidence.

Forces on the impeller shaft resulting from the downstream static pressure distortion are strongly dependent on the impeller geometry. They are much smaller for radial ending blades than for impellers with backward-leaned blades.

Integration of the static pressure at the impeller outlet section does give a good approximation of the total radial force on the impeller for backward-leaned blades. It is completely wrong for radial ending blades where the variation in radial momentum compensates the pressure forces.

Future development could be the coupling of the unsteady impeller flow calculation with a volute flow calculation, such as the one by Ayder (1993), to obtain a full-stage prediction program.

Acknowledgments

The authors gratefully acknowledge the computer time on a CRAY Y-MP2E/116 provided under contract No. IT/SC/33 by the Belgian Federal Services for Science Policy, Technical, and Cultural Affairs.

References

Ayder, E., 1993, "Experimental and Numerical Analysis of the Flow in Centrifugal Compressor and Pump Volutes," Ph.D. thesis RUG-VKI, Apr.

Badie, R., Jonker, J. B., and van Essen, T. G., 1992, "Calculations on the Time-Dependent Potential Flow in a Centrifugal Pump," ASME Paper No. 92-GT-151.

Childs, D. W., 1992, "Pressure Oscillation in the Leakage Annulus Between a Shrouded Impeller and Its Housing Due to Impeller-Discharge-Pressure Disturbances," ASME *Journal of Fluids Engineering*, Vol. 114, pp. 61–67.

Croba, D., 1992, "Modélisation de l'écoulement instationnaire dans les pompes centrifuges. Interaction roue-volute," Ph.D. thesis, Institut National Polytechnique de Grenoble.

Eckardt, D., 1976, "Detailed Flow Investigations Within a High-Speed Centrifugal Compressor Impeller," ASME *Journal of Fluids Engineering,* Vol. 98, pp. 390–402.

Erdos, J. I., and Alzner, E., 1977, "Computation of Unsteady Transonic Flows Through Rotating and Stationary Cascades," NASA CR 2900.

Fatsis, A., 1993, "Three Dimensional Unsteady Flow Calculations in Radial Components," presented at VKI LS 1993-01 "Spacecraft Propulsion."

Fatsis, A., and Van den Braembussche, R., 1994, "Evaluation of an Euler Code With Non-reflecting Boundary Conditions for the Analysis of 3D Flow in Radial Impellers," ASME Paper No. 94-GT-147.

Iversen, H., Rolling, R., and Carlson, J., 1960, "Volute Pressure Distribution, Radial Force on the Impeller, and Volute Mixing Losses of a Radial Flow Centrifugal Pump," ASME *Journal of Engineering for Power,* Vol. 82, No. 1, pp. 136–144.

Jameson, A., Schmidt, M., and Turkel, E., 1981, "Numerical Solutions of the Euler Equations by Finite Volume Methods Using Runge–Kutta Time Stepping Schemes," AIAA Paper No. 81-1259.

Lorett, J. A., and Gopalakrishnan, S., 1986, "Interaction Between Impeller and Volute of Pumps at Off Design Conditions," ASME *Journal of Fluids Engineering,* Vol. 108, No. 1, pp. 12–18.

Meier-Grotian, J., 1972, "Untersuchungen der radialkraft auf das laufrad einer Kreiselpumpe bei verschiedenen Spiralgehauseformen," Ph.D. thesis, T. U. Braunschweig, Germany.

Morfiadakis, E. E., Voutsinas, S. G., and Papantonis, D. E., 1991, "Unsteady Flow Calculation in a Radial Flow Centrifugal Pump With Spiral Casing," *International Journal of Numerical Methods in Fluids,* Vol. 12, pp. 895–908.

Pfau, H., 1967, "Temperaturmessungen zur Stroemungsuntersuchung, insbesondere an Radialverdichtern," *Konstruktion,* Vol. 12, pp. 478–484.

Pierret, S., 1994, "Unsteady Flow in Centrifugal Impellers. Parametric Study by Means of an Euler Solver," VKI Project Report 1994-16.

Sideris, M., 1988, "Circumferential Distortion of the Flow in Centrifugal Compressors Due to Outlet Volutes," Ph.D. Thesis, RUG-VKI, Belgium, Apr.

Uchida, H., Inayoshi, M., and Sugiyama, K., 1987, "Effect of a Circumferential Static Pressure Distortion on Small-Sized Centrifugal Compressor Performance," presented at the International Gas Turbine Congress held in Tokyo, Japan, Oct. 26–31.

Design and Flow Field Calculations for Transonic and Supersonic Radial Inflow Turbine Guide Vanes

A. W. Reichert
Siemens AG,
Power Generation (KWU),
Gas Turbine Technology,
45473 Mülheim, Federal Republic of Germany

H. Simon
Institute of Turbomachinery,
University of Duisburg,
47048 Duisburg, Federal Republic of Germany

The design of radial inflow turbine guide vanes depends very much on the discharge conditions desired, especially if the choking mass flow is reached. Because of the choking mass flow condition and supersonic discharge Mach numbers, an inverse design procedure based on the method of characteristics is presented. Various designs corresponding to different discharge Mach numbers are shown. Viscous and inviscid flow field calculations for varying discharge conditions show the properties of the guide vanes at design and off-design conditions. In a previous paper (Reichert and Simon, 1994), an optimized design for transonic discharge conditions has been published. In the present paper, additional results concerning the optimum design are presented. For this optimum design an advantageous adjusting mechanism for a variable geometry guide vane has been developed. The effect of guide vane adjustment on the discharge conditions has been investigated using viscous flow field calculations.

Introduction

To provide more understanding of the flow through radial inflow turbines and give improved recommendations for design parameters, an investigation was instigated at the University of Duisburg. During the first stage of the project, a code was written to simulate the turbine flow field realistically. In the next stage, the flow through the guide vanes has been investigated by numerical simulations. Generally applicable parameters have been developed and their influence has been investigated. The study was started by neglecting the flow viscosity and the heat conduction. Promising results have been presented last year (Reichert and Simon, 1994).

The results presented are limited to operating conditions characterized by a mass flow less than the choking mass flow. If a higher specific work is projected, operating conditions with choking mass flow are needed. For these operating conditions, the guide vanes have to be shaped very carefully to prevent additional losses due to shocks and to gain uniform rotor inlet conditions. To attain these aims, an inverse design method based on the theory of characteristics has been developed. Guide vanes, which are designed using this method, are presented in this paper.

As regards operating conditions for guide vanes with a mass flow below the critical one, the investigations have been extended to the influence of the flow viscosity and the heat conduction. As a result, the influence of some design parameters on the loss coefficient has been evaluated. Furthermore, the investigations are extended to three-dimensional flow field calculations.

Numerical Schemes

Governing Equations. The flow of a perfect gas in an arbitrary domain may be described by conservation equations for the physical quantities specific momentum $\rho\mathbf{v}$, specific mass ρ, and specific total internal energy u_t, all quantities related to volume. For simplicity, these conservative variables are combined in a vector $\mathbf{u}$. One can find the conservation law for this vector in a fixed domain V with the surface S to be

$$\frac{\partial}{\partial t}\int_V \mathbf{u}dV + \oint_S \mathbf{F}^I ds = \oint_S \mathbf{F}^V ds. \tag{1}$$

In these equations, the flux tensors $\mathbf{F}^I$ and $\mathbf{F}^V$ are introduced, describing the convective ($\mathbf{F}^I$) and diffusive ($\mathbf{F}^V$) transport of the conservative variables. The flux tensors connect the three-dimensional physical space with the five-dimensional vector space of the vector $\mathbf{u}$, which contains the physical one as a subspace. For inviscid flow, the components of the tensor $\mathbf{F}^V$ are equal to zero and Eq. (1) becomes the Euler equation. The flux tensor of the inviscid flow $\mathbf{F}^I$ depends on the vector $\mathbf{u}$ only, because the tensor $\mathbf{F}^V$ mainly depends on **grad u**. These dependencies are described by the equations

$$\mathbf{u} = \begin{bmatrix} \rho\mathbf{v} \\ \rho \\ u_t \end{bmatrix}, \tag{2}$$

$$\mathbf{F}^I = \mathbf{u}\bigcirc\mathbf{v} + p\begin{bmatrix} \mathbf{E} \\ \mathbf{0} \\ \mathbf{v} \end{bmatrix} \quad p = (\kappa - 1)\left[u_t - \frac{\rho}{2}\mathbf{vv}\right], \tag{3}$$

$$\mathbf{F}^V = \begin{bmatrix} \mathbf{T} \\ \mathbf{0} \\ \mathbf{Tv} - \mathbf{q} \end{bmatrix}, \tag{4}$$

$$\mathbf{T} = \eta(\mathbf{grad}\ \mathbf{v} + \mathbf{grad}^T\ \mathbf{v} - \tfrac{2}{3}\,\mathrm{div}\ \mathbf{vE}), \tag{5}$$

$$\mathbf{q} = -\lambda\mathbf{grad}T. \tag{6}$$

In these equations, $\mathbf{v}$ denotes the velocity vector, p the static pressure, T the static temperature, κ the specific heat capacity ratio, η the viscosity, λ the molecular heat conductivity, and $\mathbf{E}$ is the unit tensor. The operator $\bigcirc$ declares the dyadic product, while the scalar product is not declared especially.

In calculations with negligible gradients of the flow quantities in one direction, a calculation in only two dimensions is possible. Equation (1) changes slightly in these cases, as the dimen-

Contributed by the International Gas Turbine Institute and presented at the 40th International Gas Turbine and Aeroengine Congress and Exhibition, Houston, Texas, June 5–8, 1995. Manuscript received by the International Gas Turbine Institute February 11, 1995. Paper No. 95-GT-97. Associate Technical Editor: C. J. Russo.

sions of the two vector spaces are reduced by one. The control volume V becomes a control area A and the control volume surface S becomes a closed loop L. If the geometry of the flow channel does not possess a constant width w in the neglected third direction, additional terms have to be added to consider the change of the cross sections. The resulting quasi three-dimensional form of Eq. (1) looks like

$$\frac{\partial}{\partial t}\int_A w\mathbf{u}dA + \oint_L w\mathbf{F}^I d\mathbf{l} = \oint_L w\mathbf{F}^V d\mathbf{l} + \int_A \mathbf{F}_D \,\mathbf{grad}\, w dA, \quad (7)$$

with:

$$\mathbf{F}_D = (p - \tau_3^3)\begin{bmatrix}\mathbf{E}\\ \mathbf{0}\\ \mathbf{0}\end{bmatrix}, \quad (8)$$

$$\tau_3^3 = \eta\left[\frac{2}{w}\mathbf{v}\,\mathbf{grad}\, w - \tfrac{2}{3}\,\mathrm{div}\,\mathbf{v}\right]. \quad (9)$$

Method of Characteristics

Basic Method. The basic method of characteristics is well known and described in detail by Shapiro (1953). The method is based on the Euler equation derived for a plane flow field with constant total temperature and pressure and written as a differential equation in two dimensions for a potential Φ, which is defined by the equation $\mathbf{grad}\,\Phi = \mathbf{v}$. Adding two differential equations for the total derivatives of the potential Φ, one gets a system of differential equations. Four differential equations, two for the change of flow quantities along characteristics and two for the slope of the characteristics itself, can be derived under the condition of a shock-free supersonic flow from that system of equations.

Discretizing these equations, an iterative solution method for supersonic isentropic flows can be found. The basic iteration of that method starts from two points of known state. Assuming locally straight running characteristics, a third point connected to both other points by one characteristic can be calculated from the discretized set of differential equations; see Fig. 1.

Inverse Algorithm. In Fig. 1, the iterative approach of the inverse algorithm is depicted in contrast to the basic method. The flow of information along one of the two types (left-/right-running) of characteristics, is inverted. Starting from a given state (e.g., the outflow conditions) the states of that one characteristic are calculated against the flow direction. In contrast to the basic method, no boundary conditions are applied to this algorithm. The unknown profile contour is calculated via a mass flow integration.

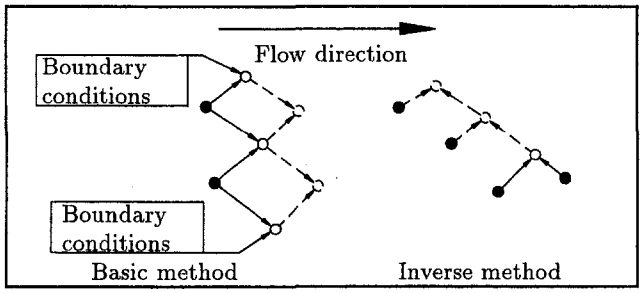

Fig. 1 Iterative approach in the basic and inverse method of characteristics

Navier–Stokes Scheme

Discretization Method. Dividing the surface S of the control volume V into a finite number of planes, given by their normal vectors $\mathbf{s}^i$, and using proper averages for the flux tensor $\mathbf{F}$ in the planes and for the unknown vector $\mathbf{u}$ in the domain, Eq. (1) becomes

$$\frac{\partial \mathbf{u}}{\partial t} = -\frac{1}{V}\sum_i \mathbf{F}\mathbf{s}^i, \quad \mathbf{F} = \mathbf{F}^I - \mathbf{F}^V \quad (10)$$

To implement Eq. (10) into a numerical scheme, an assumption has to be made: Since there is only one set of equations to determine the averages of the unknown values (at the domain center), the mean value of the flux tensor at the surface has to be assumed by an interpolation procedure. To indicate the assumption which is made, the flux tensor determined at the domain surface shall be called numerical flux tensor $\mathbf{F}^N$.

Introducing a unit vector $\mathbf{g}^i$ with the same direction as the plane normal-vector $\mathbf{s}^i$, one can define the product with the flux tensor

$$\mathbf{f}^{iN} = \mathbf{F}^N\mathbf{g}^i, \quad (11)$$

which is called flux vector or numerical flux function. Using the norm s^i of the plane vector $\mathbf{s}^i$, Eq. (10) becomes:

Nomenclature

$\dot{a}$ = physical quantity in general, local velocity of sound
A = area
$\mathbf{A}^{\pm}$ = flux Jacobians with eigenvalues of positive/negative sign
b = cross-sectional width
c = velocity component
$\mathbf{E}$ = unit tensor
$\mathbf{F}$ = flux tensor
$\mathbf{f}^i$ = flux vector
$\mathbf{g}$ = base vector
L = closed integration path
$\mathbf{l}$ = line normal vector
p = static pressure
$\mathbf{q}$ = heat flux vector
r = radius
R = gas constant
S = surface
$\mathbf{s}$, s = surface normal vector, its norm
t = time
T = temperature
$\mathbf{T}$, τ = stress tensor, its component
u_t = specific total energy related to volume
$\mathbf{u}$, u = state vector, component
$\mathbf{v}$ = velocity vector
V = volume
w = control volume width orthogonal to computational plane
α = flow angle
γ = blade angle
ζ = loss coefficient = $1 - p_t/p_{t_{in}}$
κ = ratio of specific heat capacities
λ = molecular heat conductivity
λ_c = eigenvalue of flux Jacobian
ρ = density
Φ = potential

Superscripts

i = contravariant component
I = inviscid
k = iteration index
N = numerical
V = viscous
$\hat{\alpha}$ = contravariant characteristic component
$\pm$ = states interpolated from right/left direction
$*$ = intermediate state

Subscripts

0 = guide vane inlet
1 = rotor inlet
g = state at the throat
L/R = states from left/right control volume
u = circumferential component, derivative with respect to u
$\hat{\alpha}$ = covariant characteristic component

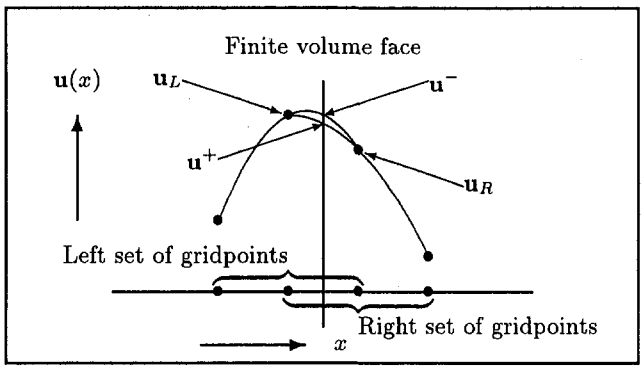

Fig. 2 Definition of states used in the flux calculation

$$\frac{\partial \mathbf{u}}{\partial t} = -\frac{1}{V}\sum_i \mathbf{f}^{iN} s^i. \tag{12}$$

This is a general finite volume formulation of the Navier–Stokes Eq. (1). The accuracy of Eq. (12) depends on the evaluation method for the flux vector. The authors have developed a new method, picking up elements from Roe's (1981) and Osher and Solomon's (1982) scheme, which shall be described briefly.

The numerical flux vector is calculated according to the State Difference Splitting technique, using an intermediate state $\mathbf{u}^*$:

$$\mathbf{f}^{iN} = \mathbf{F}^I(\mathbf{u}^*)\mathbf{g}^i - \mathbf{F}^V\mathbf{g}^i. \tag{13}$$

This technique is used by Osher and Solomon (1982) and differs from the flux difference splitting technique, which is used in Roe's scheme, where an intermediate flux vector is calculated.

The intermediate state $\mathbf{u}^*$ is calculated from the two states $\mathbf{u}^+$ and $\mathbf{u}^-$, which are interpolated from two different sets of gridpoints (Fig. 2). The interpolation is done using the van Albada et al. (1982) limiter or a polynomial fitting. It is carried out in characteristic variables $u_{\hat{\alpha}}$, which are those components of the vector $\mathbf{u}$, to which known propagation speeds $\lambda_c(\hat{\alpha})$ can be related. They are generated by a proper choice of base vectors $\mathbf{g}_{\hat{\alpha}}$ and $\mathbf{g}^{\hat{\alpha}}$. These base vectors and the propagation speeds $\lambda_c(\hat{\alpha})$ are evaluated using the density-weighted average proposed by Roe (1981).

Since the linear transformation to characteristic variables is only applicable to differences, the left cell values (L) are chosen as a reference state at each cell face. Using the abbreviation $s = \frac{1}{2} - \lambda_c(\hat{\alpha})/\Delta\lambda_c(\hat{\alpha})$, the complete algorithm becomes:

$$\mathbf{u}^* = \mathbf{u}_L + \sum_{\hat{\alpha}} \Delta u_{\hat{\alpha}} \mathbf{g}^{\hat{\alpha}}; \tag{14}$$

$$\Delta u_{\hat{\alpha}} = \begin{cases} (\mathbf{u}^- - \mathbf{u}_L)\mathbf{g}_{\hat{\alpha}} + \min(1, \max(0, s)) \\ \quad \times (\mathbf{u}^+ - \mathbf{u}^-)\mathbf{g}_{\hat{\alpha}} \quad \text{for} \quad \Delta\lambda_c(\hat{\alpha}) > 0 \\ (\mathbf{u}^- - \mathbf{u}_L)\mathbf{g}_{\hat{\alpha}} \quad \text{else for} \quad \lambda_c(\hat{\alpha}) > 0 \\ (\mathbf{u}^+ - \mathbf{u}_L)\mathbf{g}_{\hat{\alpha}} \quad \text{else for} \quad \lambda_c(\hat{\alpha}) \le 0 \end{cases} \tag{15}$$

$$\Delta\lambda_c(\hat{\alpha}) = \frac{\partial\lambda_c(\hat{\alpha})}{\partial \mathbf{u}_{\hat{\alpha}}}[\mathbf{u}^+ - \mathbf{u}^-]_{\hat{\alpha}}. \tag{16}$$

This is a highly accurate difference splitting method, preventing unphysical solutions as known from Roe's scheme (Harten and Hyman, 1983) but using its simple algebra for the difference split.

The components of the stress tensor $\mathbf{T}$, which are needed to calculate the components of the flux vector $\mathbf{F}^V\mathbf{g}^i$, are discretized using central differences. The influence of turbulence is modeled by the use of the well-known algebraic turbulence model proposed by Baldwin and Lomax (1978).

Iterative Method. In the investigation, only steady-state solutions are considered. For high convergence rates, an implicit Newton–Raphson-like iterative method is used (Rai and Chakravarthy, 1986). According to this method, Eq. (12) is rewritten:

$$\frac{1}{\Delta t}\Delta\mathbf{u}^{k+1} + \frac{1}{V}\sum_i [(\mathbf{A}^+\Delta\mathbf{u}^{k+1})_L + (\mathbf{A}^-\Delta\mathbf{u}^{k+1})_R]\mathbf{s}^i = -\frac{1}{V}\sum_i (\mathbf{f}^{iN})^k s^i. \tag{17}$$

The split flux Jacobians $\mathbf{A}^{\pm} = \mathbf{grad}_u \mathbf{F}^{\pm}$ are evaluated using "first-order" Roe flux difference splitting. The indices L and R denote values from the left (L) and right (R) cells sharing the surface $\mathbf{s}^i$. The different treatment of the discrete operators on the left and right sides of Eq. (17) allows the use of a very accurate solution method combined with a low effort implicit operator. On the other hand, the method results in a mild restraint on the time step size, which is locally calculated using a constant Courant number.

At the boundaries, either the prescription of a physical quantity or the extrapolation of this quantity from the interior to the boundary is needed. The physical quantity can be chosen from a large variety of quantities, including characteristic components for nonreflecting boundary conditions. All boundary conditions have the form

$$a(\mathbf{u}) = a_{\text{target}}, \tag{18}$$

with a being the physical quantity or its extrapolation function. To keep the convergence rate high, this equation is implemented to the iterative method in a Newton–Raphson formulation.

$$(\mathbf{grad}_u a)^k \Delta\mathbf{u}^{k+1} = a_{\text{target}} - a^k \tag{19}$$

Guide Vane Design

General Design Principles. The guide vanes of radial turbines build a flow channel, which may be divided into two sections, upstream and downstream of the throat. In the channel section, upstream of the throat the main acceleration and turning of the flow take place. To reduce the turbine size and the manufacturing costs, this section of the flow channel should be designed to be as short as possible. To prevent the appearance of pronounced velocity maxima, resulting in adverse pressure gradients at the suction side downstream of the throat, care has to be taken. These velocity maxima may introduce supersonic regions into the flow field, terminated by shocks, because the adverse pressure gradient has a negative influence on the boundary layer at the suction side.

To prevent such velocity maxima at the suction side, the surface curvature should be controlled by the surface velocity outside the boundary layer. The curvature should be low at places of high velocity and vice versa. The flow acceleration in the channel formed by the guide vanes results, in combination with this design principle, in a continuous reduction of the suction side curvature starting from the leading edge radius. A construction method for such a suction side geometry is shown in Fig. 3.

Having chosen a shape for the section of the suction side upstream of the throat, the flow channel is formed by the design of the pressure side. As shown in Fig. 4, there are different design principles concerning the shape of the channel at the throat. At that section, the contours of suction and pressure side may be parallel or converging, curved or almost straight. By choosing a combination of these items, one can control the velocity gradient in the throat and the location of the velocity maximum at the suction side.

A curvature of pressure and suction side at the throat produces a velocity gradient in this section. This velocity gradient de-

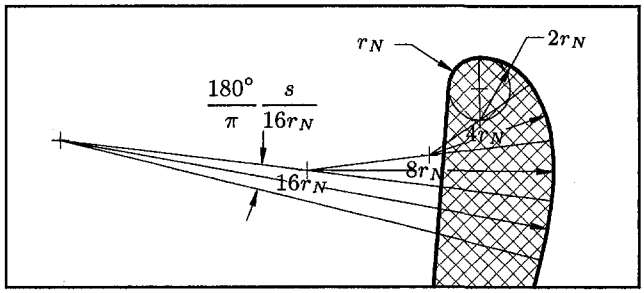

Fig. 3 Construction of the front of the suction side (radii ratio = 2, $s = 2r_N$)

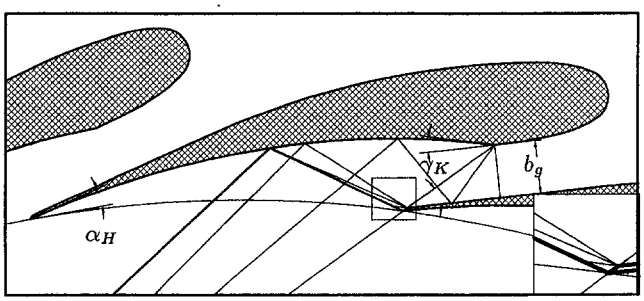

Fig. 5 Design of guide vanes operating with supercritical pressure ratio

creases the pressure at the suction side and increases the pressure at the pressure side near the trailing edge. A higher pressure at the trailing edge decreases the losses generated in the wake flow. On the other hand, the pressure drop at the suction side together with the pressure rise at the trailing edge produces an increase of the boundary layer thickness at the suction side. This effect is superimposed on the effect that has already been described and may result in an overall rise of the wake losses. Furthermore, a supersonic region with additional losses due to shocks may occur at the suction side. To avoid this supersonic region, guide vanes operating near the critical pressure ratio should be designed to be almost straight at the throat.

Increasing the convergence of the contours of the pressure and suction sides, one can shift the velocity maximum at the suction side downstream. In this way the maximum velocity is increased. These aspects will be discussed by using an example in a following section.

The shape of the suction side downstream the throat depends to a great extend on the operating conditions of the guide vanes. Operating conditions characterized by a choking mass flow, supercritical pressure ratio, and supersonic outflow result in a converging–diverging channel shape with a severe curvature of the suction side downstream of the throat. On the other hand, this section of the suction side should be only slightly curved if the pressure ratio of the guide vanes remains subcritical.

Supercritical Pressure Ratio

Design Principles. The proposed design for guide vanes operating at supercritical pressure ratio is depicted in Fig. 5. The contours of the suction and pressure sides at the throat run nearly parallel and uncurved to obtain a straight sonic line. Downstream of the throat the suction side continues with a kink of a certain degree to create an expansion fan accelerating the flow. The downstream section of the suction side is designed with a smooth turn, ending up with the outflow angle. The pressure side is designed uncurved downstream of the throat. It is terminated at that position, where the projected outflow Mach number is reached. The trailing edge is shaped at one side only to prevent expansion waves and shocks from running straight towards the rotor. As shown in Fig. 5, only the weakened reflections of the trailing edge waves leave the guide vanes toward the rotor.

Numerical Results. To summarize, guide vanes with different design exit Mach numbers and a design exit angle of 14 deg have been shaped using the inverse method of characteristics. To ensure the high accuracy of the inverse method, the kink in the suction side is replaced by a circular arc of a small radius. Due to the known and unknown sections of the flow field boundaries and the shape of the characteristics, there exist two different regions, influenced by different boundaries (Fig. 6). The flow field in the region influenced by the known boundaries may be predicted by the usual method of characteristics, starting from the throat. The flow field in the other region, which is influenced by the guide vane exit, needs to be calculated by the inverse method.

In Fig. 7, the net of characteristics calculated for an exit Mach number of 2.0 is shown. The superimposed contour of the suction side is calculated by mass flow integration. The contours that correspond to different design exit Mach numbers are given in Fig. 8.

The contour, which is calculated for an exit Mach number of 2.0, is completed with the subsonic sections of suction and pressure sides and for which an inviscid flow field calculation has been carried out. The results depicted in Fig. 9 show the

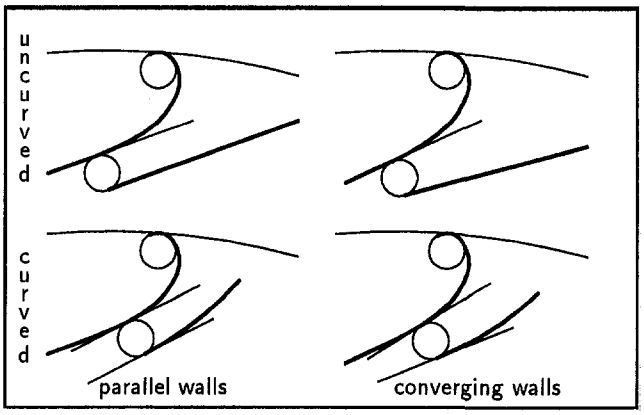

Fig. 4 Different flow channel designs at the throat

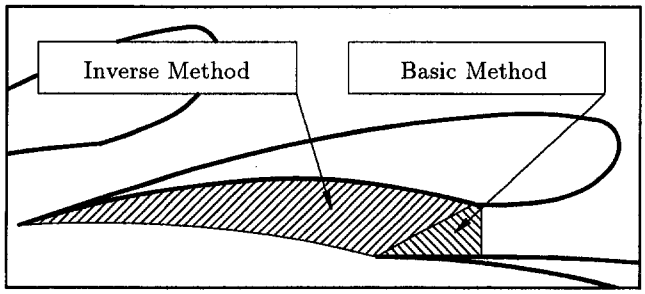

Fig. 6 Regions of application for the different methods of characteristics

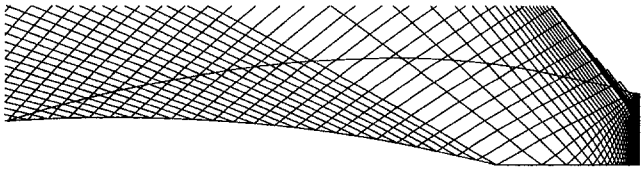

Fig. 7 Calculated net of characteristics (reduced) and superimposed guide vane contour

Fig. 8 Comparison of guide vane contours designed for different exit Mach numbers

success of the inverse design method: The flow field has almost constant states along lines of constant radius.

To investigate the influence of the viscosity, a Navier–Stokes calculation with a turbulence model according to Baldwin and Lomax (1978) has been carried out. The results of this calculation (Fig. 10) give an impression of the moderate disturbance of the flow field, which is caused by the viscosity.

The guide vane profiles presented so far have been designed with a zero trailing edge thickness, because the shocks resulting from a nonzero trailing edge cannot be considered within the proposed inverse method of characteristics. To get a realistic profile design, the trailing edge thickness has to be added to the calculated contour. The contour is changed downstream from the point where the disturbances caused by the trailing edge strike the suction side. Starting from that point, the contour has been continuously completed with two circular arcs, ending up with a trailing edge thickness of 5 percent of the throat. For the contour with thick trailing edge, the results of inviscid calculations at design conditions and of viscous calculations at design and off-design conditions are shown in Fig. 11. Due to the thick trailing edge, disturbances are generated in contrast to the disturbance-free flow field, which is shown in Fig. 9. These disturbances are increased by the influence of the boundary layers. Strong disturbances become visible at off-design conditions.

Generally, the proposed method succeeded in minimizing flow-field nonuniformities at the rotor inlet. However, small disturbances due to the boundary layers and trailing edge thickness seem to be unavoidable.

Subcritical Pressure Ratio

Design Principles. For a high efficiency, the flow should remain everywhere subsonic in guide vanes designed for a subcritical pressure ratio. As the operating point for radial turbine guide vanes is located near the choking mass flow, supersonic regions in the flow channel can only be avoided by having almost straight contours of suction and pressure side. Therefore the construction of the suction side upstream of the throat is similar to the one described in the previous section. Downstream of the throat, the suction side is continuously completed by a circular arc, ending at the trailing edge. As shown in Fig. 12, the guide vane design is completed by the prescription of the trailing edge wedge angle γ_H and the convergence angle γ_C of the throat walls.

Parameter Variation. By varying the convergence angle of the throat walls, different variations in the resulting flow fields can be observed. Maintaining the parameters given in Table 1 unchanged, the suction side unguided turning angle variation is almost identical to the variation of the convergence angle. The variation of this angle results in different surface pressure distributions and therefore in different exit flow angles. Prescribing the exit pressure, the flow angle variation influences the mass

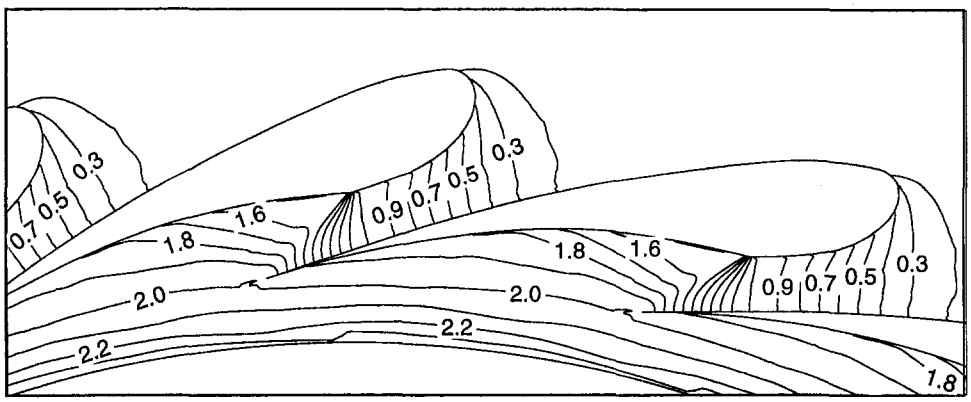

Fig. 9 Mach number distribution from inviscid calculation for the profile generated with the inverse method of characteristics

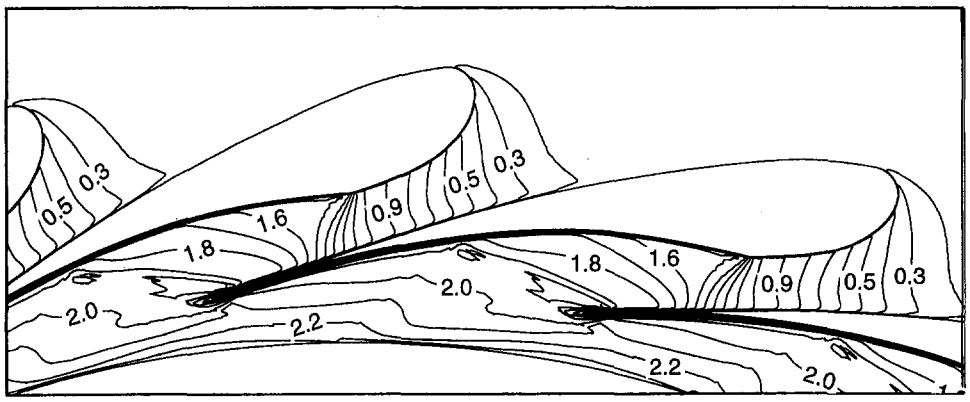

Fig. 10 Mach number distribution from viscous calculation for the profile generated with the inverse method of characteristics

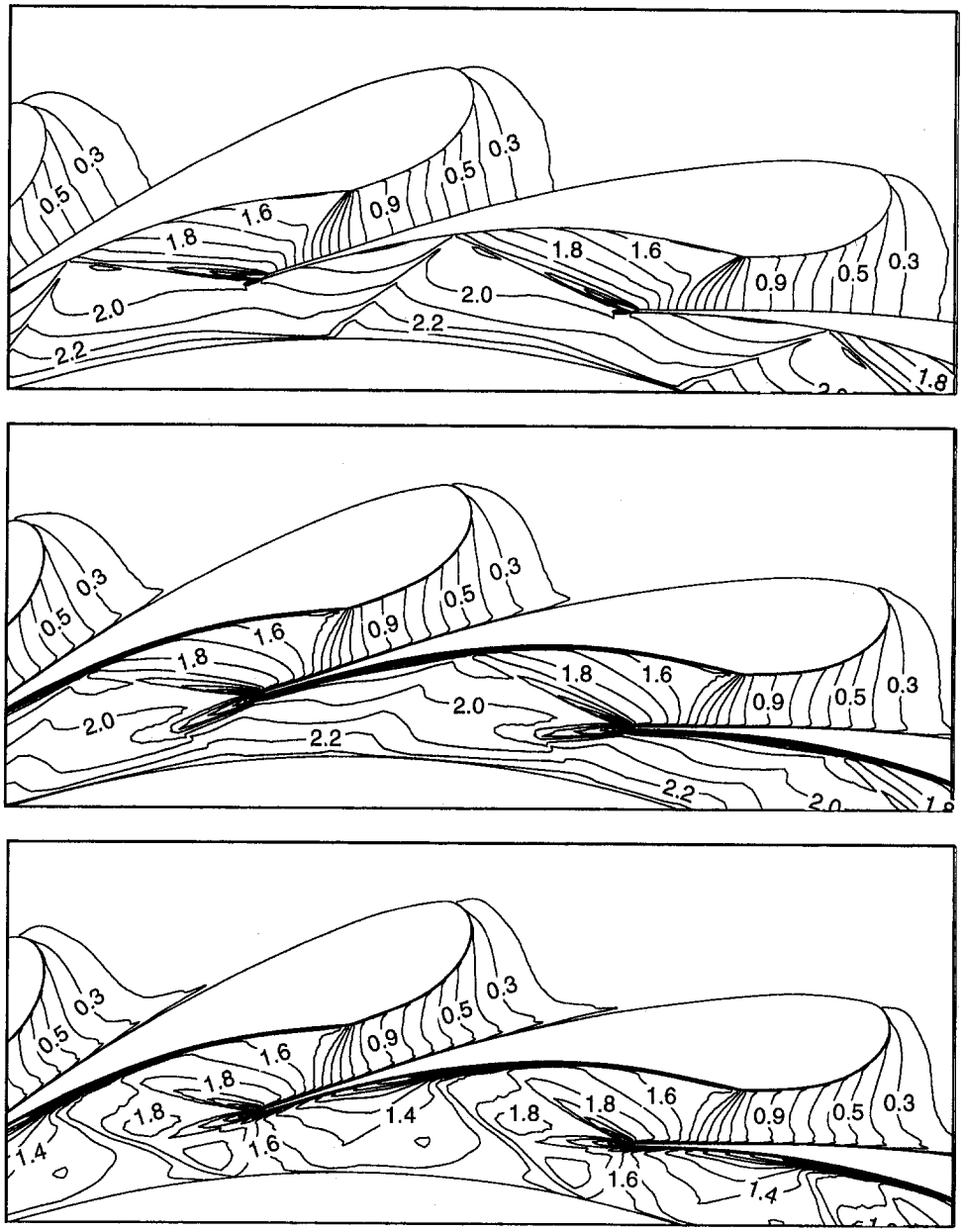

Fig. 11 Mach number distribution from various calculations for the profile with thick trailing edge: (*a*) inviscid calculation; (*b*) viscous calculation, design conditions, $p_{exit}/p_{tin} = 0.128$; (*c*) viscous calculation, off-design conditions, $p_{exit}/p_{tin} = 0.2$

flow through the guide vanes. The mass flow influenced by the convergence angle determines the mean velocity in the throat, which influences the flow field losses.

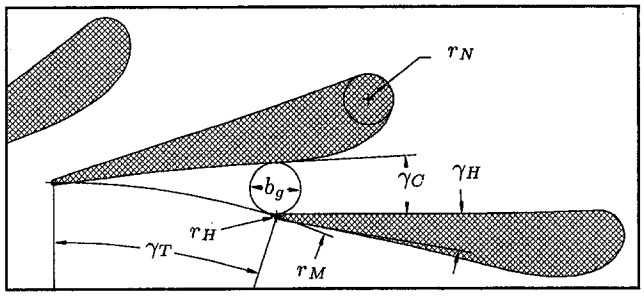

Fig. 12 Design parameters for subcritical pressure ratio

Throughout our investigations, two mechanisms with contrary influence on the loss generated by the wake flow have been observed. One part of the wake flow losses is generated in the profile boundary layers. This part of the losses is determined by the surface pressure distribution along the surfaces. In particular a reduced unguided turning increases the boundary layer losses because of an increased pressure rise at the suction side. This pressure rise results in an enlarged pressure at the trailing edge. This pressure corresponds with the flow-field velocity at the trailing edge and influences the other loss generation mechanism.

Table 1 Design parameters for subcritical pressure ratio maintaining unchanged in this study

$b_g = 0.0775 r_1$	$r_H = 0.05 b_g$	$\gamma_H = 10°$
$r_M = 1.1 r_1$	$r_N = b_g/2$	$\gamma_T = 18°$

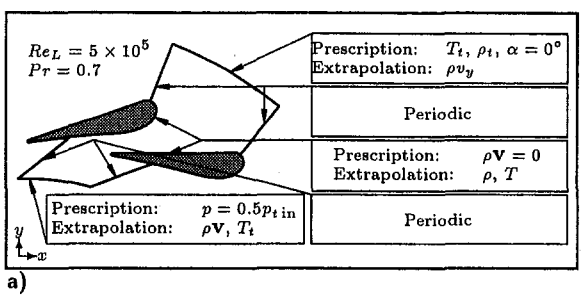

a)

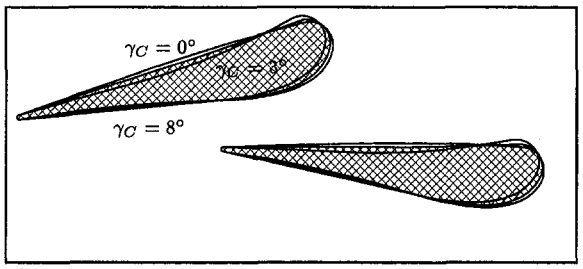

b)

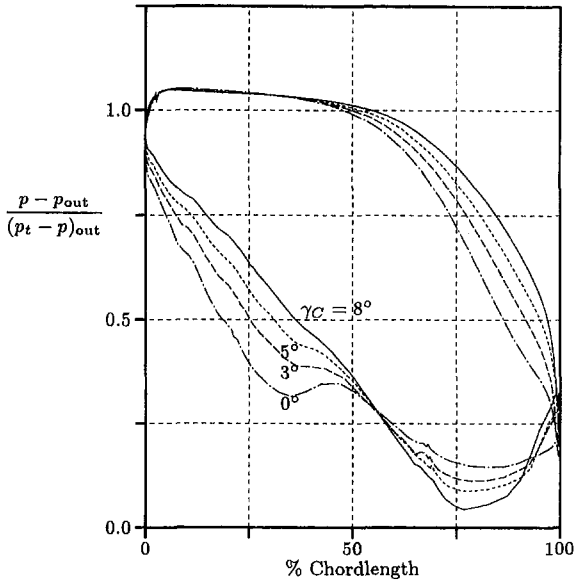

c)

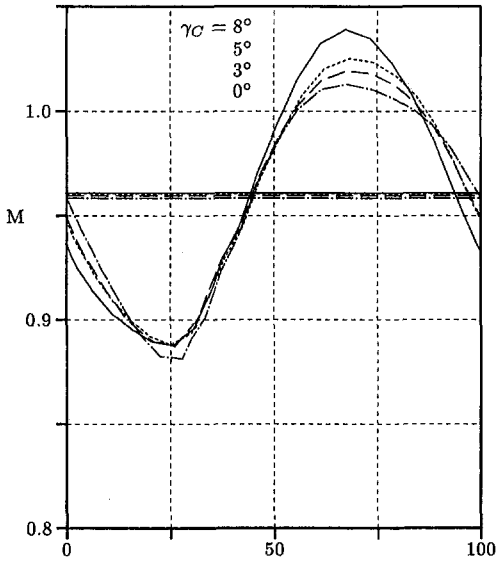

d)

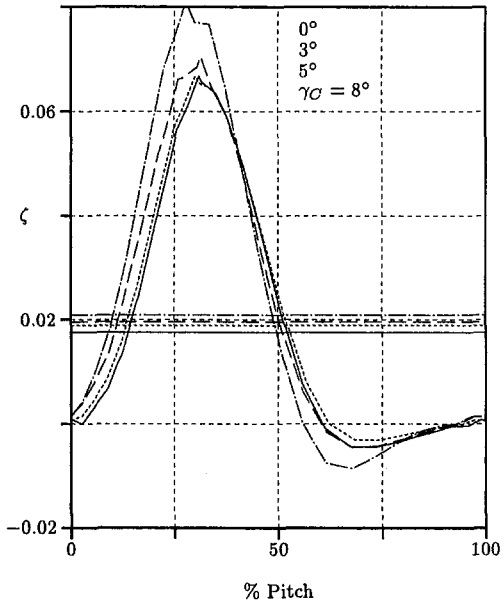

e)

f)

γ_C	0°		3°		5°		8°	
r	$1.5r_1$	r_1	$1.5r_1$	r_1	$1.5r_1$	r_1	$1.5r_1$	r_1
$\overline{M}$	0.091	0.958	0.089	0.960	0.088	0.961	0.086	0.961
$\overline{\zeta}$	0.0	0.0209	0.0	0.0196	0.0	0.0188	0.0	0.0175
$\overline{c_u/a_t}$	0.0	0.855	0.0	0.856	0.0	0.858	0.0	0.859
η_{pol}	96.5%		96.7%		96.9%		97.1%	

Fig. 13 Several results for guide vanes with different angle γ_C: (*a*) boundary conditions; (*b*) guide vane profiles; (*c*) surface pressure distributions; (*d*) Mach number; and (*e*) loss coefficient distributions at rotor inlet location; (*f*) mean values at locations of constant radius. Legend: γ_C = 0 deg: — · —, 3 deg: - - -, 5 deg: ----, 8 deg: ——.

For the low velocities in the wake flow at the trailing edge, the static pressure at the trailing edge is almost identical to the total pressure there. The total pressure of the wake flow corresponds with the losses transported within that flow. Because the wake mass flow is influenced by the trailing edge thickness, the second loss generation mechanism is determined by the trailing edge pressure and thickness. The trailing edge pressure is enlarged if the unguided turning angle is reduced. Therefore, the losses generated by the second loss generation mechanism are reduced if the unguided turning angle is reduced.

Besides the influence of the unguided turning angle on the wake flow losses, there exists an influence on the flow field uniformity downstream of the guide vanes. To avoid additional rotor stresses, a uniform flow field is desired at the rotor inlet location.

The results of flow field calculations for four guide vanes with different convergence angle γ_C are given in Figs. 13 and 14. These results show the dependencies discussed above. It becomes clear that one has to decide between a flow field high uniformity or high efficiency for a flow field at the rotor inlet location. For the relatively small deviations in the efficiency

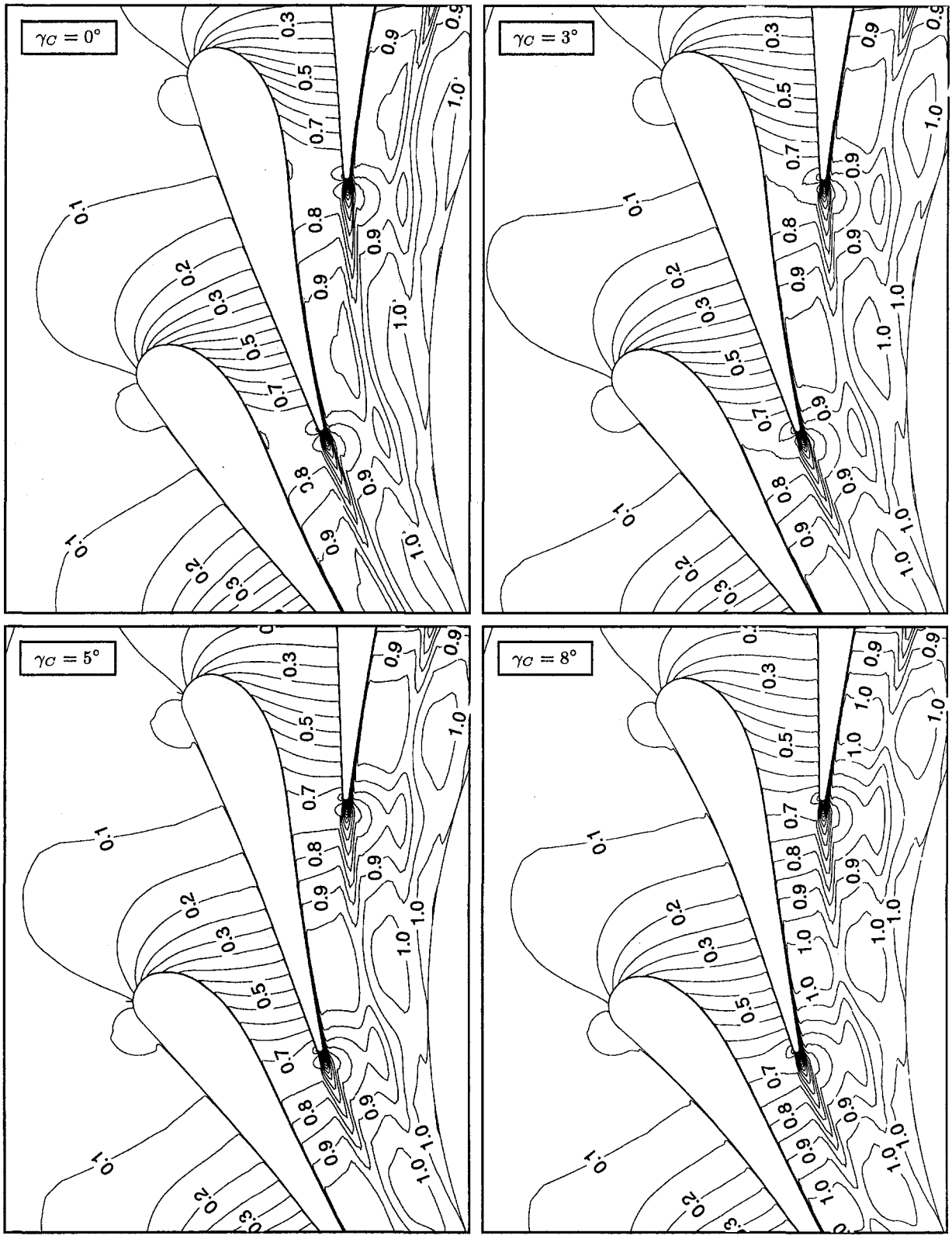

Fig. 14 Calculated Mach isolines for guide vanes with different angles γ_c

values, the optimum value for the convergence angle γ_c was chosen to be $\gamma_c = 3$ deg. For a guide vane profile with that convergence angle, a flow field calculation in three dimensions was made.

Calculations in Three Dimensions. The guide vane height in the third dimension is set to $0.1 \times r_1$. Twenty planes of 38×101 gridpoints were staggered into the third dimension to build the computational grid. For reasons of symmetry only half the channel was calculated. The results of this calculation are given in Fig. 15. Because of the negligible curvature of the flow channel near the throat, a positive effect of the proposed design principles on loss generation due to the secondary flow is observed. The magnitude of the pressure difference between suction and pressure side

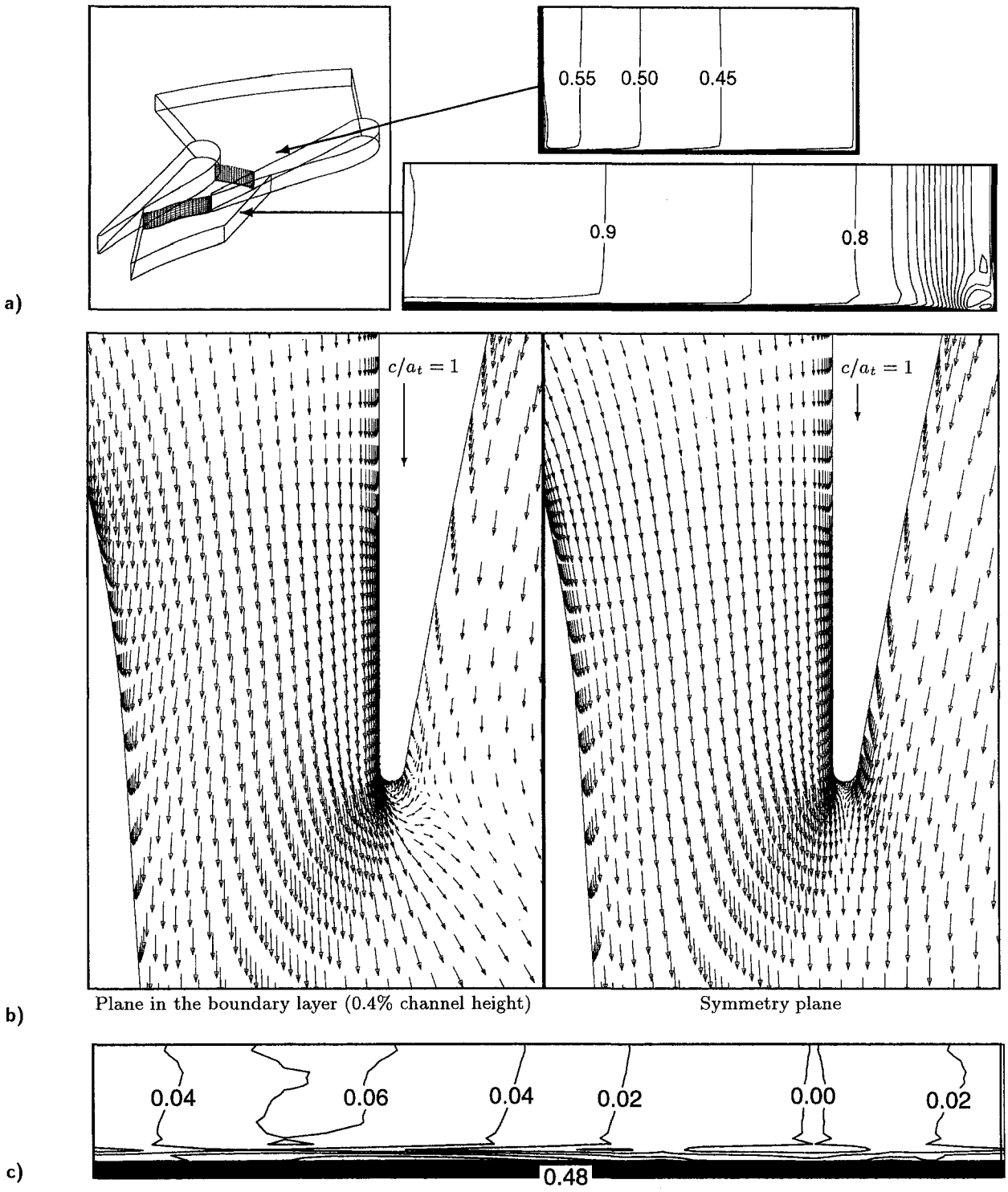

Fig. 15 Several results from the flow field computation of the optimum guide vane: (*a*) Mach number distributions in planes of maximum secondary flow; (*b*) velocity vectors; (*c*) loss coefficient at the rotor inlet location

perpendicular to the streamlines is low, resulting in small secondary flow pattern. The uncurved pressure side prevents the secondary flow pattern from spreading over the whole cross section between suction and pressure side.

However, as shown in Table 2, the side wall boundary layers have a large influence on the overall loss generation. Although only a small secondary flow pattern has been observed in the three-dimensional results, the loss coefficient is more than doubled when three-dimensional calculations are used.

Table 2 Computational results of mean values at locations of constant radius for calculations in two and three dimensions

	2D		3D		Change relativ to 2D	
r	$1.5r_1$	r_1	$1.5r_1$	r_1	$1.5r_1$	r_1
$\overline{M}$	0.089	0.960	0.090	0.956	+0.6%	−0.4%
$\overline{\zeta}$	0.0	0.0196	0.0	0.0435	—	+122%
$\overline{c_u/a_t}$	0.0	0.856	0.0	0.851	—	−0.6%
η_{pol}	96.7%		92.9%		−3.9%	

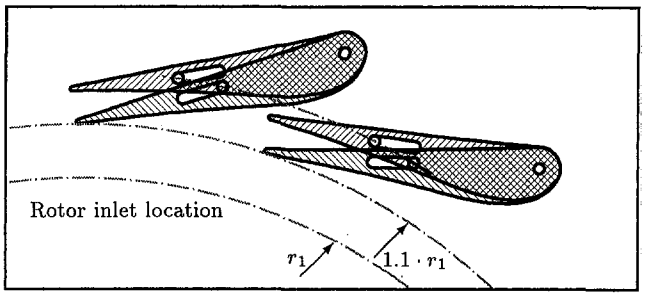

Fig. 16 Guide vane adjustment mechanism

Guide Vane Adjustment. Adjustable guide vanes allow the turbine to operate with independently chosen mass flows and pressure ratios. The question is, how the adjustment mechanism has to be designed to enable the equipment to function under certain operation conditions with minimum flow field losses. As discussed previously, the flow field losses depend to a considerable extend on the mean velocity apparent in the throat. Applying one-dimensional theory, one can derive the following relation between circumferential velocity at the rotor inlet c_{u1} and the velocity at the throat c_g (Reichert and Simon, 1994):

$$c_{u1} = c_g \frac{r_g}{r_1} \cos \alpha_g \tag{20}$$

Increasing the throat mean radius r_g with a fixed velocity component c_{u1}, one decreases the velocity c_g and therefore reduces the losses. As a result, the largest possible radius should be aspired to when the guide vanes are adjusted toward decreasing the throat area corresponding with decreasing flow field losses. A simple mechanism fulfilling that aim is constructed by turning the guide vanes around the leading edges. Such a mechanism is depicted in Fig. 16. The guide vanes are turned around −7 deg, changing the throat area to 44 percent of the original value. To get additional information on the loss generation mechanisms, flow-field simulations with identical mean velocity at the throat but different mass flows have been carried out. The results of these computations are depicted in Fig. 17 and Table 3.

Table 3 Computational results of mean values at locations of constant radius for differently adjusted guide vanes; the mass flow corresponds to the adjusted throat width

	100% $\dot{m}$		44% $\dot{m}$		Change relativ to 100% $\dot{m}$	
r	$1.5r_1$	r_1	$1.5r_1$	r_1	$1.5r_1$	r_1
$\overline{M}$	0.089	0.960	0.039	1.021	−56%	+6.0%
$\overline{\zeta}$	0.0	0.0196	0.0	0.0499	—	+154%
c_u/a_t	0.0	0.856	0.0	0.923	—	+7.8%
η_{pol}	96.7%		92.8%		−4.0%	

Concerning the swirl generation, the computational results generally confirm the validity of Eq. (20). According to this equation, the circumferential velocity component should rise about 6 percent in the reduced mass flow case. The development of the loss coefficient gives an interesting insight into further loss generation mechanisms. The influence of the velocity near the trailing edge, discussed above, has no effect for the chosen boundary conditions in this case. The large rise of the loss coefficient shows a good correlation with the change of the trailing edge thickness, which is related to the throat width. This related thickness rises to 127 percent. The additional rise of the loss coefficient above this value may be explained by the stronger loading of the boundary layer, which can be seen in Fig. 17.

Conclusions

In this paper, detailed investigations on design parameters for radial inflow turbine guide vanes are presented. The investi-

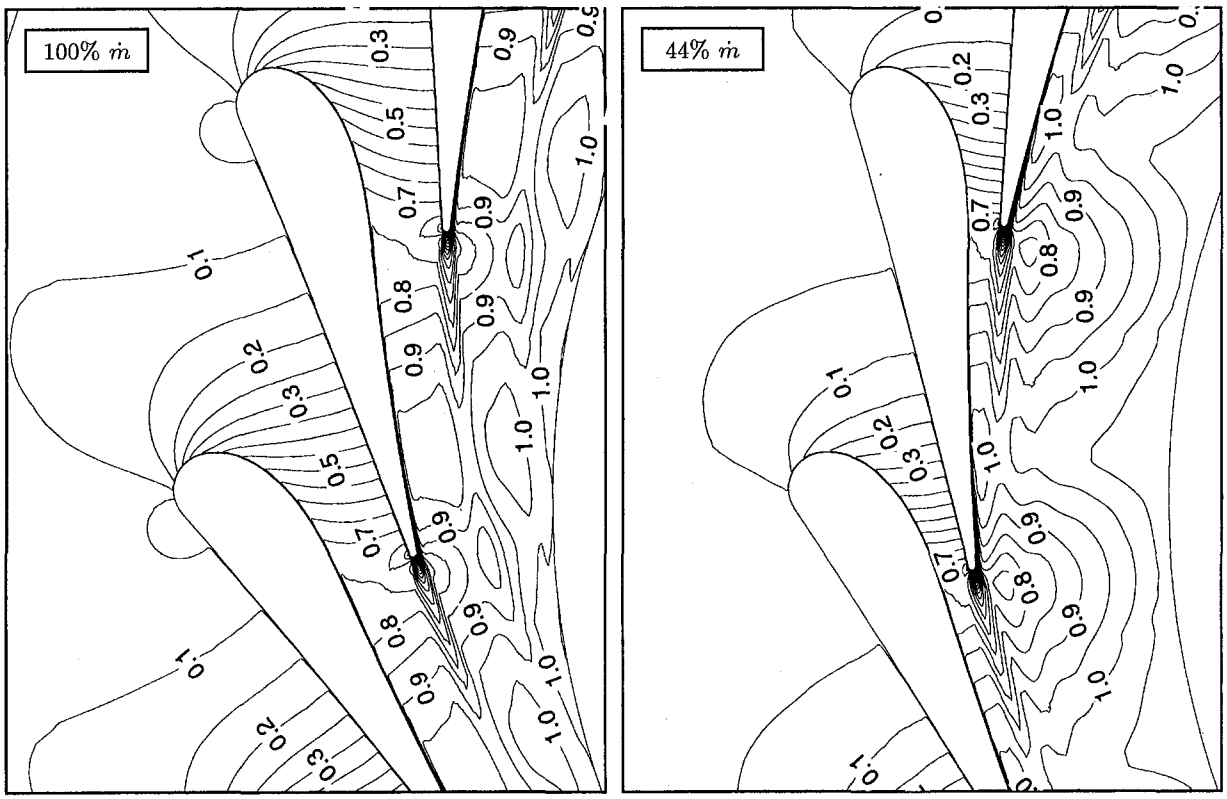

Fig. 17 Mach number distributions for differently adjusted guide vanes; the mass flow corresponds to the adjusted throat width

gations are divided into two parts according to the operating conditions for the guide vanes. General remarks on the design of the suction side applicable to both operating conditions are given. In particular, the effect of different suction and pressure side curvature at the throat on the loss generation is discussed. Generally applicable design principles are proposed.

A subsequent part of the paper deals with guide vanes designed for supercritical pressure ratios. For the design of these guide vanes, an inverse method of characteristics is applied. Inviscid flow-field calculations show the high uniformity of the exit flow field obtained with this method. This uniformity is disturbed if the flow viscosity is considered and a trailing edge thickness is incorporated into the design.

As a sequel to a previous paper (Reichert and Simon, 1994), design parameters of radial turbine guide vanes for subcritical pressure ratios are discussed. In this paper the investigations are concentrated on the loss generation mechanisms in the turbine guide vanes. The investigations are carried out with a parameter study, which allows additional insight into the effect of some design parameters on loss generation and flow field uniformity at the rotor inlet.

To extend the investigations to the secondary flows, a three-dimensional calculation has been carried out for an optimum guide vane profile. In this calculation, the previously supposed positive effect of the proposed design principles has been proved. Only a little effect of the secondary flows appears on the loss generation.

Finally, an adjusting mechanism is applied to the proposed optimally shaped guide vanes. The resulting flow field at off-design conditions is investigated by means of flow field simulations. The swirl generation in the guide vanes is found to be well described by the simple Eq. (20). The flow-field losses show a strong dependency on the trailing edge thickness relative to the throat width.

References

Baldwin, B. S., and Lomax, H., 1978, "Thin Layer Approximations and Algebraic Model for Separated Turbulent Flow," AIAA Paper No. 78-257.

Harten, A., and Hyman, J. M., 1983, "Self Adjusting Grid Methods for One-Dimensional Hyperbolic Conservation Laws," *Journal of Computational Physics,* Vol. 50, pp. 235–269.

Osher, S., and Solomon, F., 1982, "Upwind Schemes for Hyperbolic Systems of Conservation Laws," *Mathematics of Computation,* Vol. 38, pp. 339–377.

Rai, M. M., and Chakravarthy, S. R., 1986, "An Implicit Form for the Osher Upwind Scheme," *AIAA Journal,* Vol. 24, pp. 735–743.

Reichert, A. W., and Simon, H., 1994, "Numerical Investigations on the Optimum Design of Radial Inflow Turbine Guide Vanes," ASME Paper No. 94-GT-61.

Roe, P. L., 1981, "Approximate Riemann Solvers, Parameter Vectors and Difference Schemes," *Journal of Computational Physics,* Vol. 43, pp. 357–372.

Shapiro, A. H., 1953, *The Dynamics and Thermodynamics of Compressible Fluid Flow,* Ronald Press Company.

van Albada, G. D., van Leer, B., and Roberts, B. B., 1982, "A Comparative Study of Computational Methods in Cosmic Gas Dynamics," *Astronomy and Astrophysics,* Vol. 108, pp. 76–84.

Boundary Layer Development in Axial Compressors and Turbines: Part 1 of 4—Composite Picture[1]

D. E. Halstead

D. C. Wisler

GE Aircraft Engines,
Cincinnati, OH 45215

T. H. Okiishi
Iowa State University,
Ames, IA 50011

G. J. Walker
University of Tasmania,
Hobart, Tasmania

H. P. Hodson
University of Cambridge,
Cambridge, United Kingdom

H.-W. Shin
GE Aircraft Engines,
Cincinnati, OH 45215

Comprehensive experiments and computational analyses were conducted to understand boundary layer development on airfoil surfaces in multistage, axial-flow compressors and LP turbines. The tests were run over a broad range of Reynolds numbers and loading levels in large, low-speed research facilities which simulate the relevant aerodynamic features of modern engine components. Measurements of boundary layer characteristics were obtained by using arrays of densely packed, hot-film gauges mounted on airfoil surfaces and by making boundary layer surveys with hot wire probes. Computational predictions were made using both steady flow codes and an unsteady flow code. This is the first time that time-resolved boundary layer measurements and detailed comparisons of measured data with predictions of boundary layer codes have been reported for multistage compressor and turbine blading. Part 1 of this paper summarizes all of our experimental findings by using sketches to show how boundary layers develop on compressor and turbine blading. Parts 2 and 3 present the detailed experimental results for the compressor and turbine, respectively. Part 4 presents computational analyses and discusses comparisons with experimental data. Readers not interested in experimental detail can go directly from Part 1 to Part 4. For both compressor and turbine blading, the experimental results show large extents of laminar and transitional flow on the suction surface of embedded stages, with the boundary layer generally developing along two distinct but coupled paths. One path lies approximately under the wake trajectory while the other lies between wakes. Along both paths the boundary layer clearly goes from laminar to transitional to turbulent. The wake path and the non-wake path are coupled by a calmed region, which, being generated by turbulent spots produced in the wake path, is effective in suppressing flow separation and delaying transition in the non-wake path. The location and strength of the various regions within the paths, such as wake-induced transitional and turbulent strips, vary with Reynolds number, loading level, and turbulence intensity. On the pressure surface, transition takes place near the leading edge for the blading tested. For both surfaces, bypass transition and separated-flow transition were observed. Classical Tollmien–Schlichting transition did not play a significant role. Comparisons of embedded and first-stage results were also made to assess the relevance of applying single-stage and cascade studies to the multistage environment. Although doing well under certain conditions, the codes in general could not adequately predict the onset and extent of transition in regions affected by calming. However, assessments are made to guide designers in using current predictive schemes to compute boundary layer features and obtain reasonable loss predictions.

1.0 Introduction

Axial compressors rely fundamentally on aerodynamic diffusion to achieve pressure rise. Since the adverse pressure gradients associated with the diffusion become strong at the high-loading levels of modern designs, boundary layers tend to separate. This has a negative impact on stall margin, efficiency and pressure rise capability.

On the other hand, low-pressure (LP) turbines rely fundamentally on aerodynamic expansion to extract work from the fluid. In those regions where expansion occurs, the fluid is accelerating and boundary layers tend to remain thin and attached because pressure gradients are favorable. Designers capitalize on this feature and produce airfoils with an extended region of accelerating flow along the suction surface to minimize boundary layer growth. Following this accelerating region is a shorter region of diffusion. This results in a so-called "aft-loaded" airfoil (Sharma et al., 1982). These airfoils operate very efficiently at the high Reynolds numbers of sea-level take-off conditions but, as all airfoils do, they suffer an inherent, continuous decrease in efficiency as Reynolds numbers are reduced to altitude cruise values (Hourmouziadis, 1989). Besides this degradation, there is the risk of an abrupt additional loss if flow separation without reattachment occurs in the diffusing region.

These difficulties present significant challenges that compel designers to address boundary layer effects when generating flowpath and airfoil configurations.

Historically, the effects have been handled with semi-empirical approaches. For compressors where range is usually limited by flow breakdown in the end walls, designers have used the diffusion factor (Lieblein et al., 1953) and effectivity (Koch, 1981) for blade row loading; V_{max}/V_{exit} limits for airfoil diffu-

[1] Editor's note: Parts 1 and 4 of this paper are being published together in this issue. Parts 2 and 3 will be published in the April 1997 issue of the JOURNAL OF TURBOMACHINERY.

Contributed by the International Gas Turbine Institute and presented at the 40th International Gas Turbine and Aeroengine Congress and Exhibition, Houston, Texas, June 5–8, 1995. Manuscript received by the International Gas Turbine Institute April 7, 1995. Paper No. 95-GT-461. Associate Technical Editor: C. J. Russo.

sion; and loss prediction models for efficiency (Koch and Smith, 1976). For turbines, designers have applied V_{max}/V_{exit} diffusion limits for airfoils in order to avoid flow separation. While some designers set more conservative limits than others, all recognize that such approaches simply establish design rules. They do not provide flow details and therefore cannot be used to optimize airfoil shapes.

The process of designing and optimizing turbomachine airfoils is conducted with inviscid flow solvers and boundary layer codes (Meauze, 1989), component testing (Wisler, 1985) and, more recently, viscous computational fluid dynamics (AGARD, 1994). Using these methods, designers have created compressors and turbines with impressive performance by cleverly engineering their way around phenomena they do not fully understand.

Yet, weaknesses still remain in even the most sophisticated turbomachine design and analysis systems currently in use. For example, the inability to accurately predict aerodynamic loss, the location and extent of boundary layer transition, flow separation, and the unsteadiness due to wakes often limits the degree of confidence in any given design. Consequently the search for improved configurations is hindered. Trying to resolve these issues by conducting studies in realistic multistage environments is difficult. The small physical size of the airfoils and axial gaps, the short time scales of phenomena, the widely varying properties of the flow, and the high cost of operation all conspire against both the experimentalist and the analyst.

The complexities of the problems described above have led many researchers to isolate individual aspects of the flow and conduct boundary layer experiments in simplified environments. Excellent fundamental studies have been reported for wind tunnel tests of transition in steady and unsteady flows (e.g., Abu-Ghannam and Shaw, 1980, Pfeil et al., 1983; Orth, 1993), cascade experiments with and without rods to simulate wakes (e.g., Hodson, 1985; Dong and Cumpsty, 1990a, 1990b), isolated blade row/single-stage compressor tests (e.g., Walker, 1975, 1989a), turbine tests (e.g., Hodson, 1983; Addison and Hodson, 1990a, b; Arndt, 1993; Hodson et al., 1994), and modeling and prediction work (e.g., Walker, 1989b; Addison and Hodson, 1990b, 1992; Mayle and Dullenkopf, 1990, 1991; Mayle, 1992). A comprehensive review of research on transition in turbomachines has been provided by Mayle (1991) and by Walker (1993).

Although well done in themselves, such studies are often of limited applicability to production turbomachines because boundary layer development is affected by many interacting processes. Reynolds number, loading level, free-stream turbulence, airfoil pressure gradient, wakes and other unsteady factors all compete to bring about transition and alter boundary layer development. Often the result is that different modes of transition arise on the same airfoil profile at the same location at different times. Consequently designers and researchers still have questions that need to be answered before further progress can be made.

In all of the work described above, no boundary layer studies that resolve these issues and put together the complete picture of boundary layer development for embedded stages of multistage compressors and LP turbines have been reported. Consequently, the design engineer still has questions about the structure of boundary layers in multistage turbomachinery, about where transition occurs, about whether the unsteady nature of the boundary layer needs to be considered during the design process, and about how well existing codes predict loss and other boundary layer features. Our paper addresses these issues.

2.0 Format and Objectives

2.1 Format of the Papers. The four parts of this paper, which are intended to be viewed as a unit, form a comprehensive study of boundary layer development in turbomachinery that culminates five years of research. Because of the complexity of data interpretation associated with the subject matter and the overall length of the complete paper, we have placed the discussion summarizing our major findings at the beginning in Section 5.0 of Part 1 instead of at the end of Part 4. Although unconventional, this approach gets the reader to the heart of the matter quickly and provides a springboard that allows the reader to turn to those sections in Parts 2 and 3 of specific interest.

The paper is structured so that those readers not interested in experimental detail can go directly from Part 1 to Part 4.

Part 1 presents the objectives and describes the experimental test program. It then discusses how boundary layers develop on

Nomenclature

A = laminar region on $s-t$ diagram
B = wake-induced transitional strip on $s-t$ diagram
C = wake-induced turbulent strip on $s-t$ diagram
D = calmed region on $s-t$ diagram
E = region of transition between wakes on $s-t$ diagram
E_0 = anemometer output voltage at zero flow
f_{BP} = blade passing frequency
f_k = reduced frequency = $f_{BP} \times$ SSL/V_{ex}
F = region of turbulent boundary layer between wakes on $s-t$ diagram
L_B = distance from leading edge to onset of wake-induced transition in region B
L_E = distance from leading edge to onset of transition between wakes in region E
LE = leading edge
NPT = number of data points per time trace
NTT = number of time traces per ensemble
P = pressure
PS = pressure surface
PSL = pressure surface length from LE to TE of airfoil
Re = Reynolds number for compressor = V_{in}(SSL)/ν; Reynolds number for turbine = V_{ex}(SSL)/ν
$\overline{\text{Re}}$ = stage average Reynolds number = 0.5 ($\text{Re}_{\text{rotor}} + \text{Re}_{\text{stator}}$)
s = distance, the abscissa in the distance–time ($s-t$) diagram
SS = suction surface
SSL = suction surface length from LE to TE of airfoil
t = time, the ordinate in the distance–time ($s-t$) diagram
TE = trailing edge
TI = turbulence intensity
U_p = pitchline wheel speed
V = velocity
V_∞ = velocity at edge of boundary layer (free-stream velocity)
δ = boundary layer thickness
Φ = flow coefficient = $\bar{V}_z/U_p$
ν = kinematic viscosity
θ = tangential direction
ρ = density
τ_w, $_q\tau_w$ = wall shear stress, quasi wall shear stress
$\bar{\omega}_p$ = profile loss coefficient, defined as Eq. (13)
Ψ' = pressure coefficient = $\Delta P/0.5\rho U_p^2$

Subscripts

ex = blade row exit
fs = free stream
in = blade row inlet
s = static
t = total
z = axial direction

Superscripts

$\sim$ = ensemble average
$-$ = time average

embedded stages of a multistage compressor and LP turbine based upon a synthesis of all of our experimental findings. Using sketches, it draws a detailed composite picture for operation at a baseline condition and then describes how this picture changes when Reynolds number, loading level, wake frequency, and wake turbulence intensity are varied.

Parts 2 and 3 provide the supporting evidence for the discussion in Part 1. They show the detailed experimental results from both the surface hot-film gages and the boundary layer surveys for the compressor and LP turbine, respectively.

Part 4 presents the results from the computational analyses and evaluates them relative to the experimental data.

2.2 Objectives. The overall objectives of this study are: (1) to describe the development of the unsteady boundary layers that form on the blading in embedded stages of axial compressors and LP turbines, (2) to assess the capabilities of several modern codes to predict this development, and (3) to evaluate the extent to which the detailed development needs to be modeled in the design and analysis process.

We seek to answer the following questions:

- What is the physical picture of unsteady boundary layer development in multistage compressors and LP turbines and how do wakes from upstream airfoils influence this development?
- Where does transition occur? What is its extent? What modes of transition are present and how do they interact?
- What is the nature, extent, and influence of the calmed region?
- What are the effects of Reynolds number, loading, unsteadiness, and turbulence intensity?
- What practical simplifications to the real flow field can be made for design and analysis purposes? To what extent are cascade and single-stage results of value to the designer for predicting flows in embedded stages?
- How well do existing codes predict profile loss, the location and extent of transition, and other relevant features?

The overall technical approach used to achieve these objectives combines experimentation and computational analyses.

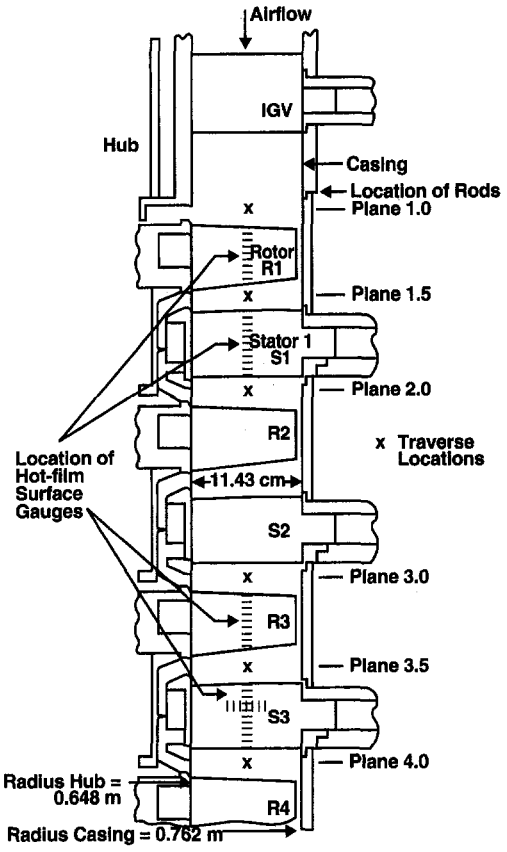

Fig. 1 Geometry of test compressor

Table 1 Compressor blading parameters (midspan)

	IGV	Rotor	Stator
Solidity	1.00	1.11	1.32
Aspect Ratio	1.36	1.25	1.44
Chord, mm	83.8	91.2	79.1
Stagger, Deg. (axial)	19.6	46.9	13.9
Camber, Deg.	3.00	22.0	44.4
No. of Airfoils	53	54	74
Axial Gap, mm	98.0	25.4	

3.0 Experimental Test Program

Test programs were conducted in the GE Low-Speed Research Compressor and Turbine to measure boundary layer development on the airfoils of multistage axial turbomachinery. High-quality blading, representative of current design practice, was used during tests conducted over a broad range of Reynolds numbers and loading levels typical of engine operation. Measurements of boundary layer characteristics were obtained by using densely packed, hot-film gages mounted on the airfoil surfaces and by making boundary layer surveys with hot-wire probes.

3.1 Low-Speed Research Compressor (LSRC). The LSRC is an experimental facility that duplicates the relevant features of the middle and rear stages of high-pressure (HP) compressor flow fields in a large, low-speed machine where very detailed investigations of the flow can be made. The facility, which has a constant casing diameter of 1.524 m (60.0 in.), is described by Wisler (1985). The compressor was set up with four identical stages in order to obtain the repeating stage environment. Measurements were made on the first and third stages.

Blading. Typical of modern designs, the compressor had high-hub/tip-ratio (0.85), low-aspect-ratio, high-solidity blading with shrouded stators and inlet guide vanes. The blading was a low-speed, aerodynamic model of an average middle stage of a nine-stage HP compressor used in modern engines currently in service. The airfoils had custom-tailored meanlines and thickness distributions to control the diffusion and give the desired surface velocity distribution. A cross section showing the geometry of the blading in the test compressor is given in Fig. 1 and the blading parameters are given in Table 1.

Performance and Test Envelope. Overall performance, shown as a four-stage average in Fig. 2, is based on measured airflow, measured work input (torque and speed), and measured pressure rise. Flow coefficient and pressure coefficient are accurate to within ±0.15 percent. Rotational speed was varied from 236 rpm to 1100 rpm in order to obtain the range of Reynolds numbers desired. Design speed was 840 ± 0.1 rpm.

Tests were conducted at the loading levels and Reynolds numbers shown partially in Fig. 2 and completely in Fig. 3 and Table 2. The numbers and letters assigned to the test points in this figure and table are used throughout the paper to identify test conditions. The baseline operating (design) point is Test Point 2B.

Normalized velocity distributions for the third-stage stator, obtained from measured static pressures, are shown in Fig. 3(*a*) for the various loading levels and in Fig. 3(*b*) for the Reynolds numbers reported herein. The distributions in Fig. 3(*b*) are normalized by the inlet velocity, V_{in}, because this best shows

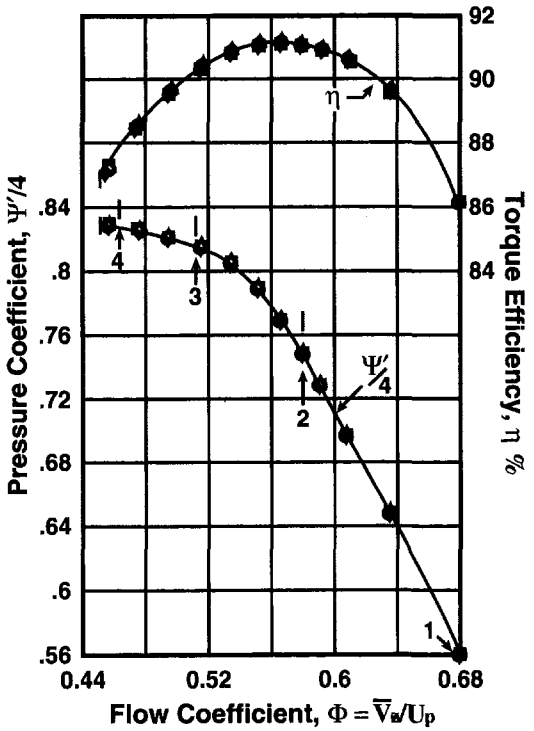

Fig. 2 Overall performance of compressor showing test points reported

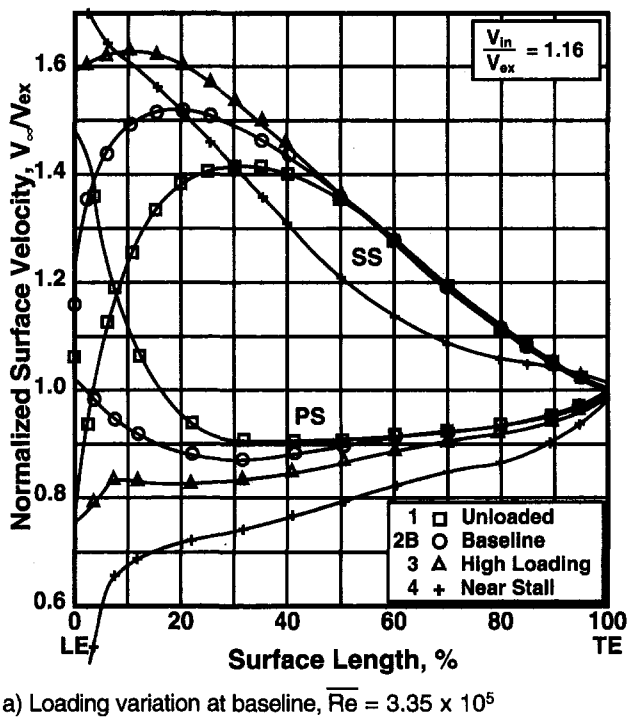

a) Loading variation at baseline, $\overline{Re} = 3.35 \times 10^5$

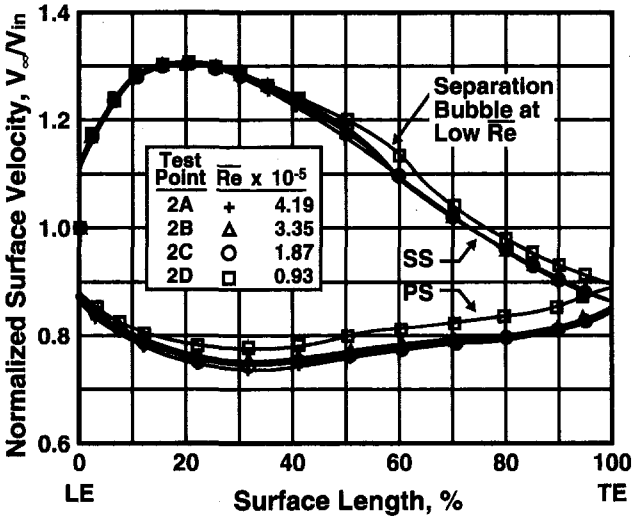

b) Reynolds number variation at design (baseline) loading

Fig. 3 Normalized surface velocity for the third-stage stator of the compressor (numbers and letters in legend correspond to those in Fig. 2 and in Table 2)

the laminar separation bubble in the data. The inlet-to-exit velocity ratio for the baseline test condition is provided in the upper right-hand corner of Fig. 3(*a*).

At the design point in Fig. 3(*a*), the leading-edge loading, the acceleration to peak velocity, and the subsequent diffusion on the suction surface were according to design intent. The change in these features as loading is varied is typical of the behavior of this type of compressor blading. Near stall in Fig. 3(*a*), a leading-edge spike appears on the suction surface. At reduced Reynolds number in Fig. 3(*b*), the presence of a separation bubble along the suction surface is suggested by the changes in slope (local decrease in diffusion) at 50–60 percent SSL (suction surface length). This feature is not present at the highest Reynolds numbers.

3.2 Low-Speed Research Turbine (LSRT). The LSRT is an experimental facility that duplicates the relevant features of LP turbine flow fields in a large, low-speed machine where very detailed investigations of the flow can be made. This vertical facility has a constant annulus area with a casing diameter of 1.524 m (60.0 in.). Ambient air is pulled through the LSRT by a large centrifugal blower. Air enters the inlet at the top and is pulled through the blading into a plenum beneath the turbine. This air, being drawn through the blading, causes the turbine to rotate. Bleed air into the plenum and IGVs on the blower, which is downstream of the plenum, allow the various operating points to be set.

Blading. The two-stage low-pressure turbine, having outlet guide vanes, is a low-speed, aerodynamic model representative of modern high-speed LP turbines currently in service. A cross section of the 0.60 hub/tip-ratio blading having shrouded nozzles is shown in Fig. 4. Design parameters are given in Table 3. The airfoils had custom-tailored meanlines and thickness distributions to give the desired surface velocity distribution. The test stage consisted of embedded Rotor 2 and Nozzle 2.

Performance and Test Envelope. Overall performance, shown as a two-stage average in Fig. 5, is based on measured airflow, measured work output (torque and speed), and measured pressure drop. Flow coefficient and pressure coefficient are accurate to within ±0.15 percent. Rotational speed was varied from 125 rpm to 610 rpm in order to obtain the range

Table 2 Compressor test points

Test point	Flow coef.	Stage avg. $\overline{Re} \times 10^{-5}$	Rotor $\overline{Re} \times 10^{-5}$	Stator $\overline{Re} \times 10^{-5}$
1	0.677	3.94	4.98	2.90
2A	0.576	4.19	5.31	3.07
2B	0.576	3.35	4.24	2.47
2C	0.576	1.87	2.37	1.36
2D	0.576	0.93	1.18	0.68
3	0.512	3.00	3.77	2.20
4	0.462	2.69	3.40	2.00

Kinematic Viscosity = 1.58×10^{-5} m²/s for 2B

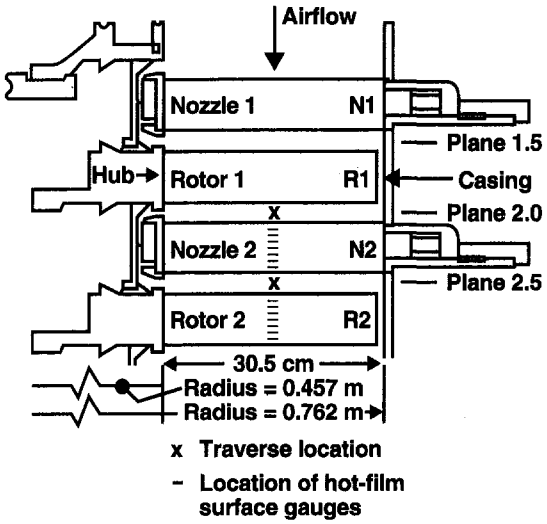

Fig. 4 Geometry of test turbine

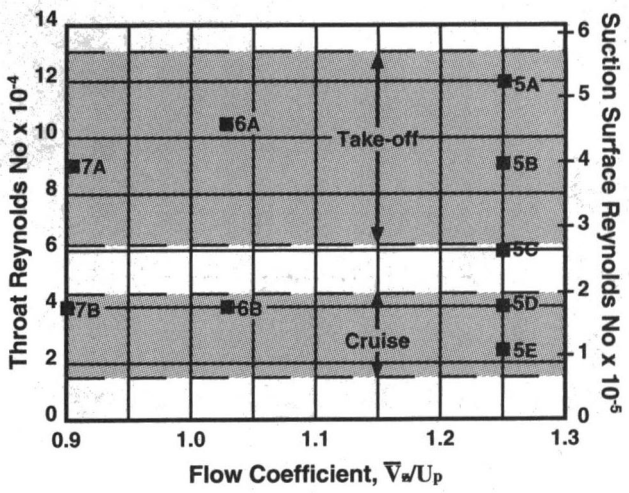

Fig. 6 Variation in Reynolds number over operating range of middle stages of LP turbines

of Reynolds numbers desired. Design speed was 610 ± 0.1 rpm.

Tests were conducted at the loading levels and the Reynolds numbers shown in Figs. 5 and 6, respectively, and in Table 4. The large difference between typical take-off and cruise Reynolds numbers for the turbine, shown by the shaded bands in Fig. 6, is representative of engine operating conditions. The numbers and letters assigned to the test points in these figures and in Table 4 are used throughout the paper to identify test conditions. The baseline operating point is Test Point 5A at increased loading and take-off Reynolds number.

The normalized velocity distributions, obtained from measured pressures on the airfoil surfaces, are shown in Figs. 7(*a, b*) for embedded Rotor 2 and Nozzle 2, respectively. The maximum velocities on the suction surface are located near 60 percent SSL. There is a 12 percent reduction in velocity over the rear portion of the airfoil. The change in velocity distribution along the forward portion of the airfoil as loading level was varied is typical. There was no significant change in normalized velocity distribution as Reynolds number was varied.

On the pressure surfaces, there are regions of considerable deceleration after the acceleration around the leading edge. The deceleration ends at approximately 30 percent PSL (pressure surface length) for the nozzle and 22 percent for the rotor. It is followed by a continuous acceleration to the trailing edge.

Table 3 Turbine blading parameters (midspan)

	N1	N2	Rotor
Solidity	1.64	1.68	1.48
Aspect Ratio	3.97	5.10	3.87
Chord, mm	76.2	59.7	78.7
Stagger, Deg. (axial)	39.8	22.9	34.9
Chamber, Deg.	60.0	102.4	96.9
No. of Airfoils	82	108	72
Axial Gap, mm	25.4	25.4	

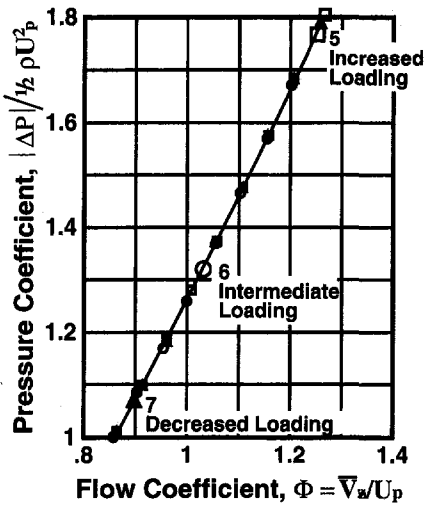

Fig. 5 Overall performance of turbine showing test points reported

3.3 Instrumentation and Data Acquisition

Hot-Wire Anemometry. Measurements of both time-resolved and time-unresolved unsteady velocities were made with a TSI IFA 100 anemometry system.

The boundary layer surveys were taken with a Dantec 55P05 hot-wire boundary layer probe that was calibrated in-situ before and after each survey. This time-saving calibration method improved accuracy and eliminated the need to continually remove and reinstall the hot-wire probe in the test vehicle. Local flow conditions were computed using detailed steady-stage measurements at each test condition. A Nusselt number formulation of the hot-wire calibration equation was employed following the method of Collis and Williams (1959). This technique facilitated a direct accounting for wall proximity effects (Walker, 1983). Measurement accuracy was estimated at ±1.5 percent for velocity.

Table 4 Turbine test points

Test point	Flow coef.	Stage Avg. $\overline{Re} \times 10^{-5}$	Rotor $\overline{Re} \times 10^{-5}$	Stator $\overline{Re} \times 10^{-5}$
5A	1.25	5.27	6.11	4.43
5B	1.25	3.96	4.59	3.33
5C	1.25	2.71	3.14	2.28
5D	1.25	1.80	2.09	1.51
5E	1.25	1.19	1.38	1.00
6A	1.03	4.53	5.25	3.81
6B	1.03	1.80	2.09	1.51
7A	0.90	3.96	4.59	3.33
7B	0.90	1.80	2.09	1.51

Kinematic Viscosity = 1.68×10^{-5} m²s for 5A
Kinematic Viscosity = 1.58×10^{-5} m²s for 5D

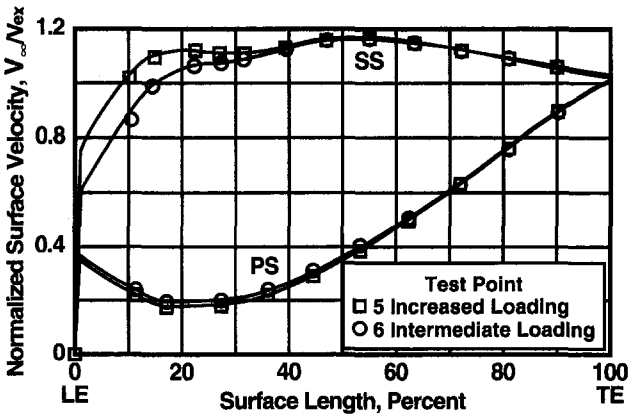

a) Second-stage rotor, R2

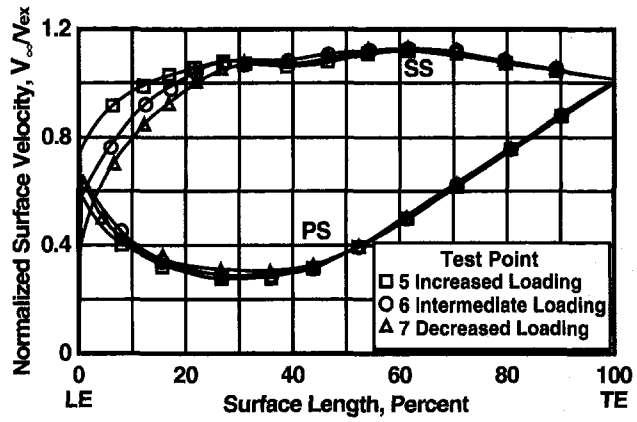

b) Second-stage nozzle, N2

Fig. 7 Normalized surface velocity for various loading levels of LP turbine (numbers correspond to those in Figs. 5 and 6 and Table 4)

The velocity, flow angle, and unsteadiness characteristics entering and exiting the airfoil rows were measured with a TSI 1240-20 "*X*" hot-film probe. Calibration was done in a free jet with measurement accuracy being ±1.25 percent for velocity and ±0.5 deg for flow angle.

Surface Hot-Film Sensors. Arrays of densely packed, hot-film sensors were mounted onto airfoil surfaces in a chordwise orientation from the leading edge to the trailing edge at 50 percent span. Both suction and pressure surfaces of a rotor blade and stator vane were instrumented in stages one and three for the compressor as marked in Fig. 1 and in stage two for the turbine at locations marked in Fig. 4. Each sensor was 0.1 mm (3.9×10^{-3} in.) in chordwise extent, 1.5 mm (5.9×10^{-2} in.) in spanwise extent, and 0.2 μm (7.9×10^{-6} in.) thick. The sensors were spaced 2.54 mm (0.10 in.) apart and mounted on a mylar substrate that was 0.05 mm (2.0×10^{-3} in.) thick. The substrate was glued onto the airfoil surface, taking great care to conform to the airfoil contour. All substrate edges were filled and sanded to remove all surface irregularities.

In addition, an array of 11 hot-film sensors was mounted onto the suction surface in a spanwise orientation on the third stator of the compressor at 35 percent chord as marked in Fig. 1. These sensors extended from 39 to 61 percent span.

The sensors were operated individually and simultaneously using a TSI IFA-100 anemometry system. The signals from the rotors were taken out through a 100-channel, mercury slip ring, which had no measurable noise.

Boundary Layer Traverses. An Aerotec precision rotary table, controlled by a stepper motor, formed the heart of the traverse instrumentation used for measuring boundary layer profiles. The rotary table held a cylindrical probe support, which was inserted radially through the casing into the axial gap between bladerows at Plane 4.0 for the compressor in Fig. 1 and at Plane 2.5 for the turbine in Fig. 4. Attached at 90 deg to this support was a small sleeve that extended upstream into the stator passage and held the hot-wire boundary layer probe. As the probe support was rotated, the probe moved very nearly perpendicular to the airfoil surface and thereby surveyed the boundary layer. Surveys were made at different chordwise positions by varying the length of the sleeve.

The rotary table had a resolution of 0.1 arc sec with a unidirectional accuracy of ±1 arc sec. This, coupled with a detection system used to find the airfoil surface while the compressor or turbine was running, allowed the hot wire to be positioned at distances above the airfoil surface within an accuracy of $\pm 1.25 \times 10^{-2}$ mm (5.0×10^{-4} in.) relative to the surface. The vibrational amplitude of the hot-wire sensors was determined to be less than 2.50×10^{-2} mm (1.0×10^{-3} in.).

Data Acquisition. Signal conditioning of all anemometry measurements was done using the IFA-100. For hot-wire boundary layer surveys, the low-pass filter was set at 50 kHz and the data sampling was done at 100 kHz. For the hot-film data the minimum low-pass filter setting was 15 times blade passing frequency with sampling done at five times the low-pass filter setting. Depending on the blade speed, these acquisition rates gave from 100 to 500 equally spaced, data-sampling increments across each blade passing period. A one-per-rev pulse from an optical encoder on a reference blade tip triggered the data gathering, which continued for at least five blade passing periods. Between 200 and 400 phase-locked records (time traces) were taken for ensemble averaging.

The hot-wire and hot-film signals were digitized with a Kinetic Systems analog-to-digital converter. Both DC- and AC-coupled data were obtained to maximize resolution. This allowed amplification gains of up to 100 to be used. A dynamic signal analyzer was used to obtain frequency-averaged spectra.

3.4 Data Reduction and Analysis

Surface Hot-Film Anemometry (Principles of Operation). The surface hot-film sensors were operated at an elevated temperature using constant-temperature anemometry. With this method, the relationship between wall shear stress at the sensor, τ_w, and the rate of heat transfer from the sensor is given in the form (Bellhouse and Schultz, 1966)

$$\tau_w = k\left(\frac{E^2 - A^2}{\Delta T}\right)^3 \tag{1}$$

where E is the instantaneous output voltage from the anemometer, ΔT is the temperature difference between the air and heated sensor, and variables k and A are calibration constants.

For the present investigation, direct calibration of each sensor was not possible. Rather, the semiquantitative approach described by Hodson et al. (1994) was employed. In earlier work, Hodson established that the rate of heat loss to the substrate, which is proportional to A^2 from Eq. (1), can be approximated using the square of the zero-flow voltage, E_0, obtained from each sensor under zero-flow conditions (Hodson, 1983, 1985). Second, if the bulk temperature of the blade is equal to the air temperature, which was the case for this investigation, the temperature difference ΔT is proportional to E_0^2. Provided the above approximations hold, the relationship between wall shear stress and sensor heat transfer can be written as

$$_q\tau_w = \left(\frac{E^2 - E_0^2}{E_0^2}\right)^3 \tag{2}$$

Here, the quantity $_q\tau_w$ on the left-hand side of Eq. (2) is referred

to as *quasi*-wall shear stress to reflect its semiquantitative nature. As further noted by Hodson et al. (1994), the relationship in the form of Eq. (2) also minimizes the effects of small differences in sensor geometry and electrical properties on measurements acquired from different sensors. As a result, *relative* magnitudes of quasi-wall shear stress obtained from various sensors along an airfoil can be compared to each other directly.

The accuracy of Eq. (2) was found to be very dependent upon the zero-flow voltage, given that $(E^2 - E_0^2)$ and E_0^2 are of the same magnitude. For this investigation, values of E_0 were obtained from all sensors before and after rig operation. Prior to data reduction, their values were adjusted to account for differences in temperature between that at which the E_0s were acquired and that associated with the test bladerow during rig operation.

Surface Hot-Film Anemometry (Signal Processing). Prior to computing any statistical quantities, all measured voltages from each ensemble are converted first to instantaneous values of quasi-wall shear stress using Eq. (2). The ensemble-averaged distribution and time-averaged value of ${}_q\tau_w$ are then determined by using Eqs. (3) and (4), respectively, where NTT is the number of time traces per ensemble and NPT is the number of data points per time trace.

$$\widetilde{{}_q\tau_{w_i}} = \frac{1}{\text{NTT}} \sum_{n=1}^{\text{NTT}} {}_q\tau_{w_{n,i}} \quad i = 1, \text{NPT} \tag{3}$$

$$\overline{{}_q\tau_w^m} = \frac{1}{\text{NPT}} \sum_{i=1}^{\text{NPT}} \widetilde{{}_q\tau_{w_i}^m} \quad m = 1 \tag{4}$$

Instantaneous (raw) time traces are presented in an AC-coupled manner determined from

$$({}_q\tau_{w_{n,i}} - \overline{{}_q\tau_w}) \quad i = 1, \text{NPT} \tag{5}$$

for a selected time trace "n."

Fluctuations in quasi-wall shear stress are quantified in terms of random unsteadiness and skew. Random unsteadiness is a measure of the fluctuation amplitude of a signal about its mean. Skew is a measure of asymmetry in the probability distributions of fluctuations about the mean. These quantities were determined by using the general relationship

$$\widetilde{{}_q\tau_{w_i}'^m} = \frac{1}{\text{NTT}} \sum_{n=1}^{\text{NTT}} ({}_q\tau_{w_{n,i}} - \widetilde{{}_q\tau_{w_i}})^m \quad i = 1, \text{NPT} \tag{6}$$

The ensemble-averaged, root-mean-square (rms) unsteadiness is computed from Eq. (6) with $m = 2$. The result is denoted symbolically as

$$\sqrt{\widetilde{{}_q\tau_{w_i}'^2}} \quad i = 1, \text{NPT} \tag{7}$$

Its time-average counterpart is determined from

$$\sqrt{\overline{{}_q\tau_w'^2}} = \sqrt{\frac{1}{\text{NPT}} \sum_{i=1}^{\text{NPT}} \widetilde{{}_q\tau_{w_i}'^2}} \tag{8}$$

Values of rms unsteadiness computed for the turbine measurements using Eqs. (7) and (8) are normalized using the ensemble and time-averaged quasi wall shear stress from Eqs. (3) and (4), respectively. Values of rms associated with the compressor are *not* normalized because near-zero values of quasi-wall shear in regions of separated flow produced distortions in the normalized quantities. Throughout this paper, values of rms unsteadiness, whether for the turbine or compressor, are referred to simply as ensemble and time-averaged random unsteadiness.

Ensemble and time-averaged values of skew are determined from the third-order statistical moment given by Eq. (6) for $m = 3$. The former is computed directly and is given symbolically as $\widetilde{{}_q\tau_{w_i}'^3}$. The time-averaged value, given as $\overline{{}_q\tau_w'^3}$, is computed using Eqs. (4) and (6) with $m = 3$. For both the compressor and turbine, values of skew, whether time or ensemble-averaged, are normalized by the absolute value of the maximum skew from the *time-averaged* distribution along a given airfoil surface length. In this paper, it is these normalized quantities that constitute the definition of skew.

Turbulence Intensity. Turbulence measurements at the inlet and exit planes of the test blading were obtained using an X hot-film probe as described in Section 3.3. The "X" probe was aligned to measure the two-dimensional velocity vector in the axial-circumferential plane. The radial component of velocity was not measured.

Turbulence intensities were determined as follows. First, the output voltages obtained simultaneously from the two sensors of the X probe were converted to instantaneous components of the velocity vector given by $\{V_\theta, V_z\}_{n,i}$. Next, the ensemble-averaged distribution and time-averaged value of velocity were determined using Eqs. (9) and (10), respectively.

$$\widetilde{V_i} = \sqrt{\widetilde{V_{\theta_i}^2} + \widetilde{V_{z_i}^2}} \quad i = 1, \quad \text{NPT} \tag{9}$$

$$\overline{V} = \sqrt{\overline{V_\theta^2} + \overline{V_z^2}} \tag{10}$$

The fluctuation velocities in the streamwise (u') and transverse (v') coordinate directions were then computed from the difference between the instantaneous velocity vector $\{V_\theta, V_z\}_{n,i}$ and the ensemble-averaged velocity (Eq. (9)). From these, the ensemble-averaged distribution and time-averaged value of turbulence intensity were computed as shown by Eqs. (11) and (12). Additional details are provided by Halstead (1996):

$$\widetilde{TI_i} = \frac{\sqrt{\frac{1}{2}(\widetilde{u_i'^2} + \widetilde{v_i'^2})}}{V_i} \quad i = 1, \text{NPT} \tag{11}$$

$$\overline{TI} = \frac{\sqrt{\frac{1}{2}(\overline{u'^2} + \overline{v'^2})}}{\overline{V}} \tag{12}$$

Profile Loss Coefficient. Measured values of profile loss coefficient were determined from circumferential traverses of total and static pressure using Eq. (13). The numerator of this relationship is the difference between the free-stream and mixed-out values of total pressure at the exit measurement plane of the blade row. The denominator is equal to free-stream dynamic head. It is based on inlet static pressure for the compressor and exit static pressure for the turbine:

$$\overline{\omega_p} = \frac{\overline{P}_{t_{ex,fs}} - \overline{P}_{t_{ex,\text{mixed}}}}{\overline{P}_{t_{ex,fs}} - \overline{P}_s} \tag{13}$$

Predicted values of profile loss coefficient were determined using an analysis based on two-dimensional wake mixing similar to that of Denton (1993). Boundary layer quantities at the trailing edge required for this analysis were obtained from two-dimensional boundary layer calculations. Values of base pressure coefficient recommended by Denton (1993) were used.

4.0 General Discussion of Transition

The development of unsteady boundary layers on turbomachinery blading is influenced significantly by laminar to turbulent transition. Therefore, to facilitate the reading of this paper, we describe the transition processes and associated terminology used throughout this work.

4.1 Transition Processes. The three fundamental processes by which transition occurs in steady flow are also relevant for the unsteady flow in turbomachinery. These are:

Tollmien–Schlichting (TS) Transition. The process of Tollmien–Schlichting, or "natural" attached-flow transition, is shown schematically in Fig. 8(*a*) (White, 1974). For very low free-stream disturbance where *TI* is less than 1.0 percent, the laminar boundary layer develops linear oscillations of well-defined frequency when the Reynolds number exceeds a critical value. This is shown as region 1 in the figure. These oscillations, called Tollmien–Schlichting (TS) waves, are two-dimensional and convect at a typical speed of 0.30–0.35 V_∞. As the amplitude of the TS waves increases, spanwise distortions of the vortical structure develop (region 2) and grow in an increasingly three-dimensional and nonlinear manner (region 3). They eventually burst into turbulent spots (region 4). Within this region, the boundary layer alternates between laminar and turbulent states. Eventually the turbulent spots originating from different locations merge and form a fully developed, continuously turbulent boundary layer as transition is completed (region 5).

Bypass Transition. This occurs when the formation and amplification process of two-dimensional TS waves in natural transition is "bypassed" due to the presence of forced disturbances of sufficient amplitude. Sources of such disturbances include higher free-stream turbulence and surface roughness. In this mode of transition, TS waves are less evident, if present at all. Rather, the first indication of transition may be the direct formation of turbulent spots thus "bypassing" regions 1–3 of Fig. 8(*a*). This process significantly reduces the length of unstable laminar flow and will promote earlier transition.

Separated-Flow Transition. Under certain instances (e.g., at high positive or negative incidence, rapid diffusion or low Reynolds number), the laminar boundary layer may separate from the airfoil surface. Rapid transition then occurs within the separated shear layer. Provided the Reynolds number is not too low or the local pressure gradient too large, the resulting turbulent-like layer will reattach to form a closed region of separated flow called a separation bubble (Roberts, 1980). The region beneath the separated laminar shear layer within the bubble is quiescent, with very low wall shear stress and nearly constant static pressure. This process is shown schematically in Fig. 8(*b*).

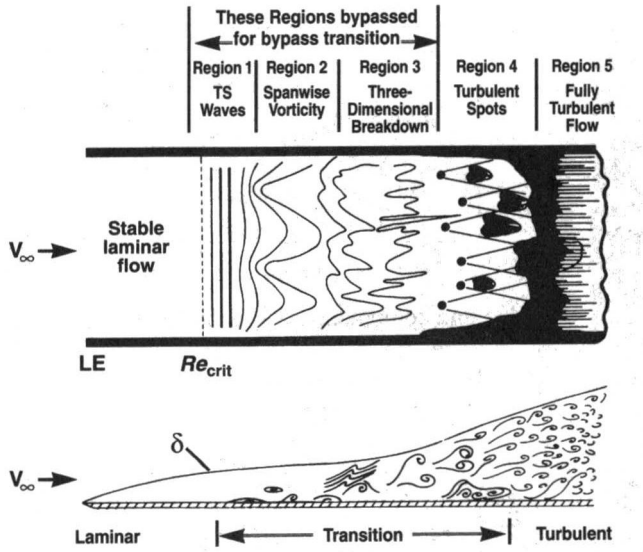

a) Tollmien-Schlichting transition (after White, 1974) and bypass transition

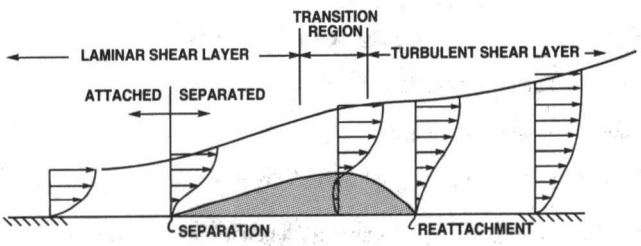

b) Separated flow transition with separation bubble shaded (after Walker, 1975 and Roberts, 1980)

Fig. 8 Schematics of transition process

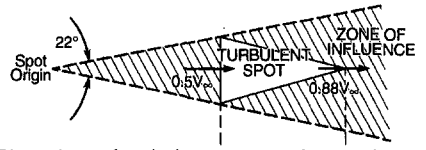

a) Plan view of turbulent spot at time t_1 in part b below (after Schubauer and Klebanoff, 1956, and as idealized by McCormick, 1968)

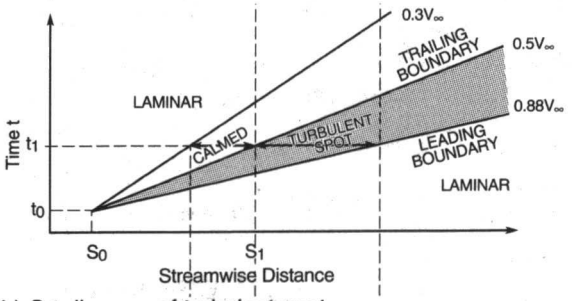

b) S-t diagram of turbulent spot

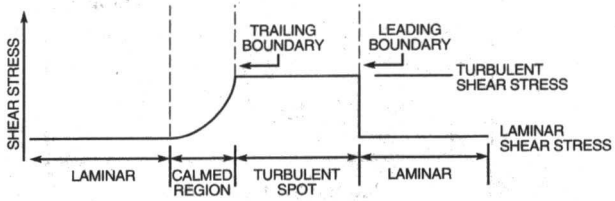

c) Variation in wall shear stress along spot centerline at $t=t_1$

Fig. 9 Characteristics of turbulent spots

4.2 Turbulent Spots, Intermittency, and the Calmed Region

Turbulent Spots. Bypass transition and the latter stages of T–S transition are characterized by the production and propagation of turbulent spots in the laminar boundary layer. As shown in Fig. 9(*a*), turbulent spots are approximately triangular in shape and spread laterally at an angle of about 22 deg as they move downstream of their origin. The region swept out by the spot is its zone of influence. The convection velocities of the leading and trailing boundaries of the spot are 0.88 V_∞ and 0.50 V_∞, respectively, as measured in zero pressure gradient by Schubauer and Klebanoff (1956). Their values do not vary with streamwise direction. Consequently, the spot maintains a self-similar shape as it moves downstream.

Various characteristics of a turbulent spot are conveniently described using a space-time (s–t) diagram as shown in Fig. 9(*b*). Lines of constant time drawn parallel to the "s" axis provide the instantaneous state of the flow along the surface. Likewise, vertical lines parallel to the "t" axis provide the unsteady behavior of the flow at a given location along the surface. Trajectories, drawn in Fig. 9(*b*) at 0.88 V_∞ and 0.50 V_∞, define the leading and trailing boundaries of the turbulent spot in the s–t diagram. For a constant streamwise velocity, the boundaries are straight lines in s–t space, otherwise they are curved. The convective velocity of each boundary is the inverse

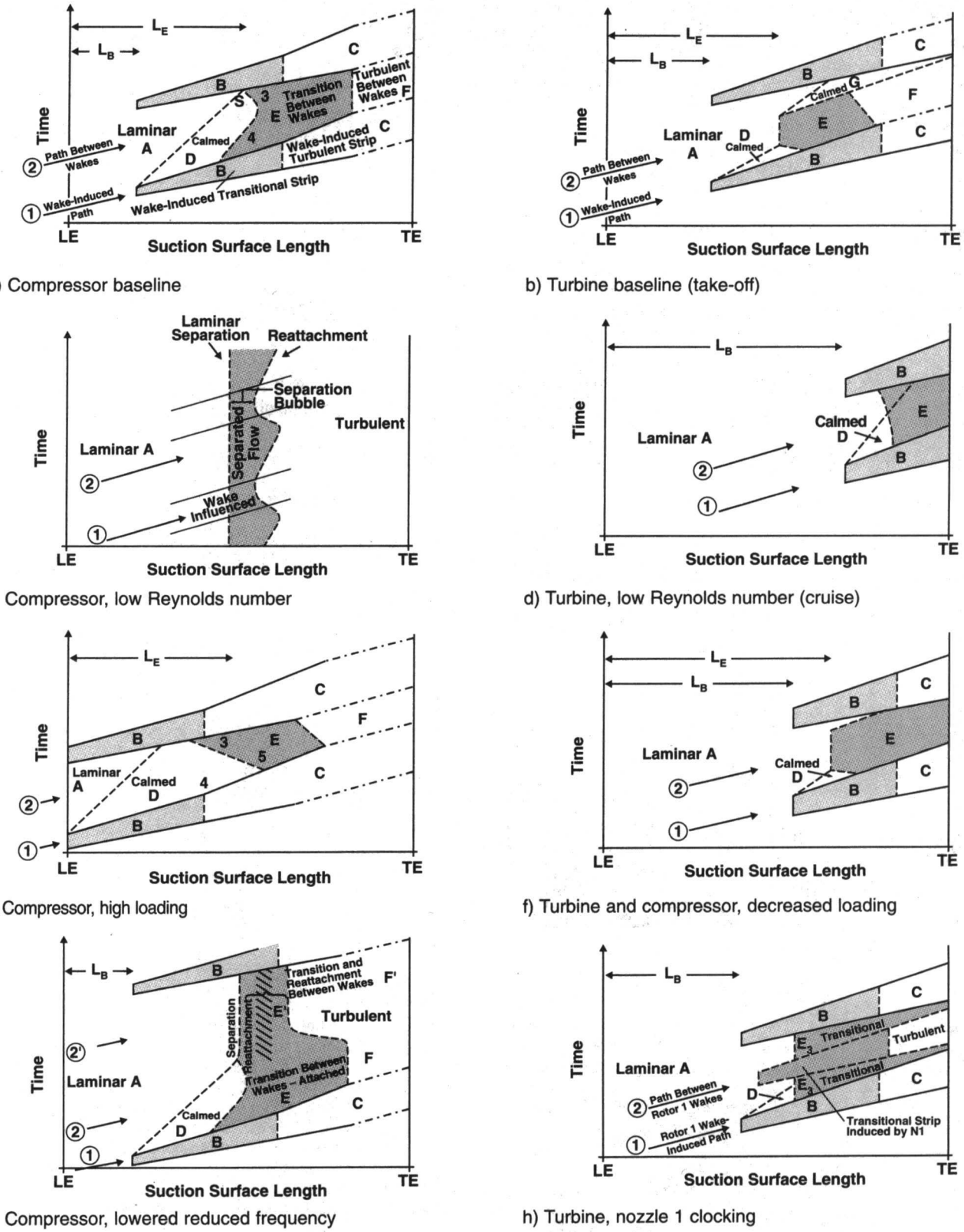

Fig. 10 Composite pictures of boundary layer development

slope of its trajectory. The shaded region in the figure describes the streamwise and temporal growth of the spot as it convects along the surface.

The streamwise distribution of wall shear stress at the spanwise position of the spot center line is shown for $t = t_1$ in Fig. 9(*c*). At the leading boundary of the spot, shear stress increases abruptly from a laminar to turbulent level. Behind the trailing boundary, shear stress gradually decreases through the calmed region to a laminar level.

Calmed Region. A "calmed" (becalmed) region of laminar-like flow occurs immediately behind a turbulent spot (Schubauer and Klebanoff, 1956) or turbulent strip (Schubauer and Klebanoff, 1956; Orth, 1993). Its existence is endemic to turbulent spots or strips regardless of the transition process that

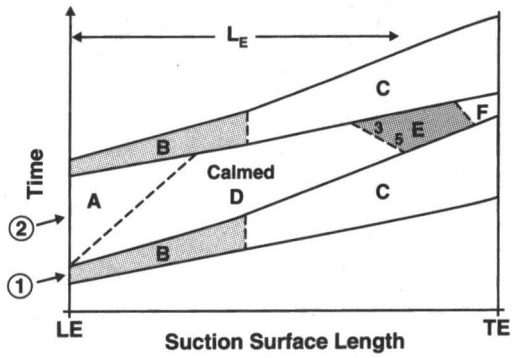

i) Compressor, increased wake turbulence intensity for baseline conditions

Fig. 10 (Continued)

brought about the turbulent event. The calmed region is identified as the region of decreasing, but still elevated, wall shear stress behind the spot or strip. An example is sketched in Fig. 9(*c*). The calmed region, whose trailing boundary convects at 0.3 V_∞, appears on an $s-t$ diagram as shown in Fig. 9(*b*).

The calmed region is not accessible to TS waves originating upstream of the spot inception point because the velocity of the trailing boundary of the spot exceeds the propagation velocity of the TS wave ($\approx$0.3 V_∞). In addition, the formation of new instabilities, whether by T-S or bypass transition processes, is suppressed within the calmed region. This occurs because the boundary layer profile, which is relaxing from a turbulent to laminar level of shear stress, is more stable than the surrounding undisturbed laminar boundary layer. The calmed region can therefore be terminated only by the merging of neighboring turbulent spots or by strong bypass transition events. In the case of pure turbulent strips, merging occurs only in the streamwise direction. This has the effect of extending significantly the streamwise length of the transition zone (Schubauer and Klebanoff, 1956; Orth, 1993).

Calmed regions are more resistant to flow separation in adverse pressure gradients due to their elevated levels of shear stress and low shape factors.

Intermittency. Transition from a laminar to turbulent flow takes place as individual spots merge together. The fraction of time the flow is turbulent is known as intermittency. Its value is equal to zero for laminar flow, varies from zero to unity from the beginning to the end of the transition region, and is unity for turbulent flow.

4.3 Transition in Turbomachines

Wake-Induced Transition is used in this paper to describe boundary layer transition brought about directly by disturbances in a convecting wake. It can occur by any of the three processes described in Sect. 4.1. In actuality, transition induced by wakes is brought about primarily by the process of bypass transition given the level of wake turbulence intensity (typically about 5 percent or greater).

Non-Wake-Induced Transition is used to categorize all boundary layer transition occurring between passing wakes. Because of the lower associated levels of turbulence, transition between wakes can occur via any of the three processes described above, although we observed only bypass and separated-flow transition in our work. In some cases, as will be reported herein, more than one process can work in concert to bring about transition along a non-wake-induced path.

5.0 Discussion of Composite Picture (Major Findings)

In this section we present our discussion of how boundary layers develop on embedded stages of multistage HP compressors and LP turbines based upon a synthesis of our experimental findings. We use sketches in the form of simplified $s-t$ diagrams to illustrate this development. We first present the picture for the baseline operation. This forms a convenient reference where compressor and turbine results are similar. We then describe how this baseline picture changes when Reynolds number, loading level, wake frequency, and wake strength (turbulence intensity) are varied.

The general physical picture was similar for compressors and turbines: both had large extents of laminar and transitional flow along the suction surface; both had wake-induced transitional strips penetrating the laminar region; both reacted similarly to variations in Reynolds number, loading, and turbulence intensity; both exhibited calming effects, but those for the compressor were much stronger. Many of the differences between the compressor and turbine are attributed to their respective adverse and favorable pressure gradients.

5.1 Composite Picture for Baseline Operation. The baseline operation for the compressor is design Test Point 2B. That for the turbine is Test Point 5A at increased loading and take-off Reynolds number. The experimental evidence for this portion of the discussion is found in Section 7.0 of Part 2 for the compressor and Section 12.0 of Part 3 for the turbine.

In a steady flow over an airfoil operating near zero incidence angle, the boundary layer develops on the suction surface in a manner similar to that described in Fig. 8, with the particular mode and location of transition dependent on the specific flow conditions and airfoil design. However in the unsteady, multistage environment of turbomachinery, this picture is modified substantially as blade rows move relative to each other and wakes from upstream airfoils periodically wash over the surface of the downstream airfoil. In this process, the increased turbulence intensity (disturbance level) in the convecting wake penetrates into the laminar boundary layer on the airfoil surface. At some location downstream from the leading edge, these wake disturbances initiate turbulent spots, i.e., the wakes initiate or induce boundary layer transition before it would have otherwise occurred in the laminar region.

As these turbulent spots within this newly created, wake-induced transitional boundary layer convect along the suction surface, they map out a wake-induced path that can be represented on an $s-t$ diagram in a manner analogous to that shown for the convecting (shaded) turbulent spot in Fig. 9(*b*). For turbomachinery, these are seen as regions "*B*" in the $s-t$ diagrams shown in Figs. 10(*a, b*) for compressor and turbine blading, respectively. We have named region *B* a "*wake-induced transitional strip.*" It has leading and trailing boundaries defined approximately by the convection velocities of the spot shown in Fig. 9(*b*). Transition onset for region *B* begins at a distance L_B from the leading edge in Fig. 10. When transition is completed within region *B* and the boundary layer becomes turbulent, this strip continues to the trailing edge as a wake-induced turbulent strip *C*, which is also marked in the figure.

In the path between wakes shown in Figs. 10(*a, b*), the boundary layer development is influenced by more than just the level of free-stream turbulence and the pressure gradient. The path between wakes can also be affected strongly by the calmed region. It is recalled in Fig. 9 that a calmed region follows a convecting turbulent spot. In turbomachines, such calmed regions, labeled "*D*" in Figs. 10(*a, b*), follow the turbulent spots generated in wake-induced regions *B*. As in Fig. 9(*b*), the trailing boundary of calmed region *D* in Fig. 10(*a*) (dashed line between regions *A* and *D*) convects at about 0.3 V_∞. Just as the shear stress decays in the calmed region behind the spot in Fig. 9(*c*), so it decays across the calmed regions between

wakes in Figs. 10(*a, b*). The higher shear stress in calmed region *D* is one of the characteristics thought to be effective in suppressing flow separation and delaying transition in the region between wakes. In addition, the periodic unsteadiness of the wake influences boundary layer growth.

Thus, the unsteady boundary layers on turbomachinery blading develop along two separate, but coupled paths marked as ① and ② in Fig. 10. The first path, called the wake-induced path, lies approximately under the wake trajectory but lags the wake somewhat. The second path lies between wakes. Along both paths the boundary layer clearly goes from laminar to transitional to turbulent, with the location of transition onset in each path strongly tied to the level and distribution of turbulence intensity, the Reynolds number, and the airfoil loading. The two paths are coupled by a calmed region which, being generated by turbulent spots produced in the wake-induced path, decays asymptotically across the region between wakes. For our case, the mode switching (in time) from the non-wake region to the wake-induced strip occurs in a small fraction of a blade passing period. Each path is described in more detail below.

The great extent of laminar and transitional flow for both the compressor and turbine blading is a most striking feature of our data. Previous assumptions of predominantly turbulent boundary layers on multistage turbomachine blading are not correct. For the compressor, the laminar region between wakes persisted well past minimum pressure to near midsurface length.

The Wake-Induced Path. This path, shown as ① in Figs. 10(*a, b*), consists of the portion of laminar region *A* that lies under the wake trajectory, the wake-induced transitional strip *B*, and the wake-induced turbulent strip *C*.

The laminar portion of this path occupies only about 20 percent of the wake-passing period. It leads directly into wake-induced transitional strip *B*. Our data show that transition does not begin at the leading edge, but rather begins some distance downstream marked as L_B in the figures. Generally, L_B is greater for the turbine than it is for the compressor due to the different nature of their surface pressure distributions.

The discovery that wake-induced strips *B* are transitional in nature and not fully turbulent is an important finding of this present investigation because it helps formulate a more general, consistent picture of boundary layer development than previously described. When constructing transition models, some have assumed that the process of wake-induced transition would immediately produce a fully turbulent strip with an intermittency of one. Our data show that this is not the case. Instead, transitional flow occupies a considerable portion of the suction surface. Transition in these strips occurs via the bypass mode at this baseline condition. The strips are well-defined and relatively narrow, being typically 20 percent of the wake-passing period.

The wake-induced turbulent strips *C*, that follow region *B*, expand in a streamwise sense more rapidly for the compressor than they do for the turbine. Region *C* extends to the trailing edge.

The Path Between Wakes. This path, shown as ② in Figs. 10(*a, b*), follows the wake in time. It consists of the remaining laminar region *A*, the calmed region *D*, and the regions of transition and turbulent flow between wakes labeled *E* and *F*, respectively.

The calmed region *D* begins at the trailing boundary of region *B* and extends into the laminar region between wakes. Since the calmed region results from turbulent spot production and growth in region *B*, its degree of effectiveness in suppressing flow separation and transition onset between wakes is related to intermittency levels within region *B*, i.e., to the fraction of the time the flow within *B* is turbulent. At locations along the airfoil surface where intermittency within *B* is relatively high, the calming can be very effective, provided this location of high intermittency is upstream of location L_E, which marks transition onset between wakes for region *E*.

In our compressor, the calmed region begins well upstream of location L_E as illustrated in Fig. 10(*a*). However the location of high intermittency within *B* does not occur until just prior to L_E. Consequently, our calmed region is only moderately effective in suppressing flow separation and transition onset. Lower intermittency over the first half of region *B* means that turbulent spots and calming are absent for some wake-passing events. This allows transition of the noncalmed flow to occur at point 4, which in turn produces a positive slope for the ensemble-average line of transition onset between wakes (line connecting points 3 and 4). Negative slopes to this line will be seen at high loading in Section 5.3 (Fig. 10(*e*)).

The calmed effect diminishes across the wake-passing period as shear stress levels decay. At location "*S*" in Fig. 10(*a*) where the least calming occurs, the boundary layer profiles become inflectional and flow separation becomes imminent. This is the location that would be most susceptible to separated flow transition when operating conditions change.

With flow separation suppressed by calming for the compressor, transition between wakes in region *E* of Fig. 10(*a*) occurs via the bypass mode. On the downstream side of region *E*, transition is progressively terminated by the growth of the adjacent wake-induced turbulent strip *C* into the region of transition between wakes *E*.

For our turbine in Fig. 10(*b*), the calmed region is less extensive. The locations of transition onset between wakes now correlate strongly with the level and distribution of incoming turbulence intensity over the blade passing period. Transition in region *E* occurs strictly via the bypass mode. A region of nonturbulent calmed flow, region *G*, persists to the trailing edge. Region *G* results for two reasons: (1) the very low incoming turbulence intensity over a small portion of the wake-passing period for this nozzle *N*1/nozzle *N*2 clocking, and (2) a calmed region created by the turbulent spots in region *E*. It will be seen that the appearance of region *G* depends on the clocking of nozzle *N*1 relative to that of nozzle *N*2.

The difference in the extent of the calmed effect between the compressor and turbine is seen by comparing the relative sizes of regions *D* in Figs. 10(*a, b*). This results from differences in intermittency along the wake-induced transitional strip, differences in time scales based on boundary layer thickness, and differences in reduced frequency, f_k, for each machine. Since reduced frequency is the ratio of convective to periodic time scales, the lower reduced frequencies for our turbine result in lower residence times (relative to wake passing) for fluid particles in the passage. Therefore the calmed region in our turbine has less time to grow than it has in our compressor.

Turbulent boundary layers between wakes, identified as regions *F* in Figs. 10(*a, b*), follow transitional regions *E* and extend to the trailing edge. Near the trailing edge for both the compressor and turbine, significant temporal variations of the integral parameters of the turbulent boundary layer occur as time proceeds from region *C* to region *F*.

On the pressure surface, wake-induced strips *B* are present. However, boundary layer transition occurs close to the leading edge because of the adverse pressure gradient in that region.

5.2 The Effect of Reynolds Number Variation. The experimental evidence for this portion of the discussion is found in Section 8.0 of Part 2 for the compressor and Section 13.0 of Part 3 for the turbine.

In general, the boundary layers on both the compressor and turbine blading respond in a similar manner to changes in Reynolds number until very low values are attained, where differences occur. As Reynolds number is reduced, the turbulence intensity in the wakes is less able to destabilize the laminar region. Consequently, the wake-induced transitional strips, *B*, weaken; they become more diffuse and the locations of transi-

tion onset, L_B in Figs. 10(*a, b*), move further downstream on the airfoil surface.

As Reynolds number is reduced for compressors, the calmed regions weaken as the wake-induced transitional strips weaken. This allows intermittent flow separation to occur between wakes at location "*S*" in Fig. 10(*a*). With continued reduction in Reynolds number, a region of separated flow at *S* grows across the wake-passing period. Transition via laminar separation increasingly replaces bypass transition as the calmed effect weakens. At stage-average Reynolds numbers less than about 10^5, separated flow transition completely replaces bypass transition across the entire wake-passing period as shown in Fig. 10(*c*). The wake now has only a modulating effect on the boundary layer rather than a mode switching effect on transition, as seen by the modulating reattachment line. For stage-averaged Reynolds numbers greater than 3.0×10^5, little variation from Fig. 10(*a*) was observed.

As Reynolds number is reduced for turbines from take-off values in Fig. 10(*b*) to cruise values, the perturbed laminar region extends very far downstream, as shown in Fig. 10(*d*). Transition in the wake-induced path does not begin until well into the region of diffusion on the aft portion of the airfoil and extends to the trailing edge. Between wakes, a rather strong calmed region *D* develops as shown in Fig. 10(*d*). This inhibits flow separation between wakes and enables a large region of attached, transitional flow in region *E* to persist to the trailing edge. This is in contrast to conventional boundary layer calculations in Part 4, which predict laminar separation to occur prior to 80 percent SSL for this blading.

These Reynolds number findings have important implications for researchers doing experimental work. For compressors, the Reynolds numbers at engine design-point operation are in the range from $5.0–8.0 \times 10^5$. To model this, one should conduct research at stage-average, aerodynamic Reynolds numbers greater than 3.0×10^5 (above the "knee" in the loss versus Reynolds number curve). As Reynolds number is reduced below this value, the flow picture becomes increasingly less relevant to the medium and large engine environment. Loss will be seen to also increase. For turbines, testing at both take-off and cruise Reynolds numbers is important.

5.3 The Effect of Loading Variation. The experimental evidence for this portion is found in Section 9.0 of Part 2 for the compressor and Section 14.0 of Part 3 for the turbine.

In general, the boundary layers on both the compressor and turbine blading respond in a similar fashion to changes in airfoil loading. As loading is increased, the wake-induced transitional strips *B* become stronger with the location of transition onset and the region of higher intermittency for the strip moving toward the leading edge. Other regions of transitional and turbulent boundary layers also move toward the leading edge.

As compressor loading is progressively increased, the location of peak velocity on the airfoil suction surface moves toward the leading edge (see Fig. 3(*a*)) and the turbulence intensity of both the incoming wakes and the region between wakes increases. The increased turbulence intensity of the wakes is more effective in initiating transition along the wake-induced path. Consequently, the location of transition onset for wake-induced transitional strip *B* moves progressively toward the leading edge. This is seen by noting the decrease in length of line L_B as one proceeds from Fig. 10(*f*) to 10(*a*) to 10(*e*).

Eventually the transitional strip begins at the leading edge as shown in Fig. 10(*e*), its transition length becomes very short and the strip functions as a wake-induced turbulent strip for all practical purposes. High levels of intermittency within the strip occur very near the leading edge and, therefore in the path between wakes, the calmed region *D* is very effective in inhibiting flow separation and delaying transition. This results in a longer region of nonturbulent (laminar-like) flow, which extends along the most calmed portion of the calmed region past point 4 all the way to point 5 in Fig. 10(*e*). This in turn produces a negative slope for the line of transition onset (line connecting points 3 and 5). Without this strong calming, as for example in the baseline in Fig. 10(*a*), there is transitional flow and a positive slope for transition onset at point 4.

As loading is increased, the wake-induced turbulent strip *C* moves upstream (compare Fig. 10(*e*) with Fig. 10(*a*) and its trailing boundary progressively terminates the region of transition between wakes, *E*. This causes this region *E* to occupy a smaller percentage of the wake-passing period. Transition occurs everywhere via the bypass mode. Near stall for this case, laminar separation occurs near the leading edge, followed by turbulent reattachment and a turbulent boundary layer to the trailing edge.

As loading of the LP turbine is progressively increased, the wake and non-wake regions retain their identity but move upstream as seen by comparing Fig. 10(*f*) with the baseline Fig. 10(*b*). Transition onset is strongly influenced by local pressure gradient and by the distribution of inlet turbulence intensity across the wake-passing period.

On the pressure surface, transition occurs near the leading edge for both the compressor and turbine as loading is varied. At negative incidence, separated flow transition occurs at the leading edge with turbulent reattachment shortly thereafter. At positive incidence, wake-induced strips and regions of transitional and turbulent boundary layers appear between wakes.

5.4 The Effect of Reducing Wake Frequency. The experimental evidence for this is found in Section 10.1 of Part 2 for the compressor.

The frequency of occurrence of the upstream wakes was reduced by removing one airfoil from the third-stage rotor of the compressor, leaving all other airfoils unchanged. This reduced the local solidity of this one effected rotor passage from 1.11 to 0.56.

The resulting picture of boundary layer development becomes more complex as multimode transition takes place between wakes. This can be seen by comparing Fig. 10(*g*) with the baseline sketch in Fig. 10(*a*). Up until the shear stress decays and the calmed effect runs out, the picture in Fig. 10(*g*) is the same as that in Fig. 10(*a*) and transition in region *E* occurs via bypass transition. However, as the calmed effect in region *D* dies out when the spacing between wakes is increased, a large region of separated flow transition, *E'*, now appears across the wake-passing period as shown in Fig. 10(*g*). The length of the transition zone in region *E'* is much shorter than that following calmed region *D*. After flow reattachment, a turbulent boundary layer *F'* extends to the trailing edge.

5.5 Effects of Nozzle–Nozzle Interaction (Clocking). The experimental evidence for this portion of the discussion is found in Section 15.0 of Part 3 for the turbine.

Significant wake interaction can occur in a LP turbine as upstream nozzle *N*1 wakes convect through the following rotor *R*1 (Arndt, 1993). Depending upon the relative circumferential position (clocking) of nozzles *N*1 and *N*2 in Fig. 4, this convection of *N*1 wakes through rotor one produces a different distribution of turbulence intensity entering the downstream nozzle *N*2. Since the boundary layer development along the surface of nozzle *N*2 is strongly tied to the distribution of inlet turbulence intensity, this interaction also produces a different boundary layer picture on *N*2.

The boundary layer development on *N*2 for *N*1 clocked about 40 percent of relative pitch compared to that for the baseline is sketched in Fig. 10(*h*). The rotor wakes still produce wake-induced transitional/turbulent strips *B* and *C*. However, the wake segments from upstream nozzle *N*1 create their own transitional/turbulent strips as shown in the figure. Consequently, the periodic variations in the boundary layer occur at twice the blade passing frequency at the trailing edge compared to those for the baseline in Fig. 10(*b*). At the relative clocking position

of Fig. 10(h), the distribution of incoming turbulence intensity is such that no region G, as seen in Fig. 10(b), is distinguishable. The implications of nozzle clocking on loss are discussed in Section 17.3 of Part 4.

5.6 Effects of Wake-Turbulence Intensity. The experimental evidence for this portion of the discussion is found in Section 10.2 of Part 2 for the compressor.

The turbulence intensity of an incoming wake was varied while leaving all other test conditions the same. This was accomplished by inserting a small-diameter rod into the rotor disk where the one rotor airfoil had previously been removed from the third-stage rotor of the compressor.

The boundary layer development when the wake-turbulence intensity from the rod is high ($\approx$16 percent) is sketched in Fig. 10(i). All other test conditions are the same as those for baseline Test Point 2B. The picture is now very different from that for the compressor baseline in Fig. 10(a) where wake-turbulence intensity is 5.5 percent. At high wake-turbulence intensity in Fig. 10(i), a very strong wake-induced transitional strip, B, forms at the leading edge and already has high intermittency near the leading edge. The wake-induced turbulent strip, C, begins much closer to the leading edge and extends to the trailing edge. The associated calmed region D is extensive and strong. The calming effect eliminates any tendency for flow separation and significantly delays transition onset. The onset of bypass transition in region E between wakes is now well aft on the airfoil surface, as seen by comparing the length of line L_E in Fig. 10(i) with that in Fig. 10(a). The slope of the boundary of transition onset (line connecting points 3 and 5) is negative. The trailing boundary of the wake-induced turbulent strip, C, progressively terminates the region of transition between wakes E.

The wake-induced strips at increased wake turbulence intensity in Fig. 10(i) look like those at high loading in Fig. 10(e). However, the region E of transition between wakes is much farther aft in Fig. 10(i) than it is in Fig. 10(e) because (1) calming is stronger, (2) the turbulence intensity between wakes is lower, and (3) the region of peak velocity is farther aft on the airfoil surface for the test conditions of Fig. 10(i).

Conclusions

The following conclusions about boundary layer development in compressors and LP turbines are drawn from our experimental work.

1 Unsteady, periodic boundary layers develop on turbomachine airfoils along the following two separate paths that are coupled by a calmed region:
   - the wake-induced path (or strip), which lies approximately under the convecting wake trajectory and generates the calmed region, and
   - the path between wakes, which follows the wake-induced path and contains the calmed region.

2 The higher shear stress in the calmed region is effective in suppressing flow separation and delaying transition onset in the region between wakes. Its effectiveness is related directly to the intermittency level in the wake-induced path.

3 Engineers can use the plan-form structure of unsteady boundary layers, as given in Fig. 10 of Part 1, to construct similar pictures for their designs and thus evaluate the extent of transition regions and calming.

4 Previous assumptions of predominantly turbulent boundary layers on multistage turbomachine blading were convincingly shown to be incorrect. Along both paths the boundary layer clearly goes from laminar to transitional to turbulent, with great extents of laminar and transitional flow being found in this research.

5 The discovery that long, wake-induced transitional strips can be present in turbomachinery shows that wake-induced transition does not immediately produce a fully turbulent strip with an intermittency of 1.0, as assumed by some researchers.

6 The mode switching (in time) from the non-wake path to the wake-induced strip within the laminar region typically occurs in a small fraction of a blade passing period. Although the strips are well defined and relatively narrow, a conventional quasi-steady analysis of these regions may not be adequate if the coupling effects of calming are not incorporated.

7 As Reynolds number is reduced, the wake-induced transitional strips weaken and form further downstream on the airfoil suction surface. Profile loss increases.
   - For compressors, the calmed regions weaken and transition via laminar separation becomes increasing more prevalent than bypass transition.
   - For LP turbines, calmed regions suppress flow separation in the aft portion of the airfoil at cruise.

8 As loading is increased, the wake-induced transitional strips form further upstream.
   - For compressors, transition length becomes progressively shorter, the strip functions as a turbulent strip for practical purposes and the calmed region becomes more effective.
   - For LP turbines, transition can be initiated by even slight diffusion in the loading distribution.

9 When wake frequency (reduced frequency) is high enough that calming does not decay before the appearance of the next wake, bypass transition dominates between wakes. Where calming runs out when wake frequency is reduced, separated-flow transition dominates.

10 Great care must be exercised when using rods to simulate airfoil wakes so that correct levels of wake turbulence intensity are produced.

11 The relative clocking of turbine nozzle rows has a substantial impact on boundary layer development and loss at midspan.

12 For the pressure surface, transition occurred in the region of adverse pressure gradient near the leading edge for the type of blading tested.

References

AGARD Lecture Series 195, 1994, "Turbomachinery Design Using CFD," May.

Abu-Ghannam, B. J., and Shaw, R., 1980, "Natural Transition of Boundary Layers—The Effects of Turbulence, Pressure Gradient and Flow History," *Journal of Mechanical Engineering Sciences,* Vol. 22, pp. 213–228.

Addison, J. S., and Hodson, H. P., 1990a, "Unsteady Transition in an Axial Flow Turbine: Part 1—Measurements on the Turbine Rotor," ASME JOURNAL OF TURBOMACHINERY, Vol. 112, pp. 206–214.

Addison, J. S., and Hodson, H. P., 1990b, "Unsteady Transition in an Axial Flow Turbine: Part 2—Cascade Measurements and Modeling," JOURNAL OF TURBOMACHINERY, Vol. 112, pp. 215–221.

Addison, J. S., and Hodson, H. P., 1992, "Modeling of Unsteady Transitional Boundary Layers," ASME JOURNAL OF TURBOMACHINERY, Vol. 114, pp. 580–589.

Arndt, N., 1993, "Blade Row Interaction in a Multistage Low Pressure Turbine," JOURNAL OF TURBOMACHINERY, Vol. 115, pp. 137–146.

Bellhouse, B. J., and Schultz, D. L., 1966, "Determination of Mean and Dynamic Skin Friction, Separation and Transition in a Low-Speed Flow With a Thin-Film Heated Element," *J. of Fluid Mechanics,* Vol. 24, pp. 379–400.

Collis, D. C., and Williams, M. J., 1959, "Two-Dimensional Convection From Heated Wires at Low Reynolds Numbers," *Journal of Fluid Mechanics,* Vol. 6, pp. 357–384.

Denton, J. D., 1993, "Loss Mechanisms in Turbomachines," ASME JOURNAL OF TURBOMACHINERY, Vol. 115, pp. 621–656.

Dong, Y., and Cumpsty, N. A., 1990a, "Compressor Blade Boundary Layers: Part 1 Test Facility and Measurements With No Incident Wakes," ASME JOURNAL OF TURBOMACHINERY, Vol. 112, pp. 222–230.

Dong, Y., and Cumpsty, N. A., 1990b, "Compressor Blade Boundary Layers: Part 2—Measurements With Incident Wakes," ASME JOURNAL OF TURBOMACHINERY, Vol. 112, pp. 231–240.

Halstead, D. E., 1996, "Boundary Layer Development in Multi-stage Low Pressure Turbines," Ph.D. Thesis, Iowa State University, Ames, IA.

Hodson, H. P., 1983, "The Development of Unsteady Boundary Layers on the Rotor of an Axial Flow Turbine," AGARD CP 351.

Hodson, H. P., 1985, "Boundary Layer Transition and Separation Near the Leading Edge of a High-Speed Turbine Blade," ASME *Journal of Engineering for Gas Turbines and Power,* Vol. 107, pp. 127–134.

Hodson, H. P., Huntsman, I., and Steele, A. B., 1994, "An Investigation of Boundary Layer Development in a Multistage LP Turbine," ASME JOURNAL OF TURBOMACHINERY, Vol. 116, pp. 375–383.

Hourmouziadis, J., 1989, "Aerodynamic Design of Low Pressure Turbines," AGARD Lecture Series 167.

Koch, C. C., 1981, "Stalling Pressure-Rise Capability of Axial-Flow Compressor Stages," ASME *Journal of Engineering for Power,* Vol. 103, pp. 645–656.

Koch, C. C., and Smith, L. H., 1976, "Loss Sources and Magnitudes in Axial Compressors," ASME *Journal of Engineering for Power,* Vol. 98, pp. 411–424.

Lieblein, S., Schwenk, F. C., and Broderick, R. L., 1953, "Diffusion Factor for Estimating Losses and Limiting Blade Loading in Axial-Flow-Compressor Blade Elements," NACA RM E53D01.

Mayle, R. E., and Dullenkopf, 1990, "A Theory for Wake-Induced Transition," ASME JOURNAL OF TURBOMACHINERY, Vol. 112, pp. 188–195.

Mayle, R. E., and Dullenkopf, 1991, "More on the Turbulent-Strip Theory for Wake-Induced Transition," ASME JOURNAL OF TURBOMACHINERY, Vol. 113, pp. 428–432.

Mayle, R. E., 1991, "The Role of Laminar–Turbulent Transition in Gas Turbine Engines," ASME JOURNAL OF TURBOMACHINERY, Vol. 113, pp. 509–537.

Mayle, R. E., 1992, "Unsteady, Multimode Transition in Gas Turbine Engines," AGARD PEP 80.

McCormick, M. E., 1968, "An Analysis of the Formation of Turbulent Patches in the Transition Boundary Layer," ASME *Journal of Applied Mechanics,* Vol. 35, pp. 216–219.

Meauze, G., 1989, "Overview of Blading Design Methods," AGARD Lectures Series No. 167.

Orth, U., 1993, "Unsteady Boundary Layer Transition in Flow Periodically Disturbed by Wakes," ASME JOURNAL OF TURBOMACHINERY, Vol. 15, pp. 707–713.

Pfeil, H., Herbst, R., and Schroder, T., 1983, "Investigation of the Laminar–Turbulent Transition of Boundary Layers Disturbed by Wakes," ASME *Journal of Engineering for Power,* Vol. 105, pp. 130–137.

Roberts, W. B., 1980, "Calculation of Laminar Separation Bubbles and Their Effect on Airfoil Performance," *AIAA Journal,* Vol. 18, pp. 25–31.

Schaubauer and Klebanoff, 1956, "Contributions on the Mechanics of Boundary Layer Transition," NACA, Report 1289.

Sharma, O. P., Wells, R. A., Schlinker, R. H., and Bailey, D. A., 1982, "Boundary Layer Development on Turbine Airfoil Suction Surfaces," ASME *Journal of Engineering for Power,* Vol. 104, pp. 698–706.

Walker, G. J., 1975, "Observations of Separated Laminar Flow on Axial Compressor Blading," ASME Paper No. 75-GT-63.

Walker, G. J., 1983, "Wall Proximity Corrections for Hot Wire Readings," *Proc. 8th Australasian Fluid Mechanics Conference,* Newcastle, pp. 6B.9–12.

Walker, G. J., 1989a, "Transitional Flow on Axial Turbomachine Blading," *AIAA Journal,* Vol. 27, pp. 595–602.

Walker, G. J., 1989b, "Modeling of Transitional Flow in Laminar Separation Bubbles," *Proc. 9th International Symposium on Air Breathing Engines,* Athens, pp. 539–548.

Walker, G. J., 1993, "The Role of Laminar–Turbulent Transition in Gas Turbine Engines: A Discussion," ASME JOURNAL OF TURBOMACHINERY, Vol. 117, pp. 207–217.

White, F. M., 1974, *Viscous Fluid Flow,* McGraw-Hill, New York, NY.

Wisler, D. C., 1985, "Loss Reduction in Axial-Flow Compressors Through Low-Speed Model Testing," ASME *Journal of Engineering for Gas Turbines and Power,* Vol. 107, pp. 354–363.

D. E. Halstead

D. C. Wisler

GE Aircraft Engines,
Cincinnati, OH 45215

T. H. Okiishi
Iowa State University,
Ames, IA 50011

G. J. Walker
University of Tasmania,
Hobart, Tasmania

H. P. Hodson
University of Cambridge,
Cambridge, United Kingdom

H.-W. Shin
GE Aircraft Engines,
Cincinnati, OH 45215

Boundary Layer Development in Axial Compressors and Turbines: Part 4 of 4—Computations and Analyses

This is Part Four of a four-part paper. It begins with Section 16.0 and concludes the description of the comprehensive experiments and computational analyses that have led to a detailed picture of boundary layer development on airfoil surfaces in multistage turbomachinery. In this part, the computational predictions made using several modern boundary layer codes are presented. Both steady codes and an unsteady code were evaluated. The results are compared with time-averaged and unsteady integral parameters measured for the boundary layers. Assessments are made to provide guidance in using the predictive codes to locate transition and predict loss. Conclusions from the computational analyses are then presented.

16.0 Description of Computational Analyses

Several different computational analyses of varying degrees of complexity were evaluated. The simplest of these were steady-flow boundary layer codes that are used regularly in the design of turbomachinery blading. They require the least amount of user orientation and computational time. Next, a steady-flow Navier–Stokes solver, which requires substantial user orientation, was run. Finally, a time-unsteady approach, developed very recently, was evaluated. Each technique is summarized below.

16.1 Steady Boundary Layer Analyses

STANX. The STANX code is a version of STAN5 originally developed by Crawford and Kays (1976). It solves the two-dimensional, compressible form of the boundary layer equations. The code utilizes a mixing-length turbulence model that has been modified to account for pressure gradient. No implicit capability to handle boundary layer transition is included in STANX. The user can specify as a program input the location of transition onset as determined using a desired correlation. The length of transition, however, cannot be specified.

KEP. The KEP code, described by Zerkle and Lounsbury (1987), is a modified version of STANX that incorporates a low-Reynolds-number $k-\epsilon$ turbulence model. Values of turbulence intensity and length scale at the blade-row inlet provide the necessary boundary conditions for the k (turbulence kinetic energy) and the ϵ (dissipation rate of turbulence kinetic energy) equations. An inherent feature of $k-\epsilon$ models is that flow transition is simulated directly by the diffusion of turbulent kinetic energy from the free stream into the laminar boundary layer. Hence, no explicit modeling of transition onset or length is employed.

16.2 Steady CFD Analysis. The second approach used a Navier–Stokes (NS) solver developed for optimizing the design of turbomachinery blade rows (Jennions and Turner, 1993). It solves the steady-state form of the compressible, Reynolds-averaged Navier–Stokes equations in two or three dimensions for a single blade row. A number of turbulence models are available. For this work, the algebraic Baldwin–Lomax turbulence model (ibid.) was used. This model, while simplistic, has the important flexibility of allowing the user to specify the location of transition onset (i.e., the point where the turbulence model is turned on).

16.3 Unsteady Boundary Layer Analysis

Fan–Lakshminarayana Code. Time-unsteady solutions were obtained using the computational approach developed by Fan and Lakshminarayana (1996). The unsteady flow field is first computed using a time-accurate, unsteady Euler solver. This solution provides the input conditions for a two-dimensional, unsteady boundary layer code. The boundary layer code employs a $k-\epsilon$ turbulence model developed for unsteady turbulent boundary layers. As with the KEP code described above, the prediction of flow transition is determined implicitly by the turbulence model.

16.4 Running the Codes. The input to the codes consisted of aerodynamic parameters and blading geometry. All aerodynamic parameters were determined directly from our experimental measurements. For unsteady flow calculations, values of reduced frequency and the time-varying distributions of blade-row inlet velocity and turbulence intensity were also provided.

Truly blind solutions from the Fan–Lakshminarayana code were generated by the code developers themselves using the required initial input and boundary conditions were provided. The experimental data were under the strict control of one of the authors (DCW) and no information of any kind concerning

Contributed by the International Gas Turbine Institute and presented at the 40th International Gas Turbine and Aeroengine Congress and Exhibition, Houston, Texas, June 5–8, 1995. Manuscript received by the International Gas Turbine Institute April 7, 1995. Paper No. 95-GT-464. Associate Technical Editor: C. J. Russo.

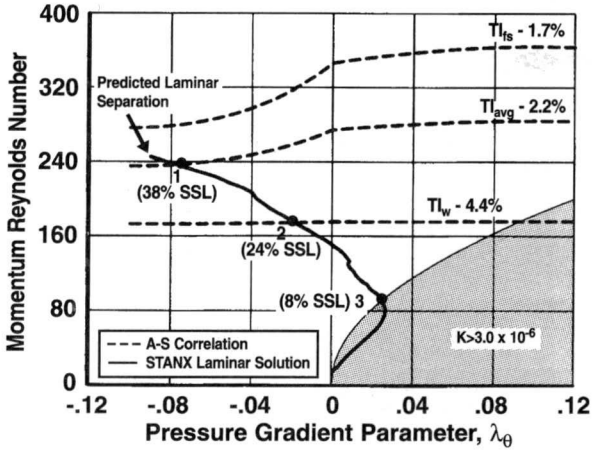

Fig. 42 Boundary layer characteristics diagram for the suction surface of the third-stage compressor stator; $\overline{Re} = 3.35 \times 10^5$, baseline Test Point 2B

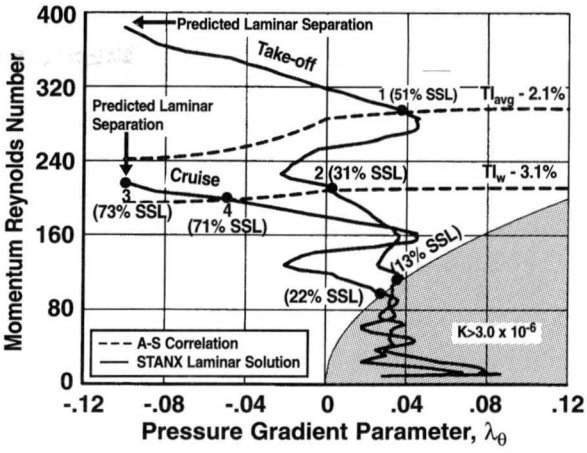

Fig. 43 Boundary layer characteristics diagram for the suction surface of the second-stage turbine nozzle: take-off $\overline{Re} = 5.27 \times 10^5$, Test Point 5A and Cruise $\overline{Re} = 1.80 \times 10^5$, Test Point 5D

the boundary layer measurements, the location of transition, etc., were provided to them *a priori.*

Running STANX. The boundary layer solution from STANX was obtained using a three-step process. First, STANX was run in a laminar-only mode until flow separation halted program execution. Second, a characteristics diagram in (λ_θ, Re_θ) coordinates was constructed using the STANX solution from step one. The location of transition onset was determined by noting where the STANX solution intersected the correlation of Abu-Ghannam and Shaw (1980), which was superimposed on the diagram. Third, STANX was re-run with the transition model turned on at the location of transition onset determined from step two above.

The characteristics diagrams for the suction surface of the compressor stator and turbine nozzle are shown in Figs. 42 and 43, respectively. The STANX laminar solutions $\lambda_\theta(Re_\theta)$ are plotted as solid lines in the figures. The Abu-Ghannam and Shaw (A–S) correlations appear as dashed lines for the relevant levels of turbulence intensity associated with the wake, the free stream, and the time-averaged values. When employing this correlation, one uses *local* values of turbulence intensity along the airfoil passage. Since our turbulence measurements indicated that dissipation effects were not significant across the blade row, we assumed frozen turbulence kinetic energy from the leading edge to compute these turbulence levels. Because the flow accelerates along the suction surface, the magnitudes of turbulence intensity were reduced relative to those at the stator inlet.

Also shown in Figs. 42 and 43 is the region where the acceleration factor, K, is greater than 3.0×10^{-6}. Such high levels of acceleration suppress transition of laminar boundary layers and relaminarize turbulent ones (Schlichting, 1979).

The location of transition onset is determined by locating the point where $\lambda_\theta(Re_\theta)$ from the STANX solution crosses the various A–S correlation lines for the local levels of turbulence intensity.

Running KEP. When we ran KEP using measured levels of turbulence intensity as input, we found that it predicted the location of transition onset too far aft on the airfoil surface compared to our measured locations and to the A–S correlation. Similar inaccuracies in predicting transition onset using $k-\epsilon$ models have been documented by Schmidt and Patankar (1991).

Nomenclature

A = laminar region on $s-t$ diagram
B = wake-induced transitional strip on $s-t$ diagram
C = wake-induced turbulent strip on $s-t$ diagram
d = diameter of cylindrical rod
D = calmed region on $s-t$ diagram
E = region of transition between wakes on $s-t$ diagram
F = region of turbulent boundary layer between wakes on $s-t$ diagram
H = shape factor = δ^*/θ
K = acceleration factor = $(\nu/V_\infty^2)dV_\infty/ds$
l = distance from rod centerline to measurement plane
LE = leading edge
Q_0 = lowest value (blue) of quantity in reference color legend for color figures
Q_{10} = highest value (red) of quantity in reference color legend for color figures
Re = Reynolds number for compressor = $V_{in}(SSL)/\nu$; Reynolds number for turbine = $V_{ex}(SSL)/\nu$
$\overline{Re}$ = stage-averaged Reynolds number = $0.5(Re_{rotor} + Re_{stator})$
Re_θ = momentum Reynolds number = $V_\infty\theta/\nu$
s = distance, the abscissa in the distance–time ($s-t$) diagram
SSL = suction surface length from LE to TE of airfoil
t = time, the ordinate in the distance–time ($s-t$) diagram
TE = trailing edge
TI = turbulence intensity
V = velocity
V_∞ = velocity at edge of boundary layer (free-stream velocity)
w = wake width
W, X, Y, and Z = trajectories on $s-t$ diagrams at constant fraction of free-stream velocity
Δ = difference
δ^* = displacement thickness
θ = momentum thickness or tangential direction
λ_θ = pressure gradient parameter = $(\theta^2/\nu)dV_\infty/ds$
ν = kinematic viscosity

Subscripts

avg = average
fs = free-stream
w = wake
z = axial direction

Given this inability of the KEP code to predict implicitly the correct location of transition onset for our data, we used an alternative approach. KEP was run using various values of inlet turbulence intensity until the location of transition onset it predicted agreed with the location obtained from the A–S correlation. We then conducted our KEP analysis with this value of turbulence intensity.

Running NS. The NS solutions were generated using a modified **H** grid containing 97 blade-to-blade and 197 streamwise nodes. To resolve the boundary layers adequately, we located 28 grid lines inside $y^+ = 30$ with the nearest wall grid point being located inside $y^+ = 1.0$. The location of transition onset was specified using the A–S correlation.

17.0 Comparison of Experimental and Computational Results

17.1 Steady Integral Parameters. Steady-state solutions are presented for the suction surface of both the compressor and turbine. Compressor results are shown for the baseline conditions (Test Point 2B) while those for the turbine are shown at take-off and cruise Reynolds number at increased loading (Test Points 5A and 5D, respectively). Computational results are presented in terms of displacement thicknesses, δ^*, momentum thicknesses, θ, momentum Reynolds number, Re_θ, and shape factor, $H = \delta^*/\theta$. In all cases, the computed values are compared directly with time-averaged experimental measurements.

Compressor Baseline (Test Point 2B)

Transition onset. The location of transition onset for the STANX, KEP, and NS solutions was determined from the A–S correlation using the time-averaged local turbulence intensity. Denoted as point 1 in Fig. 42, this location is approximately midway between the observed locations of wake-induced and non-wake-induced transition found in Fig. 13(*a*) of Part 2. Additional aspects relating to Fig. 42 are noteworthy. At the local level of turbulence intensity of the wake, $TI_W = 4.4$ percent, transition onset is predicated to occur at 24 percent SSL (point 2 of Fig. 42). This is in reasonable agreement with the measured location of 19 percent SSL for wake-induced transitional strip B shown in Fig. 13(*a*). At the local turbulence level occurring between wakes, $TI_{fs} = 1.7$ percent, laminar separation is predicted to occur *prior* to transition onset. However, our data show no flow separation occurring between wakes. Thus as a result of calming, the nonturbulent flow between wake-induced strips remains attached significantly farther downstream than predicted by this "classical" calculation for steady laminar boundary layers.

Integral parameters. A comparison of measured and computed values of integral boundary layer parameters is shown in Fig. 44. The KEP solution was obtained with an inlet turbulence intensity of 4.9 percent. Calculations from the Fan–Lakshminarayana code were obtained from a time average of their unsteady solution. Time-averaged values of the measurements are shown as symbols for the six streamwise locations where boundary layer surveys were made. In addition, values for trajectories *W* and *Z* are also shown to illustrate the variation of the unsteady parameters about the average.

The computed solutions are in quite good agreement with the time-averaged boundary layer measurements in Figs. 44(*a–c*). Changes in the rate of increase of the parameters are apparent at about 38 percent SSL, the location of transition onset. Near the trailing edge, values of computed momentum Reynolds number in Fig. 44(*c*) vary within about 15 percent of the measurements.

The difference in the nature of transition between the measured and computed boundary layers is shown by the variation in shape factor in Fig. 44(*d*). The sharp decrease of shape factor from laminar to turbulent levels at 38 percent SSL characterizes the "point-transition" nature of the STANX and NS solutions. This illustrates the consequence of not accounting for transition length downstream of the onset location. KEP shows only a slightly more gradual decline. The Fan–Lakshminarayana solution predicts a longer transition length with transition onset located near 42 percent SSL. Consequently, the distribution of shape factor follows the measured trend more closely.

Values of shape factor predicted by the NS code for the laminar region ($s < 40$ percent SSL) are about 10 percent less than those from the other solutions. This follows from the slight overprediction of momentum thickness in this region (Fig. 44(*b*)) and likely is caused by limitations in grid density near the leading edge.

The computed solution at increased loading (Test Point 3) showed the same trends.

Turbine Baseline (Test Point 5A). At the take-off Reynolds number, calculations were obtained from the KEP and STANX steady codes and from the Fan–Lakshminarayana unsteady code.

The location of transition onset for STANX and KEP was determined using the A–S correlation at the time-averaged local turbulence intensity in Fig. 43. Transition onset (point 1) occurs at 51 percent SSL. This coincides with the earliest observed location of transition onset between wakes shown at 52 percent SSL (point 17) in Fig. 28(*a*) of Part 3. Along the wake-induced path, transition onset was predicted by the correlation to occur at 32 percent SSL (point 2, Fig. 43), which agrees with the measured value at point 3 in Fig. 28(*a*).

For the KEP solution, a value of $TI_{\mathrm{KEP}} = 2.5$ percent was required to locate transition onset at the desired value of 51 percent SSL. The actual location of transition onset predicted by KEP was found to be very sensitive to the selected value of inlet turbulence intensity. Lowering TI_{KEP} just 0.3 percent moved transition onset downstream to about 70 percent SSL.

Agreement between measured and computed values of displacement thickness, momentum thickness, and momentum Reynolds number is generally good in Figs. 45(*a–c*). The sharp decrease of shape factor from laminar to turbulent levels at 48 percent SSL in Fig. 45(*d*) again characterizes the "point-transition" nature of STANX. The Fan–Lakshminarayana code appears to predict the correct location and extent of transition. In actuality, this code predicts a shorter-than-observed transition length along all trajectories *W*, *X*, *Y*, and *Z*. However, because the *location* of transition onset varies along the trajectories, the predicted *time-averaged* distribution of shape factor appears to match the measurements. This will be seen in the unsteady solution presented below.

Turbine Cruise Reynolds Number (Test Point 5D). Boundary layer calculations were obtained at cruise Reynolds number of 1.80×10^5 for the STANX and KEP codes only. The Fan–Lakshminarayana code had convergence problems of the Euler solver because of the low Mach number.

The STANX laminar-only solution for this test case predicted that laminar separation occurs *prior* to boundary layer transition associated with the time-averaged, local turbulence intensity. However, the experimental data showed that the flow remained attached to the trailing edge as a result of wake-induced transition and the calmed effect. Consequently, transition onset for both STANX and KEP solutions was placed just prior to predicted separation (point 3 in Fig. 43). This is just downstream of the measured location of the onset of wake-induced transition at 71 percent SSL (point 4 in Fig. 43). For the KEP solution, a value of $TI = 3.3$ percent was required to locate transition just prior to laminar separation.

The resulting distributions of momentum thickness and momentum Reynolds number in Figs. 46(*b–c*) agree reasonably well with the measurements. Downstream of the imposed location of transition onset, both codes underpredict shape factor in

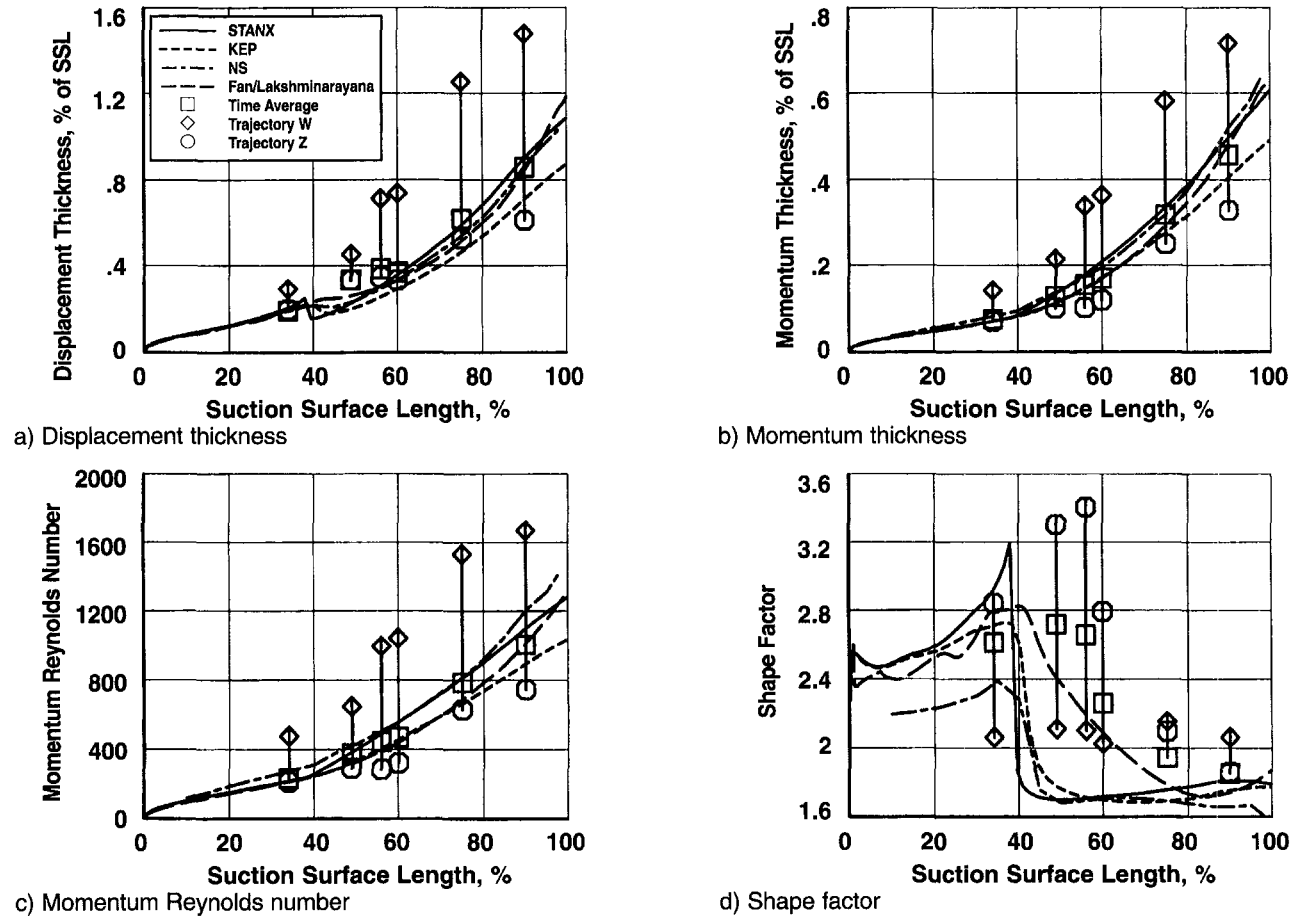

Fig. 44 Comparison of measured and computed boundary layer parameters for the suction surface of the third-stage compressor stator; baseline $\overline{Re} = 3.35 \times 10^5$, Test Point 2B

Fig. 46(d), which results from a lower-than-measured displacement thickness in Fig. 46(a) near the trailing edge.

17.2 Unsteady Computations. Unsteady boundary layer calculations were obtained using the Fan–Lakshminarayana code for both the compressor and turbine baseline test cases.

Compressor Baseline (Test Point 2B). Computed s–t diagrams of shape factor and momentum Reynolds number along the suction surface are shown in Figs. 47(a, b) for the third-stage stator operating at baseline conditions. Distributions of shape factor along trajectories W, X, Y, and Z are shown in Fig. 47(c). The relative phases of these trajectories and the letters describing the regions of boundary layer development are the same as those used in Part 2 for the compressor. The distribution of inlet turbulence intensity used for the computation, labeled TI, is superimposed onto the s–t diagrams.

The laminar region A in Figs. 47(a, b) extends downstream from the leading edge to about 40 percent SSL. Up until peak velocity, values of shape factor in this region are consistent with those of an accelerating laminar flow. Very little periodic variation associated with wake interaction is evident. Along the wake-induced path W, the shape factor of the laminar boundary layer remains nearly constant up to point 1 in Fig. 47(a) and in Fig. 47(c). Between wakes from 20 to 40 percent SSL, indicated by points 2 and 3 in Figs. 47(a, c), the shape factor increases in response to the adverse pressure gradient.

The start of wake-induced transition near 40 percent SSL is identified by the significant decrease in shape factor along trajectory W (point 4 in Figs. 47(a, c)). This is brought about by the higher level of turbulence in the rotor wake. The predicted location of the onset of wake-induced transition occurs about 20 percent farther downstream than that measured in Fig. 13(a) of Part 2. The wake-induced transitional region that develops downstream of transition onset is labeled region B in Figs. 47(a, b). As indicated in Fig. 47(c), transition along W extends from 40 to 52 percent SSL giving a predicted transition length of 12 percent of SSL, which is significantly shorter than the measured extent of 43 percent of SSL. The turbulent boundary layer occurring along the wake-induced path is labeled region C.

Between the wake-induced paths the turbulence intensity is lower and transition onset modulates along the surface aft of points 2 and 3, as shown by the dashed line. The highest values of shape factor occur just prior to transition onset at point 3 in Figs. 47(a, c). Unlike the conclusions drawn from the measurements, this increase in shape factor is *not* attributed to calming effects since this computational approach does not account for them. Rather, much of this variation is likely due to periodic effects captured in the unsteady solution.

The region of flow transition between wake-induced paths is labeled E in Figs. 47(a, b). The length of transition varies across this region as the line of transition completion also modulates. In general, the location of transition onset and the extent of transition along trajectories X, Y, and Z agree reasonably well with the measurements.

A turbulent boundary layer in region F follows region E and extends to the trailing edge. The momentum Reynolds number for the turbulent boundary layer in Fig. 47(b) increases significantly. Near the trailing edge, shape factors along all trajectories increase slightly due to the continued flow deceleration.

Time-Varying Integral Parameters. Computed boundary layer parameters across one wake passing period are shown in Fig. 48 for the same six streamwise locations where traverse

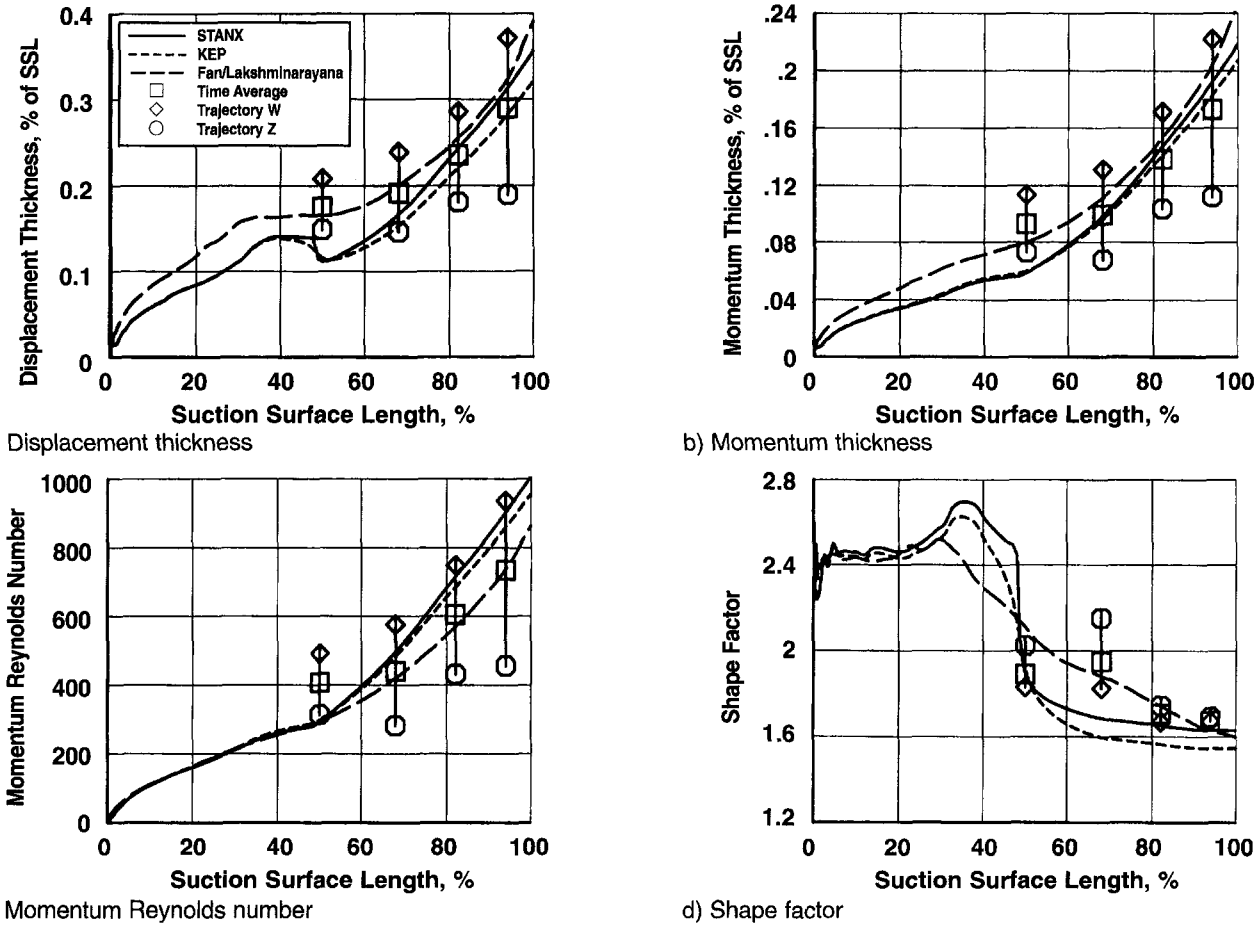

Fig. 45 Comparison of measured and computed boundary layer parameters for the suction surface of the second-stage turbine nozzle; take-off $\overline{Re} = 5.27 \times 10^5$, Test Point 5A

measurements were shown in Fig. 16 of Part 2. Ordinate scales for like parameters are identical to facilitate comparison. The unsteady computations exhibit some of the general features shown by the measurements. The computations of δ^*, θ, and Re_θ show a periodic variation with peak values occurring along the wake-induced regions. However, the computed periodic variations are more sinusoidal than the measurements, which show a more defined peaking of the wake-induced region. This is likely due to the diffusive character of the turbulence model and uncertainties in accounting for unsteady effects.

The computed shape factors are all below 3.0 in Fig. 48(d), while the measurements in Fig. 16(d) show that the flow is on the verge of separation along trajectory Z near 50 percent SSL.

Turbine Baseline (Test Point 5A). Computed $s-t$ diagrams of shape factor and momentum Reynolds number are shown along the suction surface in Figs. 49(a, b) for the second-stage turbine nozzle operating at baseline conditions. Distributions of shape factor for trajectories W, X, Y, and Z are shown in Fig. 49(c). Results are presented in a manner similar to that described for the compressor.

A prominent region A of laminar flow extends downstream from the leading edge. Shape factors, being equal to about 2.4, have little periodic variation.

Along a wake-induced trajectory W, the higher levels of turbulence initiate wake-induced transition directly downstream of 30 percent SSL at point 1. This location agrees with the measured start of transition in Fig. 28(a) of Part 3. However, the predicted length of the wake-induced transitional region B (17 percent of SSL) in Fig. 49(a) is significantly shorter than that observed experimentally (48 percent of SSL).

Between wake-induced regions, the decreasing shape factors along points 1-2-3 denote transition onset and parallel the distribution of turbulence intensity in Fig. 49(a). The computed location and character of transition onset at point 2 agrees with the measurements at point 17 in Fig. 28(a). The computed shape factors for point 3 in Fig. 49(a) remain at laminar levels to 90 percent SSL, which is well aft of minimum pressure. This region is similar to region G of Fig. 28(a), although the measured location of transition onset occurs significantly earlier (55 percent SSL). It is important to note, however, that both decreased turbulence, calming and flow periodicity are responsible for region G in the measurements, while only turbulence level and periodicity produce this region in the unsteady computations. This is an important distinction in the physics of this model, which contains no explicit calming.

As noted in Section 17.1, the predicted length of transition along each trajectory in Fig. 49(c) is relatively short compared to the measurements. However, because the location of transition onset varies along the trajectories, the predicted time-average distributions seen in Fig. 45(d) appears to match the measured length and onset location of transition.

Turbulent boundary layers, denoted as regions C and F, develop downstream of transitional regions B and E in Figs. 49(a, b). While shape factors in these regions are nearly uniform, the momentum Reynolds number shows considerable periodic variation.

Time-Varying Integral Parameters. The individual distributions of displacement thickness, momentum thickness and momentum Reynolds number shown in Fig. 50(a–c) agree reasonably well in both magnitude and trend with the measurements in

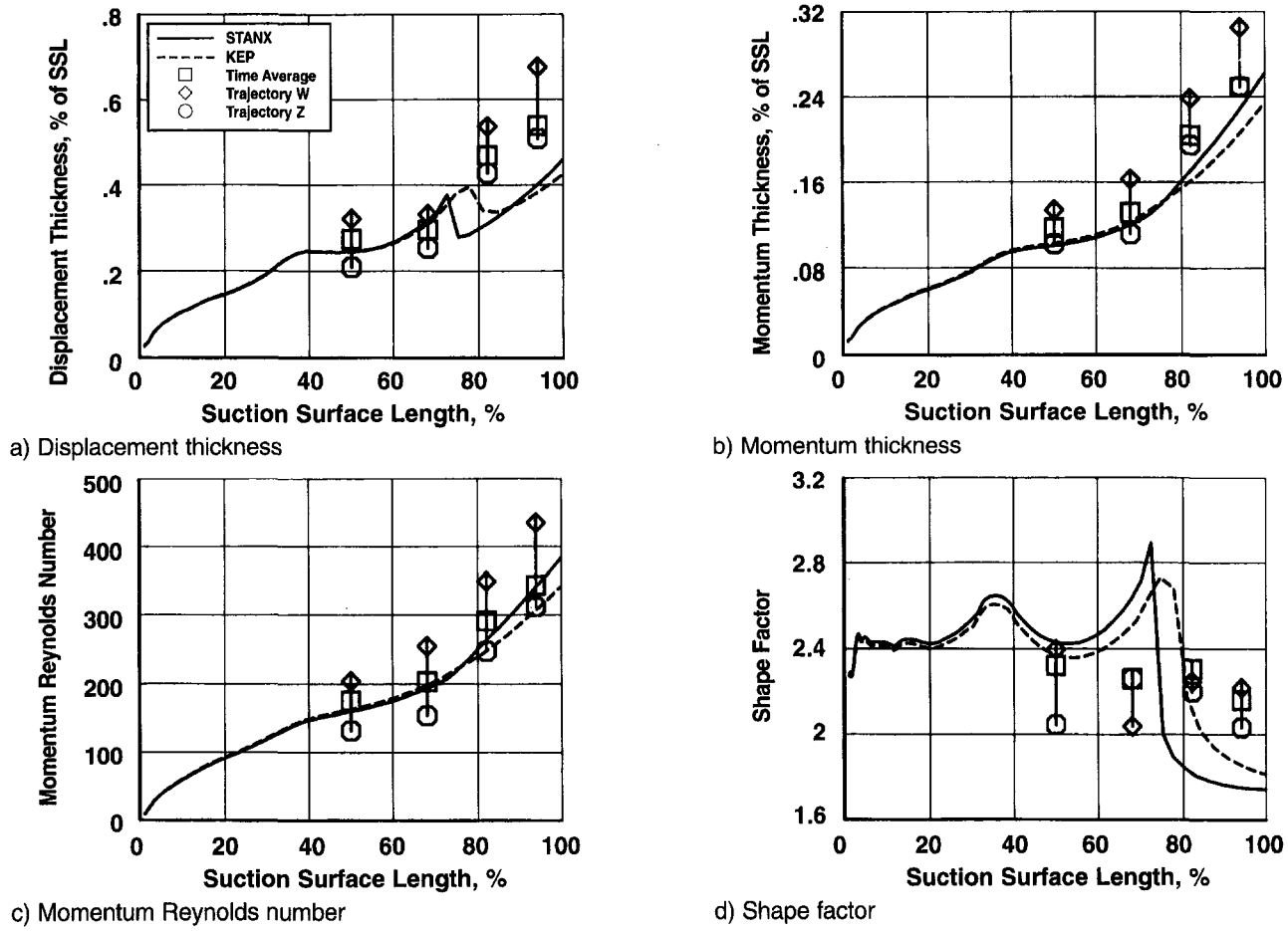

Fig. 46 Comparison of measured and computed boundary layer parameters for the suction surface of the second-stage turbine nozzle; cruise $\overline{Re} = 1.80 \times 10^5$, Test Point 5D

Fig. 30(a–c). In the vicinity of trajectory W, the computations indicate a double peak with the maximum values lagging W values by about 10 percent of the period. This feature is not present in the measured distributions and may be due to uncertainties in accounting for unsteady effects. For both the measurements and computations, the momentum Reynolds number is lowest in general near trajectory Z where turbulence intensity is low.

The distributions of shape factor at 50 percent SSL in Fig. 50(d) show significantly greater magnitudes along the nonwake paths than observed experimentally. This difference may reflect the inability of the computational model to account for the influence of high levels of turbulence on nontransitional laminar boundary layers.

17.3 Aerodynamic Loss

Compressor. A comparison of measured and predicted values of profile loss coefficient is presented in Fig. 51 for the third-stage compressor stator. Loss was computed using Eq. (13) of Part 1. Measurements are shown as open symbols and are identified by Test Point number. The curve adjoins measurements obtained at high Reynolds numbers and over a range of flow coefficients. The remaining open symbols show loss variation with Reynolds number at one flow coefficient.

At the baseline Test Point 2B, the stator operates at near-optimal incidence. Its measured loss coefficient is 0.020. Loss increases with incidence for Test Points 3 and 4, as expected. At Test Point 4, the compressor is near stall. Loss also increases as Reynolds number is reduced for Test Points 2C and 2D. Compared to the baseline, the loss has more than doubled at the lowest Reynolds number.

Predictions of loss coefficient determined for Test Point 2B using the KEP and STANX boundary layer solutions are denoted in Fig. 51. The upper values of each prediction were obtained with transition occurring at or very close to the leading edge. The lower values were obtained with transition onset located using the A–S correlation as described in Section 17.1. For the latter case, the loss coefficient predicted using STANX agreed closely with the measured value while that using the KEP solution was underpredicted by 16 percent. This is consistent with the differing predicted values of displacement and momentum thickness at the trailing edge as shown in Figs. 44(a, b).

The effect that varying the location of transition onset has on predicted loss coefficient is shown further in Fig. 52 for the STANX solutions. The ordinate is percent change in loss coefficient from the reference value obtained with transition onset specified by the A–S correlation. Five locations of transition onset were evaluated. The loss coefficient computed with transition specified at the leading edge is nearly 20 percent greater than the reference value. As the location of transition onset is placed farther aft, the magnitude of the overprediction decreases as expected. Downstream of peak velocity, the difference is less than about 10 percent.

Turbine. A comparison of measured and predicted values of loss coefficient for the second-stage turbine nozzle at increased loading is provided in Fig. 53. As before, measurements are shown using open symbols and are identified by Test Point.

The lowest value of measured loss occurs at Reynolds number 5.27×10^5 (Test Point 5A). As Reynolds number is reduced from take-off to cruise levels, the loss coefficient increases

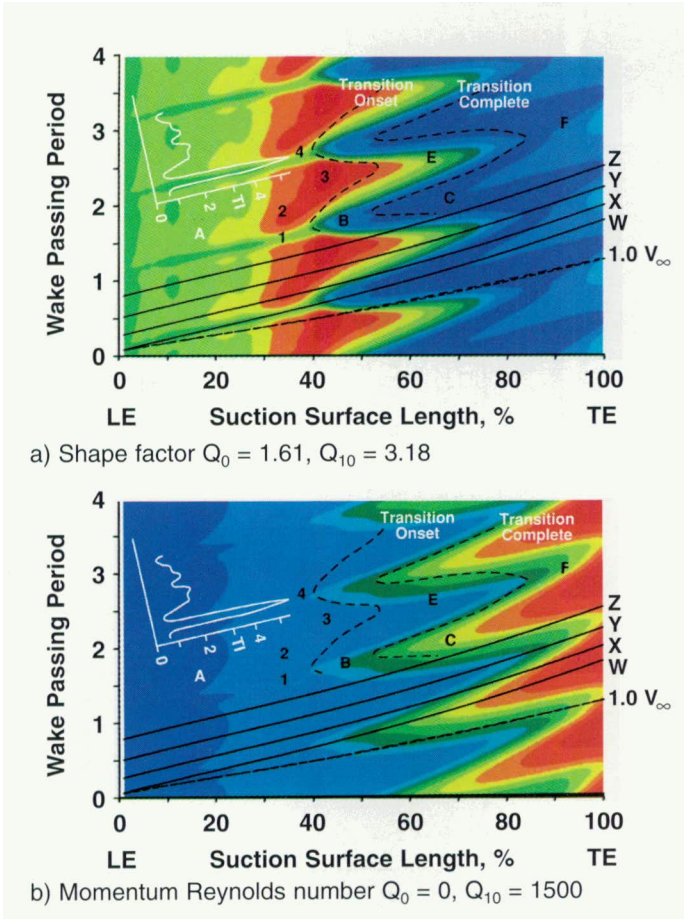

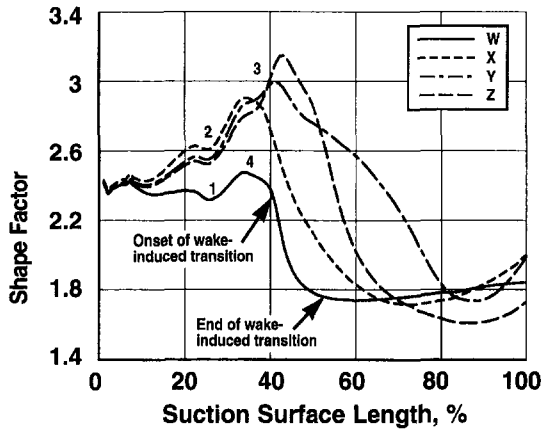

Fig. 47 Unsteady boundary layer calculation for the suction surface of the third-stage compressor stator. (*a–b*) *s–t* diagrams, (*c*) trajectories *W*, *X*, *Y*, *Z*. Baseline $\overline{Re} = 3.35 \times 10^5$, Test Point 2B.

monotonically. At Test Point 5E, it has increased by 65 percent from its value at 5A.

Additional loss measurements included in Fig. 53 were obtained at Test Point 5B for six different circumferential orientations of nozzle 1 relative to nozzle 2. Nearly a 25 percent variation in the profile loss coefficient for nozzle 2 was observed as nozzle 1 was clocked circumferentially relative to nozzle 2. This variation is nearly 40 percent of that caused by the reduction in Reynolds number from take-off to cruise values. Thus, nozzle clocking can have a significant impact on LP turbine loss at midspan. Similar findings have been reported by Sharma et al. (1994) for a low-aspect-ratio turbine.

Predicted values of loss coefficient are also shown in Fig. 53 for take-off and cruise Reynolds numbers, Test Points 5A and 5D, respectively. As denoted, the range in predicted loss was obtained by varying the location of transition onset along the suction surface from the leading edge (solid square symbol) to just prior to laminar separation (solid circle). The symbol "*X*" denotes loss prediction with transition specified using the A–S correlation as detailed in Section 17.1. For the latter, loss predictions determined from KEP and STANX solutions overpredict measured loss by 42 and 56 percent, respectively. The magnitude of predicted loss varied by as much as 35 percent depending on the specified location of transition.

At cruise Reynolds number, loss determined with transition located just prior to separation was overpredicted by 6 and 25 percent using KEP and STANX solutions, respectively. As expected, the maximum value of loss occurs when assuming turbulent flow from the leading edge.

18.0 Discussion

A discussion of our findings relative to our objectives in Section 2.2 is presented below.

18.1 The Composite Picture. This discussion relating to our first objective of describing boundary layer development on multistage turbomachinery blading has already been presented in Section 5.0 of Part 1.

18.2 Computational and Modeling Considerations. The second overall objective was to assess the capabilities of several modern codes to predict the measurements. This issue is addressed and answers are provided to describe how well these codes predict profile loss, the location and extent of transition, and other relevant features.

General Accuracy of Computations

Steady flow codes. In general, only when appropriate locations of transition onset were provided by the user did the steady-flow calculations of displacement thickness, momentum thickness and momentum Reynolds number from KEP, STANX and NS, agree well with measurements. For STANX and NS, the distributions of shape factor decrease abruptly from laminar to turbulent levels, which is characteristic of point-transition models. The comparison of measured and calculated values of displacement and momentum thickness suggests that accounting for transition length may improve agreement. The $k-\epsilon$ turbulence model in KEP did not reliably predict transition onset. Its computed transition length was also significantly underpredicted.

Unsteady code. The unsteady solution obtained using the Fan–Lakshminarayana code successfully captured some general unsteady features observed experimentally. Time-averaged boundary layer parameters obtained from the unsteady solution showed good agreement with the measurements. Locations of wake-induced-transition onset for the turbine baseline and non-wake-induced-transition onset for the compressor baseline were predicted especially well. In general, transition lengths for both the compressor and turbine, especially along the wake-induced path, were underpredicted. Because calming effects are not accounted for in this code, it predicted midchord laminar separation for compressor Test Point 3 where none was observed experimentally. Improvements in modeling the essential physics of turbulent spot formation and the associated calmed effect as well as addressing flow separation issues would likely improve predictions.

Given the strong correlation between the unsteady flow field and the subsequent boundary layer solution, it is imperative when utilizing such codes that the initial conditions of the flow field be accurately documented in terms of inlet velocity, turbulence intensity, and turbulence length scale.

Aerodynamic loss prediction. Predictions of aerodynamic loss obtained using STANX boundary layer calculations

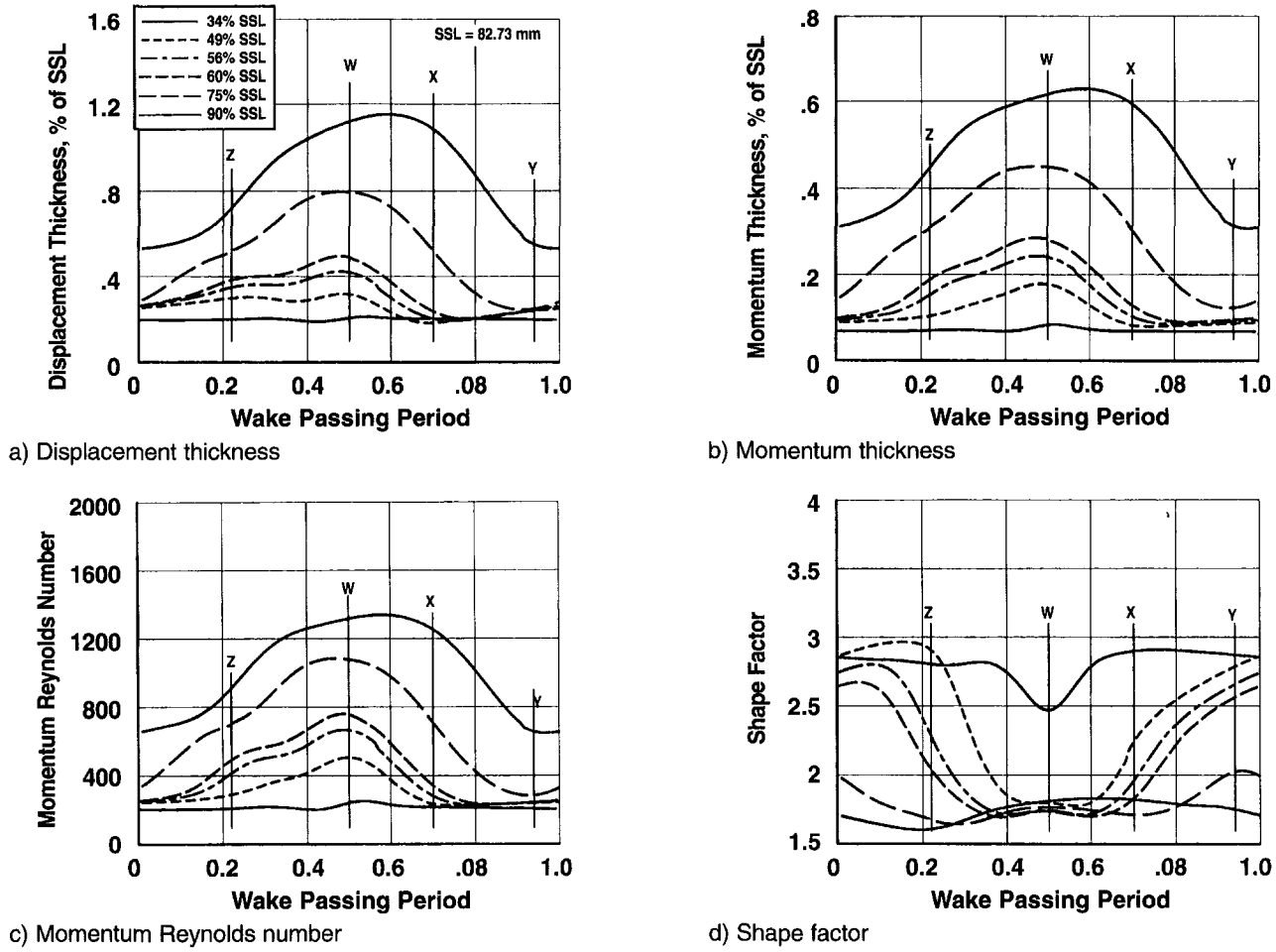

Fig. 48 Variation of computed boundary layer parameters across wake-passing period for the suction surface of the third-stage compressor stator; trajectories *W*, *X*, *Y*, and *Z* from Fig. 47 are identified; baseline $\overline{Re} = 3.35 \times 10^5$, Test Point 2B

matched well with the compressor measurements while those from KEP are about 15 percent lower than measured. For the turbine, profile loss was overpredicted slightly at cruise and more so at take-off Reynolds numbers. The general trend of increasing loss with decreasing LP turbine Reynolds number was captured by the predictions; however, the slopes of the predicted and measured trends differ. For the compressor, predicted values obtained with turbulent flow assumed from the leading edge were about 20 percent greater than those obtained with transition onset located to better coincide with the measurements. Differences as large as 35 percent were observed for the turbine.

Computational/Modeling Deficiencies at LPT Cruise. Comparisons of our computational results with measurements at cruise (low) Reynolds number for the turbine showed that no reliable means to compute these flows is yet available. The A–S correlation predicted separation to occur prior to transition onset. However, the measurements showed that no separation took place due to calming effects in the regions of nonturbulent flow. In order to predict accurately when large increases in LP turbine loss associated with laminar separation without reattachment will occur, one must understand and appropriately model the *unsteady* transition process. Designers may then be able to increase V_{max}/V_{exit} ratios with more confidence to get fewer airfoils and less weight while staying clear of performance deterioration at low cruise Reynolds numbers.

Steady Versus Unsteady Computations. As noted previously, there was strong agreement between the time-averaged unsteady solution (Fan–Lakshminarayana) and the steady-flow boundary layer calculations for the compressor. Given this agreement, one must ask whether the extra effort associated with obtaining the unsteady solution is warranted. One important feature of the unsteady calculation is the prediction of the time-varying turbulent boundary layer at the trailing edge. This is entirely consistent with the boundary layer measurements. An implication is that, as compressor loading is increased, the portion of the turbulent boundary layer with high-momentum Reynolds number near the trailing edge will separate first. The unsteady code should capture this feature. In actuality, however, flow breakdown in compressors generally occurs first in the end walls.

Accounting for Transition. Both the measurements and computations clearly underscore the need for designers to consider the transitional nature of boundary layers in both compressors and low-pressure turbines, especially as it relates to loss prediction.

Locating transition onset. For steady-flow calculations at relevant compressor Reynolds numbers and at take-off Reynolds numbers for the LP turbine, reasonable predictions of transition onset were obtained using the A–S correlation evaluated at time-averaged, local turbulence intensities. In addition, reasonable agreement for the onset of wake-induced transition was found when applying the correlation using the local value of wake-turbulence intensity. This may be especially attractive for modeling approaches that attempt to capture both the wake-induced and non-wake-induced paths.

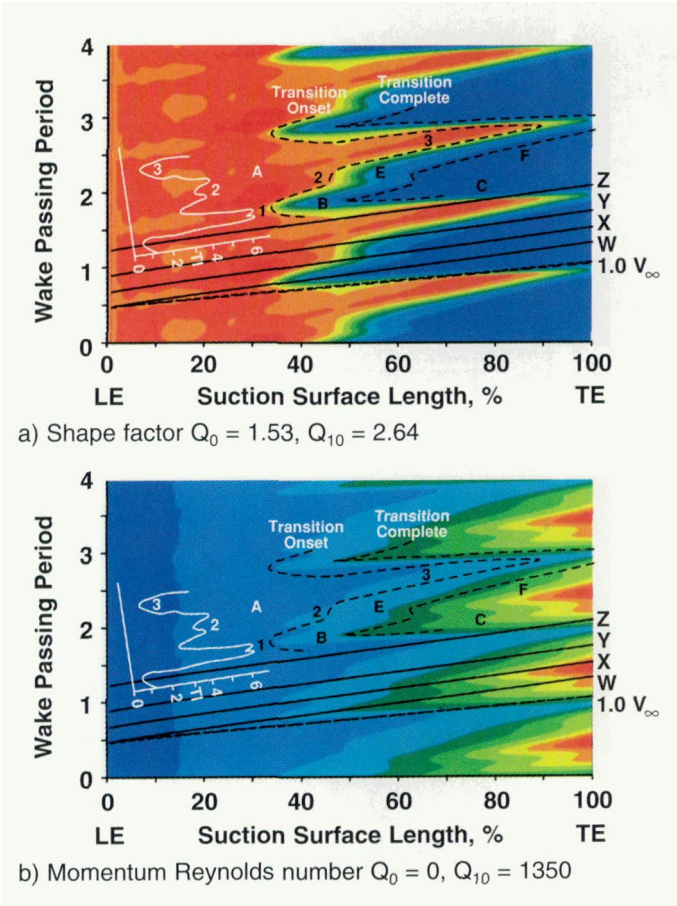

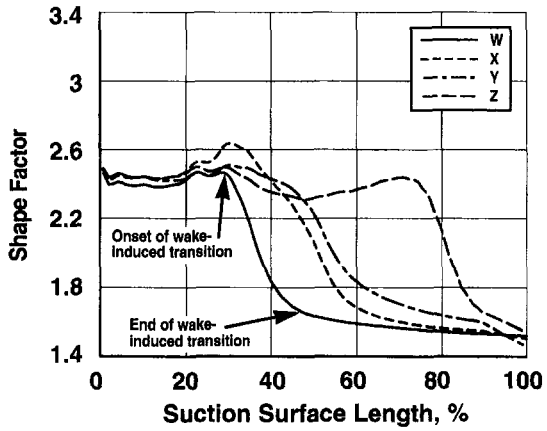

Fig. 49 Unsteady boundary layer calculation for the suction surface of the second-stage turbine nozzle: (*a–b*) *s–t* diagrams, (*c*) trajectories *W*, *X*, *Y*, *Z*; take-off $\overline{Re} = 5.27 \times 10^5$, Test Point 5A

Consequences of calming. Additional insight was gained concerning boundary layer solutions and the prediction of transition onset when calming effects were strong. Especially for the compressor, levels of local free-stream turbulence occurring between wake-induced strips were such that the A–S correlation consistently predicted laminar separation to occur prior to transition onset. However, the measurements showed no flow separation. Instead, the flow remained attached due to the elevated shear stress produced by calming. In this instance, the A–S correlation could not adequately predict onset for the region between wakes because, while the flow is nonturbulent, it is also not conventional laminar flow either. This further implies that boundary layer prediction schemes using a traditional linear combination approach, which at first looks attractive given the distinct wake and non-wake paths, would not be adequate. In regions where calming is significant, the nonturbulent portion of the solution cannot be treated in a conventional (i.e., laminar) fashion since separation would be inaccurately predicted.

Effect on loss prediction. Our analysis for the turbine at take-off Reynolds numbers and for the compressor at relevant Reynolds numbers suggests that finding the precise location of transition onset is not critical for steady-flow calculations of loss prediction. Rather, a sound engineering approach based on proven transition correlations appears to be adequate. If the location of transition onset is determined using a reasonable correlation, the predicted values of loss are not *strongly* influenced by small variations in this location. However, for both compressors and LP turbines, assuming turbulent flow from the leading edge is an oversimplification that can produce significant errors in loss prediction. For our tests, loss was overpredicted by as much as 35 percent.

Length of transition. In general, neither the steady nor the unsteady codes could predict transition length accurately. In most cases the codes significantly underpredicted this length. This is suggested especially by comparing the computed and measured distributions of shape factor. Not accounting for transition length may explain a portion of the loss overprediction for the turbine at take-off Reynolds number.

Use of $k-\epsilon$ models. Implicit predictions of transition onset and length using the $k-\epsilon$ model as implemented in KEP were less accurate than desired. However, efforts to improve this aspect of $k-\epsilon$ models have been made elsewhere (Schmidt and Patankar, 1991). Such an approach is appealing in that the capability to compute transitional flows is enhanced while maintaining the attractive features of the $k-\epsilon$ turbulence model.

18.3 Design Considerations. The third and final overall objective was to evaluate the extent to which the detailed picture of boundary layer development needs to be modeled in the design and analysis process. What practical simplifications to the real flow field can be made for these purposes? To what extent are cascade and single-stage results of value to the designer for predicting flows in embedded stages?

Although this part of the discussion is subjective and we obviously cannot discuss the details of particular design systems, we can provide some insights.

Aerodynamic Loss. Designers want to know whether the loss prediction from the boundary layer portion of their design system is reliable enough to allow meaningful comparisons of loss associated with different airfoil shapes, loading distributions and vector diagrams. The emphasis here is on relative comparisons so that the best configuration can be chosen.

For well-designed turbomachine airfoils operating at the design point, we found that there can be a large extent of laminar or laminar-like flow on the suction surface, extending in some cases to near midchord for compressors and farther downstream for LP turbines. Thus, in estimating loss, our results show designers should not simplify things by assuming a turbulent boundary layer beginning from the leading edge, as this can overpredict the profile loss significantly and possibly underpredict achievable diffusion. Applying this assumption for LP turbines, especially at cruise Reynolds numbers, may yield entirely misleading results.

Our results suggest the following practical approach when using conventional boundary layer codes. By incorporating a correlation like that of Abu-Ghannam and Shaw to locate the onset of transition, reasonably good boundary layer solutions and loss predictions can be obtained from steady codes for compressors and LP turbines at take-off Reynolds numbers. Predictions are much less reliable for LP turbines at cruise Reynolds numbers where laminar separation may occur.

For turbines, our results confirm the notion of keeping a continuously accelerating flow to peak velocity. Even the slight-

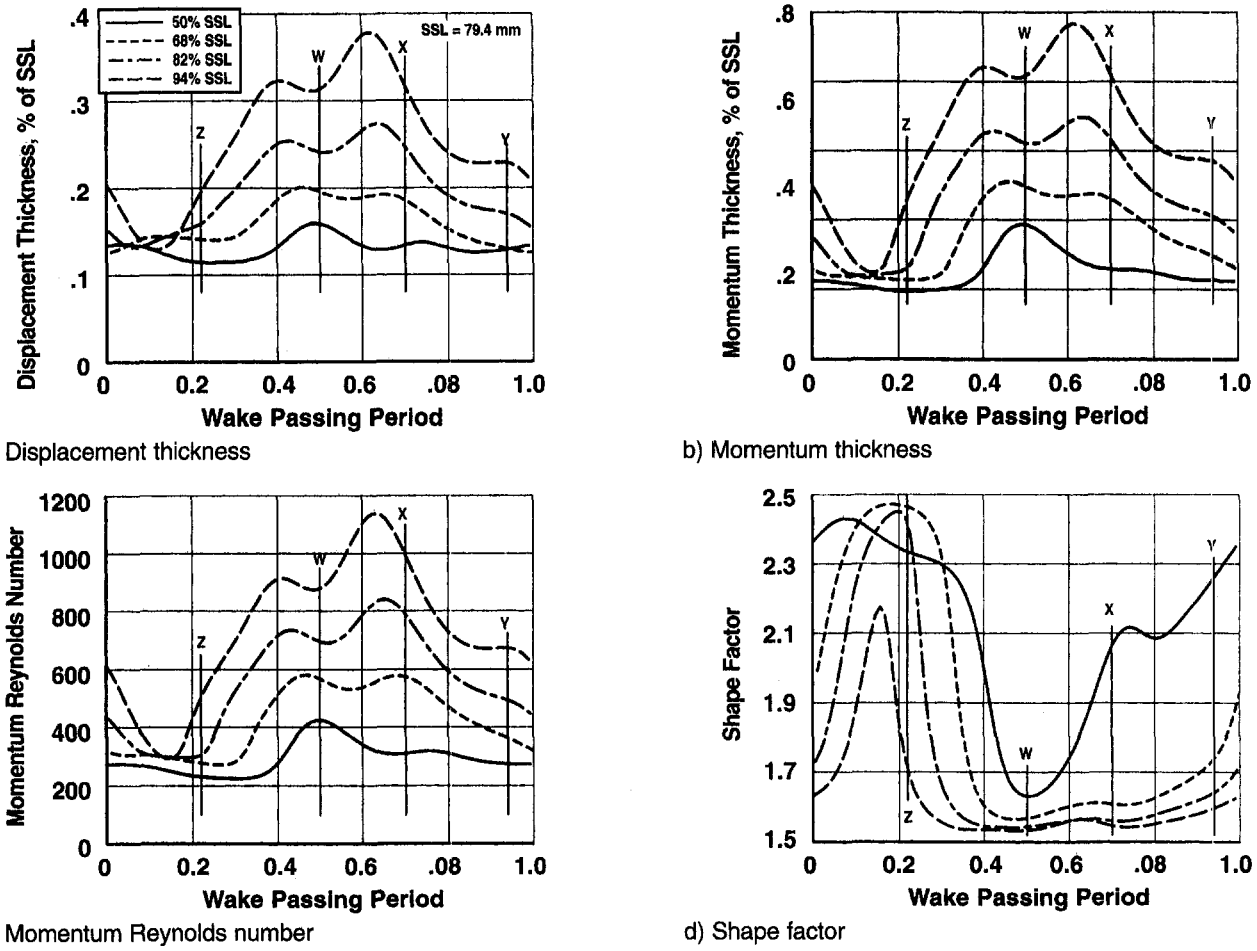

Fig. 50 Variation of computed boundary layer parameters across wake-passing period for the suction surface of the second-stage turbine nozzle; trajectories *W*, *X*, *Y*, and *Z* from Fig. 49 are identified; take-off $\overline{Re} = 5.27 \times 10^5$, Test Point 5A

est diffusion along the way may be enough to trigger transition and possibly additional loss.

Nozzle–nozzle clocking was shown experimentally to have a substantial influence on profile loss at midspan, as the boundary layer on the downstream nozzle is strongly influenced by wake interaction from the upstream nozzle. Designers should continue to consider blade-row clocking as a variable.

Airfoil Shapes. We recognize that there are airfoil loading (velocity) distributions other than the ones shown in Figs. 3 and 7 that we tested. However, we think that the same generic regions *A–F*, which define boundary layer development, will also be found along the airfoil surfaces for these other loading distributions. The locations and extent of these regions will, of course, depend on the design.

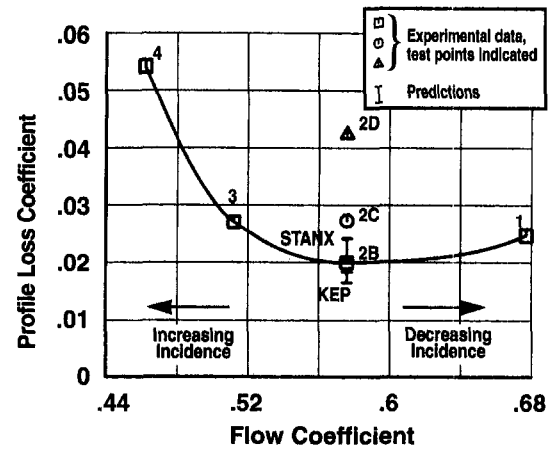

Fig. 51 Comparison of predicted and measured values of profile loss coefficient for the third-stage compressor stator

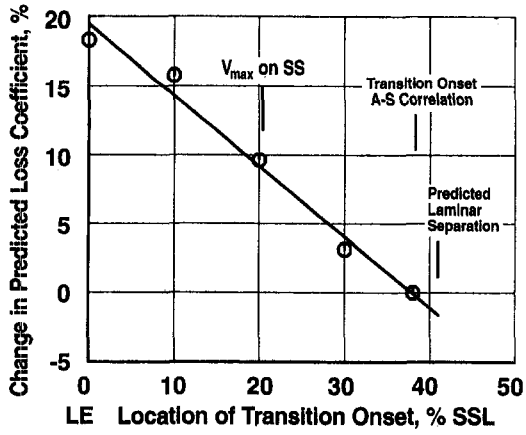

Fig. 52 Effect of transition onset location on predicted values of profile loss coefficient for the third-stage compressor stator, Test Point 2B, boundary layer calculations from STANX

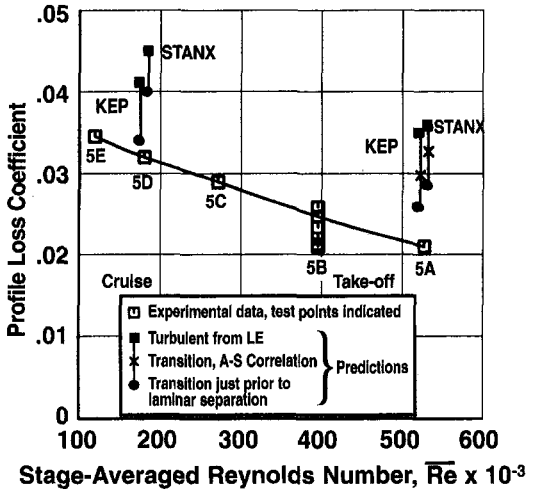

Fig. 53 Comparison of predicted and measured values of profile loss coefficient for the second-stage turbine nozzle

Based upon our results, we address features associated with other airfoil velocity distributions shown in Fig. 54. Profile A in Fig. 54(a) was used for the compressor tests reported in this paper. Profile A in Fig. 54(b) was used for the turbine tests.

For the compressor, profile B in Fig. 54(a) has a more rapid accelerating region, a peak velocity that is closer to the leading edge, a higher value of V_{max}/V_{exit}, a much more rapid diffusion immediately after peak velocity, and a much more gentle diffusion over a long region from midchord to the trailing edge. This type of profile loads the forward portion of the airfoil and unloads the aft portion, giving a characteristic ski-jump shape to the diffusing region.

Profile B in Fig. 54(a) will tend to have a shorter extent of both laminar and calmed regions on the suction surface relative to profile A. This is because peak velocity has been moved toward the leading edge and the calmed regions have less time to grow before peak velocity. Transition will likely take place rapidly in the strong diffusion that occurs immediately following peak velocity. With a diminished extent of calming, intermittent flow separation may be more prone to occur near the end of the wake passing period in the strong diffusion right after peak velocity. Early transition along both the wake and the non-wake paths would create a longer extent of turbulent boundary layer. Profiles between A and B that have a reduced diffusion gradient in the aft portion of the airfoil have been used with good success to reduce turbulent flow separation as loading increases (Wisler, 1985).

For profile C, the peak velocity was moved aft and the diffusion gradient is increased in the rear portion of the airfoil. Relative to profile A, profile C in Fig. 54(a) will likely have a longer extent of laminar regions. However the steeper diffusion gradient may cause separated-flow transition in the aft portion of the airfoil as loading increases. This type of airfoil was reported by Wisler (1985) to work well in tip sections of rotors where tip vortex and secondary flows dominate wake-induced effects.

For LP turbines, profile A in Fig. 54(b) is representative of what we tested. The diffusion levels are not high and the airfoil is separation free. Some designs incorporate more aggressive loadings such as that of profile B. In this case, as values of V_{max}/V_{exit} increase and diffusion gradients steepen in the aft portion of the airfoil, the flow is more likely to undergo separated flow transition sooner after peak velocity. Increasing V_{max}/V_{exit} limits, which could permit the use of fewer airfoils, must be balanced by the risk of flow separation, which is especially detrimental to performance if the flow does not reattach. The calmed effect needs to be examined more closely relative to its ability to suppress this separation and allow higher loading.

Exploiting the Calmed Region? Can designers exploit the calmed effect to improve turbomachinery performance? Some general thoughts follow.

We observe that a great deal of optimization has already been achieved since designers are very clever in engineering complex, efficient machines without fully understanding all flow details. Thus, a good portion of the benefits of the calmed effect may already be incorporated into modern designs, perhaps unknowingly. Since the trend in compressor design over the past 25 years has been to higher solidity blading, airfoils are now placed closely enough circumferentially that the calmed region generally does not completely decay before the next wake-induced strip occurs. The practical benefit of this has been to prevent intermittent laminar-flow separation with possible associated loss that was shown to occur in the region between wakes at the reduced solidity (airfoil count) and wake frequency typical of earlier designs. Consequently higher loadings are achieved at midspan without laminar flow separation. The same can be said for LP turbines where designs have trended to aft-loaded velocity distributions with increasing V_{max}/V_{exit} ratios. In retrospect, perhaps we researchers have just caught up to where designers have been sitting for years.

For turbines, the discovery that the calmed effect can suppress flow separation at cruise (low) Reynolds numbers in the region between wakes may have important design implications. It provides evidence that an additional effect is at work to help combat flow separation. This allows increased loading in the aft region of the airfoil beyond that suggested using conventional analyses.

Knowing about the existence of the calmed effect may now give designers more confidence in "pushing" the velocity distributions beyond the limits determined using conventional anal-

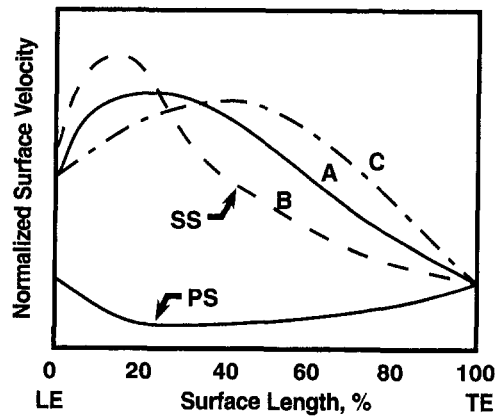

a) Compressor profiles

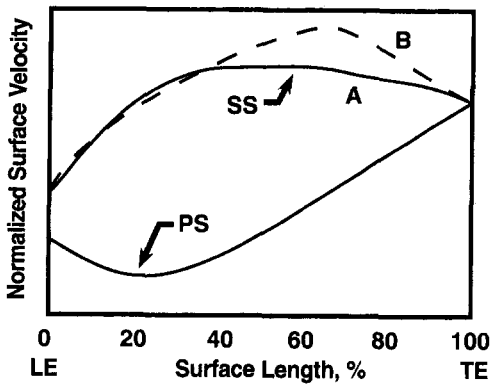

b) Turbine profiles

Fig. 54 Generic profiles showing different loading distributions for compressor and turbine airfoils

yses. Understanding the plan-form structure of unsteady boundary layers, as described in Fig. 10 of Part 1, now allows engineers to construct this picture for their design and assess the extent and influence of the calmed region.

Conclusions

The following conclusions are drawn from our computational analyses:

1 Conventional, steady flow codes predicted the general features of the boundary layer reasonably well for compressors and turbines at high Reynolds numbers, provided transition onset was adequately specified. This has important design implications.

2 At cruise (low) Reynolds numbers for turbines, no reliable codes were available to compute the flows. While the codes predicted laminar separation, the measurements show that separation was suppressed by calming.

3 Solutions from the unsteady Fan and Lakshminarayana code agreed reasonably with time-averaged measurements. While these solutions captured some of the unsteady features observed experimentally, they did not always predict the time-varying onset and length of transition well.

4 Airfoil profile loss can be significantly overpredicted when transition is forced to occur at the leading edge. For our tests, loss was overpredicted by as much as 35 percent. To achieve reasonable accuracy in loss predictions, designers should locate transition onset using proven, steady-state correlations.

5 No codes of which we are aware incorporate the calming effect. This can cause them to predict laminar separation when it is not present on the airfoil or to predict the onset of transition prematurely between wakes in the case of unsteady or quasi-steady codes.

6 Incorporating calming effects may allow designers to "push" the velocity distributions beyond the limits determined using conventional analyses.

Acknowledgments

The authors are deeply indebted to Prof. Nicholas Cumpsty for several useful discussions of this work, especially relative to his own findings about the calmed effect in compressors. These discussions took place in 1993–94.

The authors are also indebted to Dr. Sixin Fan and Prof. Budugur Lakshminarayana of the Pennsylvania State University for running the unsteady boundary layer code and providing blind solutions to our test cases, to Mr. Scott Hunter for running the N-S code, to James Cahill and William Groll for building the instrumentation to traverse the boundary layers, and to technician Donald Menner for operating the test vehicles. The authors also wish to thank GEAE for permission to publish this paper.

References

Abu-Ghannam, B. J., and Shaw, R., 1980, "Natural Transition of Boundary Layers—The Effects of Turbulence, Pressure Gradient and Flow History," *Journal of Mechanical Engineering Sciences,* Vol. 22, pp. 213–228.

Crawford, M. E., and Kays, W. M., 1976, "STAN-5—A Program for Numerical Computation of Two-Dimensional Internal and External Boundary Layer Flows," NASA CR 2742.

Cumpsty, N. A., 1993–94, private communications.

Fan, S., and Lakshminarayana, B., 1996, "Computation and Simulation of Wake-Generated Unsteady Pressure and Boundary Layers in Cascades: Part 1—Description of the Approach and Validation, Part 2—Simulation of Unsteady Boundary Layer Flow Physics," ASME JOURNAL OF TURBOMACHINERY, Vol. 118, pp. 96–122.

Jennions, I. K., and Turner, M. G., 1993, "Three-Dimensional Navier–Stokes Computations of Transonic Fan Flow Using an Explicit Flow Solver and an Implicit $k-\epsilon$ Solver," ASME JOURNAL OF TURBOMACHINERY, Vol. 115, pp. 261–272.

Schlichting, H., 1979, *Boundary Layer Theory,* McGraw-Hill, New York.

Schmidt, R. C., and Patankar, S. V., 1991, "Simulating Boundary Layer Transition With Low-Reynolds-Number $k-\epsilon$ Turbulence Models: Part I—an Evaluation of Prediction Characteristics: Part II—an Approach to Improving the Predictions," ASME JOURNAL OF TURBOMACHINERY, Vol. 113, pp. 10–26.

Sharma, O. P., Ni, R. H., and Tanrikut, S., 1994, "Unsteady Flows in Turbines—Impact on Design Procedure," AGARD LS 195.

Wisler, D. C., 1985, "Loss Reduction in Axial-Flow Compressors Through Low-Speed Model Testing," ASME *Journal of Engineering for Gas Turbines and Power,* Vol. 107, pp. 354–363.

Zerkle, R. D., and Lounsbury, R. J., 1987, "The Influence of Freestream Turbulence and Pressure Gradients on Heat Transfer to Gas Turbine Airfoils," AIAA Paper No. 87-1917.

Assessment of the Cold-Wire Resistance Thermometer for High-Speed Turbomachinery Applications

R. Dénos

C. H. Sieverding

von Karman Institute for Fluid Dynamics, Rhode Saint Genèse, Belgium

The paper first describes the fundamentals of cold-wire resistance thermometry. The transfer functions with and without wire-prong heat conduction effects are discussed and a new method for the description of complicated transfer functions describing both the prongs and wire frequency response is proposed. The experimental part of the paper starts with an investigation of the transfer function of various probes differing by the wire diameter, the l/d ratio, and the wire-prong connection using two simple methods: (1) electrical heating of the wire by a sine current and (2) a temperature step test consisting in injecting the probe into a hot air stream. The first test provides information on the wire response, whereas the second serves to study wire prong heat conduction effect. The tests cover a wide range of velocities and densities. A frequency bandwidth of 2 kHz is obtained with a 2.5 μm wire probe at an air velocity of 200 m/s at atmospheric pressure. A numerical compensation system allows us to extend the use of this probe to much higher frequencies. Finally, the probe is mounted onto a wheel in a high-speed rotating test rig allowing probe traverses through a stationary hot air jet at rotational speeds up to 5000 rpm with the probe positioned at a radius of 0.380 m. The probe signal is transmitted via an opto-electronic data transmission system. It is demonstrated that using the numerical compensation method, it is possible to reconstruct the hot jet temperature profile at frequencies up to 6 kHz.

Introduction

To date, the use of the cold-wire probe has been limited apparently to the investigation of small temperature fluctuations in turbulent flows at low speed, typically 10 m/s; see LaRue et al. (1974), Hojstrup et al. (1976), Millon et al. (1978), Weeks et al. (1988), Fournier (1990). The limitation to such low speeds may be attributed partially to the use of probes with diameters well below 1 μm to reduce the wire response time. The highest frequency response was obtained by LaRue et al. (1974) with a wire diameter of 0.25 μm providing a cut-off frequency of 12 kHz at 9 m/s. DISA has offered since 1973 cold-wire probe with a 1 μm wire for applications up to 60 m/s with a maximum cut-off frequency of 2 kHz.

Several methods can be used in order to determine the transfer function of the wire. LaRue et al. (1974) used an electrical heating method, which consists in heating the wire internally using a sine current. Weeks et al. (1988) and Fournier (1990) generated heat pulses on the wire by means of a chopped laser beam focused on its active part. All results concluded that the response of the wire is similar to the response of a first-order system.

Neither of the methods given above is able to test the unsteady prong-wire conduction. A modelization was proposed by Maye (1970) for the steady conduction case. Hojstrup et al. (1976), Millon et al. (1978), and Fournier (1990) gave an analytical expression of the transfer function accounting for unsteady conduction with prongs. A more complete theoretical study describing unsteady prong-stub-wire thermal interaction was presented by Tsuji et al. (1992). Problems of thermal boundary layers forming on the prongs and flowing partially on the active part of the wire may also influence the transfer function, especially at low speed as mentioned by Paranthoen et al. (1982). An experimental determination of the transfer function accounting for conduction was carried out by Hojstrup et al. (1976) who generated sinusoidal temperature variations with a loudspeaker. Paranthoen et al. (1992) also derived transfer functions by placing the probe in the wake of another wire heated by a sine current.

When the conduction effect is negligible (large l/d ratio), correction for the roll-off of the wire at high frequency can be realized with an electronic compensation (RC filter) (Paranthoen et al., 1982; Weeks et al., 1988). LaRue et al. (1974) applied a correction on the signal spectrum. In a recent catalog, Dantec proposes a probe with two wires; one measures the velocity in order to tune the compensation.

Finally, the electronic circuit driving the probe must not limit the frequency of the whole system. For this purpose, Cho and Kim (1993) developed a simple circuit with a broad frequency bandwidth (13 kHz) and low signal-to-noise ratio.

The present paper is a feasibility study for the use of a cold-wire probe for unsteady temperature measurements in turbomachines. The velocity range is one order of magnitude higher than in all previous low-speed studies and, depending on the engine size, blade passing frequencies are typically of the order of 2 to 20 kHz. The upper frequency range is obviously not accessible to cold-wire probes. The authors' interest was in the lower frequency range as illustrated by the following example: a transonic model turbine of 790 mm tip diameter with 43 guide vanes and 65 rotor blades running at 6500 rpm in a short duration tunnel with 0.5 seconds running time. A cold-wire probe mounted onto the rotor blade would experience blade passing frequencies of the order of 4.6 kHz.

Contributed by the International Gas Turbine Institute and presented at the 40th International Gas Turbine and Aeroengine Congress and Exhibition, Houston, Texas, June 5–8, 1995. Manuscript received by the International Gas Turbine Institute February 16, 1995. Paper No. 95-GT-175. Associate Technical Editor: C. J. Russo.

Theoretical Analysis

The main heat transfer mode is the forced convection due to the air flowing around the wire surface:

$$Q_h = -hS_w(T_w - T_a) \tag{1}$$

The frequency response of the wire is mainly due to its thermal inertia:

$$Q_s = V_w\rho_w c_w \frac{\partial T_w}{\partial t} \tag{2}$$

The wire is fastened onto prongs that have a large thermal inertia. The prongs will not be able to follow high-frequency fluctuations and a conduction phenomenon will take place between the wire and the prongs; T_p is a boundary condition of:

$$Q_k = -k_w A_w l_w \frac{\partial^2 T_w}{\partial x^2} \tag{3}$$

In these equations, it is assumed that the gradient in the radial direction of the wire can be neglected because the wire diameter remains small compared to the length.

Provided the wire is at the same temperature as the flow at all time, a linear law relates the wire temperature and the wire resistance in a limited range of temperature:

$$R_w = R_0(1 + \alpha_w(T_w - T_0)) \tag{4}$$

The wire resistance is measured in a Wheatstone bridge (see Fig. 1) through the voltage V_{out}:

$$V_{out} = I_0 \frac{R_3(R_2 + R_4) - R_4(R_1 + R_3)}{(R_1 + R_3) + (R_2 + R_4)} \tag{5}$$

This relation can be approximated by a linear law when the bridge is not too far from equilibrium ($R_1R_4 = R_2R_3$) and if the change in the wire resistance is not too large.

In order to measure V_{out}, a current has to cross the wire; this brings a heat source term due to the Joule effect:

$$Q_j = R_w I_w^2 = R_0(1 + \alpha_w(T_w - T_0))I_w^2 \tag{6}$$

Probe Response Neglecting Conduction Effects. In a steady case assuming neglegible conduction, the thermal balance expresses as $Q_h + Q_j = 0$, which can be rearranged to give:

$$T_w = \frac{h\pi^2 d_w^3 T_a + 4\sigma_0^{-1} I_w^2(1 - T_0\alpha_w)}{h\pi^2 d_w^3 - 4\sigma_0^{-1} I_w^2 \alpha_w} \tag{7}$$

Theoretical values of T_w can be derived from this equation as well as the sensitivity to velocity $\partial T_w/\partial v$ in order to estimate the error due to the Joule effect.

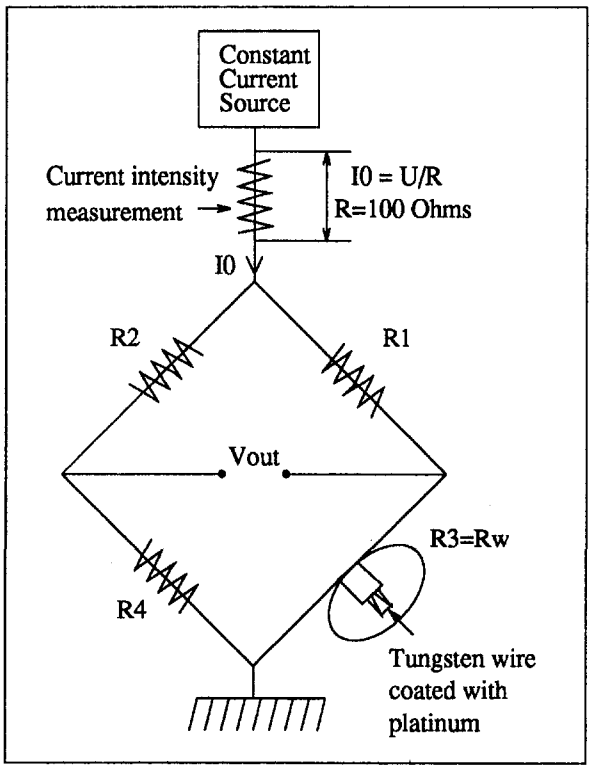

Fig. 1 Principle of resistance thermometer

The heat transfer coefficient $h = \mathrm{Nu}k_a/d_w$ is computed with experimental correlations of the kind $\mathrm{Nu} = A + B\mathrm{Re}^n$. The correlation of Collis and Williams (1959):

$$\mathrm{Nu} = 0.24 + 0.56\ \mathrm{Re}^{0.45} \tag{8}$$

in the range $0.02 \le \mathrm{Re} \le 44$ is commonly used.

Physical properties for the tungsten wire and for the air are extracted from Lide (1990): e.g., at $T_a = 340$ K, $k_a = 0.03$ W/(mK), $\mu_a = 2.17 \times 10^{-5}$ kg/(ms), $\rho_w = 20000$ kg/m^3, $c_w = 134$ J/(kgK), $k_w = 178$ W/(mK), $\alpha_w = 0.003541$/K. The wire resistance R_0 at T_0 is derived from $R_0 = (\sigma_0^{-1} l_w)/A_w$ with $\sigma_0^{-1} = 5.65E - 08\ \Omega$/m at $T_0 = 300$ K. Calculations show that for a 2.5-μm wire, if I_w remains below 1 mA, the error induced by the Joule effect is less than 0.1 K at an air velocity of 50 m/s and less than 0.05 K at 200 m/s.

However, the Joule effect becomes significant when using the electrical heating method to determine the frequency response. The unsteady equation without conduction but including the Joule effect is derived from $Q_s = Q_h + Q_j$ and results in a first-order nonhomogeneous linear equation:

Nomenclature

I = current intensity, A
Q = heat flux, W
R = resistance, Ω
T = temperature, K
c_w = heat storage capacity, J/(kg K)
f = frequency, Hz
$g = (T_{w\,\mathrm{mean}} - T_p)/(T_a - T_p)$
h = heat exchange rate by convection, W/(m^{2}K)
k = conductivity, W/(mK)
t = time, s
u = peripheral speed m/s
v = velocity, m/s
w = relative speed, m/s
d_w = wire diameter, m
l_w = wire length, m
$A_w = (\pi d_w^2)/4$ = wire cross-sectional area, m^2
$S_w = \pi d_w l_w$ = wire area available for convection, m^2
$V_w = (\pi d_w^2 l_w)/4$ = wire volume
$\mathrm{Re} = (\rho v_a d_w)/\mu_a$ = Reynolds number
$\mathrm{Nu} = (hd_w)/k_a$ = Nusselt number
α = temperature coefficient $= (1/R_0)(\partial R/\partial T)$, K^{-1}
τ = time constant, s
σ_0^{-1} = resistivity, Ωm
ρ = density, kg/m^3
μ = dynamic viscosity, kg/(ms)
ω = pulsation $= 2\pi f$, rad/s

Subscripts

0 = total
a = air
p = prong
s = static
w = wire

$$\tau \frac{\partial T_w}{\partial t} + T_w = f(t) \tag{9}$$

$$\tau = \frac{\rho_w c_w A_w}{\pi h d_w - \dfrac{\sigma_0^{-1} \alpha_w I_w^2}{A_w}} \tag{10}$$

$$f(t) = \frac{\pi \, \mathrm{Nu} k_a T_a + \dfrac{\sigma_0^{-1} I_w^2 (1 + \alpha_w T_0)}{A_w}}{\pi \, \mathrm{Nu} k_a - \dfrac{\sigma_0^{-1} \alpha_w I_w^2}{A_w}} \tag{11}$$

The time constant τ is a typical feature of a first-order equation and characterizes the time response of the wire. Notice that increasing the current intensity reduces τ. Calculations show that for a 2.5 μm wire, intensities up to 10 mA can be used without reducing significantly the cut-off frequency.

In the following, the probe is assumed to be used in normal mode with a low current intensity; the Joule effect is neglected. The unsteady equation simplifies to $Q_s = Q_h$, which leads to the same kind of first order equation as Eq. (9) but with:

$$\tau = \frac{d_w^2 \rho_w c_w}{4 k_a \, \mathrm{Nu}} \tag{12}$$

$$f(t) = T_a(t) \tag{13}$$

Notice that τ does not depend on the wire length. The transfer function of a first-order system is well known and can be written as:

$$H(\omega) = \frac{1}{1 + j\omega\tau} \tag{14}$$

$$|H(\omega)| = \frac{1}{\sqrt{1 + (\omega\tau)^2}} \tag{15}$$

$$\hat{H}(\omega) = a \tan(-\omega\tau) \tag{16}$$

where $|H(\omega)|$ and $\hat{H}(\omega)$ are the corresponding gain and phase and $\omega = 2\pi f$ is the pulsation.

Another characteristic value for a first-order equation is the cut-off frequency defined as the frequency for which $|H(\omega)| = \sqrt{2}/2 = 0.707$. A straightforward relationship exists between the cut-off frequency and the time constant, namely:

$$f_{\mathrm{cut}} = \frac{1}{2\pi\tau} \tag{17}$$

With those relations, the cut-off frequency of a 2.5 μm wire at 200 m/s is 2.8 kHz.

Probe Response Including Conduction Effects. The thermal balance for steady conduction is $Q_k + Q_s = 0$:

$$\frac{\partial^2 T_w}{\partial x^2} = \lambda^2 (T_w - T_a) \tag{18}$$

where $\lambda^2 = 4h/k_w d_w$. This is a classical equation for which an analytical solution exists (see Kay and Nederman, 1974). Boundary conditions and solution are given by:

$$T_w(x = 0) = T_p \tag{19}$$

$$Q_k\left(x = \frac{l_w}{2}\right) = 0 \tag{20}$$

$$\theta = \theta_p \frac{\cosh\left(\lambda\left(\dfrac{l_w}{2}\right) - x\right)}{\cosh\left(\lambda \dfrac{l_w}{2}\right)} \tag{21}$$

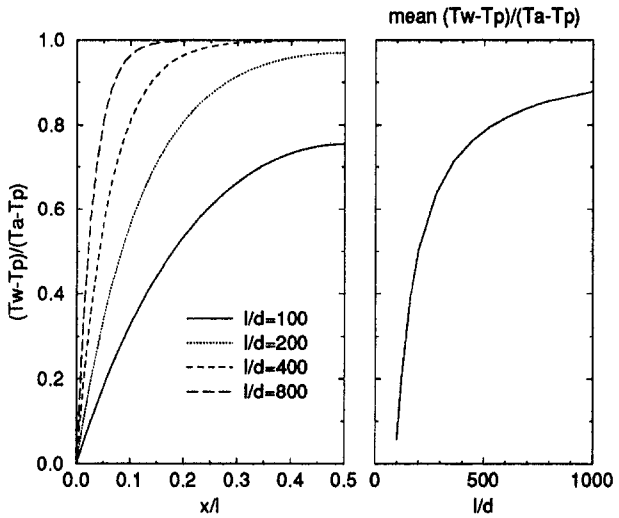

Fig. 2 Influence of l/d ratio on the temperature profile

where x measures the distance from the prong, $\theta = (T_w - T_a)$ and $\theta_p = (T_w - T_p)$. The heat flux at the prong can be determined by:

$$Q(x = 0) = -k_w A_w \left(\frac{d\theta}{dx}\right)_{x=0} = \lambda k_w \theta_p \tanh\left(\lambda \frac{l}{2}\right) \tag{22}$$

In Fig. 2 profiles are shown for several l/d ratios for a 5 μm wire in a 100 m/s flow. The graph on the right indicates the mean temperature of the wire as a function of l/d. Of course, the larger the l/d ratio, the closer the average wire temperature approaches the air temperature. On the other hand, a bigger probe volume is obtained as well as a structurally weaker probe. For a given l/d ratio, increasing the velocity results in a higher convectionnal exchange and in a wire temperature closer to T_a.

The unsteady equation including conduction is derived from $Q_s = Q_h + Q_k$:

$$\frac{\partial T_w}{\partial t} = \alpha \frac{\partial^2 T_w}{\partial x^2} - \frac{1}{\tau}(T_w - T_a) \tag{23}$$

where $\alpha = k_w/(\rho_w c_w)$ [W/m^2] and $\tau = (d_w \rho_w c_w)/4h$ [s].

The equation can be discretized with a Crank–Nicholson scheme. Instantaneous temperature profiles have been calculated and the transfer function was established assuming the prongs were behaving like a first order system. This equation was found to have the same behavior in the time as well as in the frequency domain as the combination of two first-order equations discretised as follows:

$$\frac{T_w(n+1) - T_w(n)}{\Delta t} = \frac{1}{\tau_w}(T_w(n) - T_a(n)) \tag{24}$$

$$\frac{T_p(n+1) - T_p(n)}{\Delta t} = \frac{1}{\tau_p}(T_p(n) - T_a(n)) \tag{25}$$

$$T(n+1) = gT_w(n+1) + (1-g)T_p(n+1) \tag{26}$$

where n is such that $t = n * \Delta t$. Notice that Eq. (24) is a simple discretization of Eq. (9); Eq. (24) modelizes the prong behavior in a similar way. Details on first-order system and their numerical discretization can be found in Oppenheim et al. (1983) or Rabiner and Gold (1975).

Starting from an initial guess of T_w and T_p at $n = 1$, this allows us to compute $T_w(n+1)$ and $T_p(n+1)$, the resulting probe temperature being $T(n+1)$. The transfer function can

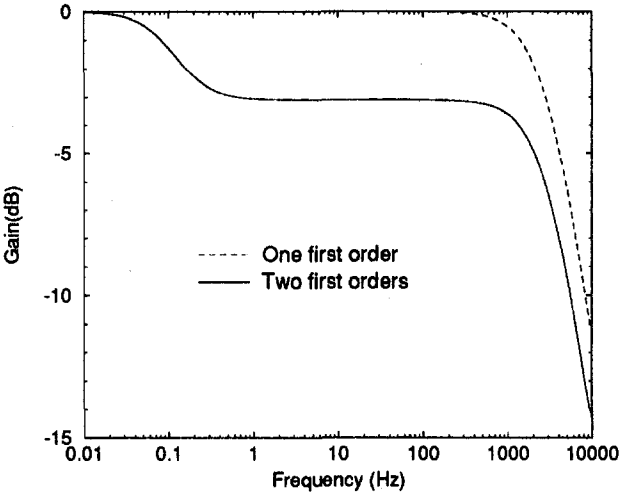

Fig. 3 Transfer function using two first orders

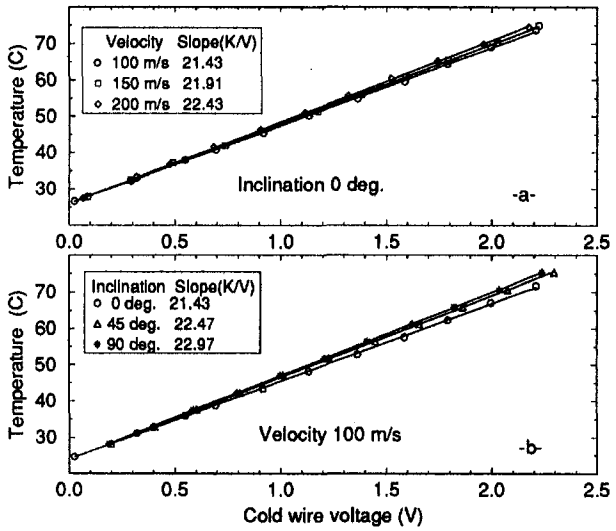

Fig. 4 Cold-wire calibration

be derived analytically from Eq. (14) and is shown in Fig. 3. The frequency response of the wire without conduction effect is plotted as a dotted line; the combination of the two first-order equations is plotted as a continuous line. At low frequency, both prongs and wire can follow the temperature fluctuations; then the prongs begin to lag behind until a plateau is reached where only the wire responds.

The plateau results from a large difference between the thermal capacity of the prongs and that of the wire. The plateau level depends on the relative importance of conduction with respect to convection in the thermal balance and is denoted by g in Eq. (26). This value corresponds to the ratio $(T_{w\,\mathrm{mean}} - T_p)/(T_a - T_p)$ plotted in the right graph of Fig. 2. Increasing l/d or the velocity would raise this level. Finally, at high frequencies, the wire also lags behind.

Extending this numerical analysis to N first-order systems allows a great freedom in the description of the transfer function shape, unlike the simple analytical expression of Paranthoen et al. (1982) or the complex expression obtained by Tsuji et al. (1992), which is limited to three first orders. Moreover, the linear system formed by those N equations can easily be reversed to compute T_a from a measurement of T_w and realize in this way a simple compensation system. Unlike the electronic compensation (RC filter) described by Weeks et al. (1988), the numerical system allows us to describe complicated transfer functions with an easy tuning through an adequate choice of the various time constants. The global transfer function is obtained by summing in the complex domain the transfer functions of the N first orders (see Eq. (14)) weighted by their respective contributions (the Laplace transform is linear).

Experimental Determination of the Probe Transfer Function

Wire Response. Static calibration of the cold-wire probe was performed in a heated jet. A platinum-plated tungsten wire with a 2.5 μm diameter was used. As expected, a linear relation relates the output voltage to the jet temperature (see Fig. 4(a)). A slight dependance of the slope on the velocity was observed. At 100 m/s, a slope of 21.43 K/V is obtained; slopes at 200 m/s and 150 m/s were respectively 4.7 and 2.2 percent higher (in all cases, probe incidence with respect to the flow was 0 deg). This effect can be attributed to the problem of recovery of the dynamic temperature $(T_0 = T_s + v^2/(2c_p))$ at high velocity, similar to thermocouples. For the same reasons, the incidence of the prongs with respect to the flow also has an influence.

Slopes at 90 and 45 deg incidence are respectively 7.2 and 4.9 percent higher than the slope at 0 deg for a velocity of 100 m/s (see Fig. 4(b)).

The wire frequency response was evaluated by the electrical heating method described by LaRue et al. (1974). A frequency generator is used to inject a sine current into the bridge. This current heats the wire and the bridge output voltage relates its temperature change. The gain is computed by dividing the output voltage obtained for a given frequency by a reference voltage, measured at a frequency sufficiently low to guarantee that the wire is able to follow the heat fluctuations perfectly. It was observed that an overly large AC current amplitude resulted in an output voltage due, not only to the wire temperature change, but also to an electrical response of the bridge, especially if it was not set at equilibrium before. In order to minimize this electrical response, a small AC current was superimposed onto a DC current for which the bridge was equilibrated. In Fig. 5 the gain in deciBell ($G(\mathrm{dB}) = 20\ \log_{10}(G)$) is plotted in function of the frequency of the AC component. Provided the AC component remains small, all data points fall onto the same line.

The gain corresponding to a first-order transfer function (see Eq. (15)) is plotted as a continuous line. The shape matches

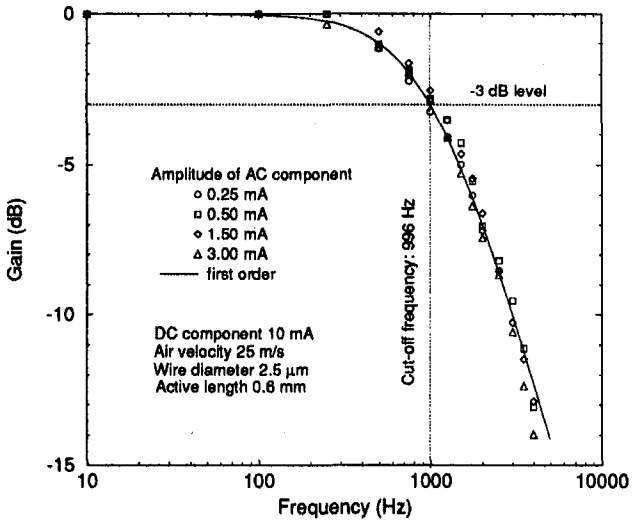

Fig. 5 Gain obtained by electrical heating for several current amplitudes

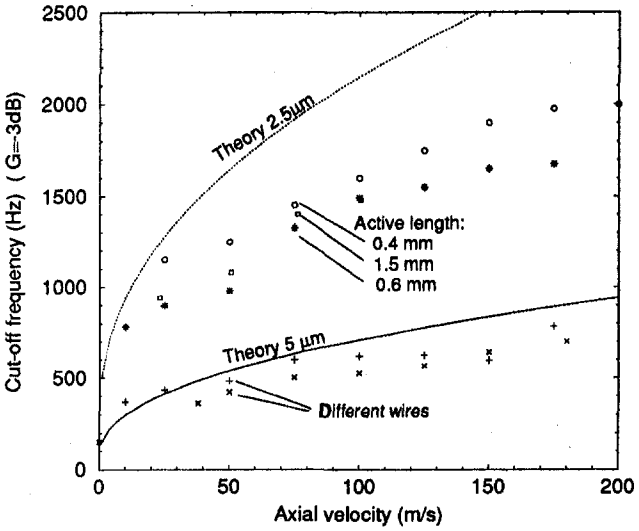

Fig. 6 Cut-off frequency in function of air velocity

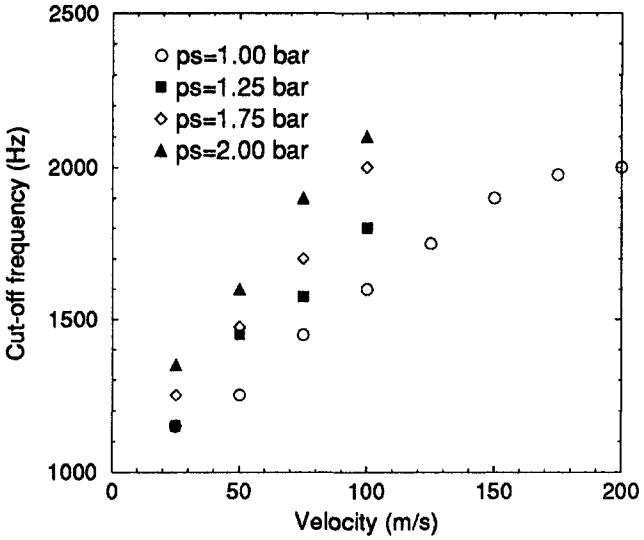

Fig. 7 Cut-off frequency in function in function of air velocity for several static pressure

the experimental curve well but the time constant τ used for this curve did not correspond to the one predicted by Eqs. (12) and (17). This problem will be adressed further when discussing Fig. 6.

Larger AC current led to a non-negligible residual output at high frequency due to the electrical response. In all following tests, a 3 mA AC current intensity was super-imposed to a 10 mA DC current intensity. It was shown in the theoretical part that this level of intensity does not significantly affect the wire dynamic response. Notice that this method only provides information on the wire response; conduction effects exist but do not affect the cut-off frequency of the wire.

The influence of the velocity on the cut-off frequency at atmospheric pressure is presented in Fig. 6 for two wire diameters (5 μm and 2.5 μm). The cut-off frequency computed from Eq. (12), Eq. (17), and the experimental correlation of Collis and Williams (Eq. (8)) is also plotted and is much higher than the measured values. This was also observed by LaRue et al. (1974), Hojstrup et al. (1976), and Weeks et al. (1988); the discrepancy tends to increase when going to smaller diameters. Hojstrup et al. even mention that in still air, no clear improvement is felt between wire diameters of 1.0 μm and 0.2 μm. Notice that the correlation of Collis and Williams (1959) was developed for constant temperature hot-wire purposes whereas the present test conditions are unsteady.

However, the experimental data show the same trends as predicted by the theory: Higher velocity improves convection and increases the frequency response; a smaller diameter reduces the thermal inertia of the wire and increases the frequency response. A 2 kHz cut-off frequency is achieved at 200 m/s with the 2.5 μm wire at atmospheric pressure. The value of the active length does not influence the cut-off frequency of the wire as expected. The cut-off frequency level can change slightly from one wire to another because of wire contamination and possibly small changes in the wire diameter. Smaller diameters were not tested because platinum-plated tungsten wires do not exist below 2.5 μm; only pure platinum wire can be found but those are much weaker.

The influence of density on cut-off frequency was investigated by performing tests with a 2.5 μm wire in a variable density chamber. The density change was achieved by setting different levels of static pressure in the measurement chamber; the results are summarized in Fig. 7. Increasing the density improves the convection around the wire and therefore the cut-off frequency. In order to take into account the influence of velocity and density on the cut-off frequency and to establish a correlation for this wire, the Nusselt number (computed by rearranging Eq. 12) was plotted against $Re^{0.45}$, causing all points to collapse onto a line. A linear regression allows us to extract the coefficients for the correlation: $Nu = 0.458 + 0.345\ Re^{0.45}$ for $4.0 \leq Re \leq 36.0$. This correlation provides a straightforward way to compute the cut-off frequency of the wire needed in the numerical compensation system.

Prong Response. The response of the stainless steel prongs to temperature variations is several orders of magnitude slower than that of the wire. Their behavior is best investigated in a temperature step test. To this end, the probe was injected from air at ambient temperature into a hot jet exiting a 12-mm-dia nozzle; the temperature difference was typically 50°C.

The probe used for this test had a 2.5 μm wire mounted onto 0.4-mm-dia stainless steel prongs. The probe response is plotted in Fig. 9(*a*). A zoomed view of the step area shows that the wire responds very fast, whereas the prongs need 10 s to reach the jet temperature. Two methods were used to compute the transfer function. For both, a numerical reconstruction of the true step is needed. The first method consists in performing a FFT on the reconstructed step and on the original wire response.

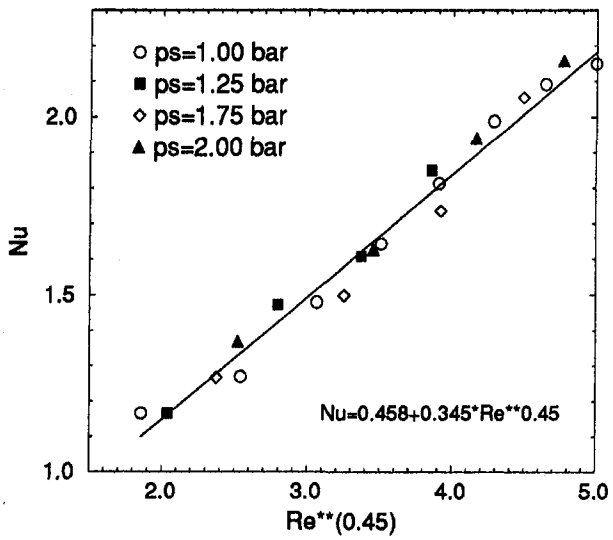

Fig. 8 Correlation $Nu = f(Re^{0.45})$

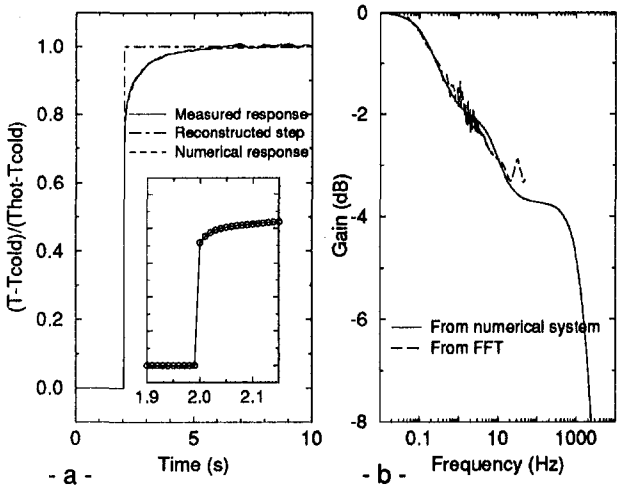

Fig. 9 Step test and prong transfer function

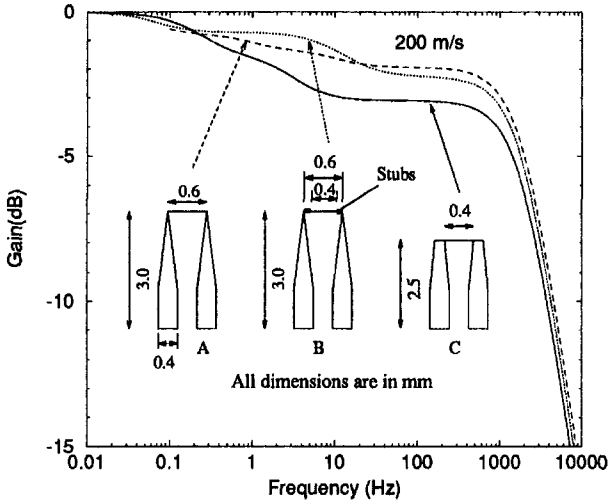

Fig. 10 Transfer function of probes *A*, *B*, and *C*

The ratio of the two FFT gives the complex transfer function from which the gain is computed (see Fig. 9(*b*)). The second method uses a numerical system comprising five first-order systems. The time constant and the contribution of each first-order system to the overall signal are adapted so that the system response to the reconstructed step fits the experimental response. The match with the FFT result is satisfactory and the transfer function of the wire is added as shown on Fig. 9(*b*) (the cut-off frequency is known from the electrical heating test). Four first-order systems were used to simulate the behavior of the prongs but only one is needed for the wire behavior.

Theoretically, the step test analysis provides information on an infinite range of frequency. Due to the existence of a 1.2 mm shear layer on both sides of the jet and a finite 0.5 m/s probe injection speed (2.4 ms to cross the shear layer), the experimental response can be analyzed only over a limited range of frequency. On a FFT plot of the experimental signal, the FFT magnitude becomes very noisy above 50 Hz. This was considered to be the highest frequency that could be analyzed in the probe response to the step.

Three probes were tested. Two of them had 3-mm-long prongs with an ogive shape at the tip, the first with a 0.6 mm wire active length extending from prong to prong, the second with a slightly reduced active length of 0.4 mm due to the presence of small stubs at the wire ends. The third probe had 2.5-mm-long prongs (part of the ogive shape was removed) with a 0.4 mm active length (prong to prong). The transfer functions at 200 m/s are shown in Fig. 10. One can clearly see that the plateau level is higher for the first probe with the 0.6 mm wire active length because the amount of heat brought by convection plays a more important part in the overall heat exchange. The presence of stubs on the second probe adds an intermediate level between low and high frequencies because the thermal capacity of the stubs is smaller than that of the prongs but higher than that of the wire. The plateau is slightly larger for the shorter prongs because the ogive shape at the end of the longer prongs extends the prong response to higher frequencies.

The influence of the flow velocity was studied on the probe with 2.5-mm-long prongs and is depicted in Fig. 11. As expected, increasing the velocity improves the convection and leads to a faster prong response. Another effect is the increase in the plateau level because the contribution of convection rises in the overall exchange.

The effect of different probe head inclinations with respect to the flow was also considered. Tests were run at 0 deg (probe is aligned with air stream), 45, and 90 deg. For a velocity of 50 m/s, the prong response is slightly faster at 0 deg. With increasing velocity, this difference becomes smaller and smaller; at 200 m/s, responses are almost identical.

Tests in Rotation, Compensation

A rotating model test rig was built to test the cold-wire probe under conditions similar to those in the transonic turbine stage referred to in the introduction. The setup is depicted in Fig. 12. The probe is fixed onto a rotating wheel at a radius of 380 mm. Instead of traversing a thermal wake issuing from a cooled turbine guide vane, the probe is rotated through a heated air jet exiting from a 12-mm-dia nozzle. At a distance of 8 mm from the nozzle exit, the cold wire sees a trapezoidal temperature profile with a thermal shear layer thickness of approximately 1.2 mm on either side of the jet. The temperatures outside and inside the jet are controlled by thermocouples. As for the step tests, the temperature difference between the ambient air and the heated jet was typically 50 K. The electronic board driving the cold wire was designed following Cho and Kim (1993). This board, as well as an opto-electronic data transmission system (Sieverding et al., 1992), is installed in the shaft of the rotating wheel. The power supply for the in-shaft electronics is provided through mechanical slip rings. The noise on the wire output signal in terms of temperature (including CW board, transmitting and receiving board) did not exceed 0.8 K (rms

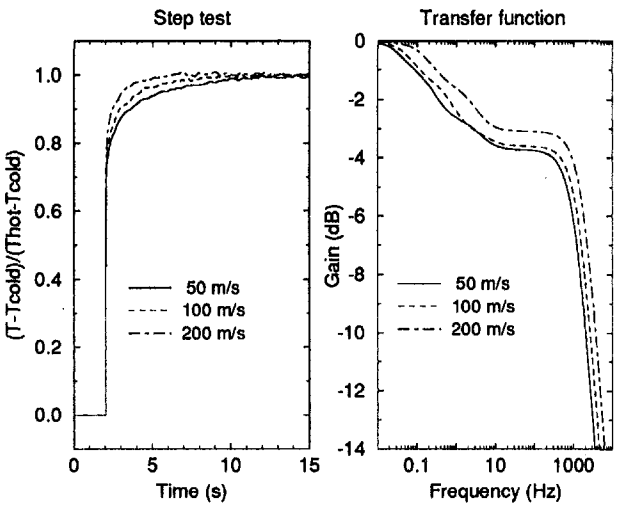

Fig. 11 Influence of velocity on type *C* prong response

value) in still air. Spun at 3000 rpm at atmospheric pressure, the noise rose up to 1.05 K (rms value).

The tests were run at atmospheric pressure. The probe used for these tests was of type *C* in Fig. 10. For all tests, the probe was aligned within ±10 deg with the relative flow direction resulting from the jet velocity v in the axial direction and the peripheral speed u of the probe. The probe measures a total relative temperature: $T_{0r} = T_s + w^2/(2c_p)$ where $w = \sqrt{v^2 + u^2}$. This temperature can be compared with the relative temperature derived from the thermocouple measurements through $T_{0r} = T_0 + u^2/(2c_p)$. Notice that $T_{0r} \neq T_0$ but $\Delta T_{0r} = \Delta T_0$. For a given rotational speed, the jet velocity is adjusted in order to obtain the desired relative velocity.

Typical measurements are shown in Fig. 13 for several rotational speeds but at a constant relative velocity of 200 m/s. The reduced temperature $(T_w - T_{\text{cold}})/(T_{\text{hot}} - T_{\text{cold}})$ is plotted as a function of time. Several jet traverses were recorded and a phase-locked average was applied (from 1 traverse at 3.2 Hz up to 50 traverses at 6000 Hz). The trapezoidal shape represents a simplified jet shape (dot-dashed lines). The frequency indicated for each experiment corresponds to the frequency of a periodic trapezoidal signal that would fit the jet shape. At low frequency (3.2 Hz), the wire responds immediately and the slight slope on the top level indicates that the prongs are warming up. At 300 Hz, the wire response is still satisfactory but the prongs do not have enough time to heat up significantly (plateau region in the transfer function in Fig. 13). At 980 Hz, the wire itself can no longer follow the temperature change. At higher frequencies (4600 and 6000 Hz) the signal is completely distorted.

The 6000 Hz signal is obtained at 4000 rpm. The rotational speed was raised to 5000 rpm (upper limit of wheel speed) without breaking the wire. The corresponding jet passing frequency is 8 kHz but the signal is severely affected by the noise.

The upper left curve in Fig. 13 represents the transfer function determined by electrical heating and step tests. For each experiment, the gain was computed from the cold-wire signal and the temperatures measured by the thermocouple and plotted as dots on the same figure. The agreement is good although the results are obtained with two distinct probes (but which have the same characteristics).

In order to correct the recorded signals for prong–wire interaction and wire roll-off at high frequency, the numerical compensation system described previously is used. The transfer function of the probe and that of the compensator are sketched in the upper left curves in Fig. 14. Injecting the measured wire

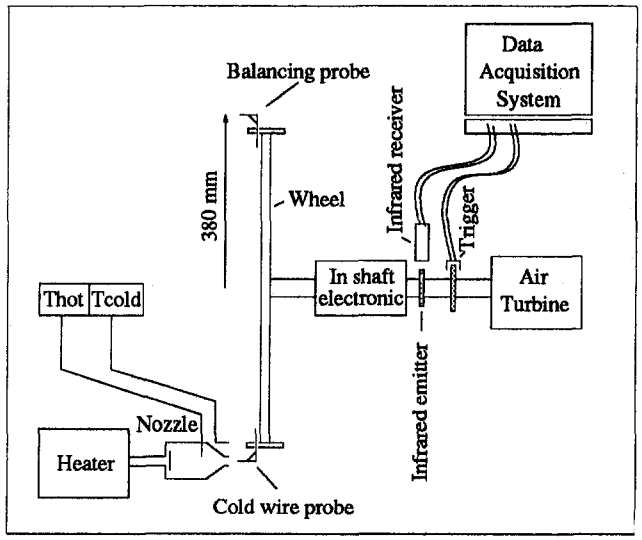

Fig. 12 Setup for measurements in rotation

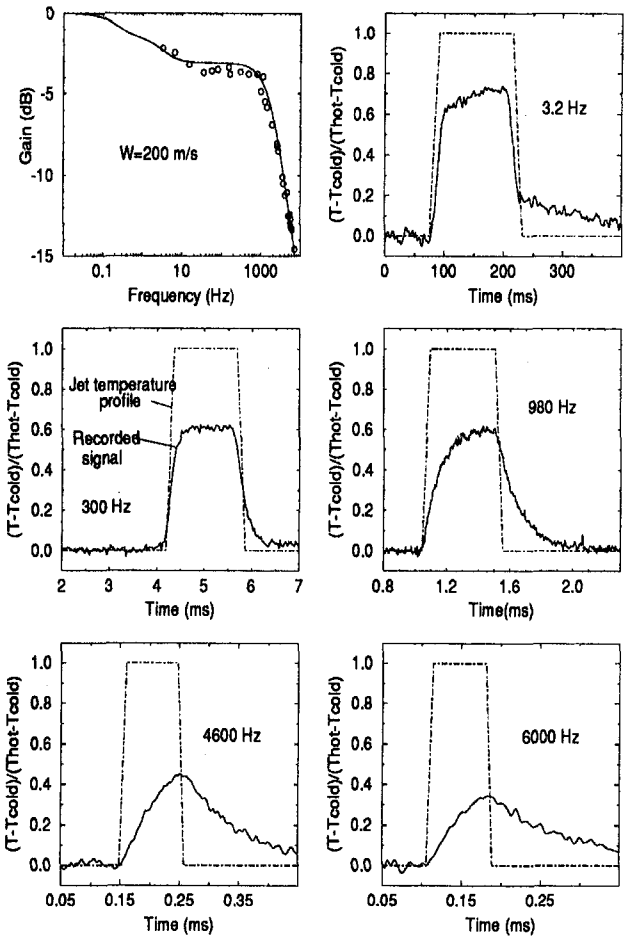

Fig. 13 Temperature signals measured in rotation

temperature T_w into the numerical compensation system immediately provides the air temperature T_a. Compensated signals are plotted in Fig. 14 as dashed lines. The compensation system seems to be efficient across the entire frequency domain.

The effect of the change in incidence and flow velocity relative to the probe across the jet shear layer will be discussed for the two extreme cases of 3.2 and 6000 Hz jet passing frequency. For the low-frequency case, the velocity changes from nearly 0 m/s to 200 m/s but in any case the cut-off frequency is at least two orders of magnitude higher than the jet passing frequency. Due to the low peripheral speed, the incidence remains close to 0 deg across the entire shear layer. For the high-frequency case, the velocity changes from 140 to 200 m/s, which corresponds to a 10 percent change in the probe cut-off frequency. The incidence changes from 45 to 0 deg, which corresponds to a 5 percent variation in the slope of the calibration curve (see Fig. 4(*b*)). The maximum error on the compensated temperature signal inside the shear layer was estimated to be 5 percent, accounting for the two phenomena.

As the compensation amplifies the high-frequency components of the signal (including the noise), the accuracy of the compensated signal decreases with increasing frequency. It is not possible to give a unique value of accuracy for the entire frequency domain. Therefore, the transfer function was decomposed in four zones of different accuracies. The first zone is the domain where both prongs and wire can follow the temperatures fluctuations. Here the accuracy is of the same order as for the thermocouple used for the calibration. This uncertainty is estimated to ±0.5 K. The second zone is the domain where the wire responds well but where the prong response lags behind. The uncertainty is assumed to be a linear transition between

the first and third zones. The third zone is the plateau level. The dispersion on the plateau level was determined through repeat step tests, leading to an uncertainty of ±1.75 K (20:1). In the fourth zone, the wire no longer follows the temperature variations. Repeat tests with the electrical heating method led to an uncertainty of ±1.85 K (20:1).

Using the compensation amplifies the error, especially in the fourth zone. This is illustrated in Fig. 15 where the error on the gain of the transfer function is plotted as well as the resulting error for the compensation (notice that the scale for the gain is not in dB but linear).

Conclusions

1 The present investigation demonstrates that the cold-wire resistance thermometry technique is of potential interest for time-resolved temperature measurements in turbomachines with blade passing frequencies of several kHz. Although the natural frequency bandwidth of the smallest commercially available platinum plated tungsten wire of 2.5 μm hardly exceeds 2 kHz, adequate compensation systems allow us to treat temperature signals of frequencies three times as high as the cut-off frequency.

2 The accuracy of the measurements depends to a large extent on the precise determination of the prong–wire transfer function over the entire frequency domain. Depending on the probe geometry, the transfer function can be rather complicated. Determined experimentally by an electrical heating method and temperature step tests, the transfer function can adequately be described by a numerical system based on the combination of

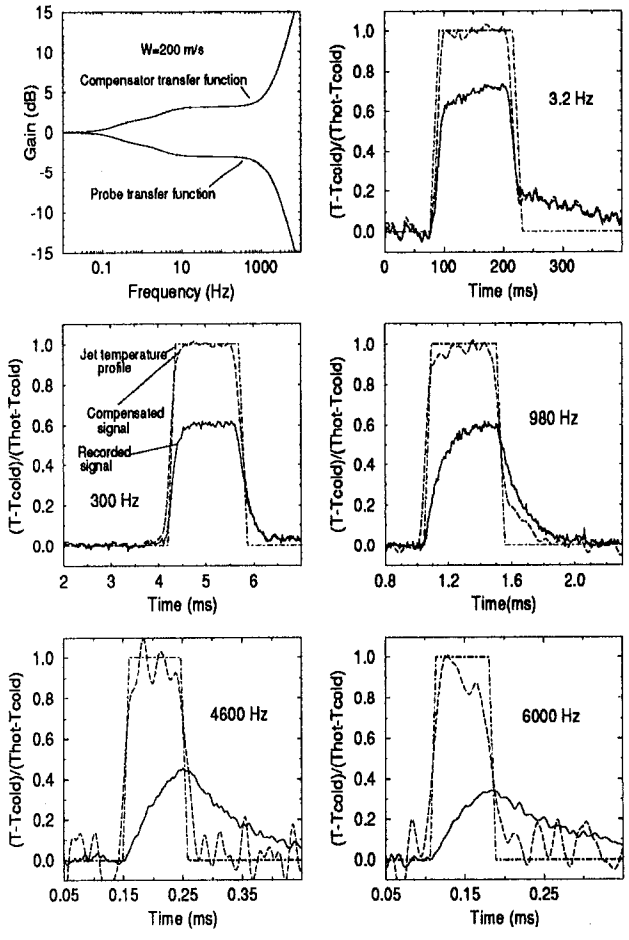

Fig. 14 Compensated signals

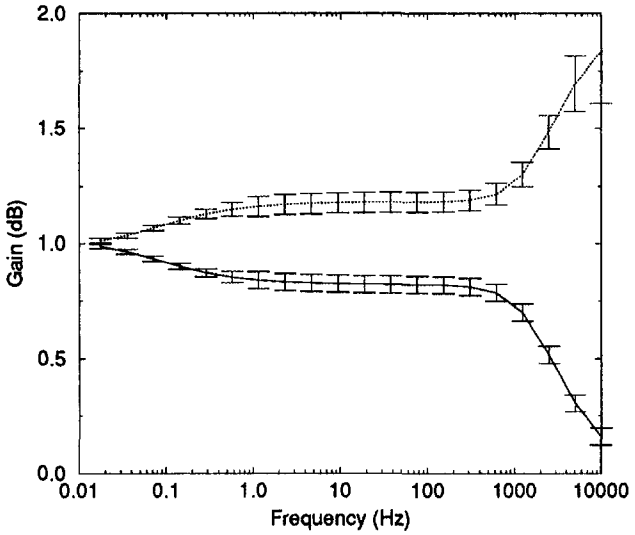

Fig. 15 Uncertainty on compensated signals

N first-order schemes. This scheme also lends itself readily for numerical compensation.

3 A probe with a wire diameter of 2.5 μm and 0.4 mm active length (prong to prong) was successfully tested in a rotating model test rig at peripheral speeds up to 200 m/s (5000 rpm). The temperature profile of a stationary hot air jet traversed by the probe could be restored with reasonable accuracy at jet passing frequencies up to 6 kHz. This test is a very severe test case because the associated temperature gradients are much steeper than those encountered in thermal wakes in turbomachines.

Acknowledgments

This research was carried out under contract for the CEC as a part of the BRITE EURAM Aero 002 project: "Wake-Blade Interference in Transonic HP Turbines." The authors wish to acknowledge this financial support as well as that of Alfa Avio, Fiat, MTU, Turbomeca, and SNECMA. The authors would also like to express their sincere thanks to Professor T. Arts who initiated this work and Mr. L. Collongeat, K. Detwiler, S. Grimmler, P. Adami, and C. Weber who took active part in the program at various stages.

References

Collis, D. C., and Williams, M. J., 1959, "Two Dimensional Convection From Heated Wires at Low Reynolds Number," *Journal of Fluid Mechanics,* Vol. 6, pp. 357, 384.

DISA elektronik Denmark, 1973, "Probe Manual."

Fournier, P., 1990, "Aréroacoustique des écoulements pulsés compressibles, metrologie et étude expérimentale du circuit d'admission d'un moteur thermique," PhD thesis, Université de Poitiers, Faculté des Sciences Fondamentales et Appliquées, France.

Hojstrup, J., Rasmussen, K., and Larsen, S. E., 1976, "Dynamic Calibration of Temperature Wires in Still Air," DISA Information No. 20, pages 22–30.

Ji Ryong Cho, and Kyung Chun Kim, 1993, "A Simple High Performance Cold-Wire Thermometer," *Meas. Sci. Technol.,* Vol. 4, pp. 1346–1349.

Kay, J. M., and Nedderman, R. M., 1974, *An Introduction to Fluid Mechanics and Heat Transfer,* 3rd ed., Cambridge University Press.

LaRue, J. C., Deaton, T., and Gibson, C. H., 1974, "Measurement of High-Frequency Turbulent Temperature," *Review of Scientific Instruments,* Vol. 46, No. 6, pp. 757–764.

Lide, D. R., 1990, *Chemistry and Physics Handbook,* Vol. 7, 1st ed.

Maye, J. P., 1970, "Error Due to Thermal Conduction Between the Sensing Wire and Its Supports When Measuring Temperatures With a Wire Used as a Resistance Thermometer," Electronic Measurements of Mechanical Events Disa information.

Millon, F., Paranthoen, P., and Trinite, M., 1978, "Influence des échanges thermiques entre le capteur et ses supports sur la mesure des fluctuations de

température dans un écoulement turbulent," *Journal of Heat and Mass Transfer,* Vol. 21, pp. 1–6.

Oppenheim, A. V., Willsky, A. S., and Young, I. T., 1983, *Signals and Systems,* Prentice/Hall International editions.

Parantheon, P., Petit, C., and Lecordier, J. C., 1982, "The Effect of Thermal Prong-Wire Interaction on the Response of a Cold Wire in Gaseous Flow," *Journal of Fluid Mechanics,* Vol. 124, pp. 457–473.

Rabiner, L. R., and Gold, B., 1975, *Theory and Application of Digital Processing,* Prentice-Hall.

Sieverding, C. H., Vanhaeverbeek, C., and Schulze, G., 1992, "An Opto-electronic Data Transmission System for Measurements on Rotating Turbomachinery Components," ASME Paper No. 92-GT-337.

Tsuji, T., Nagano, Y., and Tagawa, M., 1992, "Frequency Response and Instantaneous Temperature Profile of Cold-Wire Sensors for Fluid Temperature Fluctuation Measurements," *Experiments in Fluids.*

Weeks, A. R., Beck, J. K., and Joshi, M. L., 1988, "Response and Compensation of Temperature Sensors," *Journal of Physics and Scientific Instrumentation.*

Performance Assessment of an Annular S-Shaped Duct

D. W. Bailey

K. M. Britchford

J. F. Carrotte

S. J. Stevens

Department of Aeronautical and Automotive Engineering and Transport Studies, Loughborough University of Technology, Loughborough, Leics., United Kingdom

An experimental investigation has been carried out to determine the aerodynamic performance of an annular S-shaped duct representative of that used to connect the compressor spools of aircraft gas turbine engines. For inlet conditions in which boundary layers are developed along an upstream entry length, the static pressure, shear stress and velocity distributions are presented. The data show that as a result of flow curvature, significant streamwise pressure gradients exist within the duct, with this curvature also affecting the generation and suppression of turbulence. The stagnation pressure loss within the duct is also assessed and is consistent with the measured distributions of shear stress. More engine representative conditions are provided by locating a single-stage compressor at inlet to the duct. Relative to the naturally developed inlet conditions, the flow within the duct is less likely to separate, but mixing out of the compressor blade wakes increases the measured duct loss. With both types of inlet condition, the effect of a radial strut, such as that used for carrying loads and engine services, is also described both in terms of the static pressure distribution along the strut and its contribution to overall loss.

Introduction

To optimize the performance of multispool compressors within gas turbine engines, the diameter of each spool must decrease as the air density increases through the compression system. Thus, the annular duct connecting the low and high-pressure spools takes the form of an "S" shape. Within this duct flow separation must be avoided if the performance of the downstream compressor spool is not to be adversely affected. In addition, the provision of a suitable flow distribution at duct exit must also be achieved and stagnation pressure loss within the duct minimized. However, these various objectives are difficult to satisfy in practice due to several conflicting requirements. For example, in addition to the change in diameter, it is often desirable for the duct to be of relatively short axial length, with the passage geometry being further complicated by the presence of radial struts carrying loads or engine services. Furthermore, the influence of inlet conditions arising from the upstream compressor affects duct performance, and future developments may include the acceptance of swirl from this upstream compressor. However, the effective design of an interconnecting passage to fulfill these various requirements is difficult to achieve in practice because of the highly complex flow field that develops.

As the flow follows a curved path within the S-shaped duct, a modification to the static pressure field occurs. Across the first bend a pressure gradient is therefore present, with the pressure close to the outer casing being higher than that adjacent to the inner. However, this situation is reversed within the second bend as the flow is returned to the axial direction. Consequently streamwise pressure gradients arise that influence the mixing out of blade wakes from the upstream compressor and the boundary layer development along each casing surface. In addition, the turbulent flow field is directly affected by streamline curvature. For example, as described by Bradshaw (1973), the imbalance that exists between the centripetal acceleration of a turbulent fluid element and its surrounding pressure field gives rise, over a convex surface, to reduced turbulence levels. In contrast, over a concave surface increased turbulence mixing is observed. Naturally these effects have a significant impact on the development of the casing wall boundary layers. Although a large number of studies have been made on streamwise pressure gradient and flow curvature effects, the majority of investigations have considered these effects in isolation. A review of the large number of reported investigations conducted on these topics is given by Britchford et al. (1994).

This paper is part of a continuing investigation at Loughborough, which includes a comprehensive measurement of the mean flow and turbulence structure within an annular S-shaped duct. Such data can be used to validate and assist in the development of CFD methods. The long term objective is to apply such methods to the design of S-shaped ducts for a variety of engine configurations. However, in this paper emphasis is placed on the overall performance of a duct geometry typical of that which may be found in a modern multispool gas turbine engine. Only a limited amount of published data is available and this information may be of more immediate use to the gas turbine engineer. For inlet conditions in which axisymmetric boundary layers are developed, along an upstream entry length, the flow development within the S-shaped duct is briefly described. This is in terms of the static pressure, shear stress, and velocity distributions that are presented, and the resulting stagnation pressure loss that arises from this flow field is defined. This overall loss and its distribution across the duct is compared with that generated when more engine representative conditions are obtained by locating an axial compressor at duct inlet. Furthermore, for both inlet conditions the effect on performance of placing a radial strut within the duct is assessed.

Experimental Facility

A comprehensive description of the experimental facility (Fig. 1) is given by Britchford et al. (1993). Air is drawn from atmosphere into a large plenum prior to passing through a scroll intake containing a honeycomb flow straightener and contraction. The flow adjacent to the inner and outer casings is then artificially tripped before entering the inlet section. Inlet conditions to the S-shaped duct are generated by either allowing the casing boundary layers to develop along the entry length to provide a "clean" condition, or alternatively more engine representative inlet conditions can be obtained by incorporating a single-stage axial flow compressor immediately upstream of the duct. The compressor rotor operates with a blade loading

Contributed by the International Gas Turbine Institute and presented at the 40th International Gas Turbine and Aeroengine Congress and Exhibition, Houston, Texas, June 5–8, 1995. Manuscript received by the International Gas Turbine Institute February 11, 1995. Paper No. 95-GT-242. Associate Technical Editor: C. J. Russo.

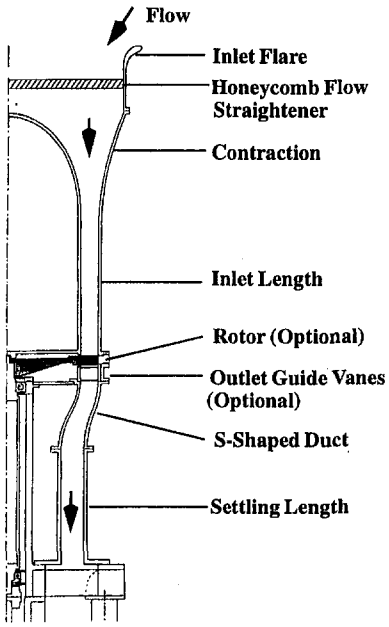

Fig. 1 Experimental facility—general layout

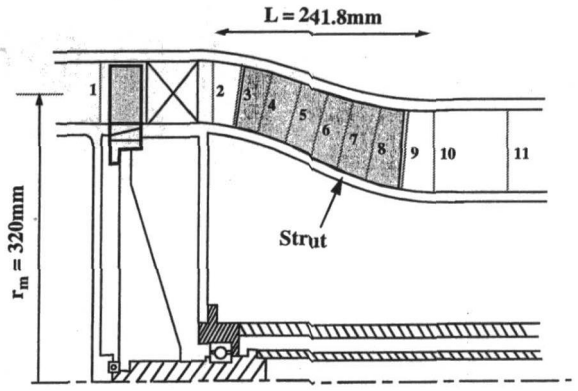

Traverse Location at Mid Passage Height

STN	1	2	3	4	5	6	7	8	9	10	11
x/L	-0.4	0.02	0.125	0.25	0.375	0.50	0.625	0.75	0.875	1.0	1.40

Strut Specifications

Hub - NACA 63 t/c = 10.4%
Mean - NACA 65 t/c = 12.0%
Tip - NACA 66 t/c = 13.8%

Fig. 2 Experimental facility—working section

coefficient of 0.285 and a flow coefficient of 0.56, with the outlet guide vanes removing 27 deg of rotor exit swirl. The duct itself is of constant flow area with an inlet passage height of 71.1 mm, an axial length of 241.8 mm, and an exit-to-inlet mean radius ratio of 0.8. Within both bends the maximum geometric curvature (h/R), at midpassage height, is approximately 0.4. Downstream of the duct air passes through the settling length and into an exhaust plenum prior to being expelled to atmosphere.

For certain tests a radial strut could be located within the S-shaped duct (Fig. 2). A single strut only was used since the significant aerodynamic blockage associated with a number of struts would require extensive modification to the facility. A NACA65 profile with 12 percent thickness/chord distribution defined the strut profile on the surface of revolution, which bisects the annulus into equal areas. This thickness distribution was then extrapolated, along radial lines, to define the distribution along each casing. Static tappings located at numerous chordwise positions allowed the static pressure distribution to be defined at 10, 50, and 90 percent of strut height.

Instrumentation

Measurements have been performed at 11 traverse planes with the data at each location being typically obtained at 23 radial positions repeated at 21 circumferential locations.

The area traversed corresponded to either one or two OGV blade spaces. With the axial flow compressor removed, the flow has been shown to be axisymmetric, and therefore traverses were performed across the passage at a fixed circumferential location.

Pressure measurements were made using a miniature five-hole pressure probe of overall diameter 1.7 mm, hole bore 0.25 mm, and was used in a non-nulled mode as outlined by Wray (1986). In addition, static pressure tappings were located in a helical path along the inner and outer walls. Measurements were also obtained using a Dantec color-separated three-channel LDA system. As described in greater detail by Carrotte and Britchford (1994), these measurements provided information on mean velocity, all six Reynolds stresses, and higher order velocity correlations. The data were obtained with an effective measurement volume of 0.1 × 0.1 × 0.3 mm with a 40 MHz frequency shift being used to eliminate fringe bias. The signals received from each channel, due to the passage of particles through the control volume, were processed in the frequency domain using 57N10 Burst Spectrum Analyzers (BSAs). All measurements were performed with coincidence filtering, i.e., data were only recorded when bursts were simultaneously registered and validated by all 3 BSAs.

Data Reduction

At each traverse point, five-hole probes provide information on stagnation and static pressure in addition to velocity magni-

Nomenclature

A = area
C_p = static pressure recovery coefficient
H = boundary layer shape parameter = δ^*/θ
L = S-shaped duct axial length
P, p = stagnation pressure, static pressure
R = radius of flow curvature
U = mean streamwise velocity component
U_{mean} = area-weighted spatial mean value
h = passage height = $n_o - n_i$
k = turbulent kinetic energy = $\frac{1}{2}(u^2 + v^2 + w^2)$
m = mass flow
r = radius
s = streamwise coordinate
n = cross-stream coordinate
$\overline{uv}$ = Reynolds shear stress component
x = axial distance
α = kinetic energy flux coefficient
δ = boundary layer thickness
λ = stagnation pressure loss coefficient
ρ = density
τ = total shear stress = $\mu\partial U/\partial n - \rho\overline{uv}$
τ_w = wall shear stress = $(\mu\partial U/\partial n)_w$

Superscripts

$-$ = time average
$\sim$ = mass-weighted spatial mean value

Subscripts

i = inner casing
o = outer casing
w = wall value

tude and direction. From the three-dimensional LDA measurements the turbulent shear stress distributions ($\overline{uv}$) are obtained, with the mean velocity information provided by this technique also being in excellent agreement with that measured by the pressure probes.

The overall mean velocity at a traverse plane (U_{mean}) was calculated using an area-weighted method, while at the same place the spatially averaged values of stagnation and static pressure were derived by mass weighting the appropriate individual values, i.e.,

$$\tilde{P} = \frac{1}{m}\int Pdm \quad \tilde{p} = \frac{1}{m}\int pdm \tag{1}$$

A kinetic energy flux coefficient (α) was also defined such that

$$\tilde{P} = \tilde{p} + \alpha \tfrac{1}{2}\rho U_{mean}^2 \quad \text{where} \quad \alpha = \int \frac{U^3}{U_{mean}^3 A}\, dA \tag{2}$$

Changes in the spatially averaged pressures between various planes within the facility are expressed in terms of a stagnation pressure loss coefficient (λ), while static pressure distributions are expressed in terms of the C_p coefficient where:

$$\lambda_{a-b} = \frac{\tilde{P}_a - \tilde{P}_b}{\tilde{P}_a - \tilde{p}_a} \quad C_p = \frac{p - \tilde{p}_a}{\tilde{P}_a - \tilde{p}_a} \tag{3}$$

where "a" and "b" are upstream and downstream planes, respectively, and p is the measured static pressure at a given location.

Differentiation of the data was achieved by calculating the gradient of a spline curve or third-order lagrange polynomial fitted to the experimental data. A detailed description of how boundary layer properties such as shape parameter (H) were obtained is given by Britchford et al. (1994).

Estimate of Experimental Errors

For the clean inlet condition the spatially averaged total and static pressures at a traverse plane were repeatable to within 0.5 mm H_2O, with discrepancies in mass flow between planes of less than 2 percent. Based on these values, it was estimated the stagnation pressure loss coefficients were repeatable to within ± 0.005. With the compressor at inlet this increased to ± 0.0075 as the compressor operating point could only be maintained to within a finite resolution. Note that although overall loss levels at a plane can vary, the nondimensional radial distributions of pressure were, within experimental error, the same.

Up to 5000 statistically independent samples were obtained with the LDA equipment at each data point. This results in the turbulent shear stress levels ($\overline{uv}$) being within ± 0.2 m^2/s^2 at most locations within the duct. Extrapolation of this data to each surface also gave reasonable agreement with wall shear stress values obtained by fitting the mean velocity to a "log law" distribution. However, it should be noted that in regions of strong favorable pressure gradient, there were insufficient data close to the surface to fit the log law distribution making the accurate definition of a wall value difficult.

Results and Discussion

Clean Inlet. At inlet to the S-shaped duct, the turbulent boundary layers that have developed along the inner and outer casings within the entry section each occupy approximately 24 percent of the passage height. The spatial average velocity for the annular passage (U_{mean}) is 28.3 m/s and this is used as a reference value for nondimensionalizing the mean velocity and shear stress data at subsequent traverse stations.

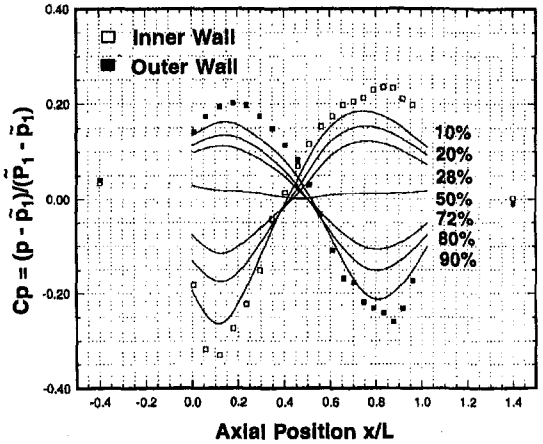

Fig. 3 Axial static pressure distribution

Flow Development. The static pressure distribution along each casing wall, and at various heights across the duct, is presented (Fig. 3) in terms of a coefficient (C_p) defined using the mass-weighted stagnation and static pressures at inlet to the duct ($x/L = -0.40$). Differences between the static pressures across the duct reflect how the pressure field adjusts to provide the required radial forces to turn the flow. As a result of the significant streamwise pressure gradients that occur, the flow along the inner casing is subjected to a predominantly positive (i.e., adverse) gradient as the static pressure coefficient rises, from -0.33 to $+0.24$ along approximately 70 percent of the duct length. In contrast, the pressure gradient is mostly negative (i.e., favorable) adjacent to the outer casing, with the coefficient reducing from $+0.20$ to -0.26 along a similar length. Note also how these gradients vary significantly across the height of each boundary layer, with the maximum streamwise variations occurring along each casing.

In addition to streamwise pressure gradients, the development of each boundary layer is influenced by curvature effects, which modify the flows' turbulent structure. Britchford et al. (1994) have already described in detail the variation of a curvature parameter (δ/R), which indicates the relative magnitude of these effects for each casing boundary layer. For example, the inner wall boundary layer is initially subject to convex curvature, the maximum value occurring at $x/L = 0.125$ ($\delta/R = 0.11$), and this will lead to a reduction in turbulence levels. However, by $x/L = 0.50$ curvature is in the opposite sense (i.e., concave), increasing up to a maximum value at $x/L = 0.80$ ($\delta/R = 0.12$) and resulting in increased turbulence mixing. Along the outer casing similar effects are present, but in this case concave ($\delta/R = 0.08$) precedes the convex ($\delta/R = 0.09$) curvature. The magnitude of the curvature parameter, as suggested by Gillis and Johnston (1983) and Barlow and Johnston (1988), indicates that the flow within each casing boundary layer is experiencing relatively strong curvature. This, combined with the continually varying pressure gradients, gives rise to the development of a complex flow along each casing.

Shear Stress Distribution. The measured distribution of shear stress ($\overline{uv}$) along the duct is presented (Fig. 4). Note that interpretation of these data has been assisted by the wall shear stress values, obtained from fitting the mean velocity profiles to the "log law" distribution, and also the total shear stress gradient at each surface is known from the static pressure distribution since $(\partial\tau/\partial n)_w = (\partial p/\partial s)_w$. Whereas the development of boundary layers within the entry length has produced near linear distributions of shear stress at $x/L = -0.40$, these rapidly change within the S-shaped duct.

The effect of the streamwise static pressure gradients is more apparent in the near-wall region where the flow is of relatively

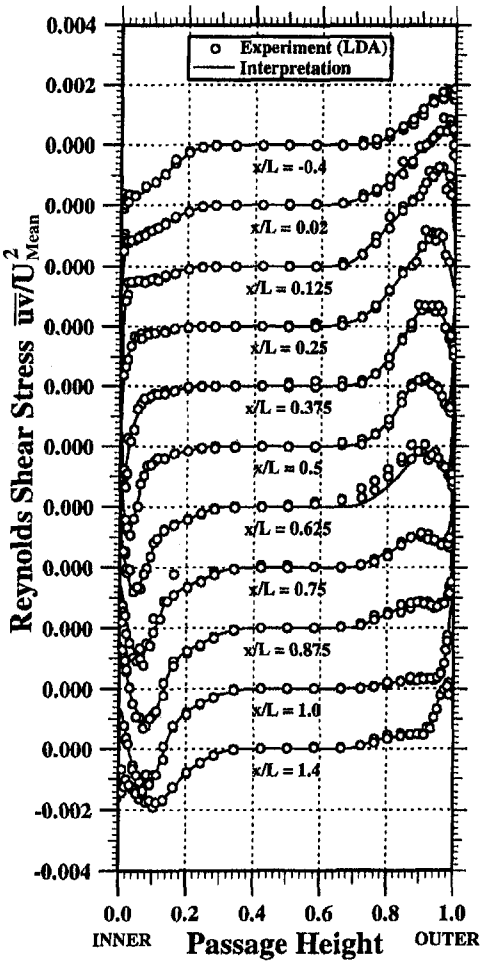

Fig. 4 Development of Reynolds shear stress

low momentum. For example, between $x/L = 0.25$ and 0.75 the sustained adverse pressure gradient along the inner casing reduces the wall shear stress, with the peak value increasing in magnitude and moving progressively away from the wall. Such an effect helps offset the deceleration of near-wall flow brought about by the increasing pressure. However, this region is preceded, and then followed by, a favorable pressure gradient throughout which the wall shear stress increases. In contrast, for the outer casing the pressure gradient is adverse during the initial and latter stages of the duct, resulting in the peak shear stress moving away from the surface and a reduced wall value. However, along most of the surface ($x/L = 0.25$ to 0.75) the pressure gradient is favorable, causing the observed increases in shear stress at the wall. For both boundary layers the streamwise pressure gradients can therefore be seen to produce complex distributions of shear stress. However, these are further modified by the direct effect of the streamline curvature on the turbulence field, which is more apparent in the outer part of each boundary layer. Thus, for the inner wall the convex curvature leads to an initial suppression of shear stress and, although concave curvature commences at $x/L = 0.50$, the low turbulence level at this location means that enhanced shear stress values are not observed until $x/L = 0.75$. For the outer casing similar effects are observed, except in this case turbulence mixing and shear stress levels are initially enhanced prior to being reduced by the convex curvature toward duct exit.

Mean Velocity Profile. At a given location the mean velocity profile is predominantly a function of the applied streamwise pressure and shear stress gradients. In this way the duct curvature directly affects the velocity profile through the static pressure field, and indirectly through the modified turbulence structure. The mean velocity profiles (Fig. 5) show the presence of a potential core region, along the entire length of the duct, which isolates the boundary layers adjacent to each casing. Of particular significance is the variation of each boundary layer's shape parameter (H) along the duct, which shows that it is the flow adjacent to the inner casing that is most likely to separate. This is due to the combined influence of the sustained adverse pressure gradient and curvature effects on the boundary layer development. This gives rise to the rapid growth in shape parameter, which reaches a maximum value of 1.66 at $x/L = 0.75$, although it should be noted that this is well below the value of approximately 2.4 associated with flow nearing separation. The avoidance of flow separation is also confirmed by the fact that at no point along each wall does the shear stress reduce to zero.

Overall Performance. As described by Gillis and Johnston (1983), the momentum equation along a streamline can be reduced to

$$\frac{\partial P}{\partial s} = \frac{\partial \tau}{\partial n} \tag{4}$$

where P and τ are the stagnation pressure and total shear stress, respectively. Now the effect of streamwise curvature and pressure gradients on the shear stress distribution (τ) within the S-shaped duct has already been discussed. Of some concern therefore is the level of stagnation pressure loss that may be generated within the duct due to these effects.

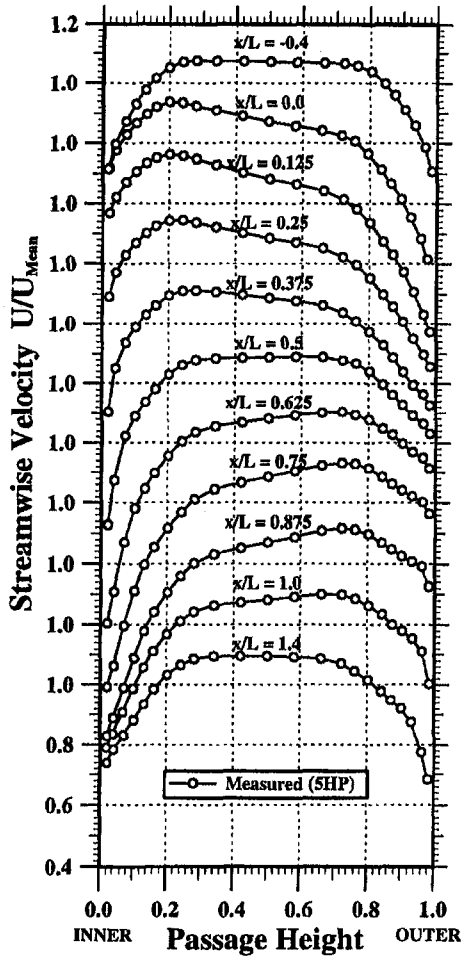

Fig. 5 Development of streamwise velocity

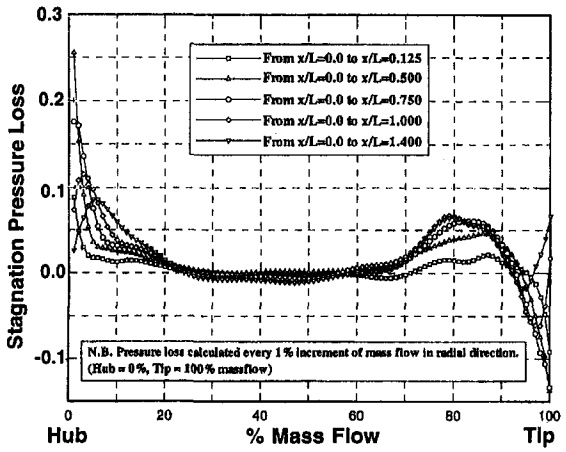

Fig. 6 Development of the radial variation of stagnation pressure loss—clean inlet

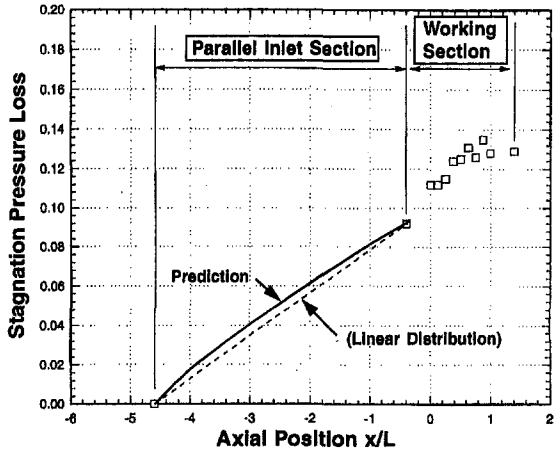

Fig. 7 Axial variation of stagnation pressure loss

The radial distribution of loss and its development within the duct can be described by monitoring the change in stagnation pressure along streamlines. At every plane the mass flow is therefore divided into 1 percent increments across the duct, with the stagnation pressures at these locations being determined by interpolation of the measured data. At several planes the loss distributions across the duct are presented (Fig. 6), based on the pressure loss along each streamline, with the area under each curve representing the overall stagnation pressure loss incurred by the flow up to that plane. As indicated from Eq. (4) these changes in stagnation pressure are a result of the shear stress gradients, which can be integrated along each streamline to give the stagnation pressure loss. Note how in certain regions of the duct, stagnation pressure can increase along a streamline and that the loss associated with each boundary layer is different in both magnitude and distribution. For example, along the inner wall the loss is mostly associated with the adverse pressure gradient applied over a significant length of the duct, with this high loss region moving away from the casing as flow proceeds toward duct exit. Alternatively, for the outer casing the majority of the loss is in the outer regions of the boundary layer and is mainly due to the initial concave curvature. This enhances turbulence levels and hence the gradient of shear stress between the peak and the edge of the boundary layer. Gradually the high levels of turbulence are suppressed by the convex curvature in the latter half of the duct. For the central core region the stagnation pressure loss should be zero with the minor variations observed being within experimental error.

Within the working section of the test facility, the loss coefficient (λ) is 0.04. This is based on the mass-weighted stagnation pressure loss between $x/L = -0.40$ and 1.40 relative to the mean dynamic head at the upstream plane ($\alpha\frac{1}{2}\rho U^2_{\text{mean}}$). Based on the conditions between duct inlet ($x/L = 0.0$) and exit ($x/L = 1.0$) the loss coefficient (λ) is approximately 0.02. However, the relative magnitude of the S-shaped duct loss can be more easily assessed by evaluating the loss incurred by the flow between rig inlet and the traverse plane being considered. This is nondimensionalized by the dynamic head ($\frac{1}{2}\rho U^2_{\text{mean}}$) and is presented relative to axial location (x/L) within the facility (Fig. 7). Note the experimental scatter due to the relatively small changes in pressure that are taking place and the finite resolution to which the pressures can be measured. It can be seen that stagnation pressure loss within the inlet section results in a loss coefficient of 0.092 at $x/L = -0.40$, which rises to 0.129 at x/L 1.40. Within the parallel-sided inlet section the rate of loss increase will initially be high and decrease toward the end of this section. However, predictions indicate that the loss increase does not differ significantly from that of a linear distribution and, as a consequence, it can be seen that the rate of loss increase through the S-shaped duct does not appear to be significantly different. Thus, despite strong curvature and pressure gradient effects, the stagnation pressure loss within the duct appears to be comparable with that which would be obtained with a parallel-sided duct. This is, of course, for a duct in which the flow is well behaved and flow separation is avoided.

The relatively small duct pressure loss is difficult to establish experimentally, while significant variations of shear stress within the duct have already been described. It is therefore desirable to validate the shear stress and pressure measurements to ensure both sets of data are consistent with each other. Based on Eq. (4) the derivatives $\partial(\overline{uv})/\partial n$ and $1/\rho\,\partial P/\partial s$ from both sets of measurements were compared and found to be in good agreement as shown for example at $x/L = 0.50$ (Fig. 8). Furthermore, based on the shear stress gradients and using Eq. (4), an estimated value of the duct stagnation pressure loss (λ) of 0.055 was obtained between $x/L = -0.4$ and 1.4. Allowing for the inherent inaccuracies associated with the differentiation of experimental data, this is thought to be in excellent agreement with the value of 0.04 obtained directly from the pressure measurements.

Compressor at Inlet. More engine representative inlet conditions are obtained by incorporating a single-stage rotor and OGV row at inlet to the S-shaped duct. Although pressure gradient and streamline curvature effects are present upstream of duct inlet ($x/L = 0.0$), the axial location of the compressor means that overall performance can only be assessed between $x/L = 0.0$ and the downstream traverse planes. For comparison

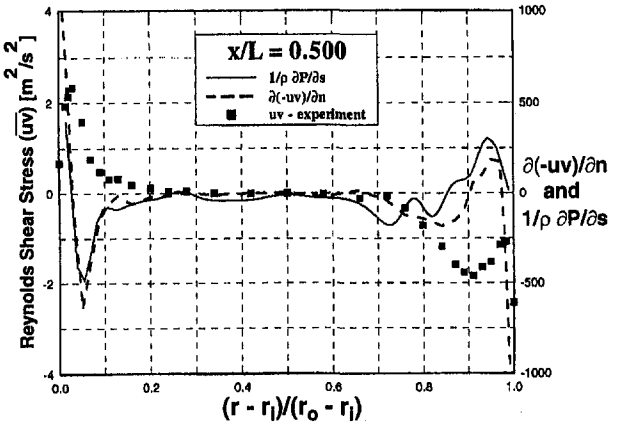

Fig. 8 Profiles of $\partial\tau/\partial n$ and $1/\rho\ \partial P/\partial s$

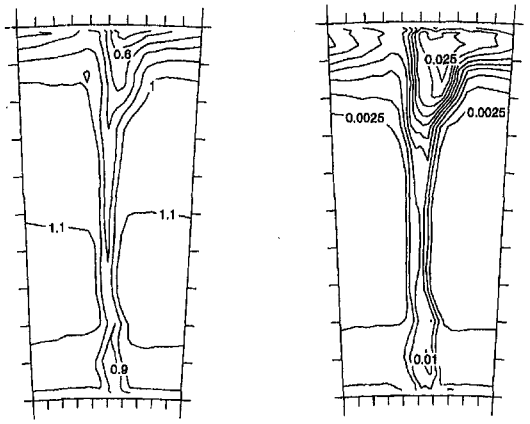

a) Streamwise Velocity Distribution at x/L = 0.0

Contours U/U_{mean} (0.1 Intervals)

b) Turbulent Kinetic Energy Distribution at x/L = 0.0

Contours $\frac{1}{2}(u^2+v^2+w^2)/U_{mean}^2$ (0.0025 Intervals)

Fig. 9 Compressor-generated inlet conditions

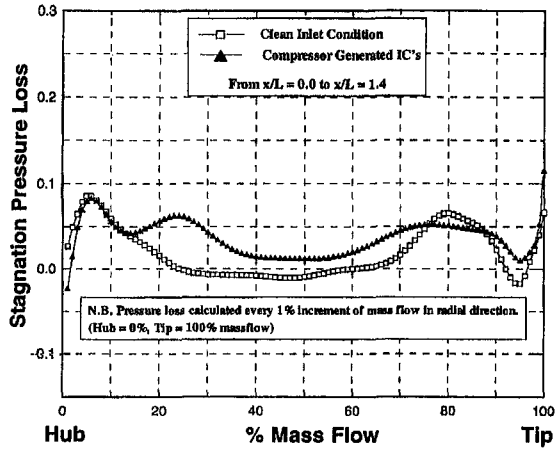

Fig. 11 Radial variation of stagnation pressure loss (clean and compressor at inlet)

purposes the clean inlet performance is therefore also defined from data observed at the same locations.

At duct inlet the mean velocity distribution (Fig. 9(a)) indicates circumferential variations in the flow field introduced due to wakes from the upstream compressor OGV row. In addition, the turbulent kinetic energy distribution (Fig. 9(b)) illustrates the change in turbulence structure of the flow entering the duct. Note, for example, the large amount of turbulent energy close to the outer casing associated with rotor tip leakage effects. The detailed response of this more complex mean and turbulent velocity field to the pressure gradients and curvature effects within the S-shaped duct is the subject of a continuing investigation at Loughborough.

In terms of overall performance it is interesting to note that the maximum shape factor (H) within the duct has been reduced from 1.66 to 1.47 (Fig. 10). It should be noted that, for the compressor, this is the value associated with the circumferentially averaged velocity profile, but at the critical location the circumferential variation is in the range 1.36 to 1.56, which is still below the clean value. This implies that the streamwise pressure gradients could be increased, for example by reducing length for the same change in mean radius, without necessarily incurring flow separation. Some of the mechanisms that may account for this change in performance have already been described by Britchford et al. (1993). For example, the radial pressure gradient tends to drive the OGV wake flow radially inward and, although this fluid has a total pressure deficit, it is less than the deficit resident in the inner wall boundary layer, thereby helping to re-energize this flow. Along the outer casing a slight reduction in shape parameter is also observed, with higher velocities being recorded closer to the casing surface. This is thought to be due to the enhanced mixing associated with the tip leakage effects noted earlier.

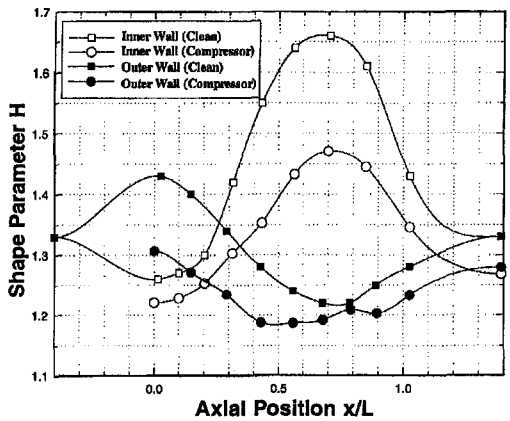

Fig. 10 Axial variation of shape parameter

The overall mass-weighted stagnation pressure loss for the duct (λ) is approximately 0.035 between $x/L = 0.0$ and 1.0, which compares with 0.020 for the clean inlet. However, this pressure loss is still relatively small and can only be defined to within ± 0.0075 of its true value. Most of the additional loss though is thought to be attributable to mixing of the OGV wakes within the duct. As described by Denton (1994), this loss can normally be estimated by assuming mixing occurs at constant momentum in a parallel sided duct. Although not strictly true here, this approach has been applied to the wake profiles observed at duct inlet and, in particular, to the wakes in the central passage region that have not been distorted by any boundary layer influences. This yielded a mixing loss value of 0.015, which is the correct order of magnitude to account for the observed loss increase. It should also be noted that mixing will occur rapidly downstream of the blade row, and so the actual mixing and overall duct loss depend on the axial location of the traverse plane with respect to the OGV trailing edge.

The radial distribution of pressure loss for the two types of inlet condition are presented (Fig. 11). Note the finite loss now occurring in the center of the duct due to wake mixing. However, within each boundary layer the similar distributions indicate the same flow mechanisms in these region are also present and contributing to the generation of stagnation pressure loss. The only exception to this is in the outer regions of the inner wall boundary layer, where a relatively high loss is apparent. This develops as the boundary layer is subjected to the sustained adverse pressure gradient within the duct and is located at the wake-boundary layer intersection.

Strutted S-Shaped Duct. Effects brought about by the presence of the strut were found to be similar with both clean and compressor-generated inlet conditions, but only the axial velocity contours obtained with the compressor are presented. At duct inlet ($x/L = 0.0$), the effect due to the downstream blockage presented by the strut is evident (Fig. 12(a)). The axial velocity contours indicate that, compared with the adjacent OGV passages, immediately upstream of the strut the casing boundary layers are relatively thicker with a smaller core region of high velocity flow. Farther downstream a well-defined wake can be observed at the strut trailing edge (Fig. 12(b)), but there are no significant regions of flow separation. The trailing

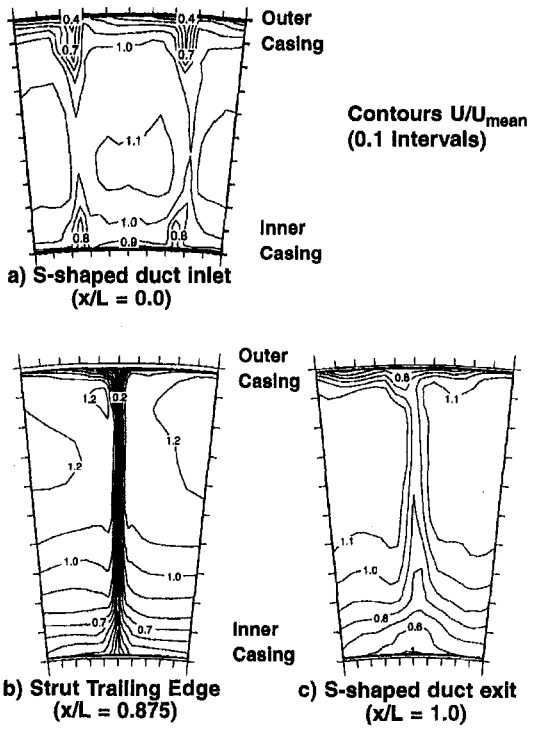

Fig. 12 Axial velocity distributions (clean inlet)

edge is deliberately positioned at the location where the pressure gradients within the duct are changing sign. Thus, mixing out of the wake and boundary layer in the more critical inner wall region is assisted by the favorable pressure gradient and the enhanced shear stresses due to curvature. However, the reverse is true along the outer casing where wake mixing will therefore be delayed. At duct exit ($x/L = 1.0$) a well-defined wake can still be observed (Fig. 12(c)) and its magnitude, relative to the remnants of the OGV wakes, can also be assessed.

The circumferential variation of stagnation pressure loss, both with clean and compressor generated inlet conditions, are presented (Fig. 13). Note that for the clean condition the loss values are referenced to $x/L = -0.4$, at which the upstream effect of the strut is not evident, but with the compressor only the duct inlet plane ($x/L = 0.0$) is available. It can be seen that the localized strut effect is relatively large, and the associated loss increment can be obtained by integration of the area under the loss curve (Fig. 13). However, the influence of a single strut on overall performance is relatively small. For example,

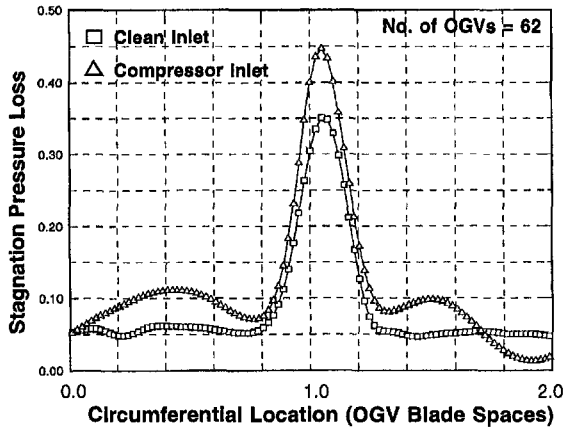

Fig. 13 Circumferential loss distribution

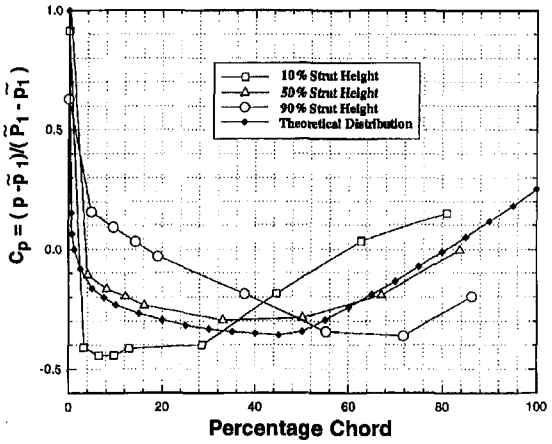

Fig. 14 Static pressure distribution about strut

the clean inlet loss coefficient would increase from 0.040 to 0.042 when a single strut is incorporated, with corresponding values of 0.035 and 0.038 with the compressor present. Normally the number of struts will be significantly greater, and if it is assumed the duct geometry is varied to account for the blockage associated with a given number of struts, and the flow field associated with each strut is independent of its nearest neighbor, then the overall effect on performance can be estimated. For example, with compressor-generated inlet conditions eight struts would increase the duct loss from 0.035 to approximately 0.058.

The static pressure distributions measured along the strut at 10, 50, and 90 percent heights are presented (Fig. 14) and, at a given height, only minor differences are apparent between the values obtained with both types of inlet condition. What is of significance though is the differences in the pressure distribution across the strut height. For example, at midheight the pressure gradients are favorable up to the 45 percent chord location, downstream of which the pressure then increases. This is in reasonable agreement with the distribution deduced from the data of Abbott and Von Doenhoff (1949) based on measurements of this NACA profile under "free-stream" conditions. However, at 10 percent strut height an unfavorable pressure gradient is present over 85 percent of the strut chord, whereas toward the outer casing the gradient is favorable over most of the strut length. Although some minor variations occur due to the changing profile across the strut height, differences between the distributions are mostly due to the streamwise pressure gradients within the S-shaped duct presented earlier. This is illustrated by considering the distribution at 10 percent height. At this location the pressure distribution within the S-shaped duct, as already presented (Fig. 15), can be subtracted from the distribution measured along the strut. The resulting distribution is a good approximation to that of the free-stream distribution for this profile as outlined by Abbott and Von Doenhoff (1949). Thus the static pressure distribution surrounding the strut is mainly a function of the strut profile and the pressure distribution of the duct in which it is located. Such a result also indicates that rather than using a standard profile, the strut design can be modified to account for the pressure field within which it operates. Thus, favorable pressure gradients can be taken advantage of while off-loading regions in which the pressure gradient is mostly adverse. Such an integrated design approach would be of even greater benefit if cambered struts were to be incorporated within the duct.

Conclusions

An experimental investigation has been undertaken to assess the performance of a compressor interconnecting annular S-

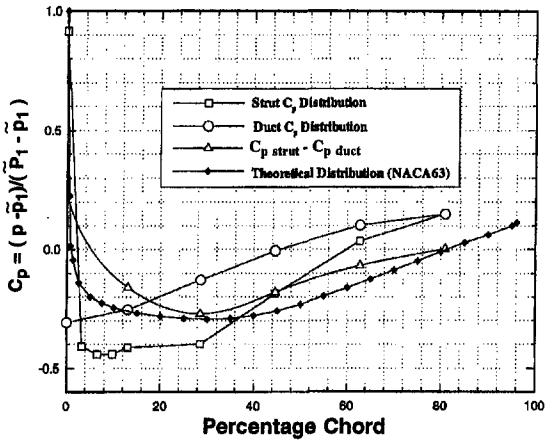

Fig. 15 Superposition of strut and duct static pressure distributions

shaped duct whose geometry is typical of that which may be found in a modern multispool gas turbine engine. The following conclusions have been drawn:

- Significant streamwise pressure gradients arise within the duct due to flow curvature, which also have a direct influence on the turbulent flow field. This effect results in the flow adjacent to the inner casing being more liable to separate.
- With no flow separation present the stagnation pressure loss within the duct was of a similar magnitude to that which would be obtained with a parallel-sided passage. The magnitude and radial distribution of loss was consistent with the measured shear stress distribution within the duct.
- When engine representative inlet conditions are provided by an axial compressor at duct inlet, the boundary layers are re-energized so reducing the likelihood of separation. However, the mass-weighted stagnation pressure loss in the duct increases due to mixing out of compressor wakes.
- Attached flow was observed over the entire surface of the 12 percent thickness-chord ratio radial strut, which is typical of that which may be used for carrying loads or engine services. The static pressure distribution around the strut is determined not only by the strut profile, but also the pressure distribution imposed by the duct itself.

Acknowledgments

The authors would like to express their thanks to Messrs. R. Marson, D. Glover, L. Monk, and W. Niven for their assistance in the manufacture of the test facility.

References

Abbott, I. H., and Von Doenhoff, A. E., 1949, *Theory of Wing Sections,* Dover Publications Inc., New York.

Barlow, R. S., and Johnston, J. P., 1988, "Structure of a Turbulent Boundary Layer on a Concave Surface," *Journal of Fluid Mechanics,* Vol. 191.

Bradshaw, P., 1973, "The Effects of Streamline Curvature on Turbulent Flow," AGARD AG-169.

Britchford, K. M., Carrotte, J. F., Stevens, S. J., and McGuirk, J. J., 1994, "The Development of the Mean Flow and Turbulence Structure in an Annular S-Shaped Duct," ASME Paper No. 94-GT-457.

Britchford, K. M., Manners, A. P., McGuirk, J. J., and Stevens, S. J., 1993, "Measurements and Prediction of Flow in Annular S-Shaped Ducts," *Proc. Second International Symposium on Engineering Turbulence Modelling and Measurements,* Florence, Italy.

Carrotte, J. F., and Britchford, K. M., 1994, "The Effect of Laser Beam Orientation on the Accuracy of 3D LDA Measurements Within an Annular Test Facility," *Proc. Seventh International Symposium on Applications of Laser Techniques to Fluid Mechanics,* Lisbon, Portugal, July.

Denton, J. D., 1994, "Loss Mechanisms in Turbomachines," ASME JOURNAL OF TURBOMACHINERY, Vol. 115.

Gillis, J. C., and Johnston, J. P., 1983, "Turbulent Boundary Layer Flow and Structure on a Convex Wall and Its Redevelopment on a Flat Wall," *Journal of Fluid Mechanics,* Vol. 135.

Wray, A. P., 1986, "The Analysis of 5-Hole Probe Data Using Generalised Computer Software," Dept. of Transport Technology, Loughborough University, Report No. TT86R06.

Journal of Turbomachinery

Technical Brief

Circumferentially Smeared Computed Effects of Rim Seal Clearance on Wheelspace Thermal Distributions

S. H. Ko,[1] D. L. Rhode,[2] and Z. Guo[3]

An advanced finite volume computer code, recently benchmarked against rotor–stator cavity measurements (Ko and Rhode, 1992), was used to obtain an enhanced partial understanding of hot gas ingress heating of a generic turbine wheelspace cavity. This problem is extremely complicated, with a three-dimensional, probably circumferentially periodic ingress/egress flow through the rim seal due to mainstream pressure asymmetries resulting from the presence of blades, etc. The present study does not assume that the complete problem can be modeled as steady and two-dimensional axisymmetric. Rather, the objective of this study is to obtain a partial understanding of the complete problem from investigating the circumferentially smeared, steady, two-dimensional axisymmetric subproblem. It was found that, contrary to the case of the nominal rim seal axial clearance, for a clearance of one-fourth of the nominal value, the temperature of the "hot spot" on the rotor is sharply reduced with increasing purge-coolant flow because the rim seal gap recirculation zone does not form. Also, it was found that smaller rim seal axial clearances give less rotational drag as well as less heat transport from the mainstream into the wheelspace.

Contents

The interface between the mainstream and the rim seal is the primary focus here. Thus only the extremely narrow axial space between an upstream vane and a downstream blade, along with the corresponding wheelspace cavity, has been modeled (see Fig. 1). Due to space limitations, details of the turbulence model, boundary conditions, etc., could not be included but are available from Ko and Rhode (1992). The complete elliptic form of the two-dimensional axisymmetric Navier–Stokes equations for compressible, turbulent flow were solved using the SIMPLER algorithm of Patankar (1980). The Coriolis and centrifugal momentum terms are handled in the conventional way, as cylindrical coordinates were used in a stationary reference frame. Temperatures, pressures, Reynolds numbers, and Mach numbers of the purge-coolant and mainstream flows, as well as the Reynolds number of the disk, which are typical of a commercial gas turbine engine, were specified. Further, adiabatic walls were specified in order to isolate the ingress heating effects, which are the focus here, from convective heat transport from the wheelspace walls to the wheelspace fluid.

The nearly uniform grid of approximately 100×150 lines in the axial and radial directions, respectively, gave a sensibly grid independent solution. Grid sensitivity comparisons with a grid of 60×117 lines, for example, gave rotor temperatures and disk friction moment coefficient values within approximately 3 percent of that for the production grid of 100×150 lines. The iteration convergence criterion was that the summation of the magnitude of the normalized residuals for each cell must be less than 0.001; also, the global mass balance was verified. The purge-coolant flow enters the wheelspace cavity through a circumferentially smeared series of orifices in the stator cavity wall at temperature T_2 and leaves the cavity radially through the rim seal. For the nominal generic cavity considered, the dimensions are given by Ko and Rhode (1992).

The effect of a very small rim seal gap recirculation zone GRZ, which was first identified by Ko and Rhode (1992), has far-reaching effects on mainstream heating of the disk and wheelspace cavity. The presence of the GRZ at actual engine operating parameters was verified by independent CFD solutions (Hendricks, 1994). Specifically, the high-speed mainstream (at a Mach number of approximately 1.0) traveling across the rim seal interface with the mainstream (see Fig. 1) "drives" the GRZ in clockwise recirculation, similar to the recirculation in the classical "lid-driven cavity" problem. The resulting overall wheelspace flow pattern causes a purge-coolant fluid particle, upon reaching the rim seal vicinity as it is centrifugally pumped radially outward within the disk Ekman-like layer, to be deflected away from the disk upon meeting the opposing (radially inward) flow of the GRZ. The fluid particle then passes through the rim seal alongside the stator shroud tip (Fig. 1) and then is abruptly swept downstream, "driving" the GRZ as it passes over the seal axial clearance. The turbulent diffusion heat transport sequence is: (*a*) from the mainstream to the thin layer of cavity fluid exiting the rim seal, (*b*) then from this exiting fluid to the GRZ at approximately the disk perimeter radius R and finally (*c*) from the GRZ to the outer portion of the disk near $r/R = 0.99$.

For the generalized configuration specified, the results in Fig. 2 show the large effect of seal axial clearance on maximum adiabatic disk temperature for various purge-coolant volumetric flow rate parameter [$C_w = Q/(\nu R)$] values. Note that the C_w value of 7200 and the rim seal axial clearance of $c/R = 0.00936$

[1] Assistant Professor, Department of Mechanical Design Engineering, Chungnam National University, 305-764, 220, Kung-dong, Yusong-gu, Taejon, Korea.
[2] Associate Professor, Mechanical Engineering Department, Texas A&M University, College Station, TX 77843.
[3] Senior Product Engineer, EGS, Inc., 36,200 Plymouth Rd., Livonia, MA 48150.

Contributed by the International Gas Turbine Institute of THE AMERICAN SOCIETY OF MECHANICAL ENGINEERS. Manuscript received at ASME Headquarters September 10, 1996. Associate Technical Editor: T. H. Okiishi.

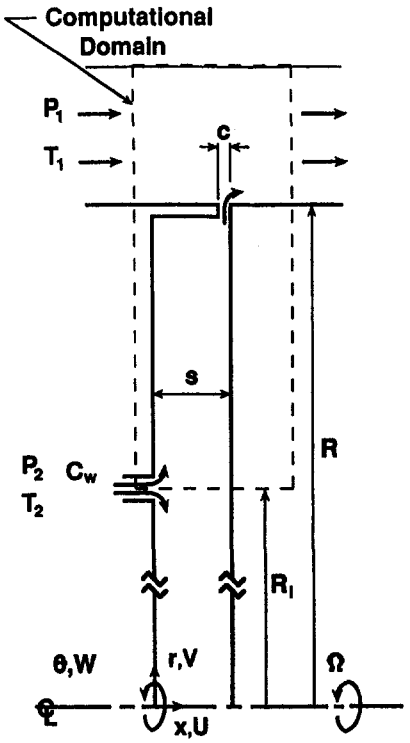

Fig. 1 Idealized configuration and computational domain

correspond to the engine nominal operating condition. Except at very small clearances T_{max} decreases slowly, and almost linearly, as the purge flow C_w increases. With the exception of potential vibration problems, a substantial advantage was found for the tightest clearance case (c/R = 0.00234) in giving a large reduction of T_{max} upon increasing C_w. The smallest clearance case is far more effective at reducing T_{max} because: (a) The GRZ does not occur (at least for C_w = 7200), which gives far less heat transport across the rim seal and (b) the disk layer of purge-coolant directly contacts the "hot spot" location due to the absence of the GRZ.

The radial distribution of adiabatic disk temperature is given in Fig. 3 for the nominal clearance case of c/R = 0.00936. Observe here that there are two regions of much different temperature. Due to the heating of the GRZ near r/R = 1.0, the outer region is very hot, whereas the inner region is cool due to the cool purge stream. Also note that the large temperature jump occurs exactly where the Ekman wall layer meets the much hotter GRZ. The stagnation point at the radially inner extremity of the GRZ is found to produce a very slight local maximum in the disk temperature distribution. Another slight temperature jump occurs at the outer edge of the disk (r/R = 1.0) where the hot mainstream transports heat to the thin egress layer, which in turn directly contacts the disk perimeter. It is also of interest to note here that higher C_w values naturally give a greater radially outward momentum, which reduces the extent of the GRZ.

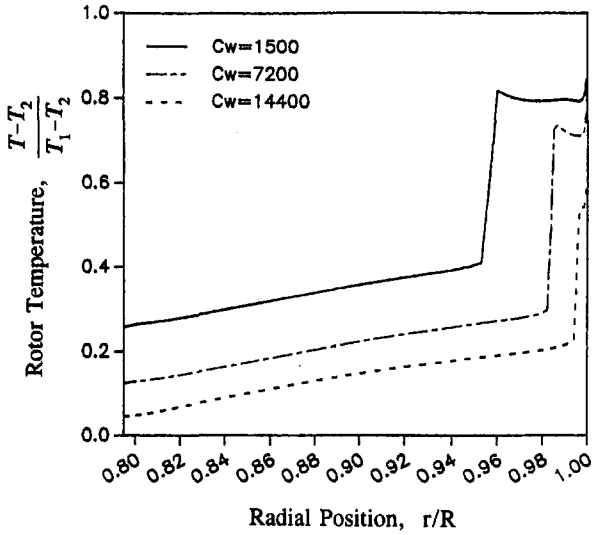

Fig. 3 Effect of cooling flow rate C_w on the temperature distribution along the rotor surface for the nominal clearance c/R = 0.00936

It has been speculated previously that, in the context of gas turbines, the disk friction moment coefficient $C_m \equiv M/(0.5\rho\Omega^2R^5)$ should decrease initially and then increase once c/R is reduced below a certain value, holding C_w fixed. However, the results for the C_m variation with c/R given in Fig. 4 show that this does not occur, at least not for clearance reductions down to 25 percent of the nominal value. The purge-coolant flow rate C_w was found to give a negligible effect on the moment coefficient, except at the smallest clearances and the lowest C_w values. When the nominal clearance is doubled (c/R = 0.01872), there

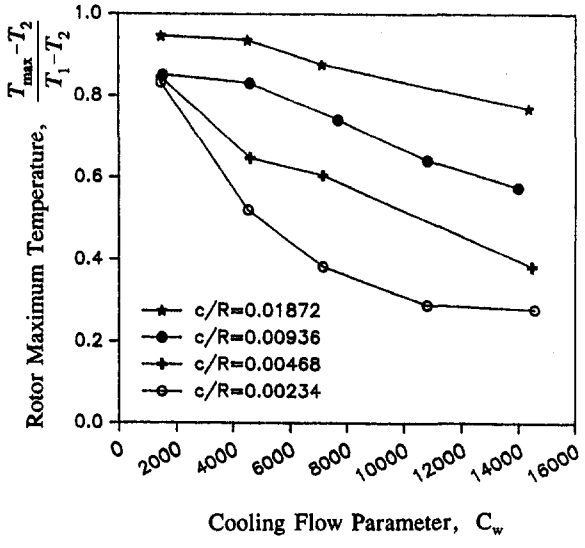

Fig. 2 Effect of rim seal axial clearance on the maximum temperature along the rotor surface

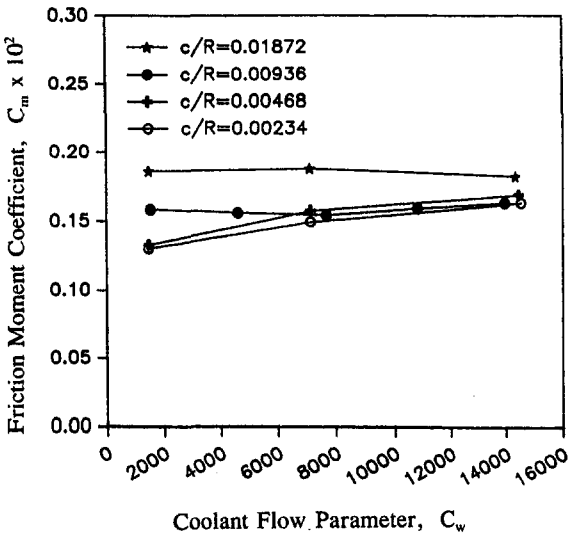

Fig. 4 Effect of rim seal axial clearance on the friction moment coefficient

is increased rotational drag, primarily because of the increased turbulent shear stresses found near the perimeter of the disk. This is the location where the drag has the most influence due to the large moment arm. From these results, it is concluded that smaller rim seal clearances are preferred from rotational drag as well as from purge minimization considerations.

Acknowledgments

The financial support of the NASA Center for Space Power and the Turbomachinery Research Consortium of Texas A & M University is gratefully acknowledged. The authors are also indebted to the Supercomputer Center at the university for a grant of CRAY-YMP CPU time.

References

Hendricks, R., 1994, personal communication.

Ko, S. H., and Rhode, D. L., 1992, "Thermal Details in a Rotor–Stator Cavity at Engine Conditions With a Mainstream," ASME JOURNAL OF TURBOMACHINERY, Vol. 114, pp. 446–453.

Patankar, S. V., 1980, *Numerical Heat Transfer and Fluid Flow,* McGraw-Hill, New York.